THE STEADY PERFORMANCE OF A POROUS AND COMPLIANT AEROSTATIC THRUST BEARING

MARC TIMOTHY EVANS

Thesis submitted for:

Doctor of Philosophy

THE UNIVERSITY OF ASTON IN BIRMINGHAM

July 1987

THE UNIVERSITY OF ASTON IN BIRMINGHAM

THE STEADY PERFORMANCE OF A POROUS AND COMPLIANT AEROSTATIC THRUST BEARING

MR MARC TIMOTHY EVANS

Thesis submitted for Doctor of Philosophy

April 1987

SUMMARY

Recent developments in aerostatic thrust bearings have included; (a) the porous aerostatic thrust bearing containing a porous pad and (b) the inherently compensated compliant surface aerostatic thrust bearing containing a thin elastomer layer. Both these developments have been reported to improve the bearing load capacity compared to conventional aerostatic thrust bearings with rigid surfaces. This development is carried one stage further in a porous and compliant aerostatic thrust bearing incorporating both a porous pad and an opposing compliant surface. The thin elastomer layer forming the compliant surface is bonded to a rigid backing and is of a soft rubber-like material. Such a bearing is studied experimentally and theoretically under steady state operating conditions.

A mathematical model is presented to predict the bearing performance. In this model is a simplified solution to the elasticity equations for deflections of the compliant surface. Account is also taken of deflections in the porous pad due to the pressure difference across its thickness. The lubrication equations for flow in the porous pad and bearing clearance are solved by numerical finite difference methods. An iteration procedure is used to couple deflections of the compliant surface and porous pad with solutions to the lubrication equations.

Comparisons between experimental results and theoretically predicted bearing performance are in good agreement. However these results show that the porous and compliant aerostatic thrust bearing performance is lower than that of a porous aerostatic thrust bearing with a rigid surface in place of the compliant surface. This discovery is accounted to the recess formed in the bearing clearance by deflections of the compliant surface and its effect on flow through the porous pad.

Key library index words to the thesis are; BEARINGS - AEROSTATIC - GAS LUBRICATION - THRUST - PERFORMANCE

In Memory of my

grandmother, May

ACKNOWLEDGEMENTS

I wish to thank;

Dr G.K.Lewis and Mr W.H.Kinsman for their guidance and encouragement during the research project.

Mr M.Clark and Mr P.Pizer, and other technician staff of the Mechanical and Production Engineering Department for their practical assistance relating to the experimental apparatus.

Mr M.Izzard (postgraduate research student in the metallurgy department) for consultation during preparation of the porous pads.

Dr M.Stanojevic (G.K.N. Vandervell Ltd.) and Dunlop Tyres Ltd. (Fort Dunlop , Birmingham) for advice on the properties and moulding of natural rubber compounds, and also the supply of natural rubber gum.

Other members of staff in the Mechanical and Production Engineering Department who have assisted during my period of study at the University of Aston in Birmingham.

The Science and Engineering Research Council for their financial funding.

CONTENTS

LIST OF FIGURES

LIST OF TABLES

LIST OF PHOTOGRAPHS

NOTATION

A_n & B_n — constants of integration.

A_{n1} & B_{n1} — constants in the elementary solutions to the elastomer layer deflections for the region $0 < r < r_n$.

A_{n2} & B_{n2} — constants in the elementary solutions to the elastomer layer deflections for the region $r_n < r < r_c$.

A_z — cross sectional area of porous pad in a plane perpendicular to the z - direction.

A_1 & A_2 — constants of integration

a — radius of piston plunger and compression cylinder in bulk modulus tester.

a_n — constant in polynomial series.

a_z — cross sectional area of a capillary bore aligned parallel to the z - axis.

a_1 — constant.

B_b — flexural constant for the porous pad in bending ($= k_b \cdot r_b + D_b \cdot \nu_b$).

$\overline{B}_b$ — non - dimensional flexural constant for the porous pad in bending $\left[= \dfrac{B_b}{p_a \cdot h_b^3} \right]$

B_1 & B_2 — constants of integration.

$2.b$ — outside diameter of compression cylinder in bulk modulus tester.

b_o — empirical constant.

b_1, b_2 & b_3 — constants of integration.

b_4 — constant $\left[= \dfrac{b_1 \cdot D_b \cdot p_a \cdot h_b^3}{(p_s - p_a) \cdot r_b^2} \right]$

b_5 — constant $\left[= \dfrac{b_3 \cdot D_b \cdot p_a \cdot h_b^3}{(p_s - p_a) \cdot r_b^2} \right]$

C_n — a constant in the elementary solutions for deflections of the elastomer layer. For a

uniform pressure profile acting on the compliant surface $C_n = 0$ and for a

parabolic pressure profile $C_n = \dfrac{2.\nu_c.p_n.t_c^2}{G_c.r_n^2}$

C_{n2} a function $\left[= \dfrac{\Lambda_u.C_2}{J_o(k_n).(k_n^2.\sinh\lambda_n + \Lambda_u.\lambda_n.\cosh\lambda_n)}\right]$

C_1 a constant ($= P_s$).

C_2 a function $\left[= \dfrac{P_s^2 - 1}{\Lambda_u^2.\sum_2^\infty E_n - \Lambda_u/8 - 1}\right]$

c bearing approach as defined in section 3.6.

$\{c\}$ coefficient matrix containing constants c_1 , c_2 and c_3.

c_1 constant in equation for a straight line fitted to experimental points using the least squares method.

c_1 , c_2 & c_3 constants.

D_b flexural constant for porous pad in bending $= \left[\dfrac{E_b.h_b^3}{12.(1-\nu_b^2)}\right]$

$\bar{D}_b$ non - dimensional flexural constant for the porous pad in bending $\left[= \dfrac{D_b}{p_a.h_b^3}\right]$

D_1 , D_2 & D_3 constants.

d_g diameter of the shear specimen.

d_k diameter of the bulk modulus specimen.

E Young's modulus of elasticity.

E_b Young's modulus of the porous pad material.

E_c Young's modulus of the elastomer layer material.

E_c' equivalent Young's modulus of the elastomer layer.

E_n — a function $\left[= \dfrac{\lambda_n}{k_n^2 . (\Lambda_u . \lambda_n + k_n^2 . \tanh\lambda_n)}\right]$

E_p — Young's modulus of the parent material in its solid non - porous form.

E_t — Young's modulus of the piston plunger material in the bulk modulus tester.

e_1 to e_8 — constants in elementary solutions to deflections of the elastomer layer.

$\left[F\right]$ — matrix containing terms with $f_1(R)$, $f_2(R)$, $f_3(R)$ and $F(R)$.

$F(R)$ — a function of R.

F_b — shear force acting on porous pad bond at $r = r_b$.

F_1 — a function $\left[= \dfrac{\alpha}{R} + \dfrac{d\alpha}{dR}\right]$

F_r — shear force per unit circumference at radius r.

f — a function of.

$f(h_d)$ — a function of h_d.

$f'(h_d)$ — first differential of $f(h_d)$.

$\left[f\right]$ — matrix containing terms with $f_1(R)$, $f_2(R)$ and $f_3(R)$.

$f_1(R)$ — a function of R.

$f_2(R)$ — a function of R.

$f_3(R)$ — a function of R.

G — shear modulus of elasticity.

G_g — apparent shear modulus of shear specimen.

G_c — shear modulus of elastomer layer material.

G_1 to G_4 — constants.

h_b — porous pad thickness.

h_d actual or derived bearing clearance at $r = r_b$.

h_k height of bulk modulus specimen.

h_k' compressed height of bulk modulus specimen when its diameter has expanded to fill the cavity of the bulk modulus tester.

h_m measured bearing clearance at $r = r_b$.

h_r local bearing clearance at radius r.

h_u uniform bearing clearance.

I maximum node number i in the r - direction.

I_o zero order modified Bessel function of the first kind.

I_1 first order modified Bessel function of the first kind.

i node number 1 to I in the r - direction.

J maximum node number j in the z - direction.

J_o zero order Bessel function of the first kind.

J_1 first order Bessel function of the first kind.

j node number 1 to J in the z - direction.

K bulk modulus of elasticity.

K_h non - dimensional ratio affecting the bearing clearance geometry $\left[= \frac{r_b^2}{\Phi_r}\right]$

K_v viscous permeability ratio for the porous pad $\left[= \frac{\Phi_r}{\Phi_z}\right]$

K_x non - dimensional bearing static stiffness

$$\left[= \frac{3.\Lambda_c^{1/3}.c.(c^2 + 6.\Phi_r).k_x}{(3.c^2 + 6.\Phi_r).\pi.r_b^2.(p_s - p_a)} = \frac{\partial W}{\partial(\Lambda_c^{-1/3})} \right]$$

(note that for a porous aerostatic thrust bearing h_d & Λ_d replaces c & Λ_c respectively in the expression for K_x).

K_o zero order modified Bessel function of the second kind.

K first order modified Bessel function of the second kind.

k_b stiffness in bending of the porous pad bond at $r = r_b$.

k_c $= \frac{1}{t_c} \cdot \sqrt{1 - \nu_c}$

k_l number of co - ordinate points x, y through which least squares line is fitted.

k_n roots of the equation $J_1(k_n) = 0$.

k_o stiffness in shear of the porous pad bond at $r = r_b$.

k_x bearing static stiffness. For the porous and compliant aerostatic thrust bearing this is = dw/dc and for a porous aerostatic thrust bearing this is = dw/dh_d.

k_1 damping factor for dynamic relaxation.

k_2 number of parabolas in elementary solutions used to approximate the actual pressure profile on the compliant surface of the elastomer layer.

k_3 number of terms in polynomial series.

L load.

l_t piston plunger length of the bulk modulus tester.

M non - dimensional bearing mass flow rate $\left[= \frac{2.m.\eta.R_{gas}.T.h_b}{\pi.r_b^2.(p_s^2 - p_a^2).\Phi_z} \right]$

M_b non - dimensional magnitude constant for the porous pad in bending $\left[= \frac{p_a.h_b^3.(B_b + 5.D_b)}{128.D_b.(B_b + D_b)} \right]$

M_{it} elastic influence matrix.

m bearing mass flow rate.

m_1 gradient of a straight line fitted to experimental points using the least squares method.

m_r radial bending moments in the porous pad.

N_b non - dimensional shape constant for the porous pad in bending $\left[= \dfrac{8.D_b}{4.B_b + 20.D_b}\right]$

n, n_1 & n_2 integers i.e. 1,2,3 etc.

P non - dimensional pressure $\left[= \dfrac{p}{p_a}\right]$

P_{ij} non - dimensional pressure of flow within the porous pad at node i, j.

P_s non - dimensional supply pressure $\left[= \dfrac{p_s}{p_a}\right]$

p pressure.

p_a ambient pressure.

p_b resulting pressure difference across the porous pad thickness at radius r.

p_c pressure profile acting on the compliant surface in a direction parallel to the z - axis for elementary solutions to the elastomer layer deflections.

p_f bearing film pressures at radius r.

p_{fh} feed hole pressure.

p_m measured pressure at the flowmeter in supply line to the bearing.

p_{mem} pressure in chamber behind membrane.

p_n magnitude of the pressure profile p_c at $r = 0$ for each elementary solution to the elastomer layer deflections.

p_{rn} magnitude of the pressure profile p_c at $r = r_n$ in elementary solutions to the elastomer layer deflections. For the uniform pressure profile case, $p_{rn} = p_n$ and for the parabolic pressure profile case, $p_{rn} = 0$.

p_s supply pressure to the porous pad.

q volumetric flow rate.

q_a volumetric flow rate at ambient pressure p_a.

q_b volumetric flow rate through the porous pad at a mean pressure of $(p_s + p_a)/2$.

q_z volumetric flow rate through a capillary aligned parallel to the z - axis.

R non - dimensional radial co - ordinate $\left[= \frac{r}{r_b} \right]$

R_c non - dimensional radial extent of the elastomer layer $\left[= \frac{r_c}{r_b} \right]$

R_{gas} gas constant.

r radial co - ordinate.

r_b porous pad radius.

r_c elastomer layer radius.

r_{fh} radius of central feed hole.

r_n radius of pressure profile for each elementary solution to the elastomer layer deflections.

r_{os} bearing outside radius.

r_1 capillary bore radius.

S_b porous pad aspect ratio $\left[= \frac{h_b}{r_b} \right]$

S_c non - dimensional thickness of the elastomer layer $\left[= \frac{t_c}{r_b} \right]$

S_o non - dimensional shear modulus of the elastomer layer $\left[= \frac{G_c}{p_a} \right]$

s_h pneumatic clearance accounting for roughness of the bearing surfaces.

T	gas temperature.
T_m	measured temperature at the flowmeter for flow in supply line to the bearing.
t	time.
t_c	elastomer layer thickness.
t_g	thickness of shear modulus specimen.
u_b	deflections of the porous pad in the z - direction.
$\bar{u}_b$	non - dimensional deflections of the porous pad in the z - direction $\left[= \dfrac{u_b \cdot h_b^3 \cdot p_a}{r_b^4 \cdot (p_s - p_a)} \right]$
$\bar{u}_{b1}$	$= \bar{u}_b$ at $r = 0$.
$\bar{u}_{b2}$	$= \bar{u}_b$ at $r = 0.7071$
u_c	deflections of the elastomer layer at the compliant surface in the z - direction.
u_r	displacements within the elastomer layer in the r - direction.
u_{rn}	displacements of the compliant surface in the r - direction for elementary solutions to the elastomer layer deflection.
u'_{rn}	the value of u_{rn} at $r = r_n$.
u_z	displacements within the elastomer layer in the z - direction.
u_{zn}	displacements of the compliant surface in the z - direction for elementary solutions to the elastomer layer deflections.
v_r	velocity of gas flow in the r - direction.
v_z	velocity of gas flow in the z - direction.
W	non - dimensional bearing load capacity $\left[= \dfrac{w}{\pi \cdot r_b^2 \cdot (p_s - p_a)} \right]$
w	bearing load capacity.
X, Y	arbitrary values.

x	horizontal graphical co - ordinate.
$\bar{x}$	the mean value of graphical points x.
y	vertical graphical co - ordinate.
$\bar{y}$	the mean value of graphical points y.
Z	non - dimensional axial co - ordinate $\left[= \frac{z}{h_b} \right]$
z	axial co - ordinate.
α	$= 1/\Lambda_r$
β	$= \lambda/S_b$
γ_{rz}	shear strain in the r - z plane.
Δp	pressure difference.
Δr	grid spacing in the r - direction.
Δt	time increment.
Δz	grid spacing in the z - direction.
δ	deflection.
δ_b	shear deflection of the porous pad bond at $r = r_b$.
ϵ_r	normal strain in the r - direction.
ϵ_z	normal strain in the z - direction.
ϵ_θ	normal strain in the θ- direction.
ϵ_{vol}	volumetric strain.
η	absolute viscosity of the gas.
η_1	linear damper.
η_2	relaxation constant in numerical solution to the lubrication equations.
θ	angular co - ordinate about the z - axis.
ι	second radial node number.

Λ_c bearing number based on approach "c"
$$\left[= \frac{12.\Phi_z.r_b^2}{h_b.c.(c^2 + 6.\Phi_r)} \right]$$

Λ_d bearing number based on clearance "h_d"
$$\left[= \frac{12.\Phi_z.r_b^2}{h_b.h_d.(h_d^2 + 6.\Phi_r)} \right]$$

Λ_u bearing number based on clearance "h_u"
$$\left[= \frac{12.\Phi_z.r_b^2}{h_b.h_u.(h_u^2 + 6.\Phi_r)} \right]$$

Λ_r bearing number based on clearance "h_r"
$$\left[= \frac{12.\Phi_z.r_b^2}{h_b.h_r.(h_r^2 + 6.\Phi_r)} \right]$$

λ_n $= k_n.S_b.\sqrt{K_v}$

ν Poisson's ratio.

ν_b Poisson's ratio for the porous pad material.

ν_c Poisson's ratio for the elastomer layer material.

ν_t Poisson's ratio of the material used for the compression cylinder of the bulk modulus tester.

ζ arbitrary variable used to introduce the Roscoe technique.

π = 3.1415927

ρ gas density.

ρ_b density of a porous material similar to that used for the porous pad.

ρ_o density of the solid parent material.

ρ_r relative fractional density of a porous material similar to that used for the porous pad $\left[= \frac{\rho_b}{\rho_o} \right]$

σ_r normal stress in the r - direction.

σ_{rn} — normal stress in the r - direction at $r = r_n$ in elementary solutions to deflections of the elastomer layer.

σ_z — normal stress in the z - direction.

σ_θ — normal stress in the θ - direction.

$\bar{\sigma}$ — mean stress $\left[= \dfrac{\sigma_r + \sigma_z + \sigma_\theta}{3} \right]$

τ_{rz} — shear stress in the r - z plane.

Φ — viscous permeability.

Φ_r — viscous permeability in the r - direction.

Φ_z — viscous permeability in the z - direction.

Φ_{eff} — effective permeability for combined viscous and inertia flow.

ϕ — inertia permeability.

ϕ_r — inertia permeability in the r - direction.

ϕ_z — inertia permeability in the z - direction.

Ψ — stress function.

∇^2 — $= \dfrac{\partial^2}{\partial z^2} + \dfrac{1}{r} \cdot \dfrac{\partial}{\partial r} + \dfrac{\partial^2}{\partial r^2}$

Subscripts

a — ambient.

b — porous pad.

c — elastomer layer or bearing approach.

d — actual or derived.

e — extent.

f — bearing film.

fh — feed hole.

g — shear modulus specimen.

h	bearing clearance.
i	at node i.
j	at node j.
k	bulk modulus specimen.
l	least squares.
m	measured.
mem	membrane.
n	integer (= 1,2,3, etc).
o	shear or shear modulus.
os	outside.
p	parent material.
r	radial direction.
s	supply.
t	bulk modulus tester.
u	uniform.
v	viscous.
vol	volume.
x	static.
z	axial direction.
ı	at node ı.

CHAPTER 1

INTRODUCTION TO THE INVESTIGATION

1.1 DEFINITION OF AN EXTERNALLY PRESSURIZED POROUS AND COMPLIANT AEROSTATIC THRUST BEARING

An externally pressurized aerostatic thrust bearing is one in which air from an external source such as a compressor, is supplied to form a thin pressurized film of air between two surfaces. This enables it to support a load with negligible frictional resistance to relative motion between the two bearing surfaces. Unlike hydrodynamic bearings which will only operate while there is relative motion between the bearing surfaces, hydrostatic and aerostatic bearings will operate while these are stationary. This is a considerable advantage when supporting static or slow moving loads.

In porous aerostatic thrust bearings (figure 1.1) air is supplied through a porous material which acts as a restricter to flow through the bearing. A uniform air film is created between two rigid flat surfaces*. As with capillary and orifice compensation in aerostatic thrust bearings the porous pad reduces the flow rate of air through the bearing, particularly under lightly loaded

* An exception to this is a bearing with an elastic porous pad. The film clearance geometry is modified by deflections of the porous pad under the pressure drop across it.

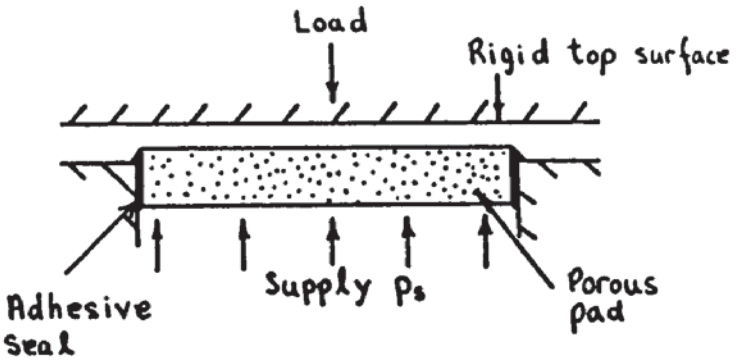

Figure 1.1a Full face porous aerostatic thrust bearing

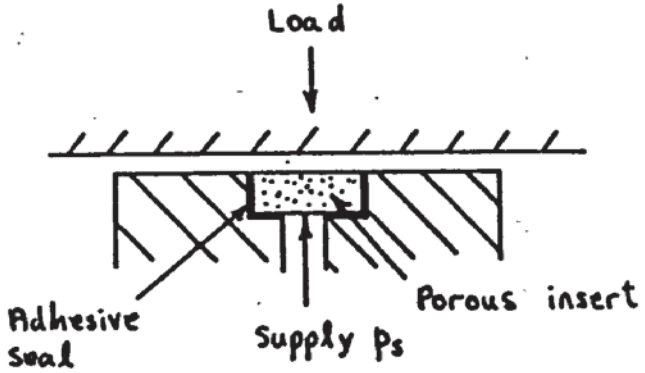

Figure 1.1b Landed porous aerostatic thrust bearing

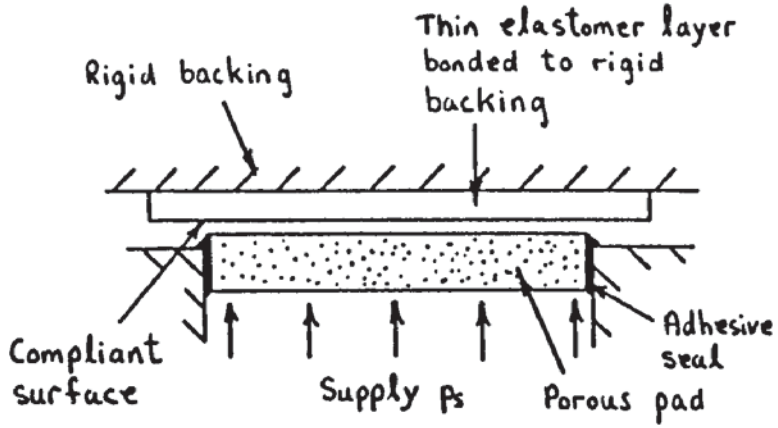

Figure 1.2a Porous and compliant aerostatic thrust bearing; compliant surface extending beyond porous pad

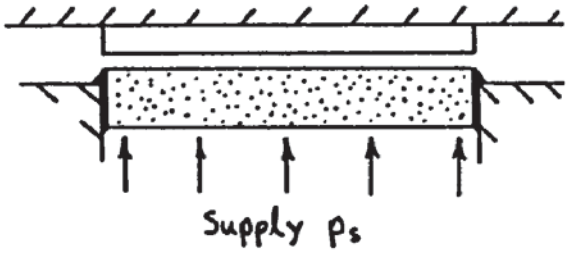

Figure 1.2b Porous and compliant aerostatic thrust bearing; compliant surface of same radius as the porous pad

conditions. This enables the supply source to remain pressurized under various operating conditions.

The porous and compliant aerostatic thrust bearing however has in addition one or more compliant surfaces which deflect under the pressures created in the film clearance. The porous and compliant aerostatic thrust bearing configurations investigated in this research project are illustrated in figure 1.2. The compliant surface is formed by a thin elastic layer opposing a full face porous pad. This elastic layer is made from a soft rubber like material which is bonded to a rigid flat surface. Its radius is greater than or equal to the bearing radius, in this case the radius of the porous pad. Typically this rubber like material is incompressible in nature which considerably affects its deflection behaviour to applied film pressures.

1.2 POTENTIAL ADVANTAGES OF USING A POROUS AND COMPLIANT AEROSTATIC THRUST BEARING

Aerostatic thrust bearings are commonly used in industry to support loads (which may be stationary or slow moving) with minimal frictional resistance against motion.

In aerostatic thrust bearings the load capacity is equal to the summation of film pressures acting over the area of the bearing clearance in a parallel direction to the applied load. The resulting load capacity therefore not

only depends on the magnitude of these film pressures but also on the shape of film pressure profile with radius. Ideally for maximum load capacity the film pressure profile should approach a uniform distribution over the whole bearing radius (figure 1.3).

However,conventional aerostatic thrust bearings with a central feed hole have relatively low load carrying capacities. This is due to the non - uniform shape of the actual film pressure profile formed in the bearing clearance (figure 1.3). Attempts to improve the load capacity by extending the region of uniform film pressures in the supply port (figure 1.4) have resulted in a form of instability known as pneumatic hammer (30). This problem is overcome in the porous aerostatic thrust bearing due to the damping characteristics of the porous pad which help to reduce the likelihood of pneumatic hammer (40). In addition the supply air is distributed more evenly in the film clearance giving rise to a more uniform film pressure profile (figure 1.5) than that for a conventional aerostatic thrust bearing (figure 1.3) and an increase in the load capacity (30).

Conventional aerostatic thrust bearings are also susceptible to roughness of bearing surfaces and blockage by contamination of supply (30). The bearing performance can also be affected by errors of bearing geometry such as flatness and parallelism between the bearing surfaces.

The presence of foreign particles in the bearing

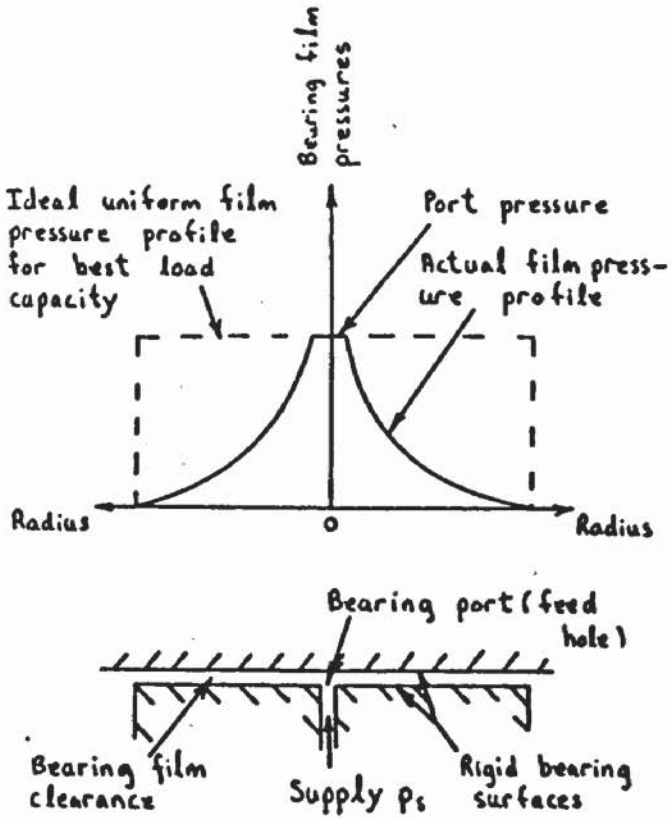

Figure 1.3 Film pressure profile for a conventional thrust bearing with central feed hole and rigid bearing surfaces

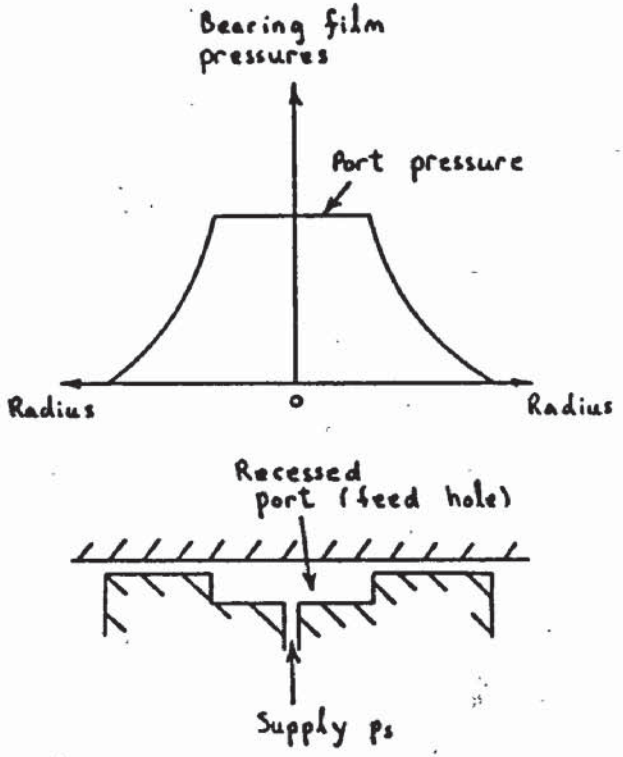

Figure 1.4 Film pressure profile for a conventional thrust bearing with a recessed central feed hole and rigid bearing surfaces

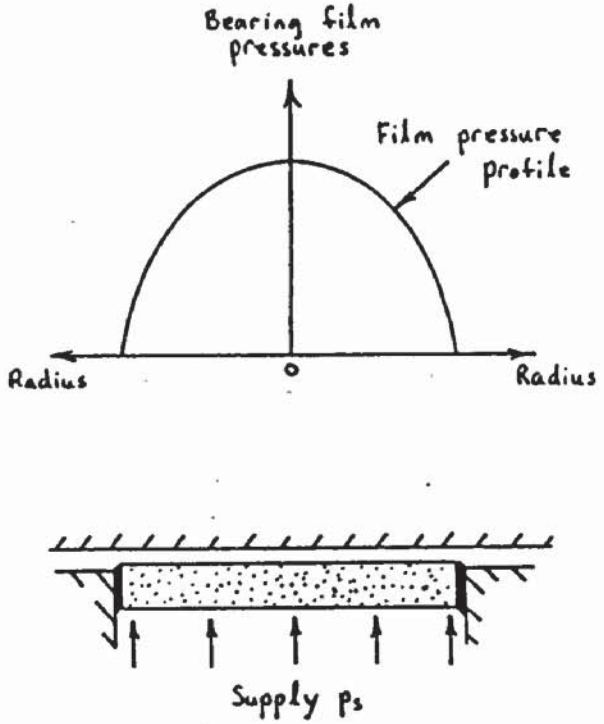

Figure 1.5 Film pressure profile for a porous aerostatic thrust bearing

clearance will distrupt bearing operation and increase its frictional resistance. In capillary compensated aerostatic thrust bearings the small capillary is easily blocked by contamination of supply in the form of fine oil droplets and other particles. Some of these problems are reduced in porous aerostatic thrust bearings because the porous pad acts as a filter to the supply. The porous pad itself may become blocked after many hours of service, but this can easily be remedied by reversing the flow through porous pad and hence unblocking it.

However due to the nature of porosity in the bearing surface formed by the porous pad, this surface is considerably rougher than normally accepted in aerostatic thrust bearings, even after grinding. Figure 1.6 shows that this limits the minimum film clearance attainable and hence reduces the potential load capacity of the bearing. This problem could be overcome if the opposing bearing surface to the porous pad is of a compliant nature such as a thin elastomer layer (figure 1.7). The elastomer layer complies to local roughness peaks to allow the effective film clearance to be reduced further. In a similar fashion, contamination by fine particles in the bearing clearance can be accomodated by local deflections of the compliant surface (figure 1.8). Due to the compliant nature of this elastomer layer a greater tolerance of bearing geometry is also acceptable. This allows the bearing to be used in lower precision applications.

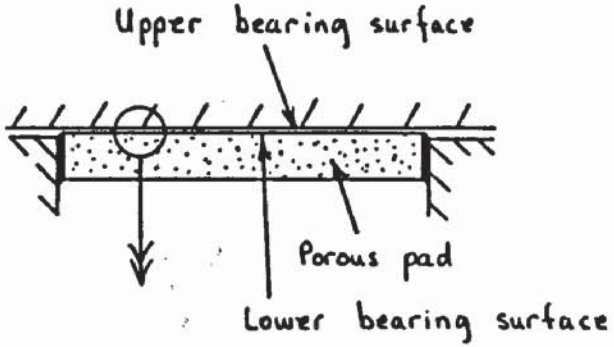

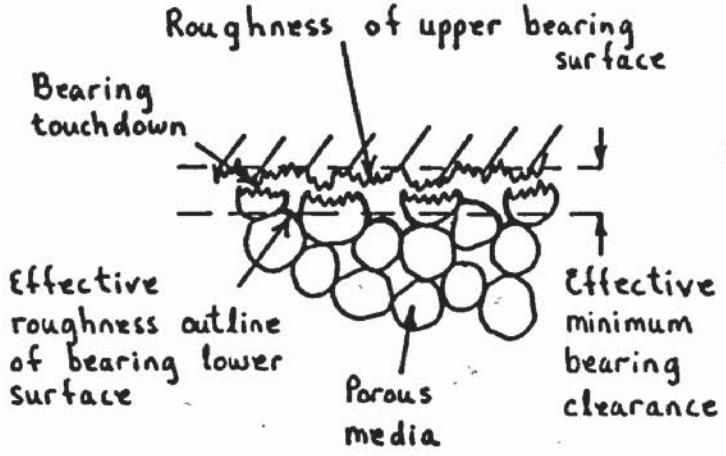

Figure 1.6 Roughness of bearing surfaces in a porous aerostatic thrust bearing: effect on minimum bearing clearance

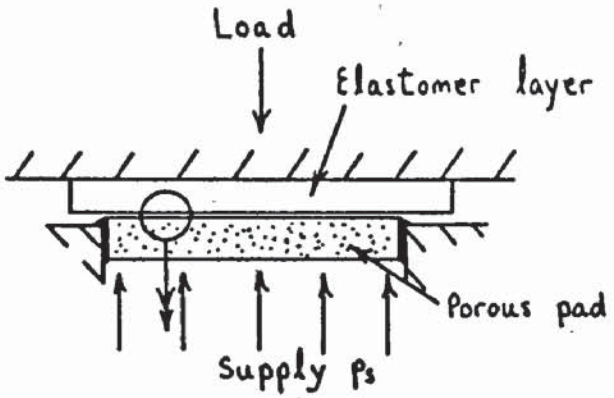

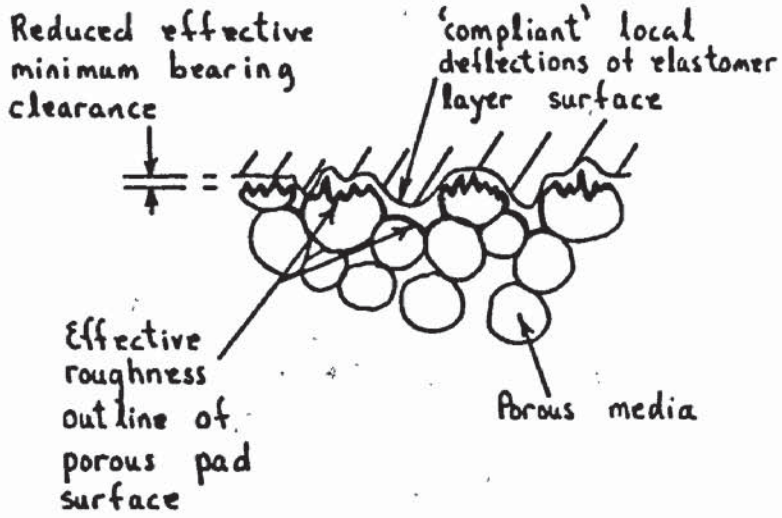

Figure 1.7 Porous and compliant aerostatic thrust bearing: compliance of elastomer layer on roughness of opposing porous pad surface

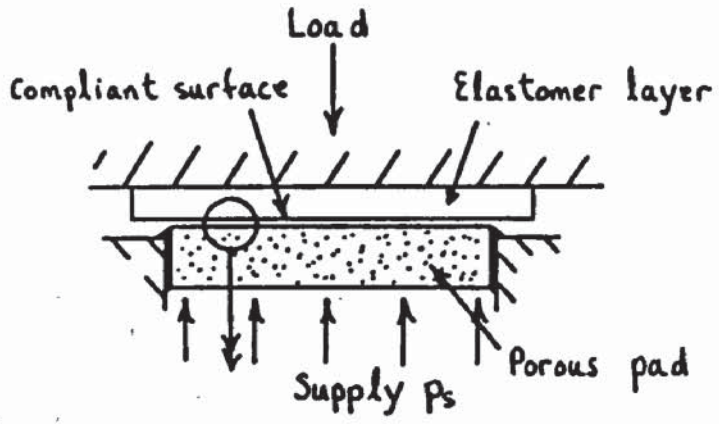

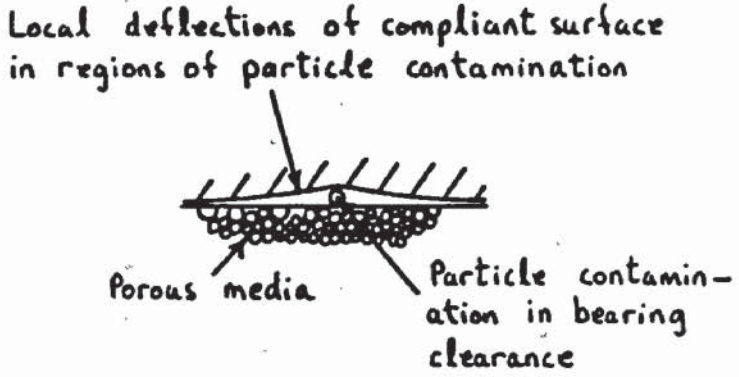

Figure 1.8 Porous and compliant aerostatic thrust bearing: compliance of elastomer layer on particle contamination in bearing clearance

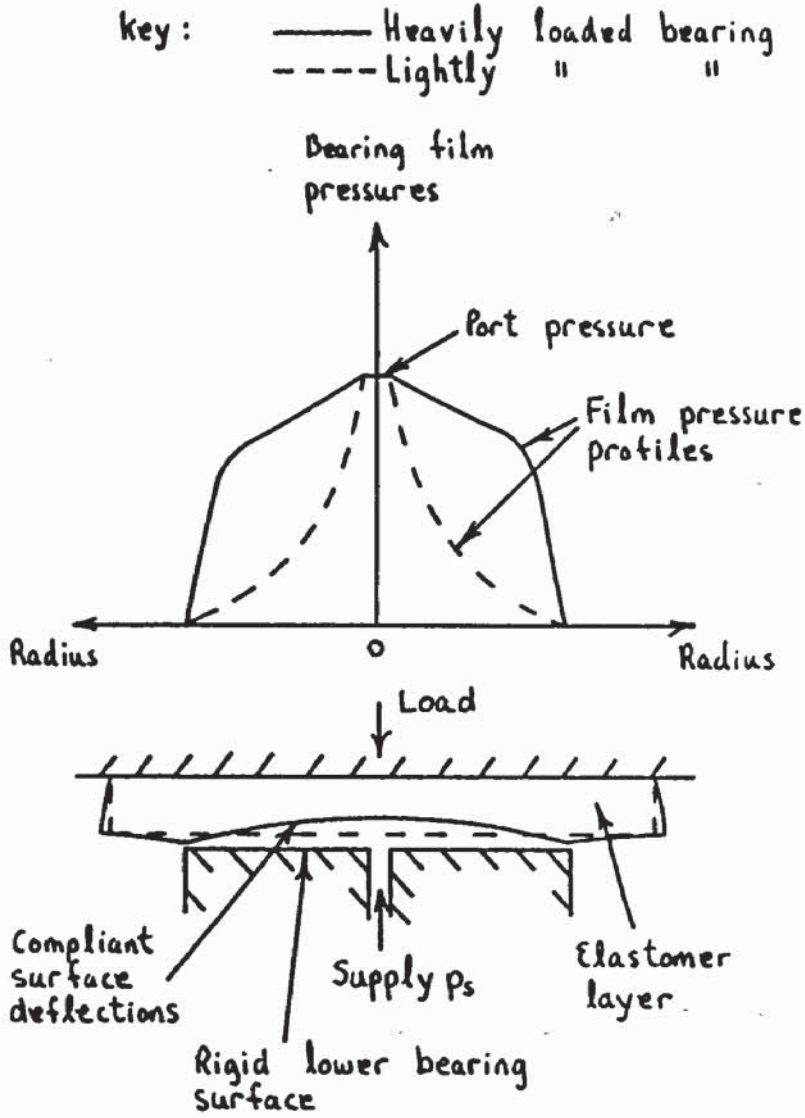

Figure 1.9 Compliant thrust bearing with central feed hole

The use of compliant surfaces in centrally fed thrust bearings (figure 1.9) has resulted in improved load carrying capacities (58 to 62) due to another phenomena. Deflections of the compliant surface under the action of film pressures modify the film clearance geometry to produce a shallow recess in central regions of the bearing clearance (figure 1.9). This recess also gives rise to a more uniform film pressure profile which in turn increases the bearing load capacity for a given port pressure. Similarly therefore in addition to the advantages already mentioned, further increases in load capacity are expected for a porous and compliant aerostatic thrust bearing compared to the more conventional porous aerostatic thrust bearing.

1.3 PRINCIPLE OF STEADY OPERATION OF A POROUS AND COMPLIANT AEROSTATIC THRUST BEARING

Consider the porous and compliant aerostatic circular thrust bearing shown in figure 1.10. Air from the external source is supplied at constant pressure p_s to the chamber below the porous pad. Flow therefore enters the lower surface of the porous pad at a uniform supply pressure p_s. 2-dimensional flow takes place within the porous pad in a predominantly axial direction but also in a radial direction, until it reaches the bearing clearance. These flows within the porous pad undergo a pressure drop whose

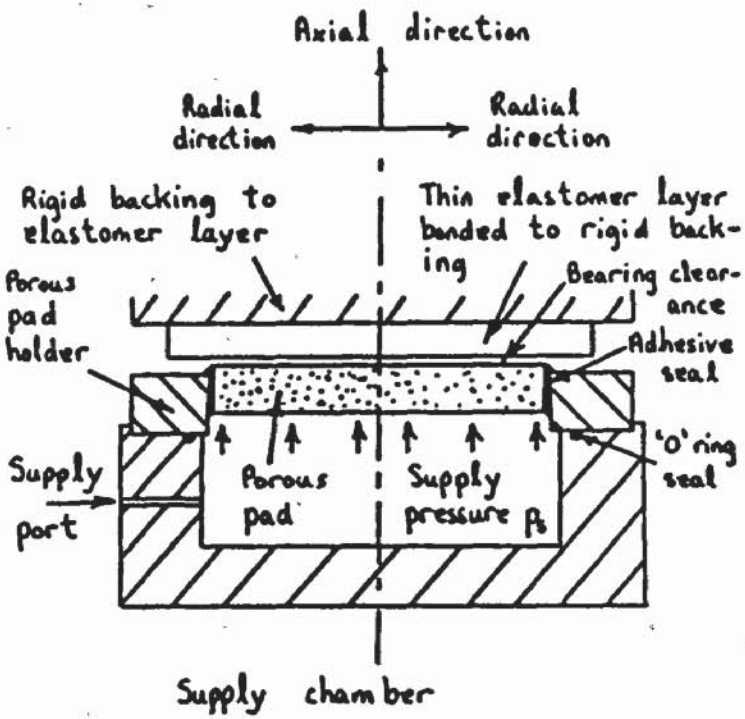

Figure 1.10 Porous and compliant aerostatic thrust bearing

(a) Initially uniform bearing clearance

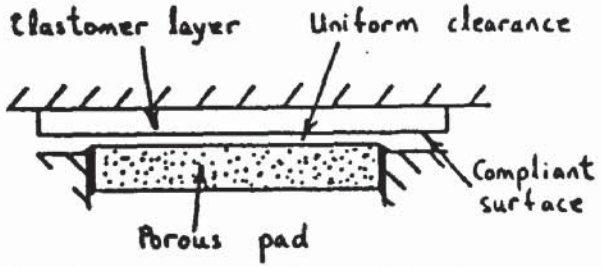

(b) Shallow recess formed in bearing clearance due to deflections of compliant surface

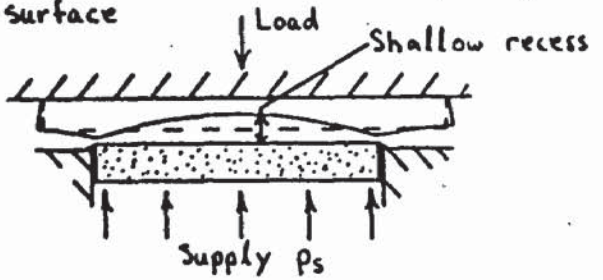

(c) Shallow recess reduced by deflections of porous pad due to the pressure difference across its thickness

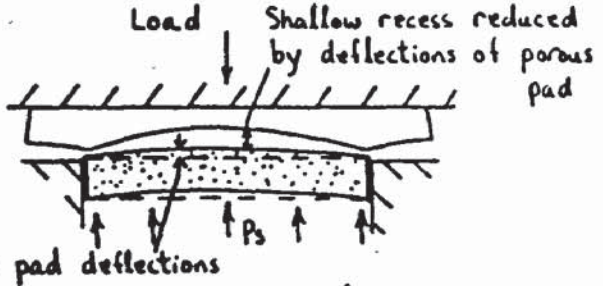

Figure 1.11 Porous and compliant aerostatic thrust bearing: bearing clearance geometry

gradient is dependant on the flow velocity. This pressure drop arises due to the restriction effect of fine capillary paths within the porous pad.

On entering the bearing clearance the flow is predominently radial towards the bearing exit. The film pressures generated in the bearing clearance have a -ve gradient in the radial direction, which is caused by the skin friction between this flow and the bearing surfaces. These film pressures will act upon the compliant surface and cause it to deflect. Since the film pressures are greatest in the central regions of the bearing clearance a shallow recess will form here to modify the bearing clearance geometry from its originally uniform state (figure 1.11(a)). In the regions of the shallow recess where bearing clearances are greatest, the film pressure gradients are reduced resulting in a more uniform film pressure profile. If the elastomer layer is incompressible in nature its deflection profile will be similar to that shown in figure 1.11(b), with bulging occurring near the bearing exit. This deepens the recess formed and further flattens the film pressure profile.

However depending on the stiffness of the porous pad, it may also deflect significantly in bending, due to the pressure difference across its thickness. This will also affect the bearing clearance geometry (figure.1.11(c)) and tend to reduce the shallow recess formed by deflections of the compliant surface. The resulting film pressure profile

will therefore depend not only on deflections of the compliant surface but also on deflections of the porous pad, the latter tending to make the film pressure profile less uniform (25).

The summation of these film pressures acting on the compliant surface area in an axial direction will equal the load carried by the bearing. The flow rate through the bearing will depend on the porous pad restriction (i.e. permeability and thickness) and the bearing clearance geometry.

CHAPTER 2

THE PROBLEM DEFINED

2.1 INTRODUCTION

In chapter 1, a porous and compliant aerostatic thrust bearing was presented. As far as the author is aware there is no published work on this new type of bearing, apart from a report by Barwell (1) that a similar bearing was developed by the National Engineering Laboratory (U.K.) for an industrial application. No further details about the bearing and its performance are given however. The problem is therefore already partially defined, i.e. it will be the purpose of this research project to investigate theoretically and experimentally the performance of this bearing and to compare results with those of a more conventional aerostatic thrust bearing.

The porous and compliant aerostatic thrust bearing may be considered a direct descendant of the following two types of externally pressurized bearings:

(a) The porous thrust bearing.

(b) The compliant thrust bearing.

A literature review will therefore be carried out on these two types of bearing. Relevant published work relating to journal bearings of a porous or compliant nature will also be included. Since there is substantial

published work on these bearings, only a proportion of this work will be reviewed which the author considers is of interest and importance to this research project.

This review of the literature will reveal other gaps in the knowledge and enable further areas of investigation to be outlined. It will also be helpful in assessing whether various analyses used by other researchers will be useful in the mathematical modelling of the new porous and compliant aerostatic thrust bearing.

2.2 LITERATURE SURVEY

2.2.1 NATURE OF FLOW IN THE POROUS PAD

One of the first papers published on porous aerostatic thrust bearings was by Sheinberg and Shuster (2). They considered that flow within a porous media could be simplified to that taking place through a series of parallel and uniformly spaced capillary tubes. In this simplified model flow takes place in one direction only, i.e. in an axial direction parallel to the thickness of the porous pad. Flow in each capillary is governed by the equation;

$$q_z = -\frac{\pi.(r_1)^4}{8.\eta} \cdot \frac{\partial p}{\partial z} \qquad 2.1$$

A permeability coefficient Φ is introduced to

characterise the permeability of the porous media. This accounts for the size, length and spacing of capillaries in this model of the porous pad. Equation 2.1 becomes;

$$q_z = - \frac{\Phi . a_z}{\eta} . \frac{\partial p}{\partial z} \qquad 2.2$$

Equation 2.2 is similar to Darcy's law, which has been used by many researchers of porous aerostatic bearings. This states that the pressure gradient is directly proportional to velocity of flow at any point in the porous media. Unlike the capillary model used by Sheinberg and Shuster (2), Darcy's law may be applied to multi - directional flow within the porous media. Its more general form is;

$$- \frac{\partial p}{\partial r,z} = \left(\frac{\eta}{\Phi_{r,z}} \right) v_{r,z} \qquad 2.3$$

Equation 2.3 suggests a constant permeability coefficient Φ for all types of flow within the porous media. However Robinson and Sterry (3) observed that this coefficient is a function of both bearing film pressures and Reynolds number. Mori et al (4) presents graphs of permeability coefficient as a function of supply pressure for several porous pads. These graphs all show reductions in permeability with increasing supply pressure, but no explanations for this phenomena are given.

A review of mathematical models for various types of

flow within a porous media is given by German (5). Darcy's law is described as governing flow at low pressures and flow velocities where viscous energy losses are dominant. At higher flow velocities inertial energy losses become more significant and Darcy's law becomes less accurate. Forchheimer (6) proposed a correction term to Darcy's law which takes into account inertia losses in the porous media. Equation 2.3 with inertia term becomes;

$$-\frac{\partial p}{\partial r,z} = \left(\frac{\eta}{\Phi_{r,z}}\right) v_{r,z} + \left(\frac{\rho}{\phi_{r,z}}\right) v_{r,z}^{2} \qquad 2.4$$

where ϕ is the inertia permeability coefficient.

The exclusion of inertia losses in Darcy's law therefore explains the apparent reduction in permeability coefficient Φ at higher supply pressures and hence higher flow velocities, as experienced by Mori et al (4).

Greenberg and Weger (7) investigated the effects of pressure and temperature on viscous and inertia permeability coefficients. While the inertia permeability coefficient was unaffected by temperatures and supply pressures in the range 15 to 60°C and 0 to 140 bars (0 to 2000 psi) respectively, the viscous permeability coefficient remained constant with respect to pressure but decreased with increasing temperature. For example the viscous permeability of the sintered bronze sample, decreased at an average rate of 2.62% per °C. This suggests therefore that it is important to monitor the temperature

while carrying out permeabilty tests on the porous material.

Morgan (8) describes in detail a technique for the accurate measurement of viscous and inertia permeability coefficients. This involves sealing a porous pad around its circumference and measuring the flowrate and uniform pressure drop across its thickness. Equation 2.4 is re - written in the form;

$$\frac{\Delta p . A_z}{q_b . \eta . h_b} = \frac{1}{\Phi} + \frac{q_b . \rho}{A_z . \eta . \phi} \qquad 2.5$$

By plotting $\frac{\Delta p\, A_z}{q_b\, \eta\, h_b}$ against $\frac{q_b\, \rho}{A_z\, \eta}$ the resulting straight line has a slope of $\frac{1}{\phi}$ and a Y axis intercept of $\frac{1}{\Phi}$. Values of Φ and ϕ are therefore obtained from this plot using least squares method to fit a straight line to the experimental points. Note that a single value of Φ and ϕ has been assumed for both r and z directions. In practice it would be difficult to determine separate values of Φ and ϕ for both r and z directions, and as far as the author is aware this has not been successfully attempted by other researchers.

Taylor and Lewis (9) introduce the concept of two distinct types of flows within the porous media. As in pipe flows there is a viscous (laminar) flow region and an inertia (turbulent) flow region with a transition region between them. The viscous flow region is governed by Darcy's law (equation 2.3). For the inertia flow region,

inertia losses are dominant and the first term in equation 2.4 is omitted , i.e.;

$$-\frac{\partial p}{\partial r,z} = \left(\frac{\varrho}{\phi_{r,z}}\right) v^2_{r,z} \qquad 2.6$$

In the transition flow region both viscous and inertia losses are significant and equation 2.4 applies. Hence in a form similar to equation 2.5, for the viscous flow region;

$$\frac{\Delta p.A_z}{q_b.\eta.h_b} = \frac{1}{\phi} \qquad 2.7$$

similarly for the transition flow region;

$$\frac{\Delta p.A_z}{q_b.\eta.h_b} = \frac{1}{\phi} + \frac{q_b.\rho}{A_z.\eta.\phi} \qquad 2.8$$

and for the inertia flow region;

$$\frac{\Delta p.A_z}{q_b.h_b} = \frac{q_b.\rho}{A_z.\phi} \qquad 2.9$$

Equation 2.7 can be re-written in logarithmic form;

$$\log_{10}\Delta p = \log_{10}\left(\frac{\eta.h_b}{A_z.\phi}\right) + \log_{10}(q_b) \qquad 2.10$$

Taylor and Lewis were able to confirm the existence of the viscous flow region by plotting $\log_{10}\Delta p$ against $\log_{10} q_b$ for uniform axial flow through the porous pad. The results gave a straight line of unity gradient as suggested by equation

2.10 (see figure 2.1). A value of Φ can be obtained from this plot by fitting equation 2.10 to the experimental points using the least squares method. In a second plot similar to that used by Morgan (8) regions of viscous and transitional flow are clearly shown figure 2.2.

Based on analytic solutions, McCrea and Donaldson (10) present a criteria which indicates whether inertia effects in the porous material are significant or negligible. Their criteria is as follows;

for viscous dominated flow

$$\frac{2.p_s^2.\phi^2}{\phi.\eta^2.h_b.R_{gas}.T} \ll 1 \qquad 2.11$$

for inertia dominated flow

$$\frac{2.p_s^2.\phi^2}{\phi.\eta^2.h_b.R_{gas}.T} \gg 1 \qquad 2.12$$

and for flows in which viscous and inertia losses are significant

$$\frac{2.p_s^2.\phi^2}{\phi.\eta^2.h_b.R_{gas}.T} = 1 \qquad 2.13$$

This criteria not only depends on supply pressure p_s but also on the ratio Φ^2/ϕ . However no account is taken of the existence of distinct flow regions as put forward by Taylor and Lewis (9). Instead they assume one region of flow in which viscous or inertial or both, losses are significant.

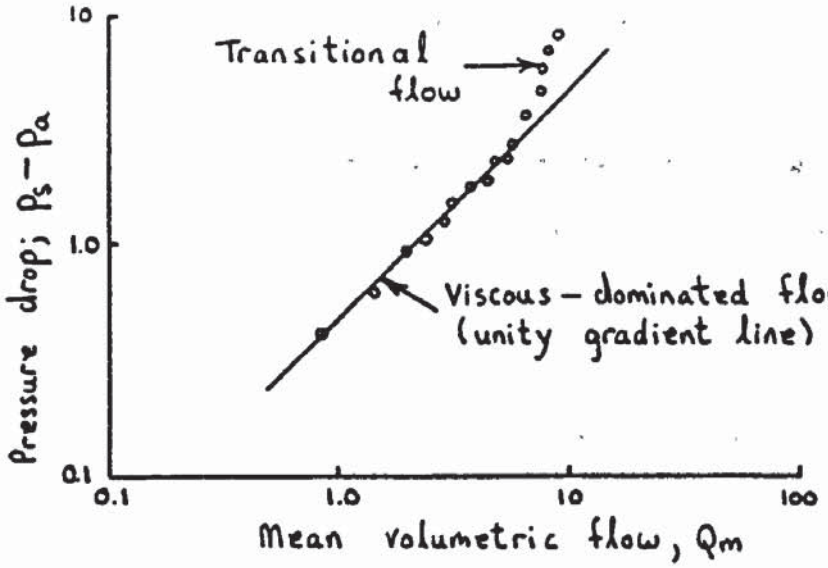

Figure 2.1 Porous pad permeability: the viscous flow region

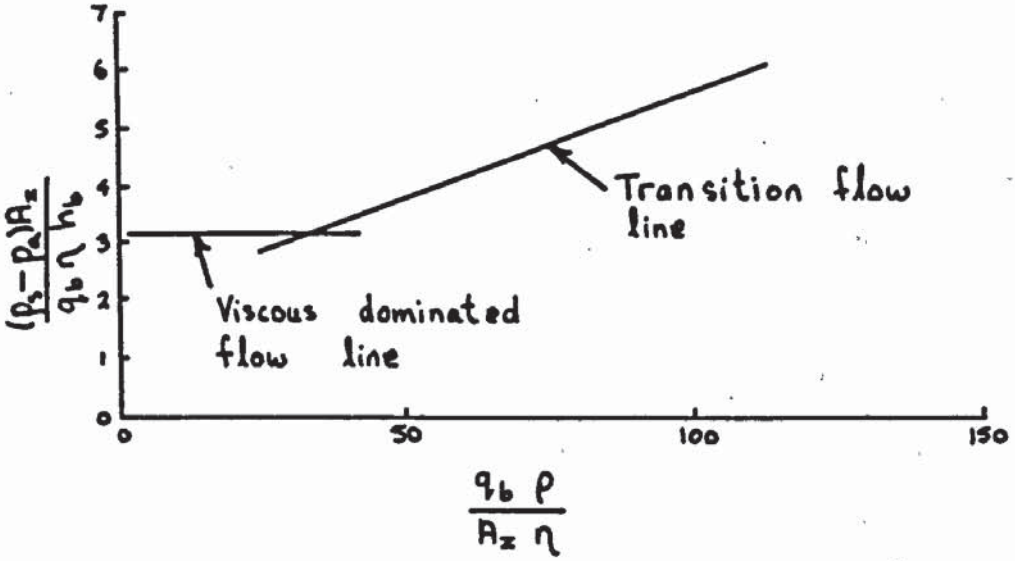

Figure 2.2 Porous pad permeability: regions of viscous and transition flow

This therefore is a major conflict of opinion between these researchers which needs further investigation.

The effects of surface machining on the flow in a porous media is investigated (11), (12). The existence of a thin highly restrictive layer is described which is created by pore blockage during surface grinding or machining of the porous material. This layer reduces the permeability of the porous pad by a significant amount by acting as a restricter to flow through it. Polome and Gorez (12) describe flow within the porous media as taking place in two regions. The first is within the homogenious porous matrix accounting for the majority of the porous media. Here the flow is 2 - dimensional and governed by Darcy's law. The second region is represented by a thin layer of parallel restricters along the machined surface of the porous media. The flow passes normal to this layer and the pressure drop is proportional to flow velocity squared.

Others (7),(9) have also reported on the effects of surface machining on permeability of the porous media. Greenburg and Weger (7) overcome this problem by removing the thin restricting layer by electo(electrolytic) - polishing and it is reported that this method is superior to conventional acid etching methods similar to that used by Taylor and Lewis (9). The author however has been unsuccessful in obtaining further references by Greenburg and Weger (7) describing this electrolytic polishing technique in more detail.

The method in which the bearing surface of the porous pad is prepared may need further investigation. This depends on whether the acid etching method is suitable as reported (9).

The review of literature in this section relating to the nature of flow in the porous pad has revealed two conflicting aspects;

(a) The existance or not of three distinct regions of flow, i.e. viscous, transitional and inertia flow regions (9), as opposed to one in which viscous or inertia or both, losses may be dominant in one region (10).

(b) The method in which the pores of a porous media may be unblocked after machining and whether any restricting effect at the surface still remains.

These aspects will contribute to the formation of an outline for the areas of investigation in section 2.3.

2.2.2 GAS LUBRICATED POROUS BEARINGS

(2),(3) and (13) are amoung the first published works on gas lubricated porous bearings. Montgomery and Sterry (13) carried out experimental work on porous journal bearings to show that a journal of 9.5 cm diameter could be rotated at speeds up to 252000 revs/min. Robinson and Sterry (3) obtained analytical solutions for an infinitely long journal bearing assuming axial flow in the porous

restrictor bushing. They verified their theoretical predictions experimentally. These researchers point out that the use of porous materials eliminates the necessity to precision machine fine holes in conventional orifice restrictor bearings.

Various circular porous thrust bearing configurations are analysed by Sheinberg and Shuster (2). Their particular interest concerns an electrically driven spindle of an internal grinding head with speeds up to 96000 revs/min. Compared to conventional centrally fed orifice bearings it is reported that the use of porous bearings have considerably increased bearing load capacity and resistance to vibration. An important practical consideration is mentioned relating to the deflection of the porous pad under the pressure difference across its thickness. It is recommended that this should be minimised by using pads of sufficient rigidity otherwise the load carrying capacity will be reduced owing to distortion of the bearing clearance geometry from its original uniform state.

At low flowrates Darcy's Law is applied by Sneck and Yen (14) to obtain analytical solutions for a full-width porous journal bearing of finite length. For higher flowrates a modified form of Darcy's Law is used similar to that for inertia flow (equ.2.6). Both solutions are obtained for the non-rotating bearing case. Sneck and Ewell (15) verified the analytical solutions (14) in an experimental investigation. Good general correlation of

theoretical and experimental results was achieved provided account is taken of the bearing surface roughnesses in the determination of bearing clearance. The amount added to measured clearance is that measured using a standard surface roughness indicator. An average peak to valley roughness value was taken.

Sneck and Yen (16) extend their analysis to take into account rotation of journal bearing shaft. They concluded from the analysis that the load capacity is not significantly affected by shaft rotation, but that the flow rate increases with increasing shaft eccentricity.

Mori et al (4) approached the solution of flow within a porous thrust bearing of the type shown in figure 2.3, by dividing the porous media into two restricting thicknesses. In this way both radial and axial flows in the porous media could be accounted for. The author considers that this analytical approach is only applicable to this type of bearing. This is because flow across the first porous media thickness and in region 1, is predominantly axial. Mainly radial flow then takes place in the second restricting thickness parallel to the bearing clearance and throughout regions 1 and 2. These restricting thicknesses are determined by matching the theoretical and experimental results. However the restricting thickness values obtained were found to be dependant on bearing load capacity. Average values for a particular bearing configuration therefore resulted in a significant error at low and high

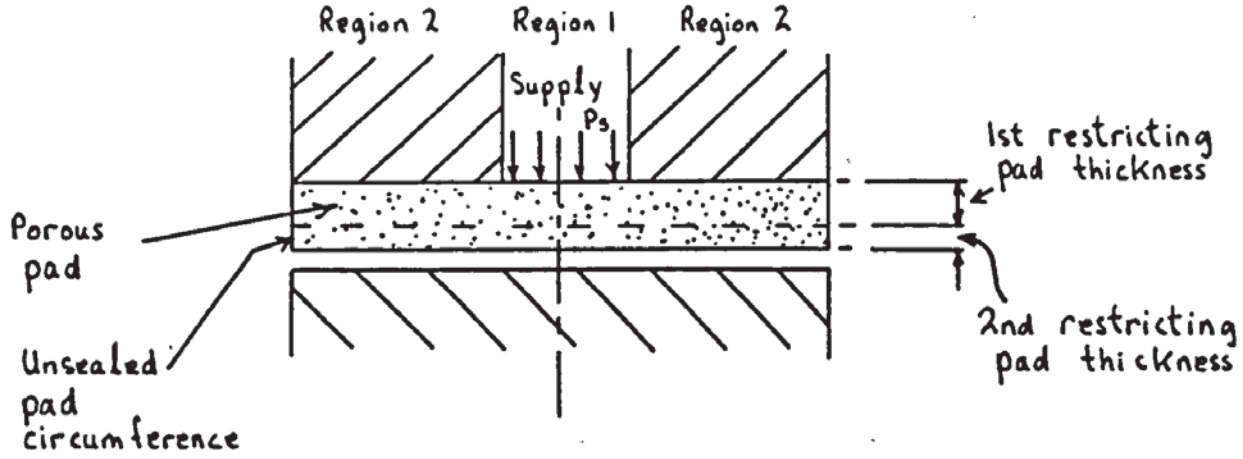

Figure 2.3 Circular porous aerostatic thrust bearing of Mori et al (4)

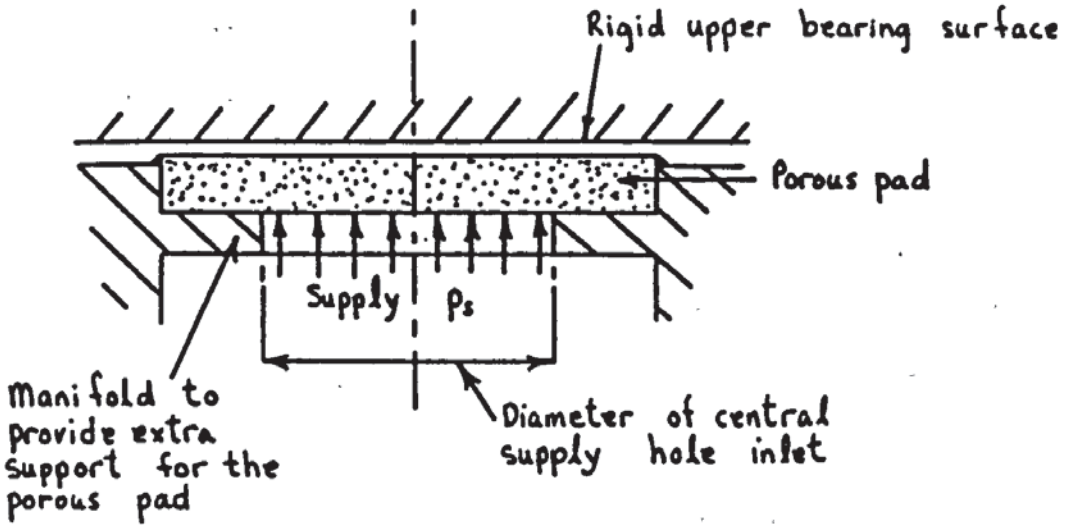

Figure 2.4 Porous aerostatic thrust bearing with inlet manifold

bearing load capacities. During their experimental programme bearing vibration (pneumatic hammer) was noted with increasing bearing clearances and supply pressures, only if the bearing was disturbed. However no vibration occurred during the experiments provided the bearing remained undisturbed.

Later Mori et al (17) presented an improved analytical solution by treating flow in the bearing clearance as a boundary value for three dimensional flow in the porous media. Both incompressible and compressible flows are considered. Several different types of porous bearing are treated including a circular thrust bearing and a journal bearing. The concept of restricting thicknesses however is still applied.

A form of porous and compliant journal bearing is investigated analytically by Barlow and Wildmann (18). Their bearing consists of a perfectly flexible foil or membrane (in which only tensile stresses are considered) moving over a porous journal restricter. Results show that this type of bearing has improved load carrying capacity compared to a foil bearing with discrete inlet restrictors. However no results are presented to show how the compliant properties of the foil affect the bearing performance.

Gargulio and Gilmour (19) have carried out a comprehensive study of aerostatic porous thrust bearings. Reynolds equation for flow in the bearing clearance is used as a boundary condition for flow in the porous pad.

Equations are solved using finite difference methods on a digital computer. This enables solutions to unusual or mixed boundary conditions, such as may occur if an inlet manifold is used (figure 2.4). This type of bearing is analysed along with the full faced type (figure 1.1a). The supply area may be reduced by reducing the central hole diameter in the manifold. Design curves are presented showing the effect of supply area (as a percentage of that for a full faced bearing) on the bearing performance. Results indicate that the load capacity reduces with supply area. However since the flow rate also reduces at twice the rate at which load capacity reduces, this can be an advantage in some applications where size limitations are not a problem but the flowrate must be minimized. Other design curves show that while the effects of anisotropic permeability on load capacity are small, the flow rate increases significantly with the permeability ratio Φ_r/Φ_z. Porous pads which are highly permeable in the radial compared to axial directions are therefore a disadvantage.

An additional advantage of using a manifold is that it can support the porous pad to reduce deflections in bending, caused by the pressure difference across it. This can change the bearing clearance geometry and affect the bearing performance (see Taylor and Lewis (25)).

Comparisons between theoretical and experimental results (19) show good correlation for load capacity at low

bearing numbers. Errors increase at higher bearing numbers and the general results for flow rate were less promising. The reasons for this are partly attributed to neglecting roughness of the bearing surfaces in the determination of bearing clearance. Also Garguilo and Gilmour (19) do not take into account the slip flow which takes place at the porous media - bearing clearance boundary. This phenomenon was first studied analytically and shown to be of significance by Ishzawa and Hori (20). They considered the flow which takes place in a radial direction within the porous pad and adjacent to the bearing clearance. Therefore by continuity, slip flow takes place in the bearing clearance at the porous wall (figure 2.5). Slip flow is an important consideration as it affects the resultant flow patterns within the bearing clearance and the porous pad.

Later Beavers et al (21), (22) confirmed the condition of slip flow experimentally for the flow in a channel having a porous wall. An empirical equation is used to predict the slip flow velocity, but the author considers that this is only applicable to the conditions of their channel experiments. In other words the condition of continuity used by Ishzawa and Hori (20) has more general application.

Jones et al (23), takes into account the slip flow condition of Ishzawa and Hori (20) in obtaining an exact

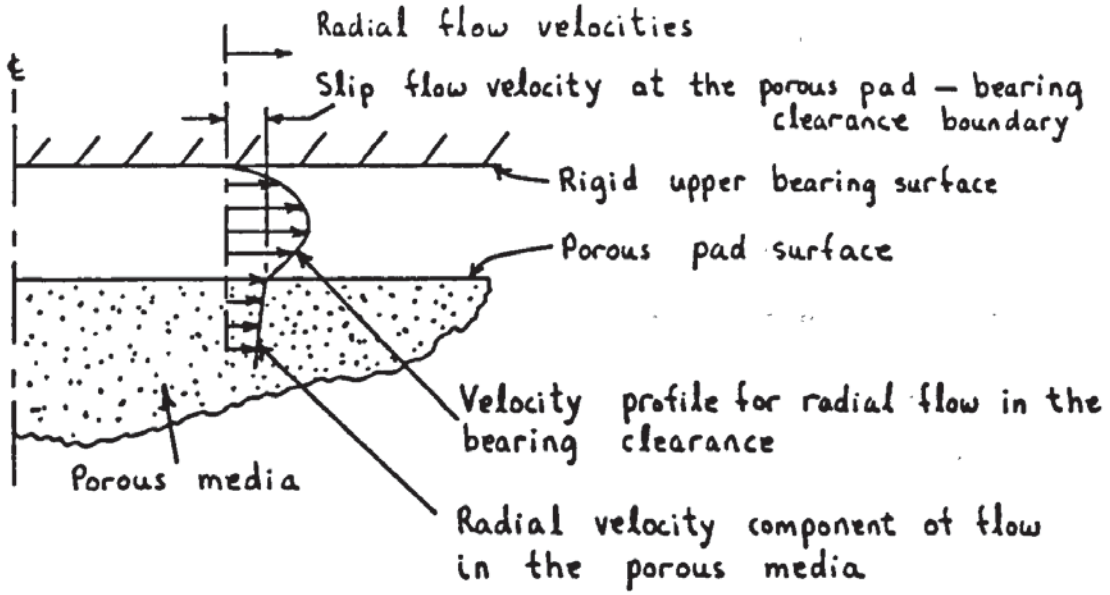

Figure 2.5 Slip flow in a porous aerostatic thrust bearing

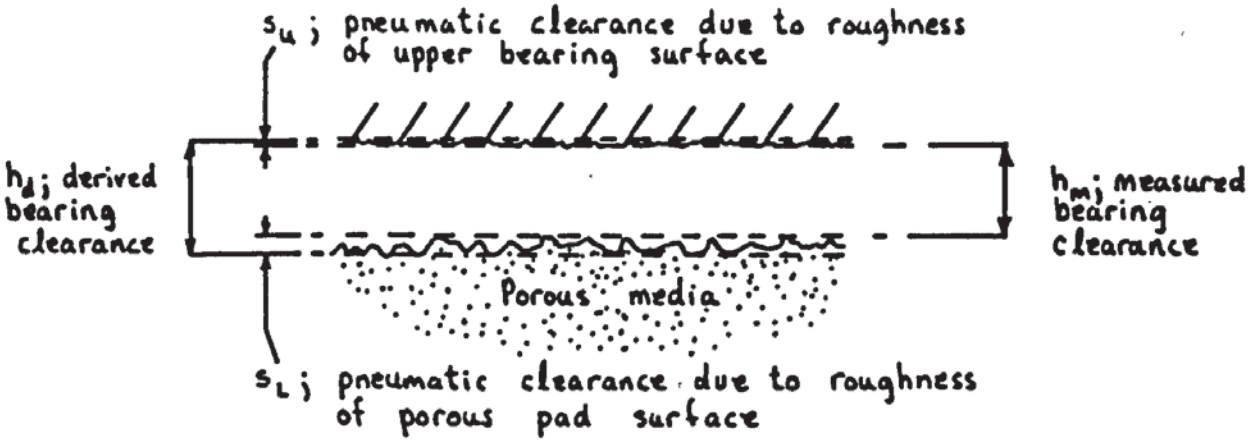

Pneumatic clearance due to roughness of both bearing surfaces; $s_h = s_u + s_L$

Figure 2.6 Pneumatic clearance due to roughness of bearing surfaces

analytical solution to the circular porous thrust bearing supplied with a compressible gas. A modified Reynolds equation is obtained which is used as a boundary condition to flow in the porous media. In a series of internal reports written by Jones et al (see Taylor (24)) a comparison of theoretical results is made with Garguilo and Gilmour (19). While close similarities existed for bearing load capacity, descrepancies arose between bearing flowrates. Also Garguilo and Gilmour obtained a reasonable correlation of theoretical and experimental results for bearing load capacity at low bearing numbers, but Jones et al however could not achieve any respectable correlation of results at any bearing number. Jones et al accounted for this to inertial flow taking place within the porous pad, invalidating their assumption of viscous flow. An attempt to obtain a solution using Forchheimer's equation (equation 2.4 in section 2.2.1) for flow in the porous media proved unsuccessful.

These discrepancies between Garguilo and Gilmour (19) and Jones et al (23) prompted Taylor and Lewis (9) and Taylor (24) to investigate possible causes and reasons for this. They put forward a number of important considerations which are listed as follows:-

(a) Roughness of the bearing surfaces particularly the porous pad.

(b) Shear deflections of the adhesive bond which supports

the porous pad in its holder. This affects the measured value of the bearing clearance.

(c) Deflection in bending of the porous pad due to the pressure drop across its thickness.

(d) Pore blockage of the porous pad surface as a result of surface machining operations (see section 2.2.1).

(e) Nature of the flow within the porous pad i.e. viscous, transitional or inertial flow (see section 2.2.1).

These all have an effect on the bearing performance and it is shown (9), (24) that provided these considerations are taken into account it is possible to achieve a close correlation between theoretical and experimental results for the theoretical solution of Jones et al (23).

It has already been mentioned that Sneck and Ewell (15) have considered surface roughness in their investigation of porous journal bearings. However their method used to measure this does not necessarily give a true pneumatic clearance accounting for the additional flow taking place in the roughness regions of the bearing surfaces. This is because they use an average peak to valley roughness reading for this pneumatic clearance. Taylor and Lewis (9) however show that it is possible to derive the bearing clearance h_d (see figure 2.6) using the modified Reynolds equation applied at the bearing clearance exit, i.e.;

$$\Lambda_d = - \frac{2.\pi.r_b^2.\Phi_z.p_a}{h_b.\eta.q_a} \left(\frac{\partial P}{\partial R} \right)_{R=1} \qquad 2.14$$

The bearing No. Λ_d and hence h_d can be obtained from equation 2.14, if the film pressure gradient at the bearing clearance exit and the bearing flowrate are measured. If the measured bearing clearance h_m is also known a pneumatic clearance s_h accounting for surface roughness, is obtained thus:

$$s_h = h_d - h_m \qquad 2.15$$

Values of s_h obtained were shown to be constant for each bearing configuration irrespective of its operating conditions, i.e. bearing clearance and supply pressure.

Shear deflections of the adhesive bond between the porous pad and its holder were measured and calibrated by Taylor and Lewis (9) while the porous pad was subject to a uniform pressure difference across its thickness (i.e. with the porous pad exhausting freely to atmosphere while pressurized). During actual bearing experiments the supply pressure minus the mean film pressure on the porous pad was calculated. This value and the calibration figures were then used to obtain the shear deflection of the porous pad bond. Hence the measured bearing clearance was corrected by subtracting this shear deflection.

In a similar way Taylor and Lewis (25) determined the

rigidity in bending of a porous pad by measuring its deflection while subject to a uniform pressure difference across its thickness and presented bearing solutions which take into account this deflection. They assume the porous pad is rigidly clamped around its circumference and apply thin plate bending theory. Because the bearing clearance is no - longer uniform it was necessary to solve the governing differential lubrication equations using numerical finite difference methods. A technique developed by Roscoe (26) was applied to discretise these equations and ensure stability in arriving at a final solution. Since deflections of the porous pad affect the resulting film clearance geometry and hence the film pressures, an iteration procedure is used. Initially a uniform bearing clearance is assumed for which the solution by Jones et al (23) can be used to obtain the first estimate of film pressures. Having obtained the film pressures, deflections of the porous pad were determined giving rise to a new bearing clearance geometry. New,more accurate,film pressures are obtained for this non - uniform clearance geometry, using the finite difference method. Hence this iteration was continued by determining new deflections of the porous pad from the last estimate of film pressures. Then new film pressures are determined from the last estimate of porous pad deflections and bearing clearance geometry. This iteration was repeated until the resulting changes in film pressures were negligible. A final solution

to the lubrication equations and deflections of the porous pad was thus achieved.

Taylor and Lewis (25) present design curves showing that the bearing load capacity reduces and flowrate increases with reducing porous pad rigidity. This is because the resulting film clearance geometry and corresponding film pressure profile become less uniform with increasing deflections of the porous pad. Taylor and Lewis point out that an optimum pad thickness exists for which the load capacity of the bearing is greatest. This is because although the throttling effect on supply pressure to film clearance reduces with pad thickness giving an increase in load capacity, the deflection of the porous pad increases due to its reduced rigidity and eventually this causes a reduction in load capacity. Previously Garguilo and Gilmour (19) had shown increases in load capacity with reducing porous pad thicknesses down to zero. This is because the porous pad rigidity was ignored.

The author considers that the assumption of a rigidly supported porous pad by Taylor and Lewis (25) has not been backed up with sufficient experimental evidence showing typical deflection profiles of the porous pad. Indeed the adhesive bond between the porous pad and its holder provides an elastic support. The rigidity of the porous pad may therefore have been underestimated because its deflection is assumed to correspond with that of a rigidly clamped plate in bending. Also bearing performance results

are presented using the minimum bearing clearance h_r at r = 0 for determination of bearing number. It is not made clear how this is measured during experiments as its value is affected by deflections of the porous pad. Since the bearing clearance at bearing exit can be obtained by direct measurement during experiments the author considers this value should be used for bearing number. In the presentation of bearing performance results this could produce a different set of results for bearing performance from which different conclusions could be drawn.

Murti (27) presents a simplified analysis of a porous gas circular thrust bearing by assuming flow in the porous pad to be predominantly axial. The simple closed form solution obtained is said to require minimal computing time compared to numerical finite difference methods. However there is probably little difference to the computing time required for the more complete solution of Jones et al (23) which the author has found to be relatively short on modern desktop mini computers. Results compare well with those of Garguilo and Gilmour (19) for thinner porous pads at low bearing numbers. Performance curves showing the affects of supply pressure are presented and the affects of each bearing parameter on the bearing performance are discussed as a useful quide to designers. However because thin porous pads may suffer relatively large deflections in bending due to their low rigidity, the usefulness of Murti's solution is considered to be limited.

Later Murti (28) extends his analysis to include the slip flow condition of Beavers and Joseph (21) which is applicable to the assumption of axial flow in the porous pad. A comparison of results for non - slip and slip flow conditions show that slip flow becomes increasingly significant at higher bearing numbers. Verma (29) has also considered the slip flow condition of Beavers and Joseph (22) in porous circular thrust bearings and obtained similar analytical results to Murti (28).

All papers that have been quoted so far in this section have been for porous bearings in which the porous restrictor extends over the whole bearing clearance. Kilmister (30) reports that some experiments with bearings containing a porous insert similar to that shown in figure 1.1b of section 1.1, have been carried out at Southampton University (U.K.). However inserts selected for optimum bearing performance were prone to self induced pnuematic instability.

Contradictory to this, Donaldson and Patterson (31,32) have carried out successful experiments with porous ceramic inserts in a landed circular thrust bearing (figure 2.7). They are able to operate the bearing without pneumatic instability though this is partly accounted to the design of their apparatus in which bearing loads are applied through an air piston which is sealed with rubber

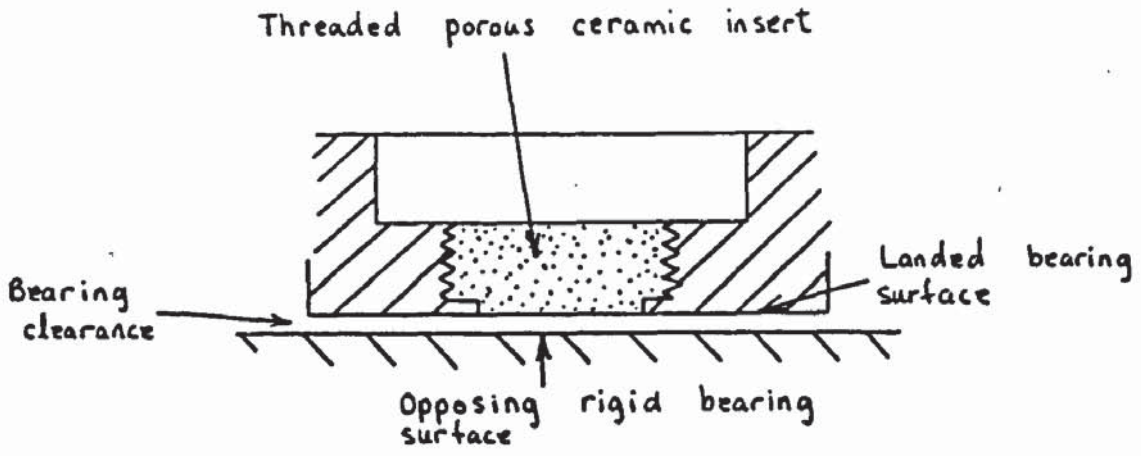

Figure 2.7 Landed porous aerostatic thrust bearing with a ceramic insert: Donaldson and Patterson (31), (32).

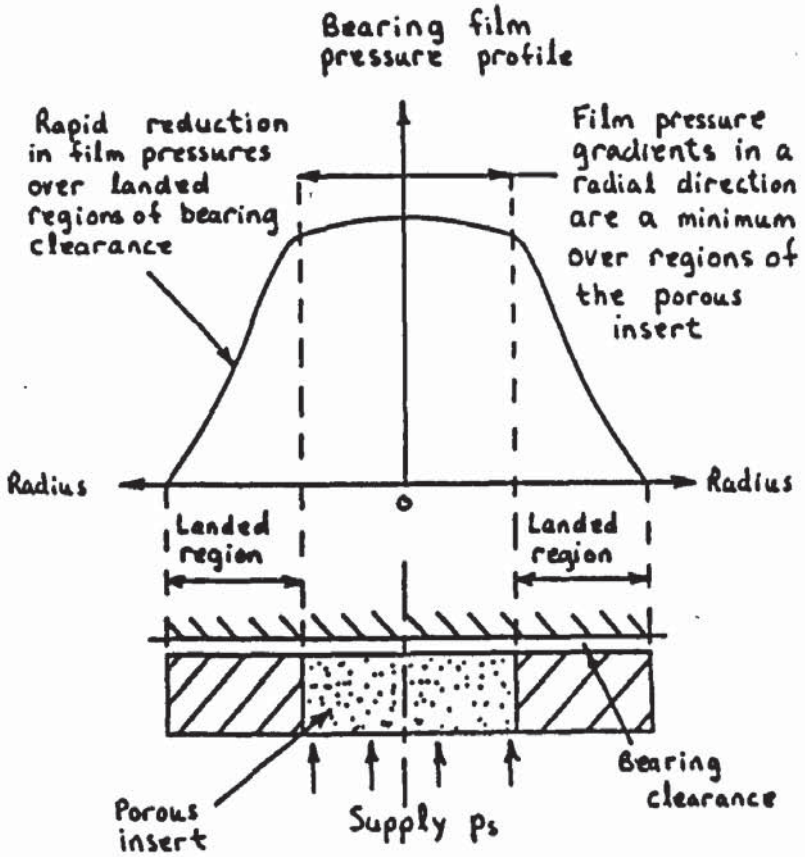

Figure 2.8 Film pressure profile for a landed porous aerostatic thrust bearing

'O' rings. Hence the bearing is externally damped by the 'O' rings and pneumatic instabilities are partly suppressed. However not all types of bearing loads are externally damped in this way and in some bearing applications the load may be applied in the form of dead weights. This could also affect the bearing stability (40) by increasing the bearing mass subject to vibration during pneumatic hammer.

Experiments (31,32) are carried out at high supply pressures up to 3.1 MN/m (450 PSI). At such pressures it is necessary to positively secure the inserts in the bearing. This is achieved by threading the porous inserts (see figure 2.7) and sealing them with epoxy resin. No account was taken of the bearing surface roughness, though provided that the bearing surfaces are precision ground the bearing clearance could be measured accurately across the landed regions where both surfaces are non - porous and therefore inherently smoother.

A theory is presented by McGrea and Donaldson (10) for this type of bearing. Account is taken of inertia effects of flow in the porous pad and slip flow at the porous wall - bearing clearance boundary. The assumption used by Murti (27),(28) that flow in the porous insert is predominantly axial is applied. The author considers that this assumption is more justifiable in landed porous bearings because the radial film pressure gradients are small over the regions of the porous insert (see figure 2.8) and therefore radial

flows in the porous media are less significant. This assumption simplifies the solution to the lubrication equations particularly when inertia effects are included in the analysis. Also the circumference of the porous insert is assumed to be a flat unthreaded surface and therefore a slight discrepancy arises in the theoretical model (10) since the actual insert used in experiments (31,32) was threaded (see figure 2.7). Taylor (24) mentions that to achieve a closer correlation between theoretical and experimental results it is important that the circumference of the porous pad is a flat surface free of grooves or threading as assumed in the theoretical model.

A criterion is presented (10) (see section 2.2.1) for viscous and inertia dominated flows in the porous insert. It is shown that with increasing supply pressures and for a porous ceramic material, inertia losses are significant. Also the inclusion of slip flow in the analysis yields the term $h_U(h_U^2+6\Phi_r)$ in place of h_U^3 in Reynolds equation. Both McGrea and Donaldson (10), and Taylor (24) show that the affect of slip flow (on the bearing performance) for typical bearing permeabilities and clearances is negligible. However Taylor points out that conditions may arise (i.e. for a highly permeable porous pad or at low bearing clearances) where slip flow becomes significant and must therefore be included in the theoretical analysis.

Rectangular externally pressurized porous thrust bearings have been studied by several researchers (33 to

36). Majumdar and Schmidt (33) predict from their analysis that the load capacity for such bearings is greater compared to a similar bearing of circular configuration and, of equal bearing area. Rao (34) later demonstrated the opposite to this in his solution which includes the slip flow condition of Beavers and Joseph (21). Rao claims that his result is more accurate since a better performance is to be expected from the more optimum circular porous thrust bearing configuration. In certain applications however size constraints may dictate a rectangular bearing as more suitable.

Rao (35) also obtained solutions for a bearing with offset loading which causes tilting of the upper bearing surface. It is shown that this significantly reduces bearing performance, causing a reduction in load capacity and an increase in the flow rate. This therefore demonstrates the importance of maintaining parallelism between the bearing surfaces for optimum bearing performance.

Naaum and Lewis (36) present a numerical finite difference solution for 3 - dimensional viscous and inertia flows within the porous media. Previous attempts by Jones et al (see reference 24) and Taylor (24) proved unsuccessfull due to the non - linearity arising in the governing differential equation for flow in the porous media. Naaum and Lewis overcame this problem by re -

arranging Forcheimer's equation (see equation 2.4 of section 2.2.1) to produce an effective permeability which represents the combined effect of both viscous and inertia flows (equation 2.16). This enables an expression similar to Darcy's Law (equation 2.17) to be used for flow in the porous media.

$$\left(\Phi_{eff}\right)_{x,y,z} = \frac{2}{\left(\frac{1}{\Phi_{x,y,z}}\right) + \sqrt{\left[\left(\frac{1}{\Phi_{x,y,z}}\right)^2 - \left(\frac{4.\rho}{\eta^2 \Phi_{x,y,z}}\right).\left(\frac{\partial P}{\partial x,y,z}\right)\right]}} \qquad 2.16$$

$$\text{and} \qquad -\frac{\partial p}{\partial x,y,z} = \left(\eta.(\Phi_{eff})_{x,y,z}\right) v_{x,y,z} \qquad 2.17$$

where in equations 2.16 and 2.17 x,y and z refer to a 3 - dimensional co - ordinate system (36).

Use of this effective permeability $(\Phi_{eff})_{x,y,z}$ therefore enables the usual numerical procedures employed for viscous flow, to be used. However since $(\Phi_{eff})_{x,y,z}$ depends on local pressure gradient $\frac{\partial p}{\partial x,y,z}$ several iterations from the first estimate of viscous flow throughout the porous media are required to obtain the final solution. This therefore greatly increases the computing time required for a solution. It was concluded (36) from the theoretical results that the bearing load capacity is a maximum while the bearing is operating in the viscous flow region, the load capacity reducing with increasing inertia flow.

Most research on porous thrust bearings has concentrated on air or gas as the externally supplied lubricant. Howarth (37) investigates such a bearing supplied with oil as an alternative lubricant. Because oil has a much higher viscosity than air or gas, porous pads with greater permeability are used, allowing the bearing to operate at higher bearing clearances for a given bearing number. This enables Howarth to use unmachined porous pads of acceptable flatness to avoid the problems associated with pore blockage during surface grinding. Even with unground porous pads it was possible to achieve dimensionless load capacities W up to 0.6. However it is questionable whether porous thrust bearings are more advantageous than conventional ported thrust bearings with a central feed hole when oil lubrication is used. This is because hydraulic instability is not a problem with these latter bearings and higher load capacities can be achieved by extending the port region (see figure 1.4 of section 1.2).

Kilmister (30) reports on the problems of permeability distribution in sintered metals. This is caused by the non - uniform compacting pressures occurring during sintering. Capone et al (38) uses an instrument similar to that shown in figure 2.9 for measuring local permeability and considerable variation was found in typical sintered bushes as supplied by the manufacturer.

This technigue could be applied to check the

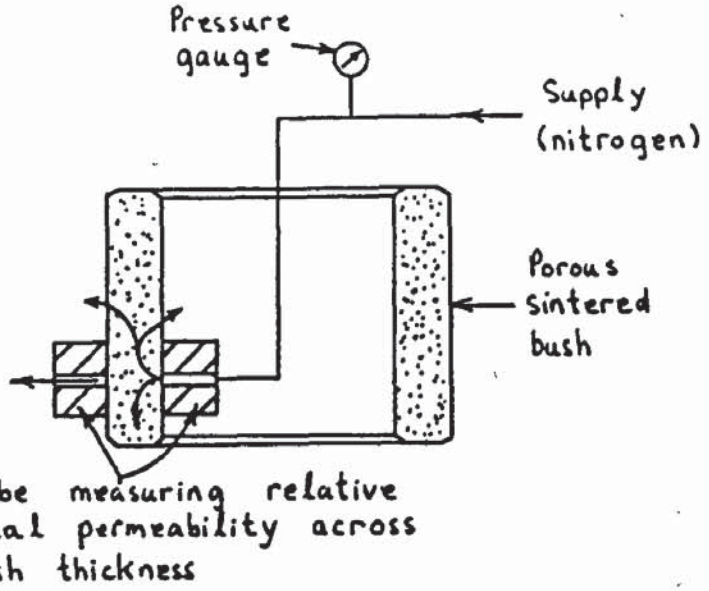

Figure 2.9 Measurement of local permeability : Capone et al (38)

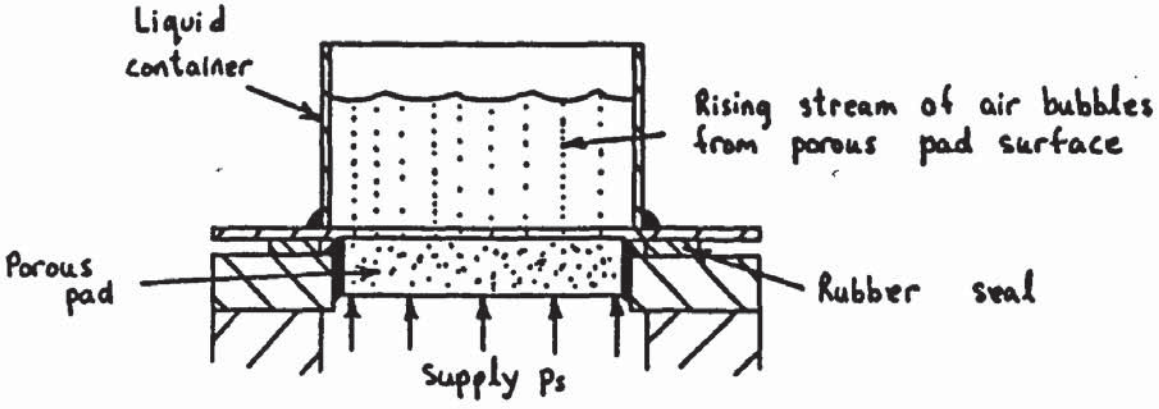

Figure 2.10 Alternative method of inspecting the permeability distribution in a porous pad

permeability distribution in porous pads. The probe would be positioned across the porous pad thickness as if to measure axial permeability. However the local permeability measurement obtained would reflect the combined effect of both radial and axial permeabilities. This is because the measuring probe (see figure 2.9) would allow the nitrogen supply to escape in both these directions within the porous pad. A misinterpretation of the resulting permeability in the predominantly axial direction would therefore occur particularly with thick porous pads. The author considers that a more accurate alternative would be to immerse the upper surface of the porous pad in a bath of water while its lower surface is pressurized with air or gas (see figure 2.10). The rising air or gas bubbles from the upper surface of the porous pad would give a visual indication of the axial permeability distribution across the surface of the porous pad. This technique is actually used by the author (refer to section 4.3.1).

Because of the pneumatic instability experienced under certain operating conditions in gas lubricated porous thrust bearings, several researchers (39 to 44) have been prompted to investigate this occurance in more detail. Gorez (39) presents a series of stability conditions in his mathematical treatment of bearing stability which assumes that the bearing film pressure profile under static conditions is unaffected by unstable disturbances of the

bearing clearance. These conditions indicate that the bearing becomes increasingly more stable with reducing porous pad porosity and thickness.

A fuller explanation of the causes of pneumatic instability in gas - lubricated porous thrust bearings is given by Dah - Chen Sun (40) (later minor corrections were made to this paper in (41)). One dimensional axial flow in a thin porous pad is assumed and only small disturbances of the bearing clearance are considered so that a linear stability theory may be applied. The governing differential equations for flow in the bearing clearance and porous media include a time dependant term to account for dynamic characteristics of the bearing. A first order perturbation method is used to obtain solutions to these equations. From the analytical results, the following conclusions are drawn:

(1) The lubricant's compressibility is the main cause of pneumatic instability. Instability will not occur if incompressible lubricants such as oil are used.

(2) The stable or unstable operating regions of the bearing depend on three main factors; (a) the compressibility of the lubricant, (b) the vicous damping properties of lubricant in the bearing clearance and (c) the floating mass of the bearing.

In some cases the load carried by the bearing is not necessarily in the form of a dead weight; for example the

thrust force from blades in a turbine or the cutting forces on a machine tool. Dah - Chen Sun therefore separates the floating mass of the bearing from the load it carries since only the former effects the bearing stability.

Figure 2.11 shows a typical stability curve obtained (40), showing regions of stable and unstable operation for a gas lubricated porous thrust bearing. A particular bearing may become unstable at certain bearing clearances as the supply pressure is increased. At a constant supply pressure and for a given floating mass, two stable regions of bearing operation can exist, one at low bearing clearances (high load capacities) and the other at large clearances (low load capacities). At low bearing clearances the viscous damping properties of the flow in the bearing clearance increase and this maintains bearing stability. At high bearing clearances the film pressures and hence compressibility of the lubricant reduce and this also results in bearing stability.

Dah - Chen Sun (40) also shows that the bearing size, mass and permeability affect the regions of stable bearing operation. The stable regions tend to reduce with increasing bearing floating mass. In some bearing applications the bearing load may be applied in the form of force rather than a dead weight. It is therefore advisable in such cases to minimise the bearing floating mass. This is probably another reason why Donaldson and Patterson (31,32) were able to operate their porous aerostatic thrust

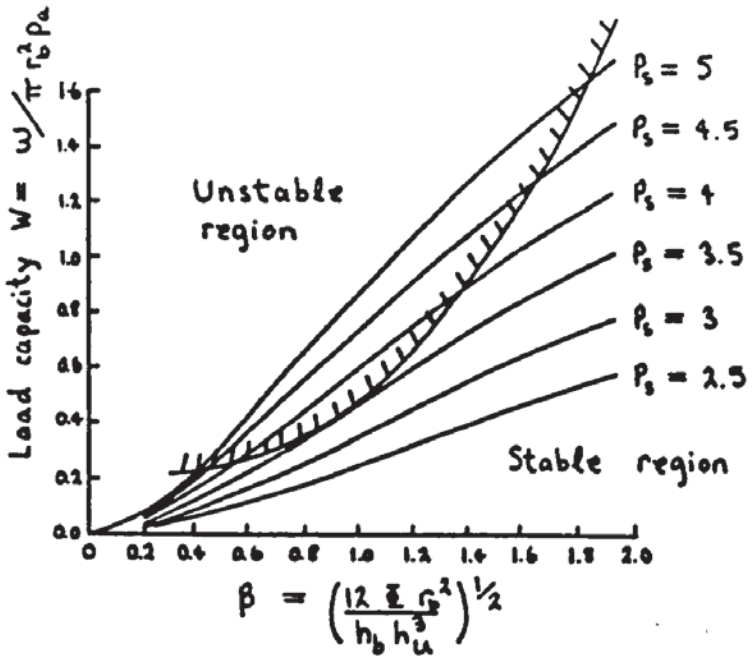

Figure 2.11 Stability regions for the operation of a porous aerostatic thrust bearing: Dah-Chen Sun (40)

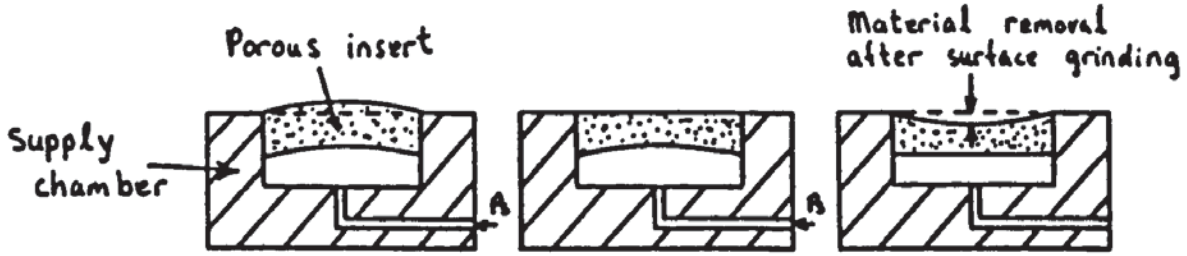

(a) Initial deflection of porous insert due to supply pressure p_s

(b) Porous insert ground flat while still pressurized at p_s

(c) Resulting porous insert shape after grinding and with supply cut-off

Figure 2.12 Grinding of porous insert while pressurized: Garez and Szwarcman (42)

bearing at high supply pressures without pneumatic instability occurring Instead of the usual dead weight loading methods used by many researchers of porous thrust bearings, they applied loads using an air piston. The resulting floating mass of the bearing was therefore minimized.

For two gas lubricated porous thrust bearings of identical radius and floating mass Dah - Chen Sun (40) showed that the one with the lesser restriction to flow through the porous pad will have the smaller region of stable operation. This is because the film pressures and hence compressibility of the bearing film are increased. For increased stability this implies a thick porous pad (and/or reduced permeability), however if the two bearings have equal restriction as defined by the ratio Φ_z/h_u, the one with the thinnest porous pad will have the larger region of stable operation.

Although Dah - Chen Sun (40) does not discuss the effects of porous pad porosity on bearing stability, the author has deduced from his conclusions that stability reduces with increasing porosity. This is therefore in agreement with Gorez (39).

Gorez and Szwarcman (42) consider the effects of 'surface loading' on bearing stability in thrust bearings having one or more porous inserts. 'Surface loading' is the blocking of pores at the surface of the porous insert caused during grinding or machining operations (see also

section 2.2.1). Their theoretical solutions take into account the presence of a highly restrictive layer at the porous insert surface which reduces its overall permeability in the axial direction. It is pointed out that if the porous insert is supplied with pressurized air during grinding, the resulting permeability may be controlled by monitoring the gas flow through it (see figure 2.12). This also results in a flattening of the porous insert which bows under the pressure drop across it. Though this may improve bearing performance the author considers that the resulting bearing geometry may be unpredictable under the varying conditions of load, supply pressure and bearing clearance. Also the grinding of the porous insert in this way will increase pore blockage in the central regions of its surface where the maximum material removal occurs (see figure 2.12). This will cause a non - uniform permeability distribution across the surface of the porous insert and could therefore considerably affect the bearing performance. However Gorez and Szwarcman show from theoretical results that for bearings of similar static performance, the one with a porous insert having a loaded surface is more stable than the one with a homogeneous porous insert. This is accounted to the elimination of the capacitance effect corresponding to the volume of pores in the porous media, i.e. the thin restrictive layer stops the pressure disturbances taking place in the bearing clearance, being transmitted to the

porous media.

Taylor and Lewis (43) and Taylor (24),(44) extend their work to include the dynamic characteristics of a full face porous aerostatic circular thrust bearing. They relate their bearing to a simple viscous damped spring - mass system and therefore assume that the bearing behaves linearly for small disturbances of the bearing clearance. In this way the dynamic forces produced by the bearing are separated into stiffness and damping forces. The bearing designer is therefore able to determine natural frequencies for a given bearing mass and check these against applied vibrational forces such as may occur in machine tools,for example. The mathematical solutions employed are similar to those used for the steady state conditions (24),(25) in that the Roscoe Technique (26) is used to discretise the governing differential equations for flow in the bearing clearance and the porous media. However in addition these equations both contain a time dependant term which accounts for small cyclic variations in pressure throughout the bearing. Numerical solutions to the governing differential equations are obtained using the Alternating Direction Implicit technique devised by Peaceman and Rachford (45), in conjunction with a form of over - relaxation to improve the convergence rate. Even with this method of solution however the computational time required was reported to be large and therefore theoretical results are limited to only one bearing configuration. However theoretical results (44)

did show that it is possible for the bearing to exhibit a negative damping force in which self induced vibration would occur as in pneumatic hammer.

Experiments are carried out (24), (43) on a porous aerostatic thrust bearing using a constant force vibrator and a sweep frequency test to obtain typical resonance frequency curves for the damped spring - mass system representing the bearing. It was confirmed that provided the amplitude of vibration is small in relation to the film clearance then the bearing behaved linearly with constant spring stiffness and damping coefficient. Predicted theoretical values of damping force were found to agree with experimental values while the dynamic stiffness was underestimated. The reasons for this were not known.

The review of literature covered in this section has revealed the following gaps in the knowledge;

(a) The treatment of an elastic porous pad by Taylor and Lewis (25) assumes a rigidly supported porous pad in bending. Many cases arise however where the porous pad is elastically supported especially if the porous pad is bonded into its holder using an adhesive. This therefore needs to be taken into account in the theoretical and experimental analysis of porous aerostatic thrust bearings having an elastic porous pad.

(b) Although several papers on the theoretical aspects of

pneumatic instability in porous gas lubricated thrust bearings have been presented, there have been limited experimental investigations to support them. Therefore many of these theories remain to be verified experimentally.

These gaps in the knowledge will contribute to a formation of an outline for the areas of investigation as part of this research project in section 2.3.

2.2.3 ELASTIC PROPERTIES OF THE POROUS MATERIAL

In section 2.2.2 a paper by Taylor and Lewis (25) concerning a porous aerostatic thrust bearing with an elastic porous pad was reviewed. A rigidly supported pad was assumed in their mathematical treatment and only the flexural constant D_b (also known as the modulus of rigidity) was required. This was determined directly from deflection measurements of the porous pad while subject to a uniform pressure difference $p_s - p_a$ across the pad thickness. However it was argued in section 2.2.2 that the porous pad may be elastically supported around its circumference by an adhesive bond. In such cases it is shown from the theoretical analysis of porous pad deflections in section 3.5 that a further flexural constant B_b is required. This constant is a function of the adhesive bond stiffness k_b in bending and Poisson's ratio ν_b for the porous pad material. It is described in section

4.3.6 how both flexural constants D_b and B_b can be obtained from deflection measurements of the porous pad after assembly in its holder and when subject to a uniform pressure difference $p_s - p_a$ across its thickness. However it is not possible to obtain a value of the stiffness k_b from the flexural constant B_b unless Poisson's ratio ν_b for the porous pad material is known.

The Young's Modulus E_b for the porous material could be determined from standard compression tests (46) on smaller test specimens. A value of ν_b can then be obtained from the following equation (47) assuming that the porous material is homogenous and isotropic:

$$D_b = \frac{E_b . h_b^3}{12.(1 - \nu_b^2)}$$

$$\text{i.e.} \quad \nu_b = \left(1 - \frac{E_b . h_b^3}{12.D_b} \right)^{1/2} \qquad 2.18$$

However even for porous materials of the same manufacturers specification their properties could vary considerably. Kilmister (30) has reported on the inconsistent permeability to flow through porous pads of the same manufacturer's grading. Similar descrepancies could occur in the elastic properties between the test specimen and the porous pad. This is especially since the specimen would be of a different size to the porous pad and uncontrollable variations may occur between them during compacting of the powder and sintering. Because of this difficulty the

following literature survey is therefore carried out. This survey may reveal other methods of predicting elastic properties of the porous material, i.e. from porosity measurements for example.

Squire (48) was among the first researchers to study the elastic properties of porous sintered materials. Using iron powder compacts it was concluded that their density or porosity was the major influencing factor on the resulting elastic modulus of the sintered material. Several attempts have since been made by other researchers to make predictions of elastic modulus from relative density ρ_r or porosity $(1 - \rho_r)$. McAdam (46) used experimental results from various sintered steel and iron based alloys to obtain the following empirical equation.

$$E_b = E_p.(\rho_r)^{3.4} \qquad 2.19$$

Conclusions drawn are similar to those by Squire (48) in that Young's modulus depends mainly on the proportion of voids in the sintered material, i.e. the relative density ρ_r rather than the material composition.

Spriggs (49) also fitted an empirical equation to experimental data for sintered Aluminium Oxide:

$$E_b = E_p.e^{-b_0.(1 - \rho_r)} \qquad 2.20$$

However the resulting value of the empirical constant b_o was found to vary significantly with the fabrication technique used.

Note that both equations 2.19 and 2.20 require Young's modulus E_p for the original parent material in its solid form. This is widely available from many literature sources.

Several theoretical predictions (50 to 53) have been made by assuming the porous medium is a homogeneous isotropic matrix whose porosity is in the form of randomly spaced spherical holes. Expressions obtained indicate reductions of shear and bulk modulus with reducing porous medium density. However Leheup and Moon (54) found that these expressions over - estimated values obtained experimentally from powder forged (hot rolled powder) and sintered samples of iron and iron - graphite. This is partly accounted by the fact that real porous materials do not have spherical pores. Experimental values of Poisson's ratio are obtained for both powder forged and sintered specimens. For the sintered specimen an increase in Poisson's ratio to 0.287 occurs at a relative density ρ_r of 0.877 (Poisson's ratio for a relative density of 1 was 0.283). Unfortunately other results for specimens of a lower density are not presented and it is therefore impossible to predict a value of Poisson's ratio ν_b for typical porous pads used in gas bearings. Note that the manufacturers (Schumacher filters Ltd.) specify a porosity

of between 30 and 50% (ρ_r = 0.7 to 0.5) for sintered stainless steel pads of the type used in porous thrust bearing applications.

Wang (55) uses a more elaborate mathematical model by assuming that the porous material consists of an array of solid spherical particles. The space between these closely packed spheres represents the material porosity. The proportion of this space and hence the porosity depends on the flattened area of contact between adjacent spheres (see figure 2.13). The solution is therefore capable of treating the transition of pore structure from interconnect to isolated (see figure 2.13). Theoretical results predict a zero Young's modulus at a relative density ρ_r of 0.5236. This is the density at which the spherical particles become isolated from each other.

A comparison between the experimental results and empirical equation of McAdam (46) and the theoretical results of Wang (55) are shown in figure 2.14. The experimental results are for an iron - copper - carbon alloy, i.e alloy steel. It is clear that the empirical equation (equation 2.19) accurately predicts within experimental scatter, the relative elastic modulus E_b/E_p down to fractional porosities (1 - ρ_r) of 0.6. The theoretical model of Wang however becomes less accurate with increasing fractional porosity (1 - ρ_r). And the predicted zero modulus at a fractional porosity (1 - ρ_r) of 0.4764 (= 0.5236 for fractional density ρ_r) gives rise to a large

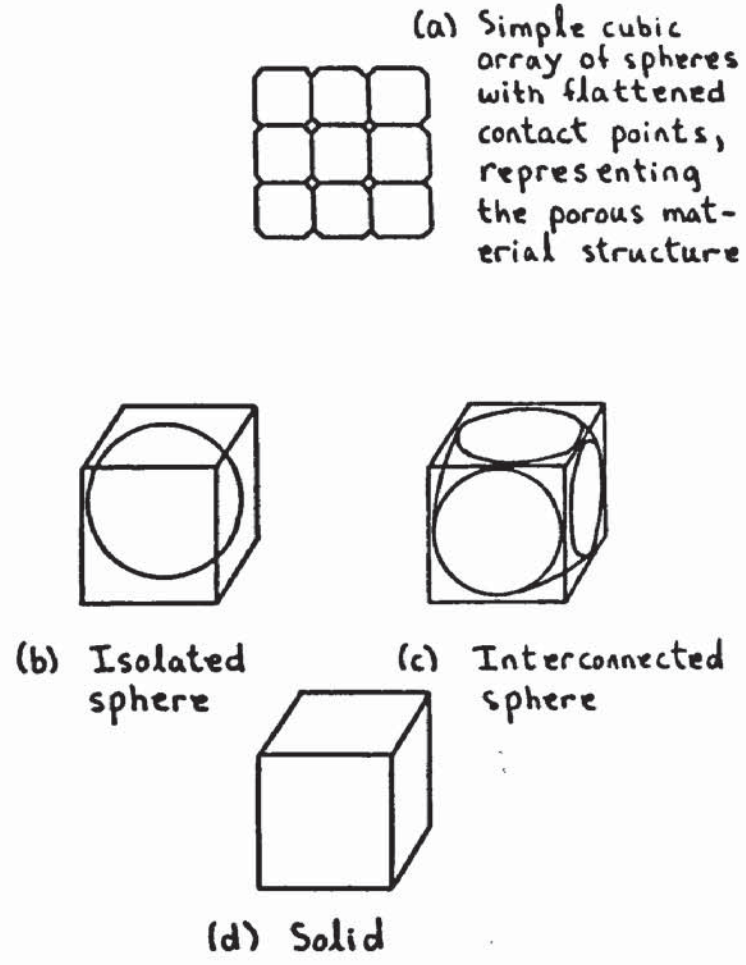

Figure 2.13 Theoretical model of Wang (55) for a porous sintered material

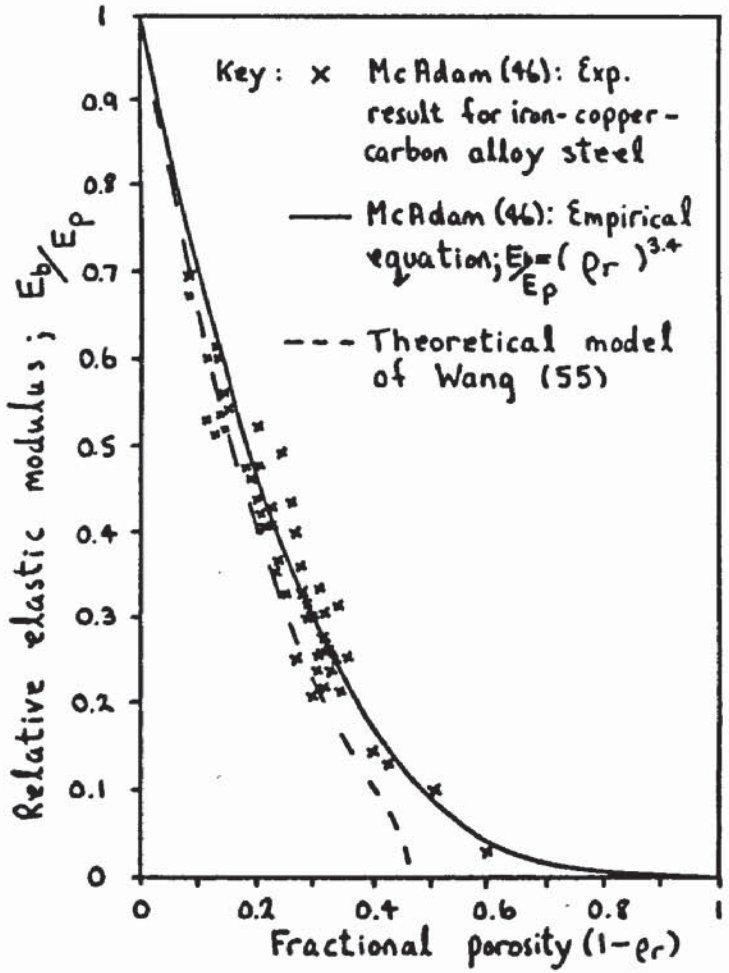

Figure 2.14 Elastic modulus of porous sintered metals

error for highly porous materials.

This completes the literature survey in this section which the author considers is of relevance. The following conclusions can therefore be drawn:

(a) The elastic property E_b of a porous sintered material can be predicted approximately from measurements of relative density ρ_r .

(b) For sintered steel or iron compounds the following empirical equation gives accurate values of Youngs modulus;

$$E_b = E_p.(\rho_r)^{3.5}$$

(c) Because insufficient information has been presented for Poisson's ratio in the literature reviewed, a value of ν_b can only be obtained from values of D_b and E_b in equation 2.18. The flexural constant D_b is directly obtainable from deflection measurements of the porous pad in bending while a value of E_b can be determined using equation 2.19.

2.2.4 COMPLIANT BEARINGS

Dowson and Taylor (56) were amoung the first researchers to investigate an externally pressurized oil lubricated thrust bearing in which one of the bearing

surfaces is compliant (see figure 1.9). Thin elastomer layers of Nitrile and Polyurethane rubber were bonded to the rigid surface of a circular thruster. The lubricant was supplied through a central feed hole in the opposing rigid bearing surface. In their mathematical treatment the elastomer layer is considered to be thin compared to its radius and restrained from any movement in the radial direction parallel to its bonded face. Also the elastomer material behaves linear - elastically for small deflections. A simple equation is thus obtained for compressive deflections of the elastomer layer;

$$w_c = \frac{p.t_c}{E_c}\left(1 - \frac{2.\nu_c^2}{1 - \nu_c}\right) \qquad 2.21$$

$$w_c = \frac{p.t_c}{E_c'} \qquad 2.22$$

where in equation 2.22 E_c' is an equivalent elastic modulus defined as;

$$\frac{1}{E_c'} = \frac{1}{E_c}\left(1 - \frac{2.\nu_c^2}{1 - \nu_c}\right) \qquad 2.23$$

Equations 2.21 and 2.22 are known as the simple column model by Castelli et at (59). By coupling this equation to Reynolds equation for flow in the bearing clearance, Dowson and Taylor obtained closed form solutions for the film pressure profile and bearing load capacity. Results show an improvement in bearing performance compared to a

conventional rigid bearing without a compliant surface.

Comparisons between theoretical and experimental results were made by assuming a value of the equivalent elastic modulus E_c' in equation 2.22 to give close agreement between experimental and theoretical results at the largest bearing clearance attained during experiments. An approximate value of Poisson's ratio was then estimated from equation 2.23 using a value of Youngs modulus E_c obtained from low strain rate compression tests on specimens of elastomer. Values of Poisson's ratio ν_c between 0.434 and 0.459 were obtained in this way.

Much research has been carried out at Columbia University U.S.A.; (57 to 63) and (68 to 70) on the theoretical and experimental study of compliant bearings. This study was initiallized after the discovery that a plastic journal bearing could be operated at very low oil feed rates while still maintaining a lubricating film.

Elrod (57) obtained exact and approximate solutions for deflections of an infinite elastomer layer, bonded to a rigid base material. Sine and Cosine functions were assumed for displacements in the radial and axial directions respectively, to obtain elementary solutions.

In a gas lubricated compliant circular thrust bearing with a central feed hole, Pirvics and Castelli (58) show further increases in load capacity at a constant recess pressure due to the gas compressibility. They conclude that the lubricating gas acts as a secondary elastomer,

enhancing the effects of the compliant surface in the bearing film clearance.

A comprehensive experimental and theorectical investigation was carried out by Castelli et al (59) using oil lubrication. The bearing configuration considered was similar to that of Dowson and Taylor (56). An exact solution to the classical elasticity equations (see section 3.4) for a linear - elastic material is obtained using Bessel functions. In order to simplify this solution by reducing the number of required boundary conditions, the elastomer is assumed to have an infinite extent in the radial direction. The final solution involves an integral which is determined numerically. For comparison with experimental results the clearance between the undeflected compliant surface and the lower rigid bearing surface is used in presenting load and flowrate graphs. This represents the liftoff of the rigid backing to which the elastomer layer is bonded and was later called the bearing approach c by Benjamin et al (61, 62).

Only a qualitative comparison of experimental and theoretical results (59) was made as an accurate value of Poisson's ratio was not known for the elastomer materials used. However it was suggested that Poisson's ratio has a value very close to 0.5 for typical soft rubber - like materials which are incompressible in nature. It was concluded that while the compliant surface in thrust bearings improves the load carrying capacity, this is

achieved with a loss in the overall stiffness of the bearing due to the soft elastomer layer. A comparison of theoretical results was also made using the simple column model of Dowson and Taylor (56) and this is shown to give accurate predictions for Poisson's ratio ν_c up to 0.45. As ν_c approaches 0.5 however equation 2.21 predicts deflections approaching zero for the compliant surface. Since Castelli et al (59) have shown this not to be true and that compliant layer deflections can occur when $\nu_c = 0.5$ then this is therefore a serious limitation of the simple column model used by Dowson and Taylor.

Although in the experimental apparatus used by Castelli et al (59) it was not possible to measure deflections of the compliant surface, their theoretical results showed the unusual nature in which incompressible materials ($\nu_c = 0.5$) can behave. Due to the compression of the elastomer layer in the central regions of the bearing clearance where film pressures are greatest, material is displaced radially outwards from this region. A bulging of the compliant surface therefore occurs at the bearing clearance exit (see figure 1.9 of section 1.2) where the film pressures reduce to ambient. This phenomena is said to improve bearing performance by reducing the rate of escaping flow from the bearing clearance exit and also enhancing the recess formed by deflections of the compliant surface which helps generate more uniform film pressures.

Solutions and results obtained by Castelli et al (59)

assume an infinite elastomer layer. Obviously this is impractical and in a design guide by Castelli and Rightmire (60) it is suggested that this case will be satisfied when the elastomer extends 3 to 5 times its thickness beyond the bearing clearance exit. Also solutions were found to be dependant on the term $1/(1 - 2\nu_c)$. This term becomes increasingly more sensitive to values of Poisson's ratio ν_c approaching 0.5 (see figure 2.15). Rightmire (63) was therefore prompted to accurately determine by experiment, values of ν_c for typical elastomer materials used in compliant bearings (refer also to section 2.2.5). Values obtained for soft rubbers were in the range 0.49881 to 0.49991. Others (64 to 66) have also obtained similar values for natural rubbers filled with carbon black.

In an attempt to find solutions for the compliant thrust bearing with an elastomer layer of finite radial extent (see figure 2.16) Benjamin (61) investigated three different solution methods to the elasticity problem. The first was by use of eigenfunctions in solving the classical elasticity equations (see section 3.4), but this proved to be too complex in the finite elastomer case. The second approach employed the Raleigh Ritz method to minimize the strain energy in obtaining a solution to the elasticity equations. However as Poisson's ratio approached 0.5 an infinitely reducing grid mesh size was required to obtain an accurate solution giving rise to an excessive computing time. It is stated that this would also occur with other

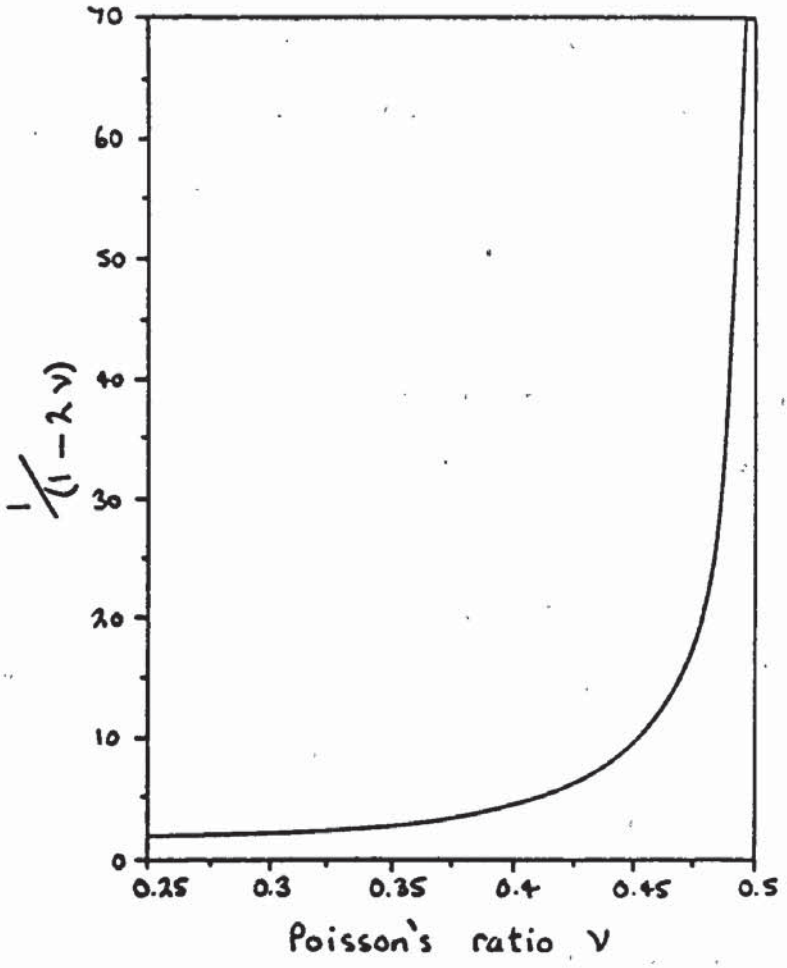

Figure 2.15 Variation of $(1-2\nu)^{-1}$ with Poisson's ratio ν

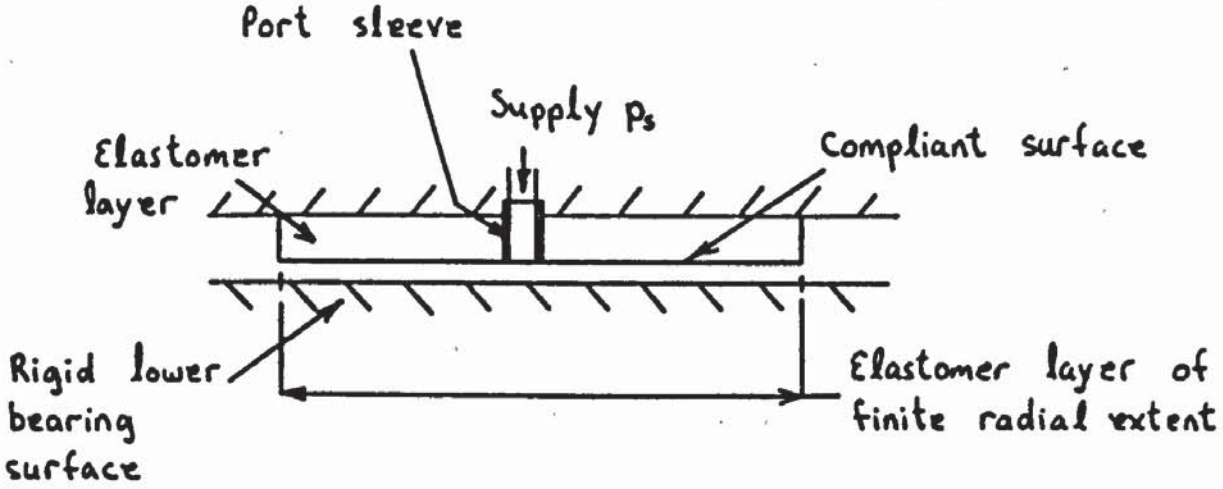

Figure 2.16 Compliant hydrostatic thrust bearing with central feed hole and elastomer layer of finite radial extent : Benjamin et al (62)

numerical methods requiring a grid mesh for their final solution, such as finite difference methods for example. The third approach which proved successful employs an integration method using Green's function approach to obtain an elementary solution to elastic field equations. The boundary conditions were then satisfied using the principle of superposition (85). This third method was particularly suitable for values of Poisson's ratio approaching 0.5. The final solution to the bearing using Reynolds equation was then achieved using the Newton - Raphson iteration technique.

A comparison of this solution with experimental results was made by Benjamin et al (62). The bearing is shown in Figure 2.16. Note the port sleeve used to stop the elastomer layer blocking the feed hole when compressed by the film pressures. A good correlation was achieved for load against recess pressure. However a small descrepancy arising at small bearing clearances was accounted to neglecting the viscous frictional heating of the lubricant in the bearing film clearance and the supply. This causes thermal distortion of the compliant surface, changes in mechanical properties of the elastomer material and a reduction in the lubricant viscosity. Results obtained for load against bearing approach were less promising, possibly due to inaccurate measurements of the bearing approach and also roughness of the bearing surfaces, particularly the compliant surface, which were ignored. These results

however clearly show that the bearing with a finite elastomer layer can operate at -ve approaches c. This occurs when compression of the elastomer layer is greater than the bearing liftoff.

The design guide presented by Castelli and Rightmire (60) gives information on several compliant thrust bearing configurations including a flexible membrane bearing similar to that studied by Levy and Coogan (67) and shown in figure 2.17. This bearing is ideal for operating over rough undulating surfaces such as floors, made possible by the flexibility of the rubber membrane.

Other research carried out at Columbia University includes work on compliant journal bearings (68 , 69) in which the compliant surface is subjected to a cyclic loading. The visco - elastic properties of the elastomer material must therefore be taken into consideration and the resulting deflections of the compliant surface are not only dependant on shaft angular position but also its rotational speed. A compliant surface in a long squeeze film journal bearing is studied theoretically by Buckholz (70). A solution is obtained using Navier equations for linear elasticity and results are presented for the special case of an incompressible elastomer and lubricant.

Lowe (71, 72) carried out an experimental analysis of compliant aerostatic circular thrust bearings with a central feed hole to verify the theoretical predictions of

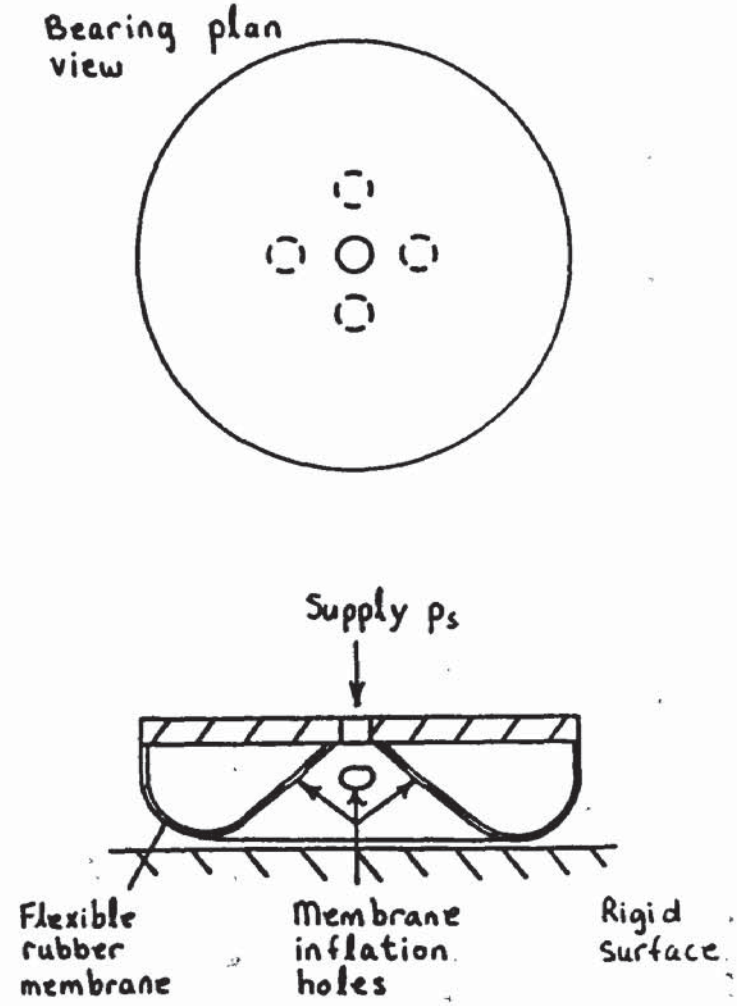

Figure 2.17 Flexible membrane aerostatic thrust bearing: Levy and Coogan (67)

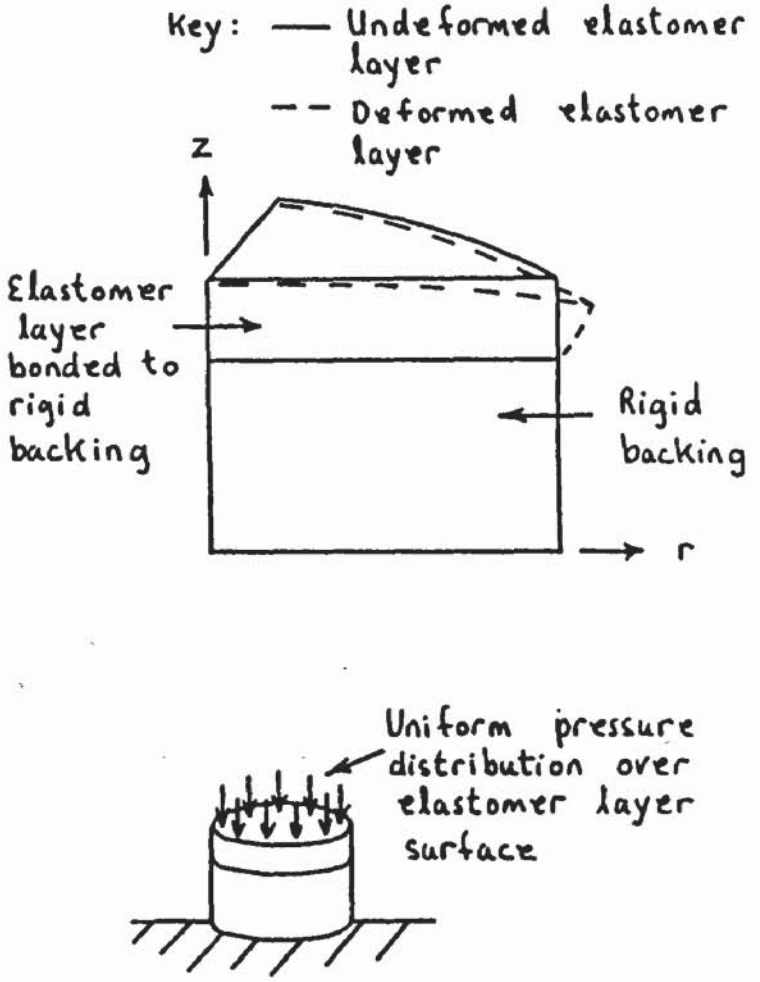

Figure 2.18 Deflections of a typical rubber like material to a uniform pressure: Rybricki et al (74)

Pirvics and Castelli (58). Inherent compensation was used to reduce the likelihood of pneumatic instability especially since a shallow recess will be formed in the bearing clearance by deflections of the compliant surface. To improve the accuracy of experimental results Lowe (72) took into account variations of the elastomer layer thickness due to changes in ambient temperature. This is because the rubber thickness was used to determine the initial zero setting of the capacitance probes used to measure the bearing approach c. Lowe achieved a good correlation of experimental results with the theory of (58) for the thinner elastomer layer cases.

Although in general Lowe found increases in load capacity for the compliant bearing compared to a conventional thrust bearing with rigid surfaces and a central feed hole, this was not always the case. For example often at medium bearing clearances a reduction in load capacity was noted. However this is possibly due to increases in bearing clearance caused by deflections of the compliant surface for a given bearing approach c. At low bearing clearances the recovery in load capacity is attributed to the static stiffness of the compliant bearing remaining virtually constant. This therefore is a significant advantage of the compliant surface bearing since the static stiffness of the rigid bearing reduces to zero at small bearing clearances. Another reason overlooked by Lowe for the increases in load capacity at low bearing

clearances is the bulging of the elastomer layer near the bearing clearance exit. As described by Castelli et al (59) this enhances the recess formed by deflections of the compliant surface to produce more uniform film pressures.

Lowe also found that an optimum elastomer layer thickness existed for which the load capacities from the compliant bearing are a maximum at a given bearing approach. This thickness depended on the hardness of the elastomer layer material and the supply pressure, i.e. the optimum thickness reduced with increasing supply pressure and reducing elastomer hardness. The reasons for this are not given but this is possibly due to deflections of the compliant surface giving rise to an increase in the mean bearing clearance for a given bearing approach. A potential recovery in load capacity would be expected at lower bearing approaches.

The experimental results obtained by Lowe also show an increase in flow rate for the compliant bearing at a given approach compared to the conventional rigid bearing. It is therefore important to operate the bearing at low bearing clearances to minimise flowrate and take advantage of the higher load capacities.

At certain operating conditions Lowe found the compliant bearing to be unstable and suffer from pneumatic hammer. Stability plots are presented which show that stable regions of bearing operation exist at lower supply pressures and for thinner or harder elastomer layers. Also

in general the bearing stability improved with increases in load capacity.

Gupta (73) considers the incipient liftoff in a preloaded plane compliant thrust bearing of finite width and infinite length with a central feed hole. This has important significance in self - caging compliant surface gyroscopic bearings for example. Here when the supply is cut off the gyro will cage in its current position because of an initial interference fit between the compliant surface and the gyro casing. The compliant layer is assumed to be of infinite extent in both width and length. The bearing is pre - loaded before the supply pressure is applied and the rigid bearing surface indents into the soft elastomer layer. It is postulated by Gupta that liftoff occurs when the lubricating film, which propagates from the central feed hole, reaches the bearing exit. Just before liftoff occurs the flowrate is zero, due to the seal maintained by the compliant surface and also the film pressure profile is uniform. This reasoning seems acceptable for compliant bearings with elastomer layers of infinite extent and particularly for elastomers that are incompressible in nature, since a bulging of the compliant surface will take place at the bearing clearance exit forming a seal here. However for a bearing with a finite elastomer layer of equal width or radius to the bearing clearance, the case for incipient liftoff may be different. This is because Rybricki et al (74) for example has shown

that deflections of the finite elastomer layer are greater towards the bearing clearance exit when subject to a uniform pressure profile (see figure 2.18). It is possible that the lubricating film will propagate instantly from the central feed hole the moment a threshold supply pressure is reached. At liftoff therefore the bearing film pressure profile is unlikely to be uniform and the criteria for incipient liftoff will be different.

Also for a compliant thrust bearing supplied through a full faced porous pad (see figure 1.1a of section 1.1), liftoff would be complete when there are no areas of the compliant surface in contact with the porous surface. And since lubricant is supplied to the full bearing face it is possible with these bearings that flow through the bearing takes place long before liftoff is complete.

Gupta however shows that the supply pressure required for bearing liftoff is a function of the properties and dimensions of the elastomer layer and the indentation due to the pre - load on the bearing. For a given indentation the liftoff pressure increases with the stiffness of the compliant layer and as Poisson's ratio ν_c approaches 0.5.

In all the research work reviewed so far on compliant bearings the surface roughness of the bearing surfaces has been ignored. This consideration is particularly important with regard to the compliant surface since although its surface roughness may be significantly greater than that of the rigid surface it had the potential capability of

complying to local roughness peaks and hence moderating the effects of roughness on bearing performance (see fig 1.7).

As far as the author is aware Lau and Harman (75) are the only researchers to take into account surface roughness in their theoretical study of a compliant hydrostatic / hydrodynamic thrust bearing. However the compliant surface is assumed to be perfectly smooth and roughness of the rigid mating surface has a random Gaussian distribution (76) typical of many machined surfaces. In the analysis the effect of local variations in the film pressure due to surface roughness are ignored. It is assumed that these have negligible effect on the bulk film pressures. Therefore the effect of compliance on local surface roughness could not be studied. This means that the results presented by Lau and Harman show the effect of the additional pneumatic clearance on the measured bearing clearance, arising from roughness of the bearing surfaces. Results show that the bearing performance reduces with increasing surface roughness as would be expected since the effective bearing clearance is increased by the roughness troughs. However since deflections of the compliant surface give rise to larger bearing clearances over most of the bearing face the relative roughness in these regions is reduced, improving the bearing performance.

Stanojevic (77) obtained two general field equations for an axisymmetric elastic material applicable to any value of Poisson's ratio from 0 to 0.5. A numerical finite

difference solution was attempted but a solution coupling both the field equations could not be achieved at the boundaries of the elastomer layer.

In experimental work (77) on aerostatic compliant thrust bearings with a central feed hole, capacitance probes are used to measure the displacement of the compliant surface which was coated with an electrically conducting paint. Stanojevic reports problems in measuring the bearing clearance in this way due to thermal distortion of the compliant surface affecting its flatness. Lowe (72) had partly overcome this problem by measuring the changes in elastomer layer thickness in a temperature controlled room. These problems however can be reduced if instead displacements of the rigid backing plate to the elastomer layer are measured. This is described in more detail in section 4.5.3.

Comparisons are made by Stanojevic (77) in the performance between bearings with bonded and unbonded elastomer layers. In general, results show that the bearing performance improves with the bonded elastomer layers compared to the unbonded cases even though deflections of the latter were greater. Reasons for this are that the bonded elastomer layers produce a deeper recess especially those that are incompressible in nature where bulging can occur at the bearing exit.

However the bearing performance resulting from the

unbonded case depended on the friction between the elastomer layer and its rigid backing. If this interface was lubricated the resulting stiffness of the elastomer layer to film pressures is reduced. This is because the elastomer material was allowed to flow unconstrained in the radial direction. The greater the friction against radial movement for the unbonded elastomer layers the greater the improvement in bearing performance.

An important recommendation made by Stanojevic is that research work should be carried out on the effects of a compensating element in compliant bearings. As far as the authur is aware no such work has been carried out to date. One form of compensation is a porous pad and therefore the work carried out in this research project on porous and compliant aerostatic thrust bearings, may have some significance to other forms of compensation such as capillary compensation.

Many researchers of compliant thrust bearings have used capacitance probes to measure bearing clearance. By incorporating several probes in the opposing rigid bearing surface to the elastomer layer an approximate measurement of the bearing clearance profile can be obtained. However some researchers have used different methods. Smith et al (78) for example uses a fibre optic probe. This was traversed above the bearing to obtain a more accurate measurement of the bearing clearance profile. Similarly Field and Nau (79) use optical interferometry to measure

the bearing clearance profile in a small hydrodynamically lubricated rubber pad sliding over a flat sheet of glass. Results show the characteristic entrapment of oil in the recess formed by deflections of the compliant rubber pad. In both methods a light source (i.e. a laser) is shone through a transparent material which forms one of the bearing surfaces. A measurement is taken using the light reflected from the two bearing surfaces. It is therefore important that both surfaces reflect the light source with approximately equal intensity. This condition may not be achieved in bearings with a porous surface for example since light may be scattered in several directions as a result of its porosity.

Compliant squeeze films subject to an oscillating vertical movement have been investigated by Hori et al (80) and Ikeuchi et al (81). Hori et al showed that at low frequencies the visco – elastic effects of the elastomer material could be ignored. Experimental bearing clearance profiles were taken during oscillations of the upper bearing portion using moire fringe topography. These results show that on the downward stroke the compliant layer deflects in a concave shape to trap escaping lubricant from the squeeze film. On the upward stroke deflections of the compliant surface take on a convex shape allowing the lubricant to flow freely back into the squeeze film. This is a further interesting example of the way in which compliant surfaces can improve bearing performance

even in squeeze films. Ikeuchi et al (81) obtained solutions for the elastomer layer which are similar to those by Castelli et al (59). Consideration is also given to a squeeze film bearing with a flexible thin plate in place of the elastomer layer.

A non oscillating compliant squeeze film bearing subject to a constant load is theoretically studied by Rybricki et al (74). A finite element solution is used for deflections of the elastomer layer but it is not shown whether this solution is suitable for the case when Poisson's ratio ν_c = 0.5. However it is shown that for ν_c = 0.48, deflections of the compliant surface are greater towards its outer edge when subject to a uniform pressure over its whole face (see figure 2.18). This illustrates the unusual nature in which incompressible materials such as rubber, which are constrained from lateral movement along one side, can behave under applied loading.

A gas lubricated externally pressurized compliant thrust bearing in which the compliant surface is formed by a thin flexible metallic plate and the lubricant is supplied through a central feed hole, is investigated by Hayashi (82). This bearing is similar to one of the squeeze film bearings studied by Ikeuchi (81). Significant improvements in static stiffness and load capacity compared to a conventional bearing with rigid surfaces was reported. However the compliance of this type of bearing to misalignment between the bearing surfaces and surface

roughness, etc. is less compared with a compliant bearing with an elastomer layer.

This completes the review of literature in this section. It has become apparent from this review that while the column model of Dowson and Taylor (56) for deflections of the compliant surface is attractive in its simplicity and therefore easily applied to complex bearing problems, its main drawback is that it is unsuitable for soft incompressible elastomer materials where Poisson's ratio ν_c approaches 0.5.

The solution offered by Castelli et al (59) can be applied where ν_c = 0.5, but is limited to the elastomer layer of infinite radial extent only. The Green's function approach by Benjamin et al (61, 62) could be applied to both elastomer layers of finite and infinite radial extent. But its complexity is a limiting factor in the application of this theory to other bearing problems. Also these solutions do not allow simpification to the column model when Poisson's ratio is less than 0.45.

A new solution for deflections of the compliant surface is therefore proposed in section 3.4.4 which is shown to be an extention of the simple column model to enable solutions for ν_c in the range 0 to 0.5 and is suitable for elastomer layers of any radial extent, i.e. finite or infinite.

The review of literature has also revealed that no published work has been presented on compliant aerostatic

thrust bearings with some form of compensation. This gap in the knowledge will be partially filled by the work in this research project on porous and compliant aerostatic thrust bearings, if the porous pad is considered as a form of compensation.

These suggestions and gaps in the knowledge on compliant thrust bearings will contribute to a formation of an outline for areas of investigation in section 2.3, as part of this research.

2.2.5 ELASTOMER MATERIAL PROPERTIES

Of the published work reviewed in section 2.2.4 most researchers of compliant bearings have assumed that the elastomer layer is a homogeneous, isotropic and perfectly linear - elastic material. A homogeneous and isotropic material is one in which the physical properties of the smallest element within the material are the same as those of the bulk material and these properties are equal in all directions. Typical soft elastomers such as rubber satisfy this condition with the exception of rubbers with a high proportion of filler. Often a filler material such as carbon black is used to increase the stiffness of the elastomer. For small proportions of the filler up to 20%, the rubber may still be considered homogeneous (83). As increasing amounts of filler are used however the rubber will become less homogeneous and take on a matrix

structure.

A perfectly linear - elastic material is one in which, when loaded, the strain is directly proportional to the applied stress and when unloaded it returns to its original undeformed state. Typical rubbers (83) have a stress strain curve similar to that shown in figure 2.19. The assumption of linear elasticity can only be satisfied therefore if small regions of this curve are linearized, i.e. for strains up to 10% the stress can be approximated by a straight line (see figure 2.19).

During the initial loading and unloading cycles with rubber, a structural breakdown occurs (83) resulting in a permanent deformation when unloaded and a reduction in the rubber stiffness with each cycle. This invalidates the assumption of a perfectly elastic material. However most of the structural breakdown takes place in the 1st cyclic loading of the rubber and by the 10th cycle the rubber is sufficiently stable to assume perfect elasticity. It is important therefore that the properties of the rubber are measured after it has reached this stable condition, i.e. after loading and unloading at least ten times.

Many researchers of compliant bearings have realised the importance of Poisson's ratio ν_c in their theoretical elasticity analysis. This is because for typical soft elastomer layers which are bonded to a rigid flat surface, as ν_c approaches 0.5, the resulting layer stiffness becomes

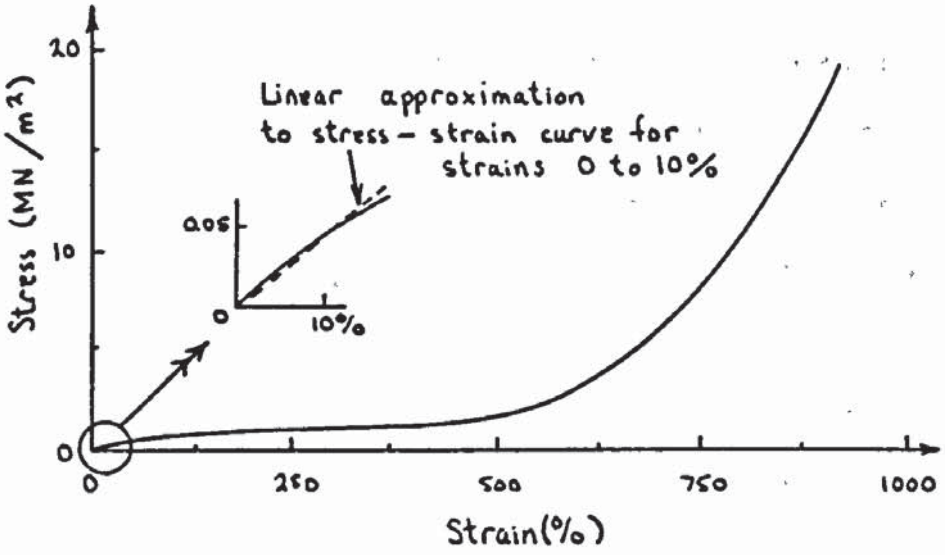

Figure 2.19 Linear approximation to a typical stress strain curve for small strains in elastomers similar to natural rubber: Lindley (83)

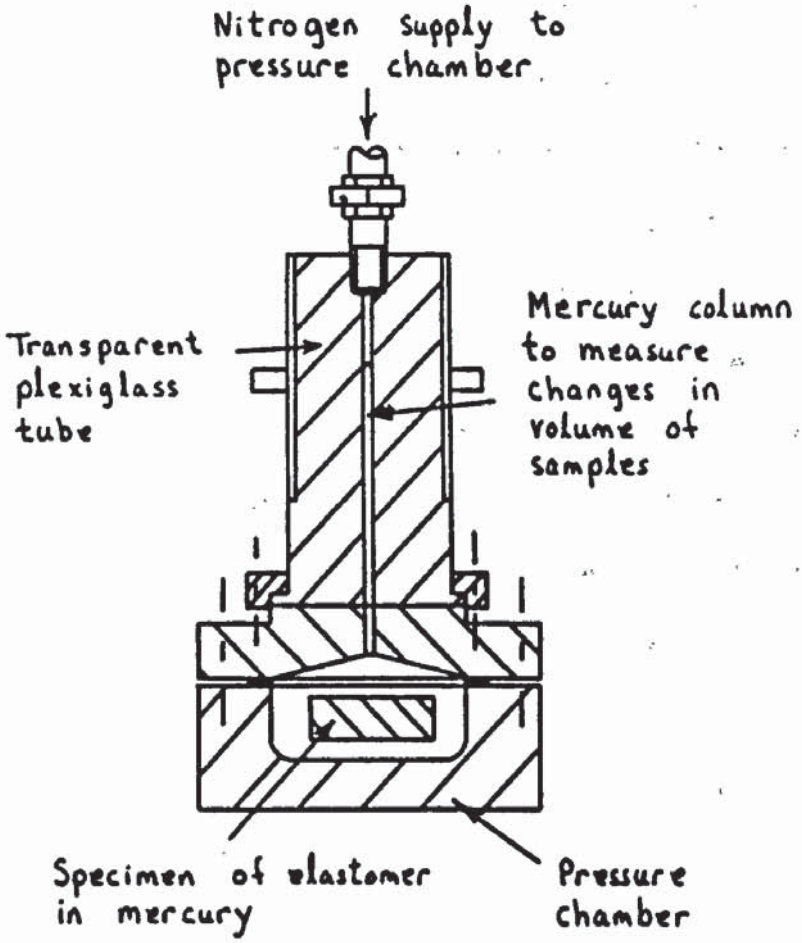

Figure 2.20 Poisson's ratio tester: Rightmire (63)

very sensitive to small changes in ν_c . For example in a study of the compression of constrained cylinders by Moghe and Neff (84), theoretical results show that the stiffness of a cylinder or disc, bonded between two flat faces is dependant on both Poisson's ratio ν and the ratio of disc thickness to diameter. For a thickness to diameter ratio of 1/10, a 20% increase in stiffness occurs for a change in Poisson's ratio from 0.4988 to 0.5 (0.24%). Similar results would be expected for the uniform compression of an elastomer layer, bonded to one flat surface whose thickness represents half that of the constrained cylinder.

This sensitivity of the elastomer layer stiffness to Poisson's ratio prompted Rightmire (63) and Holownia (64, 65) to establish experimental techniques for accurately measuring its value for soft elastomers. The apparatus used by Rightmire is shown in figure 2.20. A specimen of disc shape is placed in the pressure chamber and changes in specimen volume are measured, at different hydrostatic pressures, from the level of liquid (mercury) in the transparent plexiglass tube. To obtain a value of Poisson's ratio for the specimen it was also necessary to measure its shear modulus G. This was achieved using the shear tester shown in figure 2.21. The accuracy of obtaining Poisson's ratio in this way was shown to improve as its value approached a maximum of 0.5.

Holownia (64, 65) devised a different technigue to obtain Poisson's ratio ν by compressing a rubber specimen

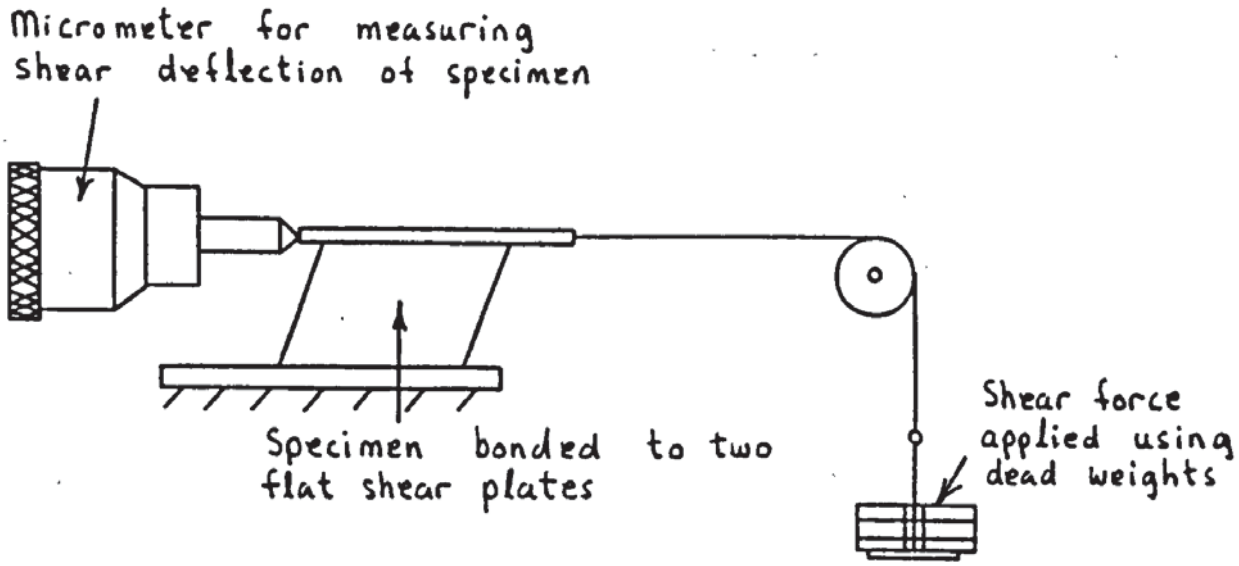

Figure 2.21 Shear modulus tester: Rightmire (63)

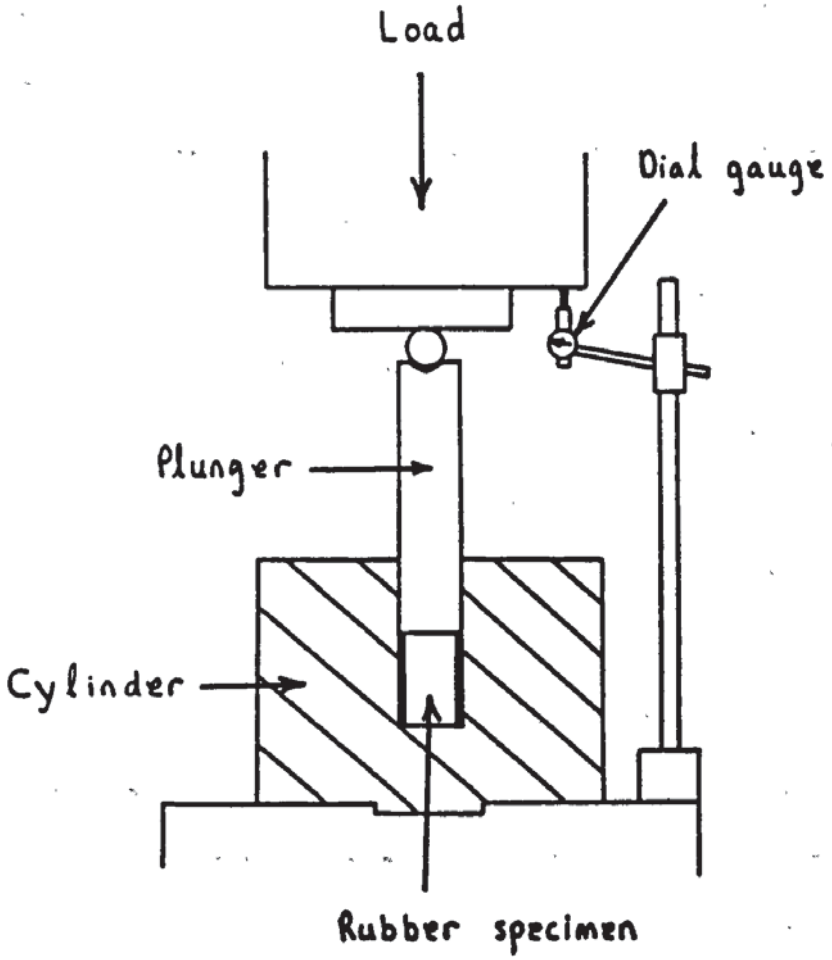

Figure 2.22 Bulk modulus tester:
Holownia (64), (65)

in a cylinder using a plunger (see figure 2.22). Values of bulk modulus K and Young's Modulus E were obtained from this apparatus for rubbers with different carbon black filler contents. The value of ν was derived from E and K (see section 4.4.2).

Stanojevic and Lewis (66) carried out a comparative study of the two test methods by Rightmire and Holownia and found that both methods gave reproducible results for bulk modulus K, to within 3%. However the cylinder and plunger method used by Holownia was prefered due to its practical ease of operation compared with Rightmires method.

Whilst it is possible to determine a value of ν from any two combinations of material elastic constants E, G and K, it was shown (66) by error analysis (refer also to section 4.4.2) that if values of E and G are used large errors in ν could occur. However for combinations E and K and also G and K, small errors would occur in ν , particularly as its value approached 0.5. For example (66) a 10% and 20% error in E and K respectively would produce an error of 0.3% in ν if this value were 0.495.

Although Stanojevic and Lewis acknowledge the way in which Holownia measures Young's modulus E and estimate an accuracy of 10% using this method, the shear modulus test of Rightmire was ignored. Rightmire estimated an accuracy of 3% for measuring shear modulus G and this would further improve the resulting accuracy in the value of Poisson's ratio ν obtained from using the combination G and K instead

of E and K. It would therefore seem appropriate to compare the values of Poisson's ratio ν obtained from both E and K and G and K measurements and this is done in section 5.3.3.

From this short review of literature on elastomer material properties the following can be summarized;

(a) The elastomer is a homogeneous and isotropic material provided its filler content does not exceed approximately 20%.

(b) Perfect linear - elasticity may be assumed for small strains up to approximately 10% and provided the elastomer is cycle loaded 10 times before testing or use.

(c) Due to the high accuracy required for Poisson's ratio it will be necessary to measure this directly from samples of rubber used for the bearing elastomer layer. The method of Holownia (64, 65) will be used to measure bulk modulus K and Young's modulus E, due to its practical simplicity. However measurements of shear modulus G will also be carried out using the shear tester by Rightmire (63). A comparison of ν derived from E and K and G and K will be made.

This completes the literature review as part of this research project. The areas of investigation will now be defined.

2.3 OUTLINE FOR THE AREAS OF INVESTIGATION

From section 2.2 the gaps in the knowledge and conflicts of opinion in the literature reviewed, in addition to proposals made, can be summarized as follows:

(a) A porous and compliant aerostatic thrust bearing; experimental and theoretical analysis to compare the performance of this new bearing with those of its predecessors the porous aerostatic thrust bearing and the compliant aerostatic thrust bearing.

(b) The existence or not of three distinct regions of flow in the porous pad as suggested by Taylor and Lewis (9) and the criteria of McGrea and Donaldson (10) for only one region of flow.

(c) The pore blockage due to surface machining operations to the porous pad; will this effect the flow through porous pad as suggested by Polome and Gorez (12)? Is the chemical etching technique used by Taylor and Lewis (9) sufficient to remove this pore blockage or will other methods such as electro - polishing (7), give better results.

(d) Consideration to the elastic support for deflections in bending of the porous pad.

(e) Experimental analysis of porous aerostatic thrust bearing stability. This could be extended to the porous and compliant aerostatic thrust bearing proposed in this research project.

(f) A new mathematical model for the deflections of the elastomer layer which extends the simple column model of Dowson and Taylor (56). This model should be suitable for elastomer layers of finite or infinite radial extent and for Poisson's ratio in the range 0 to 0.5. Also it must be suitable for application in more complex bearing problems such as the porous and compliant aerostatic thrust bearing proposed in this research project.

(g) The effect of a compensating element on compliant thrust bearing performance. In this respect the porous pad could be considered as a form of compensation.

(h) A comparison of the accuracy in determining Poisson's ratio using either shear or Young's modulus with bulk modulus for the elastomer layer.

It will be the objective of this research project to attempt a fulfilment of all aspects listed in this section.

CHAPTER 3

THEORETICAL ANALYSIS

3.1 INTRODUCTION

In this chapter a mathematical model and the solution of this model for the porous and compliant circular aerostatic thrust bearing described in chapter 1, will be presented. This will enable the bearing performance to be predicted.

The model may be sub - divided into two groups of equations as follows:

(a) The lubrication equations; these govern the compressible flow within the porous pad and the bearing film clearance. Consideration must be given to a non - uniform bearing clearance caused by defections of the compliant surface and the porous pad.

(b) The elasticity equations; these equations will predict (i) deflections of the compliant surface due to film pressures and (ii) deflections of the porous pad due to the pressure drop across its thickness.

The lubrication equations and methods of solution by Jones et al (23) and Taylor (24) for a porous aerostatic thrust bearing will be used. It was shown by Taylor and Lewis (9) that the analytic solution of Jones et al (23) gave accurate predictions for the performance of a porous

aerostatic thrust bearing with rigid bearing surfaces and a uniform bearing clearance. Though this solution cannot be applied to the non - uniform bearing clearance cases, it will be useful for a theoretical comparison between the porous and compliant aerostatic thrust bearing of this research project and the porous aerostatic thrust bearing with a uniform bearing clearance. It can also be used to obtain a first estimate of the pressures in the bearing clearance, for a numerical solution to the lubrication equations by Taylor (24). This numerical solution is suitable for non - uniform bearing clearances (25) and may therefore be used in the mathematical modelling of the porous and compliant aerostatic thrust bearing. Taylor (24) showed that this numerical solution gave accurate results when compared to the analytic solution of Jones et al (23) for a porous aerostatic thrust bearing with a uniform bearing clearance, hence verifying the numerical solution. Both these solutions by Jones et al (23) and Taylor (24) will be described in more detail in section 3.3.

With regard to the elasticity equations for deflections of the compliant surface a description of various solutions by other researchers is given in section 3.4.3. This then forms a background to the authors own solution presented in sections 3.4.4 and 3.4.5. Also, as mentioned in sections 2.2.2 and 2.2.3, although Taylor and Lewis (25) obtained equations for the deflections in bending of the porous pad due to the pressure drop across its thickness, these were

for a pad supported rigidly around its circumference. Therefore a new solution is presented in section 3.5 allowing for the elastic support of the porous pad which the author considers is a more accurate model for deflections of the porous pad.

To predict the performance of the bearing the solutions obtained from the lubrication equations and the elasticity equations must be coupled together. An iterative technique is used to match film pressures and the bearing clearance geometry with deflections of the compliant surface and the porous pad. This technique is described in section 3.6.

3.2 THE LUBRICATION EQUATIONS

The bearing configuration and the co - ordinate system used for analysis in this section are shown in figure 3.1.

3.2.1 ASSUMPTIONS FOR FLOW IN THE POROUS PAD

These are as follows:

(i) The flow in the porous pad is viscous dominated and governed by Darcy's law;

$$\frac{\partial p}{\partial r,z} = -\left(\frac{\eta}{\phi_{r,z}}\right).v_{r,z} \qquad 3.1$$

(ii) While the viscous permeabilities Φ_r and Φ_z in

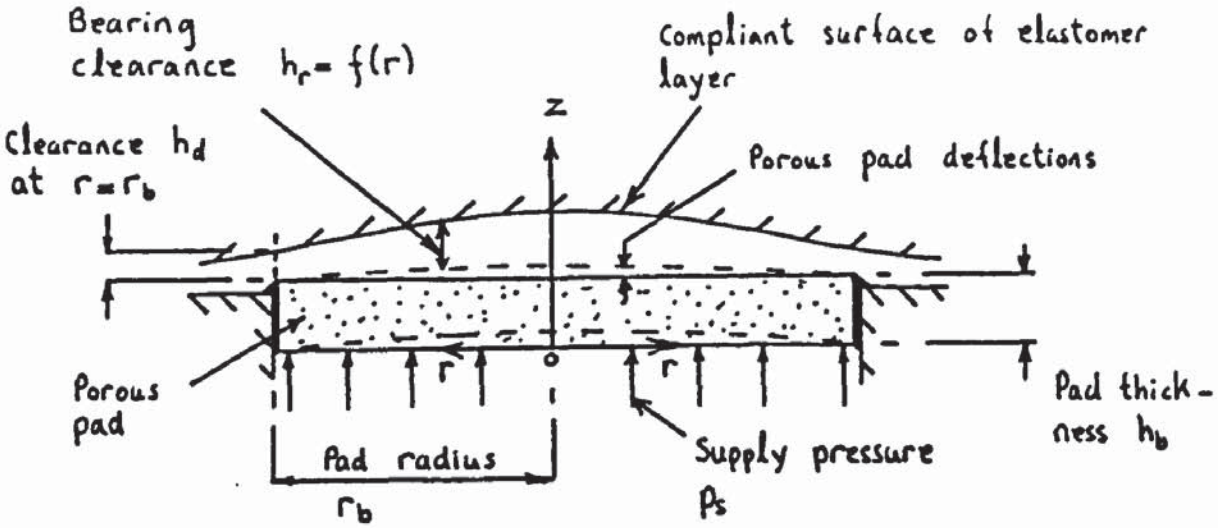

Figure 3.1 Bearing configuration for lubrication equations

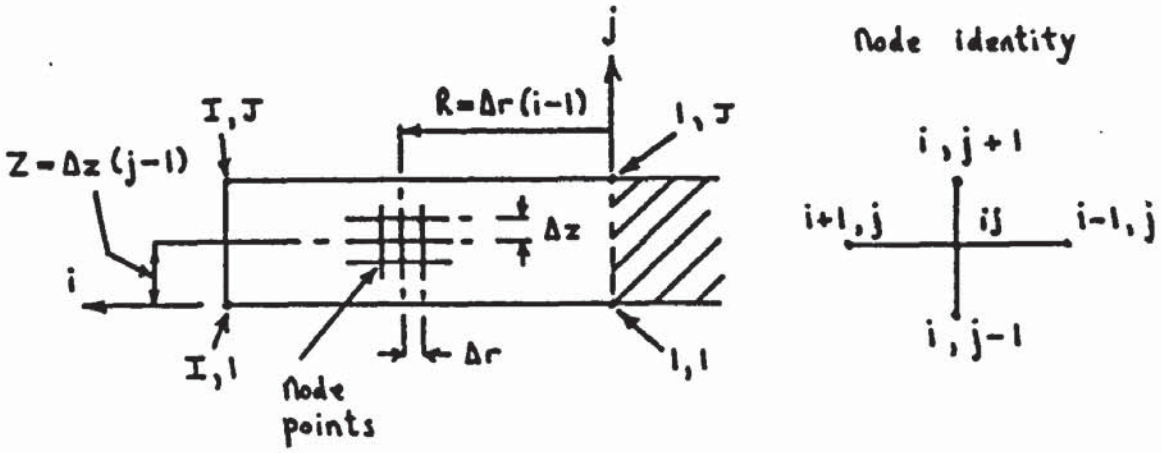

Figure 3.2 Porous pad finite difference discretisation

equation 3.1 may not be equal they are constant for each porous pad.

(iii) The lubricant is compressible and obeys the perfect gas equation of state;

$$\frac{p}{\rho} = R_{gas}.T \qquad 3.2$$

(iv) The flow is isothermal, i.e. T = constant in equation 3.2 and isoviscous, i.e. η = constant in equation 3.1.

(v) No swirl of flow takes place in the θ direction and the flow is axisymmetric about the axis r = 0.

(vi) The bearing is operating in a stable and steady state condition.

3.2.2 GENERAL DIFFERENTIAL EQUATION FOR FLOW IN THE POROUS PAD

The continuity equation for compressible flow is:

$$\frac{1}{r}.\frac{\partial(\rho.v_r.r)}{\partial r} + \frac{\partial(\rho.v_z)}{\partial z} = 0 \qquad 3.3$$

From Darcy's law, equation 3.1:

$$v_r = -\frac{\phi_r}{\eta}.\frac{\partial p}{\partial r} \qquad 3.4$$

and

$$v_z = -\frac{\Phi_z}{\eta}.\frac{\partial p}{\partial z} \qquad 3.5$$

Substituting equations 3.4 and 3.5 into equation 3.3 and using equation 3.2 gives;

$$\frac{1}{r}.\frac{\partial}{\partial r}\left(\frac{p}{R_{gas}.T}.\frac{\Phi_r}{\eta}.\frac{\partial p}{\partial r}.r\right) + \frac{\partial}{\partial z}\left(\frac{p}{R_{gas}.T}.\frac{\Phi_z}{\eta}.\frac{\partial p}{\partial z}\right) = 0 \qquad 3.6$$

The constants R_{gas} , T, η , Φ_r and Φ_z can be taken out of the differential brackets. Also since $2p\partial(p)=\partial(p^2)$ equation 3.6 may be written:

$$\frac{\Phi_r}{r}.\frac{\partial}{\partial r}\left(r.\frac{\partial(p^2)}{\partial r}\right) + \Phi_z.\frac{\partial}{\partial z}\left(\frac{\partial(p^2)}{\partial z}\right) = 0 \qquad 3.7$$

Equation 3.7 is the general differential equation for steady flow in the porous pad. It applies in the region r = 0 to r_b and z = 0 to h_b.

3.2.3 ASSUMPTIONS FOR FLOW IN THE BEARING CLEARANCE

These additional assumptions to those already mentioned in section 3.2.1 are as follows:

(vii) The flow is viscous, inertia effects are neglected.

(viii) Only pressure and velocity gradients in the radial direction are considered. The pressure across the bearing clearance is assumed constant.

(ix) By continuity, the velocity of flow across the porous pad - bearing clearance interface is constant.

(x) The bearing film pressures are equal to the pressures within the porous pad at the porous pad - bearing clearance interface.

(xi) The velocity of flow at the compliant surface is zero.

Assumption (ix) is similar to that used by Ishizawa and Hori (20) to account for the slip flow that takes place along the porous pad - bearing clearance interface (see figure 2.5 of section 2.2.2) and the injection of flow into the bearing clearance from the porous pad.

3.2.4 MODIFIED REYNOLDS EQUATION FOR FLOW IN THE BEARING FILM CLEARANCE

For flow within the bearing clearance consideration must be given to the injection of flow from the porous pad and the slip flow taking place at the porous pad - bearing clearance interface. The injection of flow from the porous pad is given by Darcy's law:

$$v_z = -\frac{\phi_z}{\eta}\cdot\frac{\partial p}{\partial z}\bigg|_{z=h_b} \qquad 3.8$$

and similarly for the slip flow:

$$v_r = -\frac{\phi_r}{\eta}.\frac{\partial p}{\partial r}\bigg|_{z=h_b} \qquad 3.9$$

From the assumptions in section 3.2.1 and 3.2.3, and using equations 3.8 and 3.9, Jones et al (23) obtained a modified Reynolds equation. For a non - uniform bearing clearance $h_r = f(r)$, this equation may be written as follows (25);

$$\frac{1}{r}.\frac{\partial}{\partial r}\left(r.\frac{\partial(p^2)}{\partial r}.(h_r^2 + 6.\phi_r).h_r \right) = 12.\phi_z.\frac{\partial(p^2)}{\partial z}\bigg|_{z=h_b} \qquad 3.10$$

Equation 3.10 applies in the region $r = 0$ to r_b and $z = h_b$ to $h_b + h_r$.

3.2.5 BOUNDARY CONDITIONS FOR FLOW IN THE POROUS PAD

While it may be possible to analyse the flow in both the porous pad and the bearing clearance and match the solutions at the porous pad - bearing clearance interface a simpler method adopted by both Jones et al (23) and Taylor (24) is to use the modified Reynolds equation (equation 3.10) as a boundary condition to flow in the porous pad. Equation 3.7 which governs flow in the porous pad is a second - order differential equation which requires four

boundary conditions. These are as follows:

(i) The supply pressure to the porous pad is constant and therefore at $z = 0$, $r = 0$ to r_b, $p = p_s$.

(ii) Since the flow is axisymmetric about the bearing axis then at $r = 0$, $z = 0$ to h_b; $\frac{\partial p}{\partial r}=0$.

(iii) The porous pad is sealed around its circumference so that $v_r = 0$ there. Therefore at $r = r_b$, $z = 0$ to h_b from equation 3.4, $\frac{\partial p}{\partial r}=0$.

(iv) Along the boundary $r = 0$ to r_b, $z = h_b$ the modified Reynolds equation (equation 3.10) applies.

In addition to the above boundary conditions, equation 3.10 for flow in the bearing clearance also has a further two boundary conditions:

(v) The film pressure is equal to the ambient pressure at bearing clearance exit. Therefore $p_f = p_a$ at $r = r_b$, $z = h_b$ to $h_b + h_r$.

(vi) For axisymmetric flow in the bearing clearance $\frac{\partial p}{\partial r}=0$ at $r = 0$, $z = h_b$ to $h_b + h_r$.

3.2.6 NON - DIMENSIONAL DEFINITIONS FOR THE LUBRICATION EQUATIONS

The following non - dimensional definitions were used by Jones et al (23) and Taylor (24) for a porous aerostatic bearing with a rigid uniform bearing clearance:

Radial position $R = r/r_b$ 3.11

Axial position $Z = z/h_b$ 3.12

Non - dimensional pressure $P = p/p_a$ 3.13

Permeability ratio $K_v = \Phi_r/\Phi_z$ 3.14

Bearing aspect ratio $S_b = h_b/r_b$ 3.15

Bearing number $$\Lambda_u = \frac{12.r_b^2.\Phi_z}{h_b.h_u(h_u^2 + 6.\Phi_r)}$$ 3.16

Because the bearing clearance h_u is no longer uniform due to deflections of the compliant surface and the porous pad, it is necessary to introduce a local bearing number as follows:

Local bearing number $$\Lambda_r = \frac{12.r_b^2.\Phi_z}{h_b.h_r(h_r^2 + 6.\Phi_r)}$$ 3.17

where h_r is the local bearing clearance at radial position r.

Equations 3.7 and 3.10 in non- dimensional form become:

$$\frac{S_b^2.K_v}{R}.\frac{\partial}{\partial R}\left(R.\frac{\partial(P^2)}{\partial R}\right) + \frac{\partial^2(P^2)}{\partial Z^2} = 0$$

for $0 \leq R \leq 1$, $0 \leq Z \leq 1$ 3.18

$$\frac{1}{R}.\frac{\partial}{\partial R}\left(\frac{R}{\Lambda_r}.\frac{\partial(P^2)}{\partial R}\right) = \left(\frac{\partial(P^2)}{\partial Z}\right)_{Z=1}$$

for $0 \leq R \leq 1$, $Z = 1$ 3.19

The boundary conditions (i) to (v) of section 3.2.5, in non - dimensional form become;

(i) $P = P_s$ at $Z = 0$, $R = 0$ to 1 3.20

(ii) $\frac{\partial P}{\partial R} = 0$ at R = 1, Z = 0 to 1 3.21

(iii) $\frac{\partial P}{\partial R} = 0$ at R = 1, Z = 0 to 1 3.22

(iv) Equation 3.19 applies at Z = 1, R = 0 to 1 3.23

(v) P = 1 at R = 1, Z = 1 3.24

Note that boundary condition (vi) of section 3.2.5 in non - dimensional form is similar to boundary condition 3.21.

3.3 SOLUTIONS TO THE LUBRICATION EQUATIONS

3.3.1 ANALYTIC SOLUTION BY JONES ET AL (23) FOR A UNIFORM BEARING CLEARANCE

For a uniform bearing clearance, the bearing number as defined by equation 3.16 can be used and since this is a constant, equation 3.19 can be written as follows:

$$\frac{1}{R}\cdot\frac{\partial}{\partial R}\left(R.\frac{\partial(P^2)}{\partial R}\right) = A_u.\left(\frac{\partial(P^2)}{\partial Z}\right)_{Z=1} \qquad 3.25$$

Using the separation of variables method Jones et al (23) showed that a solution to equation 3.18 can be expressed using Bessel functions in the form:

$$P^2 = (A_1 J_0(\beta R) + A_2 K_0(\beta R)).(B_1\cosh(\lambda Z) + B_2\cosh(\lambda Z)) \qquad 3.26$$

where $\beta = \lambda/S_b$

To satisfy boundary condition 3.21 this equation reduces to:

$$P^2 = J_0(\beta R).(C_1\cosh(\lambda Z) + C_2\sinh(\lambda Z)) \qquad 3.27$$

By using boundary conditions 3.20 and 3.22 the following expression was obtained:

$$P^2 = P_s^2 + C_2 Z + \sum_{n=2}^{\infty} C_{n2}.\sinh(\lambda_n Z)J_0(k_n R) \qquad 3.28$$

where k_n (n = 1,2,etc.) are the roots of the equation

$$J_1(k_n) = 0 \qquad 3.29$$

$$\lambda_n = k_n.S_b.\sqrt{K_v} \qquad 3.30$$

Equation 3.28 is differentiated with respect to Z and the value of the derivative obtained at Z = 1. The result is substituted into equation 3.25 which is subsequently integrated twice with respect to R to obtain an expression for P . The constants of integration are evaluated from boundary conditions 3.21 and 3.24 and the following solution was obtained for the pressure squared in the porous pad at Z = 1:

$$P^2 = 1 + \frac{\Lambda_u . C_2 . (R^2-1)}{4} + \Lambda_u \sum_{n=2}^{\infty} \lambda_n C_{n2} \left(\frac{J_0(k_n)}{k_n^2} - J_0(k_n . R) \right) \cosh(\lambda_n) \quad 3.31$$

Equations 3.28 and 3.31 are equated at Z = 1 to obtain expressions for constants C_2 and C_{n2} i.e;

$$C_{n2} = \frac{\Lambda_u . C_2}{J_0(k_n).(k_n^2 \sinh(\lambda_n) + \Lambda_u . \lambda_n . \cosh(\lambda_n))} \quad 3.32$$

$$C_2 = \frac{P_s^2 - 1}{\Lambda_u^2 \sum_{n=2}^{\infty} E_n - \frac{\Lambda_u}{8} - 1} \quad 3.33$$

where $$E_n = \frac{\lambda_n}{k_n^2 . (\Lambda_u . \lambda_n + k_n^2 . \tanh(\lambda_n))} \quad 3.34$$

Equation 3.31 gives the bearing film pressures at Z = 1. Details of a programme to evaluate this equation are given in appendix 1.

3.3.2 THE NUMERICAL FINITE DIFFERENCE SOLUTION OF TAYLOR (24)

Taylor (24) presented a second solution to the lubrication equations by finite difference methods using the Roscoe technique (26). Later Taylor and Lewis (25) showed in their study of porous pad deflections on bearing

performance that this solution is applicable to the non - uniform bearing clearance case.

The Roscoe technique is a method of discretising differential equations for a finite difference solution, which when applied to equations of a similar form to 3.18 and 3.19, ensure a valid and stable solution.

For a differential equation of the form:

$$D_1.\frac{\partial^2\xi}{\partial R^2} + D_2.\frac{\partial\xi}{\partial R} + D_3.\frac{\partial^2\xi}{\partial Z^2} = 0 \qquad 3.35$$

the Roscoe technique gives the following discretised equation:

$$\frac{D_2}{\Delta r(1 - e^{-D_2\Delta r/D_1})}.(\xi_{i+1,j} - \xi_{i,j}.(1 + e^{-D_2\Delta r/D_1}) + \xi_{i-1,j}.e^{-D_2\Delta r/D_1})$$

$$+ \frac{D_3}{(\Delta z)^2}.(\xi_{i,j+1} - 2.\xi_{i,j} + \xi_{i,j-1}) = 0 \qquad 3.36$$

Let the porous pad be discretised as shown in figure 3.2. The first term in equation 3.18 may be expanded as follows:

$$\frac{\partial}{\partial R}.\left(R\,\frac{\partial(P^2)}{\partial R} \right) = R\,\frac{\partial^2(P^2)}{\partial R^2} + \frac{\partial(P^2)}{\partial R} \qquad 3.37$$

Substituting this expansion back into equation 3.18 gives:

$$S_b^2.K_v.\frac{\partial^2(P^2)}{\partial R^2} + \frac{S_b^2.K_v}{R}.\frac{\partial(P^2)}{\partial R} + \frac{\partial^2(P^2)}{\partial Z^2} = 0 \qquad 3.38$$

Equation 3.38 is of a similar form to equation 3.35 where:

$$D_1 = S_b^2.K_v \ , \ D_2 = \frac{S_b^2.K_v}{R} \ , \ D_3 = 1 \text{ and } \xi = P^2$$

Therefore the discretised form of equation 3.18 is:

$$\frac{S_b^2.K_v}{(\Delta r)^2.(i+1).(1-e^{-1/(i-1)})}.(P^2_{i+1,j} - P^2_{i,j}.(1+e^{-1/(i-1)}) + P^2_{i-1,j}.e^{-1/(i-1)})$$

$$+ \frac{(P^2_{i,j+1} - 2.P^2_{i,j} + P^2_{i,j-1})}{(\Delta z)^2} = 0 \qquad 3.39$$

Similarly equation 3.19 in discretised form becomes:

$$\frac{F_1}{\Delta r.(1-e^{-(F_1.\Delta r/\alpha)})}.(P^2_{i+1,j} - P^2_{i,j}.(1+e^{-(F_1.\Delta r/\alpha)}) + P^2_{i-1,j}.e^{-(F_1.\Delta r/\alpha)})$$

$$= \left. \frac{P^2_{i,j} - P^2_{i,j-1}}{\Delta z} \right|_{j = J} \qquad 3.40$$

where $$F_1 = \frac{\alpha}{R} + \frac{d\alpha}{dR} \qquad 3.41$$

$$\alpha = \frac{1}{\Lambda_r} \qquad 3.42$$

$$\text{therefore;} \quad \frac{d\alpha}{dR} = h_b \cdot \left(3.h_r^2 \frac{dh_r}{dr} + 6.\Phi_r \frac{dh_r}{dr} \right) \qquad 3.43$$

$$\text{and} \quad \frac{\alpha}{R} = \frac{1}{\Lambda_r . \Delta r . (i - 1)} \qquad 3.44$$

Values of h_r and dh_r/dr are taken at each node i for i = 1 to I, j = J. The boundary conditions 3.20 to 3.24 become:

(i) $P_{i,j} = P_s$ at j = 1, i = 1 to I 3.45

(ii) $P_{i+1,j} - P_{i-1,j} = 0$ at i = 1, j = 1 to J 3.46

(iii) $P_{i+1,j} - P_{i-1,j} = 0$ at i = I, j = 1 to J 3.47

(iv) Equation 3.40 applies at j = J, i = 1 to I. 3.48

(v) P = 1 at j = J, i = I 3.49

An iterative procedure for a numerical solution using equations 3.39 to 3.49 is described by Taylor (24). This solution gives the bearing film pressures at each node i, j = J.

In a comparison of results with the analytic solution of Jones et al (23) (section 3.3.1), Taylor (24) showed that the numerical solution gave an accuracy of 2.515% for the film pressures. The numerical equations 3.39 to 3.49, therefore give a valid solution to the lubrication equations. These equations will be used in a solution to the porous and compliant aerostatic thrust bearing where the bearing clearance is non - uniform i.e. $h_r = f(r)$.

3.4 THE ELASTICITY EQUATIONS FOR DEFLECTIONS OF THE COMPLIANT SURFACE

The elastomer layer configuration and co - ordinate system for analysis are shown in figure 3.3.

3.4.1 GENERAL ASSUMPTIONS

The general assumptions for analysis of the elastomer layer are as follows:

(i) The elastomer layer is circular and of uniform thickness in the undeformed state.

(ii) The elastomer material is isotropic, homogeneous and behaves linear - elastically for small strains in the order of 10%.

(iii) Deflections and stresses applied at the compliant surface will be axisymmetric.

(iv) The elastomer layer will be statically loaded.

(v) Body forces such as gravity will be ignored. These are insignificant compared to the bearing film pressures.

(vi) A perfect bond exists between the elastomer layer and its rigid backing. Therefore displacements u_r and u_z at $z = 0$ will be zero.

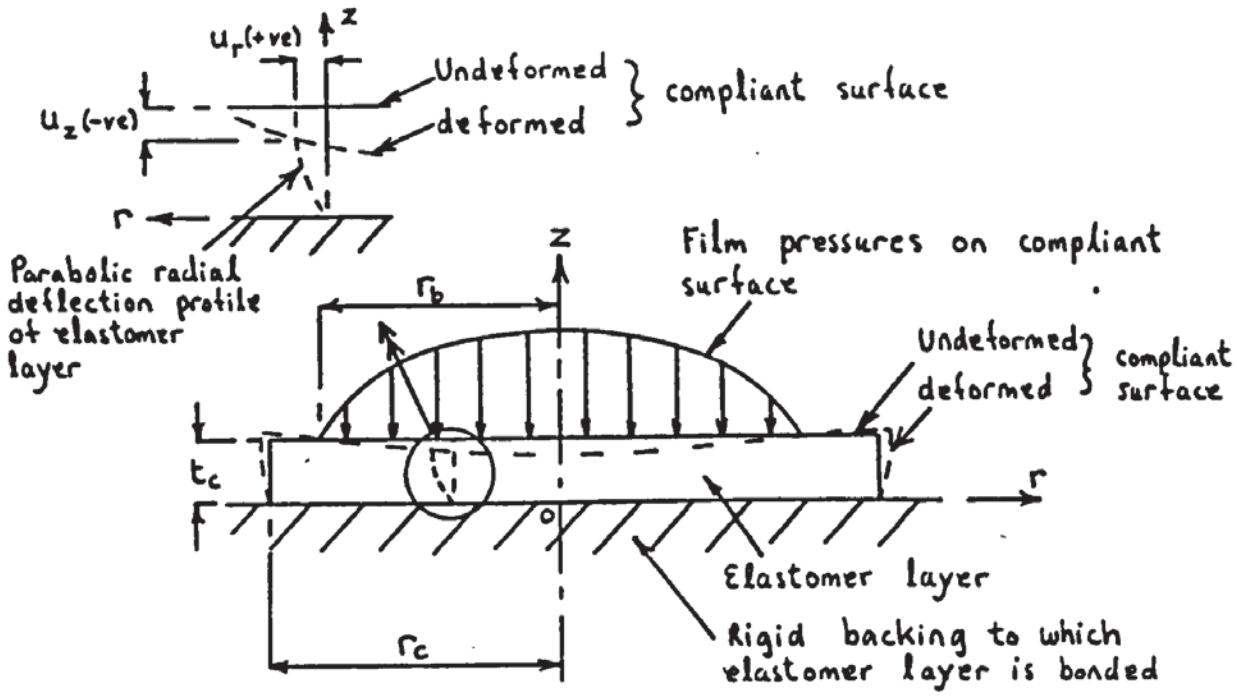

Figure 3.3 Elastomer layer configuration

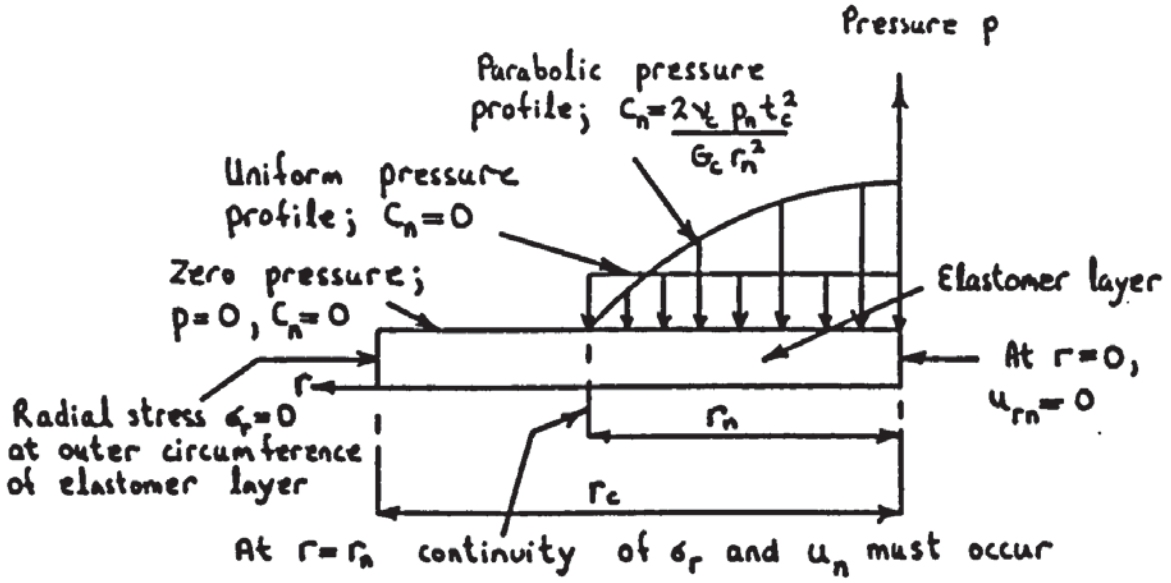

Figure 3.4 Boundary conditions for analysis of elastomer layer deflections

3.4.2 GENERAL ELASTICITY EQUATIONS FOR AN AXIALLY SYMMETRICAL STRESS DISTRIBUTION IN AN ELASTIC BODY

The equilibrium equations in polar co - ordinates, ignoring inertia and body forces are (85):

$$\left.\begin{aligned} \frac{\partial \sigma_r}{\partial r} + \frac{\partial \tau_{rz}}{\partial z} + \frac{\sigma_r - \sigma_\theta}{r} &= 0 \\ \frac{\partial \tau_{rz}}{\partial r} + \frac{\partial \sigma_z}{\partial z} + \frac{\tau_{rz}}{r} &= 0 \end{aligned}\right\} \qquad 3.50$$

For a linearly - elastic isotropic homogeneous material the stress - strain relationships are:

$$\left.\begin{aligned} \varepsilon_\theta &= \frac{1}{E_c}(\sigma_\theta - \nu_c(\sigma_r + \sigma_z)) \\ \varepsilon_r &= \frac{1}{E_c}(\sigma_r - \nu_c(\sigma_\theta + \sigma_z)) \\ \varepsilon_z &= \frac{1}{E_c}(\sigma_r - \nu_c(\sigma_\theta + \sigma_r)) \end{aligned}\right\} \qquad 3.51$$

The strains are related to displacements of the elastic body by the following equations:

$$\left.\begin{aligned} \varepsilon_r &= \frac{\partial u_r}{\partial r} \\ \varepsilon_\theta &= \frac{u_r}{r} \\ \gamma_{rz} &= \frac{\partial u_r}{\partial z} + \frac{\partial u_z}{\partial r} \end{aligned}\right\} \qquad 3.52$$

It is sometimes convenient to use a stress function Ψ in order to obtain a solution which satisfies equations 3.50. The stresses σ_r , σ_z , σ_θ and τ_{rz} may be expressed in terms of Ψ by the following equations (85):

$$\left.\begin{aligned} \sigma_r &= \frac{\partial}{\partial z}\left(\nu.\nabla^2\Psi - \frac{\partial^2\Psi}{\partial r^2} \right) \\ \sigma_\theta &= \frac{\partial}{\partial z}\left(\nu.\nabla^2\Psi - \frac{1}{r}\frac{\partial\Psi}{\partial r} \right) \\ \sigma_z &= \frac{\partial}{\partial z}\left((2-\nu).\nabla^2\Psi - \frac{\partial^2\Psi}{\partial z^2} \right) \\ \tau_{rz} &= \frac{\partial}{\partial r}\left((1-\nu).\nabla^2\Psi - \frac{\partial^2\Psi}{\partial z^2} \right) \end{aligned}\right\} \qquad 3.53$$

Equations 3.53 satisfy the equilibrium equations 3.50 provided the stress function Ψ satisfies the so called compatability equation. This equation in terms of stresses using equations 3.51, 3.52 and 3.53 is (85):

$$\nabla^2.\nabla^2\Psi = 0 \qquad 3.54$$

$$\text{where } \nabla^2 = \frac{\partial^2}{\partial z^2} + \frac{1}{r}\frac{\partial}{\partial r} + \frac{\partial^2}{\partial r^2} \qquad 3.55$$

In a solution using the stress function Ψ, equation 3.54 must be satisfied. The stress function Ψ must also satisfy the boundary conditions at the surface of the elastic body.

3.4.3 VARIOUS SOLUTIONS TO THE ELASTICITY EQUATIONS

There are several different methods by which the elasticity equations in section 3.4.2 can be solved. These are described as follows:

(i) THE SIMPLE COLUMN MODEL: Dowson and Taylor (56) assumed that strains in the r and θ directions are zero. Using equations 3.51 and for axial strain $\epsilon_z = u_c/t_c$ the following equation was obtained for deflections of the compliant

surface due to a pressure p:

$$u_c = - \frac{p.t_c}{E_c} \left(1 - \frac{2.\nu_c^2}{1 - \nu_c} \right) \qquad 3.56$$

The deflection of the elastomer layer using equation 3.56 is analogous to the compression of a bed of unconnected springs, each one depressing according to the pressure applied to it. The elastic modulus of each spring is given by:

$$\frac{1}{E_c'} = \frac{1}{E_c} \left(1 - \frac{2.\nu_c^2}{1 - \nu_c} \right) \qquad 3.57$$

and its deflection is:

$$u_c = - \frac{p.t_c}{E_c'} \qquad 3.58$$

As already mentioned in section 2.2.4 this solution is unsuitable when Poisson's ratio ν_c of the elastomer is equal to 0.5, since equation 3.56 predicts zero deflection for this case. However this solution is attractive in its simplicity and Castelli et al (59) showed that reasonable accuracy could be obtained for Poisson's ratio ν_c in the range 0 to 0.45.

(ii) ANALYTIC SOLUTIONS: In these solutions an attempt is made to define the stress function Ψ. Along each boundary of the elastic body at least two conditons must be specified. In the case of a circular elastomer layer, this may be a deflection or stress in the r and z directions. Therefore a total of six boundary conditions must be satisfied by the stress function Ψ. This would lead to a very complex and unmanageable equation defining Ψ (61). To avoid this problem Castelli et al (59) assume an elastomer layer of infinite radial extent. This reduces the number of required boundary conditions to four. The following stress function was proposed:

$$\Psi = \left[(G_1 + G_2 z).\sinh(nz) + (G_3 + G_4 z).\cosh(nz)\right] J_0(nr) \qquad 3.59$$

which satisfies equation 3.54. The constants G_1, G_2, G_3 and G_4 were determined from the following boundary conditions:

(a) From assumption (vi) in section 3.4.1, both defections u_r and u_z are zero at $z = 0$, the interface between the elastomer layer and its rigid backing.

(b) Shear stresses from the lubricating bearing film acting along the compliant surface are negligible, hence $\tau_{rz} = 0$ at $z = t_c$.

(c) Pressure stress along the compliant surface assumes the form of a Bessel function, i.e. $p = J_0(nr)$ at $z = t_c$.

The resulting solution gave the deflection of the

compliant surface due to a pressure distribution in the form of a Bessel function $J_o(nr)$. This is known as the elementary solution and to obtain a solution to the actual film pressure profile, the elementary solutions are superimposed one on top of the other until their summation closely approximates the film pressures. The resulting deflection of the compliant surface was then equated to the summation of deflections from each elementary solution. The final solution involved an integral which was solved numerically.

(iii) NUMERICAL FINITE DIFFERENCE AND FINITE ELEMENT SOLUTIONS: In these solutions the elastic body is discretized into a grid pattern. Otter et al (86) describes a finite difference solution to the elasticity equations using dynamic relaxation. The equilibrum equations 3.50, including a time dependant term become:

$$\left.\begin{aligned} \frac{\partial \sigma_r}{\partial r} + \frac{\partial \tau_{rz}}{\partial z} + \frac{\sigma_r - \sigma_\theta}{r} &= \rho\left(\frac{\partial u_r}{\partial t} + \frac{k_1 . u_r}{\Delta t}\right) \\ \frac{\partial \sigma_z}{\partial z} + \frac{\partial \tau_{rz}}{\partial r} + \frac{\tau_{rz}}{r} &= \rho\left(\frac{\partial u_z}{\partial t} + \frac{k_1 . u_z}{\Delta t}\right) \end{aligned}\right\} \qquad 3.60$$

where k_1 is a damping factor for convergence in the numerical solution.

It is important to note however that although dynamic

relaxation is used, the object was to obtain solutions to a static stress and displacement problem. Initial estimates of stress or displacement within the elastic body are dynamically damped to converge on the final solution. Holownia (87) showed that this method of solution is satisfactory for Poisson's ratio very close to 0.5 but the computing time required increased rapidly as ν approached 0.5. Holownia does not give the computing times or the number of iterations required to converge on the final solution. However in a solution by Otter et al (86) for a concrete structure having a value of $\nu = 0.2$, 39 iterations were required to achieve an accuracy of less than 0.1%. This is a large number of iterations compared to that required for a finite difference solution to the lubrication equations in section 3.3.2 (these have required only 3 to 8 iterations to achieve an accuracy of 0.1% in P). And since the number of iterations increases as ν approaches 0.5, use of this dynamic relaxation method for deflections of the compliant surface in a coupled solution with the lubrication equations would require considerable computing time.

A finite element programme known as Texgap and suitable for rubber like materials is reported by Collins et al (88). While the Raleigh Ritz method is often used in finite element solutions, Benjamin (61) had found this method to be unsuitable for typical rubber like materials where ν approaches 0.5. In the Texgap programme the

elasticity equations are said to be reformulated so that the case $\nu = 0.5$ can be treated. Unfortunately further references relating to this Texgap programme have been unobtainable. However it is mentioned that the main disadvantage of a finite element solution for rubber, is the large computing times and memory allocation required for the mathematical manipulation and storage of the matrix equations.

It can be concluded therefore that a numerical finite difference or finite element solution for the elastomer layer in a coupled numerical solution to the lubrication equations as described in section 3.3.2 would be impractible because of the large computational times required.

(iv) GREEN'S FUNCTION APPROACH: This method was applied by Benjamin et al (61, 62) for the solution to a compliant thrust bearing with a central feed hole. The elastomer layer was of finite radial extent. The Green's function approach involves an elemental solution to the equilibrium equations 3.50 which contain unknown coefficients. These coefficients are determined by superimposing the elemental solutions such that they satisfy the boundary conditions at a fixed number of points along the boundary surface. An elemental solution was obtained such that the singularity occurring at $\nu_c = 0.5$ is removed. Deflections of the compliant surface are related to the film pressures by the matrix equation;

$$u_c(r)_i = \sum_{l=1}^{I} M_{i,l}(p)_l \qquad 3.61$$

where $(p)_l$ are the film pressures acting at any node along the compliant surface which results in a deflection $u_c(r)_i$ at node i also on the compliant surface. The determination of the matrix $M_{i,l}$ involves solving the elemental solutions such that they satisfy the boundary conditions one of which are the film pressures.

Compared to other numerical methods such as finite difference and finite element solutions, the Green's function approach is more efficient in terms of computer processing time. However in a similar way to finite element solutions it still requires the storage and mathematical manipulation of large matrix equations.

From this description of various solution methods to the elasticity equations in section 3.4.2 the following conclusions can be drawn:

(i) The simple column model of Dowson and Taylor (56) does not give sufficiently accurate results for Poisson's ratio in the range 0.45 to 0.5.

(ii) Of the more complex solutions the analytic solution of Castelli et al (59) requires the least computational time and memory allocation compared with the other numerical solutions. It is therefore ideally suited to a coupled solution involving the lubrication and elasticity equations

especially since the presence of a porous pad in a porous and compliant aerostatic thrust bearing makes the overall solution much more complex. However the main limitation of this solution is that only elastomer layers of infinite radial extent can be considered.

A simplified analytic solution to the elasticity equations in section 3.4.2 is therefore proposed and presented in section 3.4.4. This solution is suitable for any value of Poisson's ratio ν_c in the range 0 to 0.5 and is suitable for elastomer layers of any radial extent beyond the bearing radius r_b. The necessary computing time will be minized since this solution does not involve a numerical process. Hence this will enable a solution to the porous and compliant aerostatic thrust bearing proposed in this research project.

3.4.4 SIMPLIFIED SOLUTION FOR DEFLECTIONS OF THE ELASTOMER LAYER

In obtaining this simplified solution the following additional assumptions to those in section 3.4.1 are made:

(i) Shear stresses at the compliant surface due to flow in the bearing film are negligible compared to the film pressure stresses (59).

(ii) For a thin elastomer layer (i.e. $t_c/r_b <= 0.25$) only the first of the equilibrium equations 3.50 for stresses in a radial direction will be satisfied. The

second of these equations 3.50 for the equilibrum of stresses in z - direction will be ignored.

(iii) Also for a thin elastomer layer the axial stress σ_z as a function of z is constant through the thickness of the elastomer layer and equal to the pressure acting on the compliant surface at radius r.

(iv) Radial deflections of the elastomer layer have a parabolic form defined by the following equation:

$$u_r = u_{rn}\left(1 - \frac{(z - t_c)^2}{t_c^2}\right) \qquad 3.62$$

Equation 3.62 satisfies assumption (vi) in section 3.4.1 that $u_r = 0$ at $z = 0$.

(v) In the third of equations 3.52 for shear strain γ_{rz} deflection gradients $\frac{\partial u_z}{\partial r}$ are ignored compared to $\frac{\partial u_r}{\partial z}$

The reasoning behind assumptions (ii), (iii), (iv) and (v) are explained as follows. Consider a thin elastomer layer constrained against radial movement by a bond to a rigid surface. Typically its stiffness is at least an order of magnitude greater than the stiffness of an unbonded elastomer layer free to expand in a radial direction (84). It can be concluded therefore that this difference is attributed mainly to the forces or stresses acting in a radial direction, particularly for the bonded elastomer layer which is constrained in this direction. These forces or stresses are represented by the first of the equilibrium

equations 3.50. This then leads to assumption (ii).

Because the elastomer layer is thin compared to its radius it is reasonable to assume that the pressure acting on the compliant surface at a radial position r will be in equilibrium with an equal and opposite pressure acting from the rigid backing to the elastomer layer. This reasoning can be extended to the axial stress σ_z at any position z through the thickness of the elastomer layer, i.e. the axial stress σ_z must be in equilibrium with the pressure acting on the compliant surface. This therefore leads to assumption (iii) that the stress σ_z through the thickness of the elastomer layer is a constant and equal to the pressure acting on the compliant surface.

In the compression of a constrained cylindrical disc bonded between two parallel rigid plates, Gent and Lindley (89) made the following assumption. If horizontal planes perpendicular to the z - axis, remain undeformed during compression of the thin cylindrical disc, then the resulting radial deflection profile across its thickness will take up a parabolic form. The compression of an elastomer layer is similar to that of the constrained cylindrical disc where the thickness of the elastomer layer represents half the thickness of the cylindrical disc. Because axial deflections of the compliant surface are small compared to its thickness and no shear stresses act here (assumption (i)) this leads to assumption (iv).

For a thin bonded elastomer layer which is incompressible in nature, axial deflections at the compliant surface can cause considerable radial bulging and hence shear straining in the radial direction. This is because the volume displaced at the compliant surface virtually equals the volume displaced in a radial direction. The bulk shear strain γ_{rz} is therefore mainly attributed to shear deflections in the radial direction. These are represented by the strains $\frac{\partial u_r}{\partial z}$. This leads to assumption (v).

In appendix 2 it is shown that these assumptions lead to the following differential equation for u_{rn} ;

$$\frac{\partial^2 u_{rn}}{\partial r^2} + \frac{1}{r}\frac{\partial u_{rn}}{\partial r} - \left(k_c^2 + \frac{1}{r^2}\right)u_{rn} = \frac{\nu_c}{2.G_c}.\frac{\partial p_c}{\partial r} \qquad 3.63$$

Using modified Bessel functions (90) the particular integral to equation 3.63 is;

$$u_{rn} = A_n.I_1(k_c.r) + B_n.K_1(k_c.r) \qquad 3.64$$

Complimentary functions c.f. may be obtained for the following pressure profiles on the compliant surface:

(a) for $p_c = p_n$ i.e. a constant

$$c.f. = 0 \qquad 3.65$$

(b) for $p_c = p_n\left(1 - \left(\frac{r}{r_n}\right)^2\right)$ i.e. a parabola

$$c.f. = \frac{2.\nu_c.p_n.t_c^2.r}{G_c.r_n^2} \qquad 3.66$$

The complete solution to equation 3.63 may be expressed as:

$$u_{rn} = A_n.I_1(k_c.r) + B_n.K_1(k_c.r) + C_n.r \qquad 3.67$$

where $C_n = 0$ for a uniform pressure profile 3.68

and $C_n = \frac{2.\nu_c.p_n.t_c^2}{G_c.r_n^2}$ for a parabolic pressure profile 3.69

(Note that it is only coincidental that one of the special cases for which a c.f. to equation 3.63 is for a

parabolic pressure profile on the compliant surface. This should not be confused with assumption (iv) in this section relating to parabolic radial deflections within the elastomer layer.)

The constants A_n and B_n in equation 3.67 can be determined from the following boundary conditions:

$$u_{rn} = 0 \quad \text{at} \quad r = 0 \qquad 3.70$$

$$\sigma_r = 0 \quad \text{at} \quad r = r_c \qquad 3.71$$

However in the more general case where the pressure on the compliant surface has a radial extent $r_n <= r_c$, equation 3.67 is applied to two regions of the compliant surface. These are $0 <= r <= r_n$ and $r_n < r <= r_c$ (see figure 3.4).

hence for $0 <= r <= r_n$;

$$u_{rn} = A_{n1}.I_1(k_c.r) + B_{n1}.K_1(k_c.r) + C_n.r \qquad 3.72$$

and for $r_n < r <= r_c$;

$$u_{rn} = A_{n2}.I_1(k_c.r) + B_{n2}.K_1(k_c.r) \qquad 3.73$$

It will be noted in equation 3.73 that the third term of equation 3.67 has been obmitted. This is because in the region $r_n < r <= r_c$, $p_c = 0$ and hence $C_n = 0$ by equation 3.68.

The constants A_{n1}, A_{n2}, B_{n1} and B_{n2} are determined such

that the boundary conditions 3.70 and 3.71 are satisfied and continuity in the values of σ_r and u_{rn} is obtained at $r = r_n$. Equations for these constants are given in appendix 2.

The axial deflection u_{zn} of the compliant surface can be related to radial displacements u_{rn} using equations 3.51 and 3.52. It is shown in appendix 2 that this gives the following expressions for u_{zn}:

for the region $0 <= r <= r_n$,

$$u_{zn} = -\frac{(1 - 2.\nu_c).p_c.t_c}{2.G_c.(1 - \nu_c)} - \frac{2}{3}.\frac{t_c.\nu_c}{(1 - \nu_c)}.(k_c(A_{n1}.I_0(k_c.r) - B_{n1}.K_0(k_c.r)) + 2.C_n) \qquad 3.74$$

for the region $r_n < r <= r_c$,

$$u_{zn} = -\frac{2}{3}.\frac{t_c.\nu_c}{(1 - \nu_c)}.(k_c(A_{n2}I_0(k_c.r) - B_{n2}.K_0(k_c.r)) \qquad 3.75$$

Equations 3.74 and 3.75 represent an elementary solution for deflections of the compliant surface in the special cases of a uniform or parabolic pressure profile of radial extent $0 <= r_n <= r_c$. Figures 3.5 and 3.6 show typical deflection profiles obtained using these equations. The deflection profile shown in figure 3.5a for a uniform pressure profile $r_n = r_c$ is similar to that illustrated by

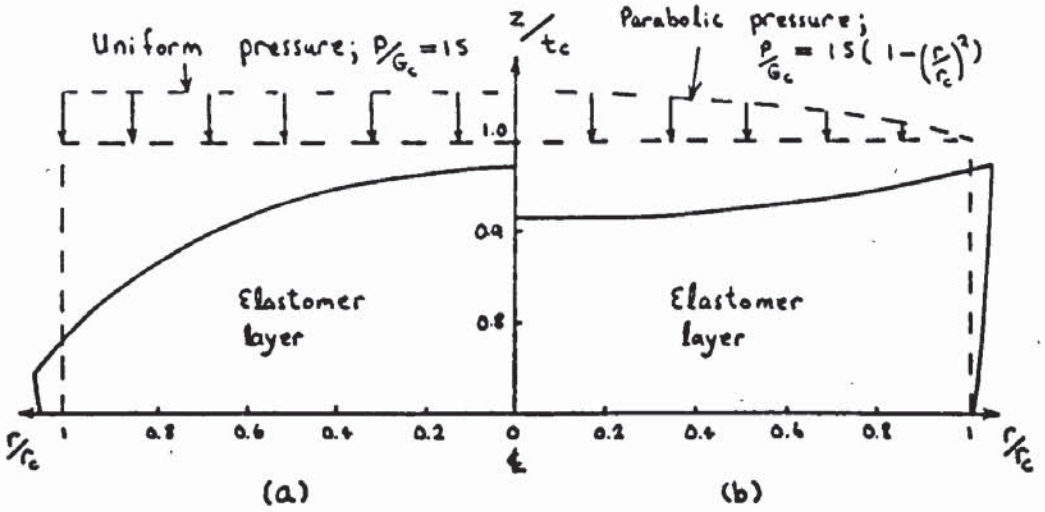

Figure 3.5 Deflections of the compliant surface for elementary solutions where $r_n/r_c = 1$, $\nu_c = 0.5$

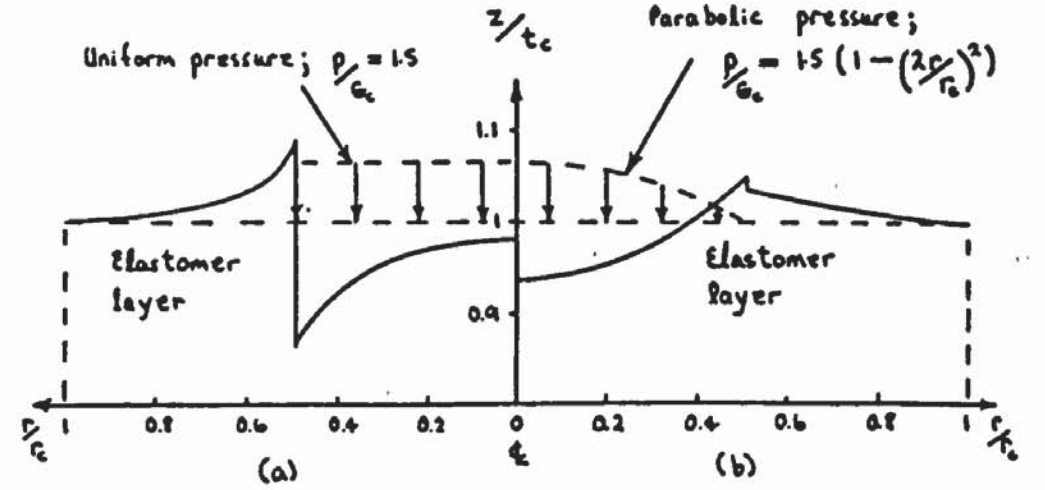

Figure 3.6 Deflections of the compliant surface for elementary solutions where $r_n/r_c = 0.5$, $\nu_c = 0.5$

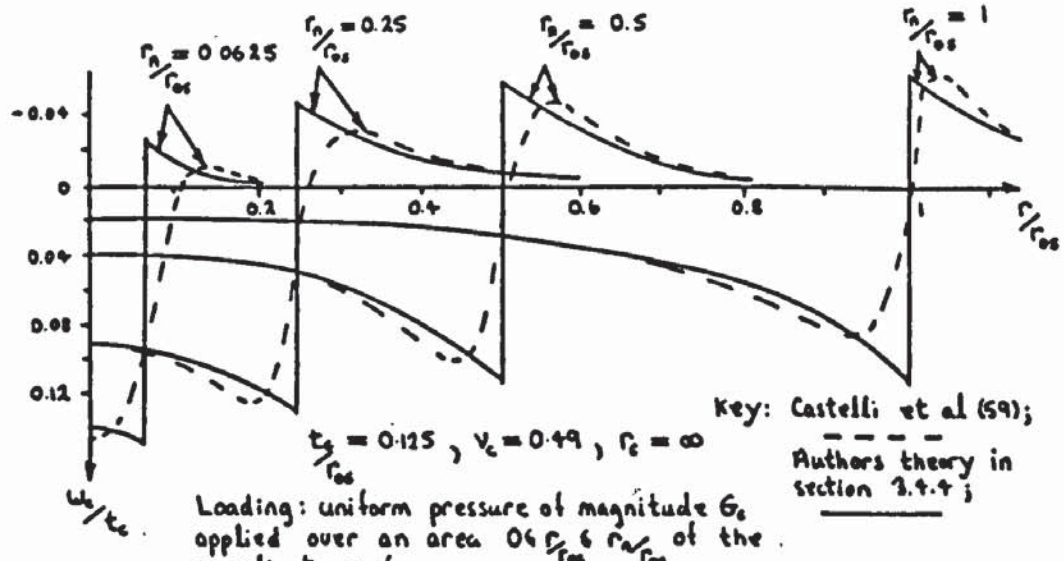

Figure 3.7 Comparison of theoretical results for deflections of the compliant surface with Castelli et al (59)

Rybricki et al (74). Note that the deflection of the compliant surface is greater at the edges than in the centre. This is an example of the unusual way in which incompressible materials can deform.

A comparison of results with those of Castelli et al (59) is also shown in figure 3.7. The deflection profiles are for uniform pressures applied over an area of radius r_n/r_{os} In general the deflection curves obtained by equations 3.74 and 3.75 compare well with those of (59) except in regions close to r_n/r_{os} This is because a discontinuity occurs here which is caused by assumptions (ii) and (v) in this section. Comparison between figure 3.6 a and b show that this discontinuity is reduced for the elementary solution to a parabolic pressure profile and hence the corresponding deflection profile is more accurate for this case.

It is interesting to note that equation 3.74 reduces to the simple column model of Dowson and Taylor (56) when ν_c approaches zero.

$$\text{i.e.} \quad u_{zn} = -\frac{(1 - 2.\nu_c).p_c.t_c}{2.G_c.(1 - \nu_c)} \qquad \text{as } \nu_c \to 0$$

and since for a linear - elastic, isotropic and homogeneous material (47), $E_c = 2.G_c.(1 + \nu_c)$ then;

$$u_{zn} = -\left(1 - \frac{2.\nu_c^2}{(1 - \nu_c)}\right)\frac{p_c.t_c}{E_c} \qquad 3.76$$

Equation 3.76 is similar to equation 3.56 for the simplified column model.

The first term on the R.H.S. of equation 3.74 therefore represents deflections of the compliant surface due to the bulk compressibility of the elastomer layer since in the column model by Dowson and Taylor (56) the strains ϵ_r and ϵ_θ are assumed zero. This term is zero when the elastomer layer material is incompressible, i.e. ν_c = 0.5. When this occurs deflections of the elastomer layer can only take place by radial shearing, i.e. the volume displaced by the elastomer layer in a radial direction is equal to the volume displaced by deflections of the compliant surface. This is represented by the second term on the R.H.S. of equation 3.74 and also the term on the R.H.S. of equation 3.75. In equation 3.75 radial shearing accounts for the total deflection of the compliant surface when $r > r_n$, since the pressure acting on the compliant surface here is zero. Equations 3.74 and 3.75 can therefore be considered as extensions of the restrained column model by Dowson and Taylor (56) to take into account strains ϵ_r and ϵ_θ due to radial shearing of the elastomer layer.

3.4.5 APPLICATION OF THE SIMPLIFIED SOLUTION TO THE ACTUAL FILM PRESSURE PROFILE

The elementary solutions obtained in section 3.4.4 are

for the special cases of a uniform or parabolic pressure profile on the compliant surface. However the actual bearing film pressure profile which acts on the compliant surface does not necessarilly take on either form. This problem can be overcome by applying the principle of superposition (85). In the context of the present analysis this can be described as follows; suppose the elementary solution for the parabolic pressure profile case is selected from section 3.4.4. As already mentioned (section 3.4.4) the discontinuity in the deflection profile at $r = r_n$ is a minimum (see figure 3.6) for this solution. The actual film pressure profile can be approximated by a series of parabolic profiles of different radius and magnitude (figure 3.8 shows a simple example). Let this series be defined by the equation:

$$p_f = \sum_{n=1,2}^{k_2} p_n \left(1 - \left(\frac{r}{r_n} \right)^2 \right) \quad \text{for } 0 \leq r \leq r_n \qquad 3.77$$

In equation 3.77, r_n represents the radial extent of each parabolic pressure profile "n" and p_n its magnitude at $r = 0$. For each parabolic pressure profile the corresponding deflection of the compliant surface can be determined using equations 3.74 and 3.75. Applying the principle of superposition the resulting deflection of the compliant surface due to the actual film pressures p_f is equal to the summation of deflection profiles obtained for

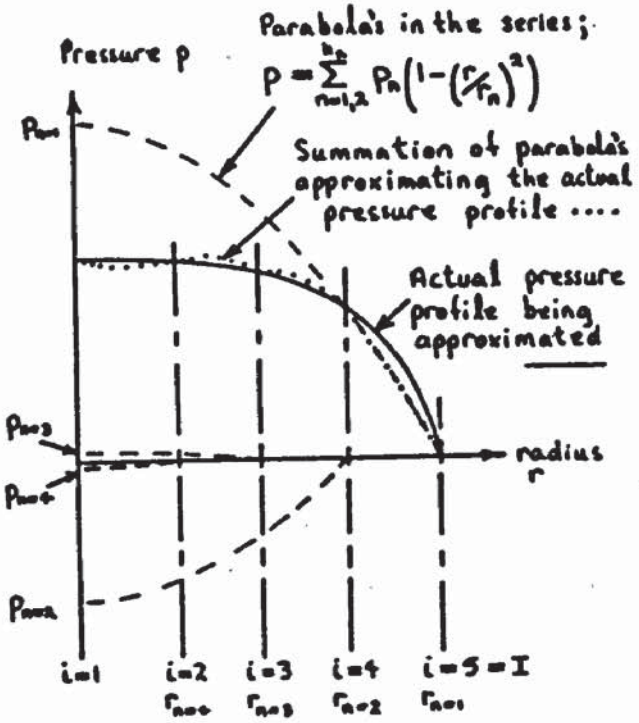

Figure 3.8 Approximating the actual pressure profile by a series of parabola's

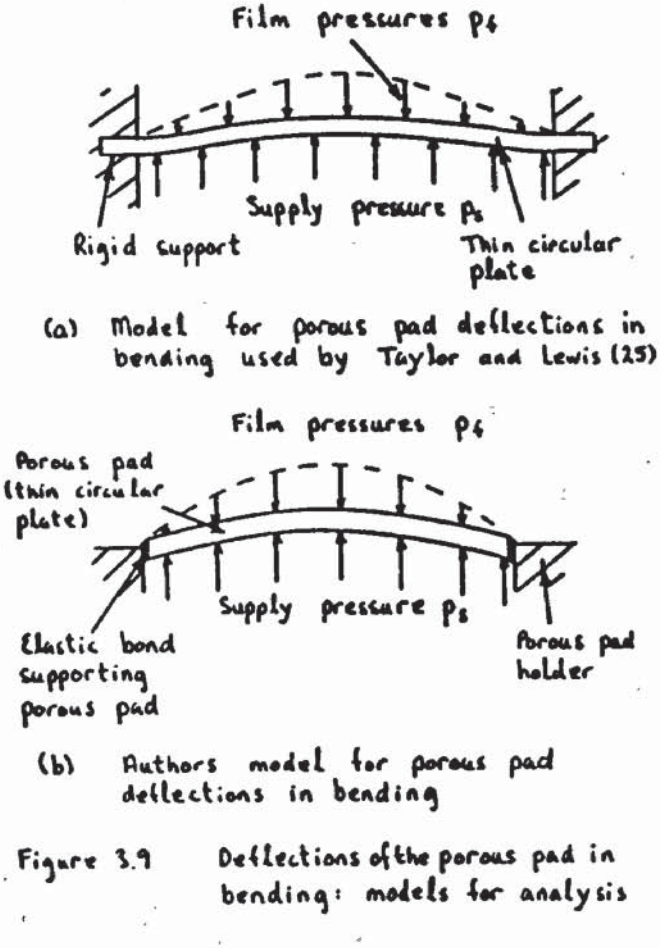

Figure 3.9 Deflections of the porous pad in bending: models for analysis

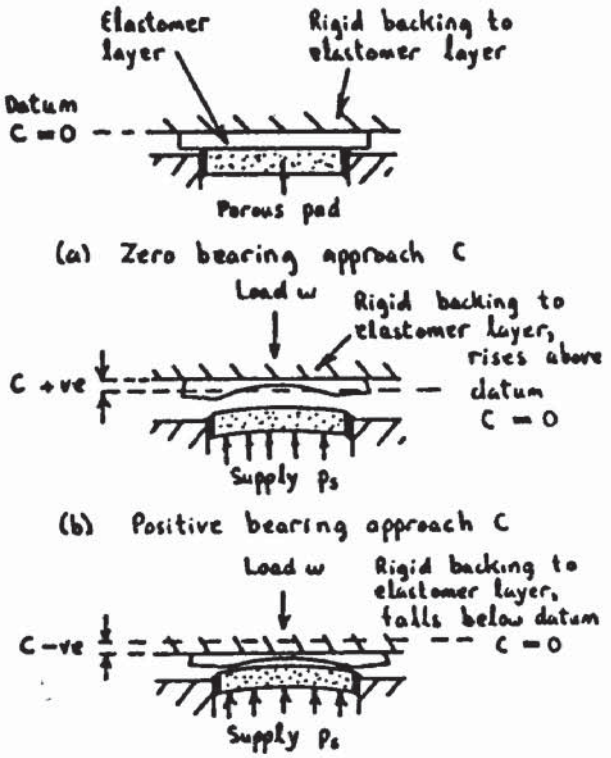

Figure 3.10 Diagrammatic description of bearing approach C

each parabolic pressure profile in equation 3.77. Hence the deflection of the compliant surface due to the actual film pressures is given by;

$$u_c = \sum_{n=1,2}^{k_2} u_{zn} \qquad 3.78$$

where values of u_{zn} are obtained from equations 3.74 and 3.75 corresponding to the parabolas "n" in equation 3.77.

It is important to note that in using the principle of superposition (85) the relationship between applied loading and corresponding deflections of the elastomer layer must be linear. This condition is satisfied by assumption (ii) made in section 3.4.1, i.e. the elastomer layer is linear - elastic for small strains in the order of 10%.

In approximating the actual film pressure profile using equation 3.77, the following procedure is used:
(i) Divide the compliant surface into I primary nodes over the region $0 <= r_i <= r_b$ starting with $i = 1$ at $r_{i=1} = 0$ and finishing with $i = I$ at $r_{i=I} = r_b$. These nodes should match the nodes used for the finite difference solution to the lubrication equations described in section 3.3.2. However to improve accuracy particularly in regions near the bearing clearance exit where film pressure gradients are greatest, further secondary nodes may be selected inbetween the primary nodes. Equation 3.77 may be re - written in the form;

$$(p_f)_i = \sum_{n=1,2}^{I-1} p_n \left(1 - \left(\frac{r_i}{r_n} \right)^2 \right) \qquad 3.79$$

$$\text{where} \quad r_n = r_i \quad \text{when} \quad i = I - n + 1 \qquad 3.80$$

(ii) Fit the first parabola of radius $r_{n=1} = r_b$ in equation 3.79 such that it intercepts the actual film pressure profile $(p_f)_i$ at the (I-1)th node position (see figure 3.8), i.e.:

$$p_{n=1} = \frac{(p_f)_{i=I-1}}{\left(1 - \left(\frac{r_{i=I-1}}{r_{n=1}} \right)^2 \right)} \qquad 3.81$$

(iii) For the second and subsequent parabolas in equation 3.79 subtract the summation of parabolas already fitted to the film pressure profile, from the value of $(p_f)_i$ at $i = I - n$. Then fit a parabola of radius $r_n = r_{i=I-n+1}$ such that it intercepts the remainder of $(p_f)_i$ at $i = I-n$. In mathematical form this may be written;

$$p_n = \frac{\left[(p_f)_{i=I-n} - \sum_{m=1,2}^{n-1} p_{n-m} \left(1 - \left(\frac{r_{i=I-n}}{r_{n-m}} \right)^2 \right) \right]}{\left(1 - \left(\frac{r_{i=I-n}}{r_n} \right)^2 \right)} \qquad 3.82$$

where $r_n = r_{i=I-n+1}$ and $r_{n=m} = r_{i=I-m+1}$.

(iv) The procedure in (iii) is repeated until (I-1)th parabolas have been fitted.

If this procedure is followed then the summation of parabolic pressure profiles as defined by equation 3.79 will equal the actual film pressure profile at the selected node points i. Between the node points however the actual film pressure profile is only approximated (see figure 3.8). The accuracy of equation 3.79 and the resulting deflections of the compliant surface, therefore will improve as more nodes I are used.

In appendix 3 equations 3.74 and 3.75 together with the procedure described in this section, are tested in a compliant thrust bearing configuration similar to those studied by Castelli et al (59) and Benjamin et al (62). A close correlation of analytical results for the bearing performance with those of (59) and (62) is achieved. This therefore verifies the accuracy of equations 3.74 and 3.75 when applied to a typical thrust bearing problem involving a compliant surface.

3.5 THE ELASTICITY EQUATIONS FOR DEFLECTIONS OF THE POROUS PAD

Taylor and Lewis (25) obtained solutions for the deflection of the porous pad assuming it is a thin linear - elastic plate in bending. The plate was rigidly clamped

around its circumference and subject to a non - uniform pressure loading from the supply pressure p_s and the bearing film pressures p_f (see figure 3.9a). In practice the adhesive bond supporting the porous pad around its circumference may flex in bending and then the porous pad is no longer rigidly clamped (figure 3.9b). For small strains and assuming the stiffness of the bond in bending is linear - elastic then the radial bending moment created by it and acting on the porous pad circumference, is given by;

$$m_r = k_b \cdot \frac{du_b}{dr} \qquad \text{at} \quad r = r_b \qquad 3.83$$

The differential equation for deflection of a thin circular plate in bending (47) is;

$$\frac{d^3u_b}{dr^3} + \frac{1}{r}\cdot\frac{d^2u_b}{dr^2} - \frac{1}{r}\cdot\frac{du_b}{dr} = \frac{F_r}{D_b} \qquad 3.84$$

This equation can be expressed in a form which allows solution by successive integration;

$$\frac{d}{dr}\left[\frac{1}{r}\cdot\frac{d}{dr}\left(r\cdot\frac{du_b}{dr}\right)\right] = \frac{F_r}{D_b} \qquad 3.85$$

F_r the shearing force per unit circumferential length, can

be expressed in terms of a pressure loading p_b (47);

$$F_r = \frac{1}{r} \int_0^r p_b.r.dr \qquad 3.86$$

Substituting for F_r in equation 3.85 gives;

$$r.\frac{d}{dr}\left[\frac{1}{r}\left(r.\frac{du_b}{dr}\right)\right] = \frac{1}{D_b}\int_0^r p_b.r.dr \qquad 3.87$$

At any radial position r the pressure loading p_b on the porous pad is;

$$p_b = p_s - p_f \qquad 3.88$$

Let this be expressed by a polynomial series which approximates the actual pressure loading p_b i.e.;

$$p_b = \sum_{n=0,2}^{k_3} a_n.r^n \qquad 3.89$$

(Note that in equation 3.89, only even values of n are taken because p_f and hence p_b are symmetrical about the axis r = 0 (assumption (v) section 3.2.1)).

Substituting for p_b in equation 3.87 and after successive integration , the deflection of the porous pad is given by;

$$u_b = \frac{1}{D_b} \sum_{n=0,2}^{k_3} \left(\frac{a_n . r^{n+4}}{(n+2)^2 . (n+4)^2} \right) + \frac{b_1 r^2}{4} + b_2 . \ln(r) + b_3 \qquad 3.90$$

In equation 3.90, deflections u_b are +ve in the direction of pressure loading p_b defined by equations 3.88 and 3.89. By equation 3.88, p_b is +ve when $p_s > p_f$ and this is likely to be the case since a pressure drop occurs across the porous pad thickness. Therefore deflections of the porous pad will be +ve in the direction of the supply pressure p_s. The constants b_1 , b_2 and b_3 can be obtained using the following boundary conditions:

(i) at $r = 0$, u_b is not equal to infinity and hence $b_2 = 0$.

(ii) at $r = r_b$ the radial bending moment m_r between the porous pad and its adhesive bond must be in equilibrium.

(iii) also at $r = r_b$ the deflection of the porous pad due to bending only is zero.

It is shown in appendix 4 that these boundary conditions lead to the following expressions for constants b_1 and b_3 .

$$b_1 = - \frac{2}{(B_b + D_b)} \left[\frac{B_b}{D_b} \sum_{n=0,2}^{k_3} \left(\frac{a_n . r_b^{n+2}}{(n+2)^2 . (n+4)} \right) + \sum_{n=0,2}^{k_3} \left(\frac{(n+3) . a_n . r_b^{n+2}}{(n+2)^2 . (n+4)} \right) \right] \qquad 3.91$$

$$b_3 = -\frac{1}{D_b}\sum_{n=0,2}^{k_3}\left(\frac{a_n.r_b^{n+4}}{(n+2)^2.(n+4)}\right) - \frac{b_1.r_b^2}{4} \qquad 3.92$$

where $B_b = k_b.r_b + D_b.\nu_b$ 3.93

The rigidity properties of the porous pad can therefore be specified by flexural constants D_b and B_b. D_b represents the rigidity of the porous pad only while B_b represents the combined rigidity of both the porous pad and its adhesive bond. It is shown in section 4.3.6 that both these constants can be determined from deflection measurements of the porous pad after it has been bonded into its holder and subjected to a uniform pressure loading. However it was found that the resulting values of D_b and B_b were very sensitive to small errors in the measurement of porous pad deflection. New constants are therefore introduced (see section 4.3.6) which overcome this problem. These constants in non - dimensional form are;

Magnitude constant; $$M_b = \frac{p_a.h_b^3.(B_b + 5.D_b)}{64.D_b.(B_b + D_b)} \qquad 3.94(a)$$

Shape constant; $$N_b = \frac{9.D_b + B_b}{4.B_b + 20.D_b} \qquad 3.94(b)$$

These constants will therefore be used to represent the rigidity properties of the porous pad in bending. Equations 3.94 may be re - written so that they are

explicit in D_b and B_b as follows;

$$D_b = \frac{p_a . h_b^3}{128 . M_b . (1 - 2 . N_b)} \qquad 3.95(a)$$

$$B_b = - D_b \left(\frac{20 . N_b - 9}{4 . N_b - 1} \right) \qquad 3.95(b)$$

Equations 3.95 are used to obtain values of D_b and B_b . in equation 3.90 to 3.92 from values of the constants M_b and N_b.

3.6 SOLUTION TO THE COUPLED LUBRICATION AND ELASTICITY EQUATIONS

An iterative method similar to that used by Taylor and Lewis (25) and Hayashi (82) is used to obtain a solution for the porous and compliant aerostatic thrust bearing. This solution must satisfy both the lubrication equations (section 3.2) and the elasticity equations (sections 3.4 and 3.5).

It is convenient here to define a bearing approach "c". This was first used in the study of compliant thrust bearings with a central feed hole by Benjamin et al (61, 62). The bearing approach c for a porous and compliant aerostatic thrust bearing is equal to the displacement of

the rigid backing to the elastomer layer relative to the porous pad bearing surface. Its value is zero when the elastomer layer in an undeformed state is resting on and in full contact with the porous pad also in an undeformed state (see figure 3.10a). From this datum position and when the porous and compliant aerostatic thrust bearing is operating under conditions of supply pressure p_s and load w, the bearing approach c will be +ve if the rigid backing to the elastomer layer moves away from the porous pad (see figure 3.10b) and -ve if the opposite occurs (see figure 3.10c). The value of c therefore depends on both the bearing clearance and compression of the elastomer layer. Note that in a porous aerostatic thrust bearing with rigid bearing surfaces or an elastic porous pad, approach c is equal to the bearing clearance h_d. This is because the rigid backing to the elastomer layer now becomes the bearing surface opposing the porous pad.

The iteration procedure is shown in figure 3.11. For the lubrication equations the porous pad is divided into I and J nodes in the r and z directions respectively. Initially a uniform bearing clearance equal to c is assumed with no deflections of the compliant surface or the porous pad.

The first estimate of film pressures at each node i for a constant supply pressure p_s, can therefore be obtained using the analytic solution of Jones et al (23) (see section 3.3.1) for a porous aerostatic thrust bearing

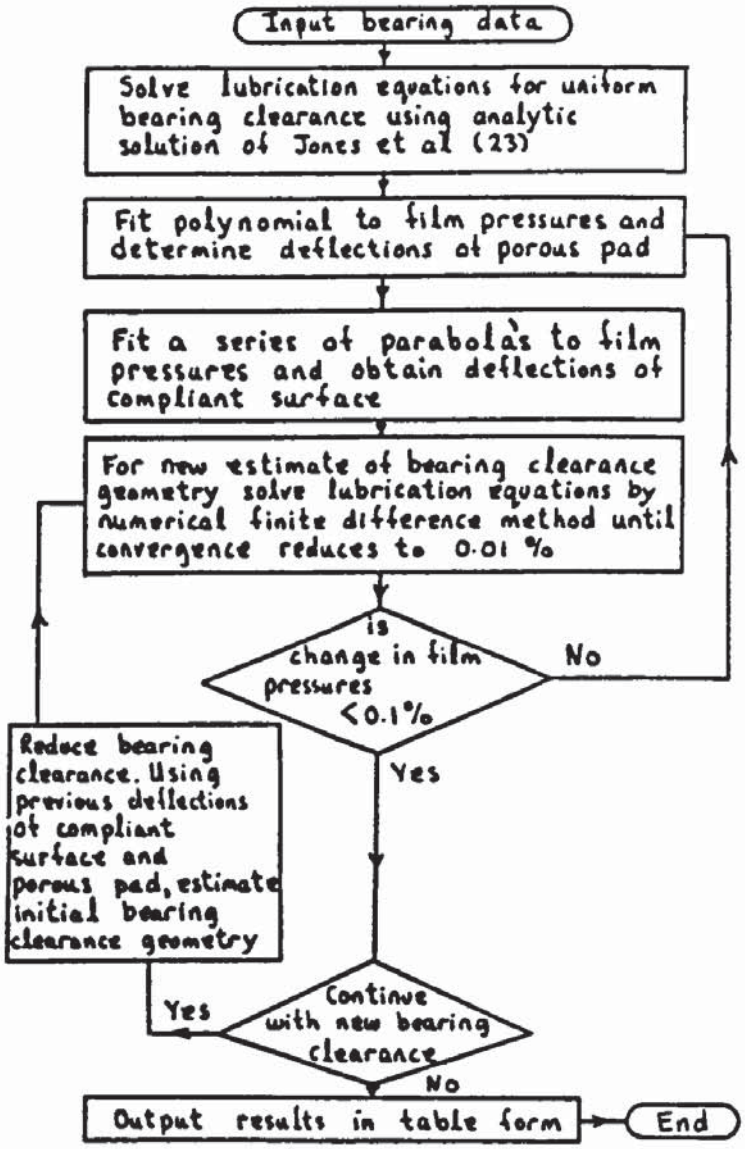

Figure 3.11 Flow diagram of iterative solution to the lubrication and elasticity equations

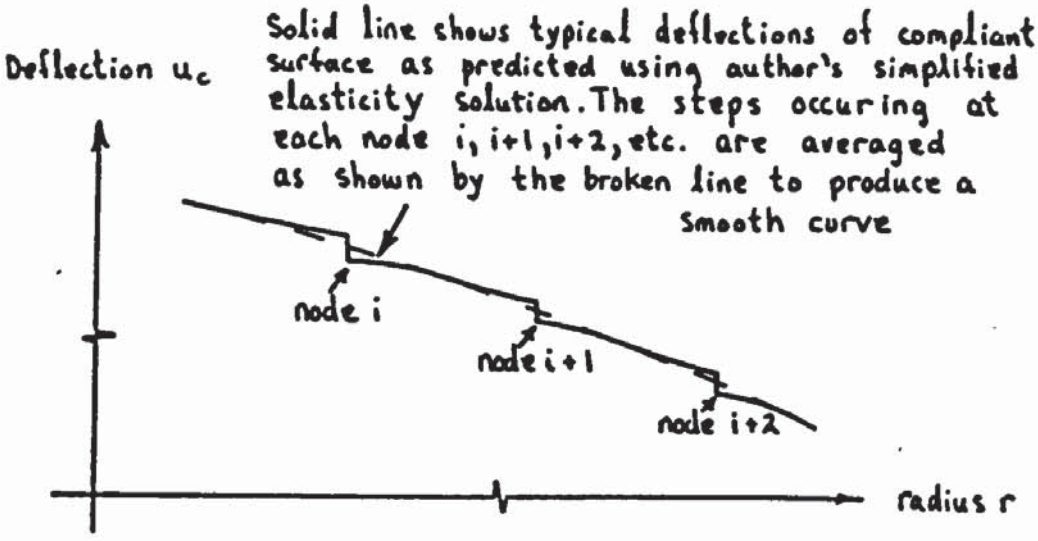

Figure 3.12 Smoothing deflections of the compliant surface

with a uniform bearing clearance.

This first estimate of the film pressures is used to determine initial deflections of the compliant surface and the porous pad in the porous and compliant aerostatic thrust bearing.

As described in section 3.4.5, deflections of the compliant surface are obtained from a summation of elementary solutions (given by equations 3.74 and 3.75) approximating the film pressure profile. The elastomer layer is therefore divided into I primary nodes in the r direction, these corresponding with the nodes already used for the porous pad. In addition, a further four secondary nodes are used between the primary nodes i = I and i = I-2. This will improve the accuracy in determination of compliant layer deflections in the region adjacent to the bearing clearance exit where the film pressure gradients are greatest.

Due to the discontinuity occuring at radius r_n in each elementary solution (refer to section 3.4.5), when these are summated the resulting deflection profile for the compliant surface will have a small vertical step at each node i (see figure 3.12). This jaggedness is removed by averaging the deflection at these nodes to obtain a smooth profile. The deflection of the compliant surface at the primary nodes is given by;

$$(u_c)_i = \sum_{n=1,2}^{I+4} (u_n)_i \qquad 3.96$$

For deflections of the porous pad a 4th order polynomial equation (i.e. equation 3.89) is fitted to the film pressure profile and deflections at each node i are obtained using equation 3.90 where $r = \Delta r(i-1).r_b$.

If deflections of the compliant surface and the porous pad are added to the bearing approach c, the new bearing film clearance geometry becomes;

$$(h_r)_i = c - (u_b)_i - (u_c)_i \qquad 3.97$$

However this gives rise to a new value of bearing clearance h_d at $r = r_b$ which often caused instability during the iteration procedure. The reason for this is attributed to the sensitivity of bearing film pressures to small changes in the bearing clearance. This problem is overcome by adding the compliant surface deflection u_c at $r = r_b$ to the bearing approach c i.e.;

$$c_{new} = c_{old} + u_c \Big|_{r=r_b} \qquad 3.98$$

The new value of c is substituted back into equation 3.97 and the bearing clearance determined at each node i.

For the new bearing clearance geometry a more accurate estimate of film pressures can be made. This is achieved using the finite difference solution to the lubrication equations, suitable for a non - uniform bearing clearance as presented in section 3.3.2. For this solution the old pressures P_{ij} at each node i, j within the porous pad are used as initial estimates in equations 3.39 and 3.40. These can be determined from the analytic solution of Jones et al (23) (see section 3.3.1) but computing time can be saved if values are estimated by linearly interpolating between the film pressures P_f and the supply pressure P_s, i.e.;

$$P_{i,j} = \frac{P_s - (P_s - (P_f)_i).(j - 1)}{J - 1} \qquad 3.99$$

Also it is necessary to determine the gradient of the bearing clearance geometry at each node i for i = 1 to I - 1 in equation 3.43. From equation 3.97;

$$\left(\frac{dh_r}{dr}\right)_i = -\left(\frac{du_c}{dr}\right)_i - \left(\frac{du_b}{dr}\right)_i \qquad 3.100$$

where $$\left(\frac{du_c}{dr}\right)_i = \frac{(u_c)_{i+1} - (u_c)_{i-1}}{2.\Delta r.r_b} \qquad 3.101$$

and differentiating equation 3.90 gives;

$$\left(\frac{du_b}{dr}\right)_i = \frac{1}{D_b} \sum_{n=0,2}^{k_3} \left(\frac{a_n . r^{n+3}}{(n+2)^2 . (n+4)}\right) + \frac{b_1 . r}{2} \qquad 3.102$$

(Note that the value of $\left(\frac{dh_r}{dr}\right)_i$ at node i = I is not required since P_{ij} at i = I, j = J is equal to 1 (see section 3.3.2)).

Having obtained a new, more accurate estimate of film pressures the solution now continues in an iteration cycle as follows. For these film pressures, new deflections of the compliant surface and porous pad are determined to give a more accurate estimate of bearing clearance geometry. This bearing clearance geometry is then used to determine new film pressures using the finite difference solution to the lubrication equations. For equations 3.39 and 3.40 initial estimates of pressures P_{ij} within the porous pad are taken from the previous iteration. This iteration cycle is repeated until the change in film pressures at any node i, j = J is less than 0.1%. A final solution is then achieved.

To obtain a set of results to enable bearing performance curves to be plotted the bearing clearance h_d at $r = r_b$ is reduced in small decrements. The decrement is such that the bearing number Λ_d (see section 3.7) is increased at a constant rate of 1, i.e. 1,2,3,4, etc. Because h_d is proportional to $(1/\Lambda_d)^{1/3}$ the decrement reduces as h_d approaches zero. This insures that stable

solutions are obtained down to small bearing clearances. As shown in figure 3.11 each iteration cycle to a new bearing clearance now starts by estimating a bearing clearance geometry using deflection profiles of the compliant surface and porous pad from the final solution to the previous bearing clearance. This helps reduce the number of iterations required to achieve a solution at each new bearing clearance.

Also film pressures are determined using the finite difference solution to the lubrication equations only. At the start of each iteration cycle to a new bearing clearance the porous pad pressures P_{ij} are carried over from the solution to the previous bearing clearance and used as initial estimates in equations 3.39 and 3.40.

As the bearing clearance reduced it was also found necessary to use a linear damper similar to that of Castelli et al (59) to maintain stability in the iterative solution. This reduces the change in bearing clearance geometry occuring after each iteration cycle to a solution at a given bearing clearance. New estimates of the bearing clearance h_r from equation 3.97 using this linear damper become;

$$(h_r)_{new} = \eta_1.(h_r)_{current} + (1 - \eta_1).(h_r)_{old} \qquad 3.103$$

also from equation 3.100;

$$\left(\frac{dh_r}{dr}\right)_{new} = \eta_1 \left(\frac{dh_r}{dr}\right)_{current} + (1 - \eta_1).\left(\frac{dh_r}{dr}\right)_{old} \qquad 3.104$$

In the analysis of compliant thrust bearings with a central feed hole, Castelli et al (59) found that their solution was stable for $\eta_1 = 1$, at large bearing clearances. As the bearing clearance was reduced however the convergence rate also reduced and when this became very slow the value of η_1 was halved. This procedure was repeated as the bearing clearance was reduced and the convergence rate once again became slow. In obtaining solutions to the authors porous and compliant aerostatic thrust bearing the same procedure has been adopted and found to work satisfactory. The convergence rate was considered to be slow when the 20th iteration was reached without converging on a final solution. At this point the value of η_1 was automatically halved from its current value.

A programme of the solution has been written in BASIC for the HP9845 desktop mini computer. A copy of this programme is given in appendix 7. This programme is divided into the following subprogrammes;

(a) Solution to the lubrication equations by Jones et al (23).

(b) Solution to the lubrication equations by the finite difference method of Taylor (24).

(c) Elasticity equations for deflections of the compliant surface.

(d) Elasticity equations for deflections of the porous pad.

The computational sequence to a solution as shown by the flow chart in figure 3.11 is controlled by a main programme. This main programme calls each subprogramme when required and passes on relevant information to the subprogramme. After the subprogramme has finished,its results are passed back to the main programme and the computational sequence is continued until a final solution is achieved.

3.7 THE PRESENTATION OF BEARING PERFORMANCE CURVES

3.7.1 NON - DIMENSIONAL BEARING PERFORMANCE PARAMETERS

In section 3.2.6 a local bearing number Λ_r (equation 3.17) was introduced. However because the bearing clearance h_r is non - uniform, Λ_r is unsuitable for the presentation of bearing performance results. For this purpose it is possible to define two bearing numbers Λ_c and Λ_d , based on bearing approach c and bearing clearance h_d respectively, as follows:

$$\Lambda_c = \frac{12.r_b^2.\phi_z}{c(c^2 + 6.\phi_r).h_b} \qquad 3.105$$

$$\Lambda_d = \frac{12.r_b^2.\phi_z}{h_d(h_d^2 + 6.\phi_r).h_b} \qquad 3.106$$

(Note bearing number Λ_c has the same sign as c which can be +ve or -ve (see section 3.6)).

While Λ_c is more useful for the bearing designer, Λ_d indicates the actual bearing clearance. Both bearing numbers will therefore be used in the presentation of bearing performance curves.

The bearing performance as a function of bearing number can be represented by its load capacity, flow rate and static stiffness. Bearing load capacity w is determined from the summation of film pressures x area which act parallel to the bearing axis at r = 0. For an axisymmetric film pressure profile;

$$w = 2.\pi. \int_0^{r_b} (p_f - p_a).r.dr \qquad 3.107$$

In non - dimensional form this can be written;

$$W = \frac{w}{\pi.r_b^2.(p_s - p_a)} \qquad 3.108$$

The non - dimensional load capacity W represents the ratio of actual bearing load to the maximum possible from the supply pressure p_s. It is therefore the load carrying efficiency of the bearing.

The mass flow rate m through the bearing can be obtained from the summation of flow velocities passing

normal to the feed face of the porous pad i.e.;

$$m = 2.\pi. \int_0^{r_b} (\rho.v_z)_{z=0} .r.dr \qquad 3.109$$

on substitution of equations 3.1 and 3.2 into 3.109 for v_z and ρ gives;

$$m = - \frac{\pi.\Phi_z}{\eta.R_{gas}.T} \int_0^{r_b} \left. \frac{\partial(p^2)}{\partial z} \right|_{z=0} .r.dr \qquad 3.110$$

In non - dimensional form;

$$M = \frac{2.m.\eta.R_{gas}.T.h_b}{\pi.r_b^2.(p_s^2 - p_a^2).\Phi_z} \qquad 3.111$$

Similarly the non - dimensional mass flow rate represents the ratio of actual mass flow through bearing to the maximum possible through the porous pad at supply pressure p_s.

In porous aerostatic thrust bearings with rigid bearing surfaces the bearing static stiffness k_x has been defined (19,23,24) as the differential of load over bearing clearance i.e.;

$$k_x = - \frac{\partial w}{\partial h_u} \qquad 3.112$$

However in a porous and compliant aerostatic thrust bearing the compression of the elastomer layer also effects the resulting bearing stiffness. This can be taken into consideration by replacing h_u in equation 3.112 with bearing approach c, i.e.;

$$k_x = -\frac{\partial w}{\partial c} \qquad 3.113$$

In their study of porous aerostatic thrust bearings with rigid bearing surfaces both Jones et al (23) and Taylor (24) use an expression similar to the following, for non - dimensional static stiffness k_x;

$$K_x = \frac{k_x.h_u.(h_u^2 + 6.\Phi_r)}{\pi.r_b^2.(p_s - p_a).(3.h_u^2 + 6.\Phi_r)} \qquad 3.114$$

Similarly this expression could be used to define the non - dimensional static stiffness for a porous and compliant aerostatic thrust bearing by replacing h_u with c, i.e.;

$$K_x = \frac{k_x.c.(c^2 + 6.\Phi_r)}{\pi.r_b^2.(p_s - p_a).(3.c^2 + 6.\Phi_r)} \qquad 3.115$$

However the bearing approach c can have a +ve or -ve

value as described in section 3.6. By equation 3.115, this would result in K_x having the opposite sign to k_x when c is -ve. Also $K_x = 0$ when $c = 0$ regardless of the value of k_x. It is therefore necessary to introduce a new definition of non - dimensional static stiffness for the porous and compliant aerostatic thrust bearing as follows:

Let

$$K_x = - \frac{dW}{d(\Lambda_c^{-1/3})} \qquad 3.116$$

$$= - \frac{dW}{dw} \cdot \frac{dw}{dc} \cdot \frac{dc}{d(\Lambda_c^{-1/3})} \qquad 3.117$$

From equation 3.113 substituting k_x for -dw/dc in equation 3.117;

$$K_x = \frac{dW}{dw} \cdot \left(\frac{dc}{d(\Lambda_c^{-1/3})} \right) \cdot k_x \qquad 3.118$$

By definition

$$W = \frac{w}{\pi . r_b^2 . (p_s - p_a)}$$

therefore

$$\frac{dW}{dw} = \frac{1}{\pi . r_b^2 . (p_s - p_a)} \qquad 3.119$$

similarly

$$\Lambda_c = \frac{12 . \phi_z . r_b^2}{h_b . c(c^2 + 6 . \phi_r)}$$

therefore

$$\Lambda_c^{-1/3} = \left(\frac{12 . \phi_z . r_b^2}{h_b} \right)^{-1/3} . (c^3 + 6 . \phi_r . c)^{1/3}$$

and

$$\frac{d\Lambda_c^{-1/3}}{dc} = \left(\frac{12.\Phi_z.r_b^2}{h_b} \right)^{-1/3} . \frac{1}{3}.(c^3 + 6.\Phi_r.c)^{-2/3}.(3.c^2 + 6.\Phi_r)$$

$$\text{i.e.} \quad \frac{dc}{d\Lambda_c^{-1/3}} = \frac{3.\Lambda_c^{1/3}.c(c^2 + 6.\Phi_r)}{(3.c^2 + 6.\Phi_r)} \qquad 3.120$$

Substituting equations 3.119 and 3.120 into 3.118 gives an expression for K_x as follows:

$$K_x = \frac{3.\Lambda_c^{1/3}.c(c^2 + 6.\Phi_r).k_x}{(3.c^2 + 6.\Phi_r).\pi.r_b^2.(p_s - p_a)} \qquad 3.121$$

The meaning of K_x is best interpreted from equation 3.116. Its value is equal to the slope $dW/d(\Lambda_c^{-1/3})$ at a bearing number Λ_c. The value of $\Lambda_c^{-1/3}$ increases with c and has the same mathematical sign, i.e. when;

c = +ve	$\Lambda_c^{-1/3}$ = +ve
c = -ve	$\Lambda_c^{-1/3}$ = -ve
c = 0	$\Lambda_c^{-1/3}$ = 0

Since for a constant supply pressure p_s, non - dimensional load capacity W in equation 3.116 is proportional to dimensional load capacity w in equation 3.113, then graphical plots of K_x versus $\Lambda_c^{-1/3}$ will show similar trends to those for k_x versus c. Note that when $c^2 >> 6.\Phi_r$ equation 3.121 reduces to;

$$K_x = \left(\frac{12.\Phi_z.r_b^2}{h_b} \right)^{1/3} \frac{k_x}{\pi.r_b^2.(p_s - p_a)} \qquad 3.122$$

i.e. $K_x \propto k_x$

and from the definition of Λ_c;

$$\Lambda_c^{-1/3} = \left(\frac{12.\Phi_z.r_b^2}{h_b} \right)^{-1/3} \times \frac{c}{3} \qquad 3.123$$

i.e $\Lambda_c^{-1/3} \propto c$

Therefore when $c^2 >> 6.\Phi_r$ the graphical plot of K_x versus $\Lambda_c^{-1/3}$ will have a similar shape to that of k_x versus c.

It is possible to use the non - dimensional static stiffness K_x given by equation 3.116 in the presentation of results for a porous aerostatic thrust bearing with rigid bearing surfaces or an elastic porous pad. For this purpose $\Lambda_c^{-1/3}$ is replaced with $\Lambda_d^{-1/3}$ in equation 3.116 and the bearing clearance h_d is used instead of approach c in equation 3.113.

3.7.2 NON - DIMENSIONAL BEARING CONSTANTS

The performance (i.e. W, M and K_x) of a porous and compliant aerostatic thrust bearing will not only depend on the bearing numbers Λ_c or Λ_d but also on the following non - dimensional constants. From section 3.2.6;

Non - dimensional supply pressure, $P_s = p_s/p_a$ 3.124

Viscous permeability ratio, $K_v = \Phi_r / \Phi_z$ 3.125

Bearing aspect ratio, $S_b = h_b / r_b$ 3.126

In addition to these constants, consideration must be given to the bearing clearance geometry. This can be expressed as a function of the following:

$$h_r = f(c \text{ or } h_d, u_c(r), u_b(r), r_b) \qquad 3.127$$

(Note that either c or h_d can be used in equation 3.127, since both relate directly or indirectly to the bearing clearance)

Equation 3.127 in non - dimensional form can be written;

$$\frac{h_r}{r_b} = f\left(\frac{c}{r_b} \text{ or } \frac{h_d}{r_b}, \frac{u_c(r)}{r_b}, \frac{u_b(r)}{r_b} \right) \qquad 3.128$$

The bearing clearance geometry can therefore be expressed by the ratios c/r_b or h_d/r_b, $u_c(r)/r_b$ and $u_b(r)/r_b$. Let each ratio in turn be considered as follows. By re - writing equations 3.105 and 3.106 the ratios c/r_b and h_d/r_b appear in the expressions for bearing number Λ_c and Λ_d respectively, i.e.;

$$\Lambda_c = \frac{12}{\left(\frac{\Phi_r}{\Phi_z}\right)\cdot\left(\frac{h_b}{r_b}\right)\cdot\left[\left(\frac{c}{r_b}\right)^3\cdot\left(\frac{r_b^2}{\Phi_r}\right) + 6.\left(\frac{c}{r_b}\right)\right]} \qquad 3.129$$

$$\Lambda_d = \frac{12}{\left(\frac{\Phi_r}{\Phi_z}\right).\left(\frac{h_b}{r_b}\right).\left[\left(\frac{h_d}{r_b}\right)^3.\left(\frac{r_b^2}{\Phi_r}\right) + 6.\left(\frac{h_d}{r_b}\right)\right]} \qquad 3.130$$

Substituting for K_v and S_b (equations 3.125 and 3.126) in equations 3.122 and 3.123, gives;

$$\Lambda_c = \frac{12}{K_v.S_b.\left[\left(\frac{c}{r_b}\right)^3.\left(\frac{r_b^2}{\Phi_r}\right) + 6.\left(\frac{c}{r_b}\right)\right]} \qquad 3.131$$

$$\Lambda_d = \frac{12}{K_v.S_b.\left[\left(\frac{h_d}{r_b}\right)^3.\left(\frac{r_b^2}{\Phi_r}\right) + 6.\left(\frac{h_d}{r_b}\right)\right]} \qquad 3.132$$

For a given value of Λ_c or Λ_d in equations 3.131 and 3.132 respectively, the ratios c/r_b and h_d/r_b which represent the bearing clearance geometry will depend on the values of K_v, S_b and the ratio r_b^2 / Φ_r. While the non - dimensional parameters K_v and S_b have already been defined the ratio r_b^2 / Φ_r has not. Therefore let this non - dimensional ratio be defined as follows:

Non - dimensional ratio, $K_h = r_b^2 / \Phi_r$ 3.133

The ratio K_h must therefore be included in the list of non - dimensional constants since its value will effect the bearing clearance geometry.

The ratio $u_c(r)/r_b$ in equation 3.128 represents the effect of compliant layer deflections on the bearing clearance geometry. For a porous and compliant aerostatic

thrust bearing operating at a constant bearing number Λ_c or Λ_d , the deflections of the compliant surface are a function of the following:

$$u_c(r) = f(G_c, t_c, r_b, r_c, p_s, \nu_c) \qquad 3.134$$

Equation 3.134 in non - dimensional form can be written;

$$\frac{u_c(r)}{r_b} = f\left(\frac{G_c}{p_s}, \frac{t_c}{r_b}, \frac{r_c}{r_b}, \nu_c \right) \qquad 3.135$$

(Note that ν_c in equations 3.134 and 3.135 is already non - dimensional)

The non - dimensional group G_c / p_s in equation 3.128 can be replaced with G_c / p_a , since p_s / p_a has already been defined as the non - dimensional supply pressure P_s , i.e.;

$$\frac{G_c}{p_s} \cdot \frac{p_s}{p_a} = \frac{G_c}{p_a} \qquad 3.136$$

Equation 3.135 becomes;

$$\frac{u_c(r)}{r_b} = f\left(\frac{G_c}{p_a}, \frac{t_c}{r_b}, \frac{r_c}{r_b}, \nu_c \right) \qquad 3.137$$

The non - dimensional groups G_c / p_a , t_c / r_c , r_c / r_a and ν_c in equation 3.137 represent the deflections u_c / r_b of the compliant surface in equation 3.128. Let these groups be

defined as non - dimensional constants for the elastomer layer;

Non - dimensional shear modulus, $S_o = G_c / p_a$ 3.138

Non - dimensional radial extent, $R_c = r_c / r_b$ 3.139

Non - dimensional thickness, $S_c = t_c / r_b$ 3.140

Poisson's ratio, ν_c 3.141

Similarly for deflections of the porous pad in bending, the non - dimensional constants M_b and N_b were introduced in section 3.5 by equations 3.94 (a) and (b). These represent deflections u_b/r_b of the porous pad in equation 3.128.

The non - dimensional constants for a porous and compliant aerostatic thrust bearing can now be summarized as follows:

Non - dimensional supply pressure, $P_s = p_s / p_a$

Porous pad aspect ratio, $S_b = h_b / r_b$

Viscous permeability ratio, $K_v = \Phi_r / \Phi_z$

Non - dimensional shear modulus, $S_o = G_c / p_a$

Elastomer layer radial extent, $R_c = r_c / r_b$

Non - dimensional elastomer layer thickness, $S_c = t_c / r_b$

Poisson's ratio, ν_c

Magnitude constant for porous pad, $$M_b = \frac{p_a . h_b^3 (B_b + 5.D_b)}{64.D_b (B_b + D_b)}$$

Shape constant for porous pad, $$N_b = \frac{9.D_b + B_b}{4.B_b + 20.D_b}$$

Non - dimensional constant, $K_h = r_b^2 / \Phi_r$

CHAPTER 4

EXPERIMENTATION

4.1 INTRODUCTION

The main objectives of experimentation in the context of aerostatic bearings, are as follows:

(a) To measure bearing performance and correlate experimental results with theoretical predictions.

(b) To show this correlation holds true under various bearing operating conditions and for various bearing constants.

(c) Account for any discrepancies between experimental and theoretical results.

(d) Discover new phenomena not already known or accounted for.

In this chapter, details of experiments to determine the performance of the porous and compliant aerostatic thrust bearing presented in chapter 1 will be described. This includes a description of the apparatus, methods of measurement and instrumentation, preparation and calibration of the porous pads and elastomer layers, etc. Various practical considerations will also be discussed which will improve the correlation between experimental and theoretical results.

The results of this experimentation along with a

comparison with theoretical predictions, are presented and discussed in chapter 5.

4.2 THE MAIN EXPERIMENTAL RIG

4.2.1 DESIGN CONSIDERATIONS

The following criteria were considered during the design of the experimental rig:

(i) Measurements to be made during bearing tests:

(a) Supply pressure p_s.

(b) Bearing load w.

(c) Mass flow through bearing m.

(d) Bearing approach c.

(e) Bearing film pressures p_f.

(f) Temperature of flow through bearing T.

In addition a means of measuring or deriving the bearing clearance h_d.

(ii) The porous pads are to be measured and calibrated for:

(a) Thickness h_b and radius r_b.

(b) Permeability Φ .

(c) Shear deflection of porous pad adhesive support.

(d) Rigidity constants M_b and N_b(see section 4.3.6).

(iii) The elastomer layers are to be measured for:

(a) Thickness t_c and radius r_c.

(b) Elastic modulus E_c, shear modulus G_c and bulk modulus K_c.

(iv) Both the elastomer layer and the porous pad must be removable from the experimental rig to allow interchanges with other elastomer layers and porous pads of different dimensions and properties.

(v) The spacing between the upper and lower sections of the bearing will not only depend on the bearing clearance but also on the thickness and deflections of the elastomer layer. The experimental rig design must therefore allow for a variation in this spacing. Consideration should also be given to the radius r_c of the elastomer layer. This may extend beyond the radius of the porous pad r_b.

(vi) During bearing operation, parallelism between the bearing surfaces must be maintained.

(vii) The load applied to the bearing must be steady and of sufficient magnitude for the higher load capacities expected from the new porous and compliant aerostatic thrust bearing.

(viii) It is logical to make comparisons between the performance of the new bearing and that of a more conventional porous aerostatic thrust bearing with porous pads of identical configuration and properties. The experimental rig should therefore be designed to allow operation with a rigid flat surface in place of the elastomer layer.

4.2.2 PRACTICAL REQUIREMENTS

Important practical aspects of the experimental rig in the design stages were considered as follows:

(a) The Measurement of Bearing Film Pressures; these can be measured using either static pressure tappings or pressure transducers. Either device would be embedded at various known radial positions within one of the bearing surfaces.

The advantage of using pressure transducers is that they respond rapidly to changes in the film pressure. Pressure tappings on the other hand are small in diameter but are slow to respond to changes in the film pressure especially since these will tend to choke at low bearing clearances. Although this may not be considered important in the steady state operation of the bearing, it will affect the time delay before film pressure readings can be taken after adjustments to bearing operating conditions.

The location of either pressure measuring device presents a problem. It would be difficult to mount a device in the elastomer layer since this is a soft material which compresses under the action of bearing loads. An alternative would be to embed each device in the rigid backing to the elastomer layer. Measurement of bearing film pressures could be achieved by drilling holes through the elastomer layer to each device (see figure 4.1a). However compression of the elastomer layer may result in blocking of these holes and its exact radial position for film

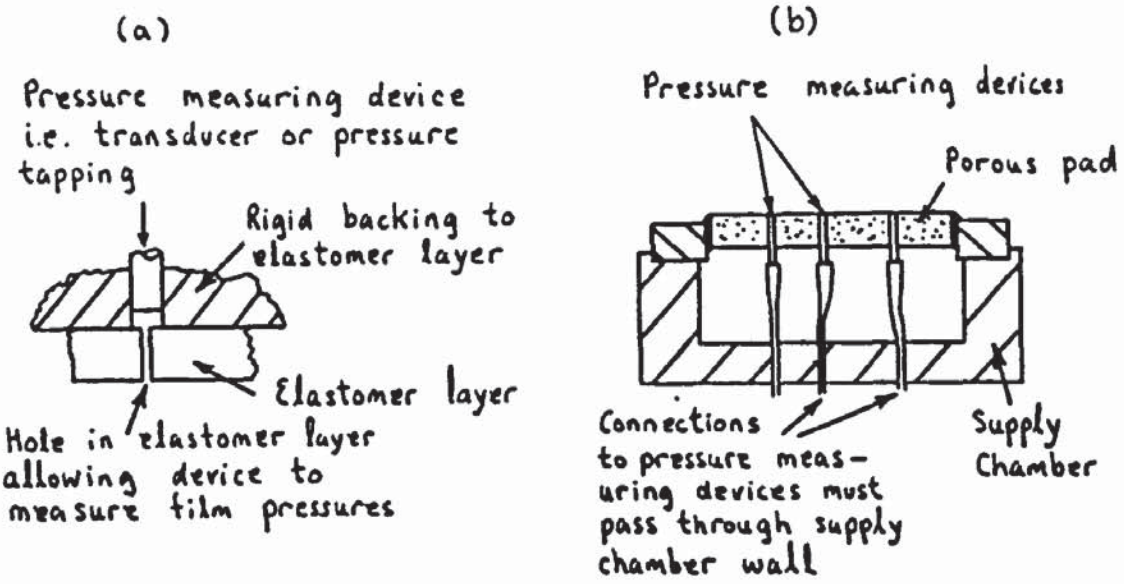

Figure 4.1 Location of pressure measuring device for measurement of bearing film pressures: (a) behind elastomer layer and (b) in porous pad

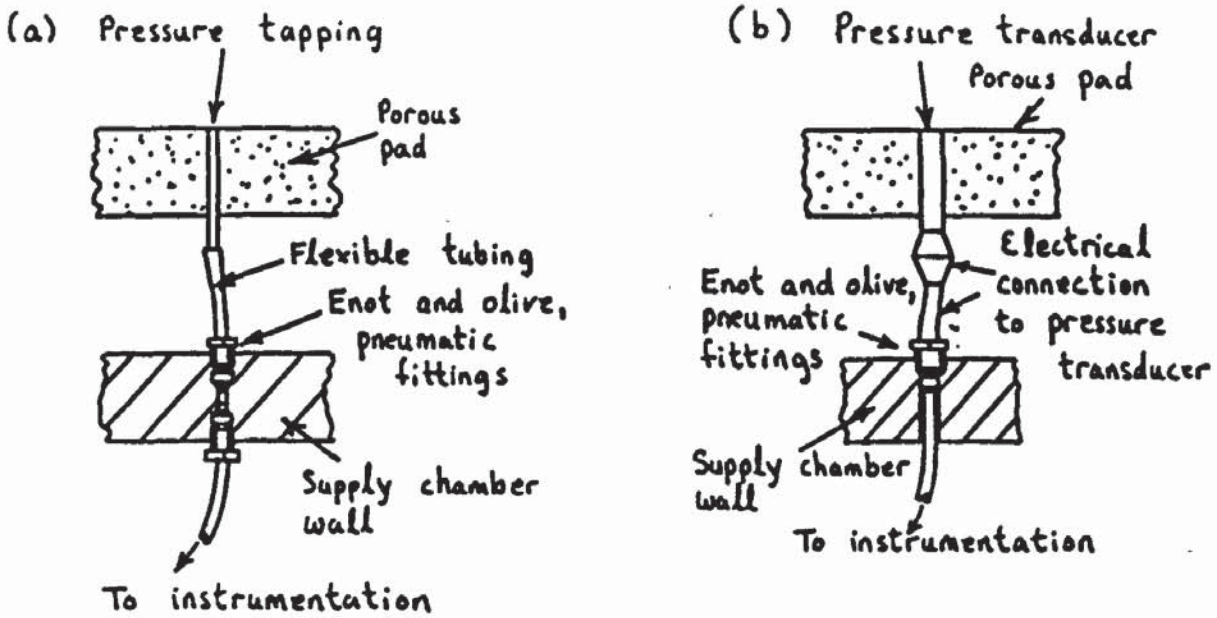

Figure 4.2 Seal through supply chamber wall for connections to film pressure measuring devices in the porous pad

pressure measurement will be altered by radial shear deflections of the elastomer layer.

For these reasons it is therefore necessary to mount the pressure measuring device in the porous pad surface. Which ever device is used it will be necessary to pass a connection through the wall of the supply chamber so that recordings of the film pressure can be made (see figure 4.1b). This connection must be sealed to stop flow escaping from the supply chamber otherwise a false measurement of flow rate through the bearing will be made. It is easy to form a seal for connections to a pressure tapping (see figure 4.2a). However in tests on an electrical connection to a capacitance probe (see figure 4.2b) air escaped through the centre of the electrical wire itself. A similar problem is likely to occur with pressure transducers as well, since the electrical connection is of similar design. For this reason it was decided to use pressure tappings in the porous pad.

To minimize the effect of the presence of pressure tappings on the flow within the porous pad these should be small in diameter relative to the porous pad radius r_b. For each pressure tapping a hole must be drilled through the porous pad and to avoid drill breakage particularly in a porous stainless steel pad, this hole should be at least 2mm diameter. Into these holes a pressure tapping of 1.5mm diameter will be inserted (see section 4.3.3 for further details of this), and the clearance sealed with a high

viscosity epoxy resin (to minimize seepage of the uncured epoxy into the porous pad). There are several pressure tappings to be mounted in each porous pad and therefore these pads should be at least 100mm diameter so that the obstruction to flow from the pressure tappings is minimal. This also ensures greater positional accuracy of the pressure tapping relative to the porous pad (for positions of the pressure tappings in the porous pad see section 4.3.3).

(b) Loading the Bearing; the available laboratory supply is approximately 8.3 bars (120 psi) from a 37 Kilowatt compressor connected to a series of large reservoir cylinders.

In experiments by Taylor (24) on a porous aerostatic thrust bearing with rigid bearing surfaces, non - dimensional load capacities (W) up to 0.3 were achieved before bearing touch down occurred. Higher load capacities than this are expected for the new porous and compliant aerostatic thrust bearing as described in section 1.2. Therefore for an estimated load capacity of 0.6 and for a porous pad of 100mm diameter, the maximum that the bearing must be loaded to is as follows:

$$\text{by definition; } W = \frac{w}{\pi . r_b^2 . (p_s - p_a)}$$

$$\text{therefore; } w = 0{\cdot}6 . \pi . (0{\cdot}05)^2 . 8{\cdot}3 \times 10^5$$

$$= 3911 \text{ N}$$

$$\simeq 400 \text{ Kgf (880 lbf)}$$

It would be impractical to apply this load using dead weights only. Alternative methods of loading are as follows:

(i) Mechanical leverage using dead weights.

(ii) Hydraulic or pneumatic rams.

(iii) A compressed spring (59).

In the application of bearing loads, consideration must be given to the stable or unstable operating regions of the bearing. It is important to determine these regions as part of the bearing experiments. It is known (40), (71), (72) that the floating mass of the bearing can affect its stable or unstable operation. For this reason the method of loading (i) is selected in the design of the main rig.

(c) Bearing Clearance Measurement; Stanojevic (77) used capacitance probes to measure the bearing clearance profile, in experiments on a compliant aerostatic thrust bearing with a central feed hole (inherently compensated). These capacitance probes were mounted in the lower rigid bearing surface. In order that a capacitance reading could be obtained it was necessary to spray the compliant surface with a metallic conducting paint. However during bearing tests the capacitance probes often shorted out when they came in contact with the compliant surface and it was necessary to stop the bearing test to clean paint from them. As a result of this the apparatus was disrupted and continuation of the bearing test produced unreliable results. The measurement of bearing clearance in this way

was therefore abandoned by Stanojevic.

If capacitance probes are used to measure the bearing clearance geometry in a porous and compliant aerostatic thrust bearing, in addition to these problems there would be difficulty in sealing the connection to capacitance probes mounted in the porous pad as already mentioned in part (a) of this section.

Because of these problems the direct measurement of bearing clearance geometry was obmitted from the experiments. However it is possible to derive the bearing clearance at the bearing exit ($r = r_b$), from measurements of the film pressure gradient and the mass flow rate through bearing. This method is described in more detail in section 4.5.2.

4.2.3 MAIN RIG DESIGN

The main experimental rig is shown diagrammatically in figure 4.3 and photographically in plates 1 and 2. It is manufactured mainly from mild steel stock and designed to accommodate porous pads up to 101.6 mm (4") diameter and 25.4 mm (1") thickness and elastomer layers of 203 mm (8") diameter and 19.05 mm (3/4") thickness. Dead weights up to 91kg (200lb) at the end of a pivot arm having a mechanical leverage of 4.4 are used to load the bearing up to 400kg (880lb). The pivot arm is supported at the pivot point by a shaft mounted in two ball bearing races. This therefore

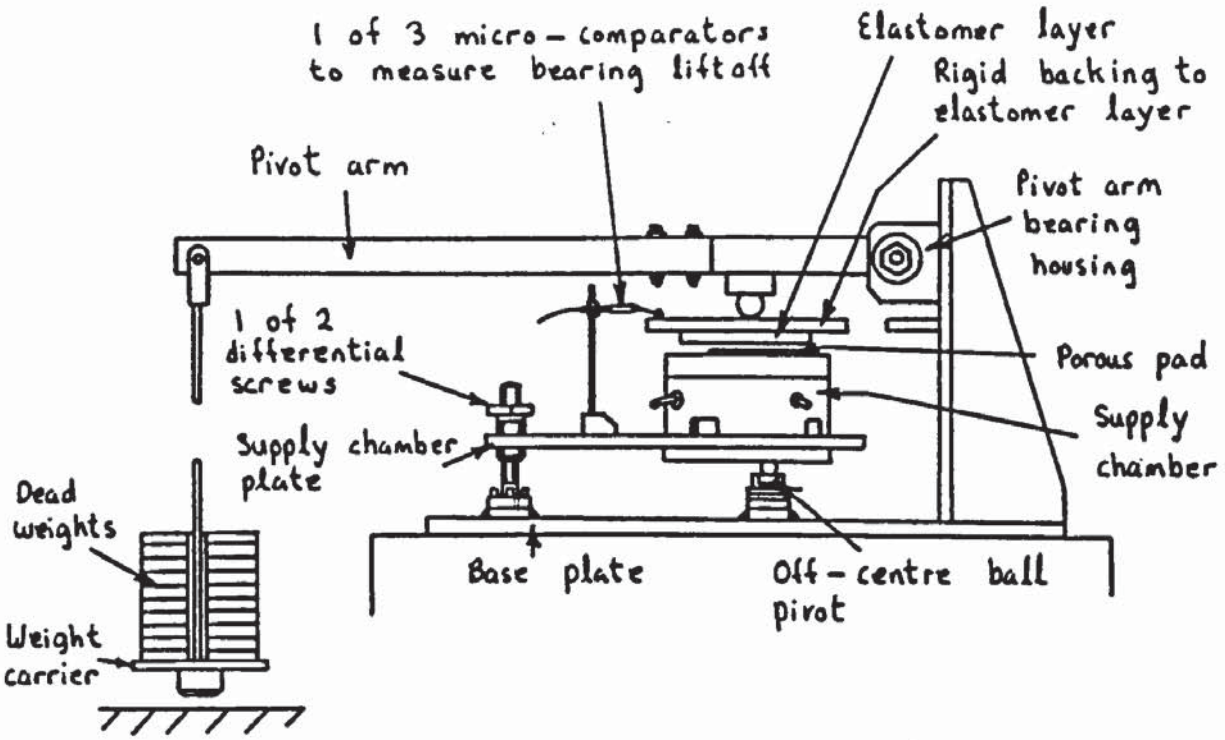

Figure 4.3 Main experimental rig

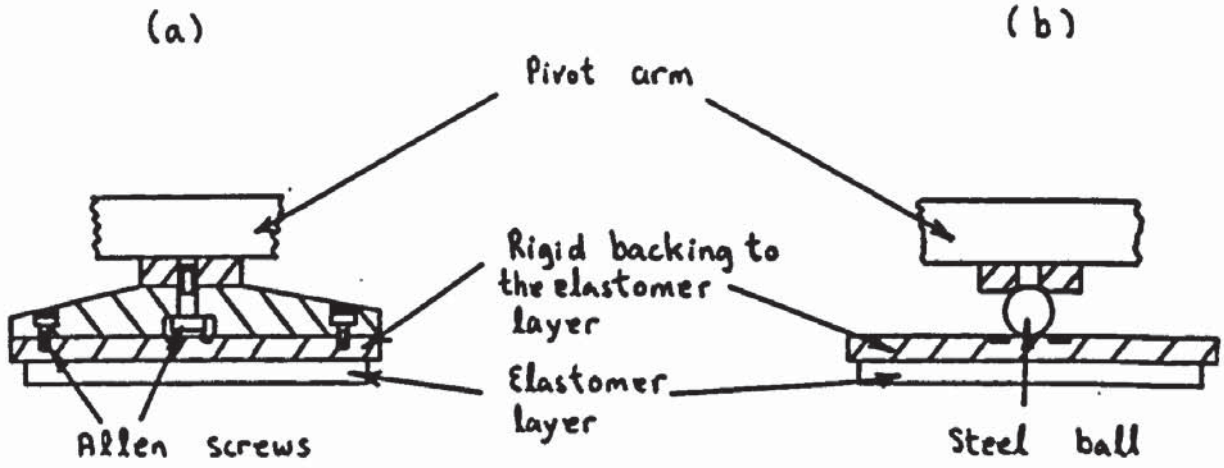

Figure 4.4 Support arrangement between pivot arm and the elastomer layer: (a) original design and (b) modified arrangement

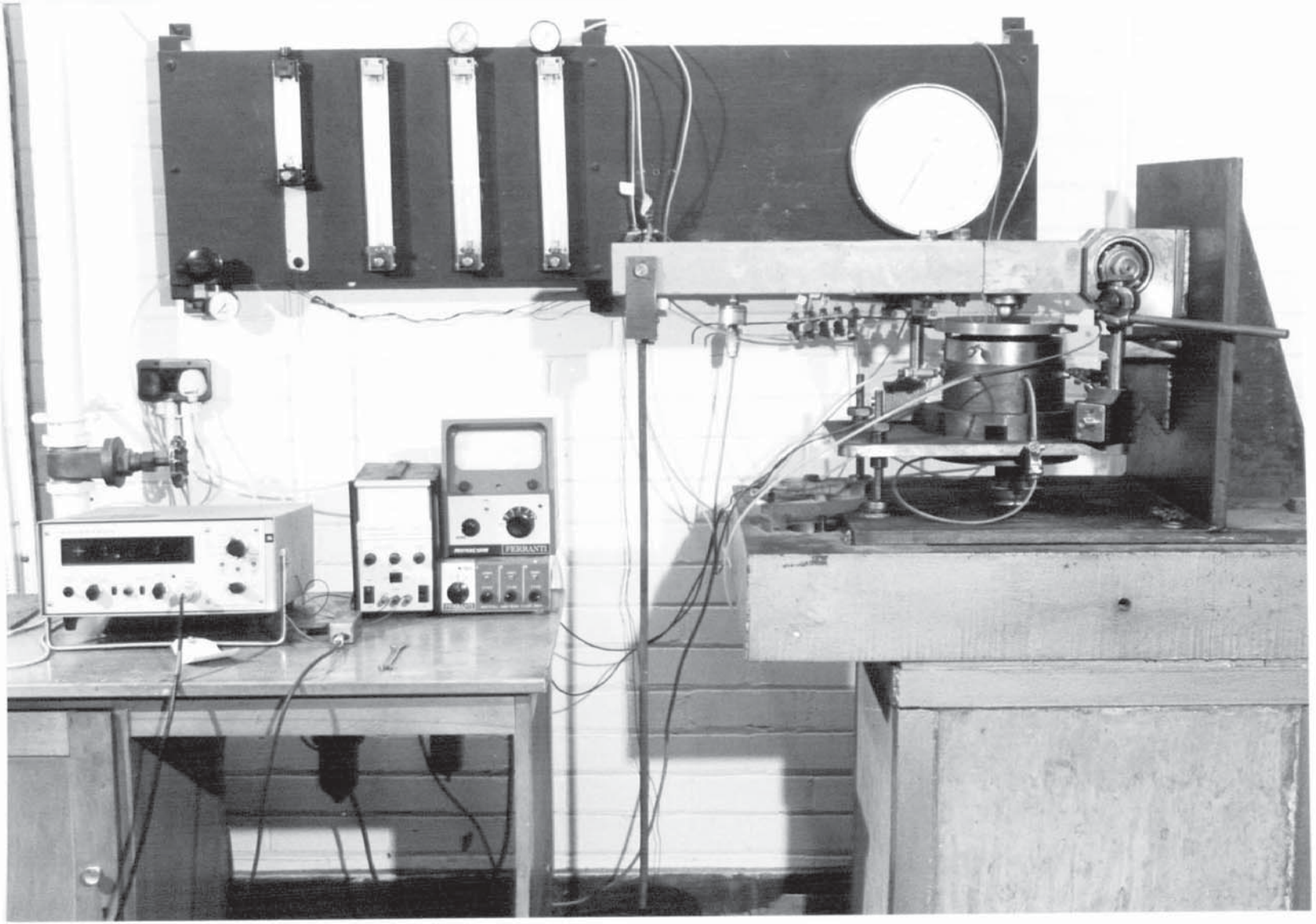

Plate 1 Main experimental rig and instrumentation.

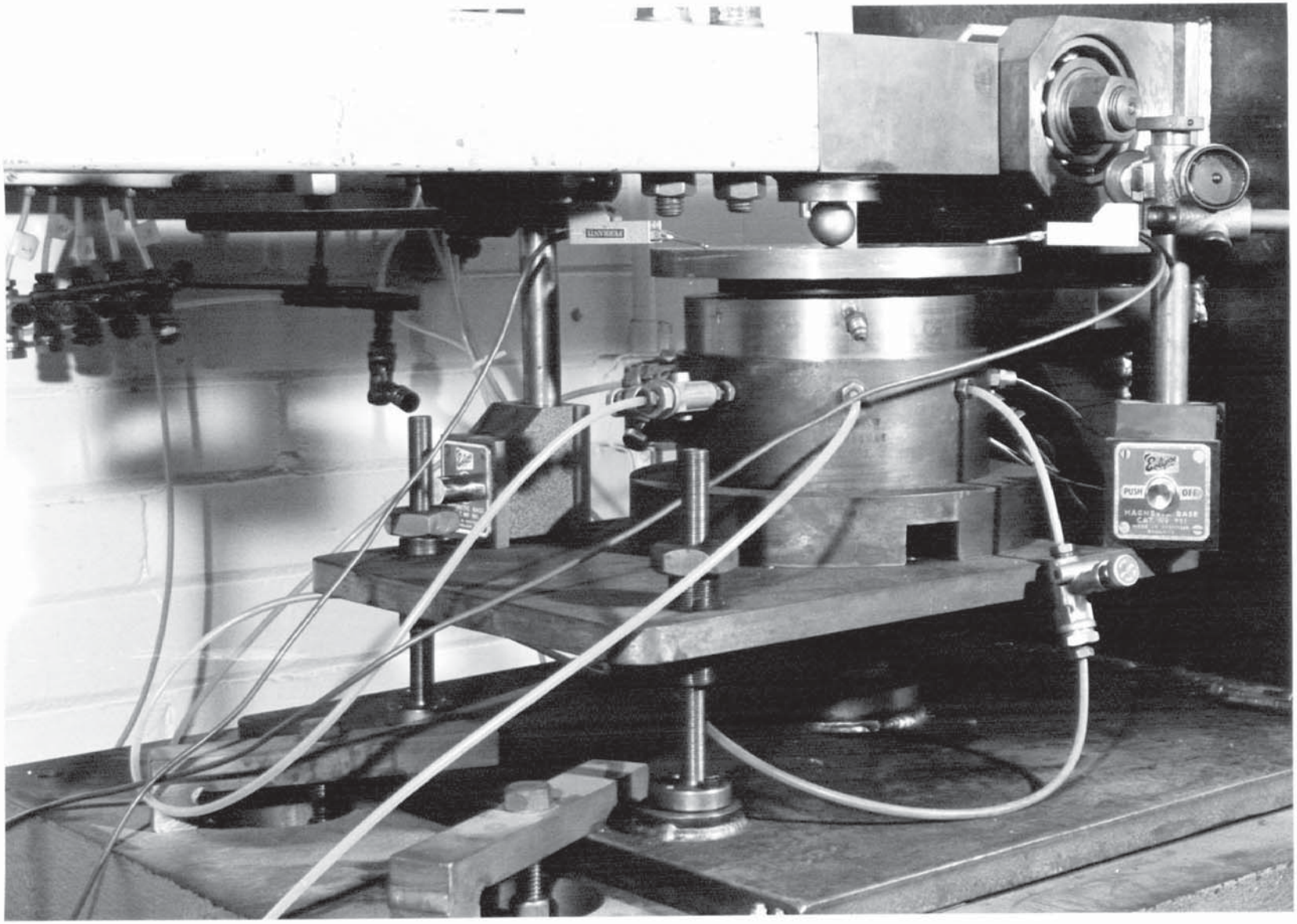

Plate 2 The bearing with micro - comparators.

minimizes the friction at the pivot point and allows the pivot arm and upper bearing surface to float freely in the vertical plane.

Initially the rigid backing to which the elastomer layer is bonded (see plate 3), was securely fixed to the pivot arm by allen screws as shown in figure 4.4(a). However later this arrangement was modified and replaced with a steel ball as shown in figure 4.4(b). This allows the bearing surfaces to self align parallel with each other during bearing tests. The lower half of the bearing containing the porous pad, is supported on two differential screws and an off - centre ball pivot (refer back to figure 4.3). The conical surfaces locating this ball are hardened by a treatment known as tuffriding. The differential screws which were originally intended for the fine parallelism adjustment of the bearing surfaces (these are now self - aligning) are now used for levelling the porous pad surface prior to bearing tests (see section 4.5.4). However details of the screw are shown in figure 4.5. The inner thread has a pitch of 20 threads per inch while the outer thread has a pitch of 1.25mm. This produces a theoretical linear adjustment of 0.02mm per 360^{o}degree turn of the outer thread. As shown in figure 4.6 the differential screws are non - linear in practice, due to manufacturing thread errors but dispite this the screws operate satisfactory for levelling of the porous pad surface.

To accommodate for different elastomer layer

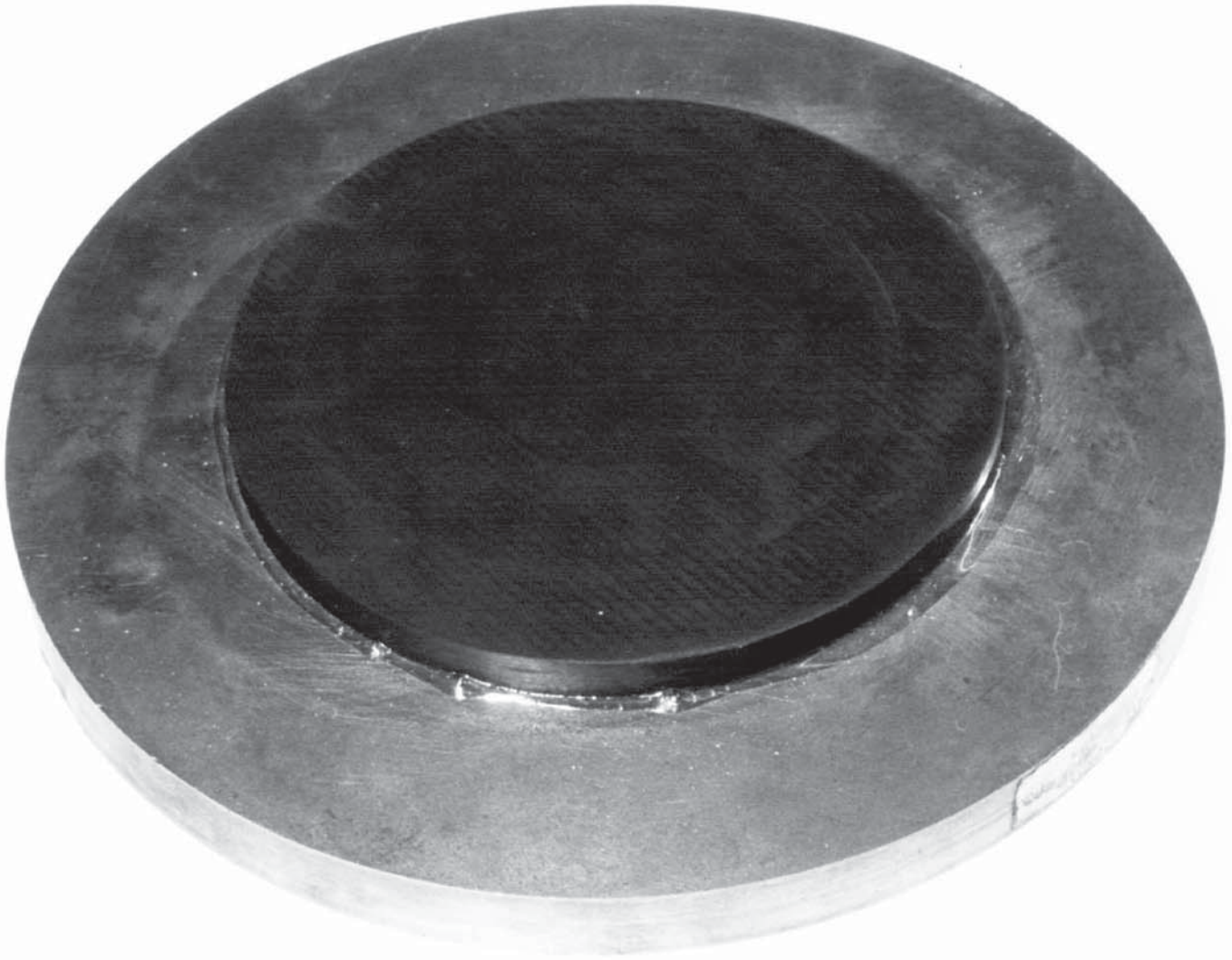

Plate 3 The elastomer layer.

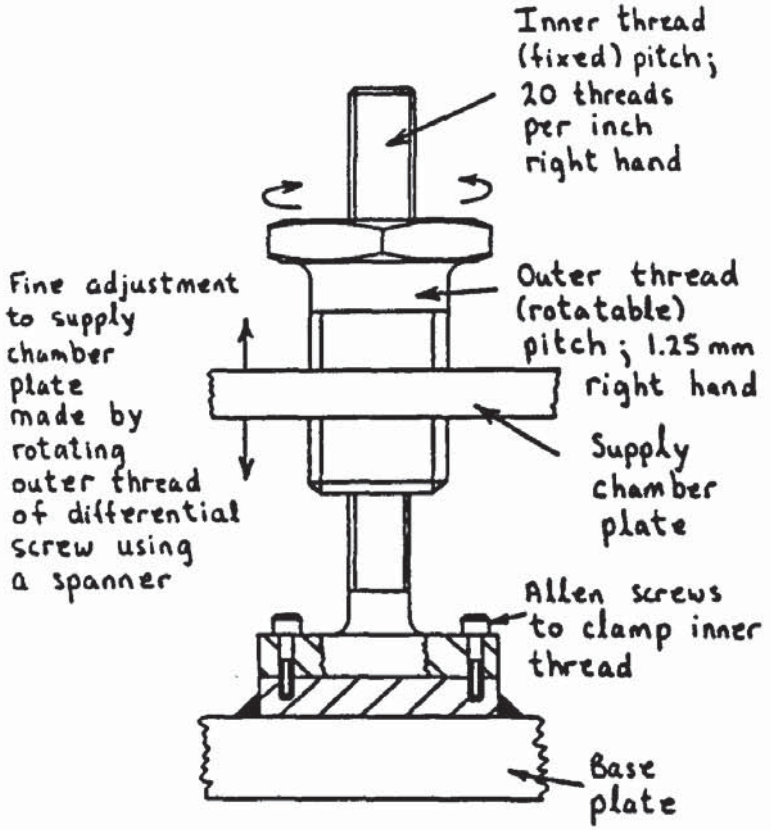

Figure 4.5 Details of differential screws

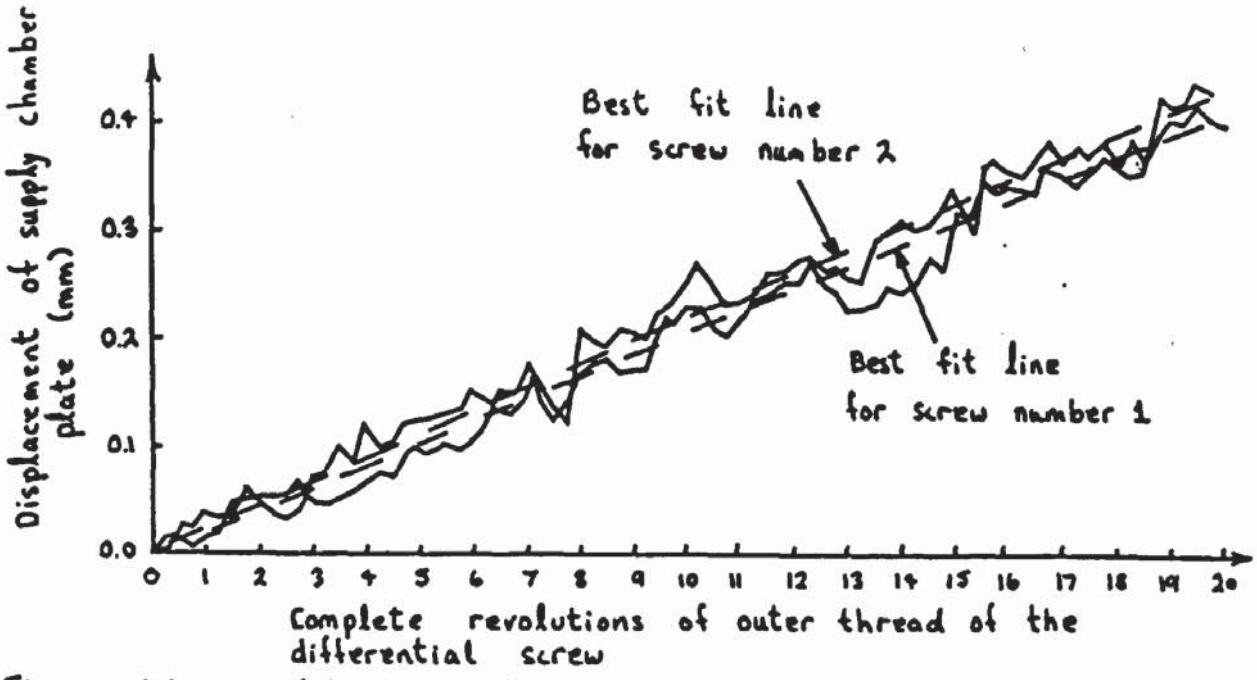

Figure 4.6 Calibration of differential screws

thicknesses, spacers and shims are used under the off - centre ball pivot (see figure 4.7). When spacers and shims are added or removed a corresponding adjustment to the differential screws is made by rotating the inner thread of the screw only. To achieve this it is necessary to unscrew the 4 allen bolts which secure the bottom of the inner screw to the rig base plate(see figure 4.5).

Figures 4.8 and 4.9 show details of the porous pad supply chamber and connections to pressure tappings in the porous pad (the mounting and sealing of pressure tappings in the porous pad is described in section 4.3.3). Photographs of the porous pad supply chamber are shown in plates 4 and 5. Originally the porous pad supply chamber was designed as shown in figure 4.8(a) and machined from aluminium (including the porous pad holder) to avoid corrosion particularly from acid attack during treatment of the porous pad surfaces (see section 4.3.4). However during deflection measurements of the porous pad (see section 4.3.6) the porous pad holder was found to deflect considerably under hydrostatic pressures within the supply chamber compared to the porous pad. Both the supply chamber and the porous pad holder were therefore modified as shown in figure 4.8(b) and machined in mild steel. After these modifications the deflection of the porous pad holder when the supply chamber is pressurized are negligible compared to deflections of the porous pad. The corrosion of the mild steel was reduced by wiping the outside of the supply

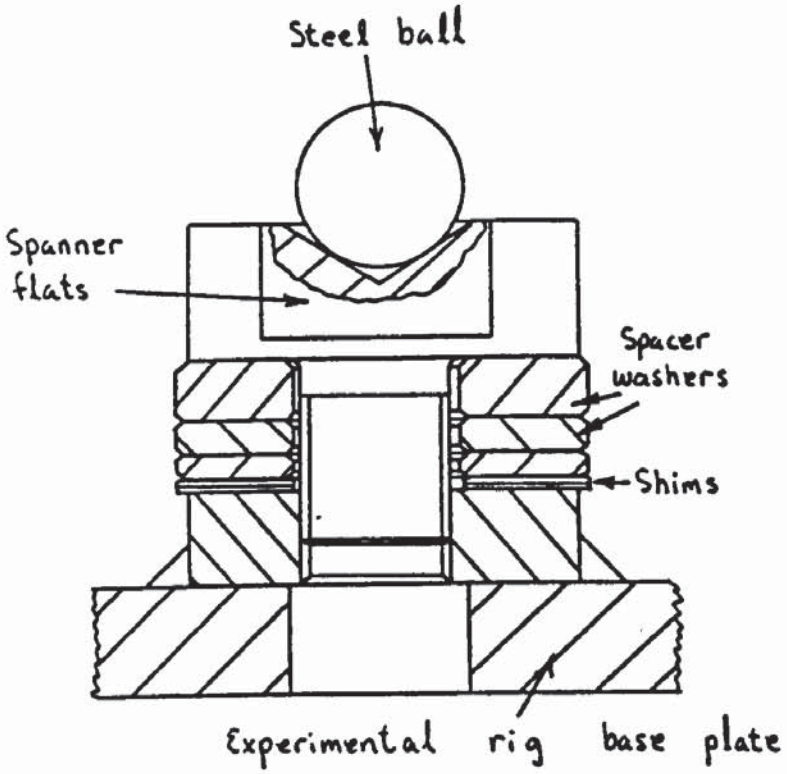

Figure 4.7 Details of the off-centre ball pivot showing spacer washers and shims to accomodate different elastomer layer thicknesses

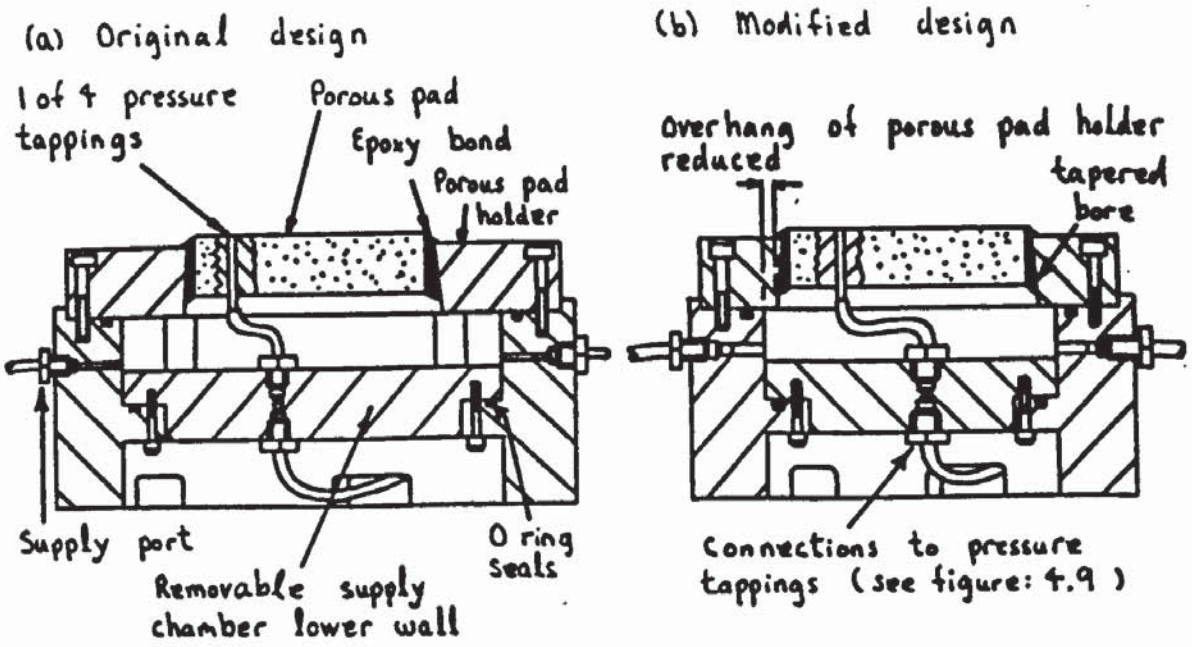

Figure 4.8 Porous pad supply chamber

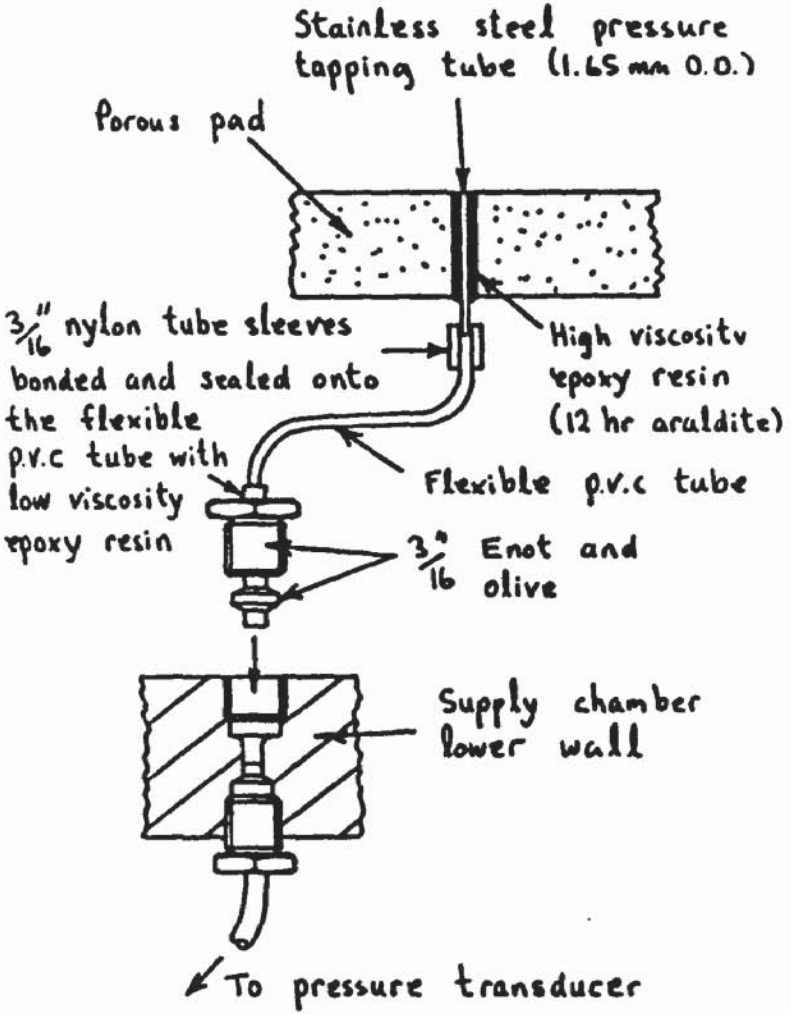

Figure 4.9 Connections to pressure tappings in porous pad

(a) For porous pad number 3 only

(b) For porous pad numbers 1, 2, 4 and 5

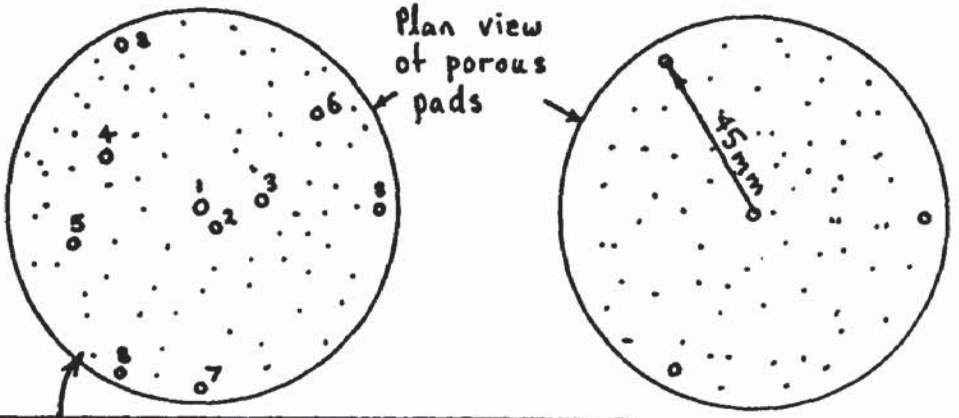

Tapping	1	2	3	4	5	6	7	8
radius (mm)	0	9·17	19·87	29·81	40	44·58	47·13	45

Figure 4.10 Location of pressure tappings in porous pads

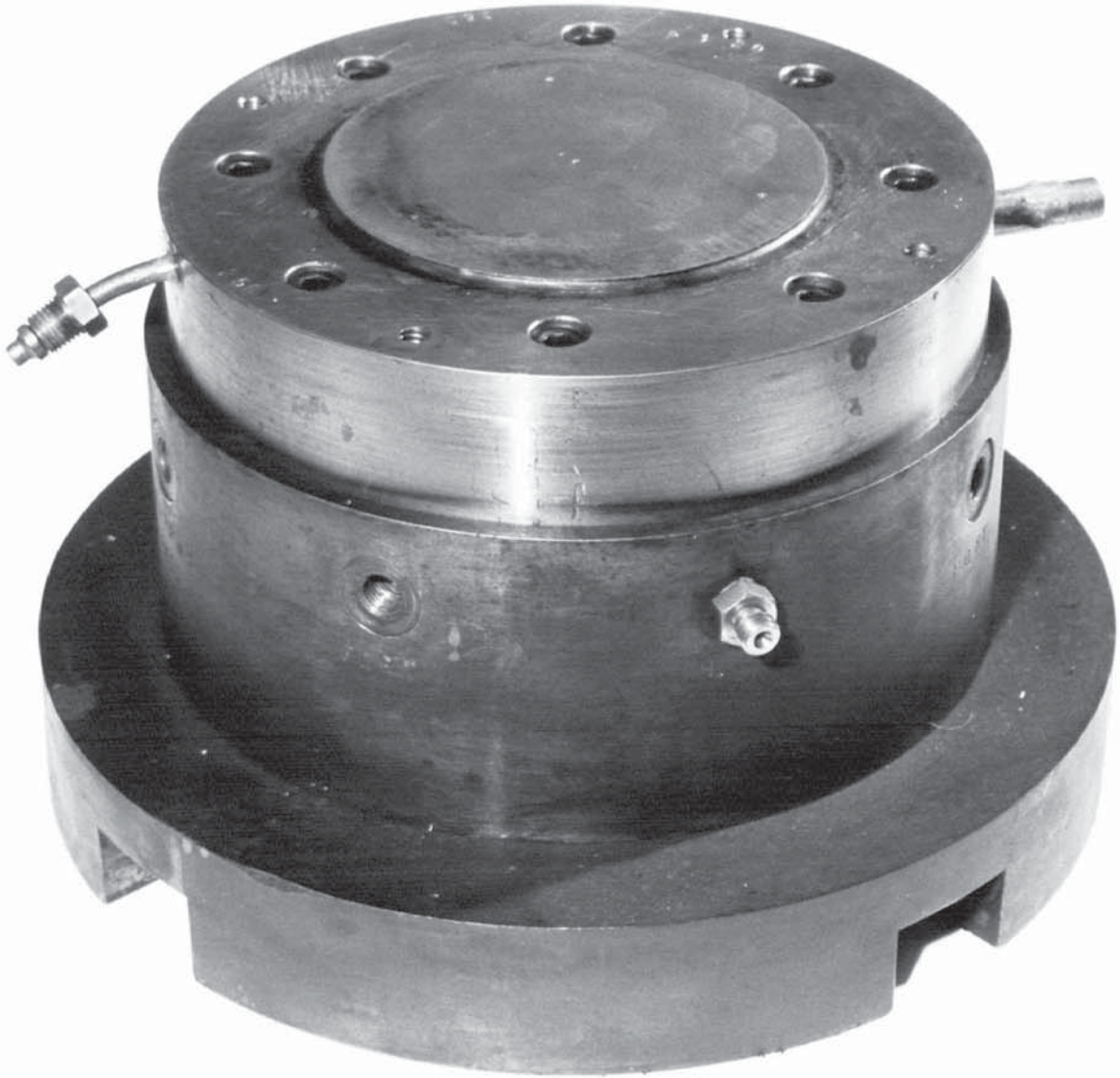

Plate 4 The porous pad supply chamber.

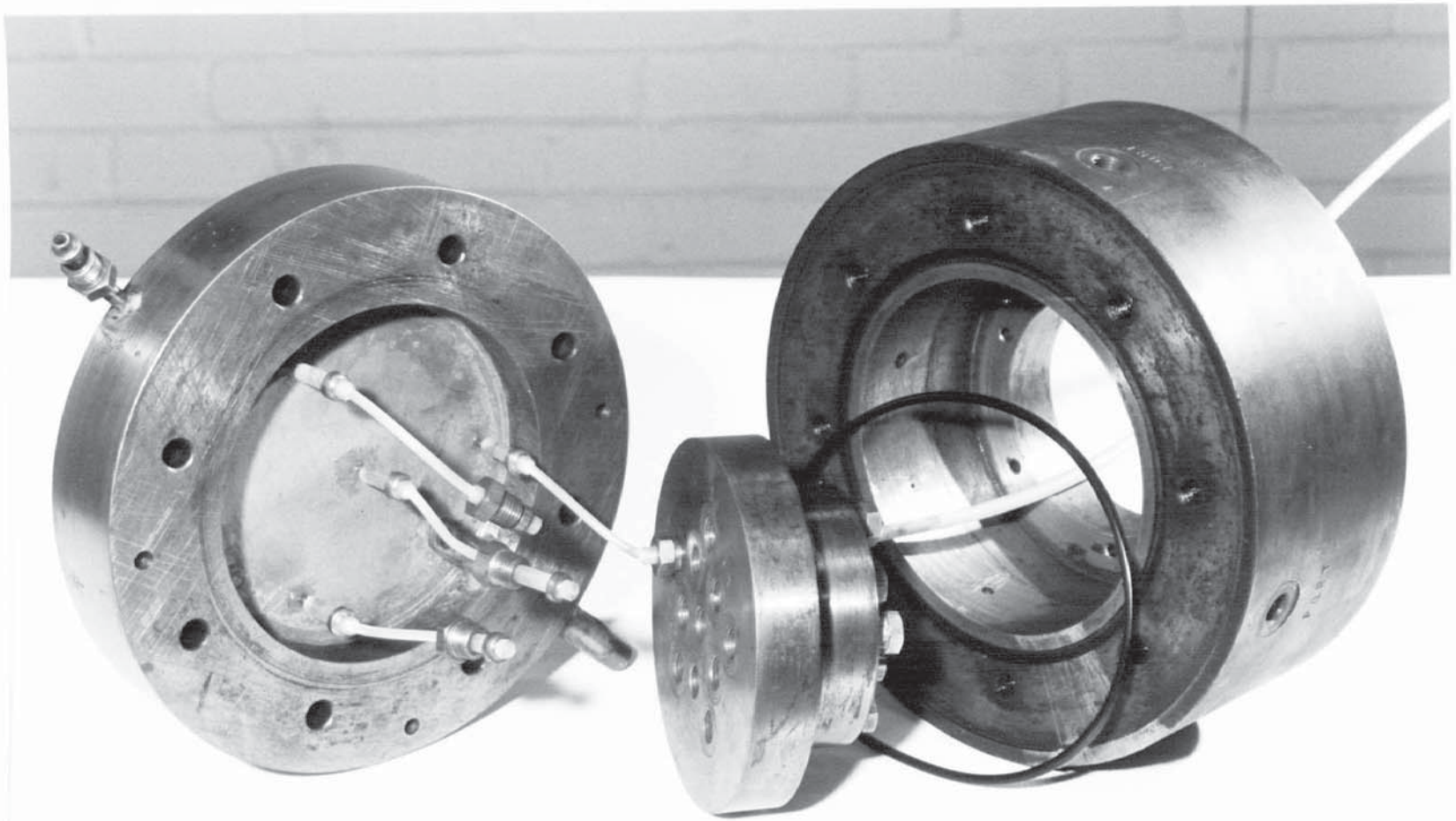

Plate 5 Unassembled porous pad supply chamber.

chamber with a partially oil soaked cloth.

For the measurement of film pressures it was initially intended to insert ten pressure tappings in each porous pad as shown in figure 4.10(a) and this was done on one of the porous pads (i.e. porous pad number 3, see chapter 5). However in attempts to assemble the porous pad on the supply chamber with all ten tappings connected (see section 4.3.3) some of the flexible tubes to each tapping crinkled and became blocked, even though this tube is only 1.7 mm outside diameter and quite flexible. It was only possible to connect four pressure tappings at a time and therefore subsequent porous pads were only fitted with four tappings as shown in figure 4.10(b). Three of these pressure tappings are placed at a radius of 45mm so as to measure the average pressure gradient at the bearing exit $r = r_b$. This was considered necessary for the accurate derivation of bearing clearance h_d (see section 4.5.2). However to obtain experimental film pressure profiles for comparison with theoretical predictions a series of experiments were carried out using porous pad 3. With this pad a maximum of four of the ten pressure tappings were connected at a time, the others being plugged using Enot fittings. By repeating the same experiment three times, film pressure readings from all ten tappings could be taken and a film pressure profile obtained.

Although the bearing clearance itself could not be directly measured, it is possible to measure displacements

of the rigid backing to the elastomer layer using three micro - comparators (one of which is shown in figure 4.3) equally spaced around the vertical axis of the bearing. Each micro - comparator gives an electrical output corresponding to displacements of the gauge tip which is measured using a Ferranti minicom meter. This meter has four ranges of measurement; 0 to 15, 0 to 30, 0 to 150 and 0 to 300 micrometers. From the micro - comparator measurements it is possible to obtain the bearing approach c (see section 4.5.3). It is also possible from the three micro - comparator readings, to check for parallelism of the bearing surfaces.

A schematic layout of the air supply system and associated instrumentation for the measurement of flowrate, supply pressure, etc. is shown in figure 4.11. Air is supplied via a series of large reservoir cylinders fed from a single stage compressor driven by a 37 kilowatt electric motor. Under no-flow conditions the supply pressure reached approximately 10.3 bars (150 psi). However this supply pressure typically reduced to 8.3 bars (120 psi) when air was used for the bearing.

The supply from the reservoir is filtered using an oil and water filter followed by a fine particle filter in series. A pressure regulator is used to control the pressure to the bearing supply chamber. Downstream of the pressure regulator is a rotameter flowmeter for the measurement of bearing flowrate. This flowmeter by Fisher

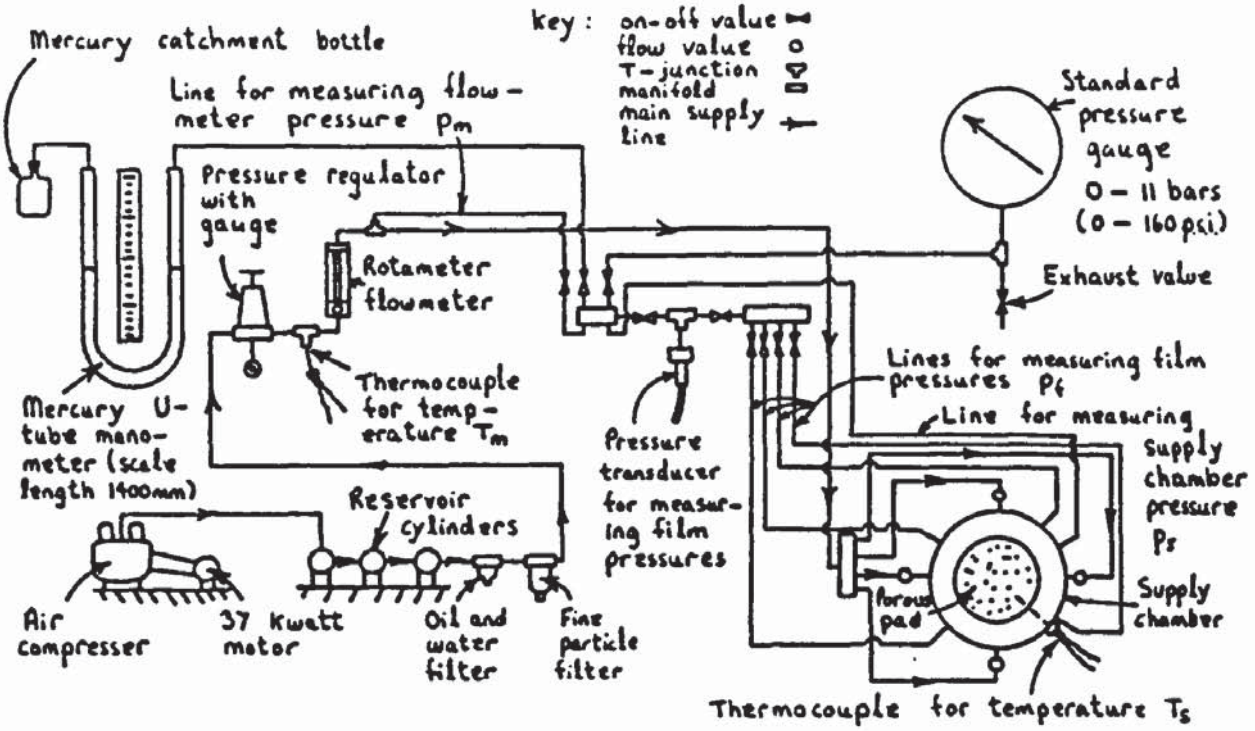

Figure 4.11 Main rig air supply and instrumentation layout

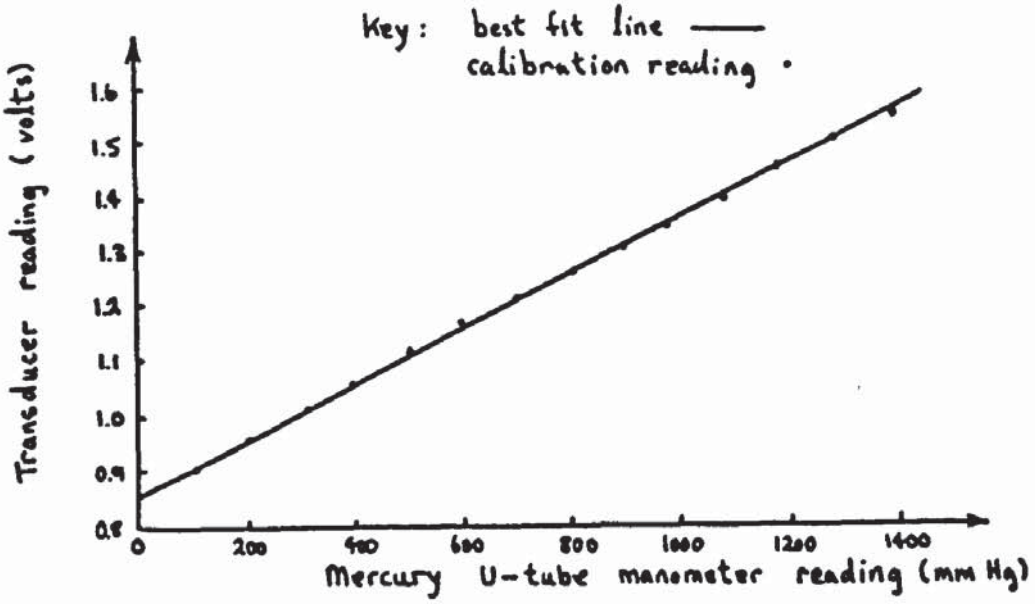

Figure 4.12 Typical calibration line for pressure transducer used to measure bearing film pressures

Controls Ltd has interchangeable tubes and floats for a wide range of flowrate measurements in the range 0.04 to 50 litres/minute at 15°C temperature and 1.013 bars pressure for air. It is important to locate the flowmeter downstream of the pressure regulator so as to minimize the correction necessary to the flow meter readings accounting for the pressure and density of flow. These corrections are given by manufacturers calibration charts supplied with the flowmeter.

From the flowmeter the supply line is connected to the bearing supply chamber via 4 ports. This ensures an even distribution of air supply to the porous pad. Both the supply chamber pressure p_s and the supply line pressure at the flowmeters p_m are measured using a standard test pressure gauge with a scale 0 to 160 psi (0 to 11 bars). This test gauge was calibrated using a dead weight pressure tester and found to have a constant error of +1 psi (0.069 bars).

For the measurement of film pressures via connections to pressure tappings in the porous pad, a pressure transducer (0 to 6.9 bars (0 to 100 psi)) is used. Initially the mercury U tube manometer with a scale length of 1400mm was intended for this purpose but it often took several minutes before the mercury column settled down to allow a film pressure reading to be taken. This is attributed to the small bore diameter of the pressure tappings in the porous pad and the large volume of air

required to displace the mercury in the U tube. The pressure transducer is supplied with 12 volts from a stabilized power supply. Transducer pressure readings in volts are measured using a digital volt meter and calibrated before each bearing test against the U tube mercury manometer. The plumbing in the main rig supply shown in figure 4.11 allows this to be carried out in isolation from the supply chamber and the pressure tappings. As shown in a typical calibration (figure 4.12) the transducer gave a very linear output over the range 0 to 1.87 bars (0 to 27 psi) which covers the range of film pressures taken during the bearing tests.

Each connection to a pressure tapping in the porous pad is isolated by an on - off valve. These valves are connected to a manifold to which the pressure transducer is also connected. This enables the pressure at each pressure tapping in the porous pad to be measured separately one at a time.

In chapter 3 the assumption was made that flow through the bearing is isothermal. It is therefore necessary to check that the supply temperature T_s of air to the bearing is equal, to within 1 ^{o}C or so of the ambient temperature T_a . To measure T_s a thermocouple is mounted through the wall of the bearing supply chamber. A second thermocouple is also mounted in the supply line near to the flowmeter. This enables a correction to be made for temperature on the flowmeter reading using manufacturers calibration charts.

The readings from both thermocouples are measured using a digital voltmeter. A calibration sheet is supplied with each thermocouple.

Before bearing tests were carried out a thorough check was made for any air leaks in the system particularly those downstream of the flowmeters and at connections to pressure gauges, etc. This was achieved by pressurizing the system, care being taken not to blow out the porous pad from its holder (see section 4.3.1), and using soapy water to detect the leaks. Note that it is important to check the epoxy seal around the circumference of the porous pad. A method of achieving this is described in section 4.3.1.

4.3 POROUS PADS

4.3.1 MOUNTING AND SEALING

Initially as suggested by Taylor and Lewis (9, 24) the porous pads were sealed around their circumference using an epoxy putty such as Devcon plastic aluminium F containing 80% aluminium and 20% epoxy plastic. After hardening the excess putty was removed by machining and the porous pad mounted in their holders using epoxy resin. However when these porous pads were assembled on the bearing supply chamber and pressurised with air, this often resulted in cracking of the putty seal at relatively low supply pressures of approximatly 1.38 bars (20 psi) for a 20mm

thickness pad. This problem was not reported (9, 24) probably because smaller diameter porous pads with higher aspect ratio's S_b were used.

This epoxy putty was used (9, 24) to stop the epoxy resin from being absorbed by the porous pad. If this occurred the flow characteristics of the porous pad could be affected along the boundary $r = r_b$, $z = 0$ to h_b ,i.e. the porous pad circumference (see figure 3.1). However for all current bearing tests low porosity porous pads are being used. Therefore the author considered it acceptable to use a low viscosity epoxy resin such as slow setting (12 hr) araldite to both seal and mount the porous pads in their holders (see figure 4.8). This was achieved in one operation and produced a more flexible bond between the porous pad and its holder. In addition the porous pad holders were tapered along their bore to give further support to the porous pads (see figure 4.8). As a result of these measures the porous pads could be pressurized to withstand a pressure difference of 0.138 bars (2 psi) per mm thickness of the porous pad, i.e. 2.76 bars (40 psi) for a 20mm thickness pad.

This epoxy bond between the porous pad and its holder was checked for leaks by attaching a perspex cylinder (originally constructed for electro - polishing of the porous pads, see section 4.3.4) over the porous pad as shown in figure 4.13, such that they can be immersed in water. By pressurizing the porous pad to between 0.138 and

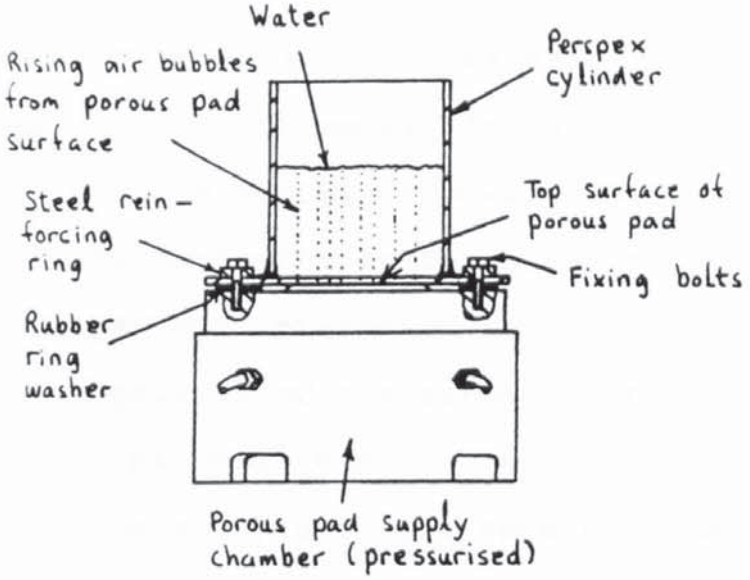

Figure 4.13 Checking the seal of the porous pad epoxy bond and visual inspection of porous pad permeability distribution

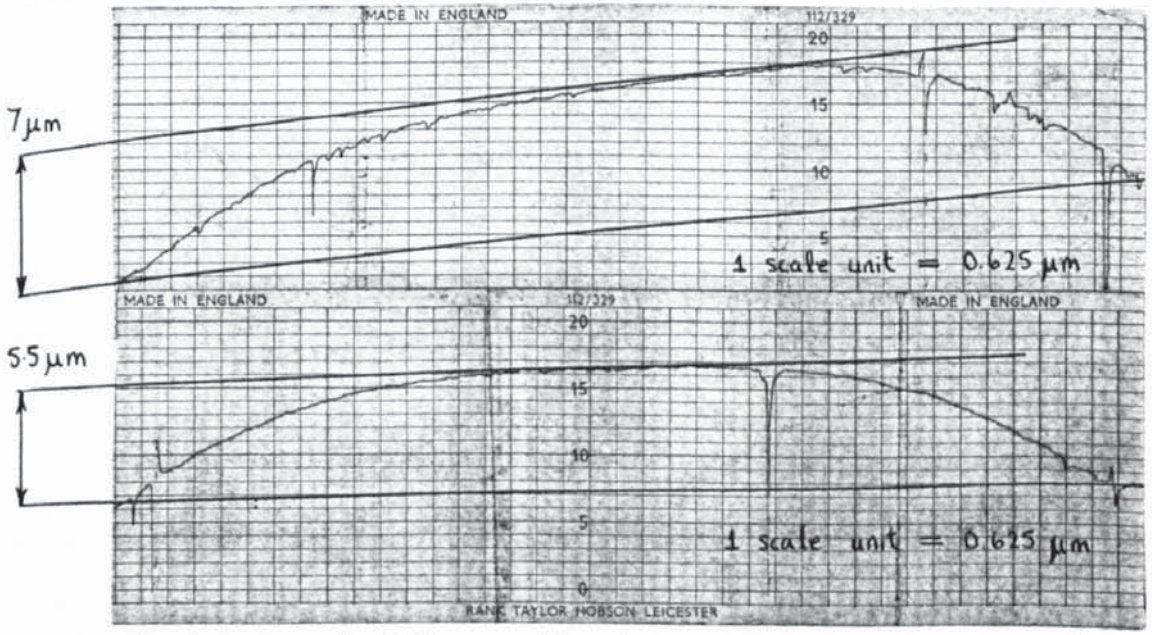

Figure 4.14 Typical flatness profiles taken across two diameters at right angles to each other for a stainless steel porous pad after surface grinding (pad grade; 150, supplier; B.S.A. Sintered Products Ltd.)

0.345 bars (2 and 5 psi) while it is assembled on the supply chamber a stream of small air bubbles will rise from the porous pad surface through the water. Leaks in the epoxy bond will be indicated by large air bubbles rising from the porous pad circumference, i.e. the epoxy bond. Also a visual inspection of the permeability distribution across the porous pad can be made. This is indicated by the distribution of air bubbles rising from the porous pad surface.

4.3.2 SELECTION OF SUITABLE GRADE AND MATERIAL

The first batch of sintered porous pads were supplied by BSA Sintered Products Ltd in both bronze and stainless steel. These were 101.6 mm (4 inches) in diameter with thicknesses of 12.7 mm (1/2 inch) and 25.4 mm (1 inch). Manufactures grading for the bronze pads were 250 and 450 and these roughly corresponded to grades 150 and 250 respectively for the stainless steel pads.

Problems were encountered during surface grinding of the bronze pads which resulted in the removal of sintered particles from this surface, causing pitting. Fine grinding depths and feed rates were tried with several different grade grinding wheels but pitting still persisted. These pads were therefore unsuitable for bearing experiments and discarded.

The stainless steel pads were however ground

successfully to a flatness of 7 micrometers (see figure 4.14) and initially acid etched as described in section 4.3.4 (note that the porous pads were later electro - polished, see section 4.3.4).

However during preliminary bearing tests using the stainless steel porous pads it was impossible to stop pneumatic hammer occurring(bearing instability). Several elastomer layers of various thicknesses and hardnesses were tried at different bearing supply pressures ps and bearing loads w with no success. The cause of this was later accounted to the high permeability of the porous pads (40), (41) which gives rise to instability in the porous aerostatic thrust bearing. In the porous and compliant aerostatic thrust bearing this condition is made worse by the recess formed in the bearing clearance by deflections of the compliant surface.

A new batch of stainless steel porous pads was therefore ordered from Schumacher Filters Ltd (BSA Sintered Products ceased to exist from March 1983). These pads were supplied in the lowest gradings of permeability offered by the manufacturer i.e. SIKA R1,3 and 5. The pads were of 100 mm diameter and in thicknesses of 10,15 and 20 mm. With the new porous pads it was now possible to operate the bearing without pneumatic hammer depending on the supply pressure p_s (refer to chapter 5). This confirmed that the selection of a low permeability porous pad is important for the stable operation of a porous and compliant aerostatic thrust

bearing.

4.3.3 PRESSURE TAPPINGS

Having selected suitable porous pads these were fitted with pressure tappings at the locations shown in figure 4.10. As described in section 4.2.3 all the porous pads except one were fitted with four pressure tappings at the locations shown in figure 4.10(b). Only one porous pad was fitted with ten pressure tappings as shown in figure 4.10(a). For this porous pad (of grade SIKA R3 and thickness 20mm) a test was carried out to find the effect of the presence of pressure tappings on the flow through the porous pad. Before inserting the pressure tappings therefore the characteristics of flow through the porous pad were measured in its as supplied condition i.e. un - ground and un - etched (see section 4.3.5 for measurement of porous pad permeability). The pressure tappings were then inserted into the porous pad and connections fitted using the following procedure:

(a) Drill 2mm holes at each pressure tapping location through the porous pad thickness.

(b) Each pressure tapping is cut from 1.65mm outside diameter stainless steel tube to a length of 35mm greater than the thickness of the porous pad.

(c) These tubes are epoxied into the drilled 2mm holes using slow setting (12 hr) araldite similar to that used to

mount the porous pads in their holders (see section 4.3.1). While the epoxy was setting the porous pad was raised on two parallel strips above a flat surface so that the tubes are 0.5mm below the surface of the porous pad (see figure 4.15). The 0.5mm clearance allows for grinding of the porous pad surface such that the tip of the tubes are not blocked by burring.

(d) After the epoxy has cured a short length (60 mm) of flexible tubing, 0.5 mm internal diameter and 0.6 mm wall thickness (available from Portex Ltd.) was inserted over the exposed ends of the pressure tapping tubes (see figure 4.9). To improve the seal at this joint it was necessary to epoxy a short sleeve from 3/16" (4.763 mm) nylon tube, over the join (see figure 4.9). For this purpose a low viscosity laminating resin was used (available from S.P. Epoxy Resins Ltd.).

(e) For the Enot connection at the other end of the flexible tube (enabling connection through the supply chamber wall, see figure 4.9) a second nylon sleeve of approximately 25 mm length and suitable for 3/16" (4.763 mm) Enot fittings is epoxied. This nylon sleeve is fitted with an olive and Enot.

After all epoxy joints had cured the flexible tube connections to each pressure tapping were checked for leakage. This was achieved by connecting the flexible tube using Enot fittings to the main air supply and pressurizing to 8.3 bars (120 psi). The other end of the pressure

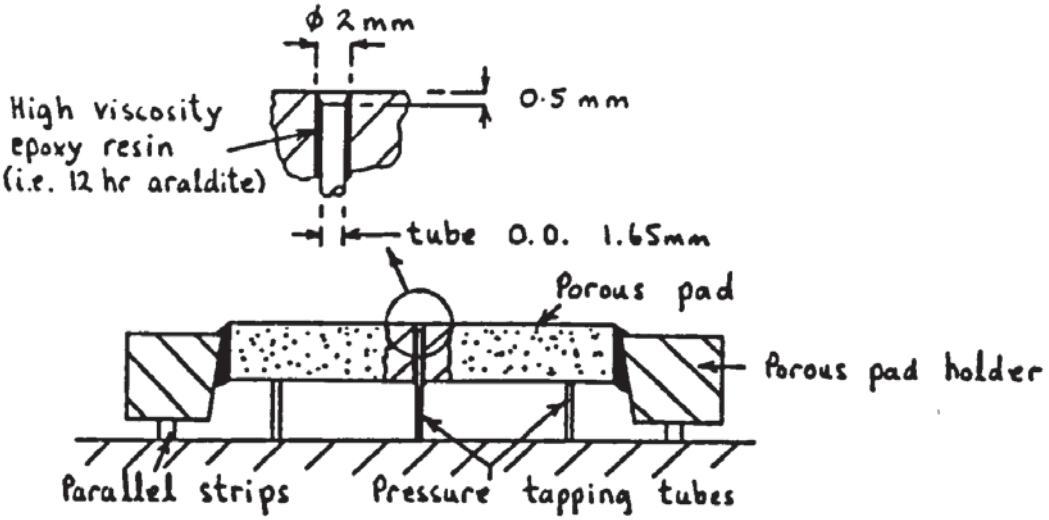

Figure 4.15 Setting of pressure tapping tubes in porous pad

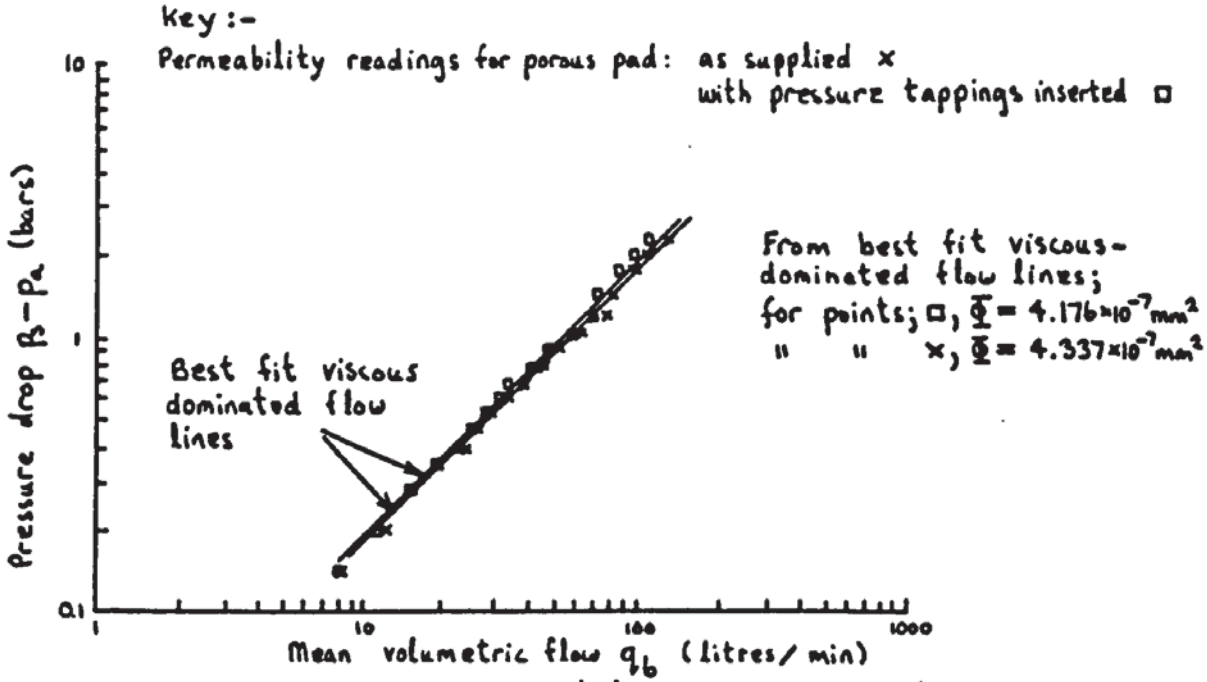

Figure 4.16 Porous pad permeability before and after inserting pressure tappings

tapping was blocked using a finger and the leaks are checked using soapy water. All the flexible tube connections tested in this way were found to be satisfactory.

During assembly of the porous pad on the bearing supply chamber the pressure tappings are connected to the bottom of the supply chamber using the Enot attached to the flexible tube. (see figure 4.8). To enable this the bottom of the supply chamber is removed from the supply chamber so that the pressure tappings are connected prior to assembly.

Having inserted the pressure tappings in the porous pad a second measurement of flow through the porous pad was made. A comparison of the flow through the porous pad before and after inserting the pressure tappings is shown in figure 4.16. It can be seen that a reduction in the porous pad permeability occurs due to the presence of the pressure tappings. But this reduction is only 4% and therefore the pressure tappings are considered to have negligible effect on the flow through the porous pad. However for all porous pads their permeability is measured after insertion of the pressure tappings.

4.3.4 BEARING SURFACE PREPARATION

After surface grinding the porous pads Taylor and Lewis (9),(24) used an acid etching technique to re - open the blocked pores in the porous pad surface caused by

machining forces during grinding. Initially the same technique was used and is described as follows;

During acid etching the porous pad is assembled on the supply chamber (this is removed from the main rig) and pressurized to 0.69 bars (10 psi) from the same supply as for the main rig. A dilute Nitric acid is spread over the porous pad surface using cotton wool and a pair of tongs. When the pores in the porous pad surface begin to re - open the excess acid is carried away by air passing up through the pressurized porous pad. This stops further corrosion taking place within the porous pad. As a safety precaution protective rubber gloves were worn and the acid etching was carried out in a vented fume cuboard for approximately 20 minutes. After etching, the porous pads were removed from the supply chamber to be soaked in water for 1 hr. Subsequent drying of the porous pads was accelerated by re - assembling them on the supply chamber and pressurizing to 0.69 bars (10 psi) so that dry air passed through the pad for approximately 2 hours.

The permeability properties of the porous pad were measured (see section 4.3.5) and presented on a graphical plot of $\log_{10}(p_s - p_a)$ against $\log_{10} q_b$ as shown in figure 4.17. Also shown in this plot is the measured permeability of the same porous pad before grinding and acid etching but with pressure tappings inserted. The viscous dominated flow line would be represented by a 45° line to the horizontal axis plotted through the results as is the case for the

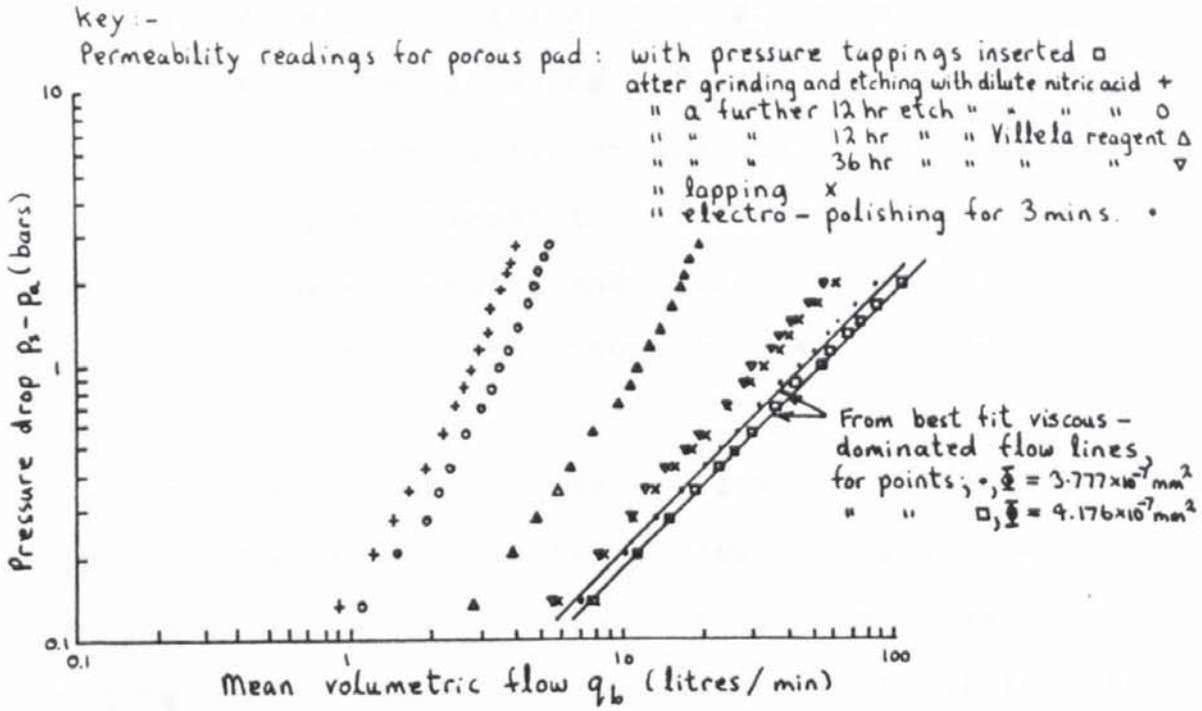

Figure 4.17 Porous pad permeability after various surface treatments

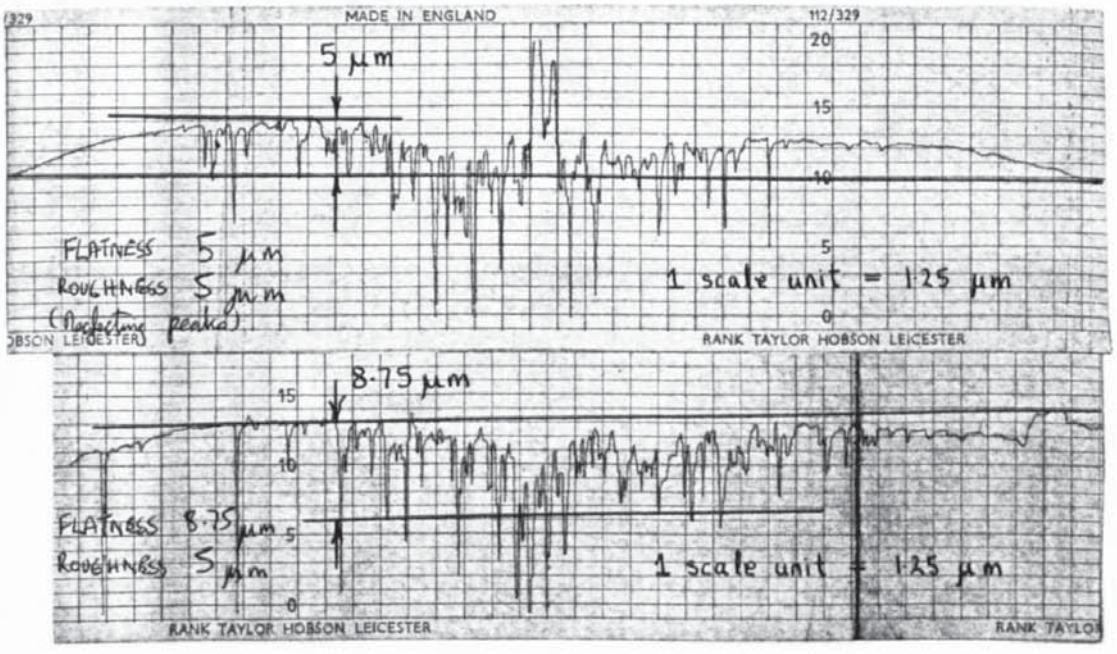

Figure 4.18 Typical flatness profiles taken across two diameters at right angles to each other for a stainless steel porous pad after lapping (pad grade; SIKA R3, supplier; Schumacher filters Ltd)

porous pad before grinding and etching. It can be seen from figure 4.17 that after grinding and acid etching the flow through the porous pad no longer has a viscous dominated flow region and the permeability of the pad is less than that before surface grinding and acid etching. This indicates that there is still pore blockage in the porous pad surface.

After consultation with Mr M. Izzard a postgraduate research student in the Metallurgy department at the University of Aston in Birmingham, a Vilella reagent containing 5mls of hydrochloric acid, 1 gm of picric acid and 100 mls of methyl alcohol was used in place of the dilute Nitric acid. However even after 48 hours of acid etching using this reagent the permeability results as shown in figure 4.17 were still unsatisfactory.

Problems of this nature were not encountered by Taylor and Lewis (9, 24) possibly because the steel pads used were less resistant to acid etching. However it appears that the stainless steel pads currently used (see section 4.3.2) are highly resistant to corrosion during acid etching. While it is possible to account for the pore blockage in the theoretical model for flow through the porous pad as Polome and Gorez (12) have done (see section 2.2.1) this would add further complication to the theoretical analysis presented in Chapter 3.

In an attempt to remedy the problem, lapping of the porous pads was tried. By lapping the ground surface of the

porous pad the thin layer of blocked pores is removed by light abrasion forces. This prevents further pore blockage. However while there was some improvement in the permeability of the porous pad after several hours of lapping as shown in figure 4.17 (this being done by hand on a lapping block), the flow through the porous pad was still not in the viscous dominated flow region even at very low pressures $p_s - p_a$ across the porous pad. And in any case the resulting flatness and roughness of the porous pad surface depended on the skill of the lapper (see flatness measurements in figure 4.18).

An alternative method to acid etching and lapping is electro - polishing. Greenberg and Weger (7) report that this technique is far superior to conventional acid etching, although further details are not given.

While it is possible to use stronger and more corrosive acid etching solutions, this often causes localized attack on the etching surface. Electro - polishing on the other hand, not only gives much higher corrosion rates but also acts uniformly over the surface being treated.

To implement electro - polishing of the porous pads again Mr M. Izzard was consulted. Although it is unusual to polish large samples such as the porous pad, he saw no reason why this could not be achieved.

The electro - polishing technique comprises an anode and cathode immersed in an acid solution while electrically

connected to a D.C. supply. The anode (D.C. supply +ve) forms the surface to be electro - polished while the cathode (D.C. supply -ve) becomes plated with irons from the anode.

Just as with acid etching it is necessary to stop the acid seeping into the porous pad during polishing. Therefore the porous pad was assembled on the bearing supply chamber (this being removed from the main rig) and pressurized between 0.345 and 0.69 bars (5 and 10 psi) from a connected gas cylinder of Nitrogen (see figure 4.19). An electrical contact with the underside of the porous pad is made through its holder (see figure 4.20). This avoids any blinding from the anode of the upper porous pad surface to be polished.

Phosphoric acid at 60^{o}C is used as a solution. This is contained above the porous pad by a flanged perspex cylinder (see plate 6) which is bolted to the porous pad holder and sealed using a rubber washer cut from sheet rubber. The acid is heated using an electrical coil heater. During heating the acid is stirred to give an even temperature distribution, the temperature being measured using a mercury glass thermometer.

The cathode in the shape of a disc was cut approximately 100mm diameter from 0.5mm thick stainless steel sheet. A tag was soldered to its centre so that it could be lowered by its electrical lead into the acid bath to a height of approximately 25mm above the porous pad. By

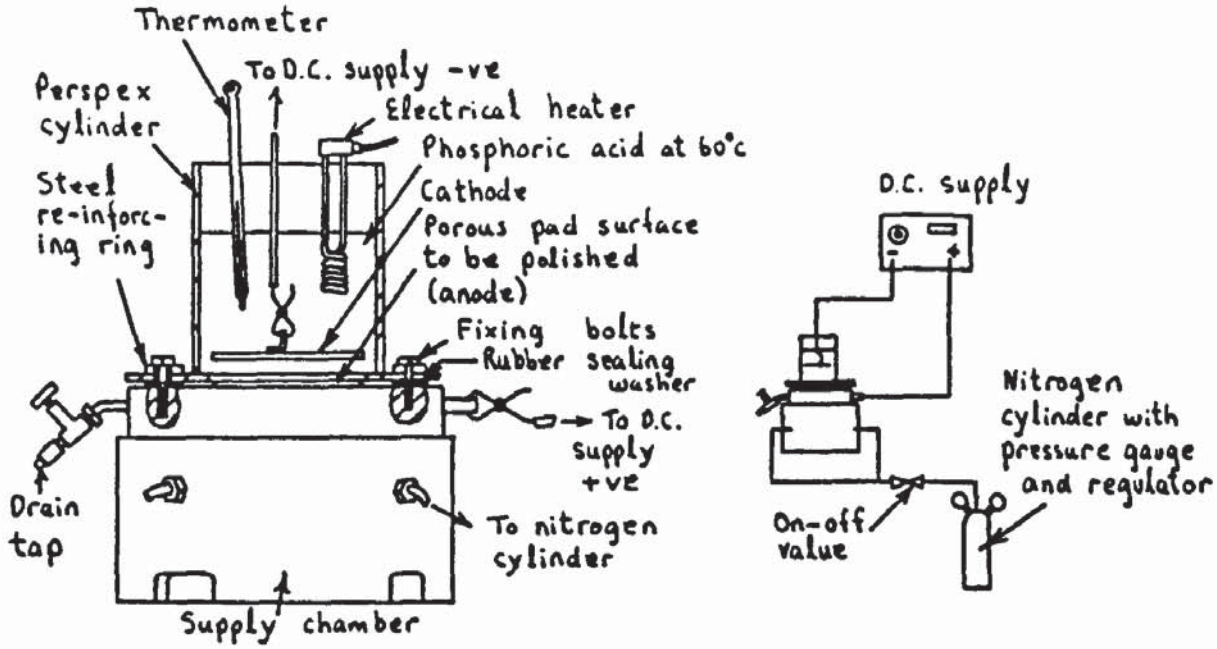

Figure 4.19 Equipment for electro – polishing of porous pads

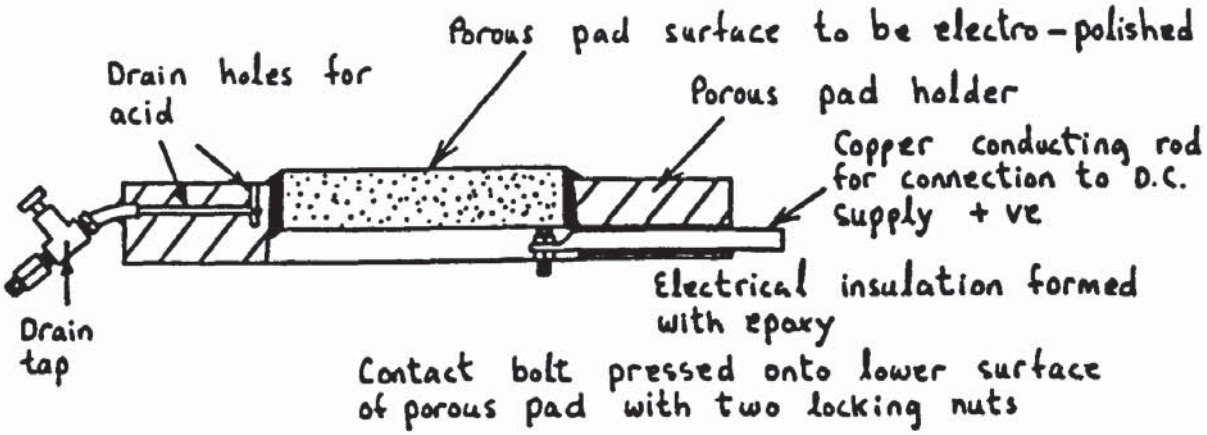

Figure 4.20 Modifications to porous pad holder for electro-polishing of the porous pad surface

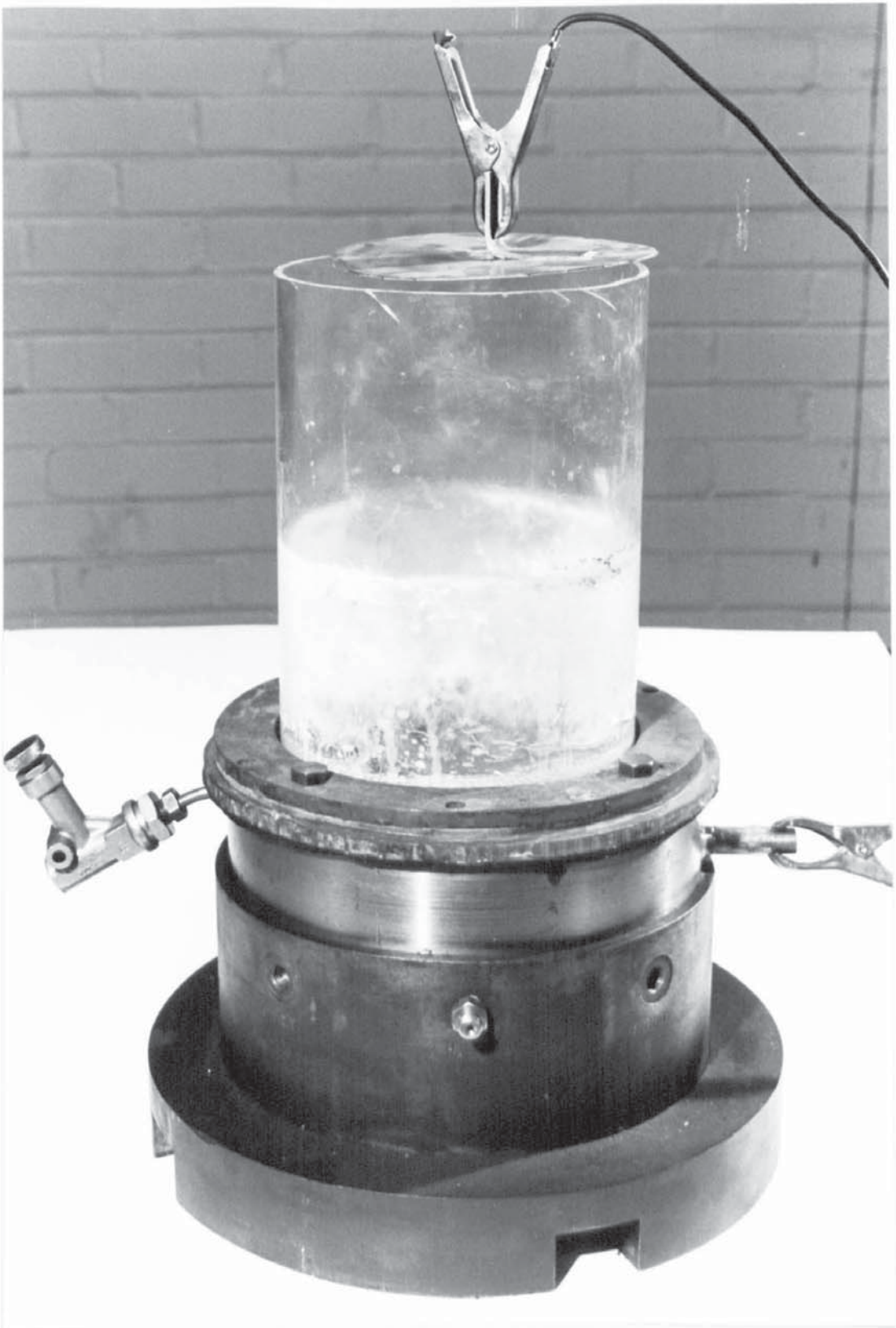

Plate 6 Perspex cylinder used in electro - polishing of the porous pads.

ensuring the cathode is parallel to the porous pad surface a constant distance is maintained between these two surfaces giving a uniform corrosion action.

When the Phosphoric acid reached 60°C the D.C. supply was switched on and the power increased to give a current of 3300 amps per m^2 of anode surface area. For a 100mm diameter porous pad this equals approximately 26 amps. After 3 mins the current was switched off and the acid drained from the perspex cylinder via a drain tap fitted to the porous pad holder (see figure 4.20).

From the first sample it was immediately obvious by visual inspection that the electro - polishing had re - exposed the original pore structure of the porous pad. In effect the thin blocked layer caused by surface grinding had been removed. Figure 4.17 shows that there is minimal difference in the permeability characteristics after electro - polishing compared to those of the original unground porous pad.

4.3.5 PERMEABILITY CALIBRATION

The permeability of the porous pads can be determined from measurements of the pressure drop across its thickness at different flow rates q_b. These measurements are made by assembling the porous pad on the supply chamber and connecting to the main rig supply so that the porous pad can be pressurized at a regulated supply pressure p_s. The

upper surface of the porous pad is allowed to exhaust freely to the atmosphere and as a result the pressure drop Δp across its thickness is uniform and equal to $p_s - p_a$. For each regulated value of p_s a flowmeter reading is taken from the rotameters together with the pressure of metered flow p_m and its temperature T_m. From these readings and using the manufacturers calibrations charts for the rotameter the mean volumetric flow rate q_b through the porous pad can be obtained.

Values of absolute viscosity η for air flow through the porous pad are read from tables (91) for dry air at low pressure and at a temperature $(T_s + T_a)/2$ (i.e. the mean temperature of flow across the porous pad). The value of η thus obtained is accurate over a wide range of pressures especially above atmospheric pressure (91).

From these measurements of pressure drop $p_s - p_a$ versus flow rate q_b, Taylor and Lewis (9) showed that the viscous dominated flow region of the porous pad could be accurately shown on a plot of $\log_{10}(\Delta p)$ against $\log_{10} q_b$. As already mentioned in the literature survey (section 2.2.1) Darcy's law in the form of equation 2.10 gives a straight line of unity gradient (i.e. 45° to the horizontal axis) on this plot. An example of such a plot is shown for convenience in figure 4.21.

Using least squares method a straight line of unity gradient can be fitted to the measured experimental points. According to the least squares principle (92) this line

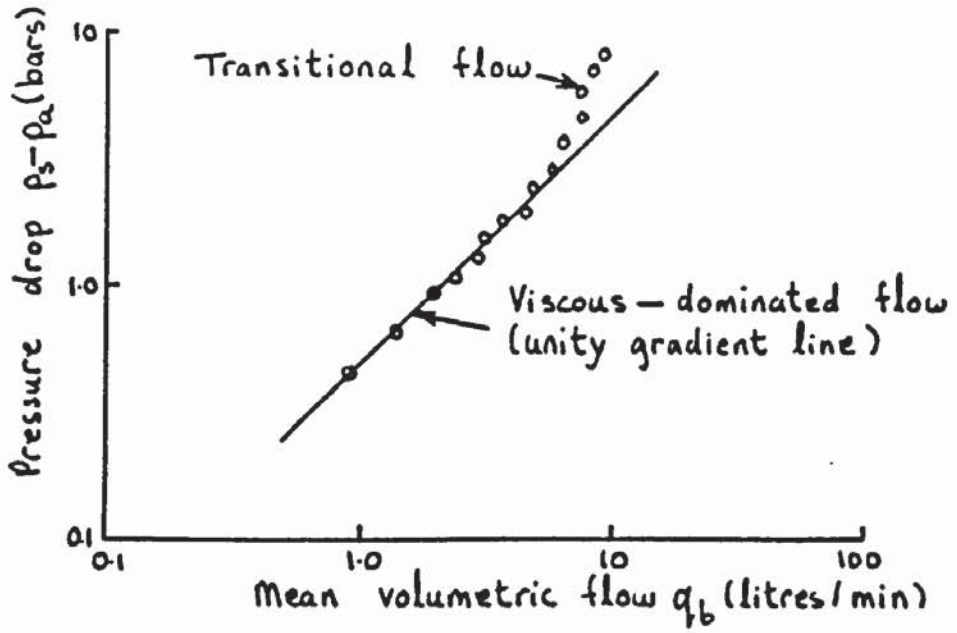

Figure 4.21 Porous pad permeability ; the viscous flow region

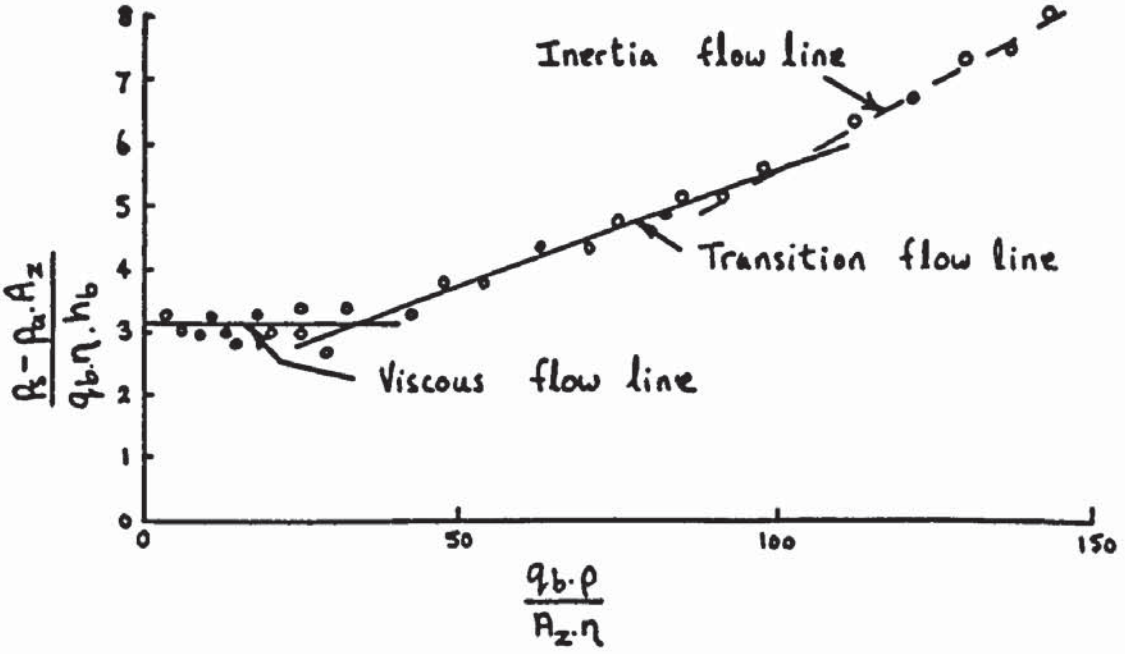

Figure 4.22 Porous pad permeability ; regions of viscous, transitional and inertia flow

must pass through the centroid of these points which lie within the viscous flow region. In section 2.2.1 equation 2.7 for the viscous flow region was re - written in the form;

$$\mathrm{Log}_{10}(\Delta p) = \mathrm{Log}_{10}(q_b) + \mathrm{Log}_{10}\left(\frac{n.h_b}{A_z.\Phi}\right) \qquad 4.1$$

This equation is of the general form for a straight line, i.e.:

$$y = m_1.x + c_1 \qquad 4.2$$

where $y = \mathrm{Log}_{10}(\Delta p)$

$x = \mathrm{Log}_{10}(q_b)$

$m_1 = 1$

$c_1 = \mathrm{Log}_{10}\left(\frac{n.h_b}{A_z.\Phi}\right)$

Applying the least squares method:

$$c_1 = \bar{y} - m_1.\bar{x} \qquad 4.3$$

where $\bar{y} = \frac{1}{k_1}\sum_{n=1}^{k_1}(y)_n \qquad 4.4$

$$\text{and} \quad \bar{x} = \frac{1}{k_1} \sum_{n=1}^{k_1} (x)_n \qquad 4.5$$

Having obtained a value of c_1 the viscous permeability of the porous pad is therefore given by:

$$\phi = \left(\frac{n.h_b}{A_z} \right) \times 10^{-c_1} \qquad 4.6$$

The viscous flow region ends when the measured points depart from the straight line as shown in figure 4.21. According to Taylor and Lewis (9) this represents the beginning of the transition flow region in which both viscous and inertial flows are significant. This region of flow is represented by equation 2.8 in section 2.2.1, i.e.;

$$\frac{\Delta p.A_z}{q_b.n.h_b} = \frac{1}{\phi} + \frac{q_b.\rho}{A_z.n.\phi} \qquad 4.7$$

Both the transition and viscous flow regions can be represented on a plot of $\frac{\Delta p A_z}{q_b \eta h_b}$ against $\frac{q_b \rho}{A_z \eta}$ (9). An example of this plot is shown in figure 4.22. This plot is known as the modified Morgan plot after Morgan (8) who only recognised a transition flow region.

In the modified Morgan plot the viscous flow region is represented by a horizontal line whose intercept with the

vertical axis equals $1/\Phi$. For measured points in the transition flow region (i.e. those points which do not lie on the viscous flow line in the $\log_{10} \Delta p$ against $\log_{10} q_b$ plot) a least squares line of gradient $1/\phi$ and intercept $1/\Phi$ is fitted.

Although Taylor and Lewis (9) do not show an inertia flow region on this modified Morgan plot, this would be represented by a line fitted to measured points in the inertia flow region, which intercepts the origin and has a gradient of $1/\phi$. An arbitrary inertia flow line is shown dotted in figure 4.22 to illustrate this.

Using these graphs of the type shown in figures 4.21 and 4.22 it is therefore possible to determine the permeability characteristics of the porous pad in any of the three types of flow regions, i.e. viscous, transitional and inertial. Permeability calibrations for several porous pads used in the bearing tests are presented and discussed in chapter 5.

4.3.6 DEFLECTIONS AND RIGIDITY OF THE POROUS PAD IN BENDING

To obtain the rigidity properties of the porous pad it is necessary to measure its deflection while subject to a known pressure loading p_b. For this test it is convenient to pressurize the porous pad with a supply pressure p_s and measure corresponding deflections of the porous pad as shown in figure 4.23. These measurements are made with the

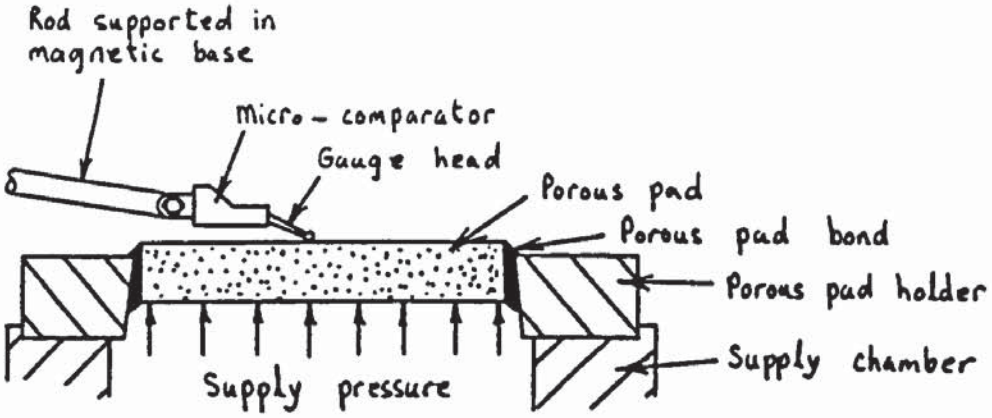

Figure 4.23 Measurements of porous pad deflections

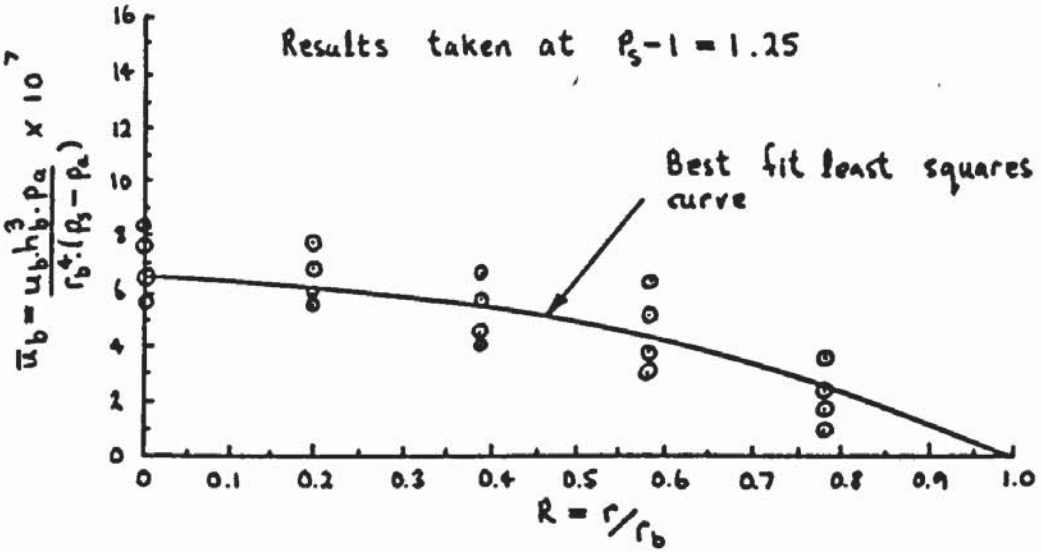

Figure 4.24 Non - dimensional plot of porous pad deflections in bending due to a uniform pressure difference across its thickness

porous pad assembled on the bearing supply chamber which in turn is connected to the main rig supply. Prior to recording deflections, the micro - comparator is calibrated and adjusted using slip gauges (see section 4.5.4) then positioned on the porous pad surface and set to zero. The porous pad is then pressurized to a maximum pressure difference $p_s - p_a$ in bars, equal to 0.138 times the porous pad thickness in mm. This is to avoid blowing the pads "out" from their holders (see section 4.3.1).

At this pressure the deflection of the porous pad was recorded from the micro - comparator instrumentation. To obtain a deflection profile of the porous pad this procedure was repeated for several different radial positions on the porous pad surface, i.e. r = 0, 10, 20, 30, 40 and 50 mm. Readings were also taken across four radii at 90° to each other to obtain an average.

While it is possible to take further deflection measurements at lower pressure differences $p_s - p_a$, it was found that these were too small to give accurate deflection profiles of the porous pad. However to check the linearity of porous pad deflections versus pressure difference $p_s - p_a$, deflection measurements were recorded at several lower pressure differences $p_s - p_a$ for the r = 0 position only.

Results are presented in non - dimensional form in a plot similar to that shown in figures 4.24 and 4.25. Note that the shear deflection of the porous pad bond at $r = r_b$ must be subtracted from deflection measurements of the

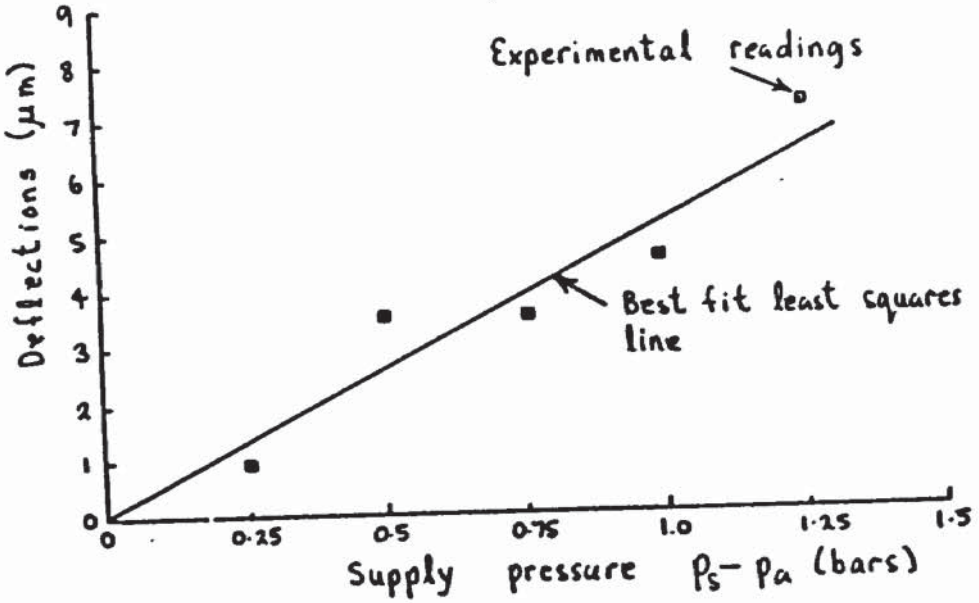

Figure 4.25 Deflections of the porous pad at r = 0 due to bending only.

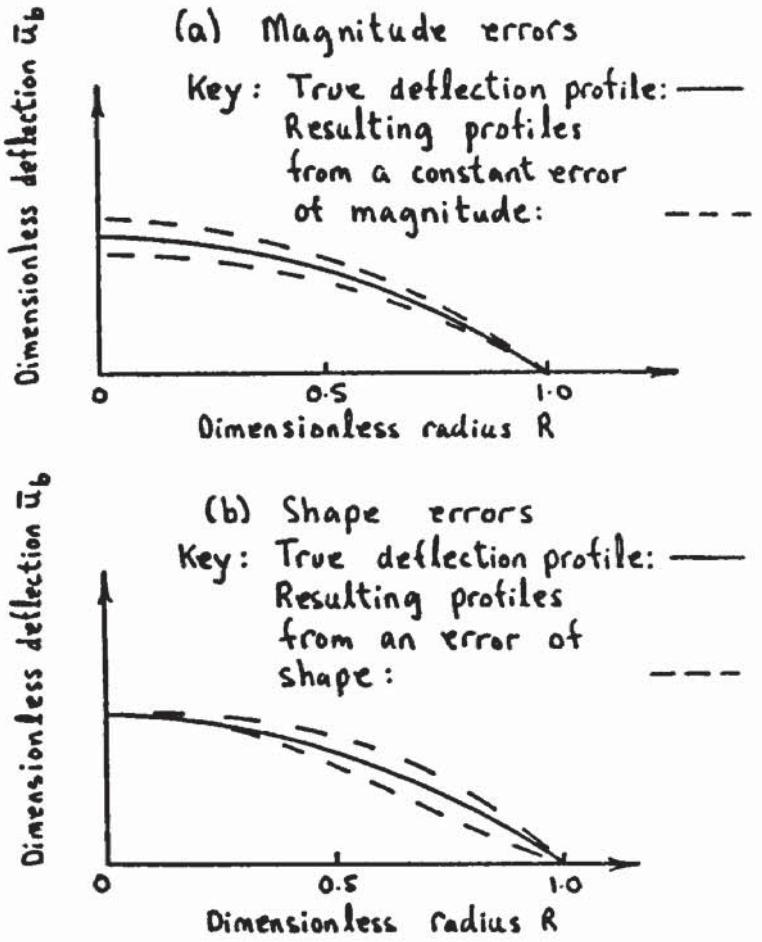

Figure 4.26 Types of error in the measured deflection profile of the porous pad in bending

porous pad at r = 0, 10, 20, etc in order to obtain its deflection due to bending only. Note that these shear deflections of the porous pad bond are calibrated separately (see section 4.5.2). Using the elasticity theory presented in section 3.5 for deflections of the porous pad in bending it is possible to fit a curve to the experimental points in figure 4.24 using least squares methods. In equation 3.88;

$$p_b = p_s - p_a = \text{constant} \qquad 4.8$$

Therefore in equation 3.89;

$$a_0 = p_s - p_a \qquad 4.9$$

$$\text{and} \quad k_3 = 0 \qquad 4.10$$

Equation 3.90 reduces to

$$u_b = \frac{1}{D_b} \cdot \frac{(p_s - p_a).r^4}{64} + \frac{b_1.r^2}{4} + b_3 \qquad 4.11$$

Equation 4.11 gives the deflection profile for the porous pad in bending subject to a uniform pressure loading $p_s - p_a$. Equation 4.11 may be expressed in the following non - dimensional form:

$$\bar{u}_b = \frac{1}{\bar{D}_b}\left(\frac{R^4}{64} + \frac{b_4 . R^2}{4} + b_5\right) \qquad 4.12$$

where $$b_4 = \frac{b_1 . \bar{D}_b . p_a . h_b^3}{(p_s - p_a) . r_b^2} \qquad 4.13$$

and $$b_5 = \frac{b_3 . \bar{D}_b . p_a . h_b^3}{(p_s - p_a) . r_b^2} \qquad 4.14$$

Consider the following general equation:

$$F(R) = c_1 . f_1(R) + c_2 . f_2(R) + c_3 . f_3(R) \qquad 4.15$$

Using least squares methods (92) the constants c_1 , c_2 and c_3 may be obtained from the matrix equation:

$$\begin{bmatrix} \Sigma(f_1(R))^2 & \Sigma f_1.(R).f_2(R) & \Sigma f_1(R).f_3(R) \\ \Sigma f_2(R).f_1(R) & \Sigma(f_2(R))^2 & \Sigma f_2(R).f_3(R) \\ \Sigma f_3(R).f_1(R) & \Sigma f_3(R).f_2(R) & \Sigma(f_3(R))^2 \end{bmatrix} \times \begin{bmatrix} c_1 \\ c_2 \\ c_3 \end{bmatrix} = \begin{bmatrix} \Sigma f_1(R).F(R) \\ \Sigma f_2(R).F(R) \\ \Sigma f_3(R).F(R) \end{bmatrix} \qquad 4.16$$

Where $\sum$ signifies the summated values corresponding to the data points in figure 4.24 to which the least squares curve is to be fitted.

Comparing equations 4.15 and 4.12, in the matrix equation 4.16 :-

$$F(R) = \bar{u}_b \qquad 4.17$$

$$f_1(R) = R^4 \qquad 4.18$$

$$f_2(R) = R^2 \qquad 4.19$$

$$f_3(R) = 1 \qquad 4.20$$

$$c_1 = \frac{1}{64.\bar{D}_b} \qquad 4.21$$

$$c_2 = \frac{b_4}{4.\bar{D}_b} \qquad 4.22$$

$$c_3 = \frac{b_5}{\bar{D}_b} \qquad 4.23$$

Values of $F(R)$, $f_1(R)$ and $f_2(R)$ are obtained from the experimental points in figure 4.24. Expressing equation 4.16 as follows:

$$[\,f\,] \times [\,c\,] = [\,F\,] \qquad 4.24$$

the constants c_1, c_2 and c_3 are obtained by inverting the matrix $[f]$ and re - arranging equation 4.24, i.e.:

$$[\,c\,] = [\,f\,]^{-1} \times [\,F\,] \qquad 4.25$$

A solution to equation 4.25 was achieved using the HP9845 desktop mini computer which can invert and multiply

matrix arrays. Values of $\overline{D_b}$, b_4 and b_5 can be determined from the constants c_1, c_2 and c_3 using equations 4.21 to 4.23. The least squares curve is thus plotted by substituting value of $\overline{D_b}$, b_4 and b_5 back into equation 4.12.

By fitting equation 4.12 to the experimental points in this way a value of $\overline{D_b}$ is directly obtained and from its definition;

$$D_b = \bar{D}_b . p_a . h_b^3 \qquad 4.26$$

In section 3.5 a second constant B_b is required for equation 3.91. Substituting for a_o and k_3 from equations 4.9 and 4.10, equation 3.91 becomes;

$$b_1 = - \frac{2}{(B_b + D_b)} \left(\frac{B_b}{D_b} . \frac{(p_s - p_a).r_b^2}{16} + \frac{3.(p_s - p_a).r_b^2}{16} \right) \qquad 4.27$$

Re - arranging equation 4.27 and using equations 4.13 and 4.26 it can be shown that;

$$B_b = -D_b \left(\frac{8.b_4 + 3}{8.b_4 + 1} \right) \qquad 4.28$$

Having obtained the flexural constants D_b and B_b for a porous pad it is possible to determine deflections for any

pressure loading p_b using the equations in section 3.5. However during the course of experimentation large variations in the values of D_b and B_b were obtained from two separate deflection measurements on one porous pad. Despite this the deflection profiles from each measurement matched to within 10% of the maximum deflection at r = 0. The reasons for this can be shown in the following error analysis.

In equation 4.12, b_5 can be eliminated since $u_b = 0$ at R = 1, i.e. substituting this condition into equation 4.12 gives;

$$b_5 = -\left(\frac{1}{64} + \frac{b_4}{4} \right) \qquad 4.29$$

and substituting for b_5 in equation 4.12 gives;

$$\bar{u}_b = \frac{1}{\bar{D}_b} \left(\frac{R^4}{64} + \frac{b_4}{4}.(R^2 - 1) - \frac{1}{64} \right) \qquad 4.30$$

Errors in the measurement of porous pad deflections can be divided into errors of magnitude (as shown in figure 4.26(a)) and errors of shape (figure 4.26(b)). The errors of magnitude can be represented by the deflection of the porous pad at R = 0. In equation 4.30 let $\bar{u}_b = \bar{u}_{b1}$ at R = 0, hence;

$$\bar{u}_{b1} = -\frac{1}{D_b}\left(\frac{b_4}{4} + \frac{1}{64}\right) \qquad 4.31$$

from equation 4.28

$$b_4 = -\frac{(3.\bar{D}_b + \bar{B}_b)}{8.(\bar{D}_b + \bar{B}_b)} \qquad 4.32$$

Substituting for b_4 in equation 4.31 using equation 4.32 gives;

$$\bar{u}_{b1} = \frac{5.\bar{D}_b + \bar{B}_b}{64.\bar{D}_b.(\bar{D}_b + \bar{B}_b)} \qquad 4.33$$

The shape of the deflection profile as defined by equation 4.30 depends on the value of b_4 only. From equation 4.31;

$$\bar{D}_b = -\frac{1}{\bar{u}_{b1}}\left(\frac{b_4}{4} + \frac{1}{64}\right) \qquad 4.34$$

Substituting for $\bar{D}_b$ in equation 4.30 using equation 4.34 gives;

$$\bar{u}_b = -\bar{u}_{b1}.\frac{(R^4 + 16.b_4.(R^2 - 1) - 1)}{(16.b_4 + 1)} \qquad 4.35$$

For a deflection profile of constant magnitude $\bar{u}_{b1}$ the space between two curves of different shape is given by;

$$\Delta\bar{u}_b = \frac{\partial\bar{u}_b}{\partial b_4} \cdot \Delta b_4$$

Using equation 4.35;

$$\Delta\bar{u}_b = -\bar{u}_{b1} \cdot \left(\frac{16.R^2.(1 - R^2).\Delta b_4}{(16.b_4 + 1)^2} \right) \qquad 4.36$$

This spacing is a maximum when;

$$\frac{\partial(\Delta\bar{u}_b)}{\partial R} = 0$$

Differentiating equation 4.36 with respect to R and equating to zero gives R = 0.7071. The spacing between two deflection profiles of equal magnitude $\bar{u}_{b1}$ but different shape as defined by b_4 in equation 4.35 is a maximum at R = 0.7071.

Let the deflection of the porous pad at this point be $\bar{u}_{b2}$. In equation 4.30;

$$\bar{u}_{b2} = -\frac{1}{\bar{D}_b} * \frac{(32.b_4 + 3)}{256} \qquad 4.37$$

Substituting for b_4 from equation 4.32 gives;

$$\bar{u}_{b2} = \frac{(9.\bar{D}_b + \bar{B}_b)}{256.\bar{D}_b.(\bar{D}_b + \bar{B}_b)} \qquad 4.38$$

Equations 4.33 and 4.38 may be written explicit in $\bar{D}_b$ and $\bar{B}_b$ as follows:

$$\bar{D}_b = \frac{1}{128.(\bar{u}_{b1} - 2.\bar{u}_{b2})} \qquad 4.39$$

$$\bar{B}_b = \frac{20.\bar{u}_{b2} - 9.\bar{u}_{b1}}{128.(\bar{u}_{b1} - 4.\bar{u}_{b2}).(\bar{u}_{b1} - 2.\bar{u}_{b2})} \qquad 4.40$$

The total differential of $\bar{D}_b$ and $\bar{B}_b$ can be expressed as;

$$\Delta\bar{D}_b = \frac{\partial\bar{D}_b}{\partial\bar{u}_{b1}}.\Delta\bar{u}_{b1} + \frac{\partial\bar{D}_b}{\partial\bar{u}_{b2}}.\Delta\bar{u}_{b2} \qquad 4.41$$

$$\text{and} \quad \Delta\bar{B}_b = \frac{\partial\bar{B}_b}{\partial\bar{u}_{b1}}.\Delta\bar{u}_{b1} + \frac{\partial\bar{B}_b}{\partial\bar{u}_{b2}}.\Delta\bar{u}_{b2} \qquad 4.42$$

In terms of the ratios $\Delta\bar{D}_b/\bar{D}_b$, $\Delta\bar{B}_b/\bar{B}_b$, $\Delta\bar{u}_{b1}/\bar{u}_{b1}$ and $\Delta\bar{u}_{b2}/\bar{u}_{b2}$ equations 4.41 and 4.42 can be written;

$$\frac{\Delta\bar{D}_b}{\bar{D}_b} = \frac{\bar{u}_{b1}}{\bar{D}_b}.\frac{\partial\bar{D}_b}{\partial\bar{u}_{b1}}.\frac{\Delta\bar{u}_{b1}}{\bar{u}_{b1}} + \frac{\bar{u}_{b2}}{\bar{D}_b}.\frac{\partial\bar{D}_b}{\partial\bar{u}_{b2}}.\frac{\Delta\bar{u}_{b2}}{\bar{u}_{b2}} \qquad 4.43$$

$$\frac{\Delta\bar{B}_b}{B_b} = \frac{\bar{u}_{b1}}{\bar{B}_b}\cdot\frac{\partial\bar{B}_b}{\partial\bar{u}_{b1}}\cdot\frac{\Delta\bar{u}_{b1}}{\bar{u}_{b1}} + \frac{\bar{u}_{b2}}{\bar{B}_b}\cdot\frac{\partial\bar{B}_b}{\partial\bar{u}_{b2}}\cdot\frac{\Delta\bar{u}_{b2}}{\bar{u}_{b2}} \qquad 4.44$$

Differentiating equations 4.39 and 4.40 with respect to $\bar{u}_{b1}$ and $\bar{u}_{b2}$ and using the same equations to replace $\bar{D}_b$ and $\bar{B}_b$ equations 4.43 and 4.44 become;

$$\frac{\Delta\bar{D}_b}{D_b} = -\left(\frac{\bar{u}_{b1}}{\bar{u}_{b1} - 2.\bar{u}_{b2}}\right)\frac{\Delta\bar{u}_{b1}}{\bar{u}_{b1}} + \left(\frac{2.\bar{u}_{b2}}{\bar{u}_{b1} - 2.\bar{u}_{b2}}\right)\frac{\Delta\bar{u}_{b2}}{\bar{u}_{b2}} \qquad 4.45$$

and

$$\frac{\Delta\bar{B}_b}{\bar{B}_b} = \frac{(9.\bar{u}_{b1}^2 - 22.\bar{u}_{b1}\bar{u}_{b2} + 48.\bar{u}_{b2}^2).\bar{u}_{b1}}{(\bar{u}_{b1}^2 - 6.\bar{u}_{b1}.\bar{u}_{b2} + 8.\bar{u}_{b2}^2).(20.\bar{u}_{b2} - 9.\bar{u}_{b1})}\cdot\frac{\Delta\bar{u}_{b1}}{\bar{u}_{b1}}$$

$$+ \frac{(-16.\bar{u}_{b1}^2 + 256.\bar{u}_{b1}.\bar{u}_{b2} - 160.\bar{u}_{b2}^2).\bar{u}_{b2}}{(\bar{u}_{b1}^2 - 6.\bar{u}_{b1}.\bar{u}_{b2} + 8.\bar{u}_{b2}^2).(20.\bar{u}_{b2} - 9.\bar{u}_{b1})}\cdot\frac{\Delta\bar{u}_{b2}}{\bar{u}_{b2}} \qquad 4.46$$

Errors in $\bar{D}_b$ and $\bar{B}_b$ are dependant not only on measurement errors of $\bar{u}_{b1}$ and $\bar{u}_{b2}$ but also on the value of $\bar{u}_{b2}$ compared to $\bar{u}_{b1}$. Consider a typical deflection profile i.e. figure 4.24. From this deflection profile $\bar{u}_{b1} = 5.8\times10^{-7}$ and $\bar{u}_{b2} = 3.3\times10^{-7}$. Substituting these values into equations 4.45 and 4.46 gives;

$$\frac{\Delta\bar{D}_b}{\bar{D}_b} = 7.5\times\frac{\Delta\bar{u}_{b1}}{\bar{u}_{b1}} - 8.5\times\frac{\Delta\bar{u}_{b2}}{\bar{u}_{b2}} \qquad 4.47$$

$$\frac{\Delta\bar{B}_b}{\bar{B}_b} = 30.32\times\frac{\Delta\bar{u}_{b1}}{\bar{u}_{b1}} - 44.5\times\frac{\Delta\bar{u}_{b2}}{\bar{u}_{b2}} \qquad 4.48$$

If the error in the fitted deflection profile curve is confined to a band of ±10% as shown in figure 4.27 then typical values of $\Delta\bar{u}_{b1}/\bar{u}_{b1}$ and $\Delta\bar{u}_{b2}/\bar{u}_{b2}$ are ± 0.1. The maximum errors in equations 4.47 and 4.48 are therefore;

$$\frac{\Delta\bar{D}_b}{\bar{D}_b} = 7.5\times(\pm 0.1) - 8.5\times(\mp 0.1)$$

$$= \pm 1.6$$

$$= \pm 160\%$$

and $$\frac{\Delta\bar{B}_b}{\bar{B}_b} = 30.32\times(\pm 0.1) - 44.5\times(\mp 0.1)$$

$$= \pm 7.482$$

$$= \pm 748.2\%$$

It can be seen that for relatively small errors in $\bar{u}_{b1}$ and $\bar{u}_{b2}$ the corresponding errors in $\bar{D}_b$ and $\bar{B}_b$ are quite large. In this respect therefore both $\bar{D}_b$ and $\bar{B}_b$ are unsuitable constants to specify the porous pad rigidity as their values are unreliable when obtained from the measurement of porous pad deflections. For this reason two new alternative constants are introduced as follows;

The magnitude constant; $M_b = \bar{u}_{b1}$ 4.49

and from equation 4.35;

$$\bar{u}_{b2} = \bar{u}_{b1}\left(\frac{(8.b_* + 0.75)}{(16.b_* + 1)}\right) \qquad 4.50$$

therefore let the shape constant N_b be defined by the equation;

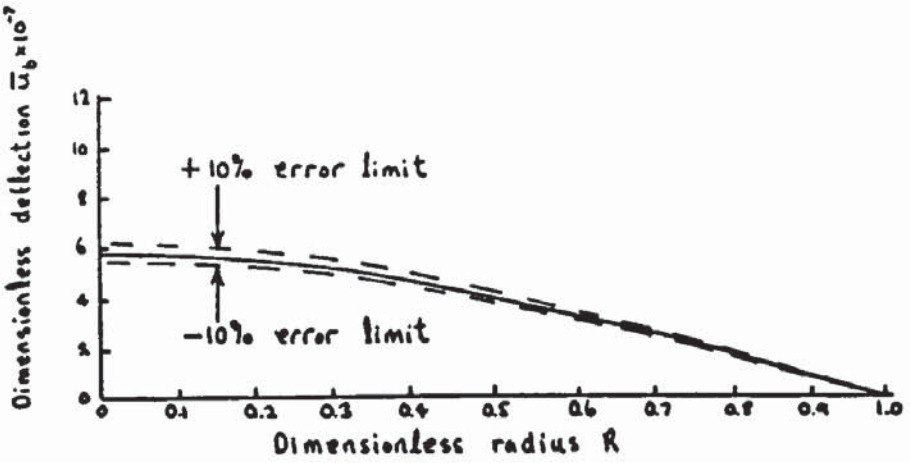

Figure 4.27 Error band ± 10% for deflections of the porous pad

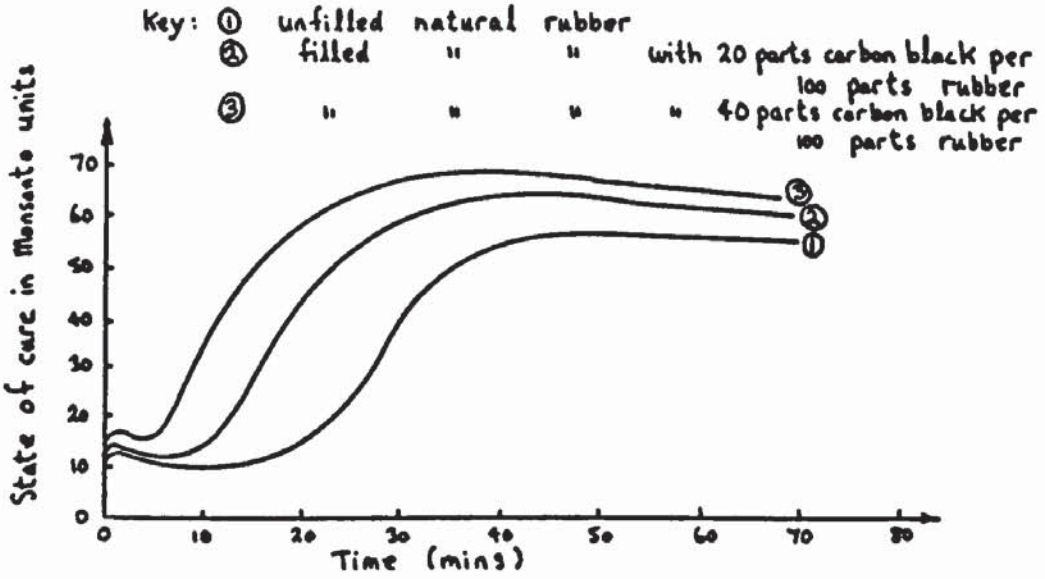

Figure 4.28 Monsanto rheographs for three natural rubber compounds of different carbon black filler content

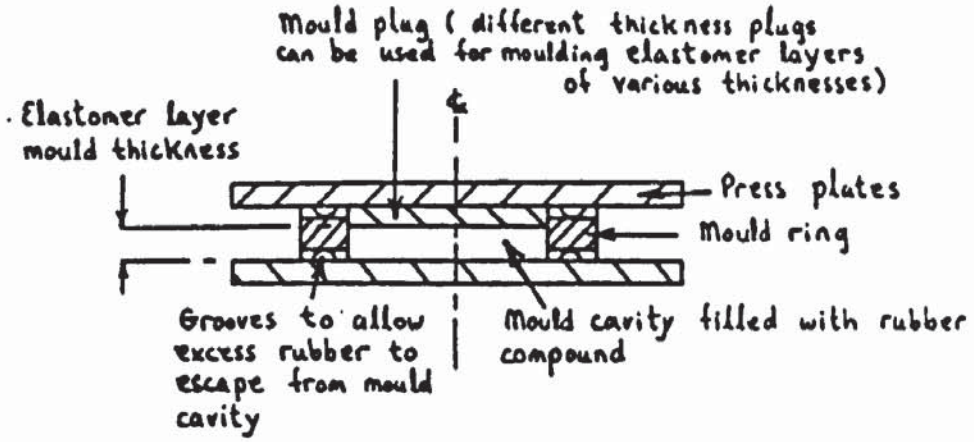

Figure 4.29 Mould design for elastomer layers

$$N_b = \frac{8.b_4 + 0.75}{16.b_4 + 1} \qquad 4.51$$

Both constants M_b and N_b define the magnitude ($\bar{u}_{b1}$) and shape ($\bar{u}_{b2}/\bar{u}_{b1}$) respectively, of the porous pad deflections in bending for the special case of a porous pad subject to a uniform pressure loading $p_b = p_s - p_a$. Repeating the error analysis for M_b and N_b the following equations are obtained;

$$\Delta M_b = \frac{\partial M_b}{\partial \bar{u}_{b1}} \cdot \Delta \bar{u}_b$$

$$\frac{\Delta M_b}{M_b} = \frac{\bar{u}_{b1}}{M_b} \cdot \frac{\partial M_b}{\partial \bar{u}_{b1}} \cdot \frac{\Delta \bar{u}_{b1}}{\bar{u}_{b1}} \qquad 4.52$$

using equation 4.49 to substitute for $\bar{u}_{b1}/M_b$ and $\partial M_b/\partial \bar{u}_{b1}$ in equation 4.52 gives;

$$\frac{\Delta M_b}{M_b} = \frac{\Delta \bar{u}_{b1}}{\bar{u}_{b1}} \qquad 4.53$$

Similarly for N_b;

$$\Delta N_b = \frac{\partial N_b}{\partial \bar{u}_{b1}} . \Delta \bar{u}_{b1} + \frac{\partial N_b}{\partial \bar{u}_{b2}} . \Delta \bar{u}_{b2}$$

$$\frac{\Delta N_b}{N_b} = \frac{\bar{u}_{b1}}{N_b} \cdot \frac{\partial N_b}{\partial \bar{u}_{b1}} \cdot \frac{\Delta \bar{u}_{b1}}{\bar{u}_{b1}} + \frac{\bar{u}_{b2}}{N_b} \cdot \frac{\partial N_b}{\partial \bar{u}_{b2}} \cdot \frac{\Delta \bar{u}_{b2}}{\bar{u}_{b2}} \qquad 4.54$$

Using equation 4.50 and 4.51, substitute for $\bar{u}_{b1}/N_b$, $\partial N_b/\partial \bar{u}_{b1}$, $\bar{u}_{b2}/N_b$ and $\partial N_b/\partial \bar{u}_{b2}$ in equation 4.54, i.e.;

$$\frac{\Delta N_b}{N_b} = \frac{\Delta \bar{u}_{b2}}{\bar{u}_{b2}} - \frac{\Delta \bar{u}_{b1}}{\bar{u}_{b1}} \qquad 4.55$$

Substituting ±0.1 errors of measurement for $\Delta \bar{u}_{b1}/\bar{u}_{b1}$ and $\Delta \bar{u}_{b2}/\bar{u}_{b2}$ in equations 4.53 and 4.55;

$$\frac{\Delta M_b}{M_b} = \pm 0.1$$

$$= \pm 10\%$$

and $$\frac{\Delta N_b}{N_b} = (\pm 0.1) - (\mp 0.1)$$

$$= \pm 0.2$$

$$= \pm 20\%$$

Hence the corresponding errors in M_b and N_b are of the same order of magnitude as the measurement errors in $\bar{u}_{b1}$ and $\bar{u}_{b2}$ from deflections of the porous pad. Values of M_b and N_b can be obtained from the least squares curve fitted to the deflection measurements of the porous pad, i.e. equation 4.12. For completeness both M_b and N_b can be expressed in terms of D_b and B_b as follows; in equation 4.33 replacing D_b and B_b with D_b and B_b respectively:

$$\bar{u}_{b1} = \frac{p_a.h_b^3.(5.D_b + B_b)}{64.D_b.(D_b + B_b)}$$

hence by definition $$M_b = \frac{p_a.h_b^3.(5.D_b + B_b)}{64.D_b.(D_b + B_b)} \qquad 4.56$$

Substituting for b_4 in equation 4.51 using equation 4.32 and replacing $\bar{D}_b$ and $\bar{B}_b$ with $\bar{D}_b$ and $\bar{B}_b$ respectively;

$$N_b = \frac{9.D_b + B_b}{20.D_b + 4.B_b} \qquad 4.57$$

Hence both constants M_b and N_b may be used to specify the rigidity properties of the porous pad in bending for any pressure loading p_b given by equation 3.88 in section 3.5. These constants are non - dimensional and depend only on the material properties of the porous pad and stiffness of the porous pad bond. This is because by definition;

$$D_b = \frac{E_b.h_b^3}{12.(1 - \nu_b^2)}$$

$$\text{and} \quad \bar{D}_b = \frac{D_b}{p_a.h_b^3} = \frac{E_b}{12.p_a.(1 - \nu_b^2)} \qquad 4.58$$

Hence in equation 4.12 $\bar{u}_b$ is independant of the porous

pad thickness h_b and radius r_b. Since the constant M_b and N_b are related to $\bar{u}_b$ by $\bar{u}_{b1}$ and $\bar{u}_{b2}$ in equations 4.49 to 4.51, then these constants are also independant of h_b and r_b.

The results of deflection profile measurements and corresponding values of M_b and N_b for several porous pads used in the bearing tests are presented and discussed in chapter 5.

4.4 THE ELASTOMER LAYER

4.4.1 MOULDING AND PREPARATION

A natural rubber compound was selected for the elastomer layer material. This could be moulded at the University of Aston in Birmingham using equipment in the Rubber Technology Department. Thus both the elastomer layers and test specimens for the measurement of shear and bulk modulus (see section 4.4.3) could be moulded from the same compounds and under controlled conditions to ensure consistency between the two. The hardness and corresponding elastic properties of the elastomer layer could be varied by the carbon black filler content in the rubber compound.

Trial and error tests of several rubber compounds with differing amounts of carbon black were carried out using a Monsanto Rheometer. This instrument cures small rubber samples of the compound and records the state of cure

versus time on a chart similar to that shown in figure 4.28. The compounds in table 4.1 were selected to give a reasonable range in elastomer properties as indicated by the separation in curves for each compound in figure 4.28.

These compounds were prepared on a Banbury mixing machine followed by milling so that the uncured rubber is rolled out into a thin sheet of approximately 5 to 10 mm thickness.

Typical moulds for the elastomer layer are shown in plate 7. The moulds are designed so that excess rubber can escape through the grooves at the top and bottom of the mould. For the elastomer layer, three moulds of diameters 105, 133 and 175 mm were used. Different size plugs are inserted into the mould as shown in figure 4.29 so that elastomer layer thicknesses of 6, 10, and 16.5 mm could be moulded.

Because it is important that the moulded properties of the elastomer layers and the test specimens are the same, both are moulded from the same Banbury mix and at 160^{o}C for 50 minutes. All moulds are pre - heated prior to filling with uncured rubber. Curing of the rubber takes place in a heated, thermo - statically controlled press at 27 tons loading.

To check for consistancy in the elastic properties between the elastomer layers and the test specimens after moulding, their hardness was measured and the results are shown in Table 4.2.

COMPOUND	1	2	3
Natural rubber (S.M.R. 10)	1000 g	1000 g	1000 g
Zinc oxide	50g	50 g	50g
Stearic acid	30g	30 g	30g
C.B.S.	6g	6g	6g
I.P.P.D.	10g	10g	10g
Sulphur	25g	25g	25g
H.A.F. carbon black	0g	200 g	400g

Key: C.B.S. Cyclo – hexyl – benzthiazyl – sylphenamide
I.P.P.D. N – ispropyl – N' – phenyl – P
H.A.F. high abrasion furnace

Table 4.1 Elastomer layer natural rubber compounds

Compound	I.R.H.D. value		
	Bulk modulus specimen	Shear modulus specimen	Elastomer layers (average and range)
1	42	42	$43.7 \pm \frac{1}{0.5}$
2	51	52	$51.4 \pm \frac{0.75}{2}$
3	67	64	$64.7 \pm \frac{3}{0.25}$

Key: I.R.H.D. International rubber hardness

Table 4.2 Hardness readings for elastomer layers and test specimens of the same natural rubber compound

Plate 7 Typical elastomer layer mould.

The close correlation of hardness readings in table 4.2 is a good indication that the properties of the elastomer layers will be accurately measured from the test specimens for the same compound.

Prior to bearing tests the elastomer layers were bonded to their rigid backings (see figure 4.3) using a slow setting (12 hr) epoxy resin. To improve adhesion the bonded surface of the elastomer layer was roughened with an emery cloth before applying the resin.

Once the epoxy resin is set the elastomer layers are ground flat to the desired thickness on a surface grinding machine. Chalk dust was used to lubricate the rubber during grinding as recommended by Lowe (71, 72). A typical flatness profile of the compliant surface after grinding is shown in figure 4.30. The flatness measurements were taken using a micro - comparator mounted on a vernier height gauge with the the elastomer layer and its rigid backing resting on a flat marble inspection table as shown in figure 4.31. A slip gauge is used to spread the contact pressure of the micro - comparator gauge head on the compliant surface. The micro - comparator was traversed to several locations on the compliant surface and a height measurement recorded. The difference in height readings between measurement locations gives the flatness of the compliant surface.

To determine the thickness of the elastomer layer additional readings are taken from its rigid backing so

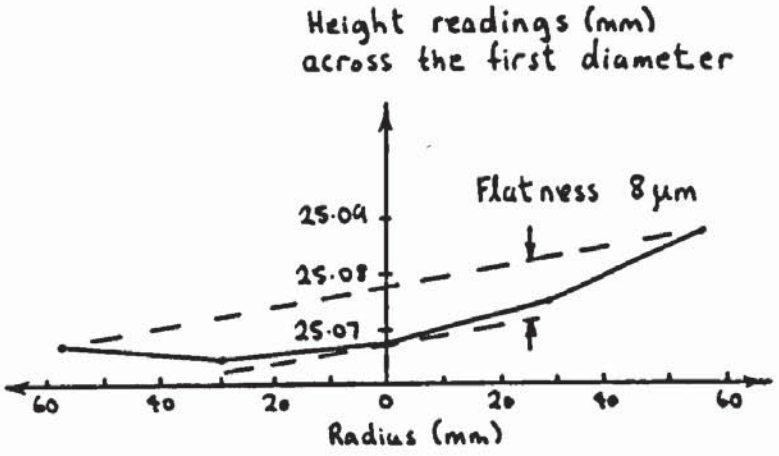

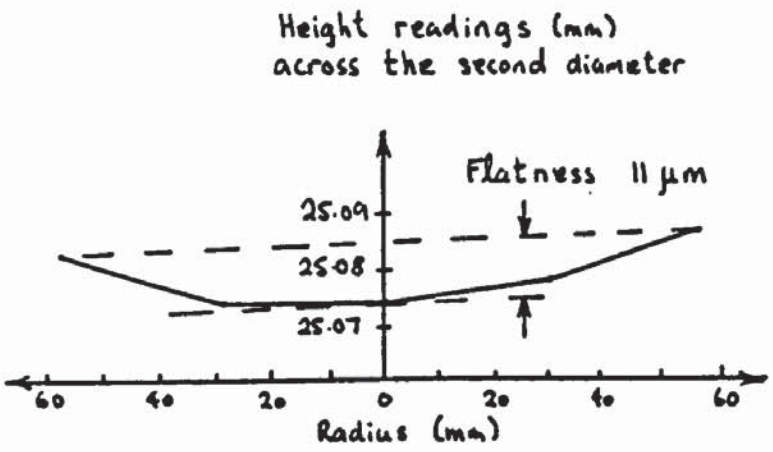

Figure 4.30 Typical flatness measurements of compliant surface after grinding

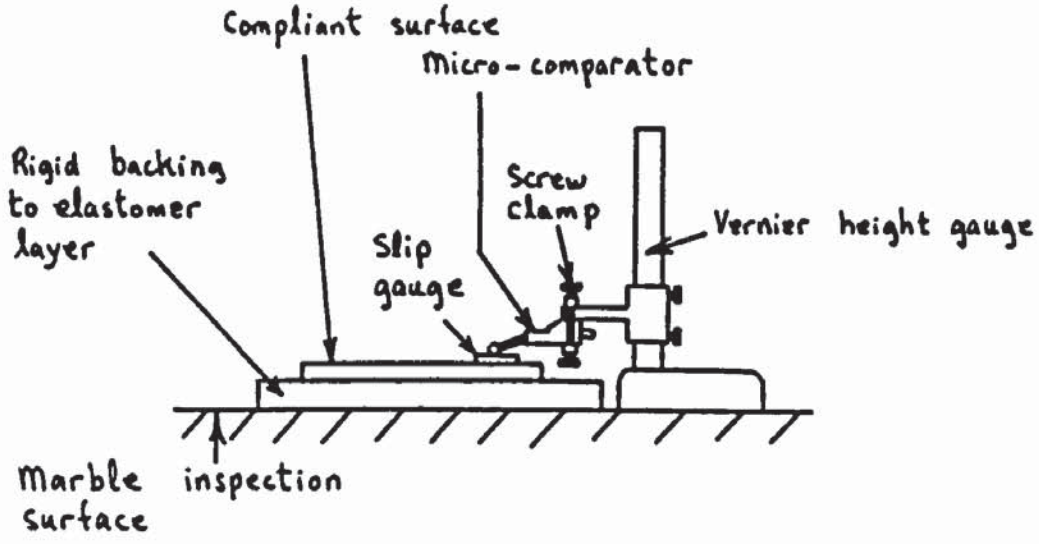

Figure 4.31 The measurement of compliant surface flatness and elastomer layer thickness

that by subtracting the average height of the rigid backing from the average height of the elastomer layer its average thickness is obtained.

4.4.2 ACCURATE DETERMINATION OF POISSON'S RATIO

In section 3.4.4 a simplified solution for deflection of the elastomer layer was presented. For this solution it is necessary to determine Poisson's ratio ν_c for the elastomer layer. It is important that an accurate value of this is obtained due to the sensitivity of bearing performance (see chapter 5) to values of ν_c approaching 0.5, which is typical for soft elastomer materials (63).

While it is possible to measure shear modulus G_c, Young's modulus E_c and bulk modulus K_c for the elastomer layer material (see section 4.4.3) a value of ν_c is normally deduced from either two of these values G_c, E_c and K_c. This is achieved using any one of the following equations applicable to a perfectly elastic, homogenious and isotropic material (63, 66):

$$\nu_c = \frac{E_c}{2.G_c} - 1 \qquad 4.59$$

$$\nu_c = \frac{1}{2} - \frac{E_c}{6.K_c} \qquad 4.60$$

$$\nu_c = \frac{1}{2} - \frac{G_c}{2.K_c} \qquad (K_c >> G_c) \qquad 4.61$$

The most obvious equation to select is 4.59 since values of E_c and G_c are the most easily obtainable of the three. However Stanojevic (77) showed that this can lead to large errors in the value of ν_c obtained. Consider the following error analysis (77);

The total differential of ν_c can be expressed as;

$$\Delta\nu_c = \frac{\partial\nu_c}{\partial E_c}.\Delta E_c + \frac{\partial\nu_c}{\partial G_c}.\Delta G_c$$

$$\text{i.e. } \frac{\Delta\nu_c}{\nu_c} = \frac{E_c}{\nu_c}.\frac{\partial\nu_c}{\partial E_c}.\frac{\Delta E_c}{E_c} + \frac{E_c}{\nu_c}.\frac{\partial\nu_c}{\partial G_c}.\frac{\Delta G_c}{G_c} \qquad 4.62$$

Using equation 4.59, equation 4.62 can be written;

$$\frac{\Delta\nu_c}{\nu_c} = \left(\frac{\nu_c + 1}{\nu_c}\right)\frac{\Delta E_c}{E_c} - \left(\frac{\nu_c + 1}{\nu_c}\right)\frac{\Delta G_c}{G_c} \qquad 4.63$$

Typical values of ν_c for soft elastomers are in the range (63);

$$\nu_c = 0.49881 \text{ to } 0.49991$$

Substituting an average figure of 0.49936 for ν_c in equation 4.63 gives;

$$\frac{\Delta\nu_c}{\nu_c} = 3.003\times\frac{\Delta E_c}{E_c} - 3.003\times\frac{\Delta G_c}{G_c}$$

Supposing that the errors in the measurement of E_c and G_c are both ±10%, then;

$$\frac{\Delta\nu_c}{\nu_c} = 3.003\times(\pm 0.1) - 3.003\times(\mp 0.1)$$

$$\frac{\Delta\nu_c}{\nu_c} = \pm 0.6$$

$$= \pm 60\%$$

The corresponding error in ν_c is relatively large. However if a similar error analysis is carried out on eqaution 4.60 for E_c and K_c the following is obtained (66);

$$\frac{\Delta\nu_c}{\nu_c} = -\left(\frac{1}{2.\nu_c} - 1\right)\frac{\Delta E_c}{E_c} + \left(\frac{1}{2.\nu_c} - 1\right)\frac{\Delta K_c}{K_c} \qquad 4.64$$

Again substituting values for ν_c , $\Delta E_c/E_c$ and $\Delta K_c/K_c$ as before except that the error in the measured value of K_c is estimated at (66) ±20%;

$$\frac{\Delta\nu_c}{\nu_c} = \pm 0.00038$$

$$= \pm 0.038\%$$

The corresponding error in ν_c is relatively small and this error reduces as ν_c approaches 0.5.

It can also be shown for G_c and K_c in equation 4.61 that;

$$\frac{\Delta\nu_c}{\nu_c} = -\left(\frac{1}{2.\nu_c} - 1\right)\frac{\Delta G_c}{G_c} + \left(\frac{1}{2.\nu_c} - 1\right)\frac{\Delta K_c}{K_c} \qquad 4.65$$

Equations 4.65 is similar to equation 4.64 and therefore the error in ν_c will also be small at 0.08%. It can be concluded therefore that accurate values of ν_c are only obtainable using equations 4.60 and 4.61 for E_c and K_c or G_c and K_c respectively and that a value of K_c must be measured.

4.4.3 THE MEASUREMENT OF ELASTOMER PROPERTIES

Theoretically it is only necessary to obtain either of the following groups;

(i) Shear modulus G_c and bulk modulus K_c.

(ii) Young's modulus E_c and bulk modulus K_c.

from which it is possible to derive an accurate value of Poisson's ratio ν_c (see section 4.4.2).

However to obtain an average value of ν_c from G_c and K_c, and E_c and K_c all three elastomer layer properties E_c, G_c, and K_c will be measured. The method and experimental apparatus used to measure these properties is described as

follows:

(a) The Bulk Modulus Tester; Stanojevic and Lewis (66) carried out a comparative study of two test methods for the measurement of bulk modulus K . The first method by Rightmire (63) involves subjecting an elastomer sample of disc shape to a hydrostatic pressure and measuring the corresponding changes in the sample volume. For the second method by Holownia (64, 65) a cylindrical sample is placed in a cavity formed by a piston and cylinder. The piston compresses the sample which is restrained from lateral expansion by the walls of the cylinder. It was concluded (66) that the second method is preferable due to its practical ease of operation and improved accuracy over the first method. The second method was therefore adopted to measure K . A diagram of the tester is shown in figure 4.32. Cylindrical samples of approximately 24.6 mm diameter and 50 mm length are moulded in each of the rubber compounds given in table 4.1 (see section 4.4.1 for moulding details). After moulding each specimen is accurately measured for diameter and length using a micrometer.

The specimen is then placed at the bottom of the compression cylinder whose bore is approximately 4% larger than the diameter of the specimen. Both ends of the specimen are lubricated with silicon grease to ensure free lateral expansion during its compression to fill the cavity. The diameter of the piston which compresses the

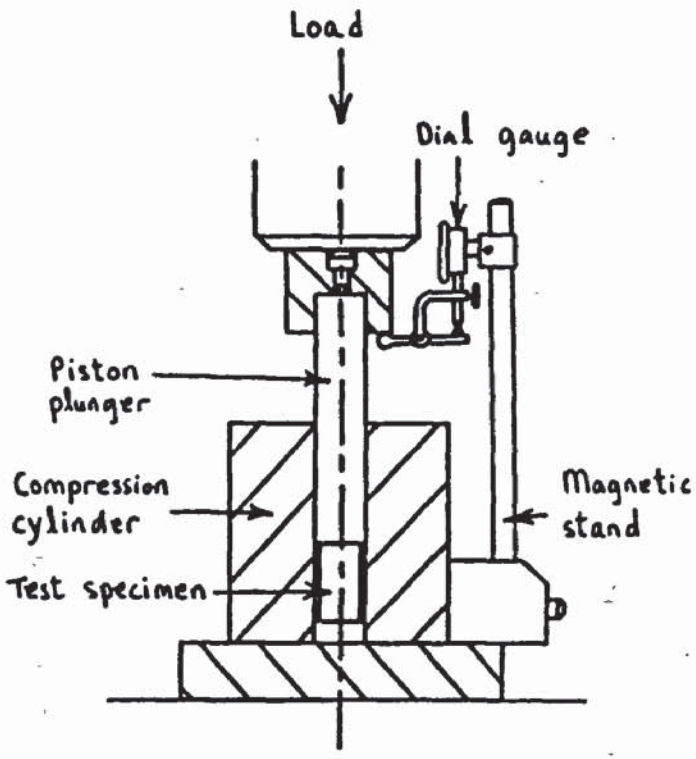

Figure 4.32 Bulk modulus tester

(a) Readings for specimen in bulk compression

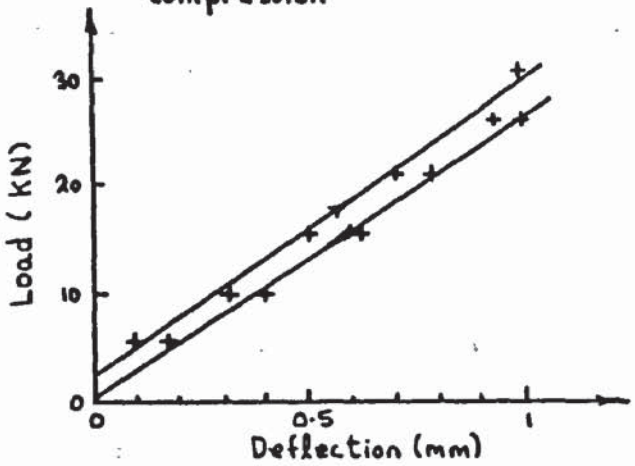

(b) Readings for specimen in axial compression

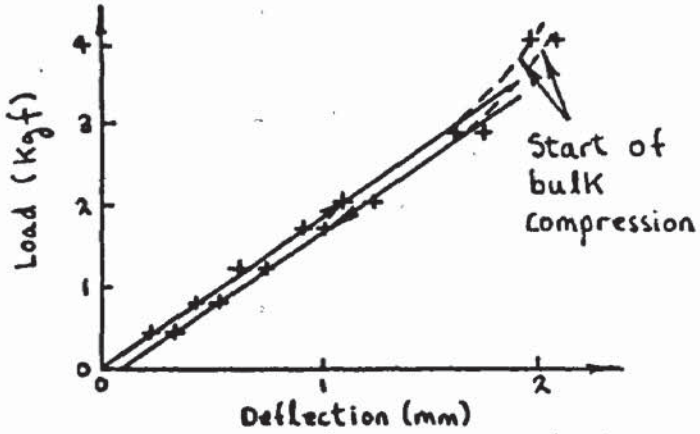

Figure 4.33 Typical experimental load against deflection plots from bulk modulus tester

specimen is 0.025 mm less than the bore diameter of the compression cylinder. This small clearance stops the soft elastomer sample from extruding past the piston during compression.

During initial loading of the piston using 2 kg weights the sample undergoes axial compression before it compresses against the sides of the compression cylinder. Therefore by taking deflection readings using the dial gauge shown in figure 4.32 it is possible to determine the Young's modulus E of the specimen for small loads on the piston. Before any deflection readings are taken however the piston must be allowed to settle on top of the specimen to allow trapped air to escape from the cylinder cavity. Also as mentioned in section 2.2.5 the specimen must be cycle loaded and unloaded at least ten times before readings are taken, to allow for the stress softening that occurs with rubber during the initial load cycles. Care is taken to zero the dial gauge before loads are applied to the piston. Deflection readings are taken during loading and unloading of the piston.

For bulk modulus readings the tester is placed in a Denison compression machine. The piston is pre - loaded to 1 kN to ensure that the specimen expands to completely fill the cavity of the bulk modulus tester. Readings of load against deflection are recorded during loading to 30kN and subsequent unloading only after cycle loading the specimen ten times prior to this.

A typical load agaist deflection graph for axial and bulk compression of the specimen is shown in figure 4.33. To obtain the slope of these graphs for the determination of E and K a straight line is fitted to the experimental points using least squares methods. Note that the slope of the bulk compression line is much greater than that of the axial compression line. This demonstrates the imcompressible nature of natural rubber.

Values of E and K are determined using equations in appendix 5 . Results for the three rubber compounds are presented and discussed in chapter 5.

(b) The Shear Modulus Tester; apparatus for the measurement of shear modulus is shown in figure 4.34. For each rubber compound in table 4.1 a disc shaped specimen of approximately 50mm diameter and 20mm thickness was moulded (see section 4.4.1 for moulding details). The flat faces of the specimen were then ground parallel to each other and then accurately measured for diameter and thickness using a micrometer. Each specimen is then bonded between two shear plates as shown in figure 4.34. Loctite 495 was convenient for this purpose as it is fast setting. Each shear plate must be degreased prior to bonding in an ultrasonic bath of 1,1,1 - trichloroethane.

During shear tests the specimen and shear plates are supported in a vertical position by an angle plate resting on a table top. A weight carrier is attached to one of the shear plates such that the shear loading passes through the

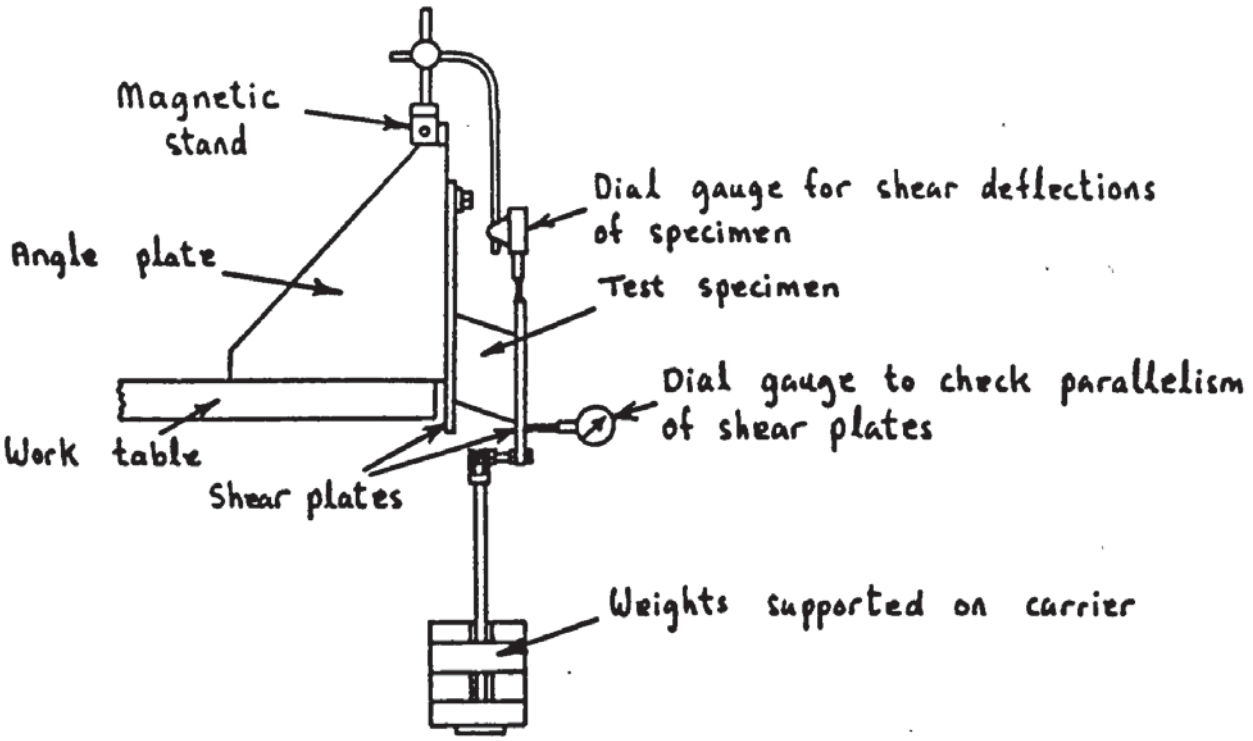

Figure 4.34 Shear modulus tester

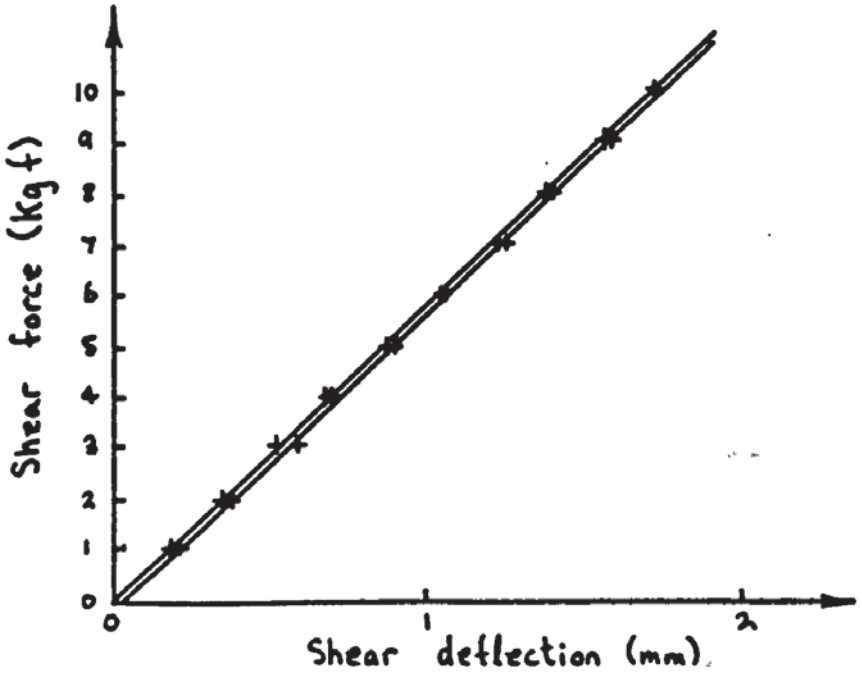

Figure 4.35 Typical experimental load against deflection plot from shear modulus tester

centre of the specimen so that parallel shearing takes place.

Two dial gauges are used with the tester, one to measure shear deflections and the other to check parallelism between the shear plates during loading and unloading of the carrier. The specimen is cycle loaded 10 times prior to taking readings during loading and unloading.

After each test the specimens were removed from the shear plates simply by placing in an oven at 160°C. Typical graphs of load against deflection are shown in figure 4.35. A least squares line is fitted to the experimental point to obtain their slopes for the determination of G using equations in appendix 5. Results for the three rubber compounds are presented and discussed in chapter 5.

4.5 THE MEASUREMENT OF BEARING PERFORMANCE CHARACTERISTICS

4.5.1 INTRODUCTION

In section 3.7.1 the bearing performance parameters Λ_c, Λ_d, W, M and K_x in non - dimensional form were presented. These parameters will be presented in graphical form in chapter 5 to represent the performance characteristics of a porous and compliant aerostatic thrust bearing. Therefore during experiments measurements of

bearing approach c, bearing clearance h_d and mass flow rate m will be recorded (or derived in the case of h_d, see section 4.5.2) for each bearing load w. During each experiment the supply pressure p_s will be kept constant.

Each set of bearing performance curves (i.e. W v Λ_c, M v Λ_c, etc) is defined by the non - dimensional constants P_s, K_v, S_b, etc presented in section 3.7.2. With the exception of P_s these constants depend on the bearing configuration and properties of the porous pad and the elastomer layer i.e. h_b, r_c, Φ, G_c, etc. It is normal practice to show the effect of each of the non - dimensional constant on the bearing performance. To achieve this one constant at a time is adjusted in a series of bearing tests while the others remain at their nominal values. At least three performance curves are then presented graphically in one plot to show the effect of that constant on the bearing performance.

Apart from the measurement of bearing performance, measurements of film pressures will also be made. These are required for the derivation of bearing clearance h_d (see section 4.5.2) and also for a comparison of experimental and theoretical film pressure profiles.

To compare the performance of the porous and compliant aerostatic thrust bearing with that of a more conventional bearing type, experimental results will also be measured for a porous aerostatic thrust bearing. For this purpose the elastomer layer is removed from its rigid backing on the main experimental rig (refer to figure 4.3). This

backing is then ground flat and used as the upper bearing surface. The experimental measurements and presentation of results for a porous aerostatic thrust bearing are similar to those for the porous and compliant aerostatic thrust bearing except of course there is no elastomer layer and the bearing approach c is equal to the bearing clearance h_d.

The comparison of performance between these two bearing types will be presented graphically in chapter 5 for bearings having identical porous pad configuration and properties.

4.5.2 BEARING CLEARANCE h_d

Taylor and Lewis (9) showed that it is possible to derive a bearing clearance for a porous aerostatic thrust bearing from measurements of pressure gradient at the bearing film exit $r = r_b$ and the flow rate through the porous pad. Though their case was for a bearing with a uniform clearance it is shown in appendix 6 that the following equation in non - dimensional form also applies for the non - uniform bearing clearance case, i.e.:

$$\Lambda_d = - \frac{2}{M.(P_s^2 - 1)} \left(\frac{\partial (P^2)}{\partial R} \right)_{R=1} \qquad 4.66$$

where from the definition of Λ_d

$$h_d.(h_d^2 + 6.\Phi_r) = \frac{12.\Phi_z.r_b^2}{h_b.\Lambda_d} \qquad 4.67$$

Equations 4.66 and 4.67 can therefore be applied to the porous and compliant aerostatic thrust bearing case. A value of h_d in equation 4.67 can be obtained using the Newton iteration method (92),i.e.;

$$(h_d)_{new} = (h_d)_{old} - \frac{f(h_d)_{old}}{f'(h_d)_{old}} \qquad 4.68$$

where from equation 4.67

$$f(h_d) = (h_d)^3_{old} + 6.(h_d)_{old}.\Phi_r - \frac{12.\Phi_z.r_b^2}{h_b.\Lambda_d} \qquad 4.69$$

and

$$f'(h_d) = 3.(h_d)^2_{old} + 6.\Phi_r \qquad 4.70$$

Taylor and Lewis (9) went on to show that the difference in the derived bearing clearance h_d and the measured bearing clearance h_m for a porous aerostaic thrust bearing was a constant accounting for the pneumatic clearance s_h due to roughness of the bearing surfaces, i.e.:

$$h_d = h_m + s_h \qquad 4.71$$

In the current research project it has not been possible to measure the bearing clearance h_m in the porous and compliant aerostatic thrust bearing for reasons described in section 4.2.2(c). It is therefore impossible to determine a value of s_h accounting for the roughness of both the soft compliant surface and the porous pad surface using equation 4.71. Other methods of surface roughness measurement such as the Talysurf or Talyline instruments are unsuitable since the soft compliant surface would deflect under the pressure from the stylus measuring tip. In any case during bearing operation the elastomer layer may comply with local roughness peaks on the porous pad surface (see figure 1.7 of section 1.2) to reduce the apparent value of s_h particularly at small bearing clearances.

For these reasons the derived bearing clearance h_d will be used in the presentation of experimental results for the bearing performance. However to confirm the accuracy of using a derived value h_d for the bearing clearance a test was carried out. For this test the main rig was operated as a porous aerostatic thrust bearing (as described in section 4.5.1) for which equation 4.71 applies and a value of h_m can be measured. For this test, porous pad number 3 (see chapter 5, section 5.2.1 for the porous pad identification) was used whose permeability $\Phi = 2.122\times10^{-8}\ mm^2$, thickness h_b = 19.4mm and radius r_b = 50.95mm. During this test measurements were taken of

bearing liftoff, flowmeter readings and film pressures at different supply pressures p_s.

Values of bearing liftoff are measured using the micro - comparators and readings must be corrected to take account of deflections in shear of the porous pad bond. These are calibrated before the test by measuring the porous pad deflections at $r = r_b$ for different supply pressures p_s using the micro - comparators in a similar way to the measurement of porous pad deflections described in section 4.3.6. An average of three shear deflection readings equally spaced around the circumference of the porous pad is taken. A graph is plotted of shear deflection ∂_b against shear force F_b as shown in figure 4.36 where;

$$F_b = \pi.r_b^2.(p_s - p_a) \qquad 4.72$$

A least squares line is fitted to the experimental points and the inverse of the slope of this line gives the stiffness k_o in shear of the porous pad bond, i.e.;

$$k_o = \frac{F_b}{\delta_b} \qquad 4.73$$

The measured bearing clearance h_m is therefore;

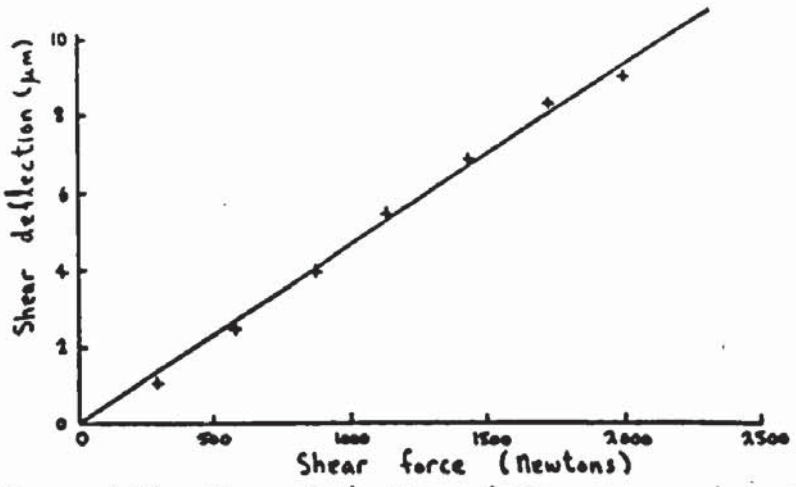

Figure 4.36 Shear deflections of the porous pad bond

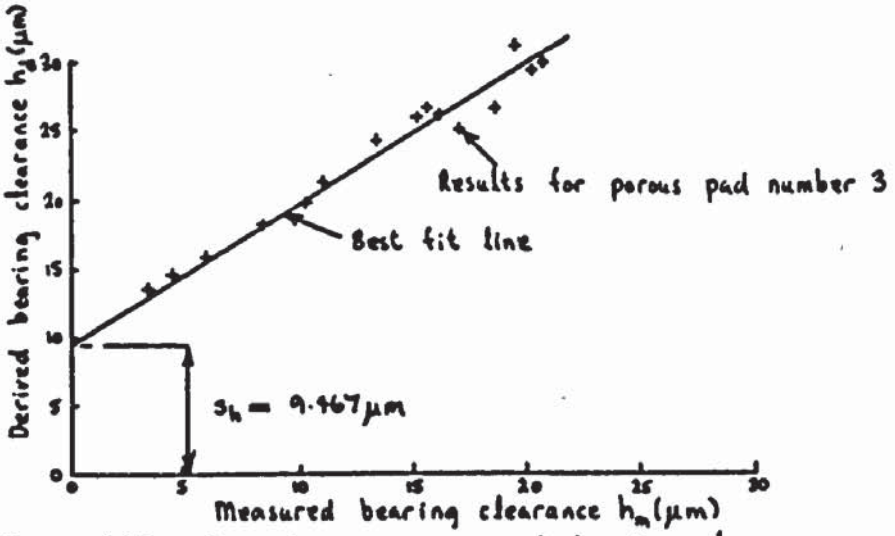

Figure 4.37 Derived versus measured bearing clearance; porous aerostatic thrust bearing

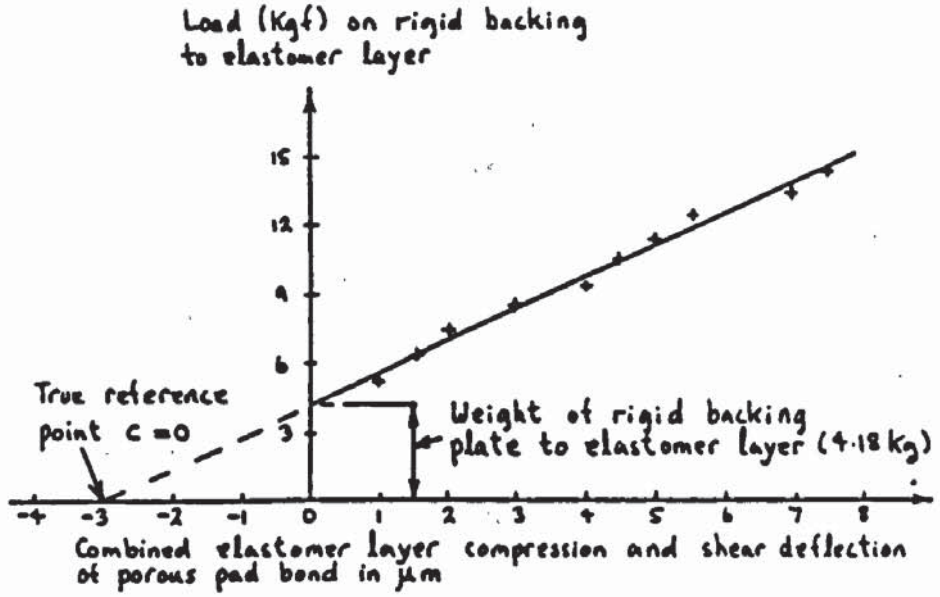

Figure 4.38 Determination of the true reference point at which bearing approach c = 0

$$h_m = \text{bearing liftoff} - \left(\frac{\pi . r_b^2 . (p_s - p_a) - w}{k_o} \right) \qquad 4.74$$

The gradient of the measured film pressure profile squared at $r = r_b$ is determined first by fitting the following polynomial equation using least squares to the film pressure profile;

$$P^2 = \sum_{n=0,2}^{8} a_n R^n \qquad 4.75$$

Only even values of n are used in equation 4.75 since the film pressure profile is symmetrical about the bearing axis $r = 0$ (assumption (v) in section 3.2.1).

Differentiating equation 4.75 and at $R = 1$;

$$\left(\frac{\partial (P^2)}{\partial R} \right)_{R=1} = \sum_{n=2,4}^{8} n . a_n \qquad 4.76$$

After calculating the mass flow rate m from the flowmeter readings the dimensionless mass flow rate M is determined at each supply pressure p_s. Substituting appropriate values in equation 4.66 to 4.70 the derived bearing clearance h_d is obtained for each supply pressure p_s. A plot of h_d versus h_m as shown in figure 4.37 produces a straight line of unity gradient giving a constant value of $s_h = 9.467$ micrometers by equation 4.71. The method for

deriving bearing clearance h_d is therefore verified and this will be used in the presentation of bearing performance results for the porous and compliant aerostatic thrust bearing.

4.5.3 BEARING APPROACH c

The bearing approach c was defined in section 3.6 as the displacement of the rigid backing to the elastomer layer relative to the porous pad bearing surface. Because the porous pad deflects in bending the reference for this displacement must be measured from $r = r_b$ on the porous pad surface.

Bearing liftoff is measured using the micro - comparators positioned as shown in figure 4.3. By equally spacing the three micro - comparators around the bearing axis an average value is obtained, accounting for small errors of alignment between the bearing surfaces.

To obtain values of c from the measured bearing liftoff it is necessary to;

(i) Zero the micro - comparatores when the elastomer layer is resting on the porous pad and there are no loads on the bearing.

(ii) Account for shear deflections of the porous pad bond and subtract these from the measured bearing liftoff.

The micro - comparators can be zeroed while the upper section of the main rig, i.e. the pivot arm (see figure

4.3) is raised so that the only load resulting in compression of the elastomer layer and shear deflection of the porous pad bond are due to the weight (4.18 kg, 9.2 lbs) of the rigid backing plate to the elastomer layer. This weight was accounted for by making an adjustment to the micro - comparator readings. This adjustment is obtained by measuring the deflections of the elastomer layer and porous pad bond for small additional loads up to 10 kg (22 lbs) placed on the rigid backing to the elastomer layer. From graphs of load against deflection similar to that shown in figure 4.38 a least squares line is fitted and its intercept with the horizontal x - axis gives the adjustment necessary to the micro - comparators i.e.;

$$\text{Micro - comparator adjustment} = -(m_1 \times 4.18) \qquad 4.77$$

Therefore instead of zeroing the micro - comparators they are initially set to read the value given by equation 4.77. In this way the micro - comparators will measure the bearing liftoff from the true reference c = 0 when there are no loads on the bearing.

During bearing tests it is necessary to place loads on the bearing carefully to avoid upsetting the micro - comparators. The bearing liftoff readings are corrected for shear deflections of the porous pad bond using an equation similar to 4.74 i.e.;

$$c = \text{bearing liftoff} - \left(\frac{\pi . r_b^2 . (p_s - p_a) - w}{k_\theta} \right) \qquad 4.78$$

where k_o is obtained from calibrations of the porous pad bond in shear deflection as described in section 4.5.2.

The measurement of bearing approach c as described in this section avoids some of the problems experienced by Lowe (72) relating to the temperature sensitivity of the elastomer layer thickness. Lowe used this thickness to determine the reference at which c = 0 and it was therefore necessary to measure changes in its value with temperature T_a.

However while the reference c = 0 is currently determined in a different way to Lowe, the micro - comparator readings will be up - set by changes in temperatures T_a and T_s due to thermal expansion or contraction of the elastomer layer thickness taking place during a bearing test. Therefore during all bearing tests these temperatures were monitored continuously and on the rare occasion that either temperature changed by more than 0.25 ^{o}C then the bearing test was discontinued and repeated when temperatures stabilized again. Also the micro - comparators are re - set at the beginning of each bearing test.

4.5.4 BEARING TEST PROCEDURE

After the preparation of the porous pads and compliant layers (see sections 4.3 and 4.4) one of each is selected for a particular bearing test (see chapter 5) and assembled

on the main rig. During assembly of the porous pad the pressure tappings must be connected to the bottom of the supply chamber as described in section 4.3.3. Note that the weight carrier attached to the pivot arm (see figure 4.3) can be removed and the pivot arm propped up in a vertical position. This allows easier access to the lower section of the main rig, i.e. the porous pad and the supply chamber.

Depending on the thickness of the elastomer layer, shims and washers are placed under the off - centre ball pivot (see figure 4.3 and 4.7) such that the pivot arm is horizontal when applying loads through the bearing. This is checked using a spirit level. Note that the angle of the pivot arm to the horizontal may change as the bearing is loaded due to compression of the elastomer layer. However this was measured during bearing tests using an inclinometer and this angle never exceeded 3^{o}. The resulting cosine error between the vertical load direction and the bearing axis is therefore negligible.

The porous pad surface is also set horizontal in two planes at right angles to each other by resting the spirit level on the porous pad surface and adjusting the differential screws on the main rig (figure 4.3).

Both the micro - comparators and the pressure transducer for the measurement of bearing liftoff and film pressures respectively are calibrated before each bearing test. When these are first switched on, 1/2 hour is allowed for their associated electronic instrumentation to warm up.

The micro - comparators were calibrated and adjusted to give the correct scale readings, by using slip gauges on a suitable smooth surface, i.e. the porous pad (see figure 4.39). A typical calibration chart for the pressure transducer against readings from the U - tube mercury manometer was shown in section 4.2.3, i.e. figure 4.12.

The elastomer layer is positioned centrally on the porous pad and the micro - comparators are positioned for measuring bearing liftoff as shown in figure 4.3. Their scale readings are then adjusted so as to measure from the true reference c = 0 as described in section 4.5.3. Making sure that the steel ball is located centrally on the rigid backing to the elastomer layer, (see figures 4.3 and 4.4(b)) the pivot arm is lowered into the horizontal position.

The porous pad is pressurized to a pressure p_s and the parallelism between bearing surfaces is checked by the readings of bearing liftoff from each micro - comparator. These were usually to within 5 micrometers of each other but if this is not the case adjustments are made to the centralization of the steel ball on the rigid backing to the elastomer layer. For each bearing load the following measurements are taken;

(i) Bearing liftoff readings from the three micro - comparators.

(ii) Flowmeter readings which include the float reading on the tube scale, and also pressure p_m and temperature

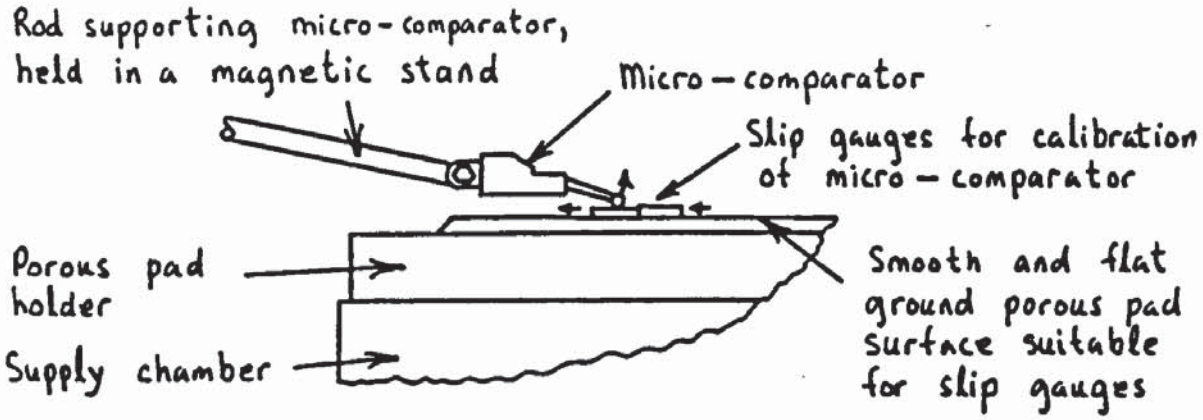

Figure 4.39 Calibration of micro-comparators using slip gauges

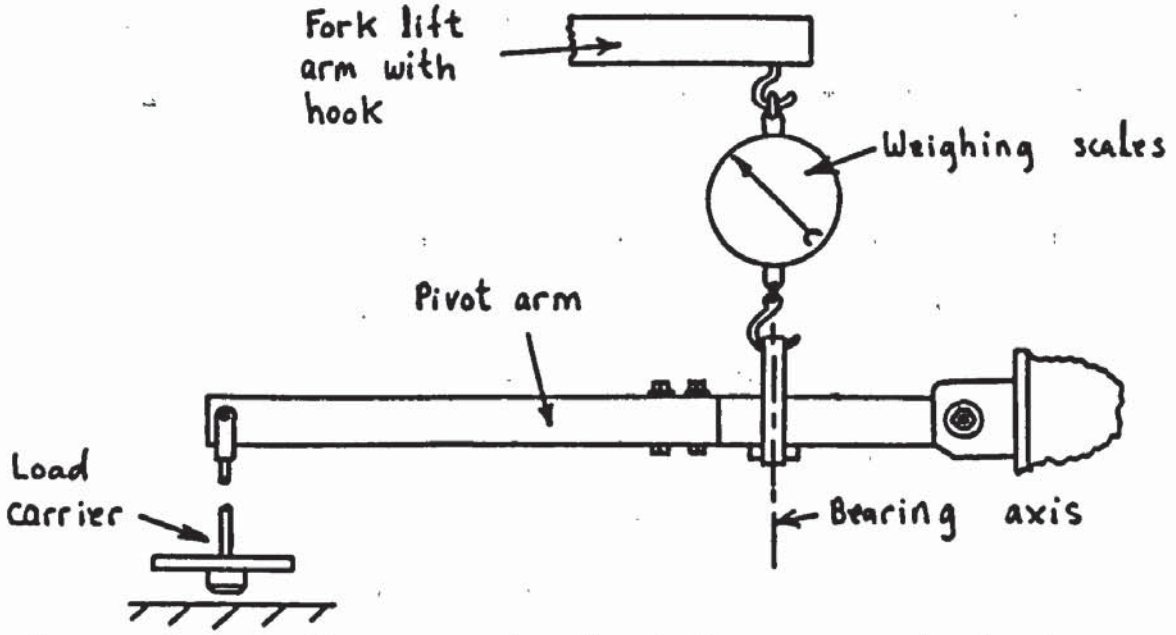

Figure 4.40 Measurement of pivot arm and load carrier weight, acting at the bearing axis

T_m of the metered flow.

(iii) Film pressure readings from the pressure transducer.

These measurements are repeated for each increment of bearing load. This bearing load is calculated from the weights on the carrier and the leverage ratio of the pivot arm, i.e.;

bearing load = 4.4xweights on load carrier+22.3kg 4.79

The additional 22.3 kg in equation 4.79 is the weight of the upper section of the rig (i.e. pivot arm, load carrier and rigid backing to the elastomer layer) acting on the bearing through its vertical axis. The weight of the pivot arm and load carrier at the bearing axis were measured using spring scales positioned as shown in figure 4.40. The scales were supported by a beam with hook on a small fork lift.

During bearing tests the ambient pressure p_a and temperature T_a were recorded together with the supply temperature T_s of air in supply chamber to the porous pad.

Each bearing test is repeated three times to average random experimental errors by rotating the elastomer layer through 120° about the vertical bearing axis.

A bearing test terminated when touchdown of the bearing surfaces occured or when pneumatic hammer made it impossible to take any further readings. Touchdown of the bearing surfaces was indicated when the elastomer layer and

its rigid backing could not be rotated freely.

CHAPTER 5

DISCUSSION OF RESULTS

5.1 INTRODUCTION

In this chapter the experimental results for a porous and compliant aerostatic thrust bearing are presented in graphical form and compared with theoretical predictions. A series of theoretical curves will also be included to show how the bearing performance varies with each of the non - dimensional constants P_s , S_b, S_o, etc.

Comparisons between the performance of a porous and compliant aerostatic thrust bearing and a more conventional porous aerostatic thrust bearing will also be made. With the aid of film pressure profiles and bearing clearance geometries (the latter from theoretical predictions only) the difference in performance characteristics between the two bearings will be discussed and conclusions drawn on the performance of a porous and compliant aerostatic thrust bearing.

In addition,results from calibration tests for permeability and rigidity of the porous pads and the elastic properties of the elastomer layer are presented and discussed.

A summary of conclusions will be made in chapter 6.

5.2 RESULTS FROM CALIBRATION TESTS ON THE POROUS PADS

5.2.1 POROUS PAD IDENTIFICATION

The porous pads selected for bearing tests (see section 4.3.2) are listed in table 5.1 and numbered 1 to 5. Note all porous pads are of stainless steel.

5.2.2 POROUS PAD PERMEABILITY

Porous pad permeability results are presented graphically in figures 5.1 to 5.6 as described in section 4.3.5. It can be seen from the plots of pressure drop against mean volumetric flow rate (figures 5.1 to 5.5) that viscous flow dominates for all five porous pads up to the maximum safe pressure specified in section 4.3.1, with the exception of porous pad number 3. For this pad there is a slight upwards departure in results from the viscous dominated flow line at $p_s - p_a = 2$ bars (see figure 5.3).

These results therefore verify the findings of Taylor and Lewis (9) that a region of viscous dominated flow exists in a porous material for which Darcy's law (equation 3.1 of section 3.2.1) applies. The author would like to make the point however of the importance in preparation of the porous pad bearing surface as described in section 4.3.4. That is the flow through the porous pad is not

Porous pad number	Manufacturers + spec. (grading)	Porous pad thickness* (mm)	Porous pad radius (mm)
1	SIKA R1	9.5	50.91
2	" R1	15.5	50.97
3	" R1	19.4	50.95
4	" R3	19.2	50.93
5	" R5	19.5	50.89

Key: + Schumacher Filters Ltd.
* After surface preparation (see section 4.3.4)

Table 5.1 Porous pad identification

Porous pad number	Viscous perm. Φ (mm^2) $\times 10^8$	Magnitude constant M_b $\times 10^7$	Shape constant N_b
1	3.691	6.578	0.5641
2	2.784	6.129	0.5497
3	2.122	5.935	0.5647
4	5.341	7.751	0.5534
5	9.184	9.227	0.5321

Table 5.2 Porous pad properties

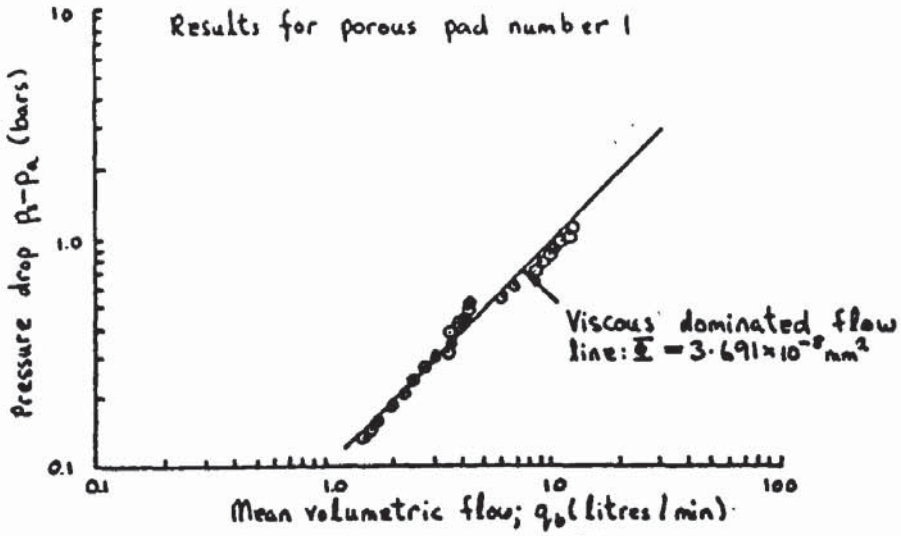

Figure 5.1 Porous pad permeability : the viscous dominated flow region

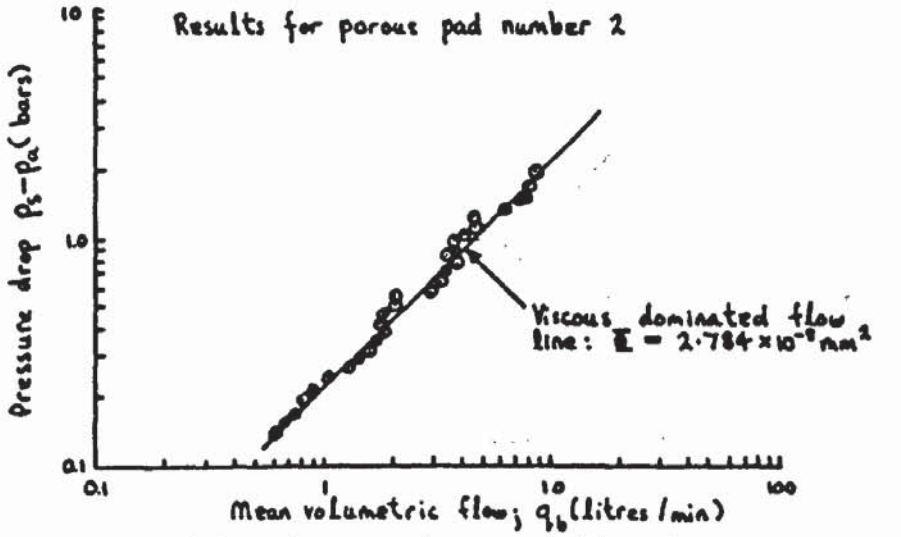

Figure 5.2 Porous pad permeability : the viscous dominated flow region

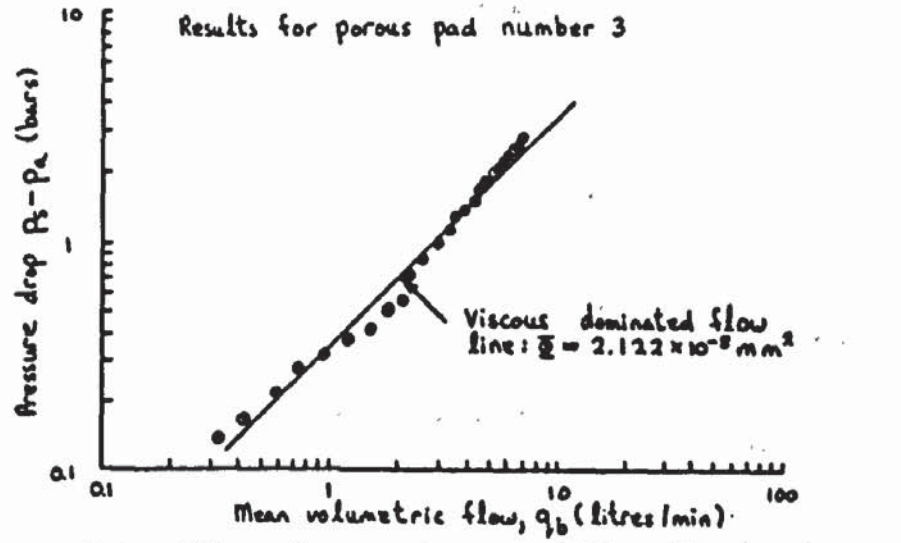

Figure 5.3 Porous pad permeability : the viscous dominated flow region

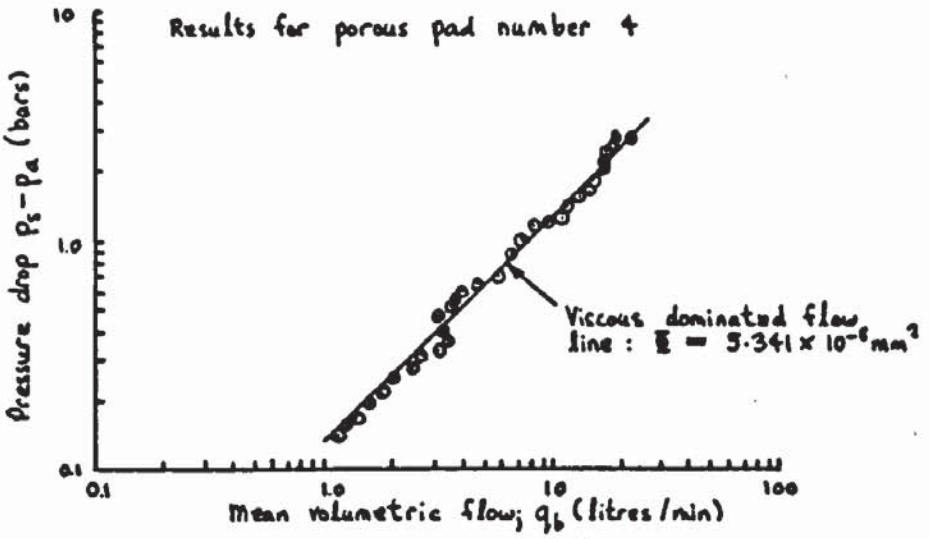

Figure 5.4 Porous pad permeability : the viscous dominated flow region

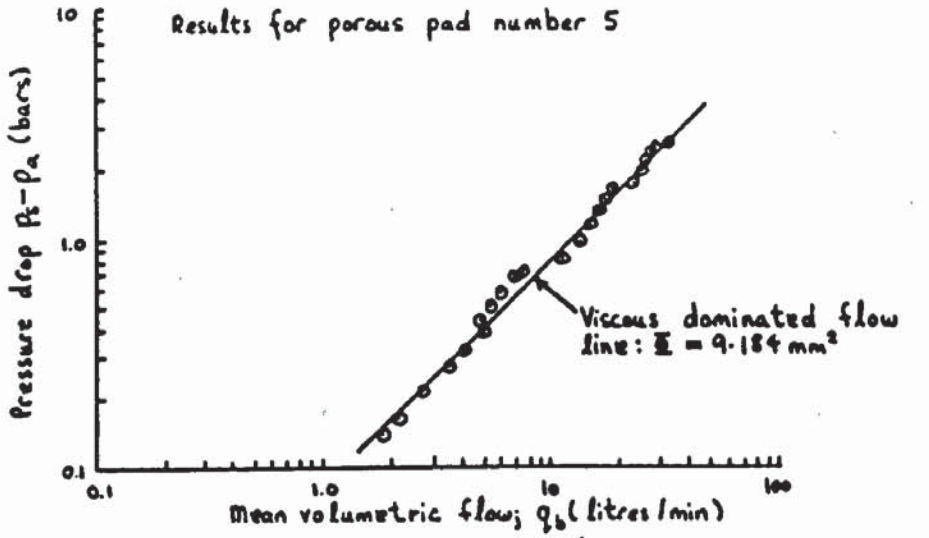

Figure 5.5 Porous pad permeability : the viscous dominated flow region

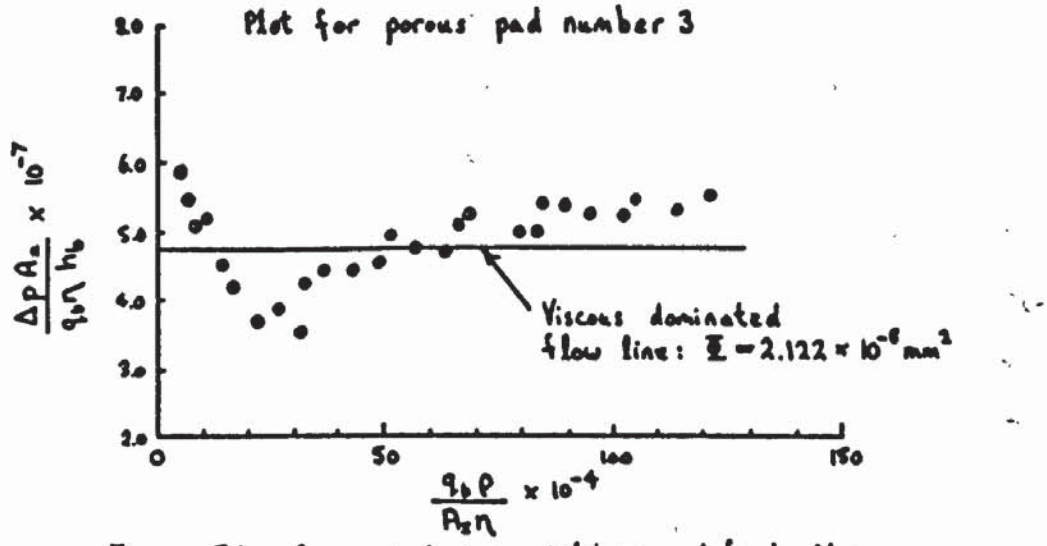

Figure 5.6 Porous pad permeability : modified Morgan plot (9), (24)

affected by the blocking of pores at this surface due to grinding.

The departure in results from the viscous dominated flow line for porous pad number 3 suggests that there is more than one region of flow through the porous pad, i.e. a transition flow region as suggested by Taylor and Lewis (9). However there are insufficient experimental points to represent this region on a modified Morgan plot as shown in figure 5.6. (see also section 4.3.5 and figure 4.22). Further results at greater pressure differences across the porous pad could not be obtained without risking damage to the porous pad bond (see section 4.3.1). The existence of a transition flow region cannot therefore be confirmed and without further substantiating evidence it would be unwise to draw conclusions in favour of Taylor and Lewis (9) or McGrea and Donaldson (10) relating to the nature of flow through the porous pad when inertia losses are significant (see section 2.2.1).

From the results in figures 5.1 to 5.5, the viscous permeability of each porous pad is obtained as described in section 4.3.5. An example calculation for porous pad number 1 is as follows. The plotted points in figure 5.1 are listed in table 5.3 together with their $\log_{10}$ values. With reference to section 4.3.5 the viscous permeability Φ is given by the equation 4.6 i.e.;

$$\Phi = \left(\frac{n.h_b}{A_z} \right) \times 10^{-c_1} \qquad 5.1$$

q_b (litres/min)	q_b (mm^3/sec) $\times 10^{-3}$	$\text{Log}_{10} q_b$	$p_s - p_a$ (bars)	$p_s - p_a$ (N/mm^2)	$\text{Log}_{10} \Delta p$
1·459	24·22	4·386	0.133	0.0133	−1.876
1·578	26·30	4.420	0.145	0.0145	−1.839
1.667	27·78	4.444	0·158	0.0158	−1·801
1·941	32·35	4·510	0·187	0·0187	−1·728
2·198	36·63	4·564	0.209	0·0209	−1·680
2·399	39·98	4·602	0·240	0·0240	−1·62
2·655	44·25	4·646	0.272	0·0272	−1·565
3·02	50·33	4·702	0·302	0·0302	−1·520
3·404	56·73	4·754	0·316	0·0316	−1·500
3·5	58·33	4·766	0·350	0·0350	−1·456
3·467	57·78	4·762	0·382	0·0382	−1·418
3·767	62·78	4·798	0·417	0·0417	−1·380
4·036	67·27	4·831	0·441	0·0441	−1·356
4·169	69·48	4·842	0·483	0·0483	−1·316
4·207	78·12	4·896	0·522	0·0522	−1·282
5·998	99·97	5·000	0·547	0·0547	−1·262
6·761	112·7	5·052	0·619	0·0619	−1·208
8·395	139·9	5·146	0·701	0·0701	−1·154
8·872	147·9	5·170	0·776	0·0776	−1·110
9·55	159·2	5·202	0·836	0·0836	−1·078
10·33	172·2	5·236	0·895	0·0895	−1·048
10·96	182·7	5·262	0·955	0·0955	−1·020
11·97	199·5	5·300	1·009	0·1009	−0·9961
12·59	209·8	5·322	1·096	0·1096	−0·9602

Summation $\Sigma \text{Log}_{10} q_b = 116·568$

and $\Sigma \text{Log}_{10} \Delta p = -33·168$

Table 5.3 Experimental plotted points in figure 5.1 for permeability of porous pad 1

Using equations 4.2 to 4.5, the value of c_1 in equation 5.1 is as follows:

$$\bar{y} = \frac{1}{k_1} \sum_{n=1}^{k_1} \text{Log}_{10}(\Delta p)$$

From table 5.3 $\sum \log_{10} \Delta p = -33.168$ and the number of experimental points $k_1 = 24$. Hence;

$$\bar{y} = -\frac{33.168}{24} = -1.382$$

similarly

$$\bar{x} = \frac{1}{k_1} \sum_{n=1}^{k_1} \text{Log}_{10}(q_b)$$

$$\text{i.e.} \quad \bar{x} = \frac{116.568}{24} = 4.857$$

Hence for a least squares line fit;

$$c_1 = \bar{y} - \bar{x}$$
$$= -1.382 - 4.857$$
$$= -6.239$$

The experimental values in table 5.3 were taken at a mean temperature $(T_s + T_a)/2$ of 22.5°C. Using (91) for dry air at low pressure, the absolute viscosity $\eta = 1.8245 \times 10^{-11}$ Nsec/mm^2. From table 5.1 for porous pad 1, $r_b = 50.95$mm and $h_b = 9.5$mm. Therefore;

$$A_z = \pi.r_b^2 = \pi.(50.95)^2$$

$$= 8142 \text{ mm}^2$$

Substituting values of η, h_b, A_z, and c_1 into equation 5.1 gives;

$$\Phi = \frac{1.8245\times10^{-11} \times 9.5 \times 10^{6.239}}{8142}$$

$$\Phi = 3.691 \times 10^{-8} \text{ mm}^2$$

The viscous permeability Φ for porous pad number 1 is therefore 3.691×10^{-8} mm^2. Values of Φ for the other porous pads are obtained in a similar fashion and presented in table 5.2.

5.2.3 POROUS PAD RIGIDITY IN BENDING

Deflection profiles of the porous pad when subject to a uniform pressure difference $p_s - p_a$ across its thickness, are presented graphically in figures 5.7 to 5.11 as described in section 4.3.6. The shape of the best fit curves to the experimental points in these graphs, indicate that the porous pads are not rigidly supported around their circumference as assumed by Taylor and Lewis (25) otherwise the slope $\frac{\partial \bar{u}_b}{\partial R}$ would be zero at R = 1. In fact the value of this slope increases with radius R for all five porous pads. This shows that the porous pad bond is considerably more flexible than the rigidity of the

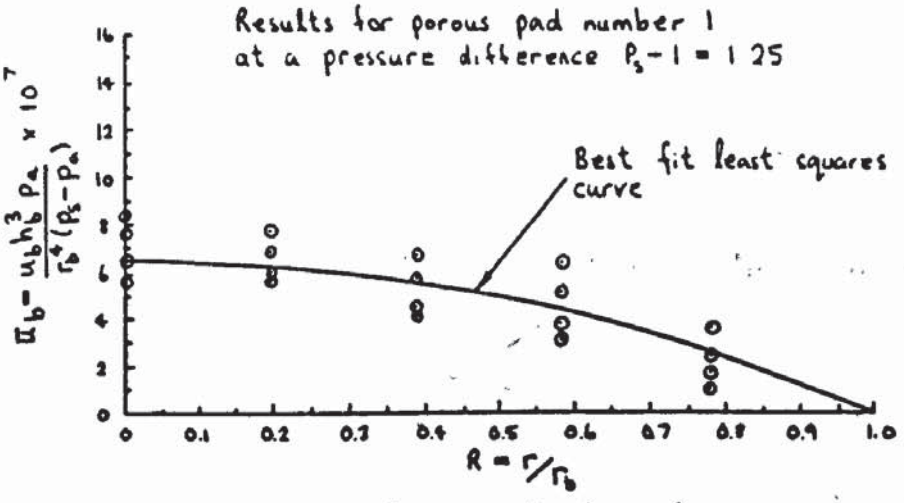

Figure 5.7 Non-dimensional plot of porous pad deflections in bending due to a uniform pressure difference across its thickness

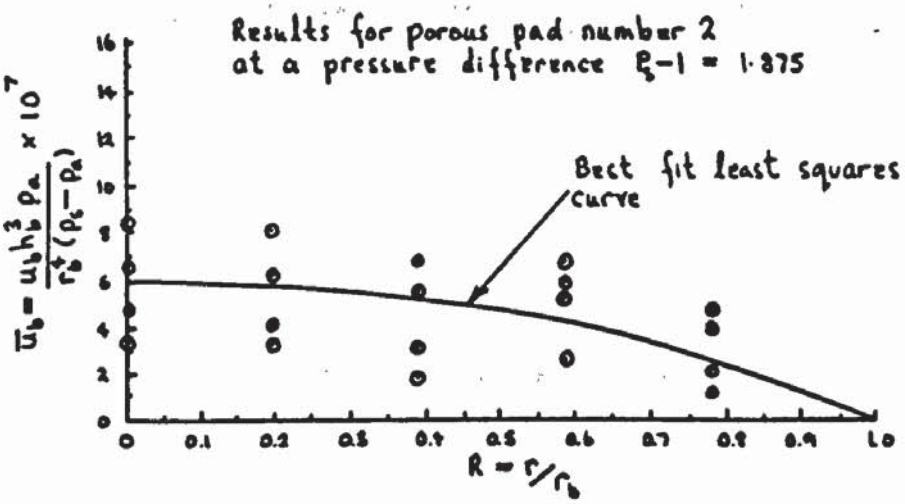

Figure 5.8 Non-dimensional plot of porous pad deflections in bending due to a uniform pressure difference across its thickness

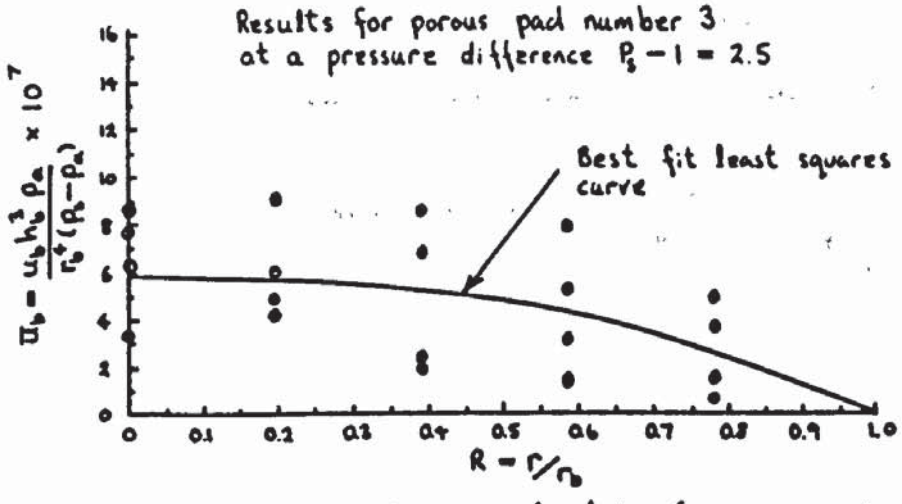

Figure 5.9 Non-dimensional plot of porous pad deflections in bending due to a uniform pressure difference across its thickness

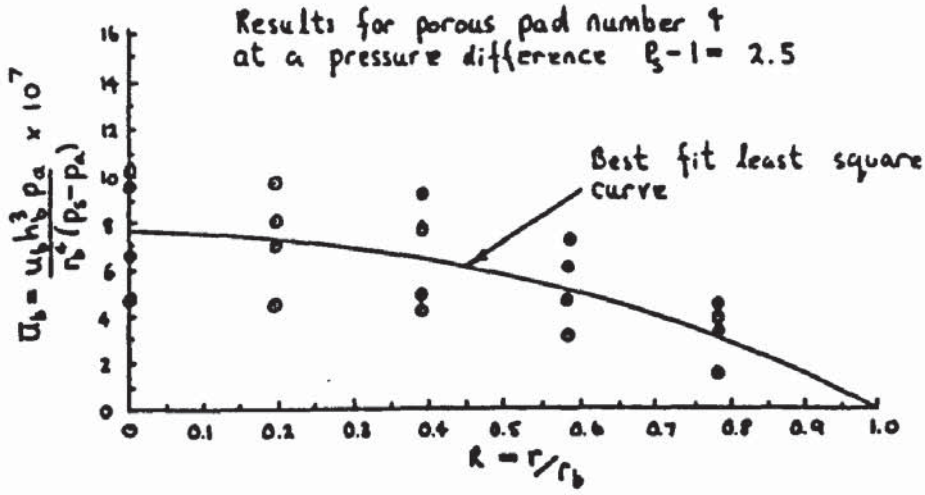

Figure 5.10 Non-dimensional plot of porous pad deflections in bending due to a uniform pressure difference across its thickness

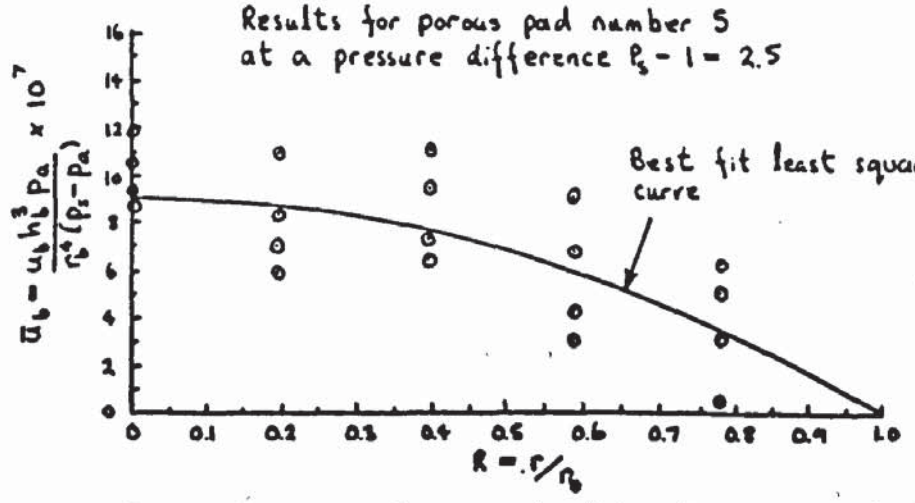

Figure 5.11 Non-dimensional plot of porous pad deflections in bending due to a uniform pressure difference across its thickness

porous pad in bending.

The importance of considering the flexibility of the porous pad bond for the analysis presented in section 3.5 is therefore justified.

Figures 5.12 and 5.13 show the variation in deflections of the porous pad (due to bending only) at its centre r = 0 for different supply pressures $p_s - p_a$. The analysis for deflections of the porous pad in section 3.5 is based on thin plate theory (47) for a linear - elastic material. A straight line has therefore been drawn through the experimental points in figures 5.12 and 5.13 which represents linear - elastic deflections of the porous pad. The apparent large scatter in experimental points (± 1 μm) about this line can be attributed to the small magnitude of the deflections of the porous pad in comparison to the resolving accuracy of the micro - comparators used to measure these deflections (see section 4.3.6). Note that the minimum scale reading for the micro - comparator is 0.5 μm. However this straight line and the assumption of linear - elasticity provides a reasonable first approximation to the experimental readings and therefore the analysis presented in section 3.5 will predict deflections of the porous pad to within ± 1 μm.

Similarly the scatter in experimental points about the best fit deflection curves in figures 5.7 to 5.11 can be attributed partly to the accuracy of micro - comparator readings and also due to non - axisymmetric deflections of

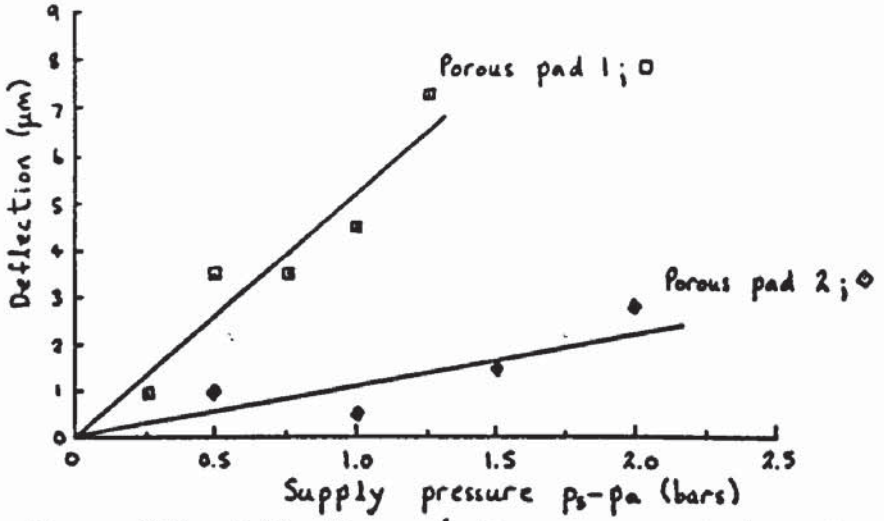

Figure 5.12 Deflections of the porous pad at r = 0 due to bending only; pads 1 and 2

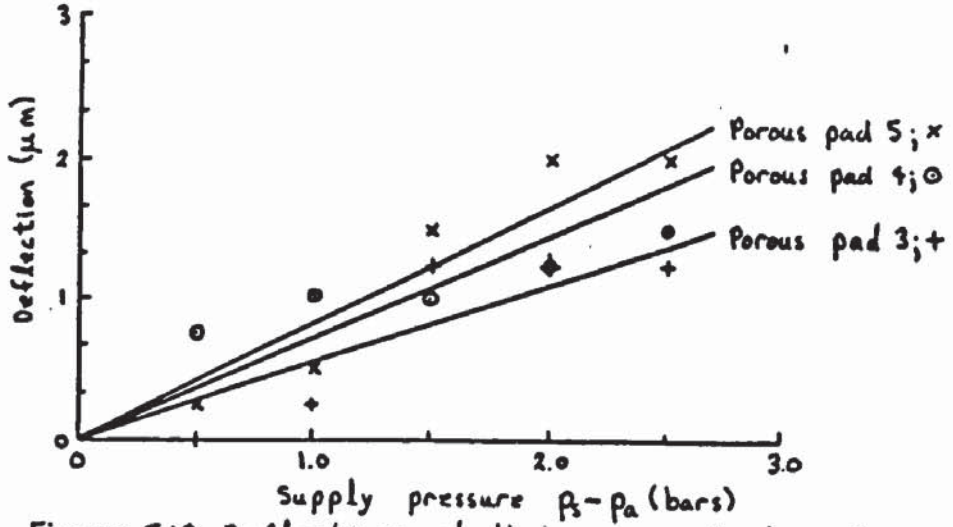

Figure 5.13 Deflections of the porous pad at r = 0 due to bending only: pads 3, 4 and 5

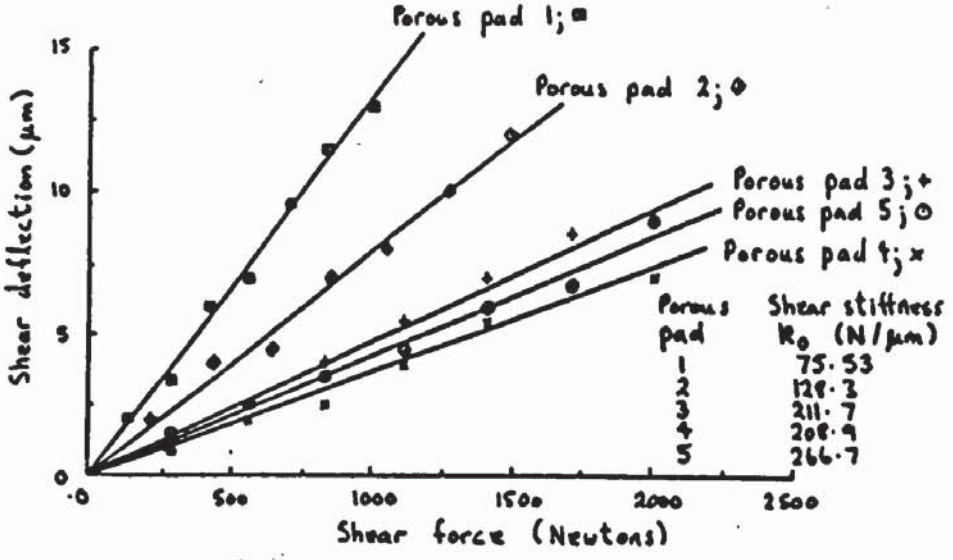

Figure 5.14 Shear deflections of the porous pad bond

the porous pad. This indicates that there are variations in the structural properties within the porous pads caused during sintering. However it is also possible that the flexibility of the porous pad bond varies with circumference. Indeed during inspection of one porous pad after it had accidently been blown out from its holder, it was discovered that the adhesive epoxy bond had only partially bridged the gap between the porous pad and its holder in parts of the circumference. This is a typical problem when two surfaces are bonded in this way and a solution would be to inject the adhesive into the gap under pressure, through access holes in the porous pad holder, i.e. in a similar method to cavity wall foam insulation in houses. To apply the adhesive in this way would require special application equipment and the author did not pursue this any further due to shortage of time.

Values of the magnitude constant M_b and shape constant N_b obtained for each porous pad as described in section 4.3.5 are presented in table 5.2. An example calculation for porous pad number 3 is as follows; table 5.4 gives values of the experimental points in figure 5.9 for deflections of porous pad 3. A least squares curve is fitted to these points by solving equation 4.25 (section 4.3.6). With reference to equations 4.16 to 4.20, 4.24 and using the calculated values in tables 5.4, then for matrix [f];

$$\Sigma(f_1(R))^2 = \Sigma(R^4)^2 = \Sigma R^8$$

①	②	③	④	⑤	⑥				⑦
R	R^2	R^4	R^6	R^8	$\bar{u}_b \times 10^{-7}$				$\sum_1^4 \bar{u}_b \times 10^{-7}$
0	0	0	0	0	3.2	7.6	6.4	4.9	22.1
0.196	0.03842	1.4758×10^{-3}	5.6699×10^{-5}	2.178×10^{-6}	4.7	6	9.1	6	25.8
0.393	0.1544	0.02385	3.6843×10^{-3}	5.6904×10^{-4}	1.96	2.36	6.72	8.46	19.5
0.589	0.3469	0.1204	0.04175	0.01449	1.3	3	5.18	7.76	17.24
0.786	0.6178	0.3817	0.2358	0.1457	0.62	1.44	3.6	4.94	10.6
1.0	1.0	1.0	1.0	1.0	0	0	0	0	0
	2.1575	1.5274	1.2813	1.1608					95.24

Key : Column's ① and ⑥ correspond to experimental points in figure 5.9 for porous pad number 3.
Column's ② ③ ④ and ⑤ are calculated from value's in column ①.
Column ⑦ equals the summation of value's along each row of column ⑥.
Values at the foot of column's ② ③ ④ ⑤ and ⑦ are the total's of values in those column's

Table 5.4 Experimental and calculated values from figure 5.9

$$= 4 \times 1.1608$$

$$= 4.6432$$

$$\Sigma f_1(R).f_2(R) = \Sigma R^4.R^2 = \Sigma R^6$$

$$= 4 \times 1.2813$$

$$= 5.1252$$

$$\Sigma f_1(R).f_3(R) = \Sigma R^4.1 = \Sigma R^4$$

$$= 4 \times 1.5274$$

$$= 6.1096$$

$$\Sigma f_2(R).f_1(R) = \Sigma R^6 = 5.1252$$

$$\Sigma f_2(R)^2 = \Sigma R^2.R^2 = \Sigma R^4$$

$$= 6.1096$$

$$\Sigma f_2(R).f_3(R) = \Sigma R^2.1 = \Sigma R^2$$

$$= 4 \times 2.1575$$

$$= 8.63$$

$$\Sigma f_3(R).f_1(R) = \Sigma R^4 = 6.1096$$

$$\Sigma f_3(R).f_2(R) = \Sigma R^2 = 8.63$$

$$\Sigma f_3(R)^2 = \Sigma 1 = 4 \times 6$$

$$= 24$$

As described in section 4.3.6 the summation sign $\sum$ refers to the summation of values corresponding to the 24 experimental points in figure 5.9. The matrix [f] is

therefore;

$$[f] = \begin{bmatrix} 4.6432 & 5.1252 & 6.1096 \\ 5.1252 & 6.1096 & 8.63 \\ 6.1096 & 8.63 & 24 \end{bmatrix}$$

The inverse of [f] as obtained using a HP9845 desktop computer is

$$[f]^{-1} = \begin{bmatrix} 4.2550 & -4.1446 & 0.4073 \\ -4.1446 & 4.3701 & -0.5164 \\ 0.4073 & -0.5164 & 0.1237 \end{bmatrix}$$

For matrix [F] ;

$$\Sigma f_1(R).F(R) = \Sigma R^4.\bar{u}_b$$

$$= (0\times22.1 + 1.4758\times10^{-3}\times25.8 + 0.02385\times19.5 + 0.1204\times17.24 + 0.3817\times10.6 + 1\times0)\times10^{-7}$$

$$= 6.6249\times10^{-7}$$

similarly

$$\Sigma f_2(R).F(R) = \Sigma R^2.\bar{u}_b$$

$$= (0\times22.1 + 0.03842\times25.8 + 0.1544\times19.5 + 0.3469\times17.24 + 0.6178\times10.6 + 1\times0)\times 10^{-7}$$

$$= 16.5313\times10^{-7}$$

and

$$\Sigma f_3(R).F(R) = \Sigma 1.\bar{u}_b$$

$$= 95.24\times10^{-7}$$

therefore

$$[F] = \begin{bmatrix} 6.6249 \\ 16.5313 \\ 95.24 \end{bmatrix} \times 10^{-7}$$

The matrix equation 4.25 in section 4.3.6 can now be solved i.e.;

$$\begin{bmatrix} c_1 \\ c_2 \\ c_3 \end{bmatrix} = \begin{bmatrix} 4.2550 & -4.1446 & 0.4073 \\ -4.1446 & 4.3701 & -0.5164 \\ 0.4073 & -0.5164 & 0.1237 \end{bmatrix} \times \begin{bmatrix} 6.6249 \\ 16.5313 \\ 95.24 \end{bmatrix} \times 10^{-7}$$

Again using the HP9845 computer to multiply matrices $[f]^{-1} \times [F]$;

$$\begin{bmatrix} c_1 \\ c_2 \\ c_3 \end{bmatrix} = \begin{bmatrix} -1.5354 \\ -4.3987 \\ 5.9434 \end{bmatrix} \times 10^{-7}$$

hence;

$$c_1 = -1.5354 \times 10^{-7}$$
$$c_2 = -4.3987 \times 10^{-7}$$
$$c_3 = 5.9434 \times 10^{-7}$$

Values of $\bar{D}_b$, b_4 and b_5 are obtained using equations 4.21 to 4.23 of section 4.3.6 as follows;

$$\bar{D}_b = \frac{1}{64.c_1} = \frac{1}{64.(-1.5354 \times 10^{-7})}$$

$$= -1.0177\times10^{5}$$

$$b_4 = 4.c_2.\bar{D}_b$$

$$= 4\times(-4.3987\times10^{-7})\times(-1.0177\times10^{5})$$

$$= 0.1791$$

$$b_5 = c_3\times \bar{D}_b$$

$$= 5.9434\times10^{-7} \times (-1.0177\times10^{5})$$

$$= 0.06049$$

The magnitude constant M_b is defined by equation 4.49 of section 4.3.6 as;

$$M_b = \bar{u}_{b1}$$

from equation 4.31;

$$\bar{u}_{b1} = -\frac{1}{\bar{D}_b}\left(\frac{b_4}{4} + \frac{1}{64}\right)$$

therefore

$$M_b = -\frac{1}{(-1.0177\times10^{5})}\left(\frac{0.1791}{4} + \frac{1}{64}\right)$$

$$= 5.935 \times 10^{-7}$$

Similarly the shape constant N_b is defined by equation 4.51 of section 4.3.6;

$$N_b = \frac{8.b_4 + 0.75}{16.b_4 + 1}$$

$$= \frac{8\times0.1791 + 0.75}{16\times0.1791 + 1}$$

$$= 0.5647$$

These values of M_b and N_b correspond with those given in table 5.2 for porous pad number 3. Similarly values for porous pads 1, 2, 4 and 5 are also listed in table 5.2. As described in section 4.3.6 the magnitude constant M_b represents the magnitude of deflections of the porous pad while the shape constant N_b relates to the shape of the deflection profile. It would be useful to compare values of N_b obtained against those for the two special cases of a rigidly and simply supported porous pad. First consider a rigidly supported porous pad. From equation 4.12 of section 4.3.6;

$$\frac{\partial \bar{u}_b}{\partial R} = \frac{1}{\bar{D}_b}\left(\frac{R^3}{16} + \frac{b_4.R}{2}\right) \qquad 5.2$$

If the porous pad is supported rigidly around its circumference $r = r_b$ then $\frac{\partial \bar{u}_b}{\partial R} = 0$ at $R = 1$. Substituting this condition into equation 5.2 gives;

$$b_4 = -\frac{1}{8}$$

Equation 4.51 of section 4.3.6 for N_b is;

$$N_b = \frac{8.b_4 + 0.75}{16.b_4 + 1} \qquad 5.3$$

Substituting for b_4 in equation 5.3 then for a rigidly supported porous pad:

$$N_b = 0.25$$

Similarly for a simply supported porous pad there would be no resistance to deflections in bending at $r = r_b$ and therefore the radial bending moment m_r is zero around the circumference of the pad. The value of m_r at any radius r is given by equation A4.5 of appendix 4 , i.e.;

$$m_r = -D_b \left(\frac{d^2 u_b}{dr^2} + \frac{\nu_b}{r} \cdot \frac{du_b}{dr} \right) \qquad 5.4$$

Substituting the condition $m_r = 0$ at $r = r_b$, equation 5.4 becomes;

$$\left(\frac{d^2 u_b}{dr^2} + \frac{\nu_b}{r} \cdot \frac{du_b}{dr} \right)_{r=r_b} = 0 \qquad 5.5$$

This equation may be written in non - dimensional form as follows:

$$\left(\frac{d^2 \bar{u}_b}{dR^2} + \nu_b \cdot \frac{d\bar{u}_b}{dR} \right)_{R=1} = 0 \qquad 5.6$$

From equation 5.2;

$$\left(\frac{d\bar{u}_b}{dR} \right)_{R=1} = \frac{1}{\bar{D}_b} \left(\frac{1}{16} + \frac{b_*}{2} \right) \qquad 5.7$$

also

$$\frac{d^2 \bar{u}_b}{dR^2} = \frac{1}{\bar{D}_b} \left(\frac{3.R^2}{16} + \frac{b_*}{2} \right)$$

$$\left(\frac{d^2\bar{u}_b}{dR^2}\right)_{R=1} = \frac{1}{\bar{D}_b}\left(\frac{3}{16} + \frac{b_4}{2}\right) \qquad 5.8$$

Substituting equations 5.7 and 5.8 into equation 5.6 gives the following expression for b_4 :

$$b_4 = -\frac{1}{8}\frac{(3 + \nu_b)}{(1 + \nu_b)} \qquad 5.9$$

The value of b_4 and hence N_b in equations 5.9 and 5.3 respectively depends on Poisson's ratio ν_b for the porous pad material. As part of the literature survey in section 2.2.3 it was described how a value of ν_b could be obtained from values of D_b, E_p and ρ_r using equations 2.18 and 2.19. However as shown in section 4.3.6 it is probable that large errors will occur in the value of D_b obtained from measured deflection profiles of the porous pad. It would therefore be erroneous to predict a value of ν_b using D_b. It was concluded in section 2.2.3 that there is insufficient literature available on ν_b for porous sintered materials and its value could be anywhere in the range 0 to 0.5 or possibly greater than 0.5. However substituting $\nu_b = 0$ in equation 5.9 gives;

$$b_4 = -3/8$$

and using equation 5.3

$$\text{for } \nu_b = 0 \quad , \quad N_b = 0.45$$

Similarly for $\nu_b = 0.5$, $N_b = 0.432$

Hence in any case the variation of N_b with ν_b is comparatively small (4%). For a simply supported porous pad therefore N_b is in the range 0.432 to 0.45.

The two special cases considered for a rigid and simply supported porous pad represents two extremes in which the stiffness of the porous pad bond k_b is infinite and zero in value respectively. However for all five porous pads the value of N_b in table 5.2 is greater than 0.45 for the simply supported case. This discrepancy can be attributed to the accuracy in measurements of porous pad deflection as discussed earlier in this section. However there is also the possibility that the deflection behaviour of a porous material is different from that of a conventional non - porous solid material on which the analysis in section 3.5 is based. This discrepancy should not adversely affect the accuracy in which deflections of the porous pad are predicted using the equations presented in section 3.5, provided values of M_b and N_b in table 5.2 for each porous pad are used. Because the values of N_b are significantly greater than 0.45 this indicates that the stiffness of the porous pad bond is small in comparison with the rigidity of the pad itself (as already mentioned earlier in this section) i.e. the porous pads are virtually simply supported around their circumference.

5.2.4 SHEAR STIFFNESS OF THE POROUS PAD BOND

Results for shear deflections of the porous pad bond are shown in figure 5.14. Values of stiffness k_o are determined as described in section 4.5.2 and are required for corrections to the measured bearing liftoff in equations 4.74 and 4.78 of sections 4.5.2 and 4.5.3 respectively.

The shear stiffness k_o for each porous pad is equal to the inverse of the slope of the best fit line passing through experimental points in figure 5.14. For example the best fit line for porous pad number 1 has a slope of 0.01324 μm/N. This gives a value of k_o = 1/ 0.01324, i.e. 75.53 N/μm.

Comparing values of k_o with porous pad thickness h_b (given in table 5.1) the stiffness of the bond increases with pad thickness. This is to be expected since the area of bond subject to shearing (i.e. $2.\pi.r_b.h_b$) increases with h_b.

5.3 ELASTOMER LAYER PROPERTIES

5.3.1 ELASTOMER LAYER IDENTIFICATION

Each elastomer layer used in bearing tests is listed in table 5.5 and identified by a letter "a" to "g". For example elastomer layer "a" is moulded in compound 1 (see

Elastomer layer	Compound+	Hardness (I.R.H.D.)*	Thickness t_c (mm)	Radius r_c (mm)	Young's modulus E_c (N/mm^2)	Shear modulus G_c (N/mm^2)	Bulk modulus K_c (N/mm^2)	Poisson's ratio ν_c
a	1	43·7	9·678	66·5	2.17	0·583	2480	0·499858
b	"	"	6·74	"	"	"	"	"
c	"	"	3·675	"	"	"	"	"
d	"	44·1	9·392	87·5	2·27	0·633	2492·5	0·499855
e	"	43·8	9·751	52·5	2.2	0·608	2485	0·499857
f	2	51·4	9·893	66·5	3·2	1	2620	0·499790
g	3	64·7	9·572	66·5	5·13	2.2	2755	0·499633

Key: + Compounds, see table 4.1
* (I.R.H.D.), International rubber hardness values

Table 5.5 Elastomer layer identification, size and properties

table 4.1 in section 4.4.1) and has a hardness value of 43.7. Its finished dimensions are 9.678mm thickness (t_c) and 66.5mm radius (r_c). For elastomer layers a,b and c a single moulding was used which was successively ground to thicknesses (t_c) of 9.678, 6.74 and 3.675mm respectively. All elastomer layers are moulded in natural rubber compounds.

5.3.2 ELASTIC MODULII E, G AND K

These are obtained from bulk modulus and shear modulus specimens as described in section 4.4.3. Load against deflection graphs from these specimens, for all three compounds are shown in figures 5.15 to 5.19. From these graphs and using the equations presented in appendix 5, values of E, G and K for each compound are obtained and listed in table 5.6. A sample calculation for compound 1 is as follows:

(a) Young's modulus E; the average slope of the two best fit lines for compound 1 in figure 5.15 is;

$$\left(\frac{L}{\delta}\right) = \frac{1.914 + 1.938}{2}$$

$$= 1.926 \quad \text{Kgf/mm}$$

$$= 18.894 \quad \text{N/mm}$$

The measured dimensions of the bulk modulus specimen for

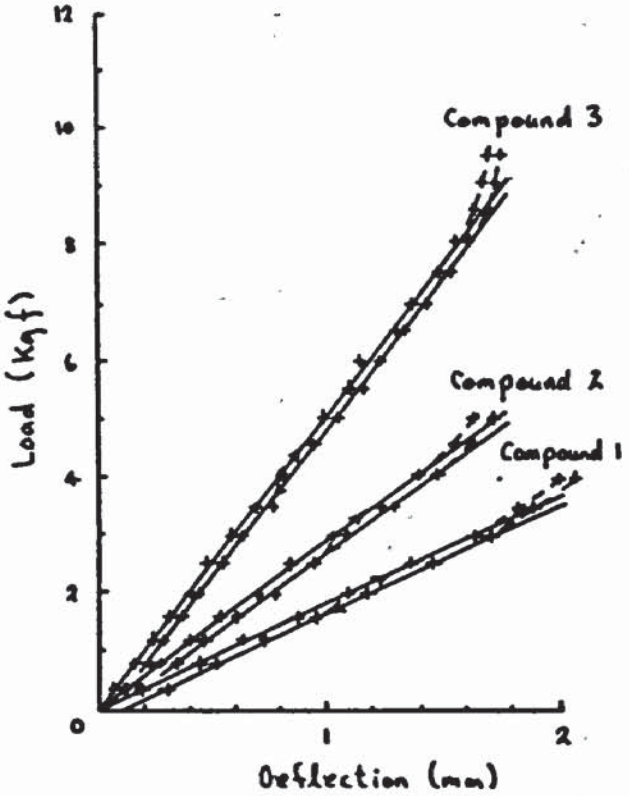

Figure 5.15 Load against deflection for bulk modulus specimen in axial compression: results for each natural rubber compound

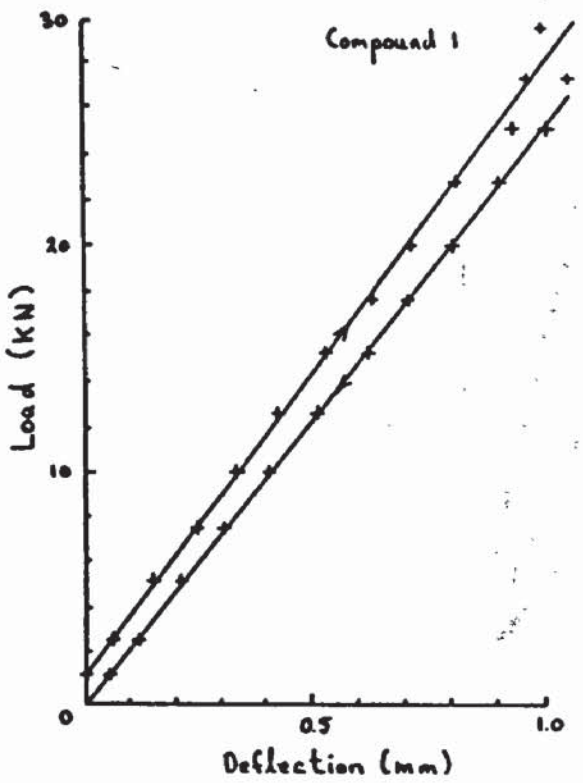

Figure 5.16 Load against deflection for bulk modulus specimen in bulk compression: results for natural rubber compound 1

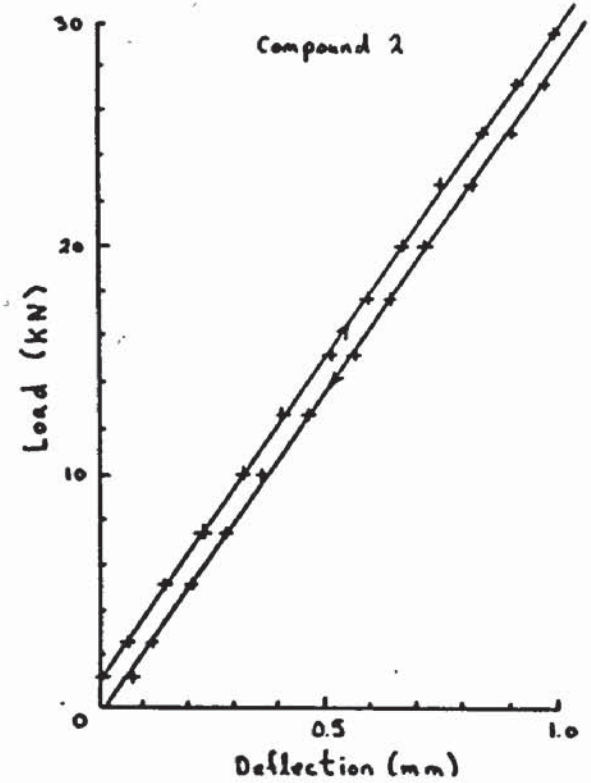

Figure 5.17 Load against deflection for bulk modulus specimen in bulk compression: results for natural rubber compound 2

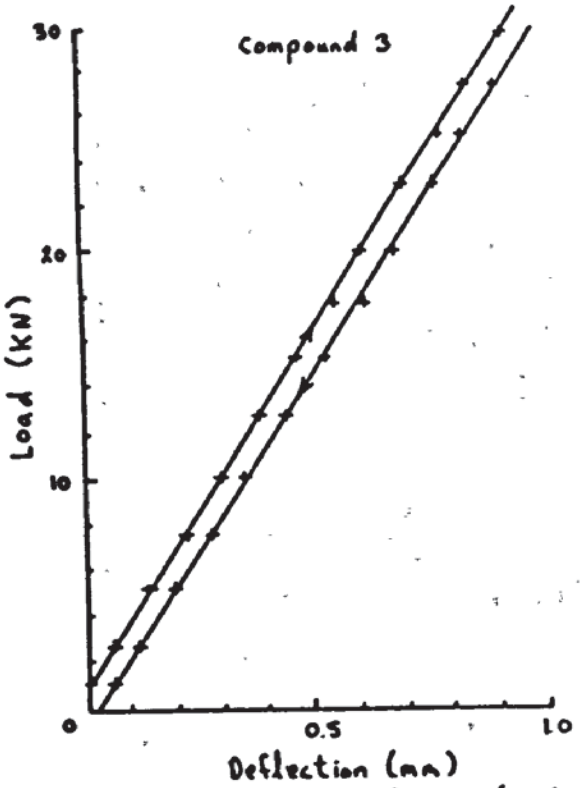

Figure 5.18 Load against deflection for bulk modulus specimen in bulk compression: results for natural rubber compound 3

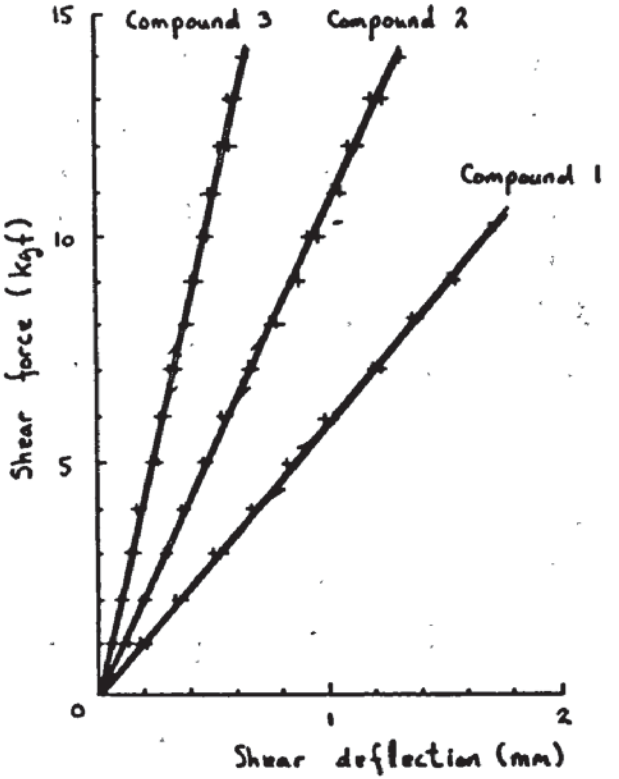

Figure 5.19 Load against deflection for shear specimens of each natural rubber compound

Compound (see table 4.2)	1	2	3
Results from bulk modulus specimen			
height h_K (mm)	49.9	50.2	50.1
diameter d_K (mm)	24.5	24.6	24.6
hardness (I.R.H.D)$^+$	42	51	67
Young's modulus E (N/mm^2)	2	3.143	5.522
bulk modulus K (N/mm^2)	2446	2610	2773
Results from shear specimen			
thickness t_g (mm)	19.05	19.61	19.61
diameter d_g (mm)	49.94	50.04	50.11
hardness (I.R.H.D)$^+$	42	52	64
shear modulus G (N/mm^2)	0.586	1.067	2.152

Key : (I.R.H.D.)$^+$, International rubber hardness value

Table 5.6 Values of E, K and G from bulk modulus and shear specimens

compound 1 in table 5.6 are; height h_k = 49.9mm and diameter d_k = 24.5mm. Using equation A5.4 in appendix 5;

$$E = \frac{4.h_k}{\pi.d_k^2}\left(\frac{L}{\delta}\right) = \frac{4\times 49.9}{\pi\times(24.5)^2}\times 18.894$$

$$E = 2 N/mm^2$$

This is the value of Young's modulus E for compound 1 in table 5.6.

(b) Bulk modulus K; the average slope of the two best fit lines for compound 1 in figure 5.16 is:

$$\left(\frac{L}{\delta}\right) = \frac{24.963 + 26.463}{2}$$

$$= 25.713 \quad KN/mm$$

This value must be corrected to take into account a small reduction in length of the piston plunger (see figure 4.32 of section 4.4.3) due to the applied load L. Equation A5.35 of appendix 5 gives the true slope as;

$$\left(\frac{L}{\delta}\right)_{true} = \frac{\left(\frac{L}{\delta}\right)_{measured}}{1 - \left(\frac{l_t}{\pi.a^2.E_t}\right)\left(\frac{L}{\delta}\right)_{measured}}$$

for the plunger l_t = 150mm, E_t = 207.10 N/mm^2 and 2a = 25.4mm. Therefore;

$$\left(\frac{L}{\delta}\right)_{true} = \frac{25.713\times10^3}{1 - \left(\frac{150}{\pi.(12.7)^2\times207\times10^3}\right) \times 25.713\times10^3}$$

$$\left(\frac{L}{\delta}\right)_{true} = 26.695 \quad KN/mm^2$$

Because the value of Poisson's ratio is very close to 0.5 equation A5.27 of appendix 5 is used to obtain a value of bulk modulus K i.e.;

$$K = \frac{h_k.d_k^2}{4.\pi.a^4}\left(\frac{L}{\delta}\right)$$

For the plunger, a = 12.7mm and from table 5.6 h_k = 49.9mm and d_k = 24.5mm. Hence;

$$K = \frac{49.9\times(24.5)^2}{4.\pi.(12.7)^4} \times 26.695\times10^3$$

$$K = 2446 \quad N/mm^2$$

This is the value of bulk modulus K for compound 1 in table 5.6. The error introduced by using equation A5.27 instead of equation A5.26 in appendix 5 is small since from equation 4.60 of section 4.4.2;

$$\nu = \frac{1}{2} - \frac{E}{6.K}$$

Substituting values of E and K for compound 1 gives a value for ν ;

$$\nu = \frac{1}{2} - \frac{2}{6\times2446}$$

$$= 0.499864$$

Using equation A5.26 instead of equation A5.27 in appendix 5 the value of K obtained would have been;

$$K = \frac{h_k . d_k^2}{12.\pi.a^4} \cdot \frac{(1+\nu)}{(1-\nu)} \cdot \left(\frac{L}{\delta}\right)$$

$$K = \frac{2446}{3} \times \frac{(1 + 0.499864)}{(1 - 0.499864)}$$

$$= 2445 \quad N/mm^2$$

The difference in values 2446 and 2445 N/mm^2 for K is only 0.04%. This therefore justifies the use of equation A5.27 in appendix 5 for K.

(c) Shear modulus G; the average slope of the best fit shear force against deflection lines in figure 5.19 for compound 1 are;

$$\left(\frac{L}{\delta}\right) = \frac{5.763 + 5.779}{2}$$

$$= 5.771 \quad Kgf/mm$$

$$= 56.61 \quad N/mm$$

From table 5.6 the dimensions of the shear specimen for

compound 1 are: t_g = 19.05mm and d_g = 49.94mm. Using equation A5.39 of appendix 5 the apparent shear modulus G_g is:

$$G_g = \frac{4.t_g}{\pi.d_g^2}\left(\frac{L}{\delta}\right)$$

$$= \frac{4\times19.05}{\pi\times(49.94)^2} \times 56.61$$

$$= 0.5506 \quad N/mm^2$$

The true shear modulus is given by equation A5.40 of appendix 5 i.e.;

$$G = 0.5506 \times \left(1 + \left(\frac{16\times(19.05)^2}{36\times(49.94)^2}\right)\right)$$

$$G = 0.586 \quad N/mm^2$$

This is the value of shear modulus G shown in table 5.6 for compound 1 and completes the sample calculation for E, K and G. Other values obtained similarly for compounds 2 and 3 are shown in table 5.6.

In obtaining bulk modulus K using equation A5.27 of appendix 5 the expansion of the compression cylinder in the bulk modulus tester (figure 4.32, section 4.4.3) was ignored. Holownia (64) took into account this expansion due to the pressure exerted by the bulk modulus specimen on the cylinder bore walls. This expansion was determined by applying two - dimensional thick cylinder theory (47), even

though the problem is three - dimensional since the bulk modulus specimen does not extend the whole length of the compression cylinder. However the following equations were obtained.

From equation 4.60 of section 4.4.2, Poisson's ratio ν is given by;

$$\nu = \frac{1}{2} - \frac{E}{6.K} \qquad 5.10(a)$$

The correction necessary to this equation to take account of the expansion of compression cylinder walls is given as (64);

$$\nu = \frac{1}{2} - \left[\frac{E}{6.K} . \left(1 - 2. \frac{\varepsilon_r}{\varepsilon_z} \right) \right] \qquad 5.10(b)$$

Where E and K are determined assuming no expansion of the compression cylinder walls. The ratio ϵ_r/ϵ_z in equation 5.10 is the ratio of radial strain to axial strain of the bulk modulus specimen. The value of this ratio is given (64) by the equation;

$$\frac{\varepsilon_r}{\varepsilon_z} = \frac{1}{E_t} \left[\frac{(b^2 + a^2)}{(b^2 - a^2)} - \nu_t \right] \left(\frac{\sigma_z}{\varepsilon_z} - E \right) \Big/ 2.\nu \qquad 5.11$$

Using equation A5.17 of appendix 5 and substituting for σ_z/ϵ_z in equation 5.11 gives;

$$\frac{\varepsilon_r}{\varepsilon_z} = \frac{1}{E_t}\left[\frac{(b^2 + a^2)}{(b^2 - a^2)} - \nu_t\right]\left(\frac{K - E}{2.\nu}\right) \qquad 5.12$$

Consider the following example. From the sample calculation for compound 1 in this section, E = 2 N/mm^2 and K = 2446 N/mm^2. Using equation 5.10a these values of E and K give; ν = 0.499864. Therefore in equation 5.12;

$$\frac{K - E}{2.\nu} = \frac{2446 - 2}{2 \times 0.499864}$$

$$= 2444.7 \quad N/mm^2$$

The compression cylinder of the bulk modulus tester used in experiments has an outside diameter of 150mm and is made from mild steel. Therefore in equation 5.12; b = 75mm, ν_t = 0.3 and $E_t = 207 \times 10^3 N/mm^2$. Also the cylinder bore 2a = 25.4mm. Substituting these values into equation 5.12 and;

$$\frac{\varepsilon_r}{\varepsilon_z} = \frac{1}{207 \times 10^3} \times \left[\frac{75^2 + 12.7^2}{75^2 - 12.7^2} - 0.3\right] \times 2444.7$$

$$= 0.009$$

Substituting 0.009 for $\varepsilon_r/\varepsilon_z$ in equation 5.10b and since E = 2 N/mm^2 and K = 2446 N/mm^2 a new value for ν is obtained i.e.;

$$\nu = \frac{1}{2} - \left[\frac{2}{6 \times 2446} \times (1 - 2 \times 0.009) \right]$$

$$= 0.499866$$

The percentage change in Poisson's ratio from expansion of the compression cylinder walls is therefore:

$$\Delta\nu = \left(\frac{0.499866 - 0.499864}{0.499866 + 0.499864} \right) \times 2 \times 100\%$$

$$\Delta\nu = 0.0004\%$$

This is small compared to the 0.04% change that may occur due to measurement errors in E and K as shown in section 4.4.2. The effects of compression cylinder expansion on the resulting value of Poisson's ratio ν can therefore be neglected.

A comparison of the results in table 5.6 for E and K with those obtained by other researchers for natural rubber filled with different carbon black contents, is shown in figure 5.20. Note that there is a considerable variation in the values of E obtained despite only a maximum difference of 8% for K. Though the author used a similar rubber compound to Stanojevic and Lewis (66) there is almost a three fold difference in the values of E obtained at H.A.F. black contents of 20 and 15 p.p.r.h. respectively. The accuracy of the authors results can be cross checked using

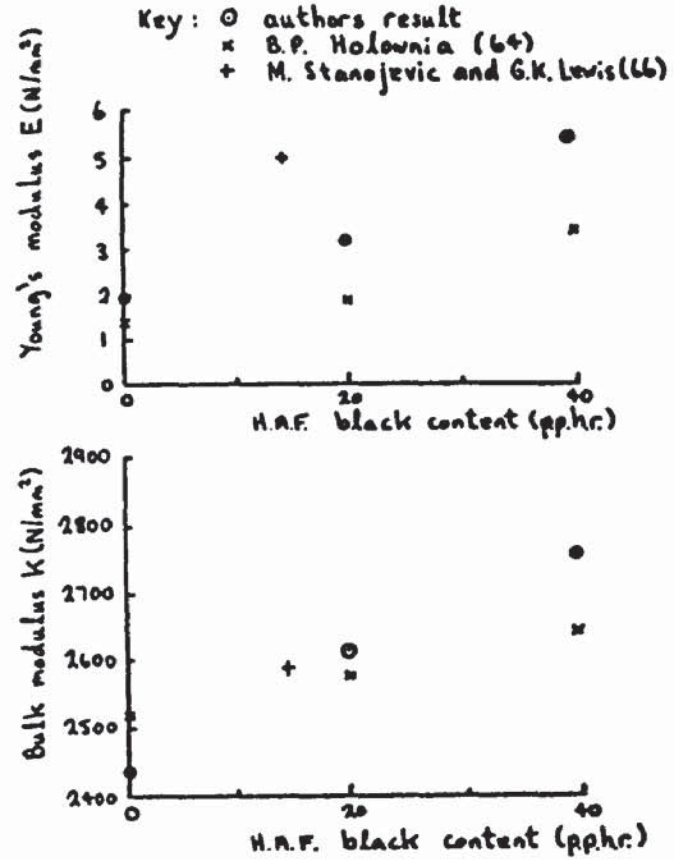

Figure 5.20 Young's and bulk modulus against carbon black content in parts per hundred parts natural rubber (pp.h.r.): comparison of results with other researchers for bulk modulus specimen.

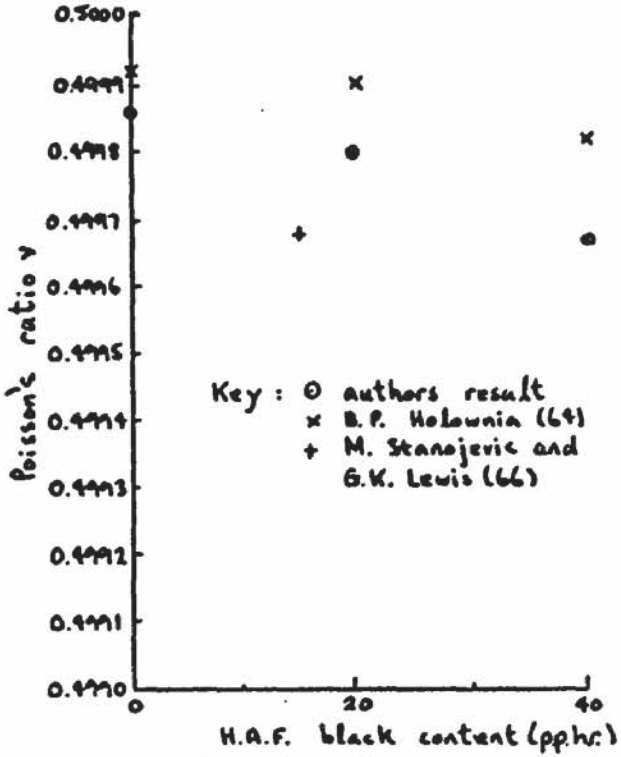

Figure 5.21 Poisson's ratio against carbon black content in parts per hundred parts of natural rubber (pph.r.): comparison of results with other researchers for the bulk modulus specimen

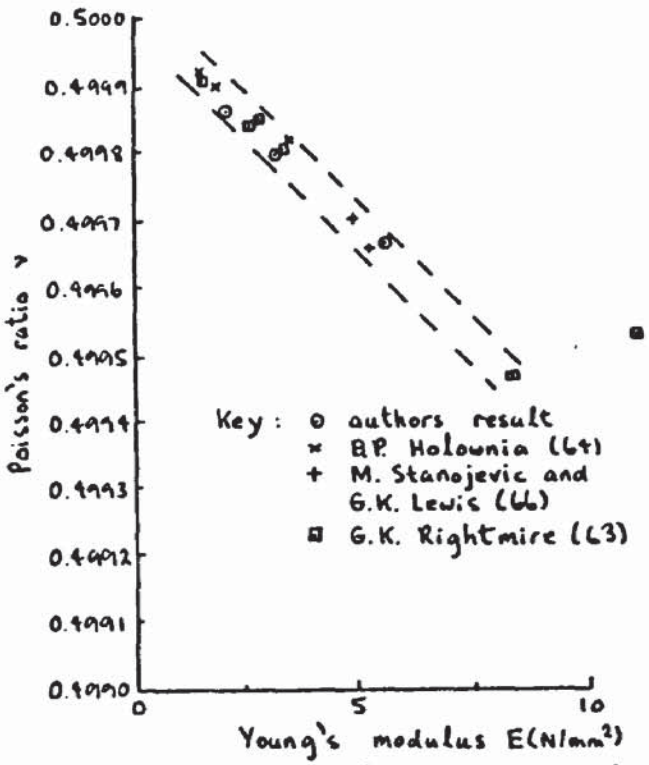

Figure 5.22 Poisson's ratio against Young's modulus : comparison of results with other researchers

the value of shear modulus G obtained from tests on the shear specimens. This can be achieved through equation 4.59 of section 4.4.2 in the form;

$$\nu = \frac{E}{2.G} - 1$$

Substituting a value of $\nu \simeq 0.5$ into this equation;

$$\frac{E}{3.G} \simeq 1$$

Using values of E and G for each compound in table 5.6 the ratio E/3G is within 1 ± 0.15 ($\pm 15\%$). Therefore the accuracy of the authors results for E in figure 5.20 is estimated at $\pm 15\%$. It is possible that the large variation in E compared to the results of other researchers in figure 5.20 may be attributed to the moulding procedure used. For example the author carried out all mouldings at 160°C for 50 mins while in (66) 140°C and 1.5 hours was used respectively. The author concludes therefore the importance of moulding all specimens and elastomer layers at the same temperature and for the same time period.

Figure 5.21 is a comparison of Poisson's ratio values ν with other researchers for natural rubber with different carbon black contents. The authors results are based on values of E and K using equation 4.60 of section 4.4.2 in the form;

$$\nu = \frac{1}{2} - \frac{E}{6.K} \qquad 5.13$$

Despite the large variation in values of E shown in figure 5.20 all values of ν in figure 5.21 are within 0.05% of each other. This demonstrates the high accuracy which ν is obtained from measured values of E and K.

A comparison of results with those of other reseachers for ν against E is shown in figure 5.22. A similar plot was presented in (66) and a straight line was fitted through the plotted points. This assumes a constant value of K in equation 5.13 which is strictly incorrect as figure 5.20 shows. However the narrow band of results indicated by the two broken lines in figure 5.22 demonstrate again the accuracy in which values of Poisson's ratio ν are obtained not only from E and K but also G and K since Rightmire (63) measures shear modulus G to obtain a value of ν .

5.3.3 ELASTIC PROPERTIES E_c , G_c , K_c AND ν_c FOR THE ELASTOMER LAYERS

Even though the specimens and elastomer layers are of the same rubber compound and are moulded under carefully controlled conditions there is still a possibility that slight variations in properties may occur between the specimens and the elastomer layers. The only indication of this is from hardness readings given in tables 5.5 and 5.6

for the specimens and elastomer layers respectively. Using the results in table 5.6 values of E, K and G have therefore been plotted against hardness readings as shown in figures 5.23 to 5.25. Using these graphs and equations 4.60 and 4.61 of section 4.4.2 in the form;

$$\nu = \frac{1}{2} - \frac{E}{6.K} \qquad 5.14$$

and $$\nu = \frac{1}{2}\left(1 - \frac{G}{K}\right) \qquad 5.15$$

two curves are drawn for Poisson's ratio ν against rubber hardness in figure 5.26. For example at a rubber hardness value of 50 values of E = 2.967 N/mm^2, K = 2593 N/mm^2 and G = 1.053 N/mm^2 are obtained from figure 5.23, 5.24 and 5.25 respectively. Using equation 5.14;

$$\nu = \frac{1}{2} - \frac{2.967}{6\times2593}$$

$$= 0.499809$$

and from equation 5.15;

$$\nu = \frac{1}{2}\left(1 - \frac{1.053}{2593}\right)$$

$$= 0.499797$$

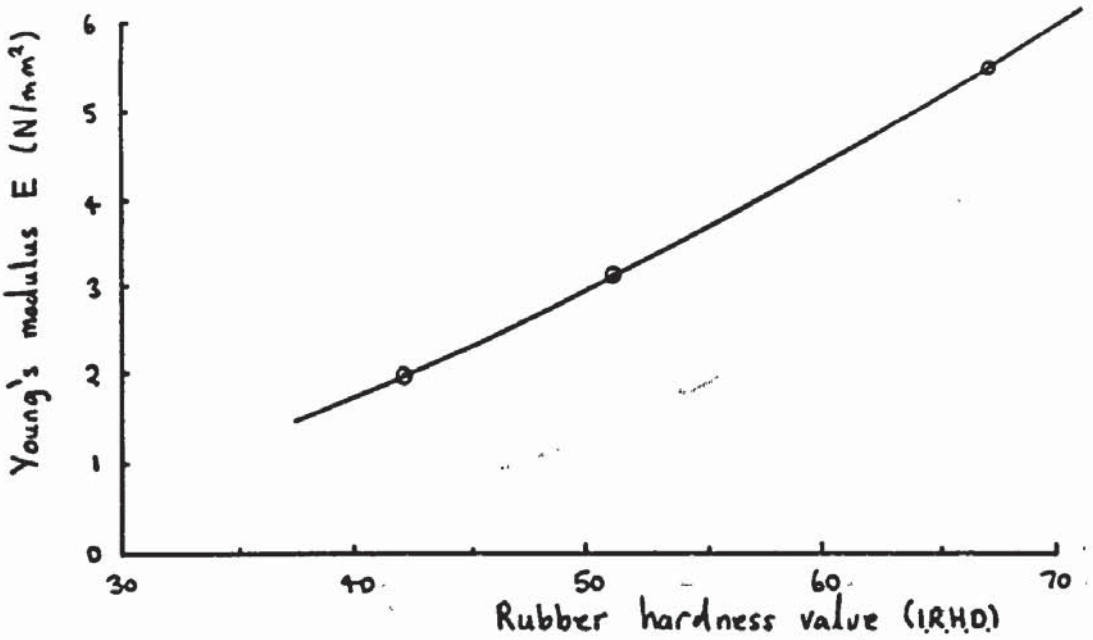

Figure 5.23 Graphical plot of Young's modulus against rubber hardness for bulk modulus specimen's

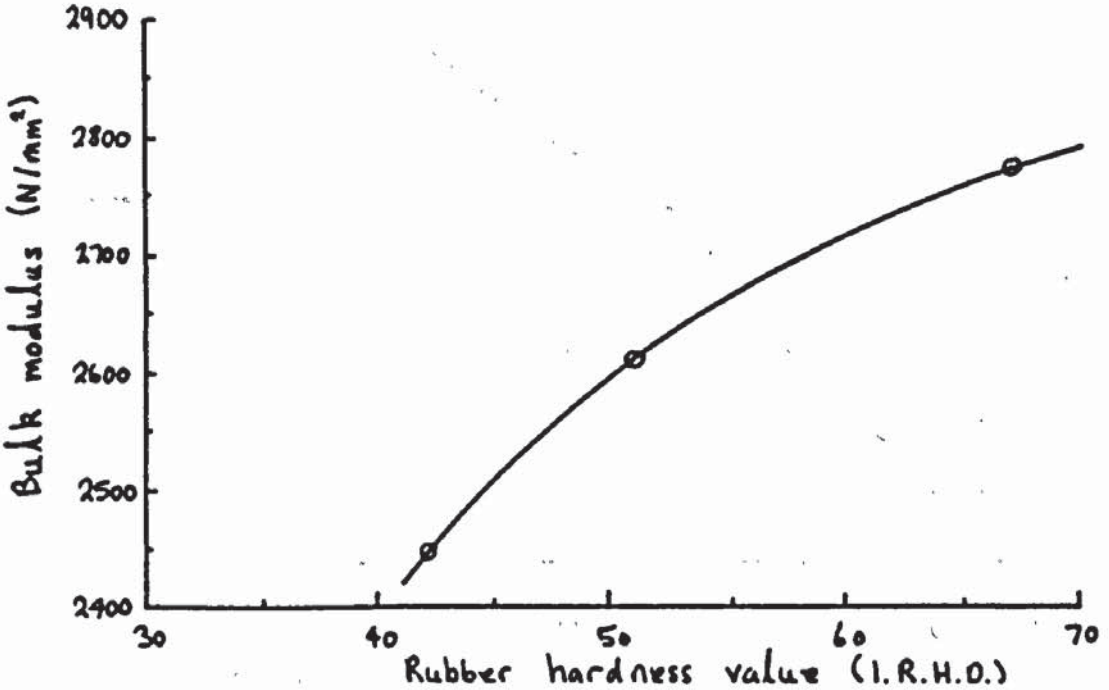

Figure 5.24 Graphical plot of bulk modulus against rubber hardness for bulk modulus specimen's

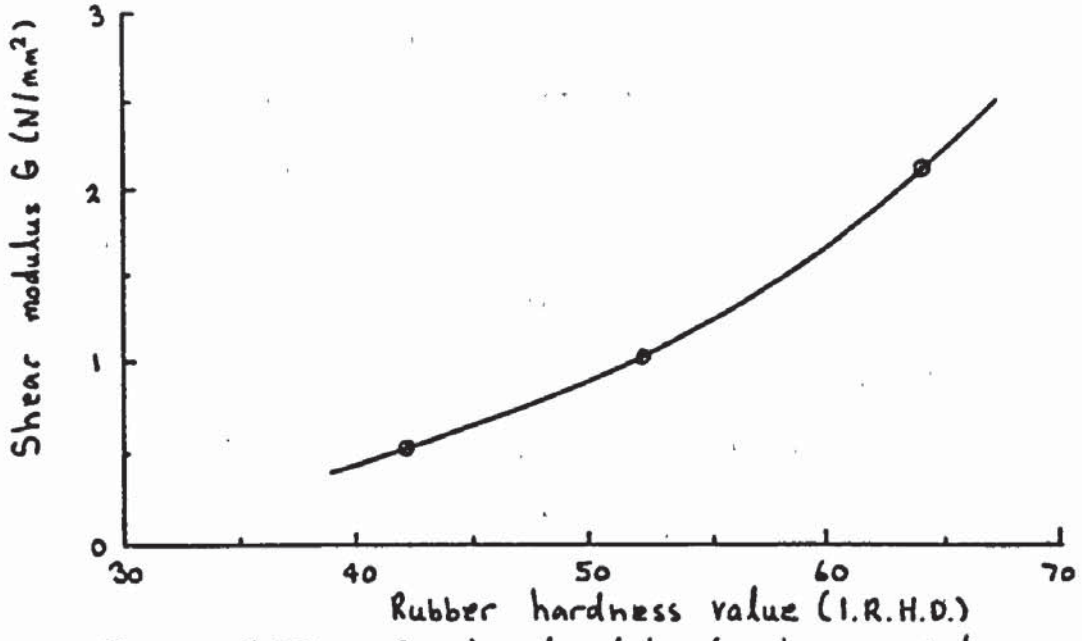

Figure 5.25 Graphical plot of shear modulus against rubber hardness for shear specimen's

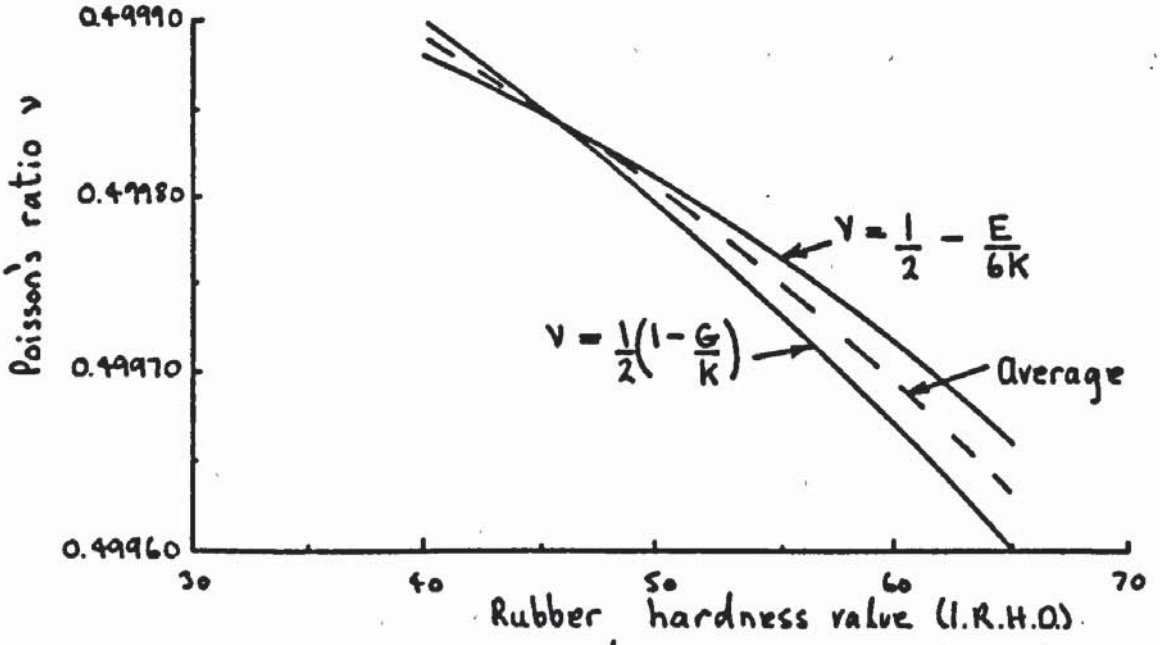

Figure 5.26 Graphical plot of Poisson's ratio against rubber hardness from values of E & K and G & K.

These values correspond with those obtainable from the two curves in figure 5.26 for a rubber hardness value of 50.

The properties of E_c, K_c, G_c and ν_c given in table 5.5 for each elastomer layer are obtained using figures 5.23 to 5.26 and correspond with their hardness value shown in the third column of this table. For ν_c an average value from the broken curve in figure 5.26 is taken. Using this procedure small differences in properties between the specimens and elastomer layers as indicated by their hardness values are accounted for.

5.4 BEARING PERFORMANCE RESULTS

5.4.1 PRESENTATION OF EXPERIMENTAL RESULTS

Experimental results for the performance of a porous and compliant aerostatic thrust bearing are presented graphically in figures 5.27 to 5.51 at the end of this chapter. Included on these graphs are curves from theoretical predictions (see chapter 3).

The bearing performance is represented by three different plots of load capacity W, flow rate M and bearing number $\Lambda_d^{-1/3}$ against $\Lambda_c^{-1/3}$, in non - dimensional form. As described in section 3.7.1 the load capacity W represents the ratio of actual load carried by the bearing to the maximum possible from the supply pressure $p_s - p_a$. Its maximum value is therefore 1. Similarly flow rate M is the

ratio of actual mass flowrate to the maximum possible through the porous pad at a supply pressure of $p_s - p_a$. It also has a maximum value of 1. Since increasing the load carrying capacity at minimum flowrate and supply pressure $p_s - p_a$ is one of the main criteria for bearing selection then the bearing performance can be said to improve as load capacity W approaches 1 and flow rate M approaches 0.

For conventional porous aerostatic thrust bearings many researchers have used a form of bearing number based on bearing clearance in the presentation of results for load capacity W and flowrate M, and this bearing number is plotted on a horizontal $\log_{10}$ scale. However for a porous and compliant aerostatic thrust bearing it is more appropriate to use a bearing number which is based on the bearing approach c. As defined in section 3.6, this represents the displacement of the rigid backing to the elastomer layer. For this reason therefore the bearing number Λ_c is used in the presentation of results for W and M. Theoretically the value of c in Λ_c can be +ve, zero or -ve (see figure 5.63 of section 3.6). Therefore it is not possible to use a $\log_{10}$ scale for Λ_c and instead $\Lambda_c^{-1/3}$ has been selected. Note that the sign of $\Lambda_c^{-1/3}$ (i.e. +ve or -ve) is the same as that for c i.e. when $\Lambda_c^{-1/3}$ is -ve, c is also -ve. Also when $c^2 >> 6\Phi_r$, $\Lambda_c^{-1/3}$ is directly proportional to c.

The additional graph of $\Lambda_d^{-1/3}$ against $\Lambda_c^{-1/3}$ shows the variation of bearing number based on bearing clearance h_d

with bearing number based on bearing approach c. This graph enables the bearing clearance h_d to be determined for a bearing operating at approach c.

During bearing tests results were recorded for several different bearing configurations and properties. For example each elastomer layer may be identified by its thickness t_c, radius r_c, shear modulus G_c and Poisson's ratio ν_c. In practice G_c and ν_c are not independant, i.e. one cannot be varied without affecting the resulting value of the other. Therefore both G_c and ν_c are replaced with a hardness value for the elastomer layer material.

Similarly the porous pads are identified by their thickness h_b, radius r_b, permeability Φ and rigidity constants M_b and N_b. The value of N_b has remained virtually constant for all five porous pads in table 5.2 (this could have been varied by increasing the stiffness of the porous pad support. But the author did not pursue this due to time limitations) and since Φ and M_b both depend on the structure and porosity of the porous pad material these are replaced with the manufacturer's grading. In addition to the bearing configuration and properties, the supply pressure $p_s - p_a$ can also be varied and this was carried out in two of the bearing tests.

It is normal practice to present results so that the effect of each property on the bearing performance is shown. There are seven separate properties i.e. t_c, r_c, hardness value for the elastomer layer, h_b, r_b,

manufacturers grading for the porous pads and supply pressure $p_s - p_a$. A change in any one of these properties will result in a corresponding change in one or more non - dimensional constants listed at the end of section 3.7.2 (i.e. S_b, K_v, S_c, etc.). However because it has been impossible to obtain porous pads larger than 51mm radius at suitable thicknesses of at least 9.5mm then r_b has been kept constant at approximately 50.9mm in the bearing tests. Smaller pads than this were not selected for the reasons explained in section 4.2.2. A change in the remaining six properties will still result in a corresponding change to all the non - dimensional constants in section 3.7.2.

During bearing tests, results are taken for at least three different values of these six properties while the others remain as constant as practically possible as shown in table 5.7. Note that each bearing is identified by a number followed by a letter, i.e. 3a for example. The number refers to the porous pads listed 1 to 5 in tables 5.1 and 5.2, and the letter to the elastomer layers listed a to g in table 5.5. Bearing 3a therefore contains porous pad number 3 and elastomer layer "a". Where a bearing is identified by a number only i.e. 3, this means that the elastomer layer has been removed and replaced with a rigid flat ground surface. Bearing 3 therefore contains porous pad 3 only. In such cases the bearing becomes a porous aerostatic thrust bearing with an elastic porous pad. As explained in section 3.6 for these bearings the clearance h_d

Bearing test	Bearing identification	Elastomer layer			Porous pad			Supply pressure p_s
		thickness t_e (mm)	radius r_e (mm)	hardness (I.R.H.D.)	thickness h_b (mm)	radius r_b (mm)	manu. grading	
1	3a	9.678	66.5	43.7	19.4	50.95	SIKA R1	3
2	3b	6.74	"	"	"	"	"	"
3	3c	3.675	"	"	"	"	"	"
4	3	-	-	-	"	"	"	"
5	3f	9.893	66.5	51.4	"	"	"	"
6	3g	9.572	"	69.7	"	"	"	"
7	3d	9.392	87.5	44.1	"	"	"	"
8	3e	9.751	52.5	43.8	"	"	"	"
9	3a	9.678	66.5	43.7	"	"	"	2
10	3a	"	"	"	"	"	"	4
11	3	-	-	-	"	"	"	2
12	3	-	-	-	"	"	"	4
13	1a	9.679	66.5	43.7	9.5	50.91	"	3
14	2a	"	"	"	15.5	50.97	"	"
15	1	-	-	-	9.5	50.91	"	"
16	2	-	-	-	15.5	50.97	"	"
17	4a	9.678	66.5	43.7	19.2	50.93	SIKA R3	"
18	5a	"	"	"	19.5	50.89	SIKA R5	"
19	4	-	-	-	19.2	50.93	SIKA R3	"
20	5	-	-	-	19.5	50.89	SIKA R5	"

Table : 5.7 Bearing test parameters

Bearing test (see table 5.7)	Termination of test due to:		Value of $\Lambda_c^{-1/3}$ at which test terminated
	bearing touchdown	pneumatic instability	
1	✓		0.63
2		✓	1.41
3		✓	1.05
4	✓		0.67
5	✓		0.94
6		✓	1.22
7	✓		0.65
8		✓	0.24
9	✓		0.61
10	✓		0.4
11	✓		0.56
12		✓	0.88
13		✓	1.0
14	✓		0.59
15	✓		1.05
16	✓		0.68
17	✓		0.50
18		✓	0.89
19	✓		0.58
20	✓		0.8

Table : 5.8 Cause of bearing test termination

is equal to the approach c and therefore $\Lambda_d^{-1/3} = \Lambda_c^{-1/3}$. Graphs of $\Lambda_d^{-1/3}$ versus $\Lambda_c^{-1/3}$ for bearings 1 to 5 have therefore been omitted.

In the presentation of experimental results graphs of static stiffness K_x versus bearing number $\Lambda_c^{-1/3}$ have been omitted . This is because K_x is not a directly measurable quantity and large errors can occur in obtaining a value of $\frac{\partial W}{\partial(\Lambda_c^{-1/3})}$ for K_x from the W versus $\Lambda_c^{-1/3}$ graph. For similar reasons both Garguilo and Gilmour (19) and Taylor (24) also chose not to present experimental graphs of static stiffness against bearing number for a porous aerostatic thrust bearing.

5.4.2 COMPARISON OF EXPERIMENTAL RESULTS WITH THEORETICAL PREDICTIONS

In general experimental results for load capacity W versus bearing number $\Lambda_c^{-1/3}$ correlate well with theoretical predictions. During bearing tests loads were increased until bearing touchdown or pneumatic instability occurred as described in section 4.5.4. For some bearing tests the range of results for bearing number $\Lambda_c^{-1/3}$ was limited due to the onset of pneumatic instability. Although one of the areas of investigation outlined in section 2.3 was for an experimental analysis of bearing instability there has been insufficient time remaining for the author to carry this out. However table 5.8 shows which bearing tests terminated

in either bearing touchdown or pneumatic instability.

In figures 5.45 and 5.50 for bearings 1 and 5 respectively a significant departure in results from the theoretical curve for load capacity W occurs at low values of bearing number $\Lambda_c^{-1/3}$. As explained in section 5.4.1 these bearings do not have an elastomer layer i.e. they are porous aerostatic thrust bearings with an elastic porous pad. This phenomena was also reported by Taylor and Lewis (9) who accounted it to touchdown of the bearing surfaces. Note that for these bearings the approach c and clearance h_d are both equal. Also bearing touchdown occurs at a value of $\Lambda_c^{-1/3}$ greater than zero. This is due to roughness and flatness of the bearing surfaces and gives rise to a pneumatic clearance s_h as described in section 4.5.2. For a porous and compliant aerostatic thrust bearing however the elastomer layer still continues to compress even after bearing touchdown. Because the elastomer layer is a soft material there is no significant departure in experimental results from the theoretical curve for load capacity W versus bearing number $\Lambda_c^{-1/3}$ with these bearings as shown in figures 5.27, 5.30, 5.33, 5.36, 5.42 and 5.47.

With the exception of results shown in figures 5.37 and 5.41, there is again a good correlation of experimental results with theoretical predictions for flow rate M versus bearing number $\Lambda_c^{-1/3}$ (see figures 5.28, 5.31, 5.34, 5.43, 5.46, 5.48 and 5.51). However in figures 5.37 and 5.41 there is a departure in experimental results from the

theoretical curve for $P_s = 4$. This discrepancy increases with bearing number $\Lambda_c^{-1/3}$. It is possible that this may be accounted to the onset of transitional flow for porous pad 3 (see section 5.22). In the transition flow region the actual flow rate for a given pressure gradient within the porous pad will reduce due to the additional inertia losses. Remembering that the non - dimensional mass flow rate M is the ratio of actual flow to the maximum possible through the porous pad at supply pressure $p_s - p_a$, this would result in a reduction in the experimental result for M because this maximum flow is based on the assumption of viscous flow within the porous pad.

For graphs of $\Lambda_d^{-1/3}$ versus $\Lambda_c^{-1/3}$ (see figures 5.29, 5.32, 5.35, 5.38, 5.44, 5.49) there is reasonable correlation of experimental results with theoretical curves for values of $\Lambda_c^{-1/3}$ down to approximately 1.2. After this there is a departure in experimental results to the left of the theoretical curves. This indicates bearing touchdown for a porous and compliant aerostatic thrust bearing because the value of $\Lambda_d^{-1/3}$ is approaching a constant value while $\Lambda_c^{-1/3}$ still reduces due to compression of the elastomer layer. This constant value of $\Lambda_d^{-1/3}$ is not zero because of the pneumatic clearance caused by roughness of the bearing surfaces.

A comparison of experimental results with theoretical predictions for the film pressure profile is shown in figure 5.39. The scatter in experimental points indicates non - symmetry of flow in the bearing film clearance (see

figure 4.10 of section 4.2.3 for pressure tapping positions). As described in section 4.3.1 and illustrated in figure 4.13 it was possible to check the symmetry of flow through the porous pad. This was achieved by observing the distribution of rising air bubbles through the water contained above the porous pad while it was pressurized through the supply chamber. There was a noticeable non - symmetry of flow through all five selected porous pads even before these were ground and electro - polished (see section 4.3.4). It appears therefore that the porosity distribution in sintered porous materials is non - uniform.

A non - symmetrical flow through the porous pads and hence flow in the bearing film can cause premature touchdown of the bearing surfaces in a porous and compliant aerostatic thrust bearing. This is due to the resulting non - symmetrical deflections of the compliant surface in a circumferential direction particularly at the bearing clearance exit $r = r_b$.

5.4.3 PRESENTATION OF THEORETICAL BEARING CHARACTERISTIC CURVES.

Theoretical curves showing the effect of each non - dimensional constant P_s, S_b, K_v, etc on the performance of a porous and compliant aerostatic thrust bearing are presented in figures 5.52 to 5.99 at the end of this chapter.

As described in section 5.4.1 for the presentation of experimental results, the theoretical bearing performance is represented by graphical plots of W, M and $\Lambda_d^{-1/3}$ against $\Lambda_c^{-1/3}$. In addition a plot of static stiffness K_x versus $\Lambda_c^{-1/3}$ is included along with theoretical film and clearance geometry profiles, similar to those shown in figures 5.54 and 5.56 respectively. The clearance geometries are the result of deflections of both the elastomer layer and the porous pad in bending. Figure 5.58 is a single plot showing separate deflections of the elastomer layer and porous pad in bending. The resulting clearance geometry from these deflections is also indicated in this figure.

5.4.4 DISCUSSION OF POROUS AND COMPLIANT AEROSTATIC THRUST BEARING PERFORMANCE

Having presented results and shown that the theoretical predictions correlate with experimental results in section 5.4.2 it is now possible to draw conclusions on the performance of a porous and compliant aerostatic thrust bearing. For reasons described at the beginning of this thesis in section 1.2 it was anticipated at the onset of this research project that the performance of a porous aerostatic thrust bearing would be improved if the solid rigid surface opposing the porous pad was compliant in the form of an elastomer layer. However the results presented

in sections 5.4.1 and 5.4.3 show that the reverse has occurred.

As an example in figure 5.27 the theoretical load capacity W decreases with increasing elastomer layer thickness for a given bearing number $\Lambda_c^{-1/3}$. The experimental results for bearings 3a and 3 also clearly show this trend. Note that the results for bearing 3a discontinues at $\Lambda_c^{-1/3}$ = 0.63 due to bearing touchdown as indicated in table 5.8 (see also table 5.7). With reference to the theoretical curves in figure 5.52 this trend persists for bearing numbers $\Lambda_c^{-1/3}$ down to zero. (Note that S_c is the non - dimensional elastomer layer thickness).

This decrease in load capacity W is made worse by a corresponding increase in the flow rate M with elastomer layer thickness as shown in figure 5.28. Again experimental results for bearing 3a and 3 clearly show the trend of increasing flowrate with elastomer layer thickness. The discrepancy between experimental results and theorectical predictions for bearing 3b is attributed to experimental error.

The reasons for this reduced performance with increasing elastomer layer thickness may be described with reference to theoretical pressure profiles and bearing clearance geometries in figures 5.56 for $\Lambda_c^{-1/3}$ = 0.4. From this figure it can be seen that the film pressure profile becomes more uniform with increasing values of non - dimensional elastomer layer thickness S_c and hence

thickness t_c (for r_b = constant). This is to be expected from the recess formed in the bearing clearance geometry due to deflections of the compliant surface. However as the film pressure profiles become more uniform the pressure gradient at R = 1 increases. From equation 4.66 of section 4.5.2 the flow rate M is given by;

$$M = - \frac{2}{\Lambda_d . (P_s^2 - 1)} \left[\frac{\partial (P^2)}{\partial R} \right]_{R=1} \qquad 5.16$$

The result of an increase in film pressure gradient at R = 1 is therefore an increase in flowrate M as shown in figure 5.53. Note also that the bearing clearance h_d at R = 1 decreases with increasing values of S_c as shown in the bearing clearance geometries, figure 5.56. This is due to bulging of the elastomer layer near the bearing clearance exit R = 1 and tends to reduce the flow rate M by a corresponding increase in Λ_d, equation 5.16. However because the increase in $\left[\frac{\partial (P^2)}{\partial R} \right]$ is greater than Λ_d in equation 5.16 the result is an increase in flow rate M with S_c. The increase in flow rate M causes a greater pressure drop across the porous pad for a given supply pressure $p_s - p_a$. As a result the magnitude of the film pressure profiles in figure 5.56 reduces with increasing values of S_c. This causes a reduction in load capacity W as shown in figure 5.52. The results are similar for film pressure profiles and bearing clearance geometries in figure 5.57 for $\Lambda_d^{-1/3}$ = 0.4, i.e. constant bearing clearance

h_d.

From this reasoning the following conclusions can be drawn. The performance of a porous and compliant aerostatic thrust bearing is compromized by the restriction to flow through the bearing caused by the porous pad. The result is that the bearing performance reduces with increasing elastomer layer compliance. This in itself is a unique discovery because previous researchers of compliant aerostatic thrust bearings with a central feed hole (58, 71, 72, 77) have used inherent compensation and ignored the effects of a restrictor, such as capillary compensation, on the bearing performance.

Although only S_c and t_c have so far been used to explain the effect of the compliant surface on porous and compliant aerostatic thrust bearing performance this will now be extended to other bearing properties and non - dimensional constants in the following section (5.4.5).

5.4.5 THE EFFECT OF BEARING PROPERTIES AND NON - DIMENSIONAL CONSTANTS ON THE PERFORMANCE OF A POROUS AND COMPLIANT AEROSTATIC THRUST BEARING

In this section reference will be made to figures 5.27 to 5.99 for both experimental and theoretical results.

(a) The effect of S_c, S_o, ν_c, t_c and rubber hardness.

These all have a similar effect on the bearing performance which can be described as reductions in load

capacity W and increases in flow rate M with increasing elastomer layer compliance. An elastomer layer is said to be more compliant when the recess formed by its deflection increases. The elastomer layer compliance increases with the non - dimensional thickness S_c and this results in a reduction in bearing performance as shown in figures 5.52 and 5.53. However the static stiffness K_x as shown in figure 5.54 can increase with S_c at lower values of $\Lambda_c^{-1/3}$. This is due to the rapid recovery in load capacity W at lower values of $\Lambda_c^{-1/3}$ as shown in figure 5.52 particularly with increasing values of S_c.

In figure 5.55 for graphs of $\Lambda_d^{-1/3}$ against $\Lambda_c^{-1/3}$ all curves for $S_c > 0$ lie to the right of the $\Lambda_c^{-1/3} = \Lambda_d^{-1/3}$ line. This is because the approach c is greater than the bearing clearance h_d and is caused by bulging of the elastomer layer near the bearing exit R = 1 as shown in figure 5.56. Note that for $S_c = 0$ there is effectively no elastomer layer and therefore $\Lambda_c^{-1/3} = \Lambda_d^{-1/3}$ since $c = h_d$. As S_c increases in value up to 0.13 the bearing approach c also increases for a given clearance h_d, this being indicated by a progressive move to the right of curves for S_c in figure 5.55. This is due to an increase in the size of the bulge occuring at R = 1 caused by increases in deflections of the compliant surface (figure 5.56). However the opposite has occurred for S_c in the range 0.13 to 0.2 i.e. there is a move back to the left for these curves in figure 5.55 with increasing S_c. This is because larger deflections of the

compliant surface are offset by a less pronounced bulging at R = 1 resulting in a reduction in the bearing approach c for a given clearance h_d. Note that the relative size of this bulge with respect to deflections of the compliant surface in the regions R = 0 to 1 increases with decreasing values of S_c. This was best illustrated in figure 3.7 of section 3.4.4 for an elastomer layer of infinite radial extent subject to a uniform pressure G_c of radius r_n. For comparison $S_c = (t_c/r_o).(r_o/r_n)$ and the value of S_c decreases with increasing values of the ratio r_n/r_o (refer to figure 3.7).

Similar reasoning for S_c may be applied to non - dimensional shear modulus S_o and Poisson's ratio ν_c. Note however the elastomer layer compliance increases with reducing values of both S_o and ν_c. For S_o the elastomer layer stiffness i.e. shear modulus G_c is proportional to S_o for p_a = constant. As ν_c approaches 0.5 the elastomer layer stiffness increases. This is because axial depression of the compliant surface causes increasing radial displacements within the elastomer layer which are restrained by the bond between the elastomer layer and its rigid backing. Bearing performance curves for S_o and ν_c are shown in figures 5.59 to 5.66. Film pressure profile and bearing clearance geometries for different values ν_c are shown in figure 5.67. Note how deflections of the compliant surface decrease as ν_c approaches 0.5 but bulging at R = 1 reduces the bearing clearance h_d at this position. This

helps reduce the mass flow rate M as shown in figure 5.64.

The results in figures 5.63 to 5.65 clearly show that the bearing performance is sensitive to ν_c as its value approaches 0.5. This can be recognized from the spacing between curves for ν_c = 0.49 and 0.5, which is greater than the spacing between curves for ν_c = 0.45 and 0.49. The importance of accurate measurement of ν_c as described in section 4.4.2 is therefore verified. In performance curves for S_c = 0 and S_o = ∞ it may have been noticed that bearing touchdown at r = 0 is indicated and this occurs at a value of $\Lambda_c^{-1/3}$ greater than zero. For example in figure 5.52 bearing touchdown occurs at an approximate value of $\Lambda_c^{-1/3}$ = 0.15 when S_c = 0. This arises due to deflections of the porous pad in bending which reduce the bearing clearance at r = 0 (see figure 5.56 for S_c = 0). Premature bearing touchdown therefore occurs when the porous pad makes contact with the opposite bearing surface. In both cases when S_c = 0 or S_o = ∞ the compliant surface is rigid and its deflections are zero. It should be noted however that this bearing touchdown is a theoretically predicted value and does not take into account roughness of the bearing surfaces which will in practice cause bearing touchdown at higher values of $\Lambda_c^{-1/3}$.

The experimental results for bearing performance in figures 5.27 to 5.29 for different elastomer layer thicknesses t_c have a similar trend to those for S_c. This is because the porous pad radius r_b is constant, t_c is

directly proportional to S_c . The elastomer layer compliance therefore increases with values of t_c .

Experimental results for rubber hardness (I.R.H.D.) are shown in figures 5.30 to 5.32. In table 5.5 for elastomer layer a, f, and g the shear modulus G_c increases with rubber hardness while Poisson's ratio ν_c reduces slightly. Because of the small reduction in value of ν_c which on its own would increase the compliance of the elastomer layer, the overall result is a reduction in compliance with increasing rubber hardness, due to the increase in G_c . The porous and compliant aerostatic bearing performance therefore increases with rubber hardness, as shown in figures 5.30 and 5.31.

(b) The effect of elastomer layer radial extent R_c and radius r_c.

Because the porous pad radius r_b is kept constant during bearing tests then the elastomer layer radius r_c is directly proportional to its non - dimensional radial extent R_c . Both therefore have a similar effect on the bearing performance.

R_c relates to the radial extent of the elastomer layer in relation to the porous pad. When $R_c = 1$, $r_c = r_b$ and when $R_c = \infty$, $r_c >> r_b$. These two values of R_c represent the lower and upper limits repectively for the elastomer layer radius. The expression "finite elastomer layer" means any elastomer layer whose radial extent is; $1 <= R_c < \infty$. Similarly an infinite elastomer layer has a radial extent

$R_c = \infty$.

Bearing performance results for various values of R_c are shown in figures 5.68 to 5.71. Film pressure profiles and bearing clearance geometries are shown in figure 5.72. With the exception of the curve for $R_c = \infty$, the bearing performance of load capacity and flow rate improve with increasing values of R_c. For $R_c = \infty$ there is a slight reduction in load capacity W and a corresponding increase in flow rate M at lower values of $\Lambda_c^{-1/3}$ in the region 0 to 0.5.

In figure 5.72 for $\Lambda_c^{-1/3} = 0.2$ there is a reduction in magnitude of compliant surface deflections from $R_c = 1$ to 1.05 giving rise to an increase in bearing performance for the same reasons as described in section 5.4.4 i.e. a reduction in elastomer layer compliance. Note that very little bulging of the elastomer layer occurs at R = 1 giving rise to a large bearing clearance here. The reason for this is because the rubber expands more freely in a radial direction at $r = r_b$ due to the limited radial extention of the elastomer layer beyond r_b. When the value of R_c reaches 1.2, significant bulging of the compliant surface occurs at R = 1. This reduces the bearing clearance here and results in improved bearing performance.

The difference in bearing performance between $R_c = 1.2$ and $R_c = \infty$ is relatively small and the bearing can be assumed to behave as though it has an elastomer layer of infinite extent when R_c is greater than 1.2.

From the theoretical results shown in figures 5.68 to 5.70 and for values of R_c = 1 and 1.05 the bearing number $\Lambda_c^{-1/3}$ and hence the bearing approach c can have a -ve value. This occurs because deflections of the compliant surface are greater than the bearing clearance and results in a low bearing stiffness as shown in figure 5.70. Note of course that in figure 5.71 the bearing number $\Lambda_d^{-1/3}$ based on bearing clearance h_d never falls below zero.

Experimental results for various elastomer layer radii r_c are shown in figures 5.33 to 5.35. Results for bearing 3e with an elastomer layer radius of 52.5mm giving a value of R_c = 1.03, do not extend down to negative values of bearing number $\Lambda_c^{-1/3}$ due to the onset of pneumatic instability at $\Lambda_c^{-1/3}$ = 0.24. Table 5.8 shows that this has occurred in several of the bearing tests. However it is not clear as to the exact causes of pneumatic instability since for example in bearing test 1 for bearing 3a which has an elastomer layer thickness of 9.678mm (see table 5.7), pneumatic instability does not occur, even though a large recess is formed in the bearing film clearance due to the greater compliant surface deflections. Note that pneumatic instability does however occur in bearing test 2 for bearing 3b which has an elastomer layer thickness of 6.74mm. It is possible therefore that unstable vibrations of the bearing surfaces are damped down by the elastomer layer. This damping may be a function of the elastomer layer thickness and other properties such as hardness.

(c) Non - dimensional ratio K_h

The effect of this constant on the bearing performance is shown in figures 5.73 to 5.76. This parameter was introduced in section 3.7.2 to account for changes in the bearing clearance geometry while the bearing number $\Lambda_c^{-1/3}$ is constant. As the value of K_h decreases at constant $\Lambda_c^{-1/3}$, the bearing approach c increases so that the relative magnitude of deflections of the compliant surface and porous pad reduce with respect to the bearing film clearance. Figure 5.77 shows film pressure profiles and bearing clearance geometries for various values of K_h. As the value of K_h decreases the bearing clearance geometry approaches a value of $h_r/c = 1$ for a uniform bearing clearance. The effect of reducing K_h is to reduce the recess formed in the bearing clearance by deflections of the compliant surface. This is similar to a reduction in compliance of the elastomer layer giving rise to an increase in the bearing performance i.e. increasing load capacity W and reducing flow rate M. For comparison a theoretical curve for a porous aerostatic thrust bearing with a uniform bearing clearance is included in figures 5.73 to 5.76. This represents the limit of porous and compliant aerostatic thrust bearing performance where $K_h = 0$. Note that the value of K_h which equals the ratio of r_b^2 / Φ_r decreases with increasing porous pad permeability and increases with increasing porous pad radius r_b.

(d) Supply pressure P_s

Theoretical performance curves for non - dimensional supply pressure are shown in figures 5.78 to 5.81. Experimental results for bearing 3a (see table 5.7) and bearing 3 are shown in figures 5.36 to 5.38 and 5.40 to 5.41 respectively. It is interesting to note that for bearing 3a which is a porous and compliant aerostatic thrust bearing, there is an increase in load capacity W with supply pressure P_s at higher values of $\Lambda_c^{-1/3}$ in figure 5.36, while the reverse occurs at lower values of $\Lambda_c^{-1/3}$. Note that for a porous aerostatic thrust bearing i.e. bearing 3 in figure 5.40 the load capacity W increases with P_s over the full range of $\Lambda_c^{-1/3}$ values.

It appears therefore that increases in the supply pressure P_s causes increases in deflections of the compliant surface resulting in a reduction in load capacity W at lower bearing numbers $\Lambda_c^{-1/3}$ .Since the bearing film pressures increase with P_s the elastomer layer can be said to behave as though it is more compliant at higher bearing supply pressure P_s . Note that the bearing film pressures also increase with reducing bearing number $\Lambda_c^{-1/3}$. Therefore the effective compliance of the elastomer layer is lower at higher values of $\Lambda_c^{-1/3}$. This is why the load capacity W increases with P_s at higher values of $\Lambda_c^{-1/3}$.

It is further interesting to note that in figure 5.37 for porous and compliant aerostatic thrust bearing 3a the flow rate M increases with increasing supply pressure P_s ,

while for porous aerostatic thrust bearing 3 the theoretically predicted flow rate M has remained constant for changes in supply pressure P_s as shown in figure 5.41.

(e) The effect of magnitude constant M_b and shape constant N_b for the porous pad rigidity.

The magnitude constant M_b represents the magnitude of non - dimensional deflections of the porous pad $\bar{u}_b$ in bending. Its value is affected by the material properties of the porous pad and also the stiffness in bending of the porous pad bond. In practice therefore M_b may change with the shape constant N_b since both relate to the stiffness of the porous pad bond. However the value of M_b is unaffected by the porous pad thickness h_b and radius r_b as explained in section 4.3.6.

Theoretical performance curves for various values of M_b are shown in figures 5.82 to 5.85. In complete contradiction to the results presented by Taylor and Lewis (25) for a porous aerostatic thrust bearing with an elastic porous pad, the performance of a porous and compliant aerostatic thrust bearing improves with reducing porous pad rigidity. Increasing values of M_b represent a reduction in the porous pad rigidity. Figures 5.82 and 5.83 show increases in the load capacity W and decreases in the flow rate M with increasing values of M_b. The reasons for this are explained as follows; in section 5.4.4 it was described how the recess in the bearing clearance was formed by deflections of the compliant surface and this had the

adverse effect on the bearing performance due to the restricting effect of flow through the porous pad. Deflections of the porous pad have the reverse effect to deflections of the compliant surface in that the recess formed in the bearing clearance is reduced (see figure 5.58). The result is a recovery in the bearing performance of load capacity W and flow rate M with increasing values of M_b as shown in figures 5.82 and 5.83. Note that for $M_b = 25\times10^{-7}$ the performance of a porous and compliant aerostatic thrust bearing is better than that of a porous aerostatic thrust bearing with a uniform bearing clearance (refer to figures 5.82 and 5.83). This suggests that a porous and compliant aerostatic thrust bearing with a flexible i.e. plastic porous pad could result in improved bearing performance.

Film pressure profile and bearing clearance geometries for various values of M_b are shown in figures 5.86 and 5.87 for $\Lambda_d^{-1/3}$ = constant, and $\Lambda_c^{-1/3}$ = constant, respectively. In figure 5.86 it is clearly shown that the recess formed by deflections of the compliant surface is progressively reduced with increasing values of M_b (note that when M_b = 0.0 the deflections of the porous pad are zero).

In figure 5.87 the larger bearing clearance at higher values of M_b may be attributed to the increase in film pressures also shown in this figure.

The shape constant N_b represents the shape of the resulting deflections of the porous pad. Theoretically the

minimum value of N_b is 0.25 for a rigidly clamped porous pad (see section 5.2.3). For a simply supported porous pad the value of N_b depends on Poisson's ratio ν_b for the porous pad material. As shown in section 5.2.3 when $\nu_b = 0$, $N_b = 0.45$ and similarly when $\nu_b = 0.5$, $N_b = 0.432$.

Bearing performance curves for various values of N_b are shown in figures 5.88 to 5.91. A curve is included for $N_b = 0.6$ which is slightly greater than the values for porous pads 1 to 5 in table 5.2 (for an explanation why $N_b > 0.45$ for these porous pads, see section 5.2.3). It can be seen from figures 5.88 and 5.89 that the bearing performance of load capacity W and flow rate M improves with increasing values of N_b. This suggests that a porous pad with a flexible support is more advantageous than a rigidly supported pad in the porous and compliant aerostatic thrust bearing. However because N_b relates only to the shape of deflection profiles of the porous pad and not their magnitude at $r = 0$, the changes in bearing performance with N_b are small in comparison with those that may be brought about by a change in magnitude constant M_b as shown in figures 5.82 and 5.83.

(f) The effect of porous pad thickness h_b and aspect ratio S_b.

Experimental results for various porous pad thicknesses h_b are shown in figures 5.42 to 5.44 for a porous and compliant aerostatic thrust bearing and in figures 5.45 and 5.46 for a porous aerostatic thrust

bearing. Theoretical performance curves for various values of S_b are presented in figures 5.92 to 5.95 for a porous and compliant aerostatic thrust bearing.

For the experimental results the porous pad radius r_b is kept constant and therefore its thickness h_b is directly proportional to S_b. As the porous pad thickness h_b and hence S_b reduce, this has two effects. The first is a reduction in the restriction to flow through the porous pad which results in higher bearing film pressures for a given supply pressure p_s. The second is a reduction in the porous pad rigidity in bending which, depending on the pressure difference across the porous pad, will increase its deflection.

Consider the experimental results for the porous aerostatic thrust bearing in figures 5.45 and 5.46 (note that the porous pad is elastic and deflects in bending). The bearing performance of load capacity W and flow rate M improves with decreasing porous pad thickness h_b. Taylor and Lewis (25) describe that the bearing performance continues to improve as the porous pad thickness h_b reduces, down to an optimum value. However from the spacing of curves in figure 5.45 and 5.46, this does not appear to be the case, i.e. the spacing increases with reducing porous pad thickness h_b. It is possible that the reason for this is that Taylor and Lewis (25) use the bearing clearance at r = 0 to present their bearing performance results while the author uses the bearing clearance h_d (= c

in a porous aerostatic thrust bearing) at $r = r_b$. Therefore for a given bearing number $\Lambda_d^{-1/3}$ ($= \Lambda_c^{-1/3}$ for a porous aerostatic thrust bearing) the mean bearing clearance from $r = 0$ to r_b is reduced by deflections of the porous pad, instead of increased as in (25). A comparison of theoretically predicted results with (25) for the performance of a porous aerostatic thrust bearing with an elastic porous pad was not possible because values of supply pressure P_s were not included with the results. There is also an error in equation (20) of reference (25) where $e^{-\alpha\Delta r/B_1}$ should be written $e^{B_1\Delta r/\alpha}$.

Both experimental and theoretical results in figures 5.42 to 5.44 and 5.92 to 5.95 respectively for a porous and compliant aerostatic thrust bearing also show improvements in bearing performance of load capacity W and flow rate M with reducing porous pad thickness h_b and aspect ratio S_b.

As described in part (e) of this section, increasing deflections of the porous pad in bending can result in a recovery of bearing performance because these reduce the recess formed in the bearing clearance by the compliant surface deflections. The deflections of the porous pad are proportional to the pressure drop across its thickness. For a given supply pressure P_s this pressure drop is approximately proportional to the porous pad thickness h_b. However the porous pad rigidity in bending reduces in proportion to $1/h_b^3$, i.e. for a given value of the constant M_b, deflections of the porous pad u_b are proportional to $1/h_b^3$.

The net overall effect is that deflections of the porous pad increase in proportion to $1/h_b^2$. From this argument therefore the bearing performance will continue to improve for reducing porous pad thicknesses down to zero. However when deflections of the porous pad are greater than the recess formed in the bearing clearance by deflections of the compliant surface, premature bearing touchdown can occur at $r = 0$ as shown in figures 5.92 to 5.95 for $S_b = 0.2$. Under these conditions the minimum bearing clearance h_d at $r = r_b$ for which the bearing can operate is limited and its potential performance reduced.

Deflections of the stainless steel porous pads 1 to 5 used in bearing tests were comparatively small and were never greater than 10 μm (refer to section 5.2.3 and figures 5.12 and 5.13). Also the theoretically predicted deflections of the compliant surface for all bearing tests never reduced below 30 μm for the range of bearing numbers $\Lambda_c^{-1/3}$ used in these tests. It is unlikely therefore that bearing touchdown at $r = 0$ instead of $r = r_b$, occurred in any of the bearing tests. However if a less rigid material such as porous plastic was used for the pad, then improvements in the bearing performance could result provided bearing touchdown at $r = 0$ does not occur before $r = r_b$. In such cases, for optimum porous and compliant aerostatic thrust bearing performance it will be necessary to carefully select properties and thicknesses of both the elastomer layer and the porous plastic pad. Use of porous

plastics in these bearings would make an interesting future research project.

(f) The effect of porous pad permeability ratio K_v

Theoretical bearing performance curves for various values of K_v are shown in figures 5.96 to 5.99. The value of K_v has only a small effect on the bearing load capacity as shown in figure 5.96. However as shown in figure 5.97 large variations in flow rate M occur with changes in the value of K_v. Since K_v is equal to the ratio of porous pad permeability Φ_r in the radial direction to the permeability Φ_z in the axial direction, the proportion of radial flow within the porous pad increases with increasing values of K_v. As shown in figure 5.97, for a constant bearing number $\Lambda_c^{-1/3}$, the mass flow rate M increases with K_v and hence increasing proportion of radial flow in the porous pad.

For the determination of K_v it would be necessary to measure both permeabilties Φ_r and Φ_z for the porous pad. The measurement of porous pad permeability as described in section 4.3.5 gives a value of Φ_z since the pad is pressurized across its thickness and flow through it is predominantly axial. However it is more difficult to produce predominantly radial flow within the porous pad for the measurement of Φ_r and no literature has been found describing a method by which this can be done. Therefore the measurement of Φ_r has not been attempted and only one value of permeability Φ is specified for each porous pad in table 5.2. For comparison of theoretical predictions

with experimental results it is assumed that $\Phi_r = \Phi_z = \Phi$, i.e. $K_v = 1$.

(h) The effect of porous pad manufacturers grading

As described in section 5.4.1 both the porous pad permeability Φ and magnitude constant M_b depend on the porosity and structure of the porous pad material. The manufacturer's (Schumacher filters Ltd. U.K.) grade their porous pads according to their permeability properties so that the resulting porosity of the porous material is not necessarily consistant with this grading. Experimental results shown in figures 5.47 to 5.51 are therefore presented for different grade porous pads rather than porosity. Of these results figures 5.47 to 5.49 are for a porous and compliant aerostatic thrust bearing and figures 5.50 to 5.51 for a porous aerostatic thrust bearing with an elastic porous pad.

In tables 5.1 and 5.2 it can be seen that for the pads 1, 4 and 5 permeability Φ and magnitude constant M_b increase with increasing manufacturer's grading, i.e. SIKA R1 to R5. Note however for porous pads 1, 2 and 3 of similar manufacturer's grading (SIKA R1, see table 5.1) there is a 54% and 10% variation of Φ and M_b respectively in table 5.2. Therefore the manufacturer's grading is only approximately representative of the porous pad properties of Φ and M_b.

The experimental results for the porous and compliant aerostatic thrust bearing in figures 5.47 to 5.49 show a

small increase in load capacity W and a reduction in flow rate M with increasing porous pad grade. This may be attributed to a reduction in the value of the non - dimensional ratio K_h (relating to the bearing clearance geometry) due to increasing porous pad permeability Φ with grading. Also the magnitude constant M_b increases with porous pad grade. Both result in improved bearing performance as described in parts (c) and (e) of this section (see also figures 5.73 to 5.74 for K_h and figures 5.82 to 5.83 for M_b). Similar improvements in bearing performance with porous pad grading occur for the porous aerostatic thrust bearing as shown in figures 5.50 and 5.51.

Although bearing performance may improve with higher grade porous pads there are two factors to consider. With increasing porous pad permeability Φ pneumatic instability may occur particularly for a porous and compliant aerostatic thrust bearing (see section 4.3.2 for the porous pad selection). Also especially for a porous aerostatic thrust bearing with an elastic porous pad, increases in the magnitude function M_b may restrict the bearing performance due to premature bearing touchdown at $r = 0$, this being caused by large deflections of the porous pad.

Problems relating to bearing stability is the reason why low grade porous pads were selected for bearing tests as described in section 4.3.2.

This completes the discussion of results in this

chapter. Conclusions from these results are made in chapter 6.

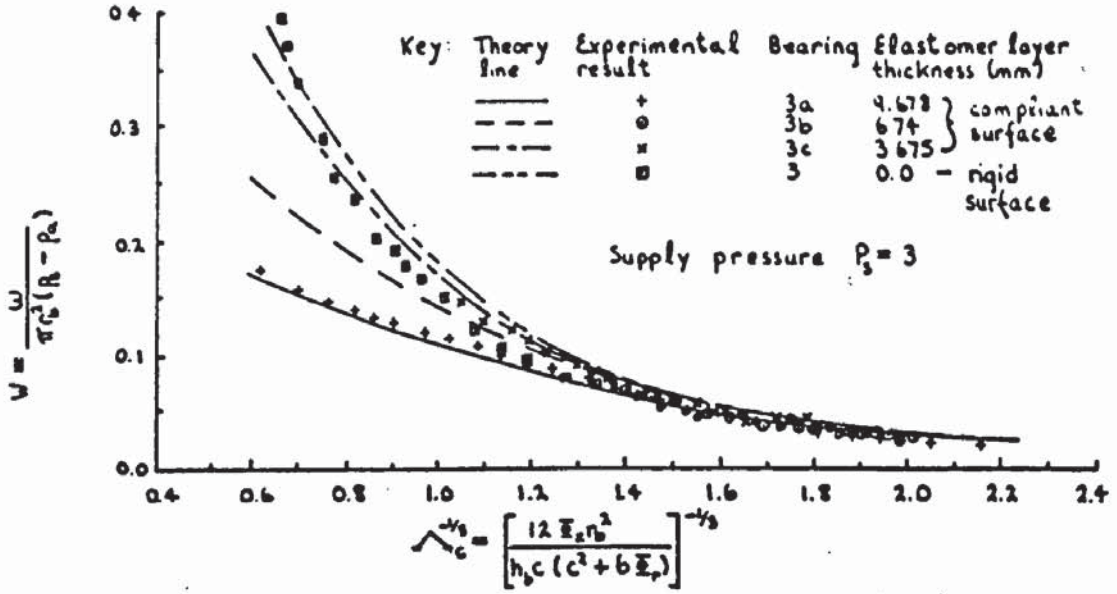

Figure 5.27 Load capacity versus bearing number for bearings of different elastomer layer thickness

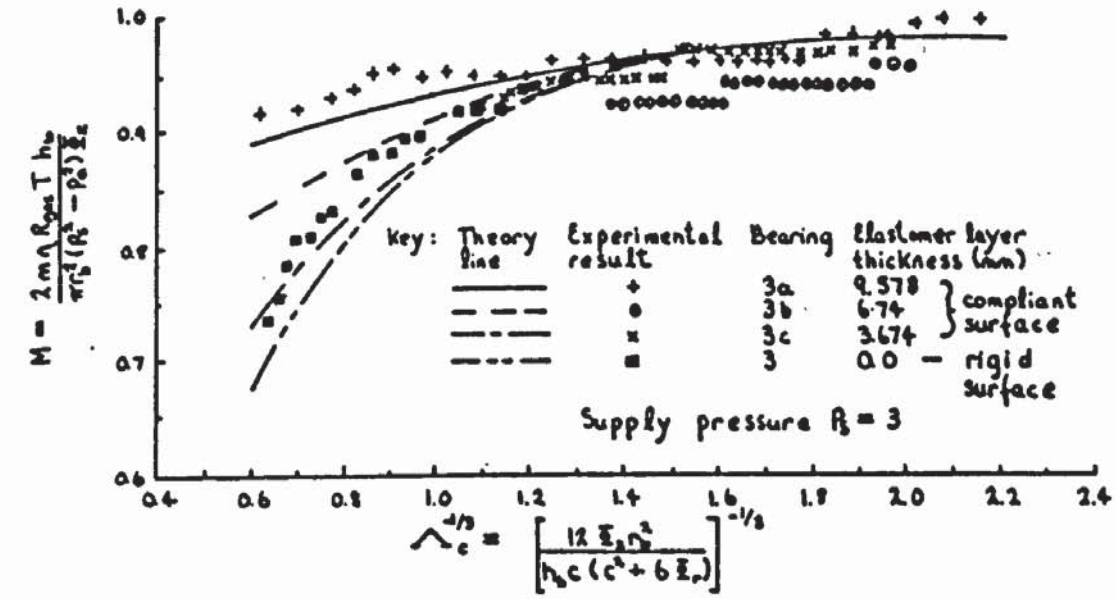

Figure 5.28 Flow rate versus bearing number for bearings of different elastomer layer thickness

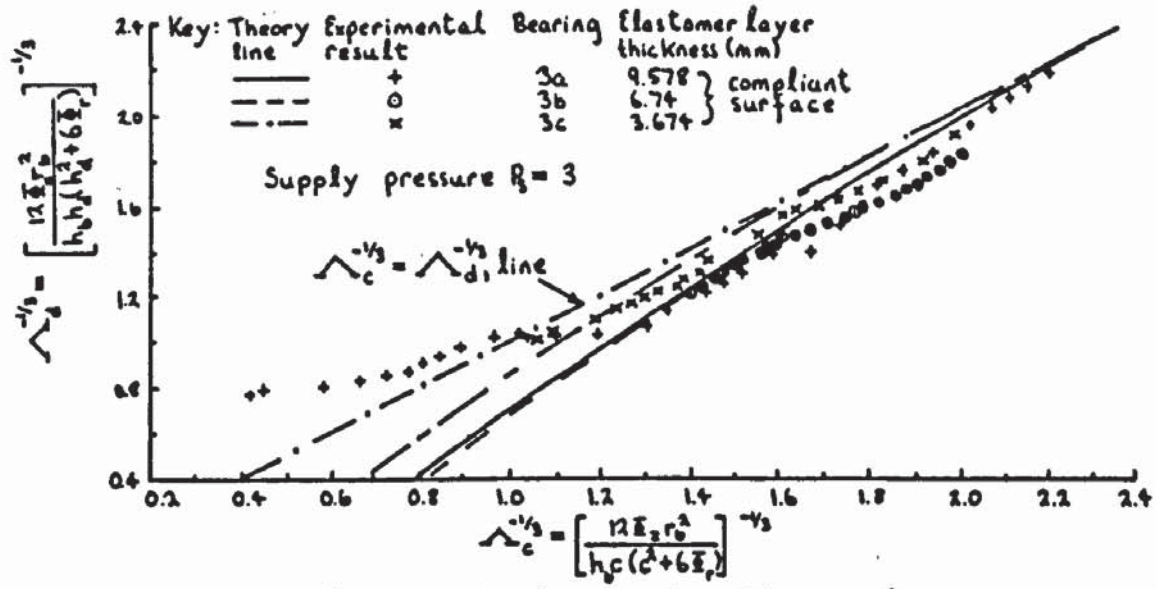

Figure 5.29 Bearing number based on derived bearing clearance versus bearing number based on bearing approach for bearings of different elastomer layer thickness

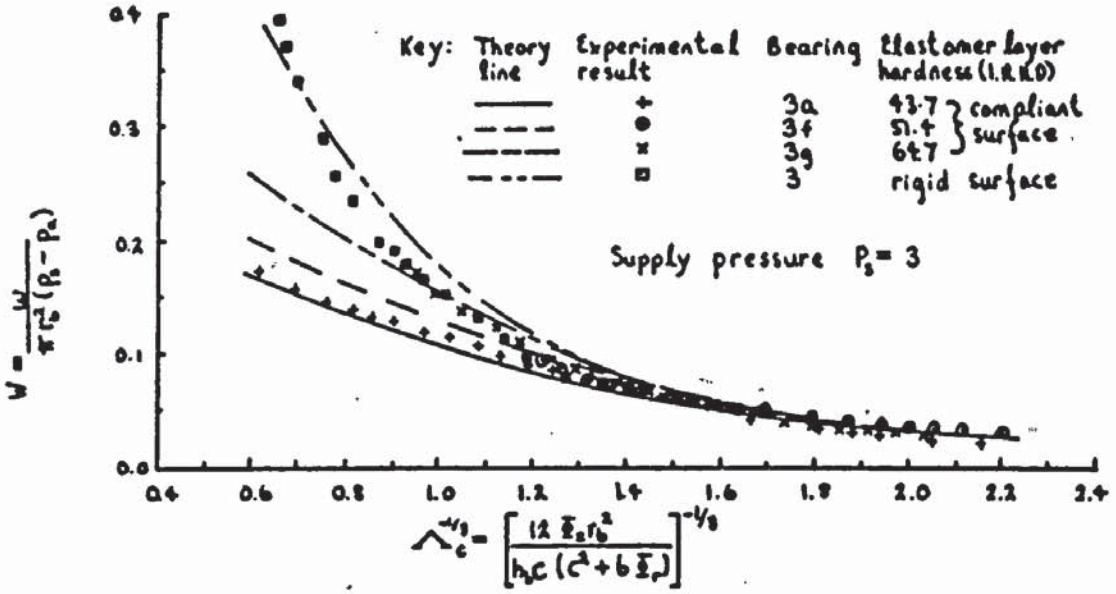

Figure 5.30 Load capacity versus bearing number for bearings of different elastomer layer hardness

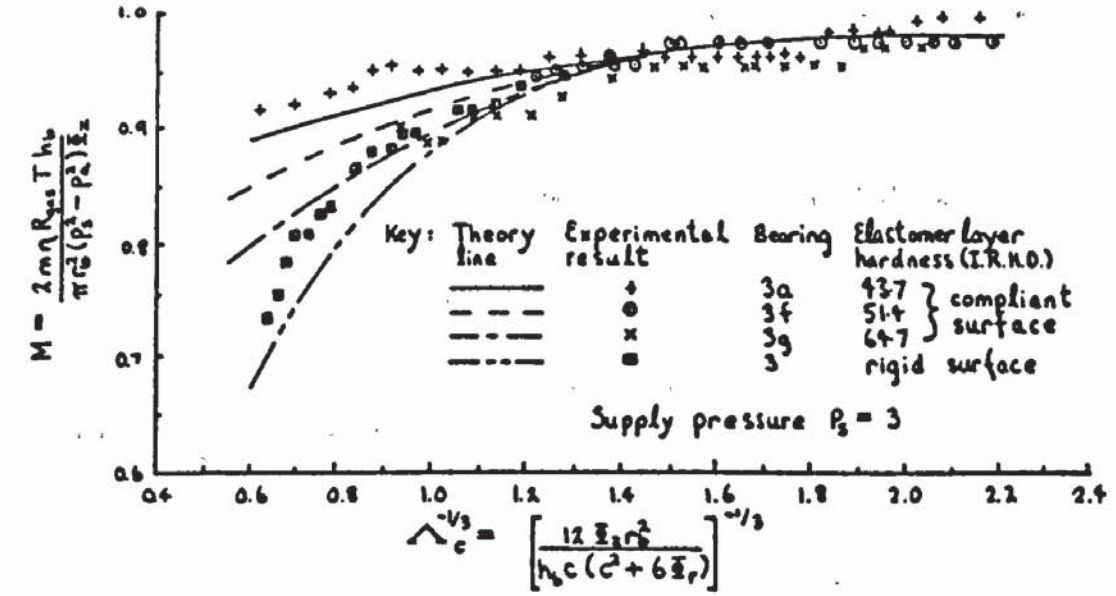

Figure 5.31 Flow rate versus bearing number for bearings of different elastomer layer hardness

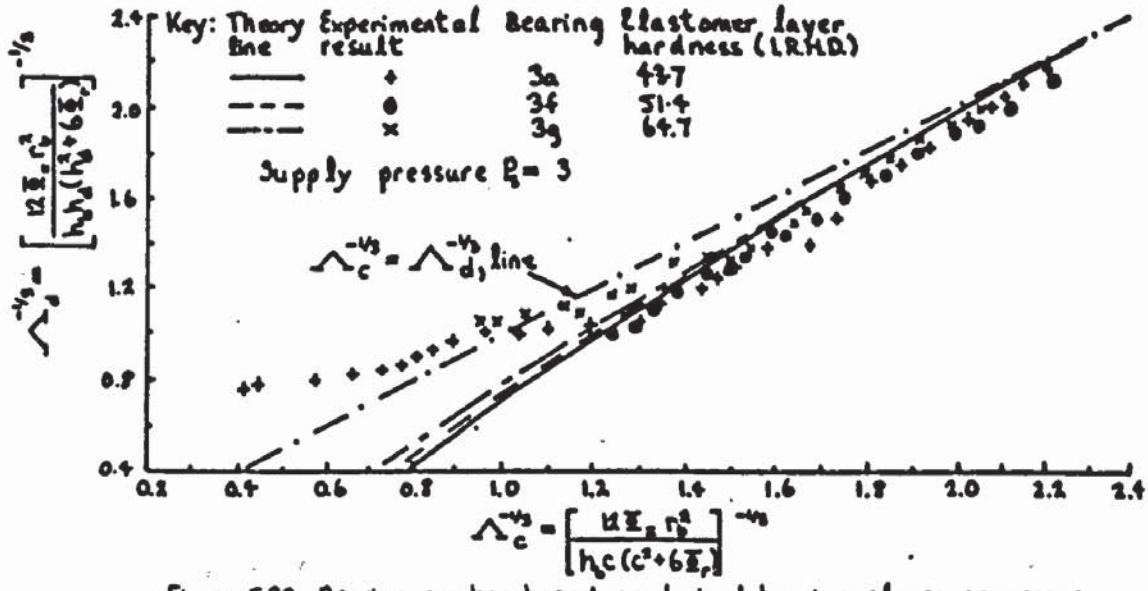

Figure 5.32 Bearing number based on derived bearing clearance versus bearing number based on bearing approach for bearings of different elastomer layer hardness

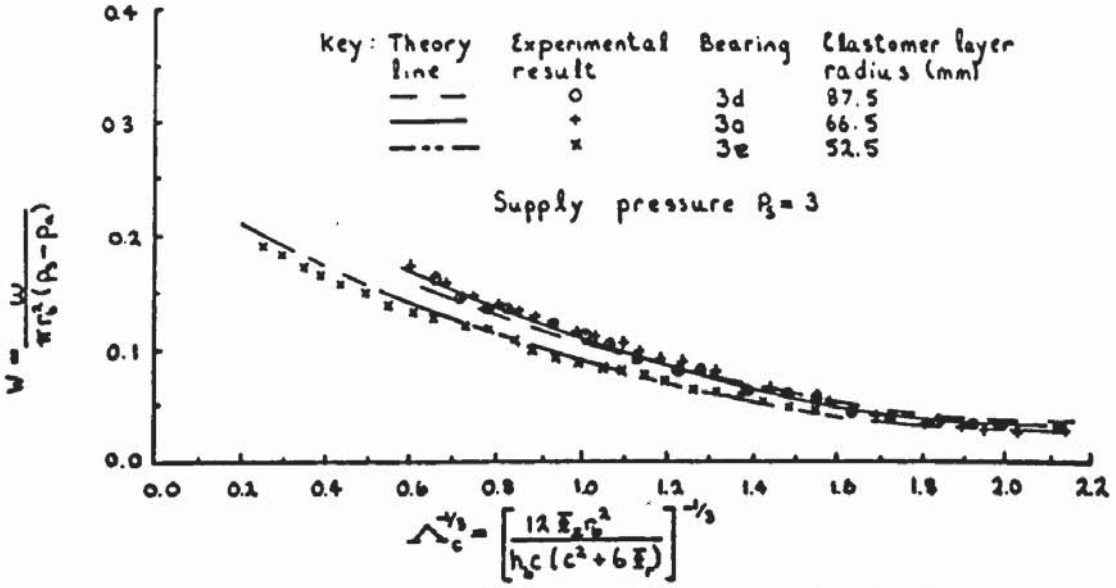

Figure 5.33 Load capacity versus bearing number for bearings of different elastomer layer radius

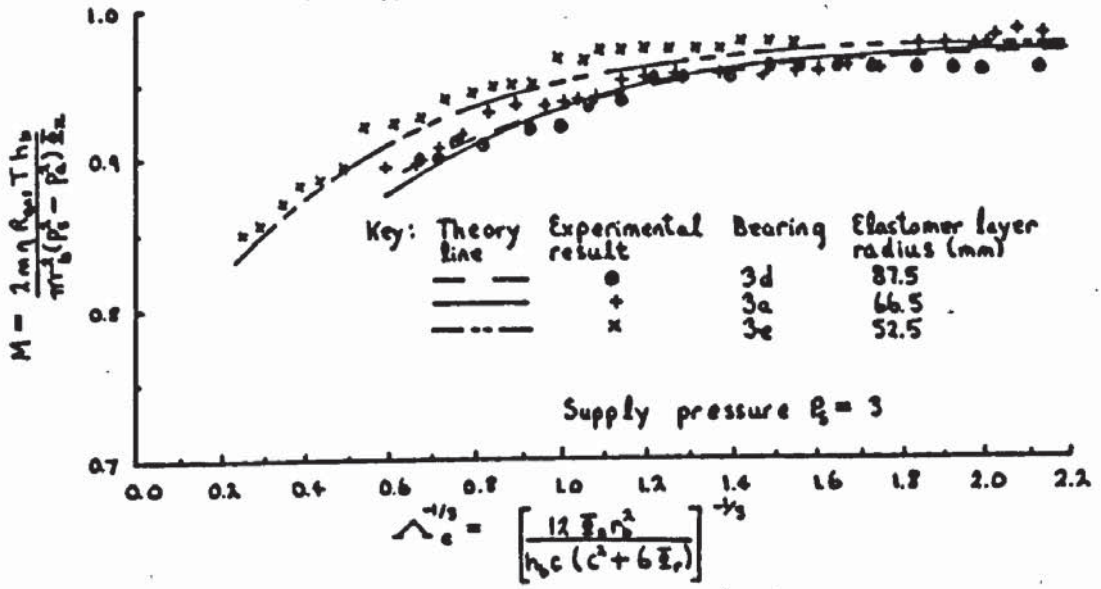

Figure 5.34 Flow rate versus bearing number for bearings of different elastomer layer radius

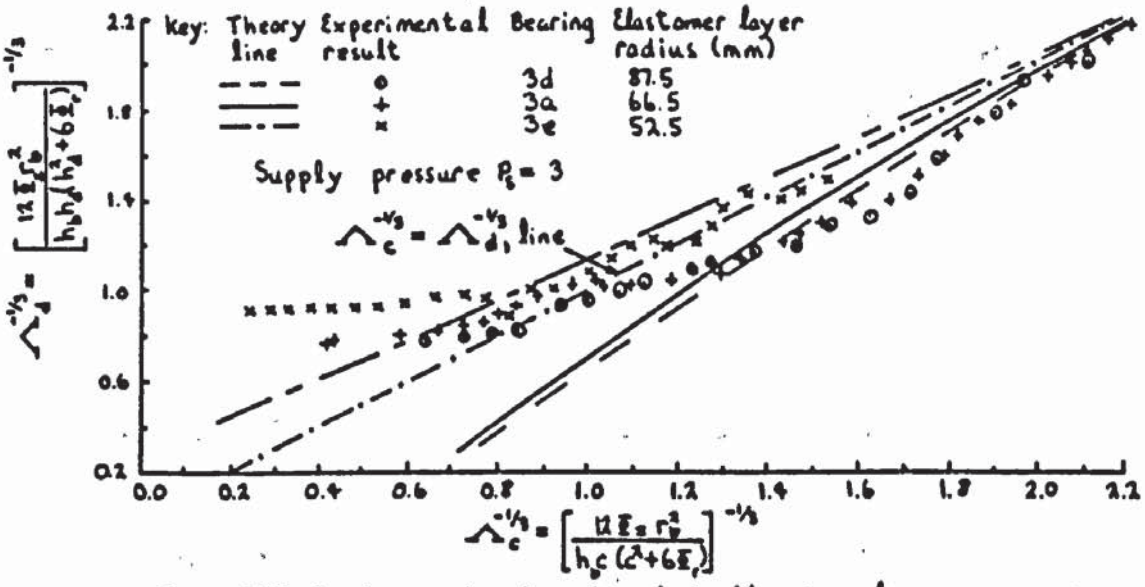

Figure 5.35 Bearing number based on derived bearing clearance versus bearing number based on bearing approach for bearings of different elastomer layer radius

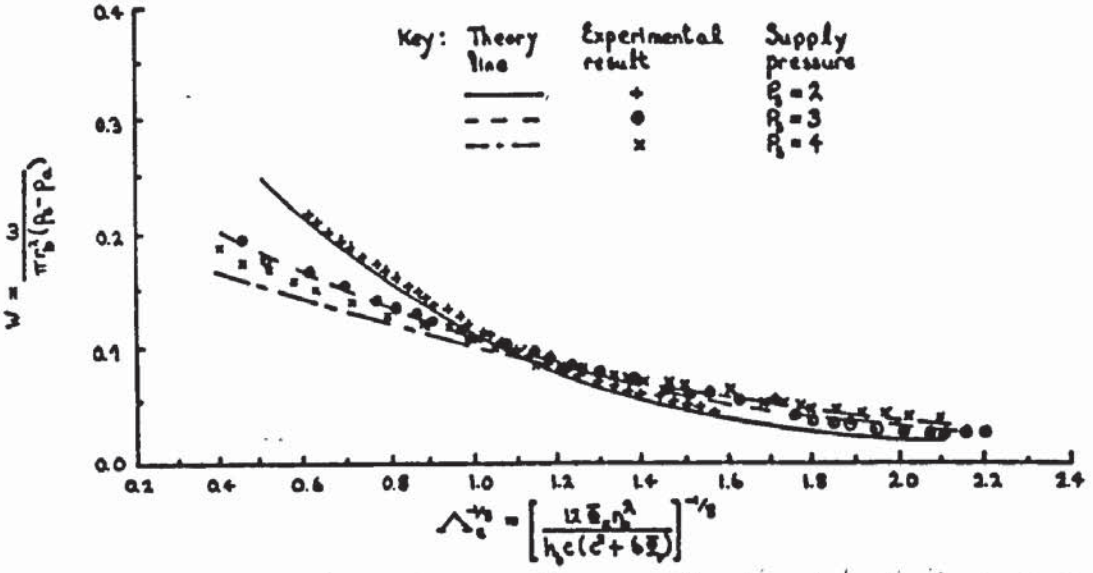

Figure 5.36 Load capacity versus bearing number at various supply pressures for bearing 3a

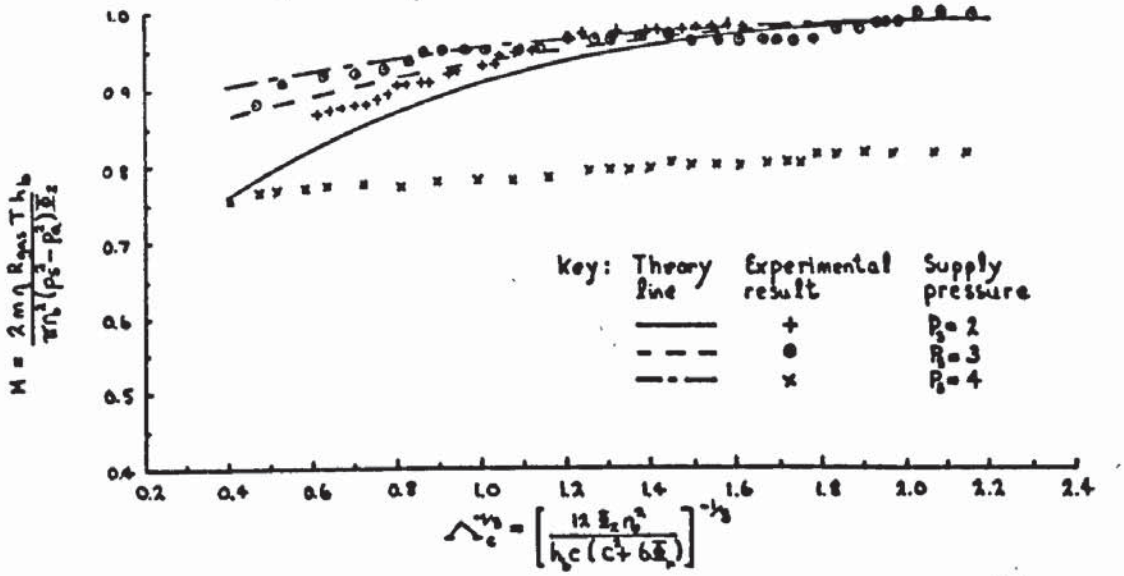

Figure 5.37 Flow rate versus bearing number at various supply pressures for bearing 3a

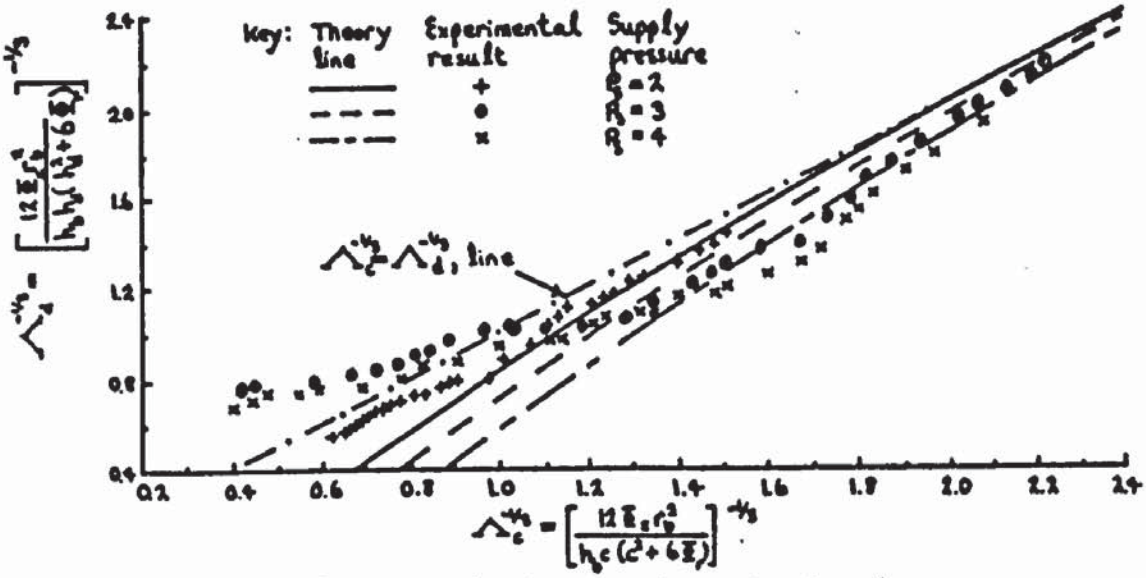

Figure 5.38 Bearing number based on derived bearing clearance versus bearing number based on bearing approach at various supply pressures for bearing 3a

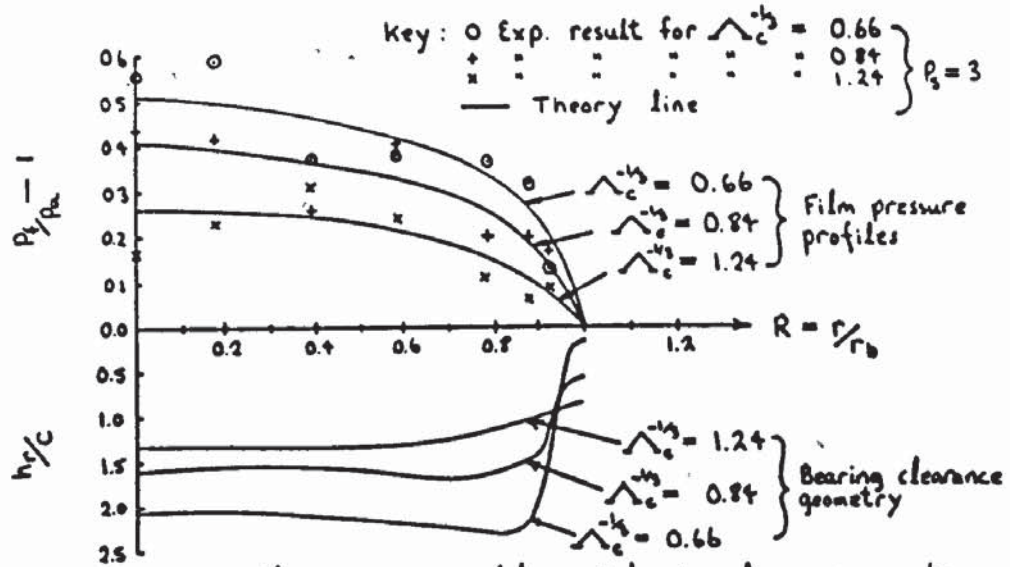

Figure 5.39 Film pressure profiles and bearing clearance geometry for bearing 3a at various bearing numbers

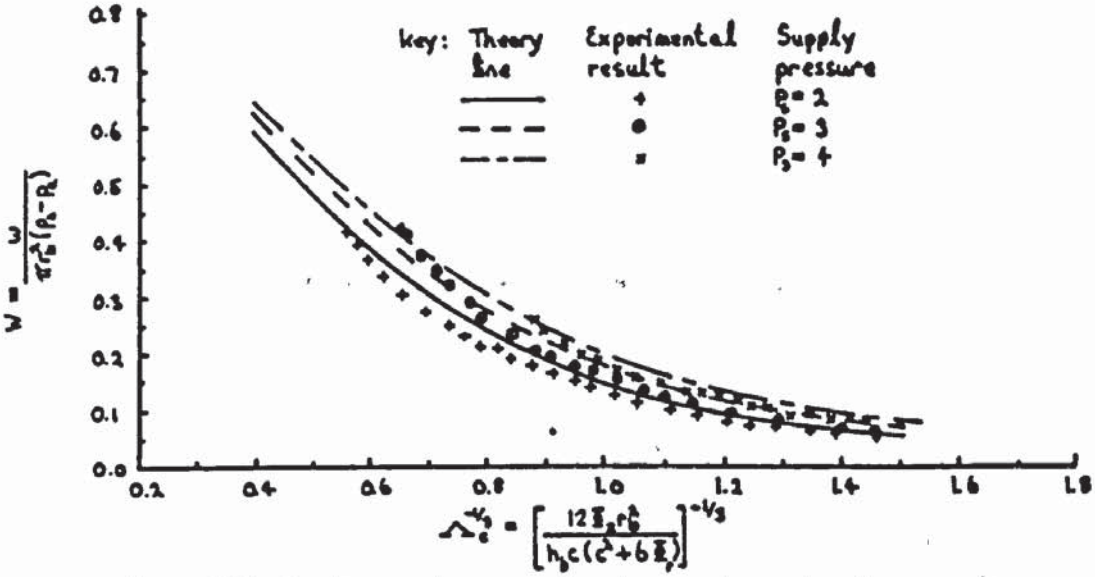

Figure 5.40 Load capacity versus bearing number at various supply pressures for bearing 3

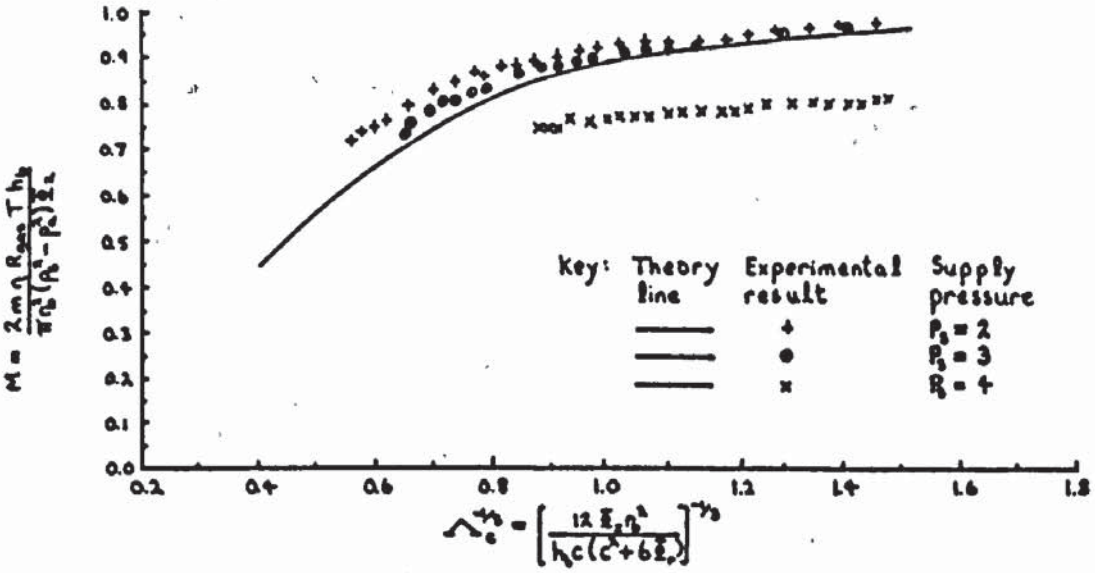

Figure 5.41 Flow rate versus bearing number at various supply pressures for bearing 3

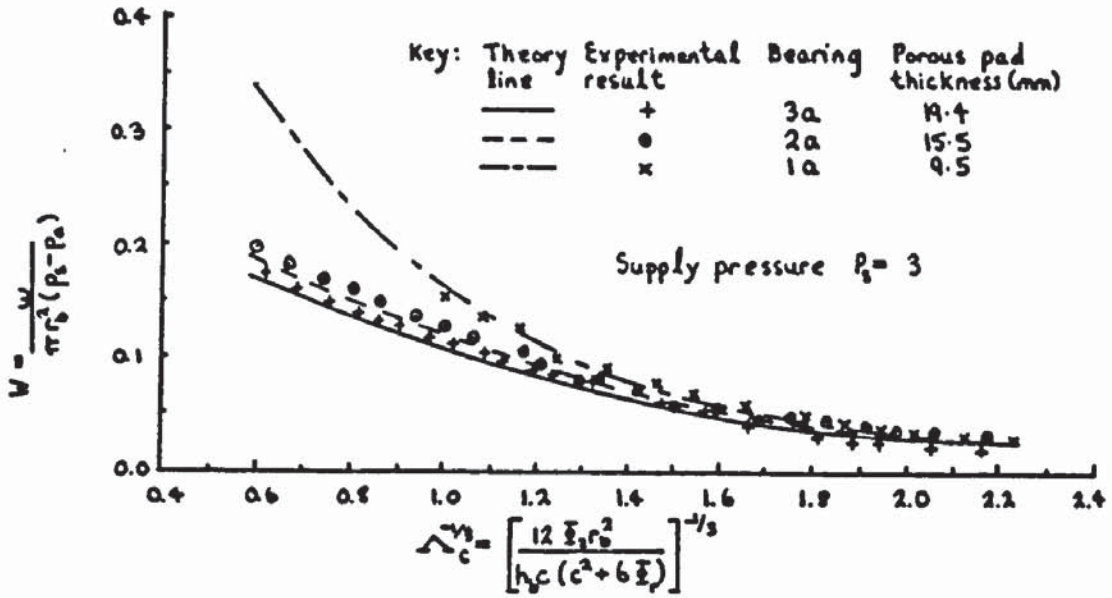

Figure 5.42 Load capacity versus bearing number for bearings of different porous pad thickness

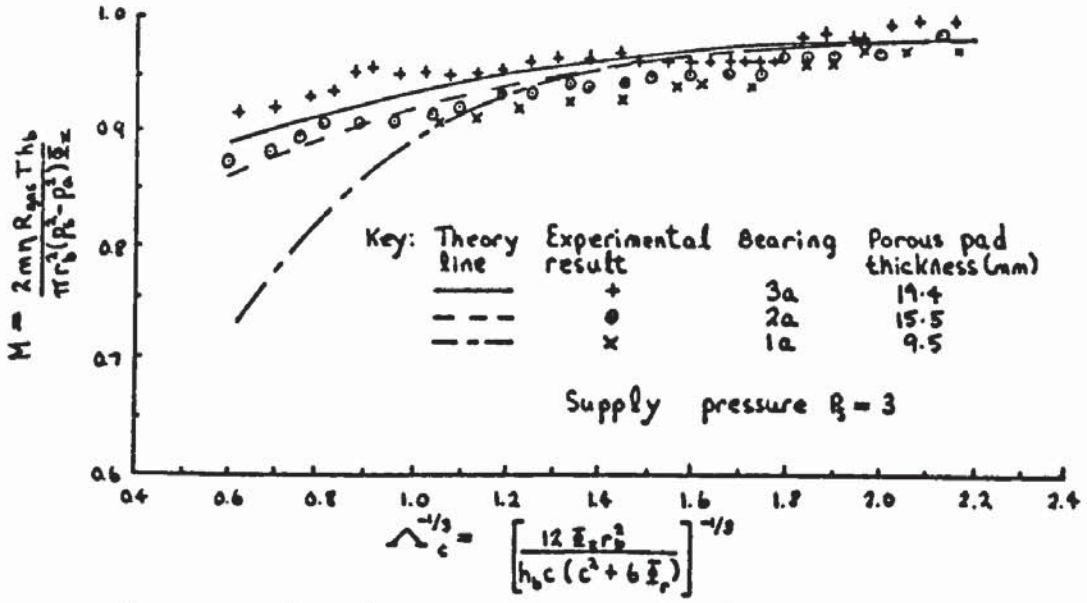

Figure 5.43 Flow rate versus bearing number for bearings of different porous pad thickness

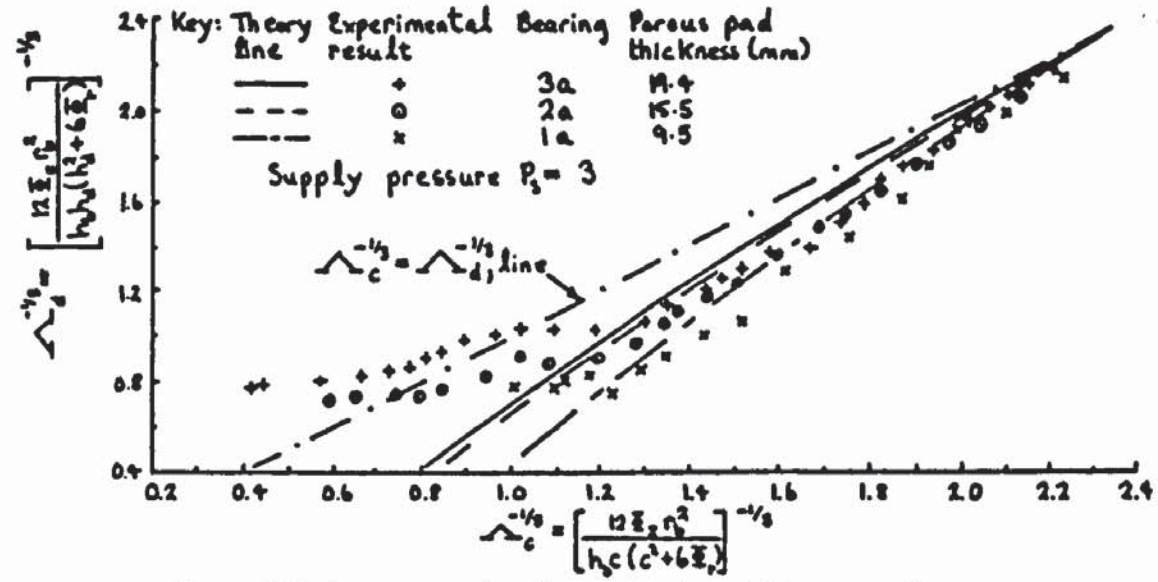

Figure 5.44 Bearing number based on derived bearing clearance versus bearing number based on bearing approach for bearings of different porous pad thickness

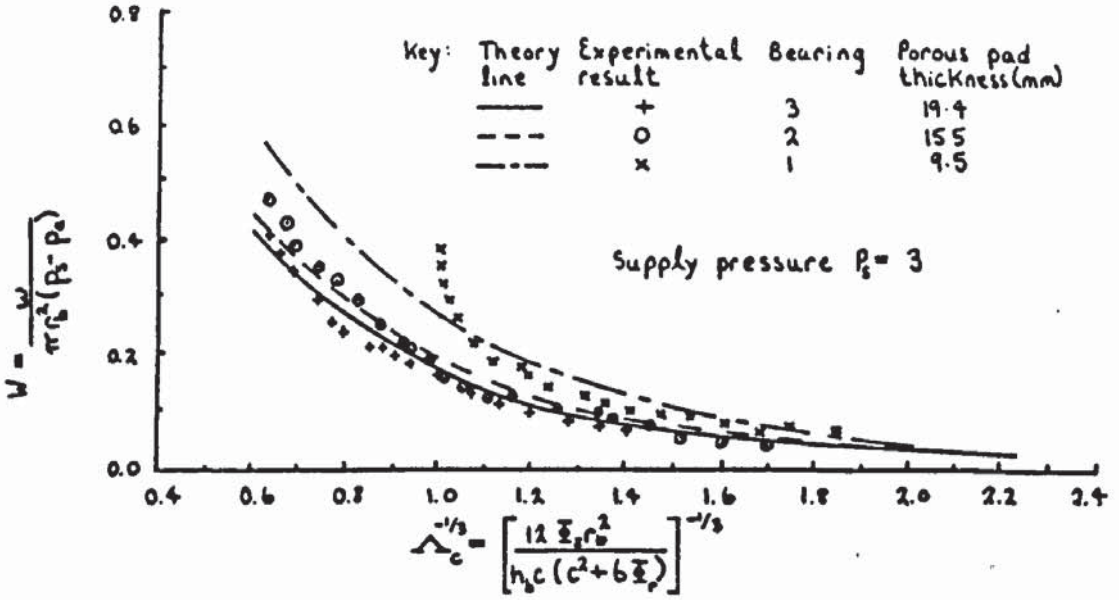

Figure 5.45 Load capacity versus bearing number for bearings of different porous pad thickness

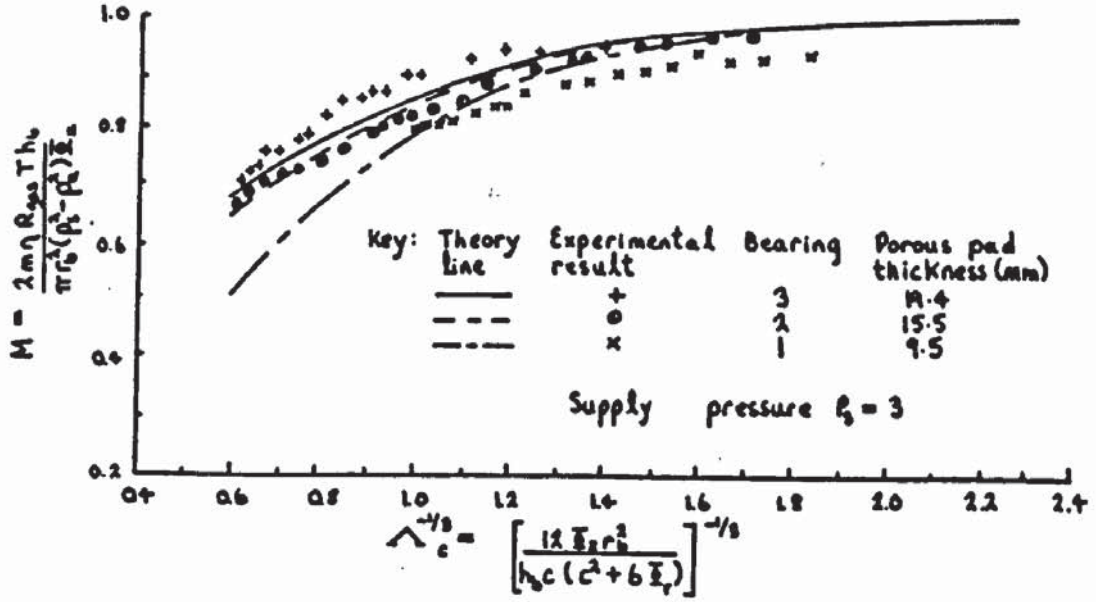

Figure 5.46 Flow rate versus bearing number for bearings of different porous pad thickness

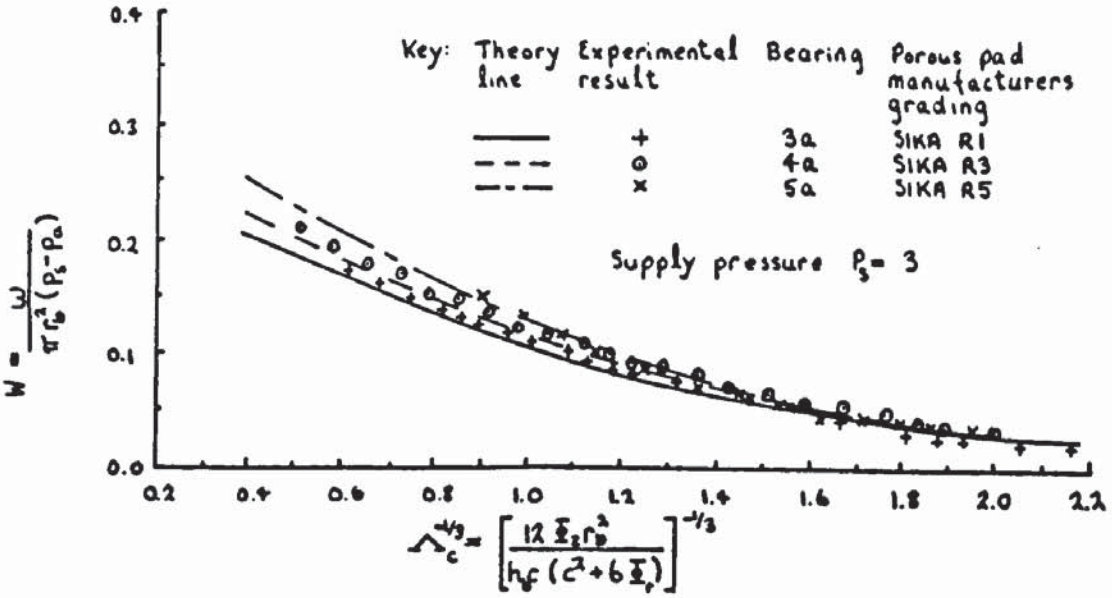

Figure 5.47 Load capacity versus bearing number for bearings with different grade porous pads

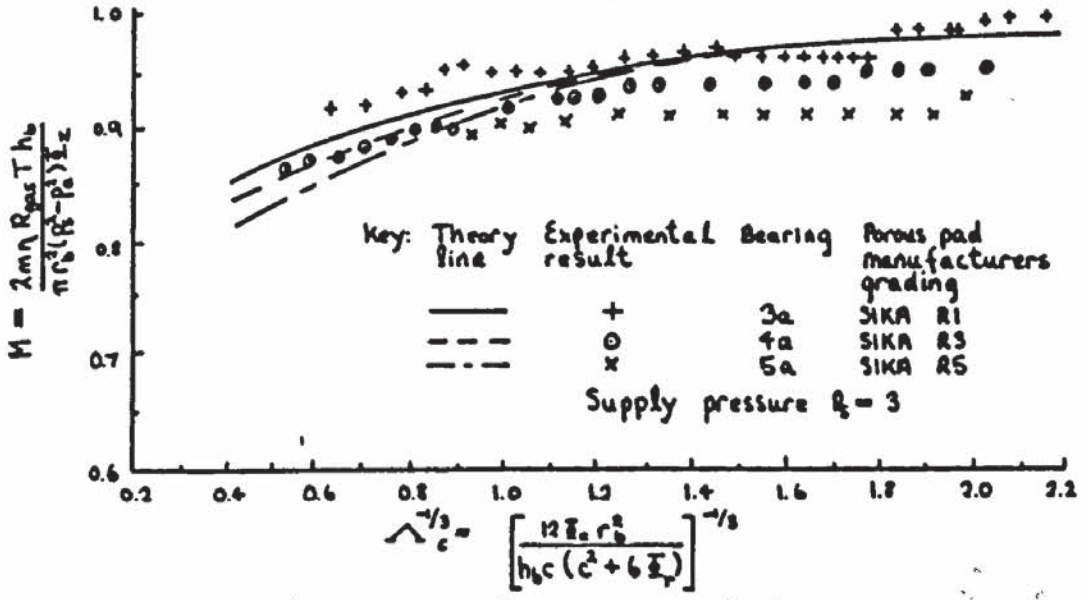

Figure 5.48 Flow rate versus bearing number for bearings with different grade porous pads

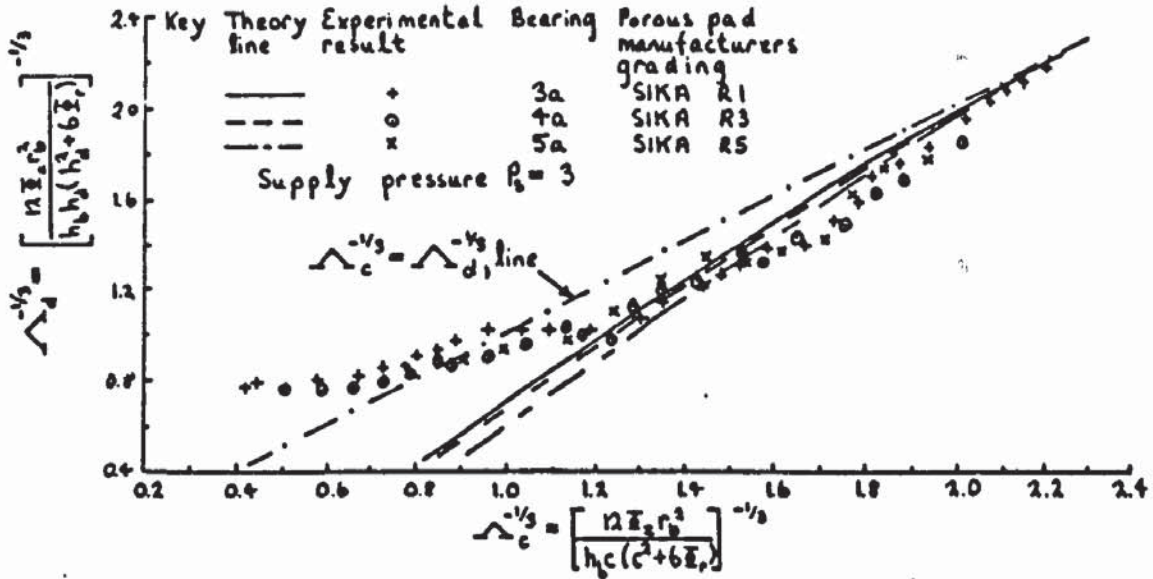

Figure 5.49 Bearing number based on derived bearing clearance versus bearing number based on bearing approach for bearings with different grade porous pads

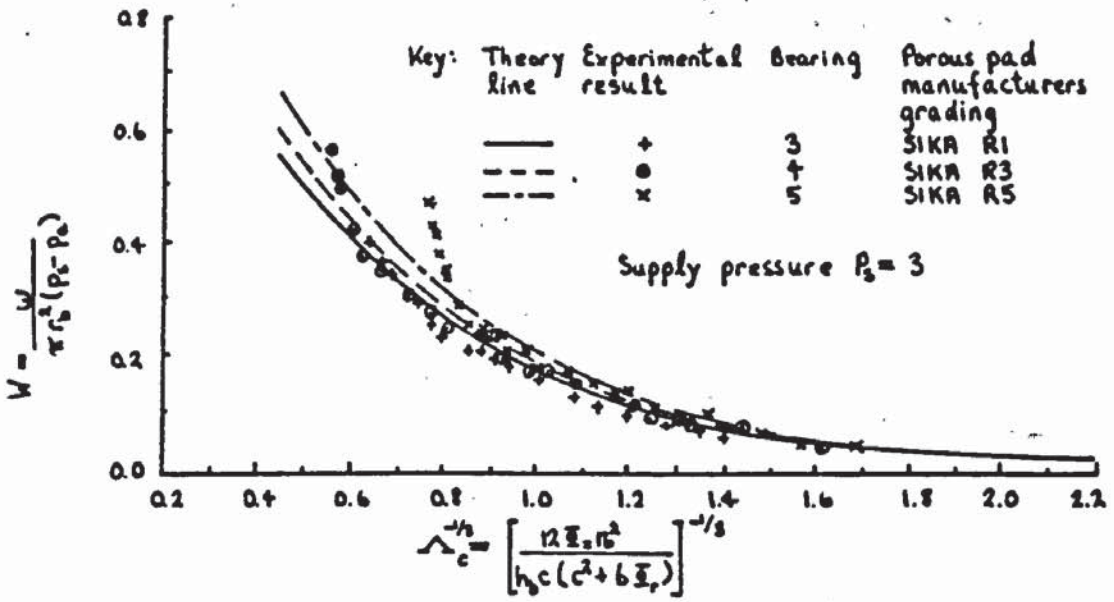

Figure 5.50 Load capacity versus bearing number for bearings with different grade porous pads

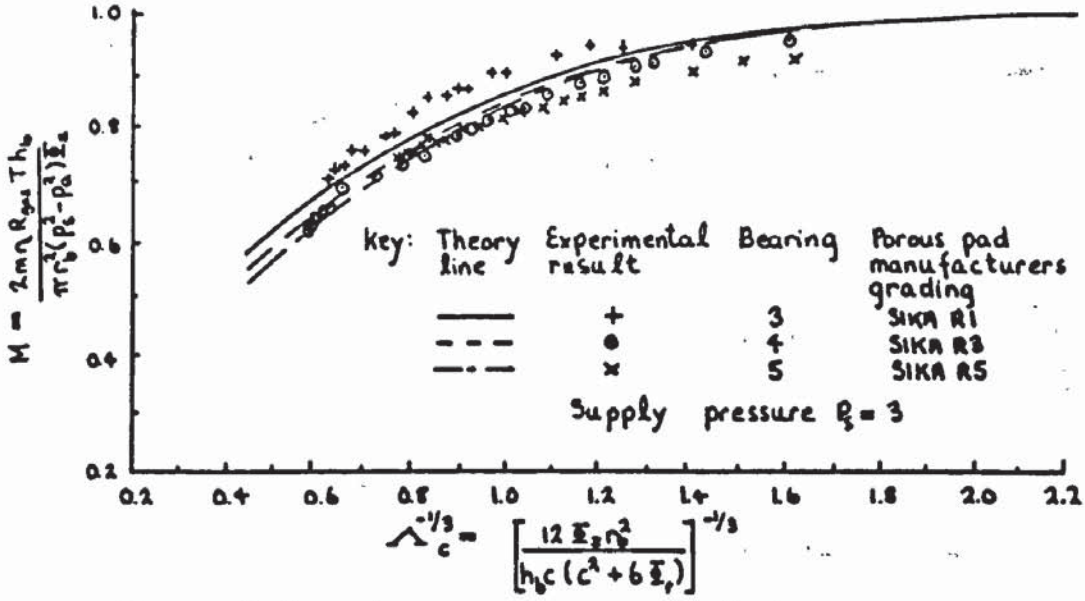

Figure 5.51 Flow rate versus bearing number for bearings with different grade porous pads

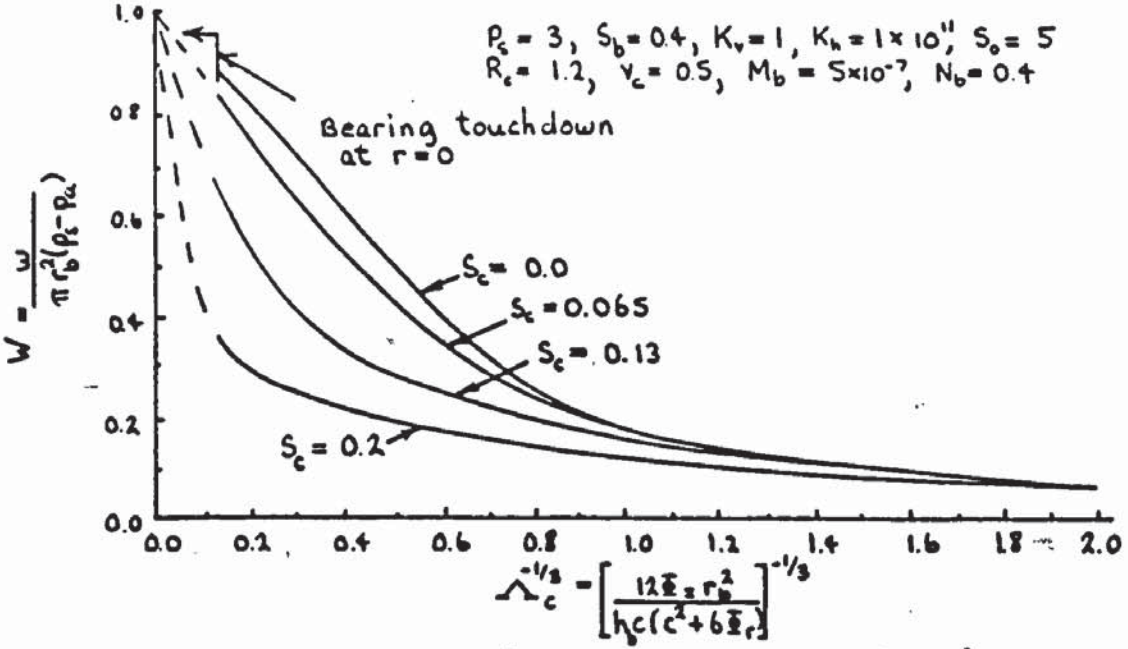

Figure 5.52 Load capacity versus bearing number for various elastomer layer non-dimensional thicknesses

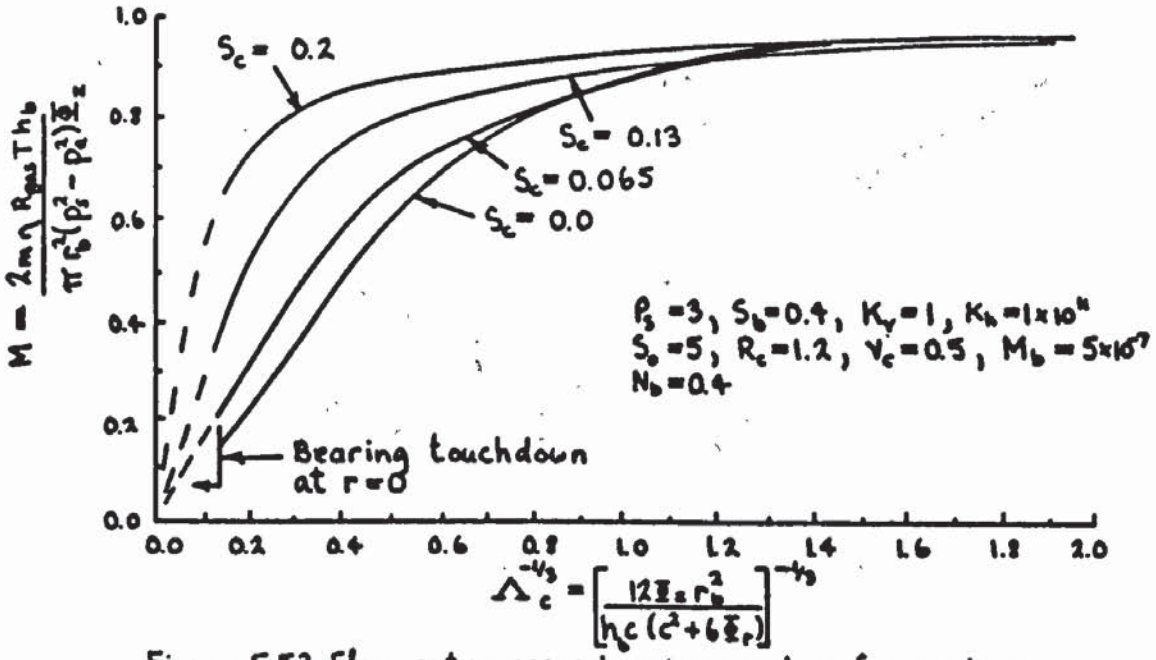

Figure 5.53 Flow rate versus bearing number for various elastomer layer non-dimensional thicknesses

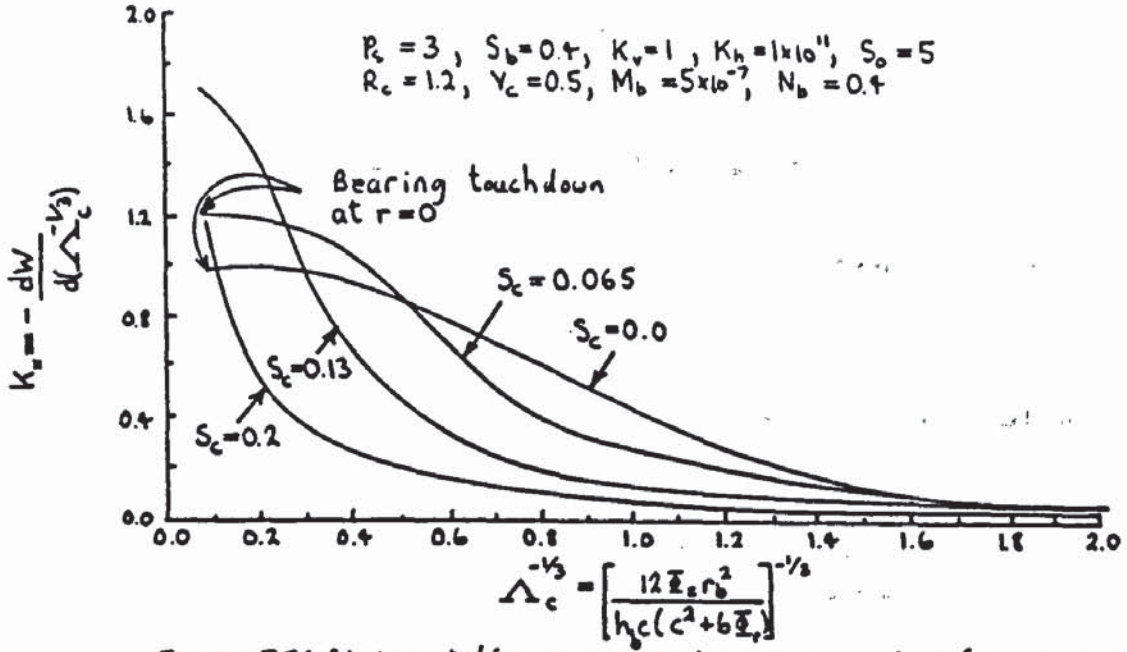

Figure 5.54 Static stiffness versus bearing number for various elastomer layer non-dimensional thicknesses

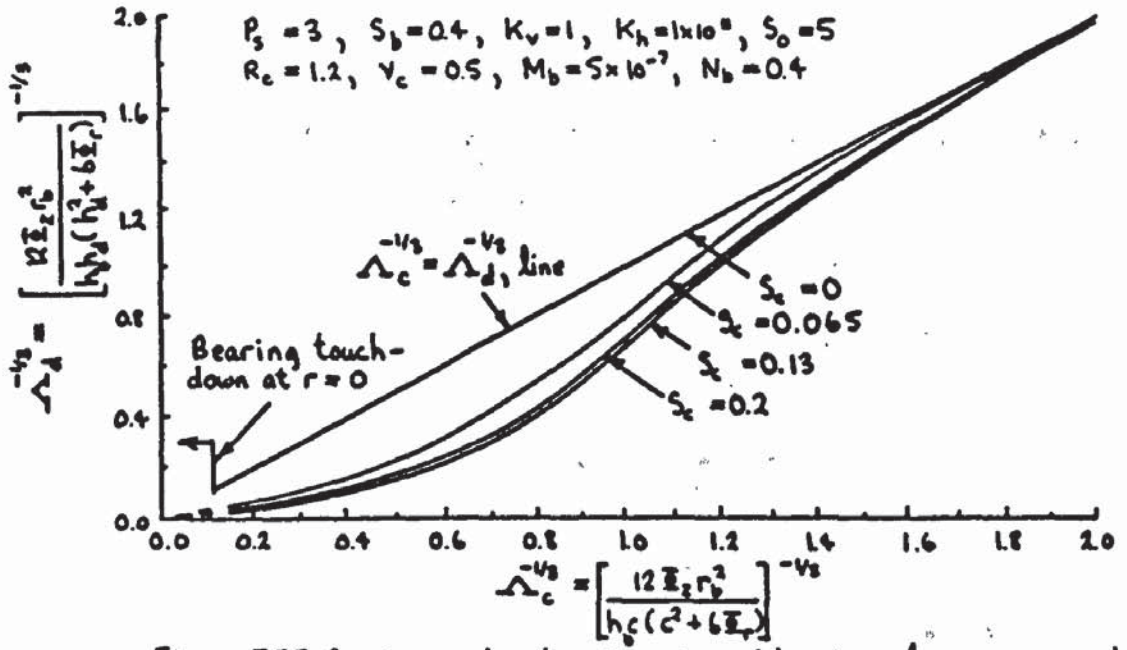

Figure 5.55 Bearing number based on derived bearing clearance versus bearing number based on bearing approach for various elastomer layer non-dimensional thicknesses

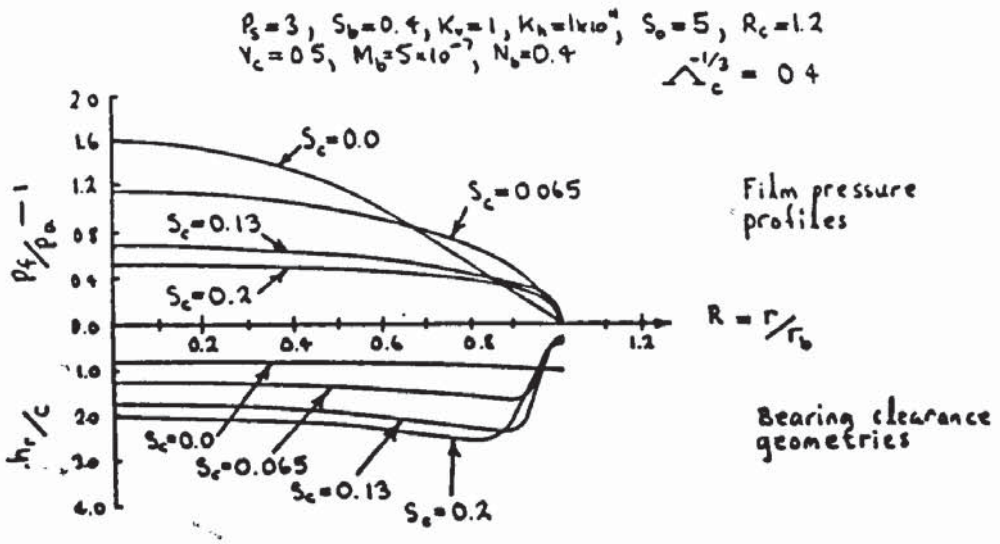

Figure 5.56 Film pressure profiles and bearing clearance geometries for various elastomer layer non-dimensional thicknesses, $\Lambda_c^{-1/3}$ = constant

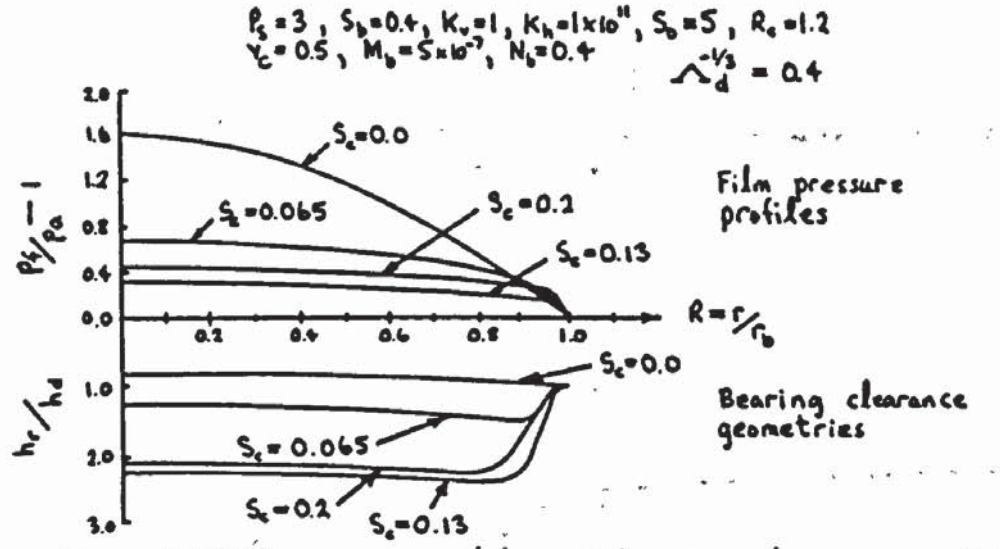

Figure 5.57 Film pressure profiles and bearing clearance geometries for various elastomer layer non-dimensional thicknesses, $\Lambda_d^{-1/3}$ = constant

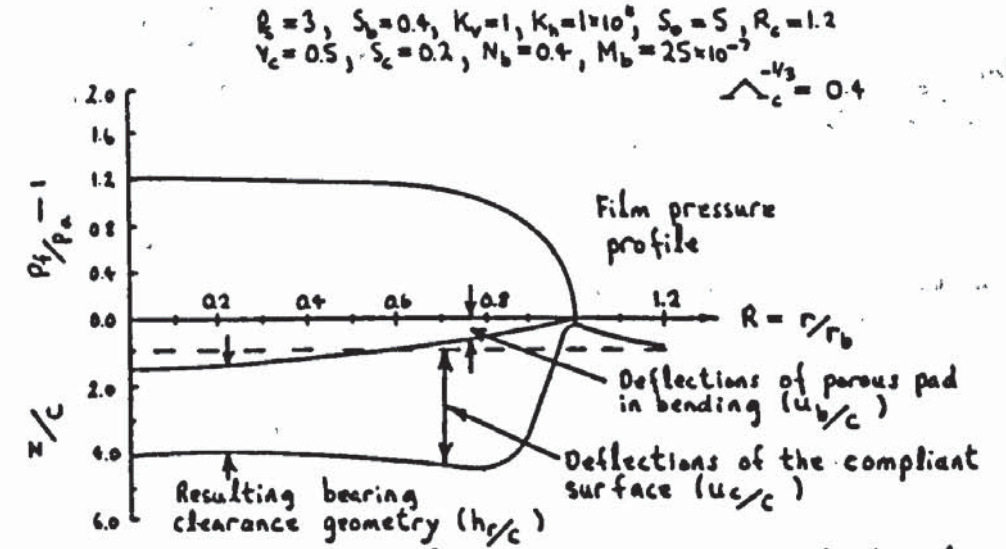

Figure 5.58 Deflections of the porous pad and compliant surface

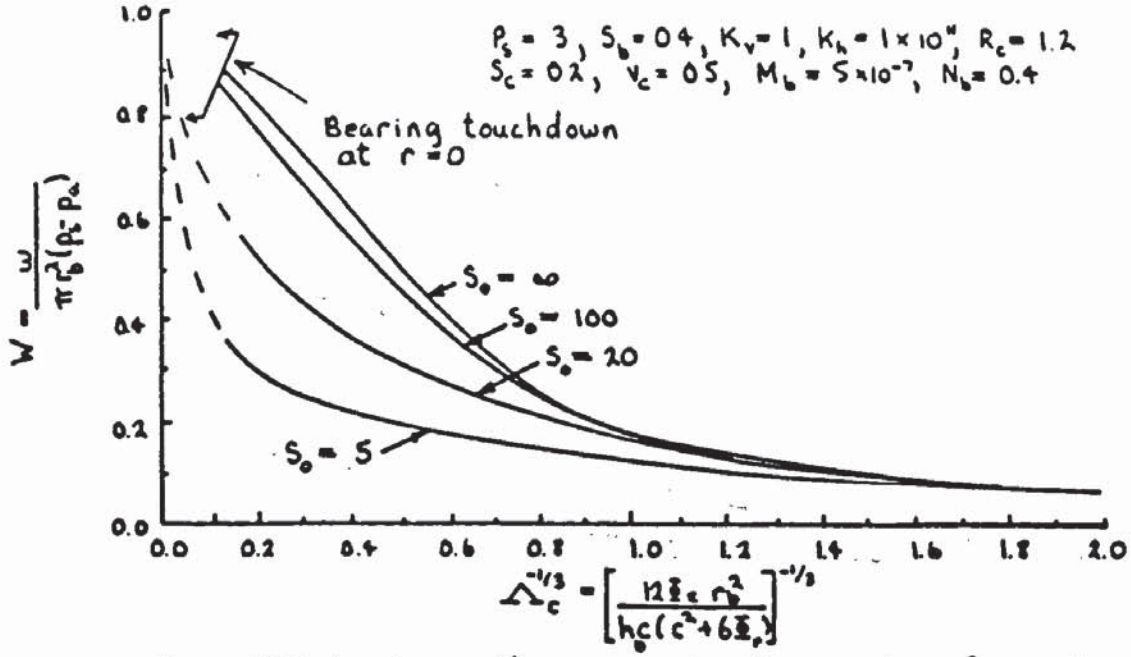

Figure 5.59 Load capacity versus bearing number for various non-dimensional shear moduli of the elastomer layer

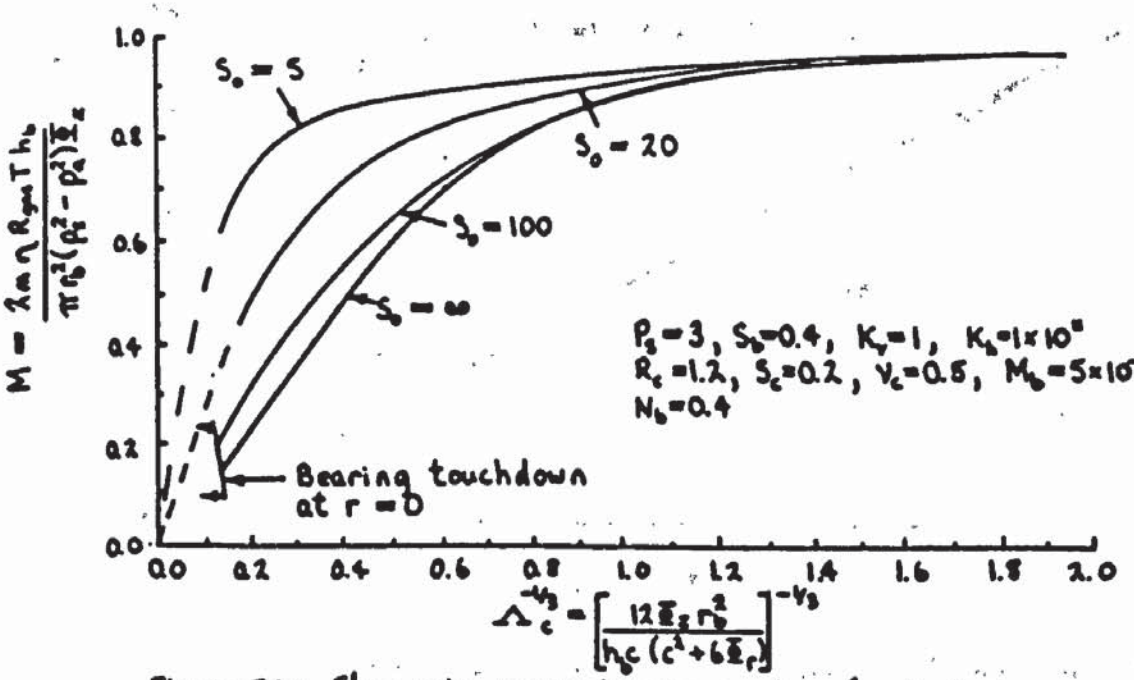

Figure 5.60 Flow rate versus bearing number for various non-dimensional shear moduli of the elastomer layer

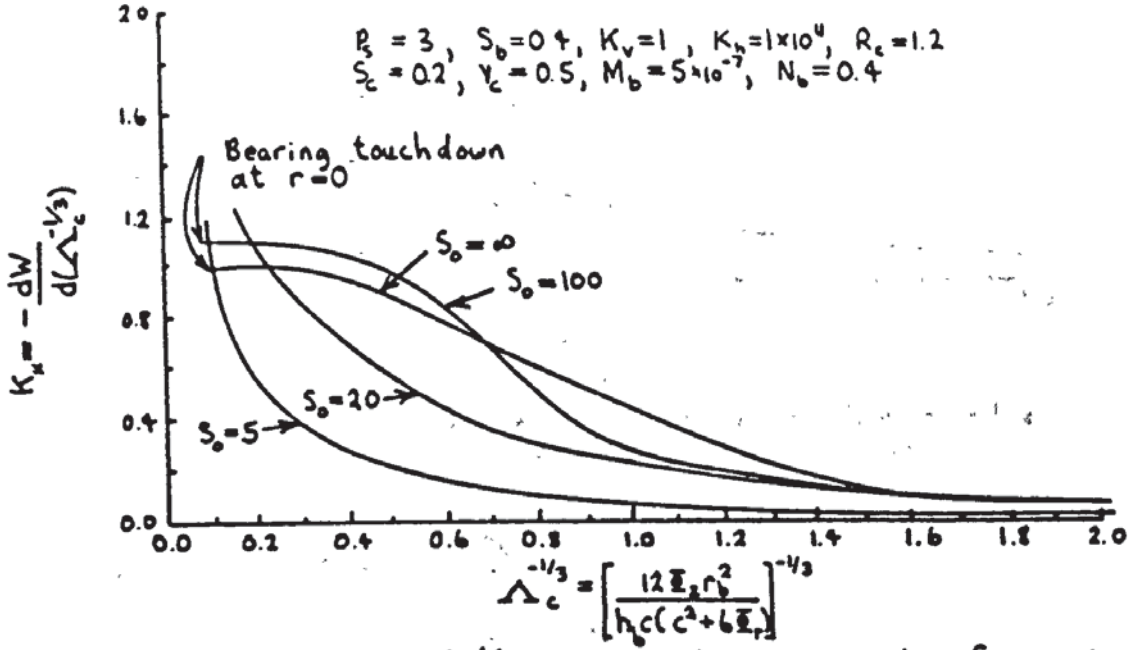

Figure 5.61 Static stiffness versus bearing number for various non-dimensional shear moduli of the elastomer layer

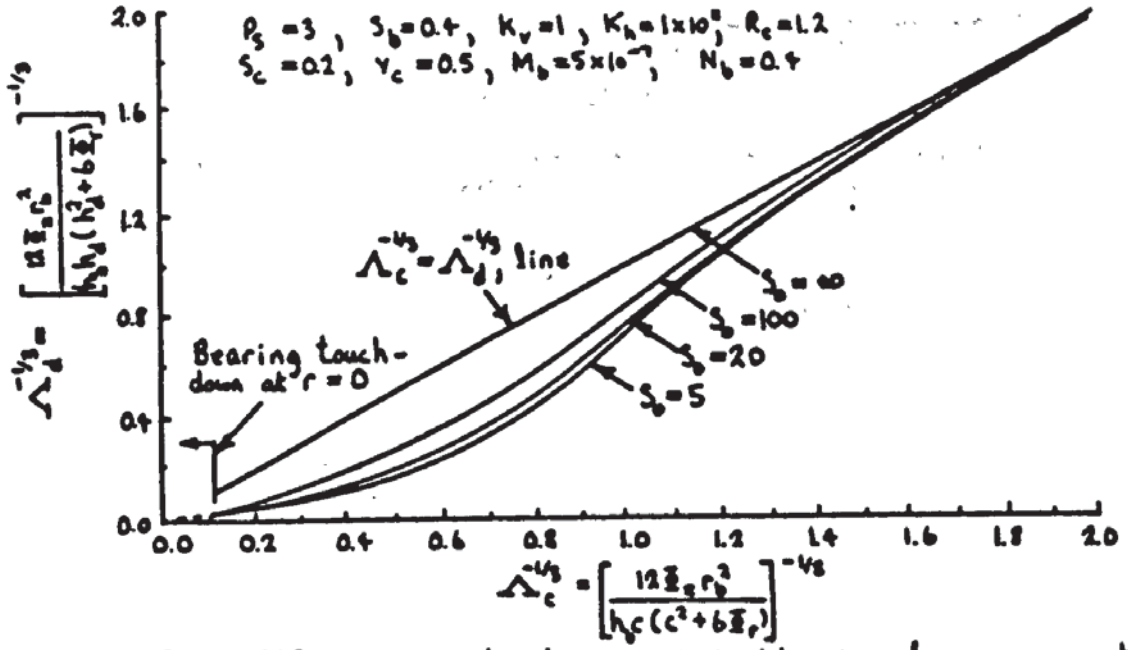

Figure 5.62 Bearing number based on derived bearing clearance versus bearing number based on bearing approach for various non-dimensional shear moduli of the elastomer layer

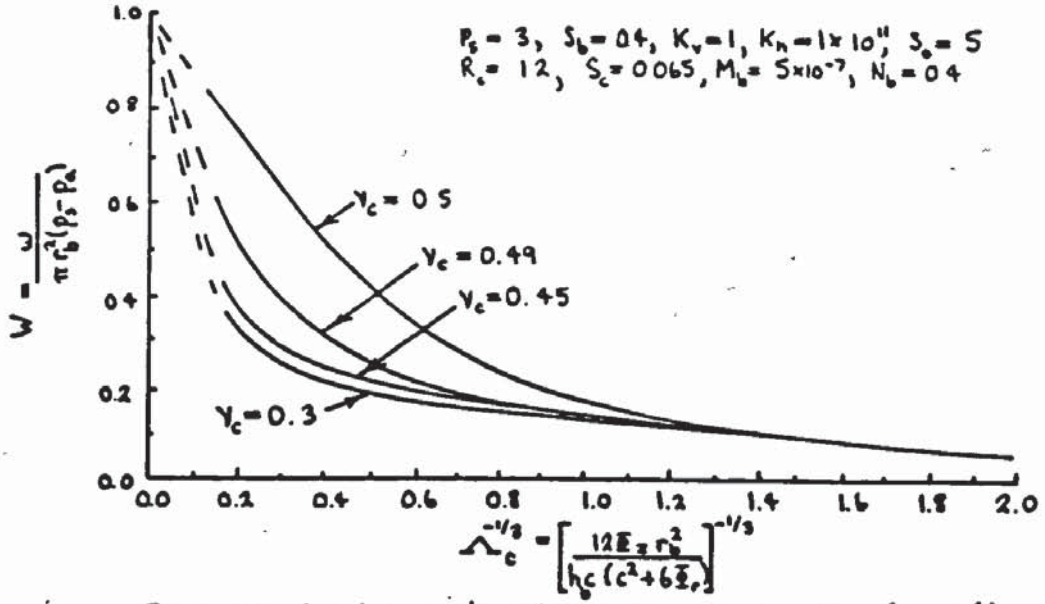

Figure 5.63 Load capacity versus bearing number for different Poisson's ratio of the elastomer layer

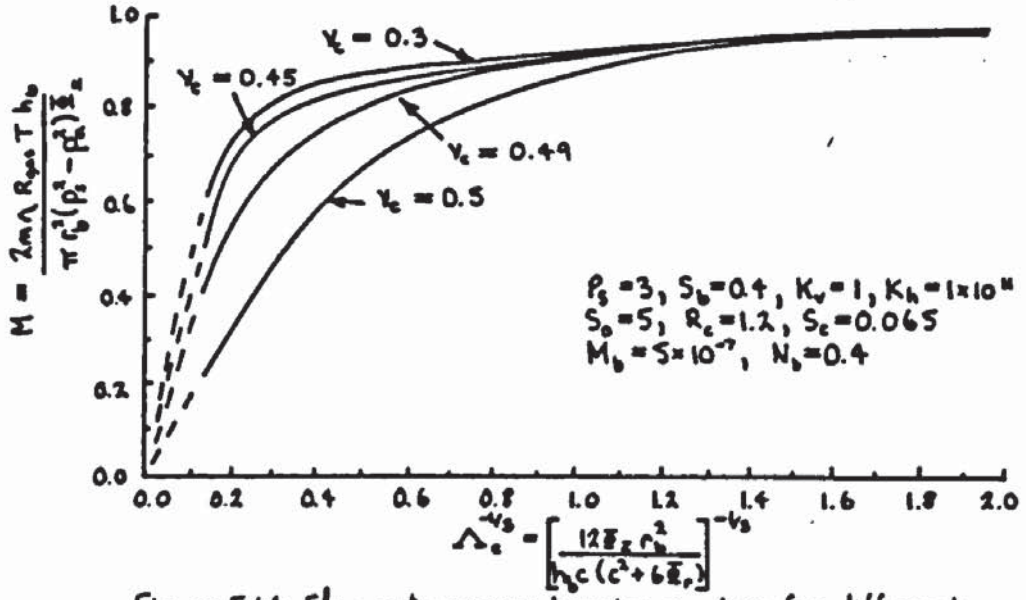

Figure 5.64 Flow rate versus bearing number for different Poisson's ratio of the elastomer layer

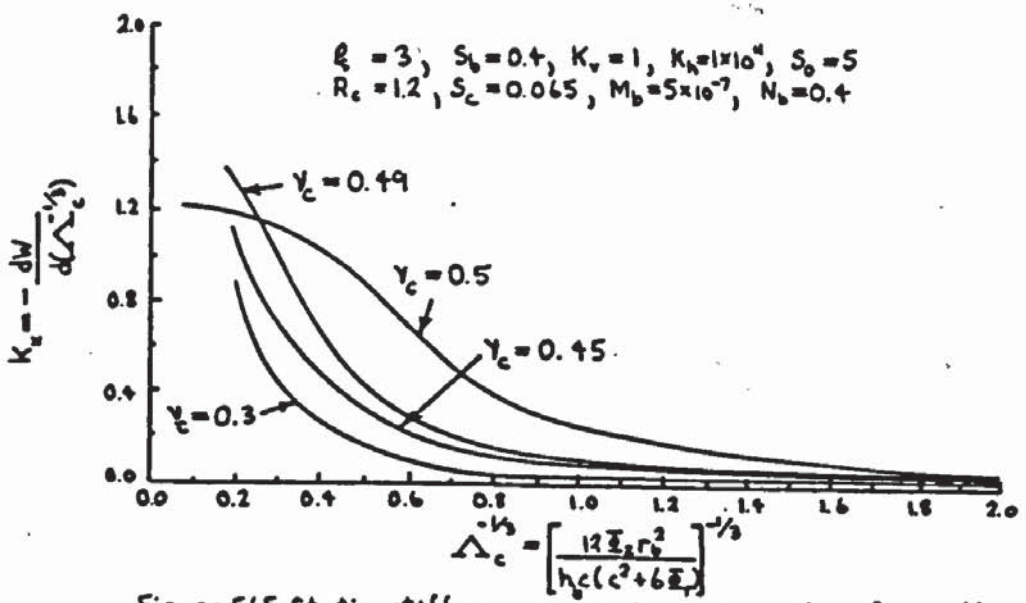

Figure 5.65 Static stiffness versus bearing number for different Poisson's ratio of the elastomer layer

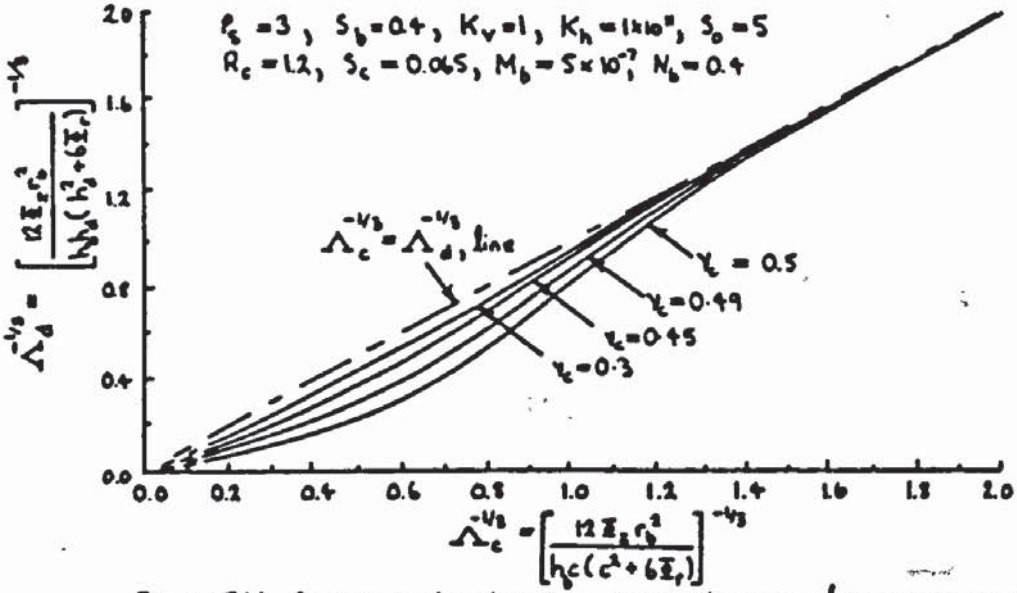

Figure 566 Bearing number based on derived bearing clearance versus bearing number based on bearing approach for different Poisson's ratio of the elastomer layer

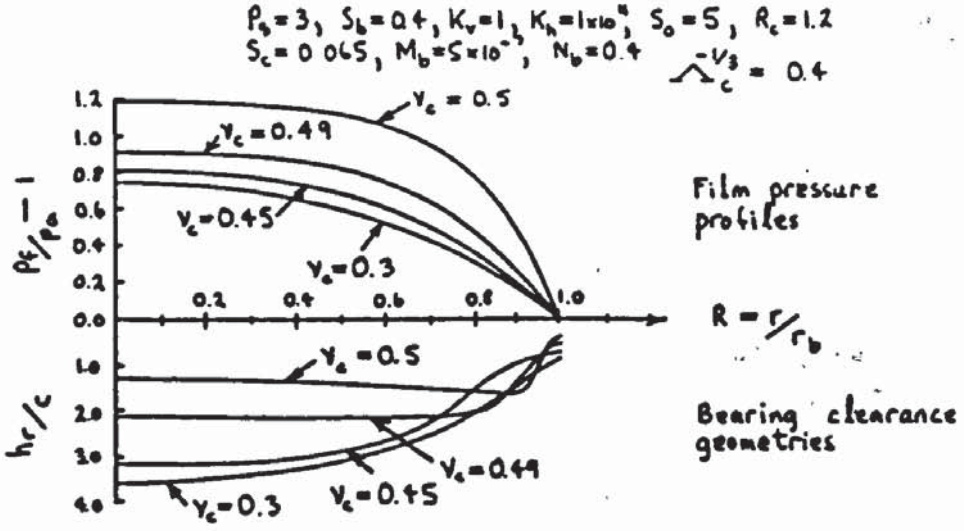

Figure 567 Film pressure profiles and bearing clearance geometries for different Poisson's ratio of the elastomer layer: $\Lambda_c^{-1/3}$ = constant

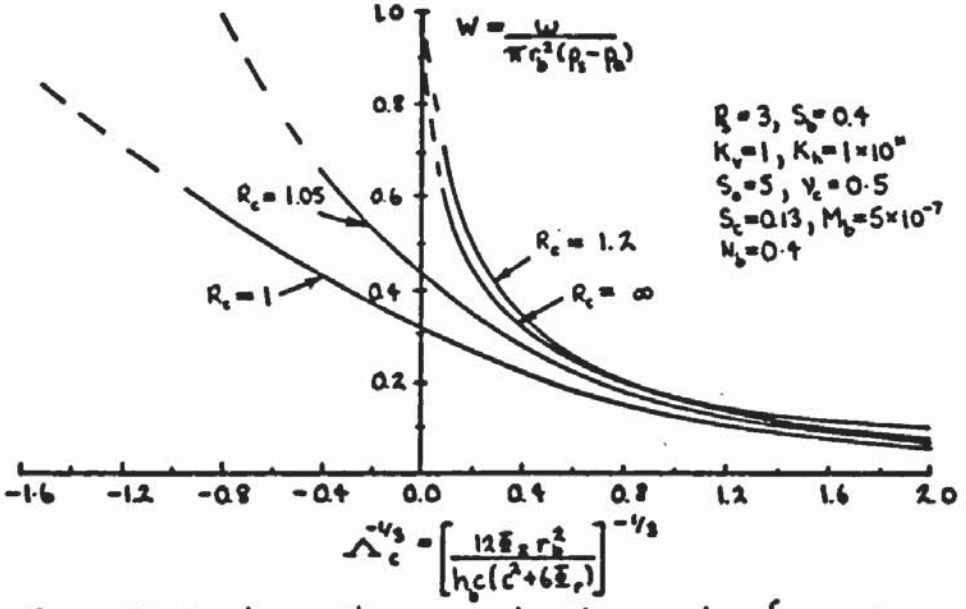

Figure 5.68 Load capacity versus bearing number for various elastomer layer radial extents

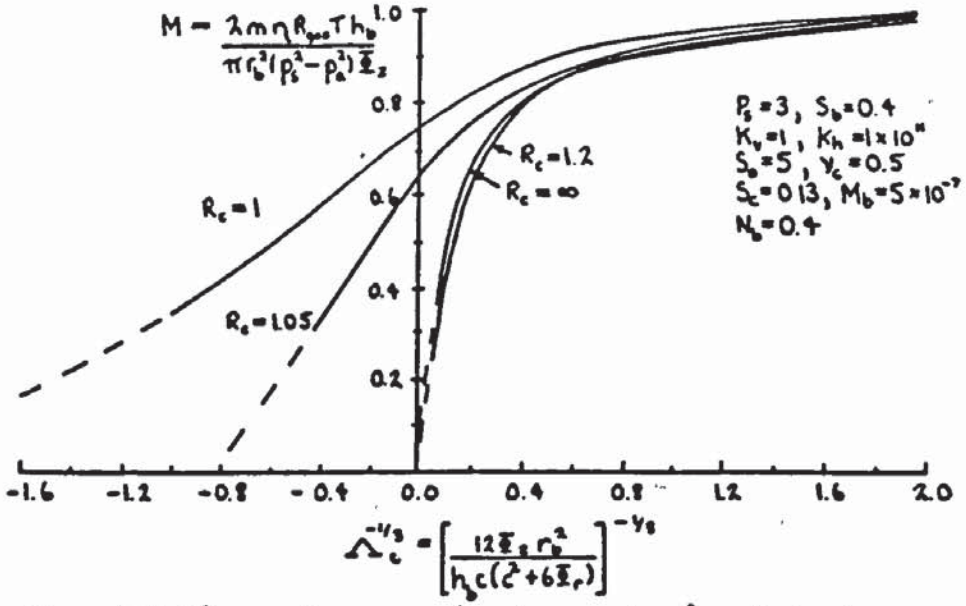

Figure 5.69 Flow rate versus bearing number for various elastomer layer radial extents

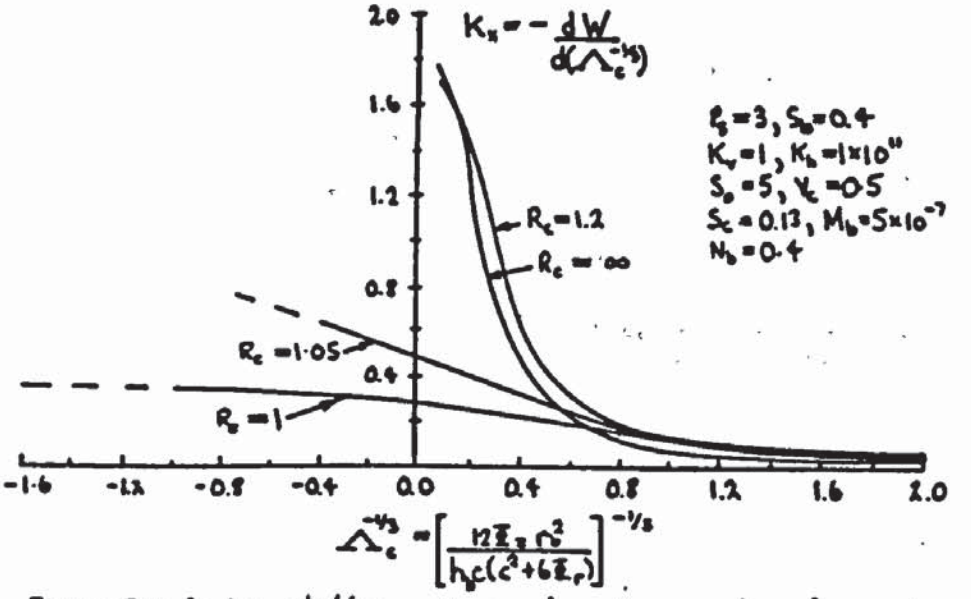

Figure 5.70 Static stiffness versus bearing number for various elastomer layer radial extents

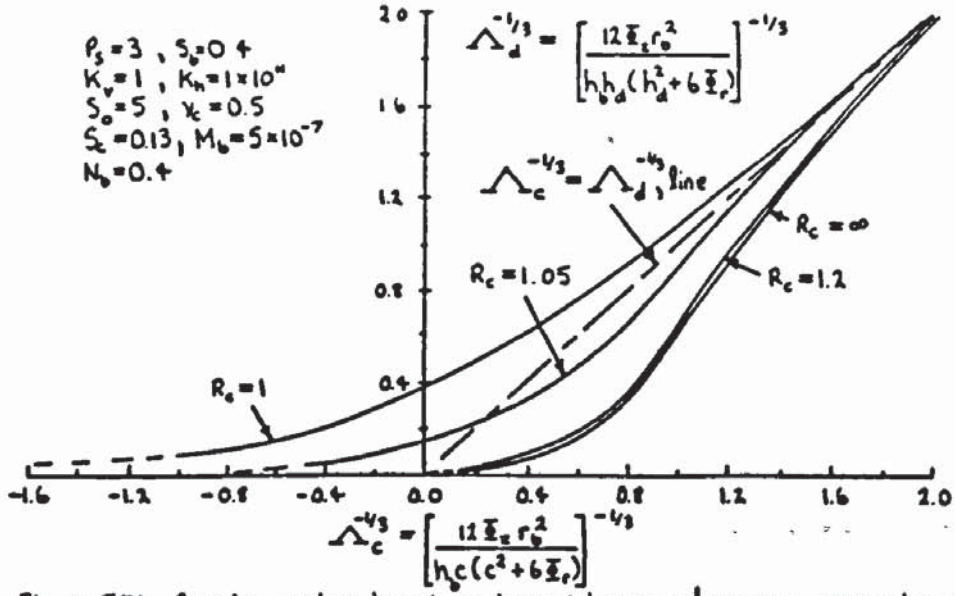

Figure 5.71 Bearing number based on derived bearing clearance versus bearing number based on bearing approach for various elastomer layer radial extents

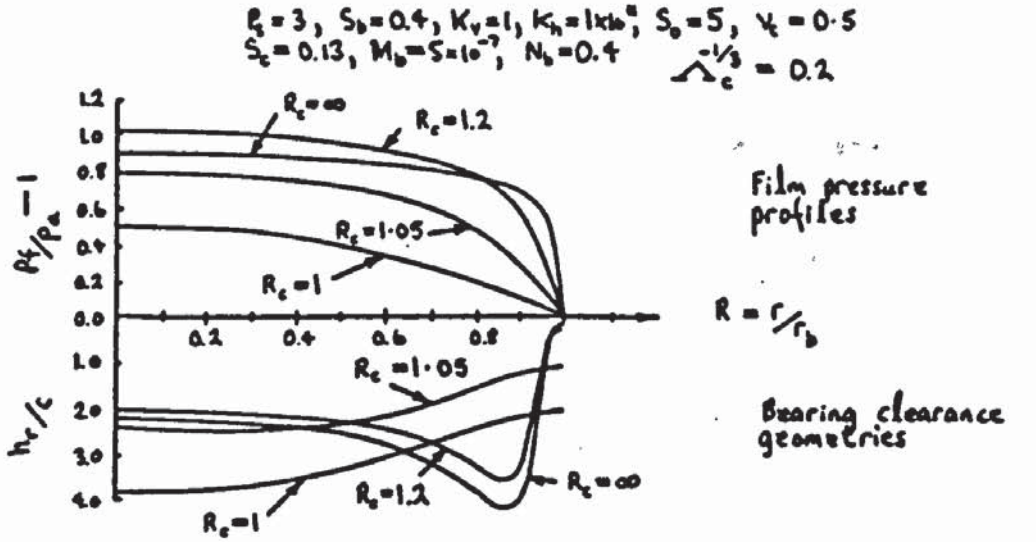

Figure 5.72 Film pressure profiles and bearing clearance geometries for various elastomer layer radial extents: $\Lambda_c^{-1/3}$ = constant

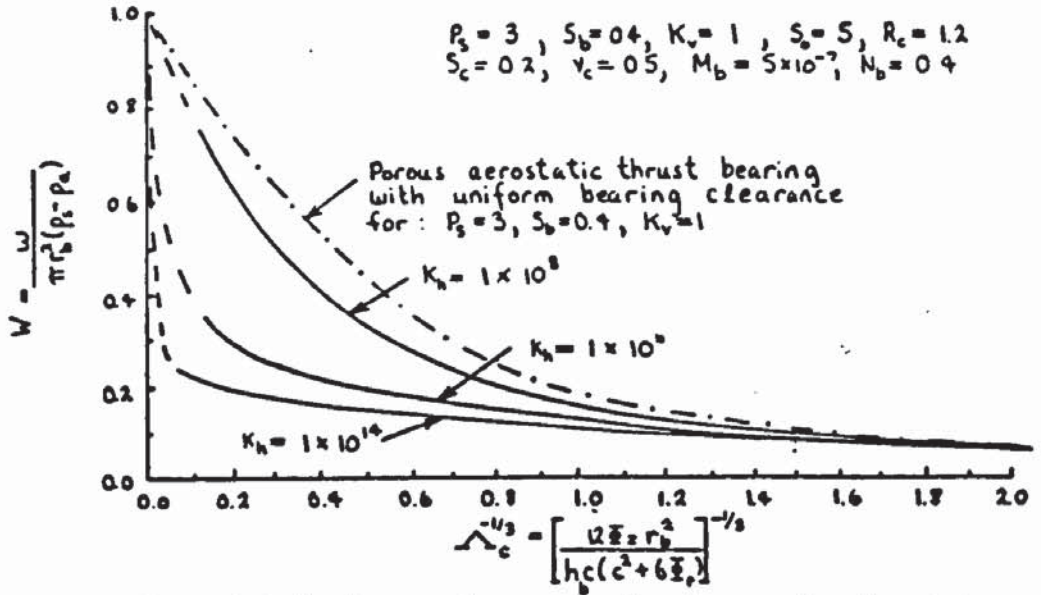

Figure 5.73 Load capacity versus bearing number for various values of the non-dimensional constant K_h, resulting in changes to the bearing clearance geometry

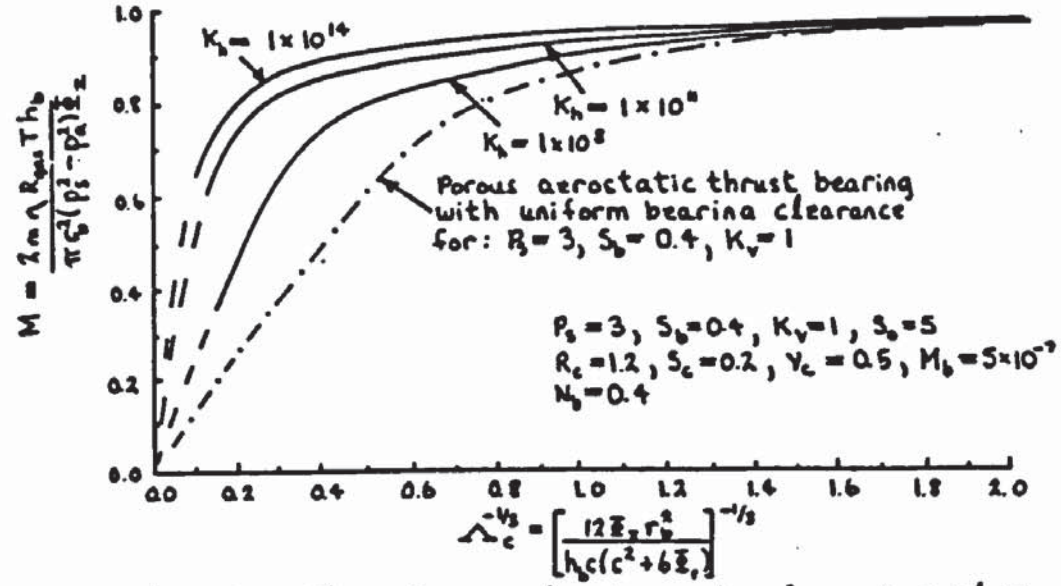

Figure 5.74 Flow rate versus bearing number for various values of the non-dimensional constant K_h, resulting in changes to the bearing clearance geometry

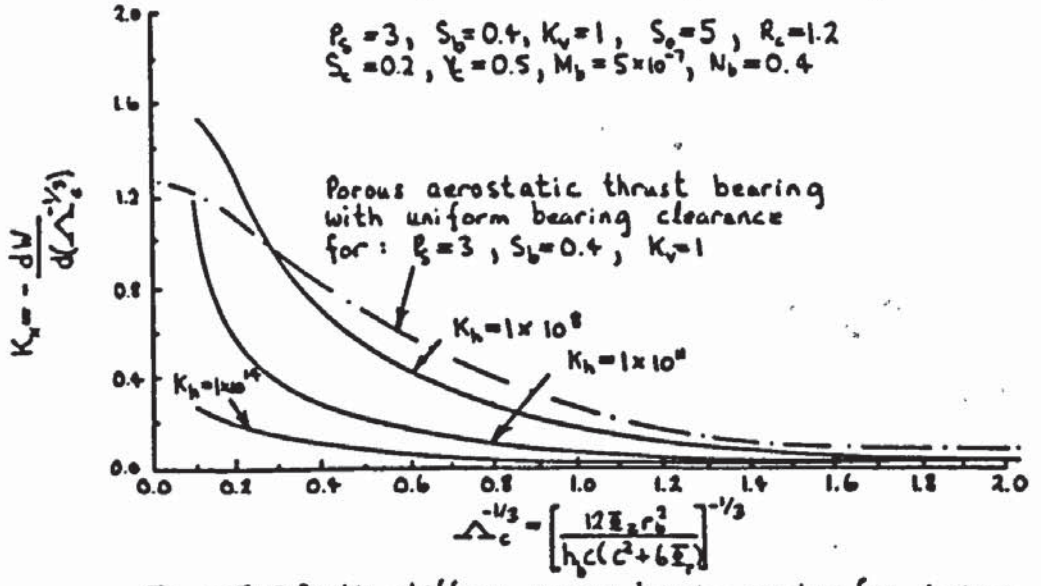

Figure 5.75 Static stiffness versus bearing number for various values of the non-dimensional constant K_h, resulting in changes to the bearing clearance geometry

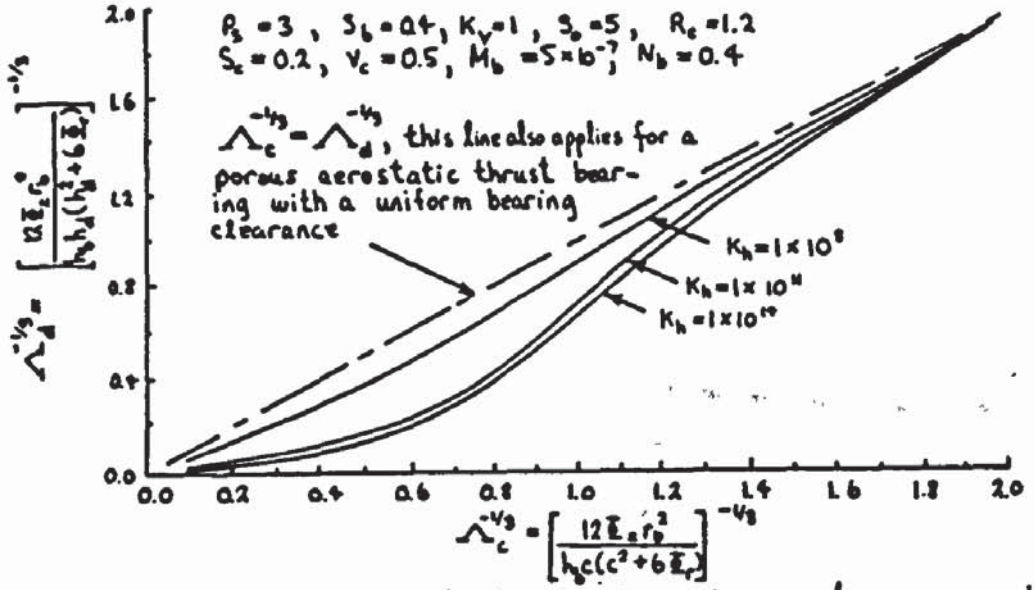

Figure 5.76 Bearing number based on derived bearing clearance versus bearing number based on bearing approach for various values of the non-dimensional constant K_h, affecting the bearing clearance geometry

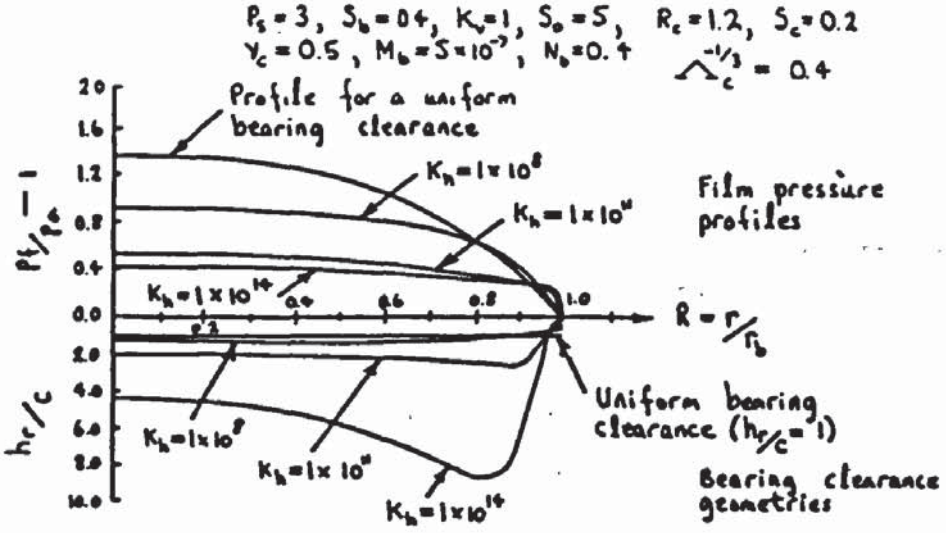

Figure 5.77 Film pressure profiles and bearing clearance geometries for various values of the non-dimensional constant K_h : $\Lambda_c^{-1/3}$ = constant.

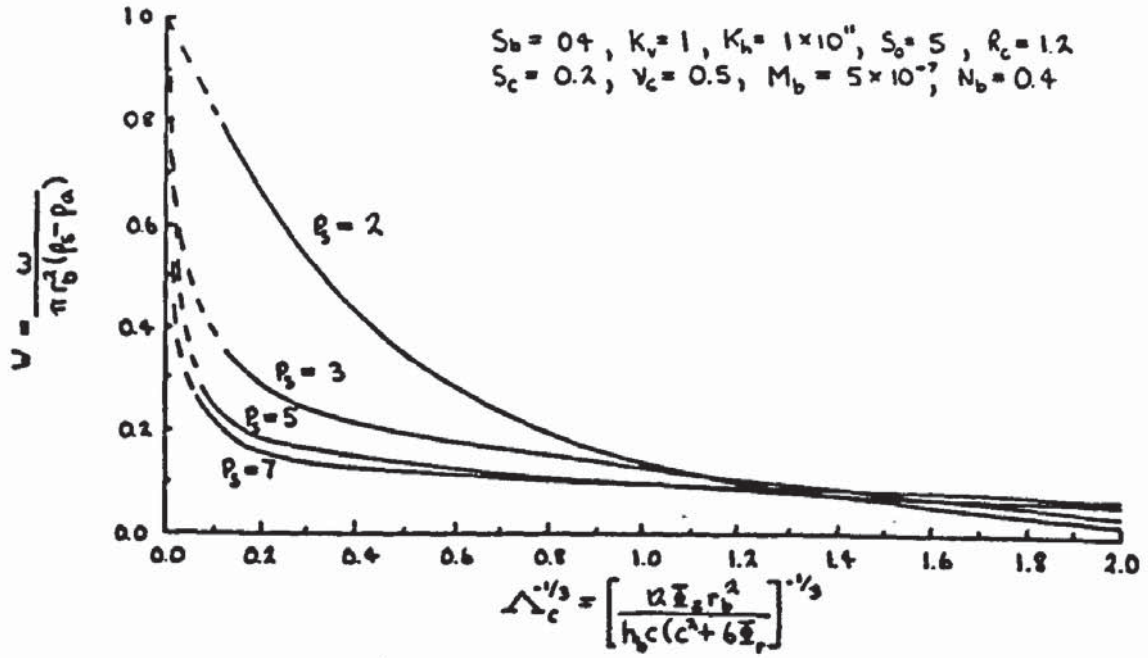

Figure 5.78 Load capacity versus bearing number at various supply pressures

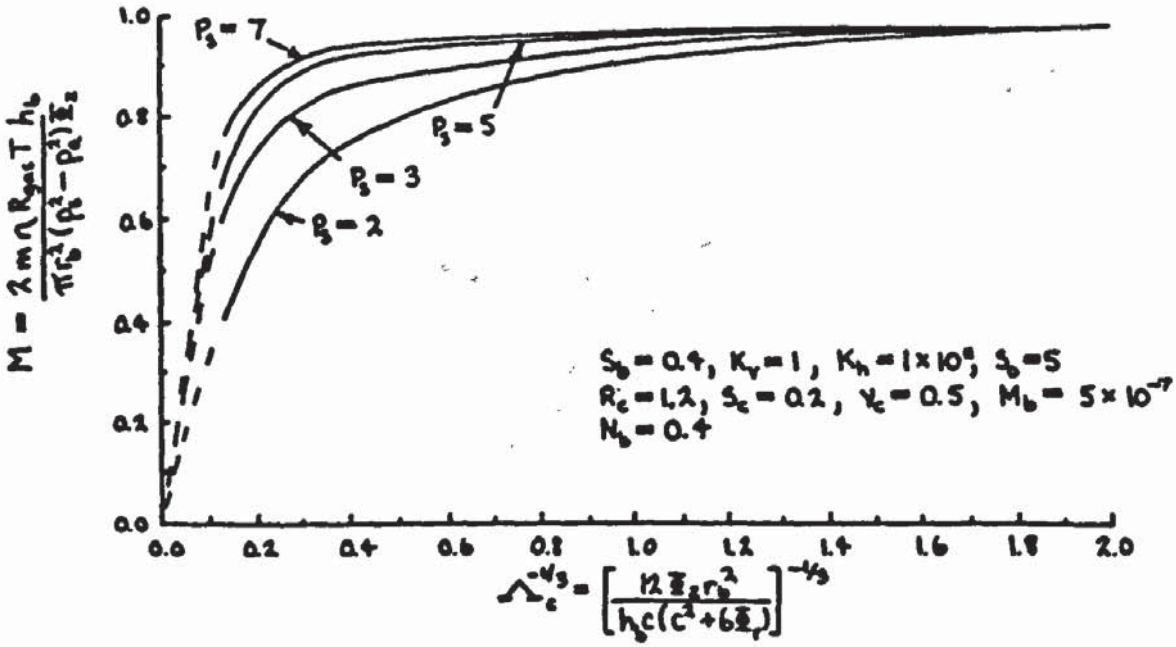

Figure 5.79 Flow rate versus bearing number at various supply pressures

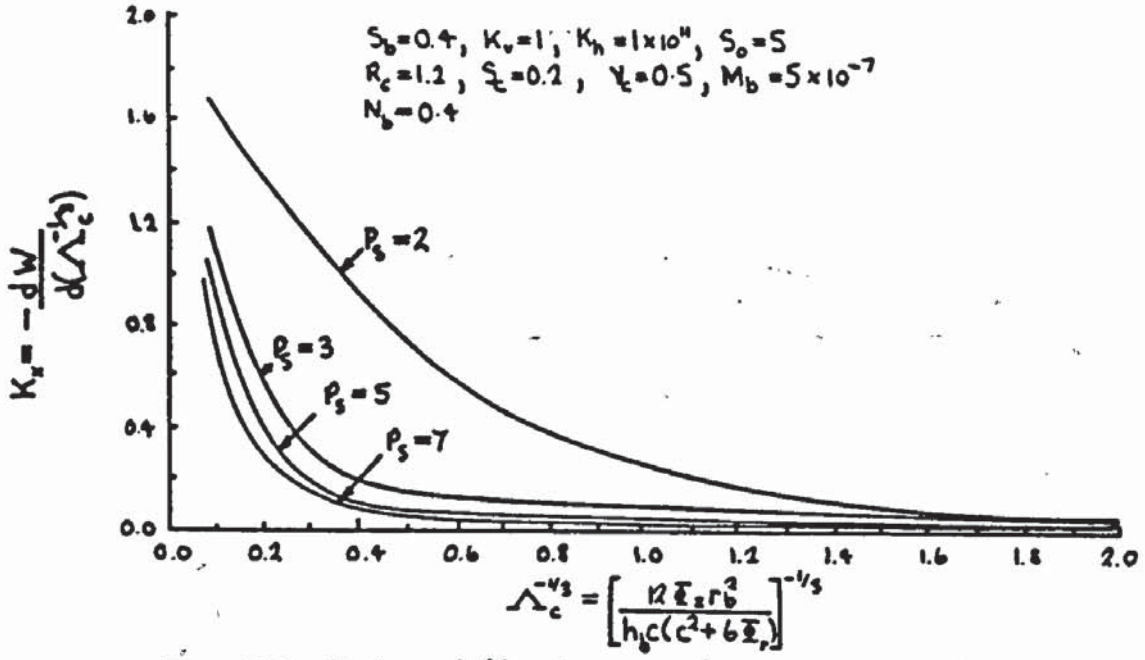

Figure 5.80 Static stiffness versus bearing number at various supply pressures

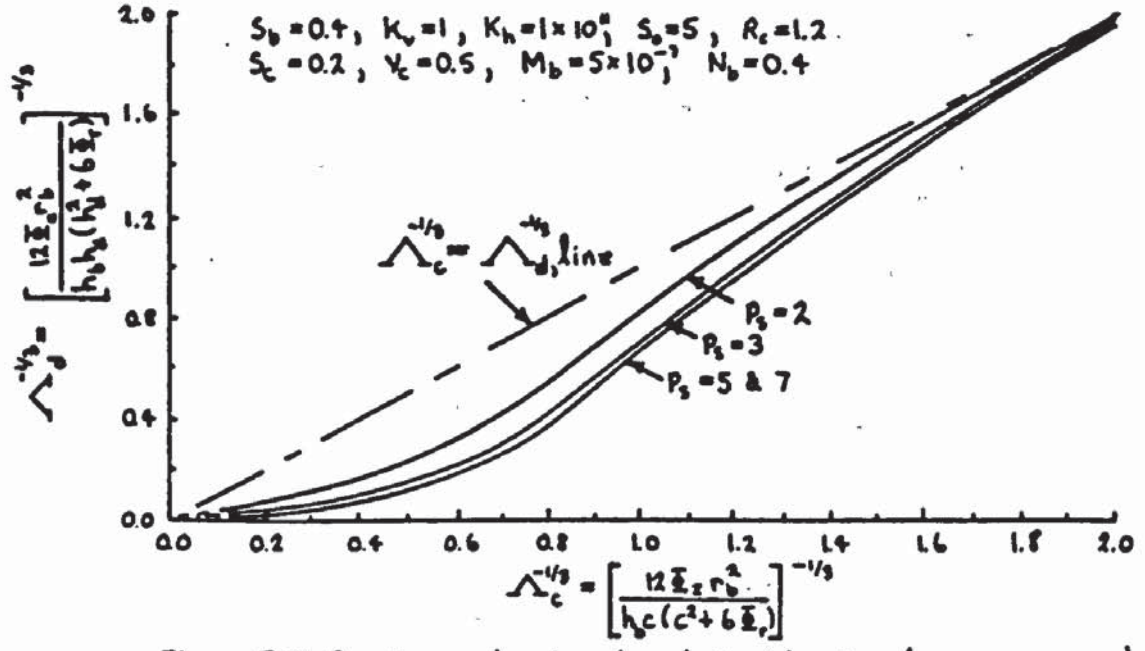

Figure 5.81 Bearing number based on derived bearing clearance versus bearing number based on bearing approach at various supply pressures

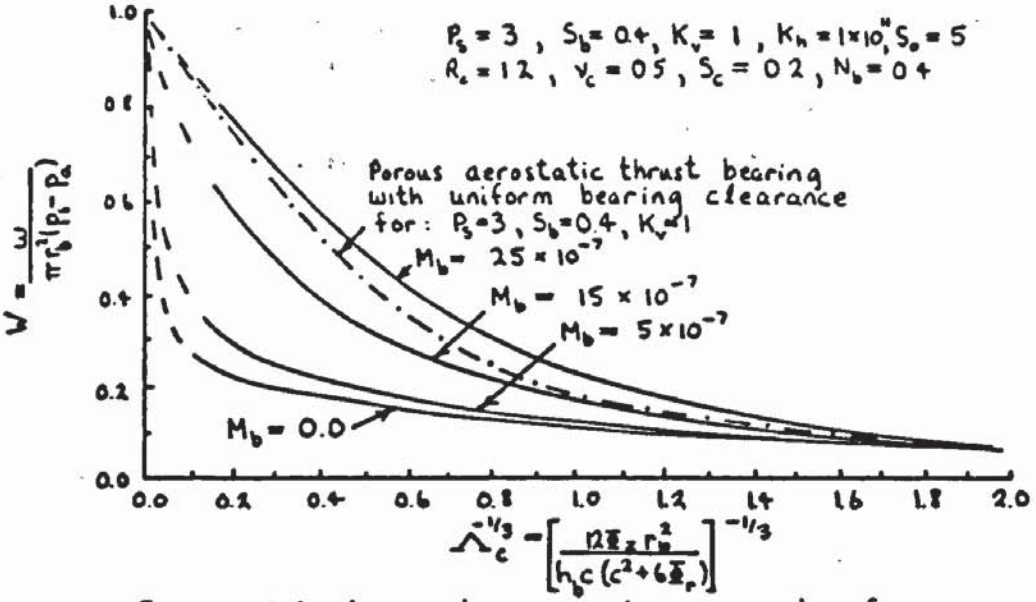

Figure 5.82 Load capacity versus bearing number for various magnitude constants of the porous pad

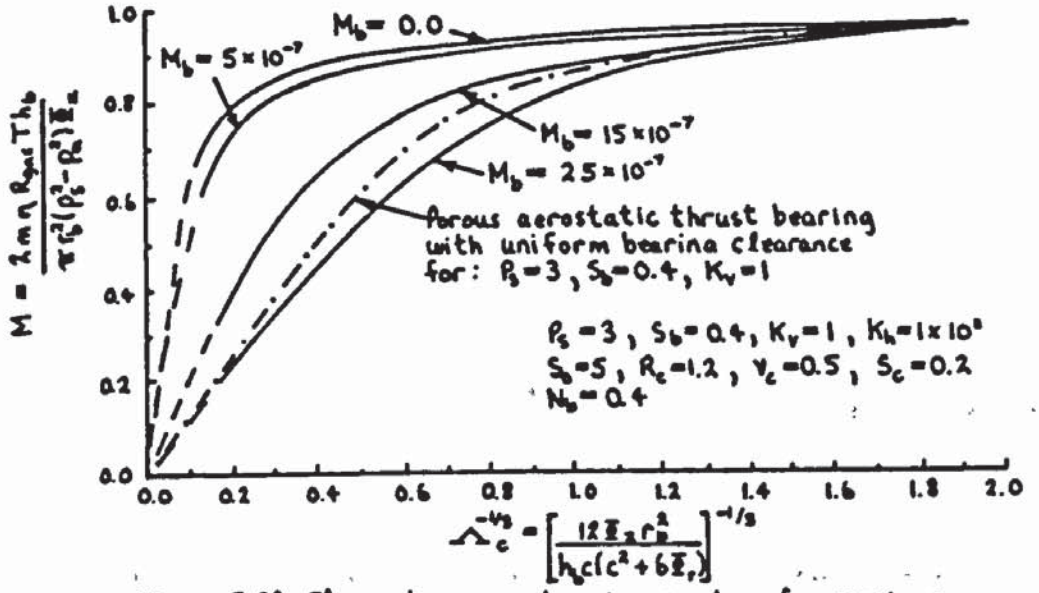

Figure 5.83 Flow rate versus bearing number for various magnitude constants of the porous pad

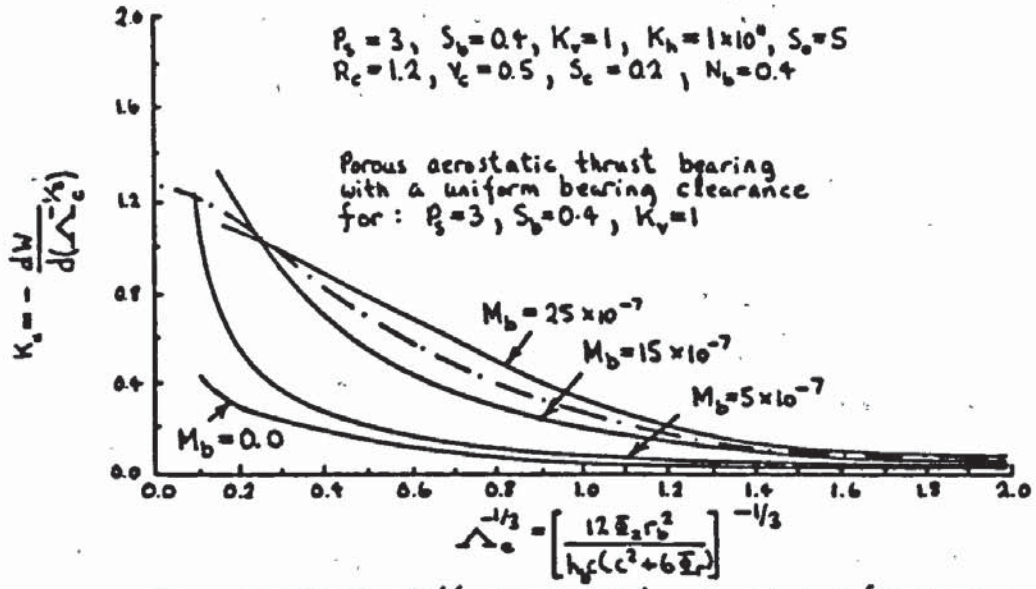

Figure 5.84 Static stiffness versus bearing number for various magnitude constants of the porous pad

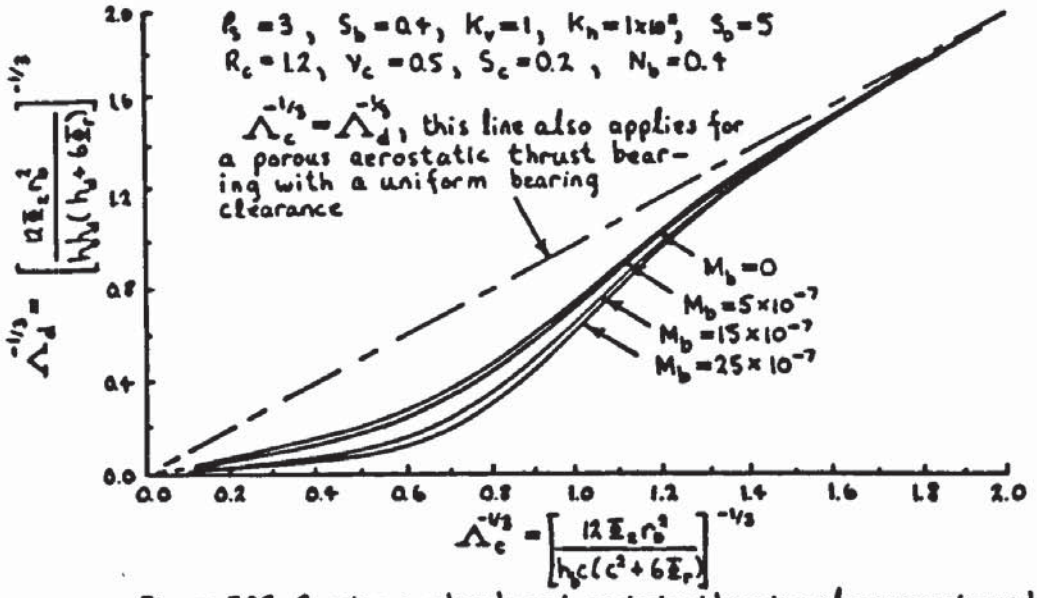

Figure 5.85 Bearing number based on derived bearing clearance versus bearing number based on bearing approach for various magnitude constants of the porous pad

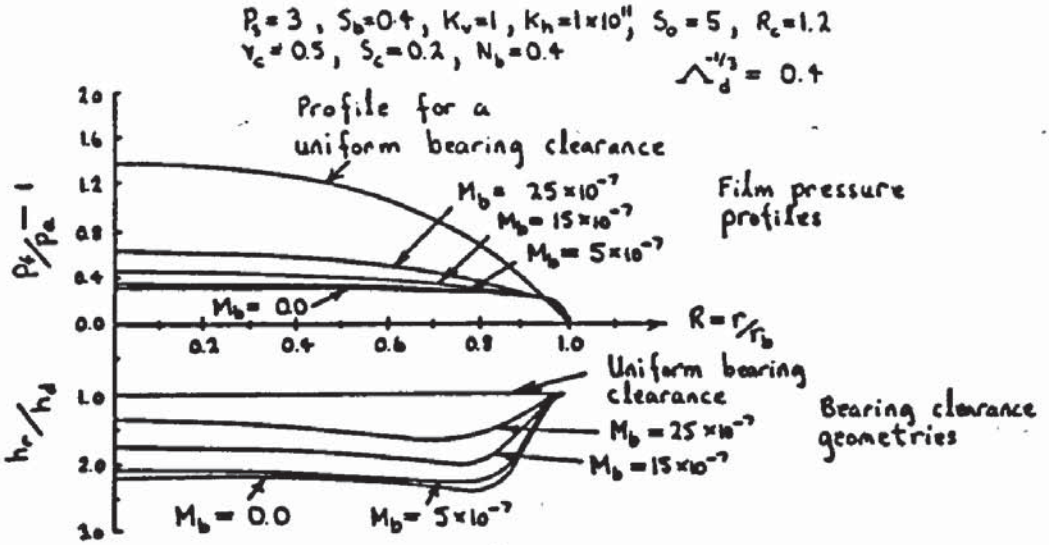

Figure 5.86 Film pressure profiles and bearing clearance geometries for various magnitude constants of the porous pad: $\Lambda_d^{-1/3}$ = constant

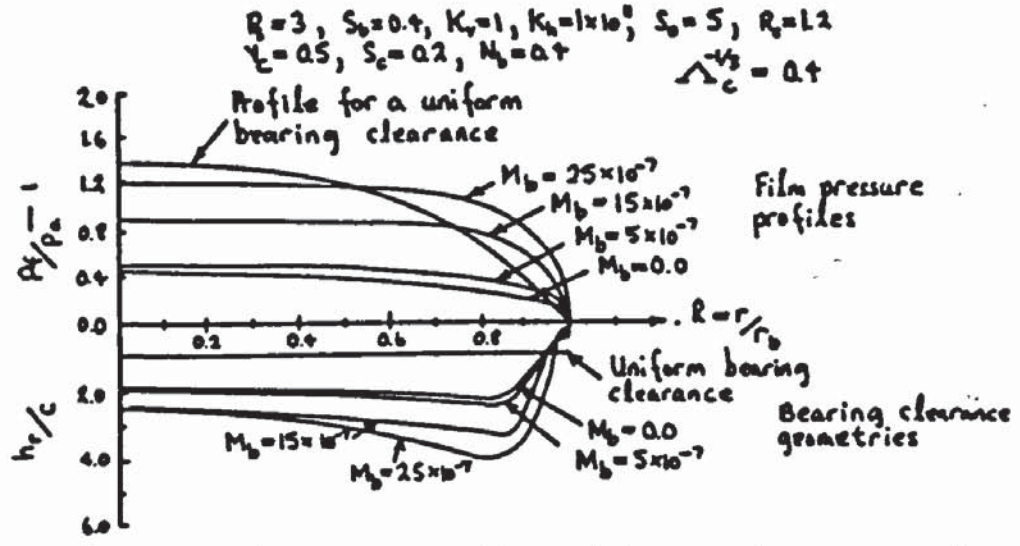

Figure 5.87 Film pressure profiles and bearing clearance geometries for various magnitude constants of the porous pad: $\Lambda_c^{-1/3}$ = constant

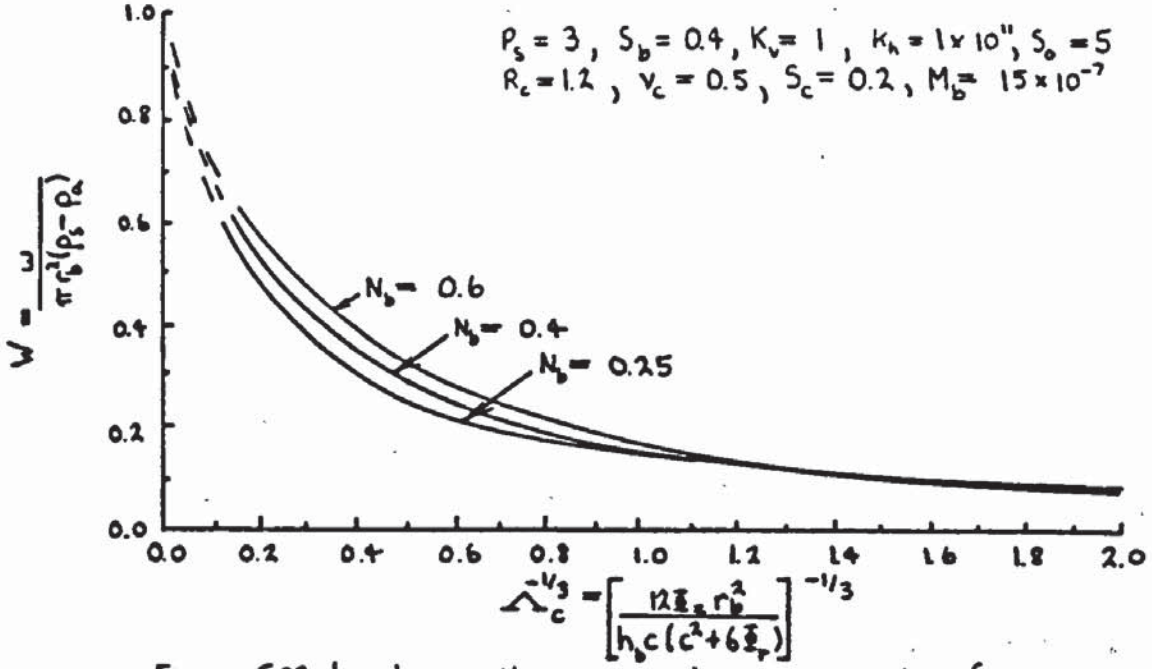

Figure 5.88 Load capacity versus bearing number for various shape constants of the porous pad

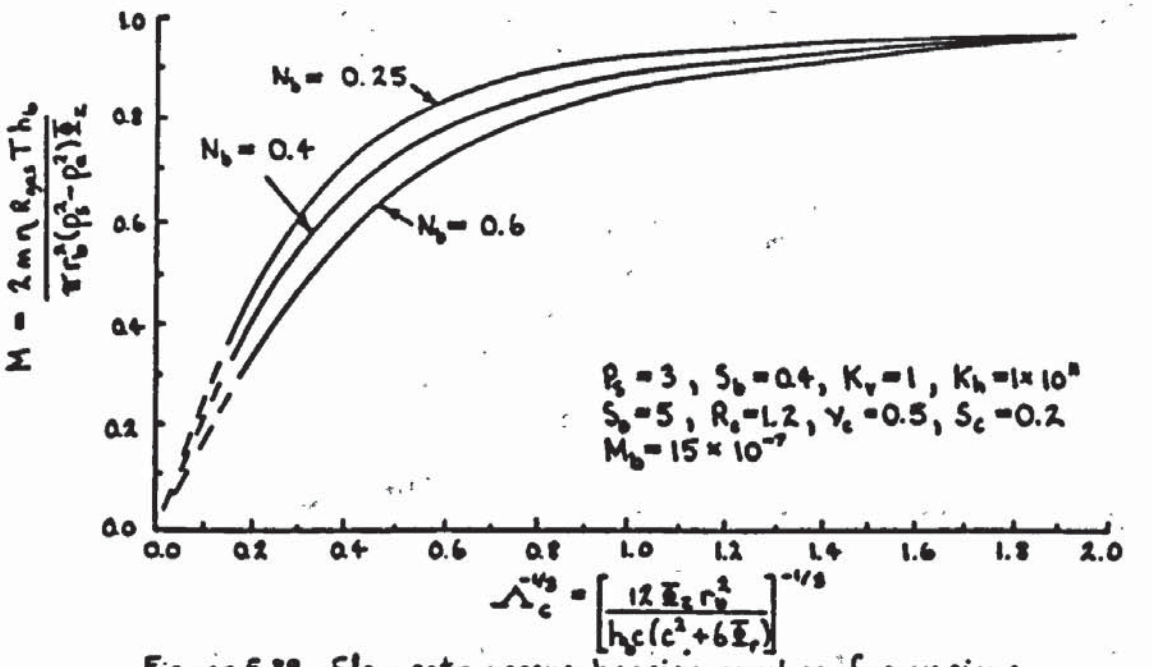

Figure 5.89 Flow rate versus bearing number for various shape constants of the porous pad

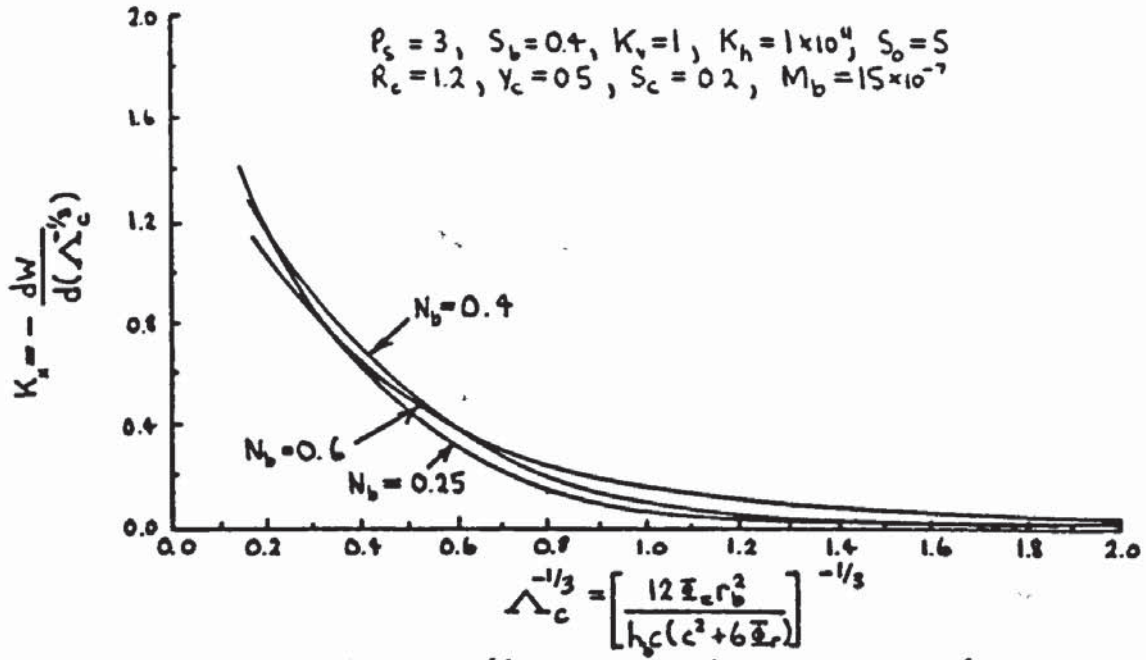

Figure 5.90 Static stiffness versus bearing number for various shape constants of the porous pad

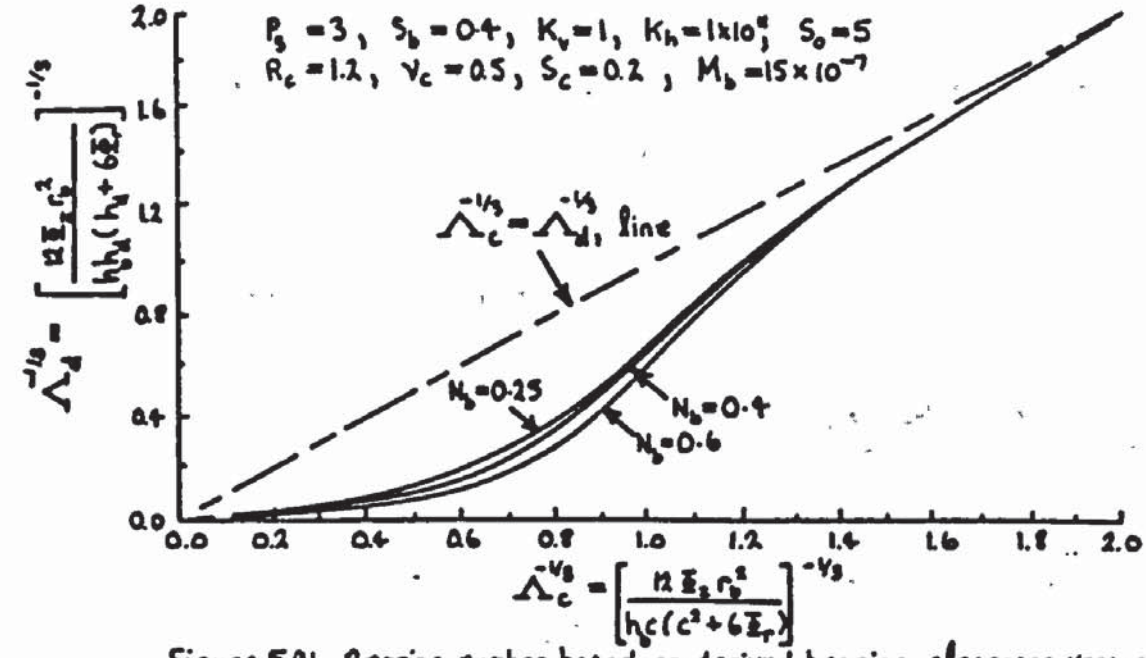

Figure 5.91 Bearing number based on derived bearing clearance versus bearing number based on bearing approach for various shape constants of the porous pad

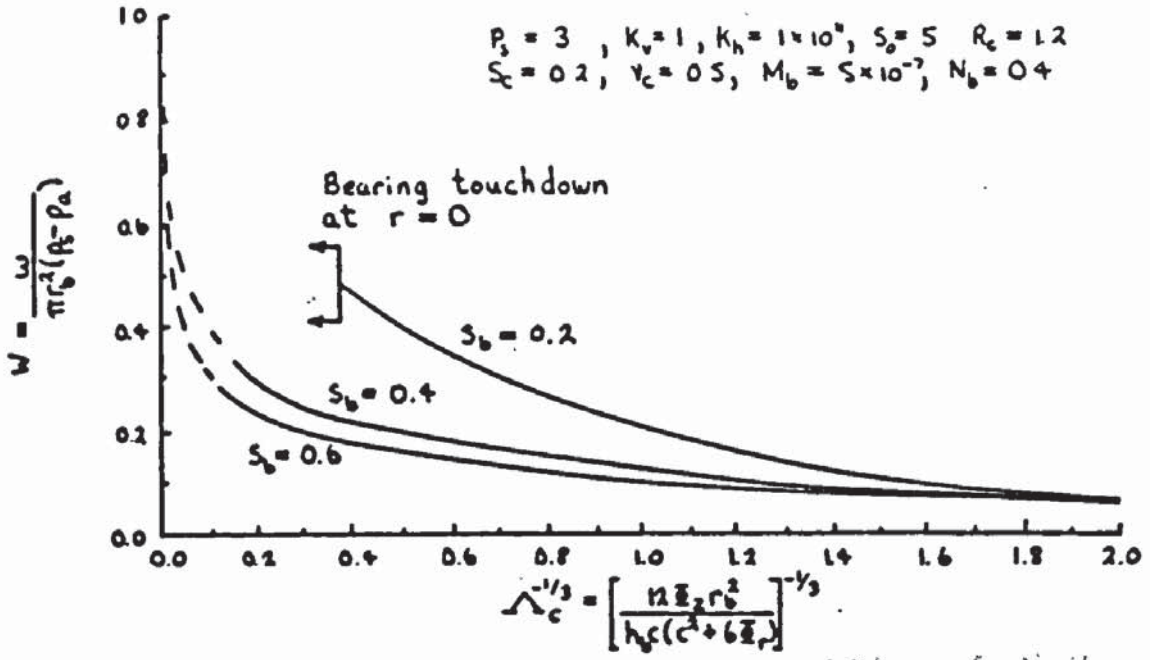

Figure 5.92 Load capacity versus bearing number for various porous pad aspect ratios

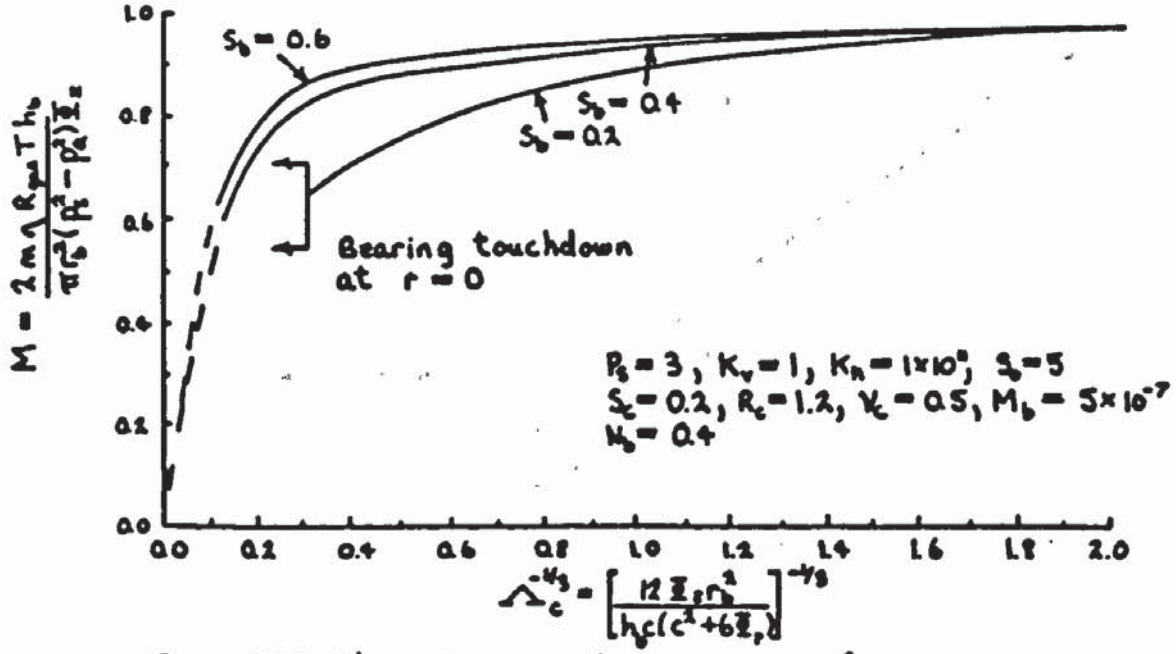

Figure 5.93 Flow rate versus bearing number for various porous pad aspect ratios

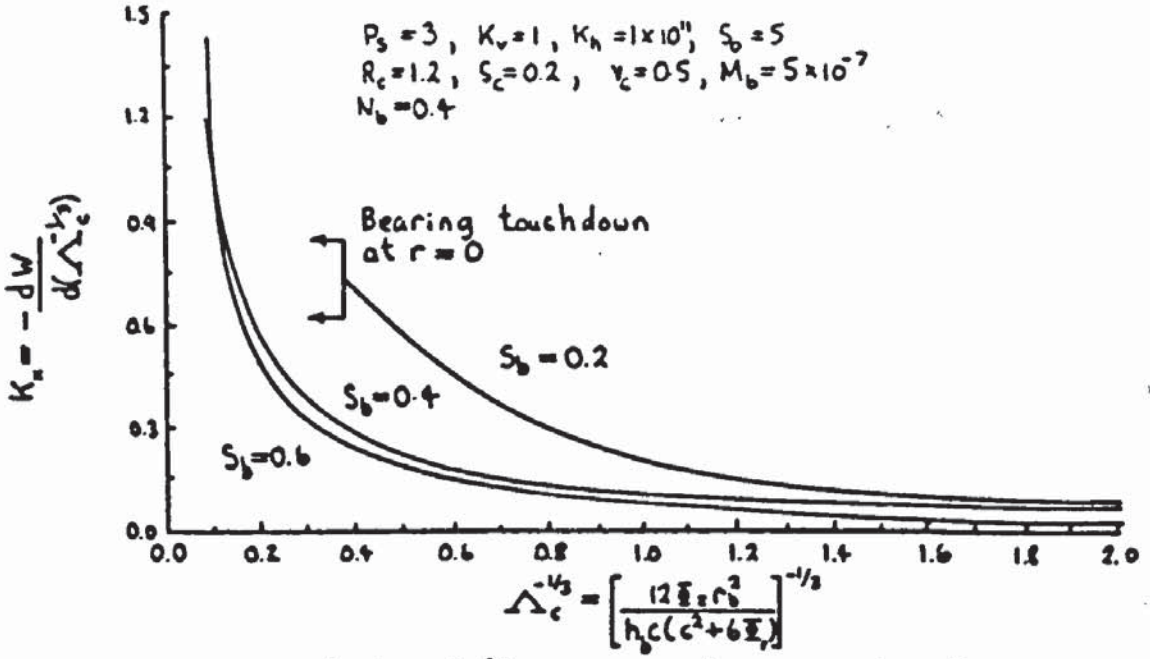

Figure 5.94 Static stiffness versus bearing number for various porous pad aspect ratios

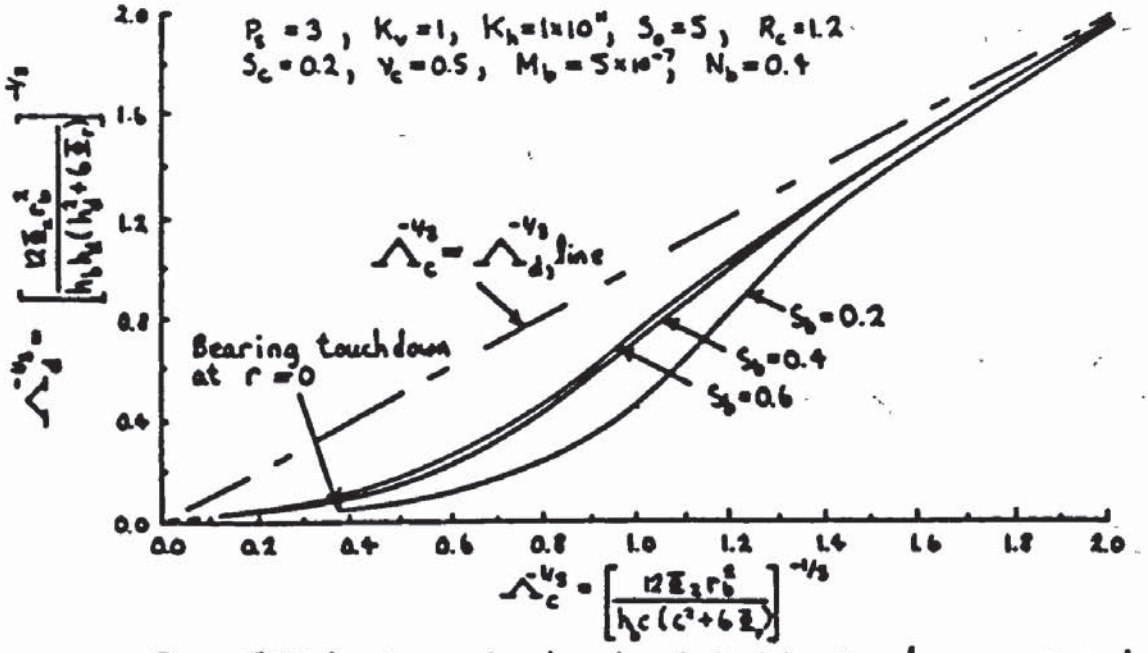

Figure 5.95 Bearing number based on derived bearing clearance versus bearing number based on bearing approach for various porous pad aspect ratios

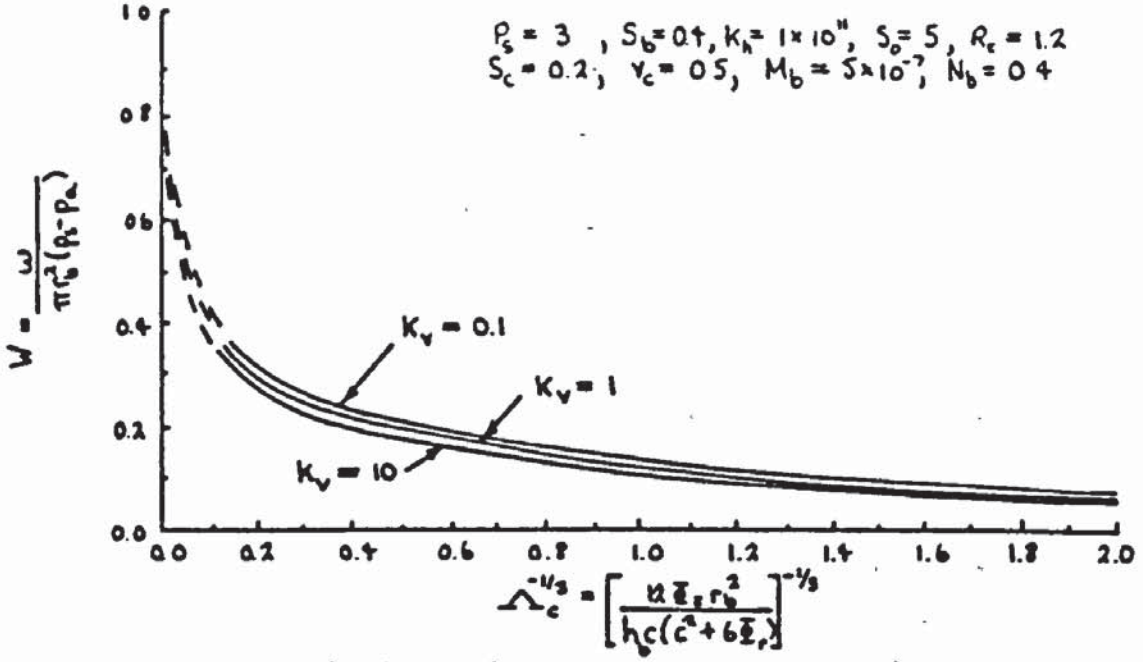

Figure 5.96 Load capacity versus bearing number for various porous pad permeability ratios

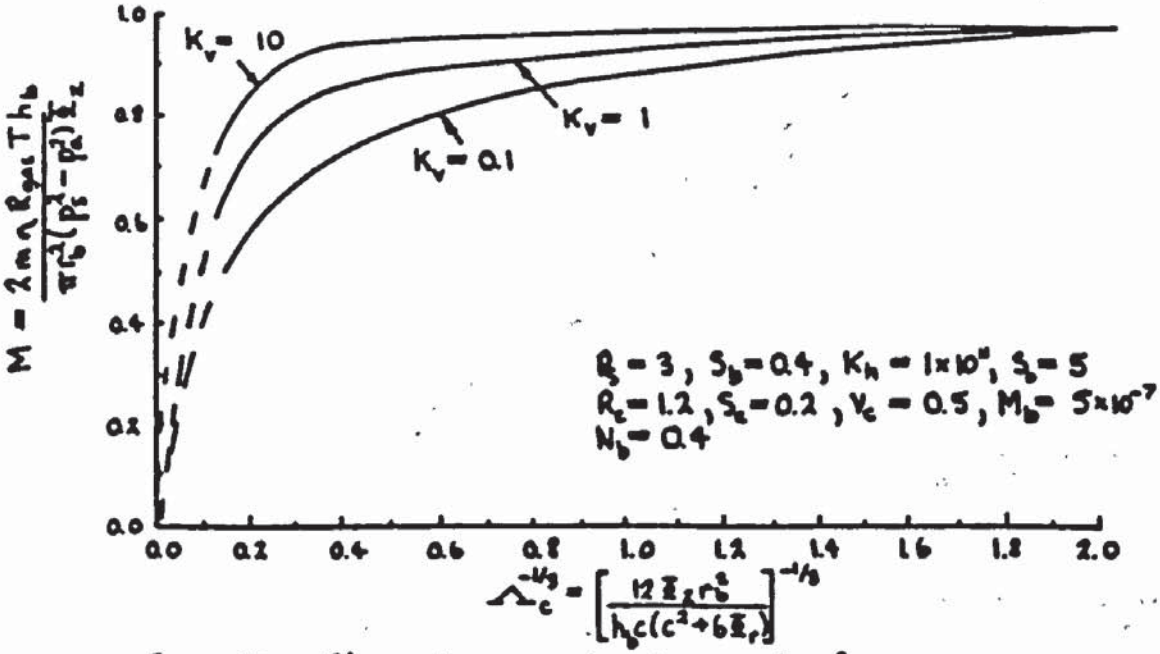

Figure 5.97 Flow rate versus bearing number for various porous pad permeability ratios

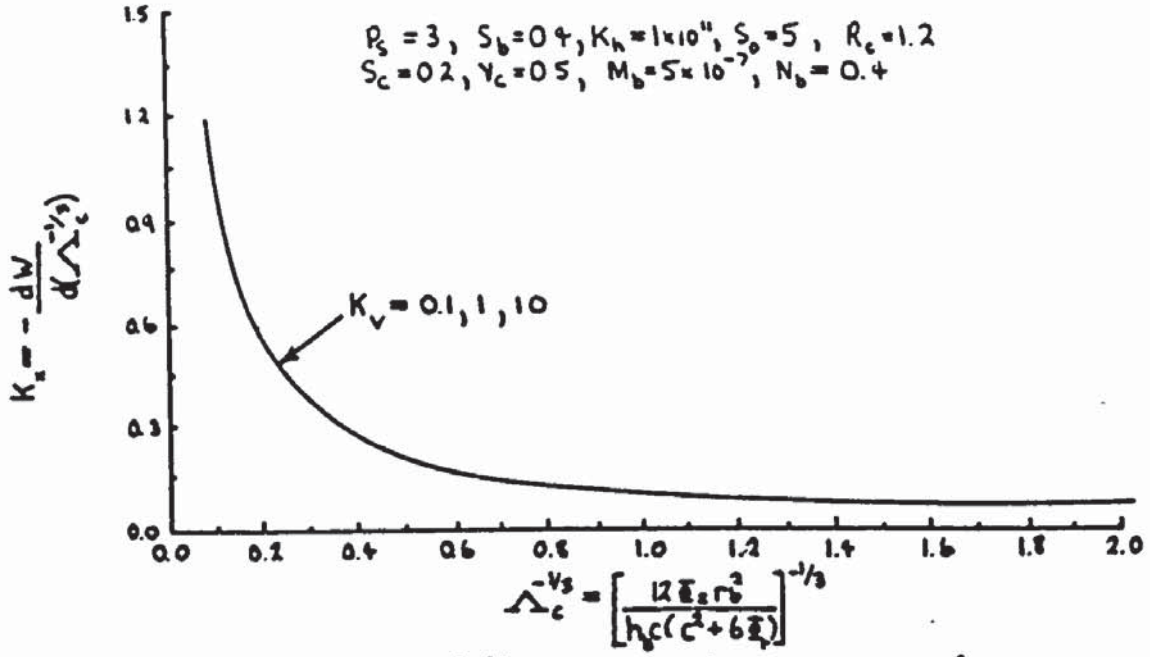

Figure 5.98 Static stiffness versus bearing number for various porous pad permeability ratios

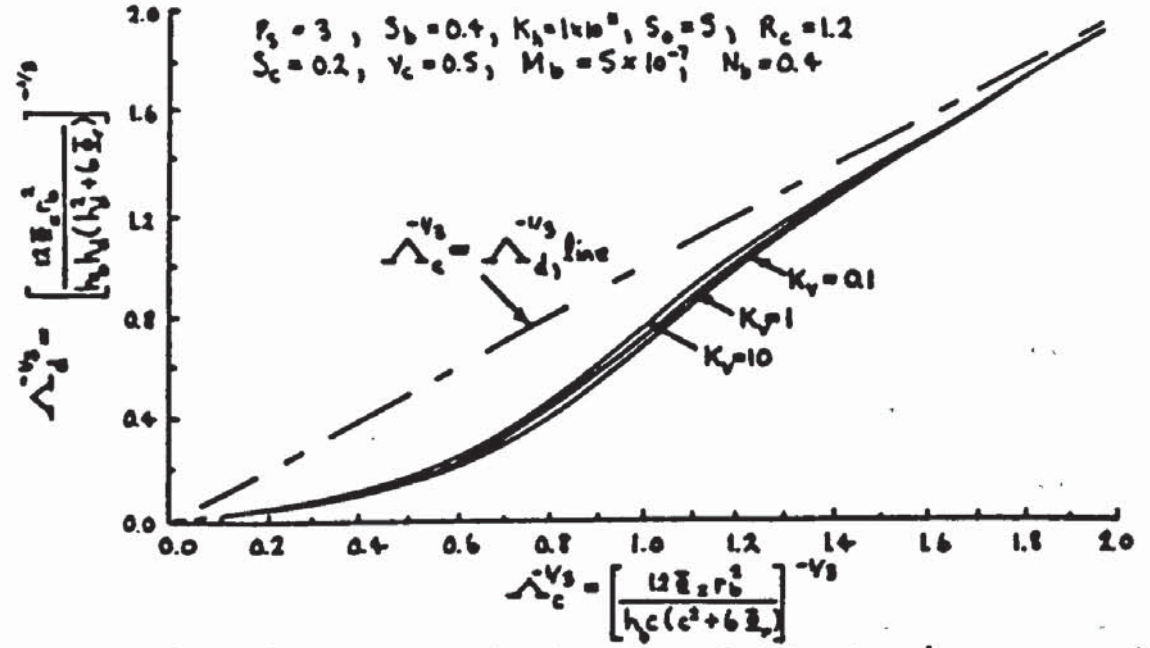

Figure 5.99 Bearing number based on derived bearing clearance versus bearing number based on bearing approach for varieas porous pad permeability ratios

CHAPTER 6

CONCLUSIONS

A mathematical model has been presented for the porous and compliant aerostatic thrust bearing configuration studied in this research project. The model includes a new simplified solution to the complex elasticity problem of the elastomer layer arising due to the incompressible nature of soft rubber like materials. This simplified solution has been shown to give accurate theoretical performance predictions when applied to a compliant thrust bearing supplied with an incompressible lubricant through a central feed hole and results compared with the more elaborate solutions of Castelli et al (59) and Benjamin et al (62). The model also includes analysis for the deflections of the porous pad in bending which take into account the flexibility of the porous pad support. Two new properties known as magnitude and shape constants, M_b and N_b respectively, have been introduced for the porous pad rigidity. These replace the modulus of rigidity D_b, Poisson's ratio ν_b and stiffness K_b of the porous pad support. The values of both constants M_b and N_b are accurately determinable from measurements of porous pad deflections in bending.

Theoretical predictions using this mathematical model have been verified by experimental results obtained from

tests on the porous and compliant aerostatic thrust bearing. These results and predictions both show that the performance of the porous and compliant aerostatic thrust bearing is reduced by increasing compliance of the elastomer layer causing a reduction in load capacity W and increases in flow rate M. This discovery is completely contradictory to that expected at the beginning of the research project and is attributed to the effect of the porous pad as a restriction on supply to the bearing film clearance. In published work on compliant thrust bearings with a central feed hole and inherent compensation results have shown increases in load capacity for a given port pressure. This is due to the recess formed in the bearing clearance by deflections of the compliant surface giving rise to more uniform film pressures. However this recess also results in an increase in flow rate through the bearing because the mean bearing clearance has increased. In the porous and compliant aerostatic thrust bearing this increase in flow rate causes a greater pressure drop across the porous pad. The result is a reduction in magnitude of the film pressures for a given supply pressure and a reduction in bearing load capacity W even though the film pressures have a more uniform profile.

Experimental results show that the elastomer layer compliance increases with increases in its thickness and reductions in hardness value. Theoretical predictions also show an increase in elastomer layer compliance with

reducing Poisson's ratio ν_c &shear modulus G_c.

In comparisons between the porous and compliant aerostatic thrust bearing and a more conventional porous aerostatic thrust bearing (both having elastic porous pads) the latter has improved performance of increased load capacity W and reduced flow rate M. As the compliance of the elastomer layer in the former bearing reduces its performance approaches that of the porous aerostatic thrust bearing.

While increasing compliance of the elastomer layer in the porous and compliant aerostatic thrust bearing reduces its performance, a recovery can occur with reducing porous pad rigidity in bending. This is because deflections of the porous pad in bending increase in relation to deflections of the compliant surface and the recess formed in the bearing clearance is reduced. However if deflections of the porous pad exceed those of the compliant surface then premature bearing touchdown will occur at r = 0, reducing the potential bearing performance.

It is shown that the porous and compliant aerostatic thrust bearing performance improves with increasing values of the magnitude constant M_b (for the porous pad rigidity) and hence increasing porous pad deflections, provided bearing touchdown does not occur at r = 0. However the shape constant N_b, which reflects the shape of resulting porous pad deflections, is shown to have a small effect on the bearing performance compared to M_b.

In porous and compliant aerostatic thrust bearings it is necessary to consider changes in the bearing clearance geometry at constant bearing number Λ_c . Apart from the elastic properties of the elastomer layer and the rigidity properties of the porous pad it is shown that the bearing clearance geometry is also affected by the non - dimensional ratio $K = r_b^2/\Phi_r$. Results show improvements in bearing performance with reducing values of K_h.

For the range of bearing numbers Λ_c covered in experimental bearing tests, the theoretically predicted static stiffness of the porous and compliant aerostatic thrust bearing is less than that of a porous aerostatic thrust bearing due to compression of the elastomer layer. Although theory predicts a steep rise in static stiffness for the former bearing at low bearing numbers Λ_c when the elastomer layer extent $R_c > 1.2$, this is at a bearing number Λ_c below the range covered in the experimental bearing tests.

CHAPTER 7

FUTURE WORK

7.1 UNCOMPLETED AREAS OF INVESTIGATION

At the beginning of this research project a list of the areas of investigation was made out in section 2.3. Due to shortage of time it has not been possible to complete this list and therefore the following may be considered for a future research project:

(a) The performance of the porous and compliant aerostatic thrust bearing presented in this research project was compared to that of a more conventional porous aerostatic thrust bearing. No comparisons of performance have been made with that of a compliant aerostatic thrust bearing having a central feed hole. This is because published work on this type of bearing are for inherent compensation only with no form of restrictor between the supply and the bearing clearance. It has been shown in this research project that the effect of the porous pad on the performance of the porous and compliant aerostatic thrust bearing, results in a reduction of the bearing performance. An extension to this work would be to look at different forms of restrictor such as capillary and orifice compensation, on the performance of a compliant aerostatic thrust with a central feed hole.

(b) In the current research project the porous pads were epoxied into their holders. Due to strength limitations this reduced the maximum pressure difference the porous pads could withstand before breaking out of their holders. As a result of this it was not possible to measure the porous pad permeability at higher flow rates where inertia losses become significant. Therefore it was not possible to verify the existence of separate regions of flow i.e. viscous, transitional and inertial, put forward by Taylor and Lewis (9). Also the criteria of McGrea and Donaldson (10) for these flows could not be tested.

If large porous pads, i.e. 100mm diameter or greater, are to be used in future research projects a stronger method of supporting the porous pads in their holders should be considered. Two possible alternative methods for supporting the porous pads are shown in figure 7.1. The thread method (a) was used by Donaldson and Patterson (31,32) and they encountered problems in sealing the porous pads along the thread line using epoxy. However the advantage of this method is that the thread itself can be made small in comparison to the porous pad radius such that it has negligible effect on flow through the porous pad along the boundary $r = r_b$, $z = 0$ to h_b. The same boundary conditions for the lubrication equations in section 3.2.5 can therefore be used. In the clamping method (b) the porous pads are sealed with epoxy around their circumference and this is allowed to cure first before

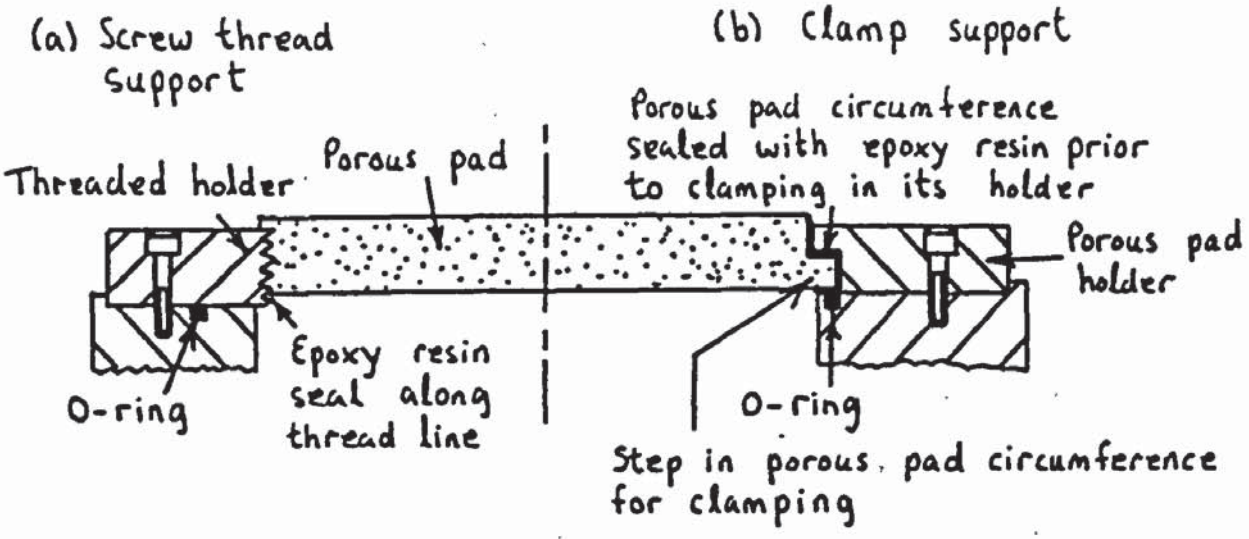

Figure 7.1 Two alternative methods of supporting the porous pad

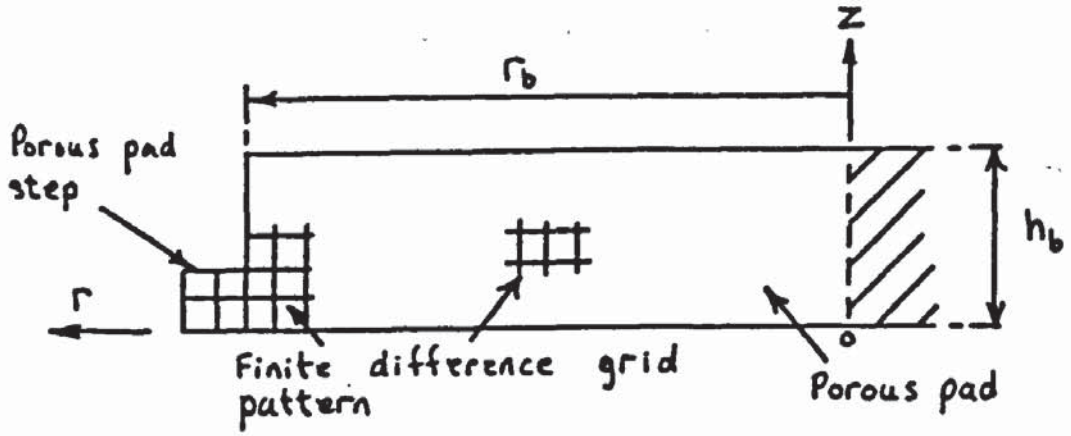

Figure 7.2 Finite difference grid pattern for a porous pad having a step around its circumference

clamping in the pad holder. This allows the porous pads to be interchanged without the need for separate holders with each porous pad. The disadvantage with this method is that if a large step is machined into the porous pad around its circumference this may affect the flow through the porous pad. In this case it will be necessary to modify the boundary conditions used in section 3.2.5 for the lubrication equations so that the discontinuity along the boundary $r = r_b, z = 0$ to h_b is accounted for. The finite difference grid pattern for a solution to the lubrication equations, will need to extend into the porous pad step as shown in figure 7.2.

(c) In this research project all porous pads were bonded to their holders using epoxy which forms a flexible support. Other types of support for example that shown in figure 7.1 (b) may be considerably stiffer in bending and support the porous pad more rigidly. In a future research project the effects of various types of porous pad support stiffness could be studied in greater depth. The stiffness of the porous pad support would have a greater influence on its resulting deflection with reducing porous pad thickness and porous pad material stiffness (such as porous plastic).

(d) Experimental work on the stability of porous aerostatic thrust bearings still remains to be done. Although several researchers have published theoretical work (39 to 44) on the stability and dynamic performance of these bearings there is very little in the way of experimental

verification of this work.

For compliant aerostatic thrust bearings with a central feed hole, Lowe (71,72) presents stability maps showing stable and unstable operating regions. These were obtained from experimental observations. As far as the author is aware there has been no theoretical work on the stability of these bearings.

7.2 NEW AREAS OF INVESTIGATION

The discoveries made in this research project open up possible new areas of investigation. These along with other types of bearing are discussed as follows:

7.2.1 POROUS AND COMPLIANT AEROSTATIC THRUST BEARING WITH A POROUS PLASTIC PAD

In chapters 5 and 6 it was described how the recess formed in the bearing clearance by deflections of the compliant surface, reduced the performance of a porous and compliant aerostatic thrust bearing. However this recess can be reduced by deflections of the porous pad in bending giving rise to a recovery in lost bearing performance. It was shown that the bearing performance improved with reducing porous pad rigidity. Therefore use of a more flexible material for the pad such as porous plastic could be used to advantage in a porous and compliant aerostatic

thrust bearing.

For such a bearing achievement of optimum bearing performance would require carefull selection of elastomer layer properties i.e. hardness and thickness, to accommodate deflections of the porous pad and to avoid premature bearing touchdown at r = 0 (see figure 7.3). Note that deflections of the porous pad in bending could be controlled by allowing for adjustments in its support rigidity. For example in support method (b) shown in figure 7.1 for the porous pad, the clamping pressure could be adjusted at the allen screws. Untightening of these screws would reduce the rigidity of the porous pad support.

It is possible to obtain porous plastic known as Vyon from Porvair Ltd. (King's Lynn) in sheet form up to 20mm thickness.

7.2.2 POROUS AEROSTATIC THRUST BEARING WITH A FLEXIBLE MEMBRANE

Instead of using an elastomer layer, deflections of the porous pad could be accomodated using a flexible membrane similar to that used by Hayashi (82) for a circular thrust bearing with a central feed hole. The porous aerostatic thrust bearing with this membrane is shown in figure 7.4. For an all plastic bearing the membrane can be fabricated from a sheet of thin plastic. If a sealed chamber is constructed behind the membrain, its

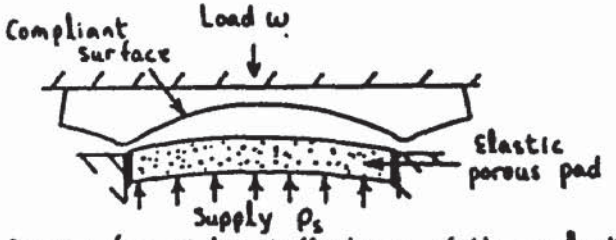

(a) Recess formed by deflections of the compliant surface reduces bearing performance; porous pad too rigid in bending

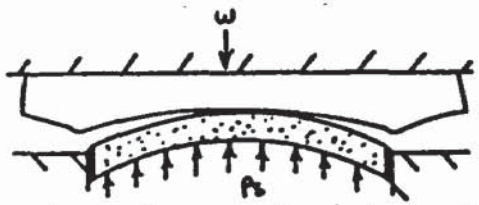

(b) Premature bearing touch down at r=0; porous pad too flexible in bending

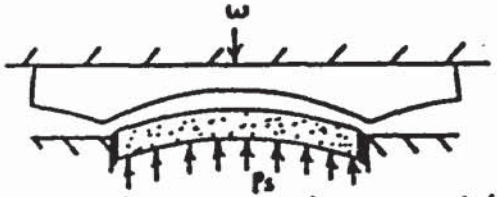

(c) Optimum bearing performance: deflections of the porous pad are of similar magnitude to those of the compliant surface recess

Figure 7.3 Optimizing the performance of a porous and compliant aerostatic thrust bearing with a flexible porous pad

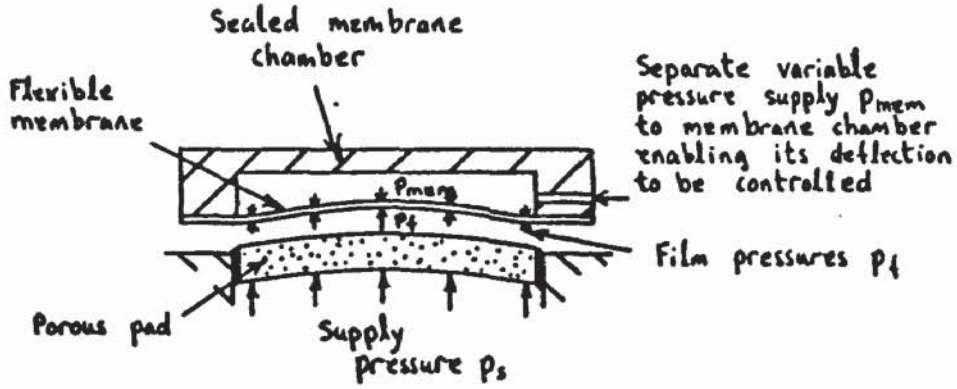

Figure 7.4 Porous aerostatic thrust bearing with elastic pad and flexible membrane

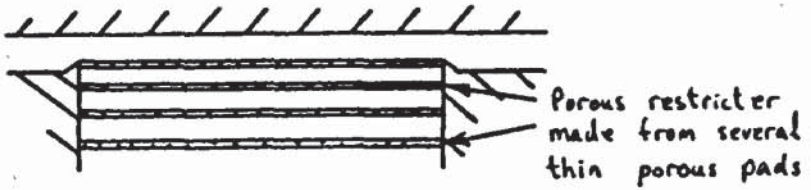

Figure 7.5 Arrangement of several thin porous pads in a porous aerostatic thrust bearing

deflection can be controlled using a separate variable pressure supply to this chamber. Deflection of the membrane due to film pressures can be reduced by increasing the chamber pressure. This would allow fine tuning of the bearing performance during its operation by matching deflections of the membrane with those of the porous pad.

7.2.3 BEARING CONTAINING A PAD MADE FROM SEVERAL THIN POROUS DISCS

There could be many potential applications for porous aerostatic thrust bearings which are larger then 100mm diameter. However manufacturers can supply large porous discs in thin sections only. For example Accumatic Engineering Ltd. (Wrexham) can supply porous discs up to 305 mm in diameter but only in thicknesses up to 3 mm.

The restriction to flow across a thin porous disc may not be sufficient to allow stable operation of a porous aerostatic thrust bearing. Also the resulting deflection of the porous disc in bending may be considerable. To overcome these problems the porous pad could be made from several thin porous discs which are parallel to each other as shown in figure 7.5. The total restriction to flow through the pad would be equal to the summation of pressure drops across each thin porous disc. Because the pressure drop across each thin disc is only a fraction of the total pressure drop across the whole porous pad, their

deflections in bending are reduced.

APPENDIX 1

COMPUTER PROGRAMME FOR THE ANALYTIC SOLUTION TO THE LUBRICATION EQUATIONS OF JONES ET AL (23)

The analytic solution of Jones et al (23) for the special case of a uniform bearing clearance was presented in section 3.3.1. This solution gave the following equation for the bearing film pressures P_f^2 at radius R, in non - dimensional form;

$$P_f^2 = 1 + \frac{\Lambda_u.C_2.(R^2-1)}{4} + \Lambda_u \sum_{n=2}^{\infty} \lambda_n.C_{n2} \left(\frac{J_o(k_n)}{k_n^2} - J_o(k_n.R) \right) \cosh(\lambda_n) \quad \text{A1.1}$$

In equation A1.1 values of k_n are given by the roots of the equation;

$$J_1(k_n) = 0 \quad \text{A1.2}$$

Also expressions for λ_n , C_2 and C_{n2} are;

$$\lambda_n = k_n.S_b.\sqrt{K_v} \quad \text{A1.3}$$

$$C_2 = \frac{P_s^2 - 1}{\Lambda_u^2 \sum_{n=0}^{\infty} E_n - \frac{\Lambda_u}{8} - 1} \quad \text{A1.4}$$

$$C_n = \frac{\Lambda_u.C_2}{J_o(k_n).(k_n^2.\sinh(\lambda_n) + \Lambda_u.\lambda_n.\cosh(\lambda_n)} \quad \text{A1.5}$$

where in equation A1.4 for C_2;

$$E_n = \frac{\lambda_n}{k_n^2.(\Lambda_u.\lambda_n + k_n^2.\tanh(\lambda_n))} \quad \text{A1.6}$$

and in equations A1.1 to A1.6; n = 2,3,4 etc.

For a computer solution to equations A1.1 to A1.6 the roots k_n of equation A1.2 must be determined and the Bessel functions $J_o(k_n)$ and $J_o(k_n.R)$ must be evaluated. An asymptotic expression for k_n is given (90) as follows;

$$k_n = Y - \frac{0.375}{Y} + \frac{0.0234}{Y^3} - \frac{0.2303}{Y^5} + \frac{6.6784}{Y^7} - \text{etc.} \quad \text{A1.7}$$

where $$Y = (n + 0.25).\pi \quad \text{A1.8}$$

The first five terms shown in equation A1.7 give a value of k_n accurate to three decimal places. For the

Bessel function $J_o(X)$ where X is an arbitrary value, two expressions are given (90) as follows;

for $0 <= X <= 8$

$$J_o(X) = 1 - \frac{X^2}{2^2} + \frac{X^4}{2^2.4^2} - .... - \frac{X^{30}}{2^2.4^2....30^2} \qquad \text{A1.9}$$

and for $X > 8$

$$J_o(X) = \left(\frac{2}{\pi.X}\right)^{1/2}. (\sin(X + 0.25\pi) + \frac{1}{8.X}.(\sin(X - 0.25\pi))) \qquad \text{A1.10}$$

The combined use of equations A1.9 and A1.10 gives an accuracy for $J_o(X)$ to less than 0.1%. For the evaluation of $J_o(k_n)$ and $J_o(k_n.R)$, X is replaced with k_n and $k_n.R$ respectively in equations A1.9 and A1.10.

A flowchart for the computer solution to eqaution A1.1 is shown in figure A1.1. Included at the end of this appendix is a copy of the programme written in BASIC language for the HP9845 desktop mini computer.

The programme starts with an input of the bearing parameters Λ_u, P_s, S_b and K_v in non - dimensional form together with a value Q which must be an integer greater than 2. This value Q equals the maximum value of n in equations A1.1 to A1.6. The larger Q is the more accurate the computed solution to equation A1.1 will be. Note however the computational time also increases with Q. For n = 2 to Q values of k_n, λ_n and E_n are calculated using equations A1.7, A1.3 and A1.6 respectively. From these values C_2 and C_{n2} are obtained using equations A1.4 and A1.5 where the Bessel functions $J_o(k_n)$ in equation A1.5 are evaluated using equations A1.9 and A1.10. Note that there is only one value of C_2 while there is a value of C_{n2} for each value of n from 2 to Q. Finally the film pressure P_f^2 are obtained using equation A1.1 by substituting C_2 and values of λ_n, k_n, $J_o(k_n)$ and C_{n2} for n = 2 to Q. However prior to this it is necessary to select positions R at which P_f^2 is required. In the programme R = 0,0.1,0.2,....1 is selected and for each value of R, $J_o(k_n.R)$ is obtained using equations A1.9 and A1.10. Equation A1.1 is evaluated at each radial position R to give a film pressure profile P_f^2.

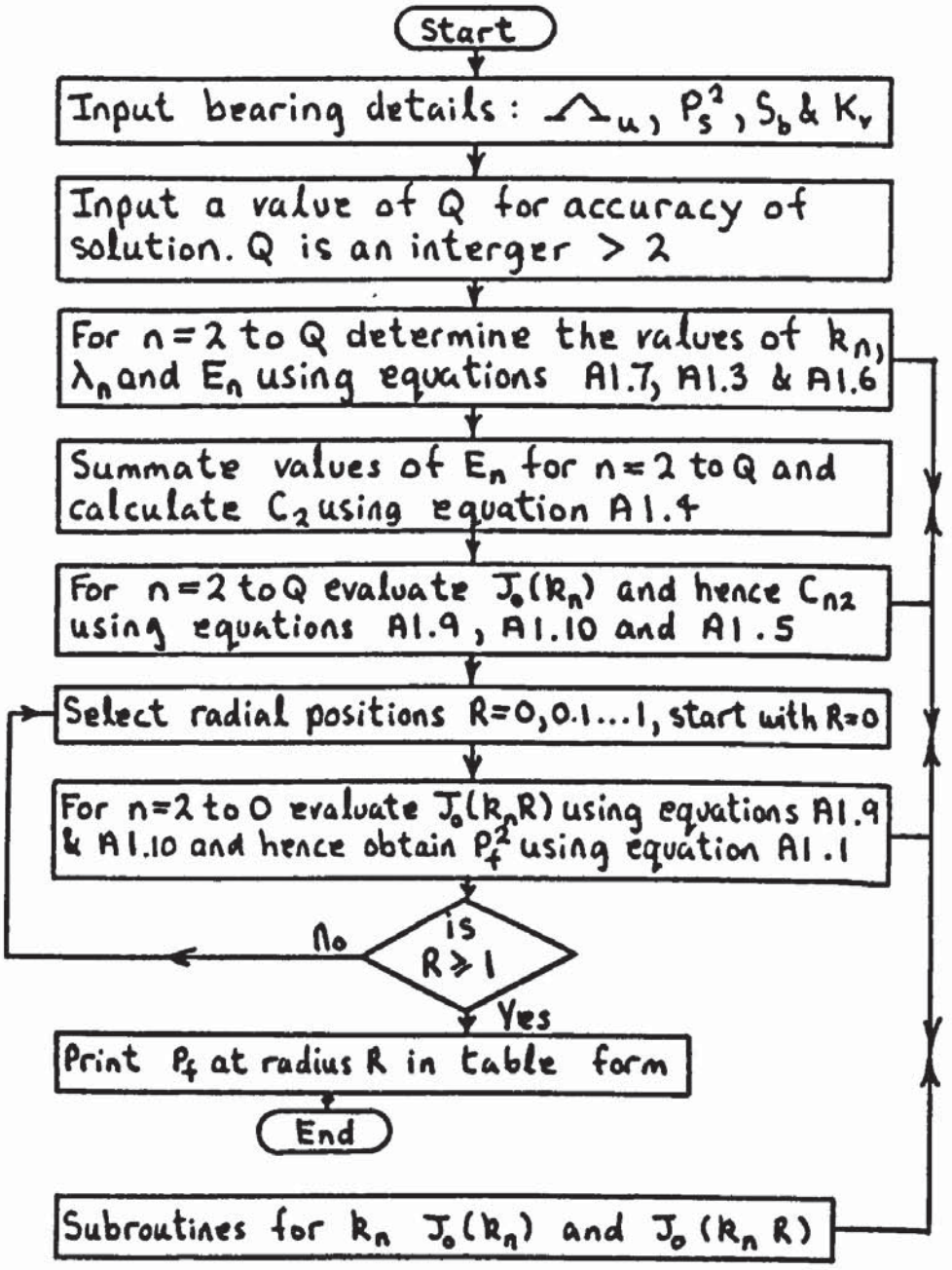

Figure: A1.1 Flow chart for computer solution to equation A1.1 from analysis by Jones et al (23)

```
10  DIM Kn(200),En(200),F(20),Jo(200,2),D(200),U(20,200),P(20),R(20)
110 REM "VALUE OF Q SELECTED FOR DESIRED ACCURACY"
210 REM "Bn=BEARING NUMBER"
310 REM "A=DIMENSIONLESS SUPPLY PRESSURE SQUARED"
410 REM "S=BEARING ASPECT RATIO"
510 REM "k=RATIO OF RADIAL PERM TO AXIAL PEPM"
610 PRINT "Q="
710 INPUT Q
810 PRINT "Bn="
910 INPUT Bn
1010 PRINT "(Ps/Pa)^2="
1110 INPUT A
1210 PRINT "S="
1310 INPUT S
1410 PRINT "Vr/Vy="
1510 INPUT K
1610 B=S*K^(1/2)
1710 REM "DETERMINE ROOTS OF J1=0"
1810 N=1
1910 E(0)=0
2010 GOSUB 8610
2110 D(N)=B*Kn(N)
2210 T=EXP(2*D(N))
2310 T=(T-1)/(T+1)
2410 REM "T=Tanh(D(N))"
2510 En(N)=D(N)/((Bn*D(N)+Kn(N)^2*T)*Kn(N)^2)
2610 En(N)=En(N)+En(N-1)
2710 IF N>Q THEN 3010
2810 N=N+1
2910 GOTO 2010
3010 C(2)=(A-1)/(Bn^2*En(N)-Bn/8-1)
3110 FOR I=1 TO 10
3210 R(I)=(I-1)/10
3310 U(I,0)=0
3410 F(I)=Bn*C(2)*(R(I)^2-1)/4
3510 N=1
3610 L=1
3710 IF Kn(N)=0 THEN 3910
3810 GOTO 4310
3910 GOSUB 8610
4010 D(N)=B*Kn(N)
4110 REM "DETERMINE Jo's"
4210 REM "Jo(N,1)=Jo(Kn) and Jo(N,2)=Jo(Kn*R)"
4310 IF Jo(N,1)=0 THEN 4510
4410 GOTO 5010
4510 M=Kn(N)
4610 IF M<=8 THEN 4910
4710 GOSUB 9110
4810 GOTO 5010
4910 GOSUB 9510
5010 L=L+1
5110 M=Kn(N)*R(I)
5210 IF L>2 THEN 5410
5310 GOTO 4610
5410 Sh=EXP(D(N))
5510 Ch=(Sh+1/Sh)/2
5610 Sh=(Sh-1/Sh)/2
5710 REM "Sh=Sinh(D(N)) &Ch=Cosh(D(N))"
5810 Cn(2)=Bn*C(2)/(Jo(N,1)*(Kn(N)^2*Sh+Bn*D(N)*Ch))
5910 U(I,N)=Bn*Cn(2)*D(N)*(Jo(N,1)-Jo(N,2))*Ch/Kn(N)^2
6010 U(I,N)=U(I,N-1)+U(I,N)
6110 IF N>Q THEN 6510
6210 N=N+1
6310 GOTO 3610
6410 REM "HENCE THE DIMENSIONLESS FILM PRESSURE IS!"
6510 P(I)=(1+F(I)+U(I,N))^(1/2)
6610 NEXT I
6710 REM "PRINTER IS 0"
6810 PRINT "DIMENSIONLESS FILM PRESSURE=P"
6910 PRINT "DIMENSIONLESS RADIUS=R"
7010 PRINT TAB(6);"P";TAB(21);"R"
7110 P(11)=1
7210 R(11)=1
7310 FOR I=1 TO 11
7410 PRINT P(I);TAB(20);R(I)
7510 NEXT I
7610 REM "DETERMINE DIMENSIONLESS BEARING LOAD CAPACITY"
7710 REM "USING SIMPSONS RULE"
7810 FOR I=1 TO 11
7910 P(I)=P(I)-1
8010 NEXT I
```

```
8110  W=2*.1*(P(1)*R(1)+4*P(2)*P(2)+2*P(3)*R(3)+4*P(4)*R(4)+2*P(5)*P(5)+4*P(6)*R
(6)+2*P(7)*R(7)+4*P(8)*R(8)+2*P(9)*R(9)+4*P(10)*R(10)+P(11)*R(11))
8210 PRINT "_"
8310 PRINT "W=",W/(3*(A^(1/2)-1))
8410 END
8510 REM "SUBROUTINE FOR ROOTS OF J1=0"
8610 Y=(N+.25)*PI
8710 Kn(N)=Y-.375/Y+.0234/Y^3-.2303/Y^5+6.6784/Y^7
8810 RETURN
8910 REM "SUBROUTINE TO DETERMINE VALUE OF Jo's"
9010 REM "WHEN M>8"
9110 Jo(N,L)=(2/(PI*M))^(1/2)*(SIN(M+.25*PI)+1/(8*M)*SIN(M-.25*PI))
9210 RETURN
9310 REM "SUBROUTINE TO DETERMINE VALUE OF Jo's"
9410 REM "WHEN M<=8"
9510 Ab=1-M^2/4+M^4/64-M^6/2304+M^8/147456-M^10/14745600+M^12/2.12336E9
9610 Bc=-M^14/4.16179E11+M^16/1.06542E14-M^18/3.45196E16+M^20/1.38078E19
9710 Cd=-M^22/6.68267E21+M^24/3.84939E24-M^26/2.60219E27+M^28/2.04011E30
9810 De=-M^30/1.8361E33
9910 Jo(N,L)=Ab+Bc+Cd+De
10010 RETURN
```

APPENDIX 2

ELEMENTARY SOLUTION TO DEFLECTIONS OF THE ELASTOMER LAYER AND ITS COMPLIANT SURFACE

For the equilibrium of stresses in a radial direction (85) and an axisymmetric problem;

$$\frac{\partial \sigma_r}{\partial r} + \frac{\partial \tau_{rz}}{\partial z} + \frac{\sigma_r - \sigma_\theta}{r} = 0 \qquad \text{A2.1}$$

Stress - strain relationships (85) for a linear - elastic isotropic material may be written in the form;

$$\tau_{rz} = \gamma_{rz} . G_c \qquad \text{A2.2}$$

$$\sigma_\theta = \frac{1}{(1 - \nu_c^2)} . (E_c(\varepsilon_\theta + \nu_c . \varepsilon_r) + \sigma_z . \nu_c . (\nu_c + 1)) \qquad \text{A2.3}$$

$$\sigma_r = \frac{1}{(1 - \nu_c^2)} . (E_c(\varepsilon_r + \nu_c . \varepsilon_\theta) + \sigma_z . \nu_c . (\nu_c + 1)) \qquad \text{A2.4}$$

$$\text{where } E_c = 2 . G_c . (1 + \nu_c) \qquad \text{A2.5}$$

Strains are related to displacements by the following equations (85);

$$\varepsilon_r = \frac{\partial u_r}{\partial r} \qquad \text{A2.6}$$

$$\varepsilon_\theta = \frac{u_r}{r} \qquad \text{A2.7}$$

$$\gamma_{rz} = \frac{\partial u_r}{\partial z} + \frac{\partial u_z}{\partial r} \qquad \text{A2.8}$$

Applying assumptions (iv) and (v) of section 3.4.4;

$$u_r = u_{rn} . \left(1 - \frac{(z - t_c)^2}{t_c^2} \right) \qquad \text{A2.9}$$

and equation A2.8 becomes;

$$\gamma_{rz} = \frac{\partial u_r}{\partial z} \qquad \text{A2.10}$$

Substituting for u_r in equation A2.6, A2.7 and A2.10 using equation A2.9 and eliminating ε_r, ε_θ and γ_{rz} in equations A2.2 to A2.4 gives;

$$\tau_{rz} = G_c \cdot \left(1 - \frac{(z - t_c)^2}{t_c^2}\right) \frac{\partial u_{rn}}{\partial z} \qquad \text{A2.11}$$

$$\sigma_\theta = \frac{1}{(1 - \nu_c^2)} \cdot \left(E_c \cdot \left(\frac{u_{rn}}{r} + \nu_c \cdot \frac{\partial u_{rn}}{\partial r} \right) \cdot \left(1 - \frac{(z - t_c)^2}{t_c^2} \right) + \sigma_z \cdot \nu_c (\nu_c + 1) \right) \qquad \text{A2.12}$$

$$\sigma_r = \frac{1}{(1 - \nu_c^2)} \cdot \left(E_c \left(\frac{\partial u_{rn}}{\partial r} + \nu_c \cdot \frac{u_{rn}}{r} \right) \cdot \left(1 - \frac{(z - t_c)^2}{t_c^2} \right) + \sigma_z \cdot \nu_c \cdot (\nu_c + 1) \right) \qquad \text{A2.13}$$

Hence from equations A2.11 to A2.13;

$$\frac{\sigma_r - \sigma_\theta}{r} = \frac{E_c}{(1 + \nu_c) \cdot r} \cdot \left(1 - \frac{(z - t_c)^2}{t_c^2}\right) \cdot \left(\frac{\partial u_{rn}}{\partial r} - \frac{u_{rn}}{r} \right) \qquad \text{A2.14}$$

$$\frac{\partial \sigma_r}{\partial r} = \frac{E_c}{(1 - \nu_c^2)} \cdot \left(1 - \frac{(z - t_c)^2}{t_c^2}\right) \left(\frac{\partial^2 u_{rn}}{\partial r^2} + \nu_c \cdot \frac{\partial}{\partial r} \left(\frac{u_{rn}}{r} \right) \right) + \left(\frac{\nu_c}{(1 - \nu_c)} \right) \frac{\partial \sigma_z}{\partial r} \qquad \text{A2.15}$$

$$\text{and} \quad \frac{\partial \tau_{rz}}{\partial z} = - \frac{2 . G_c . u_{rn}}{t_c^2} \qquad \text{A2.16}$$

A differential equation for radial displacements u_{rn} can be obtained by substituting $z = t_c$ in equations A2.14 to A2.16 and substituting the results into equation A2.1, i.e.;

$$\frac{\partial u_{rn}^2}{\partial r^2} + \frac{1}{r} \cdot \frac{\partial u_{rn}}{\partial r} - \left(k_c^2 + \frac{1}{r^2} \right) . u_{rn} = \frac{\nu_c}{2 . G_c} \cdot \frac{\partial p_c}{\partial r} \qquad \text{A2.17}$$

$$\text{where} \quad k_c = \frac{1}{t_c} \times \sqrt{1 - \nu_c}$$

Equation A2.17 satisfies the equilibrium of stresses in a radial direction within the elastomer layer. Therefore by assumption (ii) in section 3.4.4 a solution to this equation will give deflections of the elastomer layer at $z = t_c$. Hence using modified Bessel functions (90) the particular integral to equation A2.17 is;

$$u_{rn} = A_n.I_1(k_c.r) + B_n.K_1(k_c.r) \qquad \text{A2.18}$$

A complimentary function (c.f.) to equation A2.17 may be obtained for the following two elementary cases;

(i) $p_c = p_n$ (uniform pressure profile)

$$\text{c.f.} = 0 \qquad \text{A2.19}$$

(ii) $p_c = p_n.(1 - (r/r_n)^2)$ (parabolic pressure profile)

$$\text{c.f.} = \frac{2.\nu_c.p_n.t_c^2.r}{G_c.r_n^2} \qquad \text{A2.20}$$

The complete solution to equation A2.17 may be expressed as;

$$u_{rn} = A_n.I_1(k_c.r) + B_nK_1(k_c.r) + C_n.r \qquad \text{A2.21}$$

where $C_n = 0$ for a uniform pressure profile,

and $C_n = \frac{2.\nu_c.p_n.t_c^2}{G_c.r_n^2}$ for a parabolic pressure profile.

The constants A_n and B_n in equation A2.21 may be determined from the boundary conditions given in section 3.4.4 by equations 3.70 and 3.71. These are;

$$u_{rn} = 0 \text{ at } r = 0 \qquad \text{A2.22}$$

$$\text{and } \sigma_r = 0 \text{ at } r = r_c \qquad \text{A2.23}$$

However in the more general case of a pressure profile of radius r_n where $r_n <= r_c$ equation A2.21 is applied in two regions; $0 <= r <= r_n$ and $r_n < r <= r_c$ (see figure 3.4 of section 3.4.4). Equation A2.21 can be written as follows;

$$u_{rn} = A_{n1}.I_1(k_c.r) + B_{n1}.K_1(k_c.r) + C_n.r \quad \text{for } 0 \leq r \leq r_n \qquad \text{A2.24}$$

and $$u_{rn} = A_{n2}.I_1(k_c.r) + B_{n2}.K_1(k_c.r) \qquad \text{for } r_n < r \leq r_c \quad \text{A2.25}$$

Note that in equation A2.25 the third term on the R.H.S. of equation A2.21 has been omitted . This is because for $r > r_n$, $p_c = 0$ (see figure 3.4 of section 3.4.4) and therefore in equation A2.21, $C_n = 0$.

The constants A_{n1} , A_{n2} , B_{n1} and B_{n2} must satisfy the boundary conditions and also continuity of radial deflection u_{rn} and stress σ_r at $r = r_n$. Let the boundary conditions A2.22 and A2.23 be changed to;

$$u_{rn} = 0 \text{ at } r = r_{fh} \qquad \text{A2.26}$$

and $$\sigma_r = 0 \text{ at } r = r_c \qquad \text{A2.27}$$

Note that it is important to consider the application of this elementary solution to bearings types such as compliant thrust bearing having a central feed hole. And because in these bearings the central feed hole may pass through the elastomer layer (61,62) (see figure A3.1 of appendix 3) the boundary condition given by equation A2.26 has been introduced. In cases where a feed hole does not pass through the elastomer layer, then $r_{fh} = 0$ and equation A2.26 reduces to A2.22.

For continuity in the elastomer layer at $r = r_n$ let;

$$u_{rn} = u'_{rn} \text{ at } r = r_n \qquad \text{A2.28}$$

and $$\sigma_r = \sigma'_{rn} \text{ at } r = r_n \qquad \text{A2.29}$$

Expressions for A_{n1} , A_{n2} , B_{n1} and B_{n2} can now be obtained as follows. Applying equation A2.26 to equation A2.24 gives;

$$0 = A_{n1}.I_1(k_c.r_{fh}) + B_{n1}.K_1(k_c.r_{fh}) + C_n.r_{fh} \qquad \text{A2.30}$$

from equations A2.28 and A2.24;

$$u'_{rn} = A_{n1}.I_1(k_c.r_n) + B_{n1}.K_1(k_c.r_n) + C_n.r_n \qquad \text{A2.31}$$

from equations A2.28 and A2.25;

$$u'_{rn} = A_{n2}.I_1(k_c.r_n) + B_{n2}.K_1(k_c.r_n) \qquad \text{A2.32}$$

Equating A2.31 and A2.32 to eliminate u'_{rn} gives;

$$0 = (A_{n1} - A_{n2}).I_1(k_c.r_n) + (B_{n1} - B_{n2}).K_1(k_c.r_n) + C_n.r_n \qquad \text{A2.33}$$

Equation A2.33 satisfies equation A2.28. To satify equation A2.29, equation A2.13 must be used together with equations A2.24 and A2.25. Substituting for E_c using equation A2.5 and at $z = t_c$ equation A2.13 may be written;

$$\sigma_r = \frac{2.G_c}{(1-\nu_c)}.\left(\frac{\partial u_{rn}}{\partial r} + \nu_c.\frac{u_{rn}}{r}\right) + \frac{\sigma_z.\nu_c}{(1-\nu_c)} \qquad \text{A2.34}$$

Substituting equation A2.24 into A2.34 and at $r = r_n$;

$$\sigma'_{rn} = \frac{2.G_c}{(1-\nu_c)}.\left(A_{n1}\left(k_c.I_0(k_c.r_n) - \frac{I_1(k_c.r_n)}{2.r_n}\right) - B_{n1}.\left(k_c.K_0(k_c.r_n) + \frac{K_1(k_c.r_n)}{2.r_n}\right) + \frac{3}{2}.C_n\right) - \frac{\nu_c}{(1-\nu_c)}.p_{rn} \qquad \text{A2.35}$$

Where p_{rn} is the pressure acting on the compliant surface of the elastomer layer at $r = r_n$. Its value is equal to p_n for the uniform pressure profile case and zero for the parabolic pressure profile case.

Similarly substituting equation A2.25 into A2.34 gives;

$$\sigma'_{rn} = \frac{2.G_c}{(1-\nu_c)}.\left(A_{n2}.\left(k_c.I_0(k_c.r_n) - \frac{I_1(k_c.r_n)}{2.r_n}\right) - B_{n2}.\left(k_c.K_0(k_c.r_n) + \frac{K_1(k_c.r_n)}{2.r_n}\right)\right) \qquad \text{A2.36}$$

Equating A2.35 and A2.36 to eliminate σ'_{rn} gives;

$$0 = \frac{2.G_c}{(1-\nu_c)}.\left((A_{n1} - A_{n2}).\left(k_c.I_0(k_c.r_n) - \frac{I_1(k_c.r_n)}{2.r_n}\right) - (B_{n1} - B_{n2}).\left(k_c.K_0(k_c.r_n) + \frac{K_1(k_c.r_n)}{2.r_n}\right) + \frac{3}{2}.C_n\right) - \frac{\nu_c.p_{rn}}{(1-\nu_c)} \qquad \text{A2.37}$$

Equation A2.37 therefore satisfies equation A2.29. Similarly equation A2.27 may be satisfied using equations A2.25 and A2.34. Substituting equation A2.25 into A2.34 gives;

$$\sigma_r = \frac{2.\nu_c}{(1-\nu_c)}.\left(A_{n2}\left(k_c.I_0(k_c.r) - \frac{I_1(k_c.r)}{2.r}\right) - B_{n2}\left(k_c.K_0(k_c.r) + \frac{K_1(k_c.r)}{2.r}\right)\right) \qquad \text{A2.38}$$

therefore from equation A2.27

$$0 = A_{n2}\left(k_c.I_0(k_c.r_c) - \frac{I_1(k_c.r_c)}{2.r_c}\right) - B_{n2}\left(k_c.K_0(k_c.r_c) + \frac{K_1(k_c.r_c)}{2.r_c}\right) \qquad \text{A2.39}$$

Equation A2.39 satisfies equation A2.27. The simultaneous solution of equations A2.30, A2.33, A2.37 and A2.39 gives:

$$A_{n1} = -(B_{n1}.e_1) - e_2 \qquad \text{A2.40}$$

$$A_{n2} = B_{n2}.e_3 \qquad \text{A2.41}$$

$$B_{n1} = \left(\frac{e_4}{e_5}\right) + B_{n2} \qquad \text{A2.42}$$

$$B_{n2} = \left(\frac{e_4}{e_5} - \frac{e_6}{e_7}\right) \Big/ \left(\frac{e_8}{e_7} - 1\right) \qquad \text{A2.43}$$

where;

$$e_1 = K_1.(k_c.r_{fh})/I_1(k_c.r_{fh}) \qquad \text{A2.44}$$

$$e_2 = C_n.r_{fh}/I_1(k_c.r_{fh}) \qquad \text{A2.45}$$

$$e_3 = \frac{(k_c.K_0(k_c.r_c) + K_1(k_c.r_c)/(2.r_c))}{(k_c.I_0(k_c.r_c) - I_1(k_c.r_c)/(2.r_c))} \qquad \text{A2.46}$$

$$e_4 = -\frac{k_c.I_0(k_c.r_n).C_n.r_n}{I_1(k_c.r_n)} + 2.C_n - \frac{\nu_c.p_{rn}}{2.G_c} \qquad \text{A2.47}$$

$$e_5 = \frac{k_c.I_0(k_c.r_n).K_1(k_c.r_n)}{I_1(k_c.r_n)} + k_c.K_0(k_c.r_n) \qquad \text{A2.48}$$

$$e_6 = C_n.r_n - \frac{I_1(k_c r_n).C_n.r_{fh}}{I_1(k_c.r_{fh})} \qquad \text{A2.49}$$

$$e_7 = -K_1(k_c.r_n) + \frac{I_1(k_c.r_n).K_1(k_c.r_{fh})}{I_1(k_c.r_{fh})} \qquad \text{A2.50}$$

$$e_8 = -K_1(k_c.r_n) - \frac{I_1(k_c.r_n).(k_c.K_0(k_c.r_c) + K_1(k_c.r_c)/(2.r_c))}{k_c.I_0(k_c.r_c) - I_1(k_c.r_c)/(2.r_c)} \qquad \text{A2.51}$$

Equations A2.40 to A2.51 give the values of the constants A_{n1}, A_{n2}, B_{n1} and B_{n2} when there is a central feed hole of radius r_{fh} passing through the elastomer layer. However when this is not the case, $r_{fh} = 0$ and the values of A_{n1}, A_{n2}, B_{n1} and B_{n2} are as follows;

When $r_{fh} = 0$, $I_1(k_c.r_{fh}) = 0$ and therefore in equation A2.50, $e_7 = \infty$. Equation A2.43 for B_{n2} therefore reduces to:

$$B_{n2} = -\frac{e_4}{e_5} \qquad \text{A2.52}$$

Hence substituting for B_{n2} in equation A2.42 gives;

$$B_{n1} = 0 \qquad \text{A2.53}$$

Similarly for A_{n2} in equation A2.41;

$$A_{n2} = -\frac{e_4}{e_5}.e_3 \qquad \text{A2.54}$$

The value of e_2 by equation A2.45 is indeterminate and therefore equation A2.40 cannot be used for A_{n1}. However A_{n1} can be determined using equation A2.33 i.e.;

$$A_{n1} = A_{n2} + \frac{B_{n2}.K_1(k_c.r_n)}{I_1(k_c.r_n)} - \frac{C_n.r_n}{I_1(k_c.r_n)} \qquad \text{A2.55}$$

When $r_{fh} = 0$ the values of A_{n1}, A_{n2}, B_{n1} and B_{n2} are given by equations A2.52 to A2.55 where e_3, e_4 and e_5 are given by equations A2.46 to A2.48. Other special cases are also considered as follows. When the elastomer layer is of infinite radius i.e. $r_c = \infty$ then equations A2.46 and A2.51 reduce to;

$$e_3 = 0 \qquad \text{A2.56}$$

and $$e_8 = - K_1(k_c.r_n) \qquad \text{A2.57}$$

provided the value of k_c is not equal to zero.

If the pressure profile p_c in this elementary solution is of equal radius to the elastomer layer, i.e. $r_n = r_c$, then the deflection u_{rn} is given by equation A2.24 only. Expressions for A_{n1} and B_{n1} are given by solving equations A2.30 and A2.35 where in equation A2.35, $\sigma'_{rn} = 0$ (by a boundary condition similar to that expressed by equation A2.27) and $r_n = r_c$, i.e.;

$$A_{n1} = - \frac{\left(C_n \left(r_{fh}.\frac{e_{10}}{e_{12}} + \frac{3}{2} \right) - \frac{\nu_c.p_{rn}}{2.G_c} \right)}{\left(e_9 + e_{10}.\frac{e_{11}}{e_{12}} \right)} \qquad \text{A2.58}$$

and $$B_{n1} = - A_{n1}.\frac{e_{11}}{e_{12}} - C_n.\frac{r_{fh}}{e_{12}} \qquad \text{A2.59}$$

where $$e_9 = k_c.I_0(k_c.r_c) - \frac{I_1(k_c.r_c)}{2.r_c} \qquad \text{A2.60}$$

$$e_{10} = k_c.K_0(k_c.r_c) + \frac{K_1(k_c.r_c)}{2.r_c} \qquad \text{A2.61}$$

$$e_{11} = I_1(k_c.r_{fh}) \qquad \text{A2.62}$$

$$e_{12} = K_1(k_c.r_{fh}) \qquad \text{A2.63}$$

and if $r_{fh} = 0$, equations A2.62 and A2.63 become;

$$e_{11} = 0 \qquad \text{A2.64}$$

and $$e_{12} = \infty \qquad \text{A2.65}$$

Hence equations A2.58 and A2.59 reduce to;

$$A_{n1} = - \frac{\left(\frac{3}{2}.C_n - \frac{\nu_c.p_{rn}}{2.G_c} \right)}{e_9} \qquad \text{A2.66}$$

$$\text{and} \quad B_{n1} = 0 \qquad \text{A2.67}$$

Having obtained expressions for the constants A_{n1}, A_{n2}, B_{n1} and B_{n2} in equations A2.24 and A2.25 it is now necessary to relate radial displacements u_{rn} with axial displacements u_{zn} of the compliant surface since it is these that are required. From stress - strain relationships (85) for a linear - elastic isotropic material;

$$\varepsilon_z = \frac{1}{E_c}.(\sigma_z - \nu_c.(\sigma_\theta + \sigma_r)) \qquad \text{A2.68}$$

$$\text{where } \varepsilon_z = \frac{\partial u_z}{\partial z} \qquad \text{A2.69}$$

From equations A2.3, A2.4 and A2.5;

$$\sigma_\theta + \sigma_r = \frac{2.G_c.(1 + \nu_c).(\varepsilon_\theta + \varepsilon_r) + 2.\nu_c.\sigma_z}{(1 - \nu_c)} \qquad \text{A2.70}$$

Substituting for $\sigma_\theta + \sigma_r$ in equation A2.68 gives;

$$\varepsilon_z = \frac{\sigma_z.(1 - 2.\nu_c)}{2.G_c.(1 - \nu_c)} - \frac{\nu_c}{(1 - \nu_c)}.(\varepsilon_\theta + \varepsilon_r) \qquad \text{A2.71}$$

Using equations A2.6, A2.7, A2.9 and A2.69 equation A2.71 can be written in the form;

$$\frac{\partial u_{zn}}{\partial z} = \frac{\sigma_z.(1 - 2.\nu_c)}{2.G_c.(1 - \nu_c)} - \frac{\nu_c}{(1 - \nu_c)}.\left(1 - \frac{(z - t_c)^2}{t_c^2}\right) \times \left(\frac{\partial u_{rn}}{\partial r} + \frac{u_{rn}}{r}\right) \qquad \text{A2.72}$$

Integrating from z = 0 to t_c gives;

$$u_{zn} = \frac{(1 - 2.\nu_c)}{2.G_c.(1 - \nu_c)} \int_0^{t_c} \sigma_z.\partial z - \frac{2.t_c.\nu_c}{3.(1 - \nu_c)}.\frac{1}{r}.\frac{\partial(u_{rn}.r)}{\partial r} \qquad \text{A2.73}$$

Applying assumption (iii) of section 3.4.4;

$$\sigma_z = - p_c \qquad \text{A2.74}$$

Substituting for σ_z in equation A2.73;

$$u_{zn} = -\frac{(1 - 2.\nu_c).p_c.t_c}{2.G_c.(1 - \nu_c)} - \frac{2}{3}.\frac{t_c.\nu_c}{(1 - \nu_c)}.\frac{1}{r}.\frac{\partial(u_{rn}.r)}{\partial r} \qquad \text{A2.75}$$

Substituting for u_{rn} using equation A2.24 and A2.25 in equation A2.75;

$$u_{zn} = -\frac{(1 - 2.\nu_c).p_c.t_c}{2.G_c.(1 - \nu_c)} - \frac{2}{3}.\frac{t_c.\nu_c}{(1 - \nu_c)}.(k_c.(A_n.I_0(k_c.r) - B_n.K_0(k_c.r)) + 2.C_n) \quad \text{for } 0 \le r \le r_n \qquad \text{A2.76}$$

$$u_{zn} = -\frac{2}{3}.\frac{t_c.\nu_c}{(1 - \nu_c)}.(k_c.(A_n.I_0(k_c.r) - B_n.K_0(k_c.r)) \quad \text{for } r_n < r \le r_c \qquad \text{A2.77}$$

Equations A2.76 and A2.77 give deflections of the compliant surface for an elementary solution to the elastomer layer. In equation A2.76 p_c is constant for a uniform pressure profile acting on the compliant surface. For a parabolic pressure profile;

$$p_c = p_n\left(1 - \frac{r}{r_n}\right)^2. \qquad \text{A2.78}$$

In equation A2.77 the first term on the R.H.S. of equation A2.75 is obmitted because $p_c = 0$ in the region $r_n <= r <= r_c$.

APPENDIX 3

ACCURACY OF THE AUTHORS SIMPLIFIED SOLUTION TO THE ELASTOMER LAYER IN COMPLIANT THRUST BEARINGS SUPPLIED WITH AN INCOMPRESSIBLE LUBRICANT THROUGH A CENTRAL FEED HOLE

A good method of testing the accuracy of the author's simplified solution presented in sections 3.4.4 and 3.4.5 for deflection of the compliant surface is to apply equations 3.74 and 3.75 together with the procedure described in section 3.4.5 to the compliant thrust bearing configurations shown in figures A3.1a and A3.1b. It is then possible to compare analytical results with those of Castelli et al (59) and Benjamin et al (62) respectively. Both types of bearings are supplied with an incompressible lubricant (i.e. oil) through a central feed hole. For the bearing configuration shown in figure A3.1b this feed hole passes through the elastomer layer. The port extension tube is designed to allow free axial deflections of the compliant surface (at $r = r_{fh}$) but stops the feed hole becoming blocked by compression of the elastomer layer.

The analysis is as follows; in a compliant thrust bearing with a central feed hole the lubrication equation for flow in the bearing clearance is given by Reynolds equation of the form (56):

$$\frac{h_r^3}{12.\eta}.r.\frac{dp_f}{dr} = -\frac{q}{2.\pi} \qquad \text{A3.1}$$

and since the lubricant is incompressible

$$q = \text{constant} \qquad \text{A3.2}$$

Equation A3.1 may be expressed as;

$$\frac{dp_f}{dr} = \frac{a_1}{h_r^3.r} \qquad \text{A3.3}$$

$$\text{where } a_1 = \text{constant} = 6.\eta.q/\pi \qquad \text{A3.4}$$

Integrating equation A3.3 between the bearing radius r_{os} and radial position r gives;

$$p_f = p_a + a_1 \int_r^{r_{os}} \frac{1}{h_r^3.r}\, dr \qquad \text{A3.5}$$

At $r = r_{fh}$ let $p_f = p_{fh}$, the feed hole pressure. Substituting this condition into equation A3.5 gives;

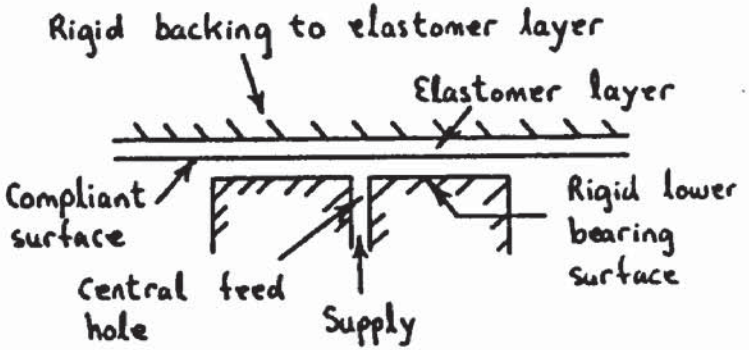

(a) Compliant thrust bearing configuration with elastomer layer of infinite radial extent: Castelli et al (59).

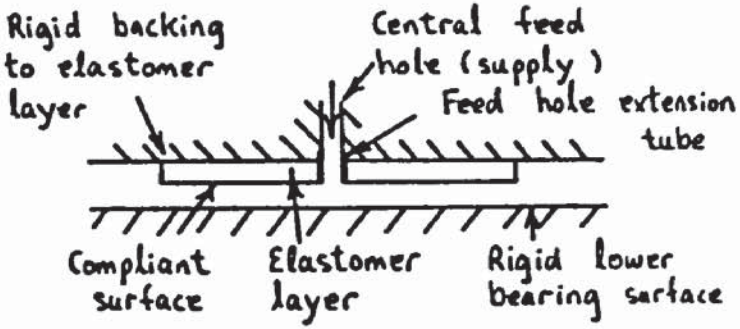

(b) Compliant thrust bearing configuration with elastomer layer of finite radial extent: Benjamin et al (62).

Figure: A3.1 Compliant thrust bearing configurations with a central feed hole

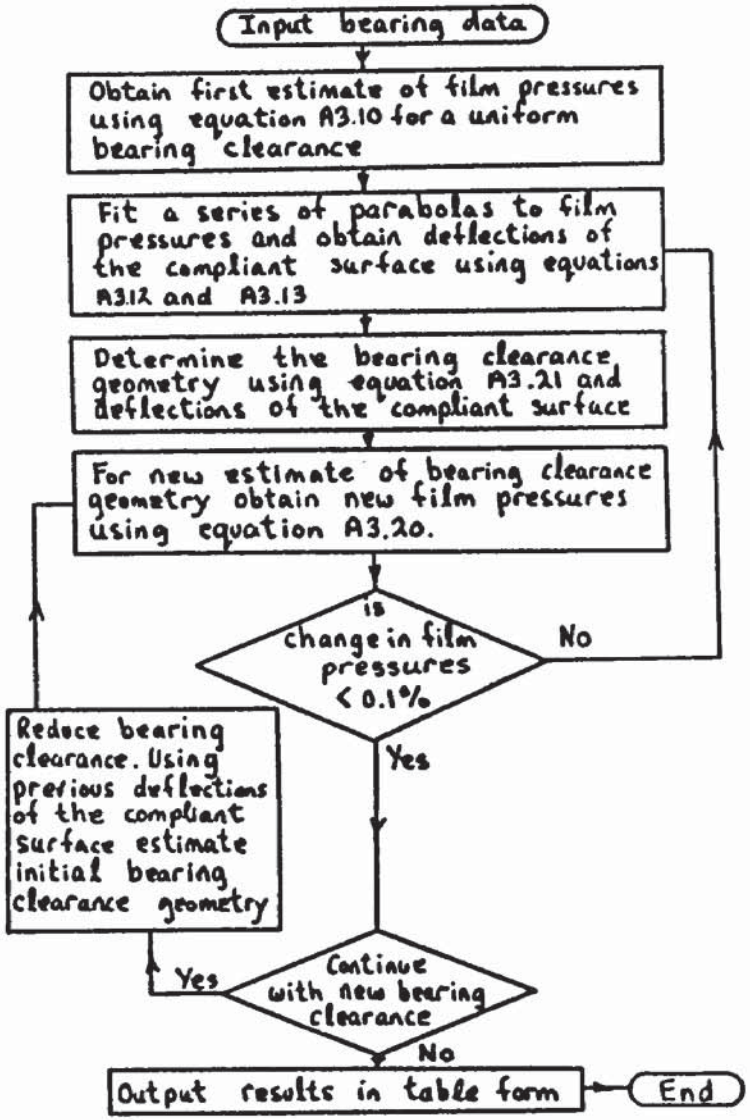

Figure: A3.2 Flow diagram of iterative solution

$$a_1 = \frac{p_{fh} - p_a}{\int_{r_{fh}}^{r_{os}} \frac{1}{h_r^3 . r}\, dr} \qquad \text{A3.6}$$

Hence equation A3.5 becomes;

$$p_f = p_a + (p_{fh} - p_a).\frac{\int_{r}^{r_{os}} \frac{1}{h_r^3 . r}\, dr}{\int_{r_{fh}}^{r_{os}} \frac{1}{h_r^3 . r}\, dr} \qquad \text{A3.7}$$

and eliminating a_1 between equations A3.4 and A3.6 gives the volumetric flow rate q;

$$q = \frac{(p_{fh} - p_a).\pi}{6.\eta \int_{r_{fh}}^{r_{os}} \frac{1}{h_r^3 . r}\, dr} \qquad \text{A3.8}$$

To obtain film pressures using equation A3.7, an iterative solution similar to that described in section 3.6 for the porous and compliant aerostatic thrust bearing case is used. The bearing clearance is divided into I nodes from $r = r_{fh}$ to $r = r_{os}$. Initially a uniform bearing clearance equal to the bearing approach, i.e. $h_r = c$ is assumed with no deflections of the compliant surface. For a uniform bearing clearance equation A3.7 becomes;

$$p_f = p_a + (p_{fh} - p_a).\frac{\ln\left(\frac{r_{os}}{r}\right)}{\ln\left(\frac{r_{os}}{r_{fh}}\right)} \qquad \text{A3.9}$$

The film pressure at each node i is determined for a constant feed hole pressure p_{fh}, i.e. from equation A3.9;

$$(p_f)_i = p_a + (p_{fh} - p_a).\frac{\ln\left(\frac{r_{os}}{r_i}\right)}{\ln\left(\frac{r_{os}}{r_{fh}}\right)} \qquad \text{A3.10}$$

$$\text{where } r_i = \Delta r.(i - 1) + r_{fh} \qquad \text{A3.11}$$

Having obtained a first estimate of film pressures, corresponding deflections of the compliant surface are determined from a summation of elementary solutions as described in section 3.4.5. For convenience this is described in brief as follows. In each elementary solution the deflections of the compliant surface are determined from equations 3.74 and 3.75 in section 3.4.4, i.e.;

$$\text{for } 0 <= r <= r_n$$

$$u_{zn} = -\frac{(1 - 2.\nu_c).p_c.t_c}{2.G_c.(1 - \nu_c)} - \frac{2}{3}.\frac{t_c.\nu_c}{(1 - \nu_c)}.(k_c.(A_{n1}.I_0(k_c.r) - B_{n1}.K_0(k_c.r)) + 2.C_n) \qquad \text{A3.12}$$

and for $r_n <= r <= r_c$

$$u_{zn} = -\frac{2}{3}.\frac{t_c.\nu_c}{(1 - \nu_c)}.(k_c.(A_{n2}.I_0(k_c.r) - B_{n2}.K_0(k_c.r))) \qquad \text{A3.13}$$

where deflections u_{zn} correspond to a parabolic pressure profile p_c on the compliant surface given by;

$$p_c = p_n\left(1 - \left(\frac{r}{r_n}\right)^2\right) \text{for } 0 \le r \le r_n \qquad \text{A3.14}$$

and the actual film pressure profile is approximated by a summation of these parabolas i.e.;

$$p_f = \sum_{n=1,2}^{k_2} p_n\left(1 - \left(\frac{r}{r_n}\right)^2\right) \qquad \text{A3.15}$$

The resulting deflection of the compliant surface is equal to a summation of deflections from each elementary solution i.e.;

$$u_c = \sum_{n=1,2}^{k_2} u_{zn} \text{ at each radial position r} \qquad \text{A3.16}$$

where values of u_{zn} are given by equations A3.12 and A3.13.

To determine deflections of the compliant surface at each node i the elastomer layer is divided into I primary nodes from $r = r_{fh}$ to $r = r_{os}$. These nodes must correspond with those used for the bearing clearance. In addition a further four secondary nodes are used between the primary nodes $i = I$ and $i = I - 2$. This is to improve the accuracy of the compliant surface deflections near the bearing clearance exit. Equation A3.15 becomes;

$$(p_f)_i = \sum_{n=1,2}^{I-1} p_n \left(1 - \left(\frac{r_i}{r_n}\right)^2\right) \qquad \text{A3.17}$$

$$\text{where } r_n = r_{i=I-n+1} \qquad \text{A3.18}$$

and equation A3.16 can be written;

$$(u_c)_i = \sum_{n=1,2}^{I} (u_{zn})_i \qquad \text{A3.19}$$

Values of p_n in equation A3.17 are determined using the procedure described in section 3.4.5. Expressions for the evaluation of constants A_{n1}, A_{n2}, B_{n1} and B_{n2} in equations A3.12 and A3.13 are given in appendix 2. Their values depend on the configuration of the elastomer layer. For example in the compliant bearing studied by Castelli et al (59) the elastomer layer is of infinite radius and therefore r_c = infinity (see figure A3.1a). Also because the feedhole does not pass through the elastomer layer then in appendix 2 the case $r_{fh} = 0$ applies for the constants A_{n1}, A_{n2}, B_{n1} and B_{n2}. In the compliant bearing studied by Benjamin et al (62) the elastomer layer is of finite length equal to the bearing radius and therefore $r_c = r_{os}$. And as shown in figure A3.1b the feed hole passes through the elastomer layer. Therefore in appendix 2 the case for $r_{fh} \neq 0$ applies for the constants A_{n1}, A_{n2}, B_{n1} and B_{n2}.

Having determined deflections of the compliant surface a new estimate of film pressures are made using equation A3.7 which can be written in the form;

$$(p_f)_i = p_a + (p_{fh} - p_a).\frac{\int_{r_i}^{r_{os}} \frac{1}{h_r^3.r}\,dr}{\int_{r_i}^{r_{os}} \frac{1}{h_r^3.r}\,dr} \qquad \text{A3.20}$$

Values of the new bearing clearance h_r at each node i in equation A3.20 are given by:

$$(h_r)_i = c - (u_c)_i \qquad \text{A3.21}$$

However as described in section 3.6 to keep the bearing clearance h_r at $r = r_{os}$, constant and improve the numerical stability during the iteration procedure a new value of c is substituted into equation A3.21. This value is given by;

$$(c)_{new} = (c)_{old} + (u_c)_{i=I} \qquad \text{A3.22}$$

The integrals in equations A3.20 are evaluated by calculating the value of $1/((h_r)^3.r)$ at each node i and summating from $r = r_{os}$ to $r = r_i$ and $r = r_{fh}$ using the trapezoidal rule.

From the new estimates of film pressures the iteration continues with a new estimate of bearing clearance geometry h_r from deflections of the compliant surface due to the new film pressures. And from the new bearing clearance geometry, new film pressures are obtained. This iteration is continued until the change in film pressures at all nodes i is less than 0.1%.

Having obtained a solution which satifies both equations A3.7 and A3.21 the bearing flow rate is determined from equation A3.8 and the load capacity is given by;

$$w = 2.\pi \int_{r_{fh}}^{r_{os}} (p_f - p_a).r.dr + \pi.r_{fh}^2.p_{fh} \qquad \text{A3.23}$$

The integrals in equations A3.8 and A3.23 are evaluated in a similar way to that described for equation A3.20 except in equation A3.23 values of $(p_f - p_a).r$ are calculated at each node i and Simpsons rule is used instead of the trapezoidal rule for greater accuracy.

To obtain a set of results to enable bearing performance curves to be plotted the bearing clearance h_r at $r = r_{os}$ is reduced in small decrements. At each new bearing clearance the iteration procedure is repeated starting with an initial estimate of the bearing clearance

geometry. For this the deflections of the compliant surface in the solution to the previous bearing clearance are used, i.e.;

$$(h_r)_{\text{initial est.}} = (h_r)_{\text{previous}} - \text{decrement} \qquad \text{A3.24}$$

In successive iterations the bearing approach c in equation A3.21 is now given by;

$$c = (h_r)_{i=I} + (u_c)_{i=I} \qquad \text{A3.25}$$

where node i = I is at the bearing clearance exit $r = r_{os}$.

As the bearing clearance is reduced it was found necessary to use a linear damper similar to that of Castelli et al (59) (and used in section 3.6) to maintain stability during iterations to a solution. This reduces the change in bearing clearance geometry occuring after each iteration cycle. New estimates of the bearing clearance h_r from equation A3.21 using this linear damper become;

$$(h_r)_{new} = \eta_1.(h_r) + (1 - \eta_1).(h_r)_{old} \qquad \text{A3.26}$$

At large bearing clearances the iteration procedure is stable for $\eta_1 = 1$ in equation A3.26. With reducing bearing clearance if a solution is not achieved by the 20th iteration the value of η_1 is halved from its current value. This was repeated every time the 20th iteration to a solution was exceeded.

A computer programme for the solution on a HP9845 desktop mini computer is presented at the end of this appendix. A flowchart of the solution is shown in figure A3.2.

Comparisons of analytical results including sample pressure and deflection profiles between the authors mathematical model presented in this appendix and those of Castelli et al (59) and Benjamin et al (62) are shown in figures A3.3 to A3.12. Also in figures A3.3 to A3.6 are analytical results using the restrained column model of Dowson and Taylor (56) for deflections of the compliant surface. These figures are presented using the following notation of (59) and (62);

c bearing approach

C' dimensionless bearing approach ($= c/(t.Q^{1/4})$)

G elastomer layer shear modulus

p pressure

P' dimensionless pressure ($= p/(G.Q^{1/4})$)

q volumetric flow rate

Q dimensionless flow rate ($= 6.\eta.q/(\pi.G.t^3)$)

R radius

R_i recess radius (feed hole radius)

R_o outside radius (bearing radius)

R' dimensionless radius ($= R/R_o$)

t elastomer layer thickness

w deflections of the compliant surface

w' dimensionless deflections of the compliant surface ($= w/(t.Q^{1/4})$)

W total load (bearing load)

W' dimensionless load ($= W/(\pi.R_o^2.G.Q^{1/4})$)

ν Poisson's ratio for the elastomer layer

The authors results compare well with those of Castelli et al (59) and Benjamin et al (62). This therefore verifies the accuracy of the authors simplified solution for deflections of the elastomer layer in a typical thrust bearing application. The solution presented in sections 3.4.4 and 3.4.5 can therefore be used with confidence in other thrust bearing applications such as the porous and compliant aerostatic thrust bearing studied in this research project.

In figures A3.3 to A3.6 it is interesting to note that the restrained column model of Dowson and Taylor (56) gives reasonably accurate predictions of compliant thrust bearing performance at $\nu = 0.45$, but significant discrepancies occur for $\nu = 0.49$. It can be concluded from this that the restrained column model is unsuitable for typical rubber like materials which are bonded to a rigid backing and have a value of ν greater than 0.49.

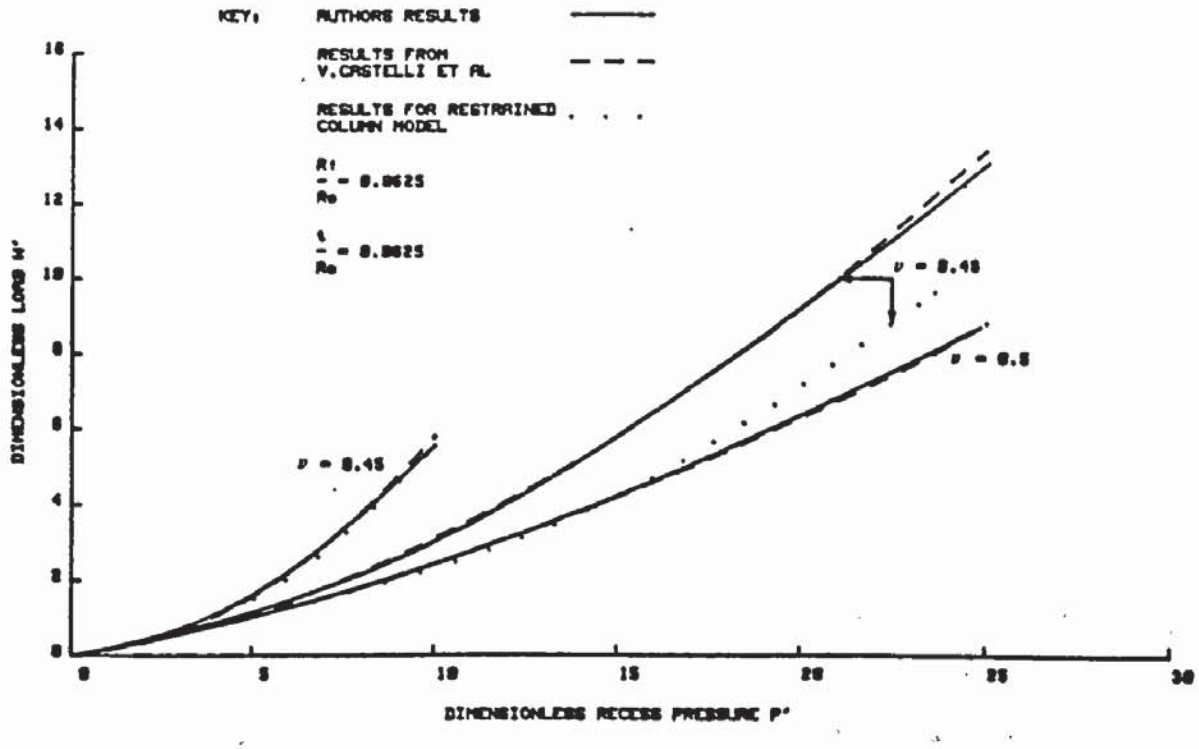

FIGURE A3.3 W' AGAINST P' FOR INFINITE ELASTOMER COMPLIANT SURFACE AXISYMMETRIC THRUST BEARING

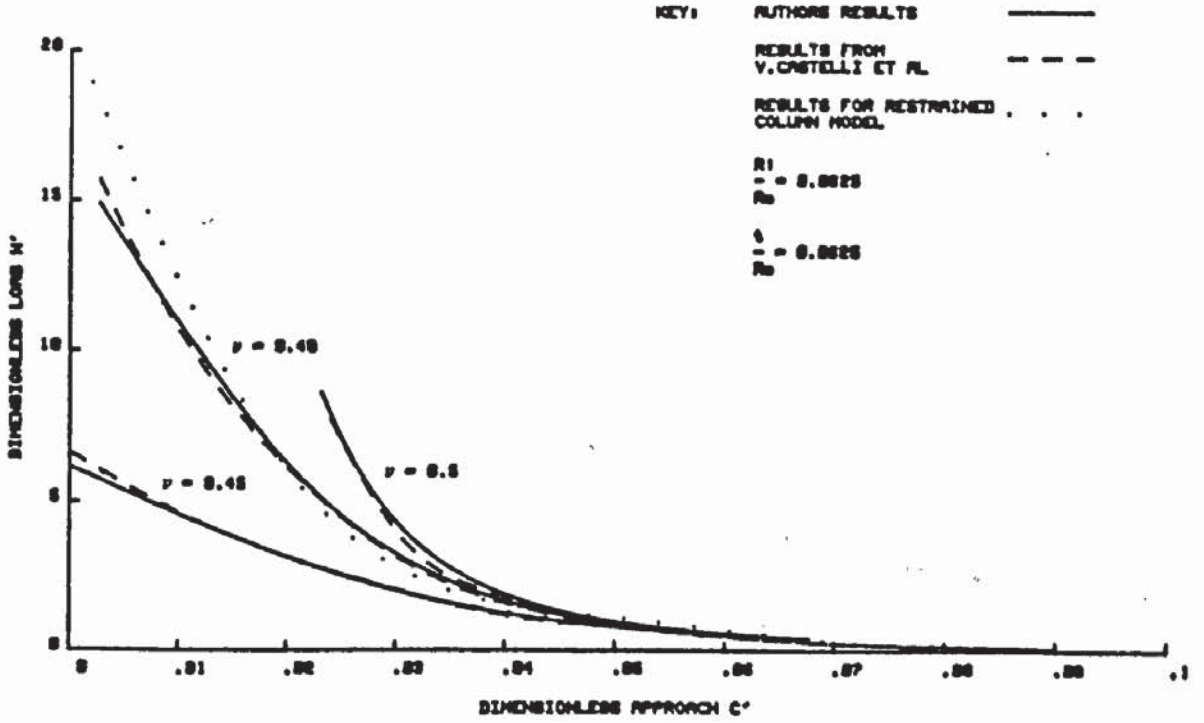

FIGURE A3.4 W' AGAINST C' FOR INFINITE ELASTOMER COMPLIANT SURFACE AXISYMMETRIC THRUST BEARING

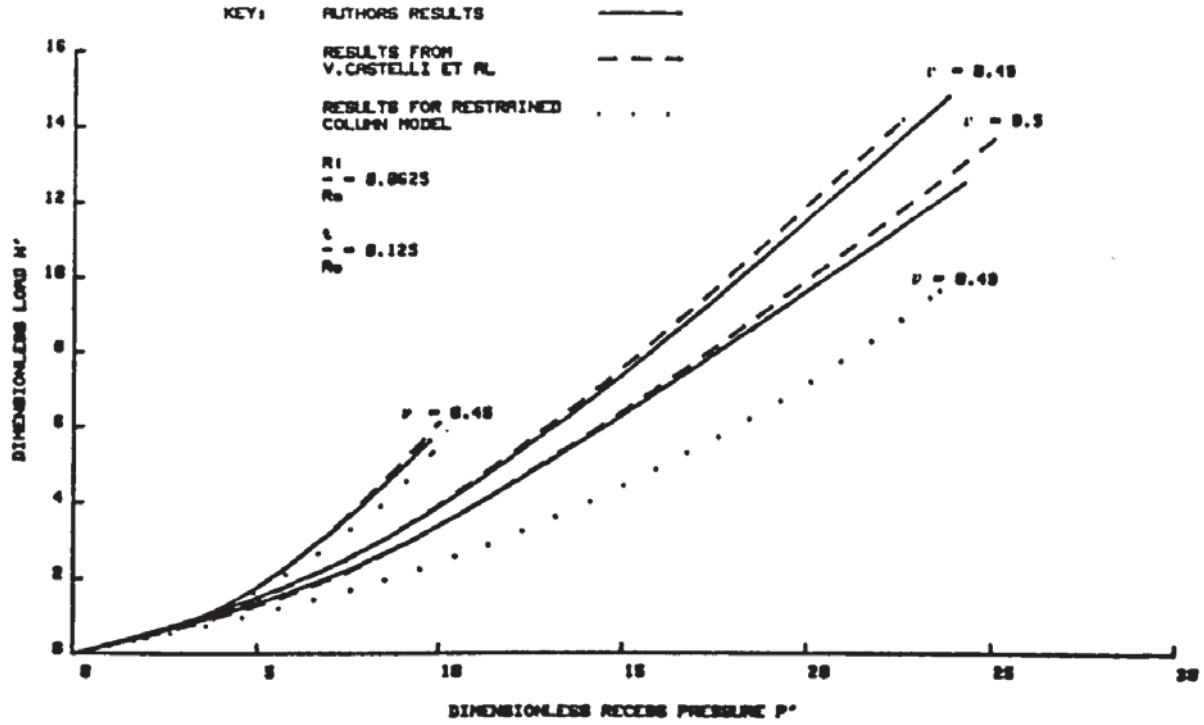

FIGURE A3.5 W' AGAINST P' FOR INFINITE ELASTOMER COMPLIANT SURFACE AXISYMMETRIC THRUST BEARING

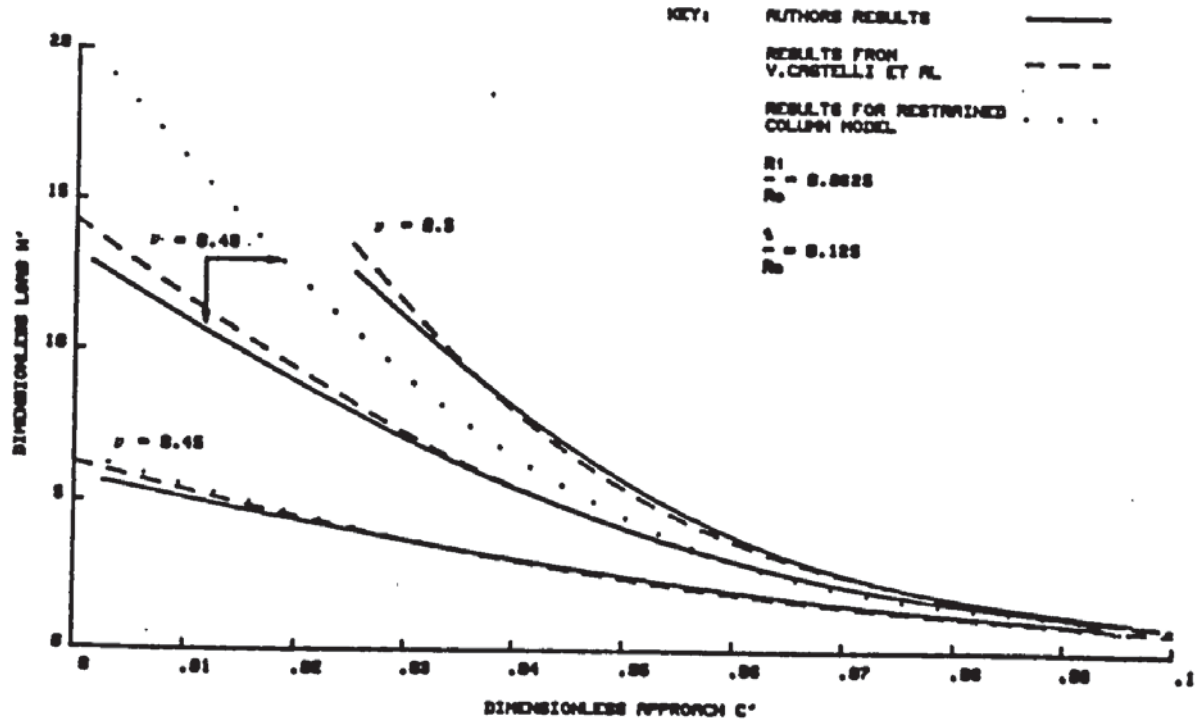

FIGURE A3.6 W' AGAINST C' FOR INFINITE ELASTOMER COMPLIANT SURFACE AXISYMMETRIC THRUST BEARING

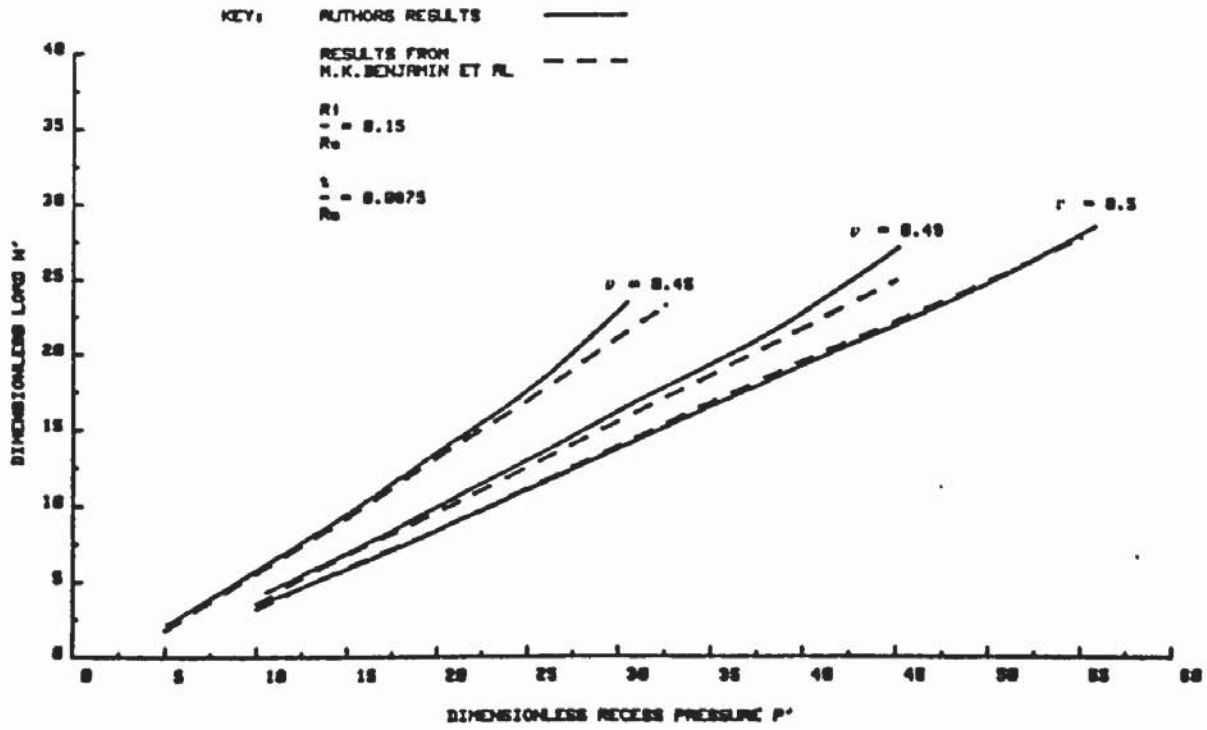

FIGURE A3.7 W' AGAINST P' FOR FINITE ELASTOMER COMPLIANT SURFACE AXISYMMETRIC THRUST BEARING

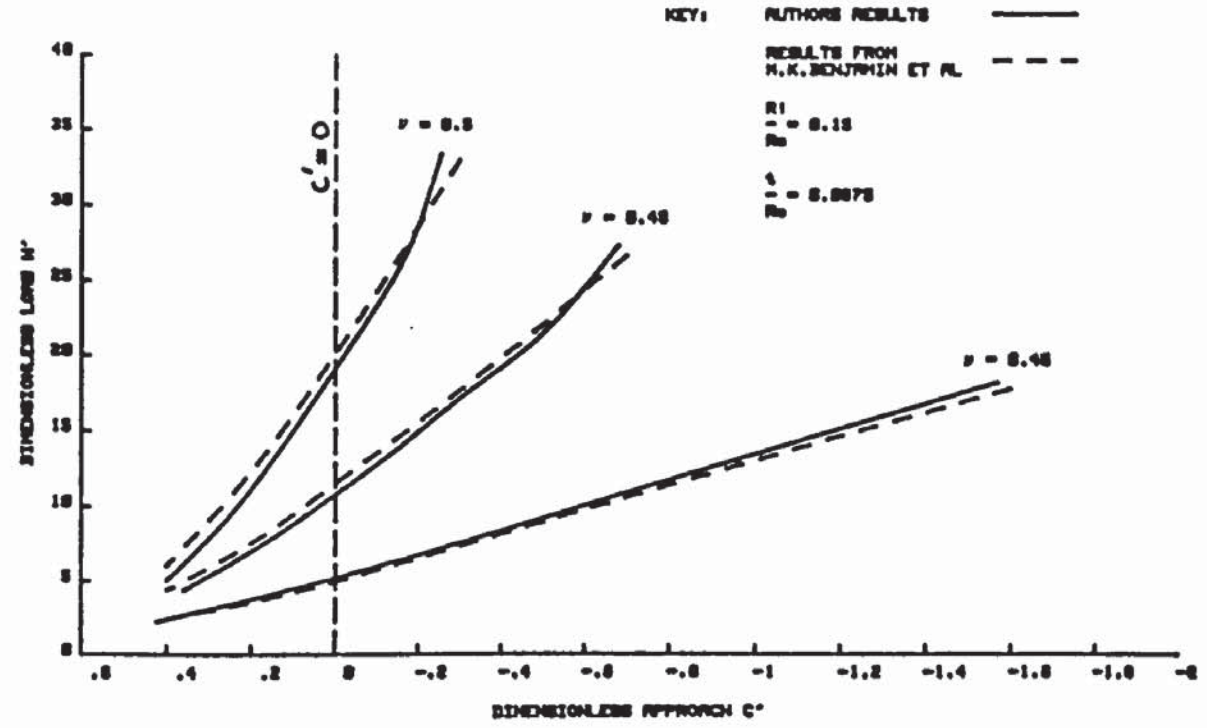

FIGURE A3.8 W' AGAINST C' FOR FINITE ELASTOMER COMPLIANT SURFACE AXISYMMETRIC THRUST BEARING

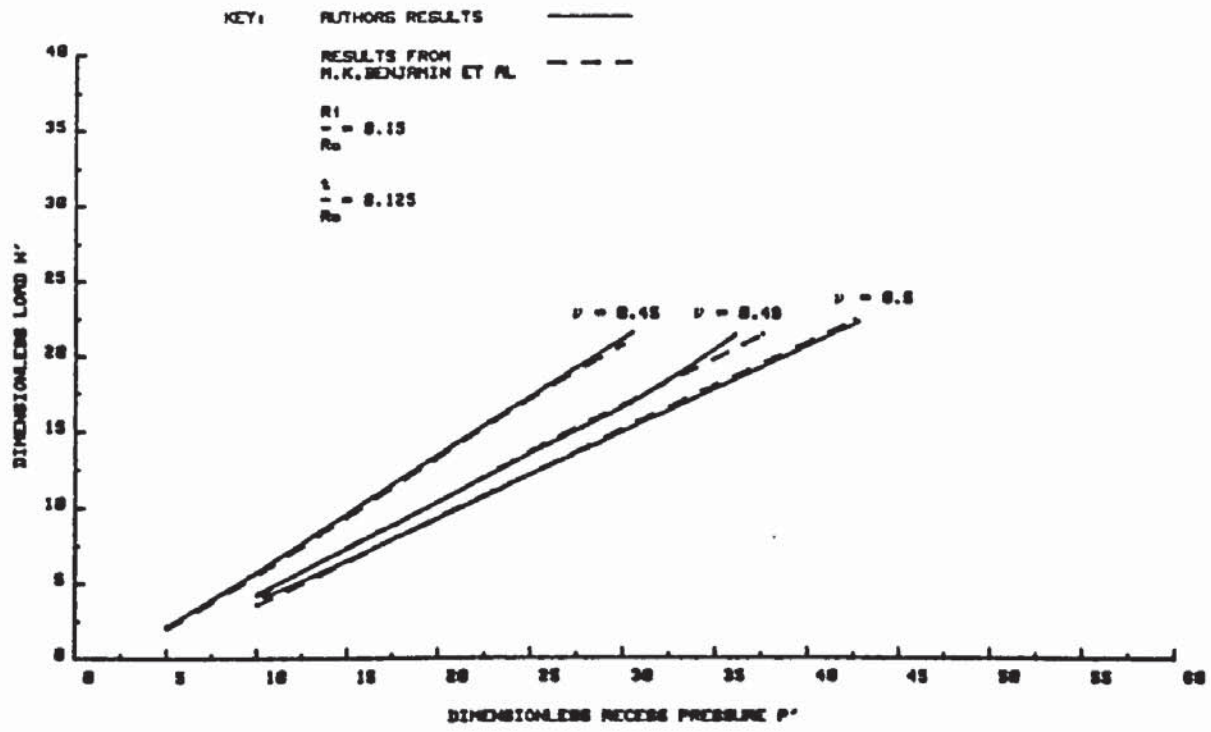

FIGURE A3.9 W' AGAINST P' FOR FINITE ELASTOMER COMPLIANT SURFACE AXISYMMETRIC THRUST BEARING

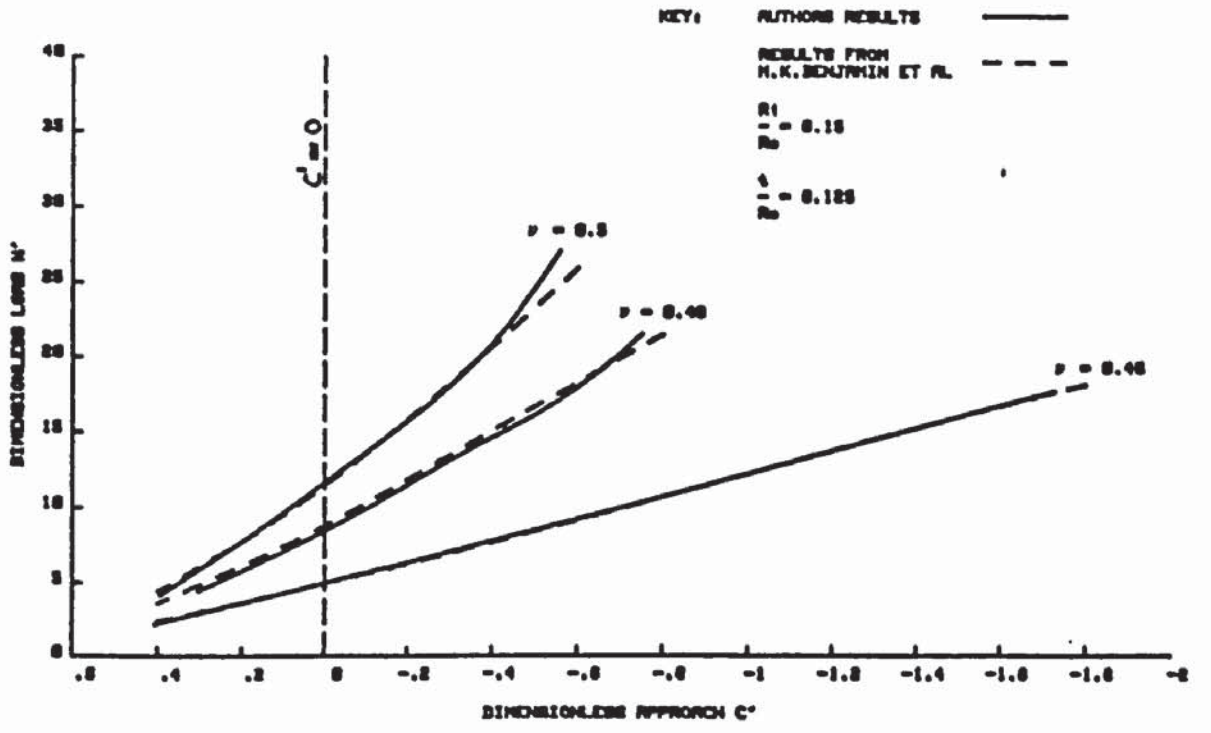

FIGURE A3.10 W' AGAINST C' FOR FINITE ELASTOMER COMPLIANT SURFACE AXISYMMETRIC THRUST BEARING

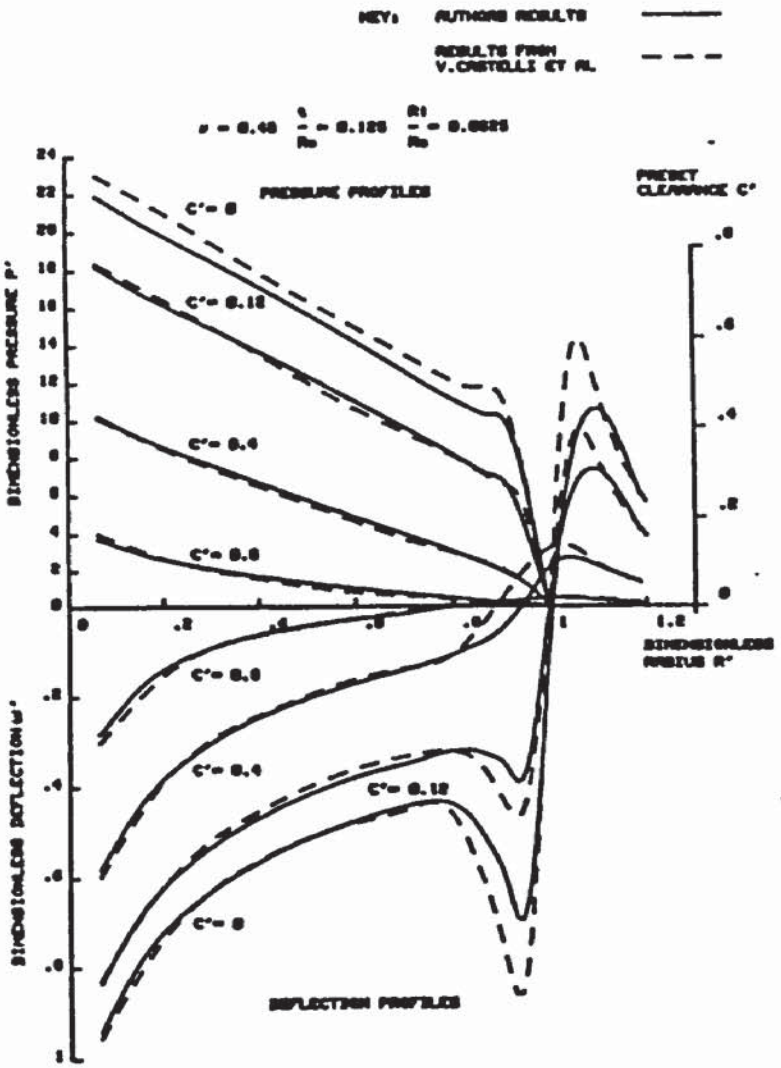

FIGURE A3.11
INFINITE ELASTOMER THRUST BEARING PRESSURE AND DEFLECTION PROFILES FOR VARIOUS PRESET CLEARANCES

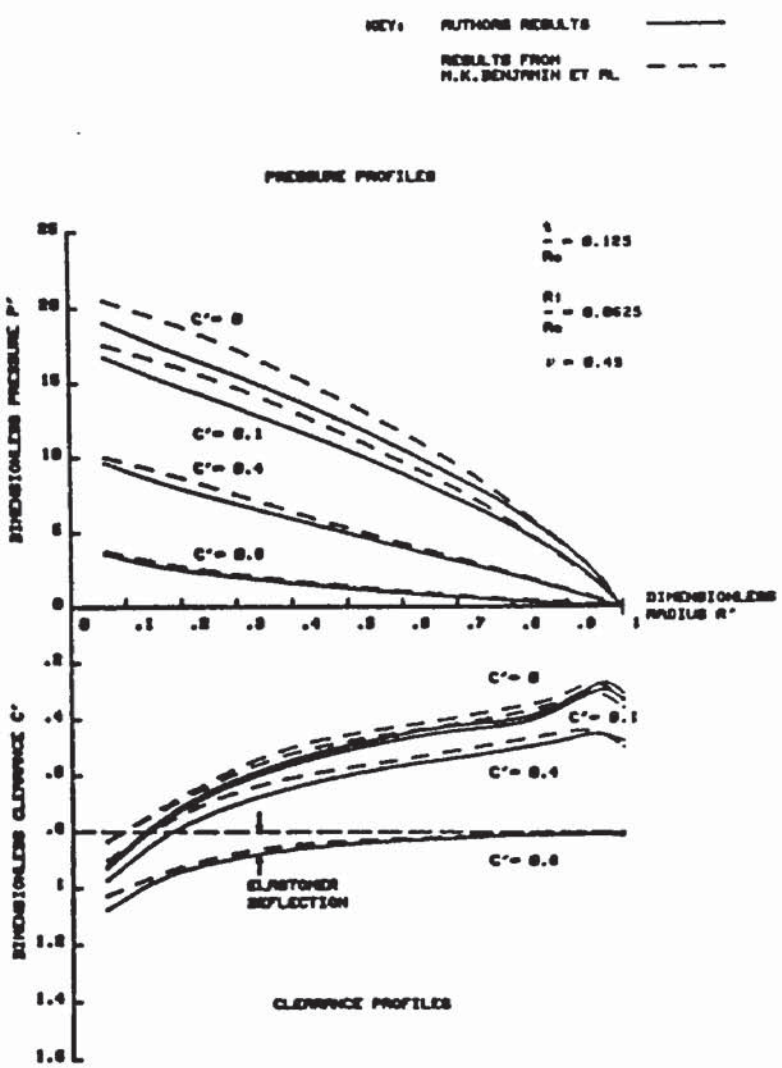

FIGURE A3.12
FINITE ELASTOMER THRUST BEARING PRESSURE AND CLEARANCE PROFILES FOR VARIOUS PRESET CLEARANCES

```
20    ! ****************************************************************
30    ! ++++++++++++++++++++++++++++++++++++++++++++++++++++++++++++++++
40    ! Programme to determine load capacity flow rate and clearance etc
50    ! for a RIGID-COMPLIANT BEARING with incompresible lubricant
60    ! ++++++++++++++++++++++++++++++++++++++++++++++++++++++++++++++++
70    ! ****************************************************************
80    !
90    ! Note this programme runs continiously overnight.It is also
100   ! suitable for any value of Vc (POISSON'S RATIO for compliant
110   ! layer).
120   !
130   PRINT "This programme computes the performance of a RIGID-COMPLIANT"
140   PRINT "BEARING supplied with an incompressible lubricant.To insure"
150   PRINT "convercence of the solution the programme is intially run"
160   PRINT "for large bearing clearances.The clearance is progressively"
170   PRINT "reduced using previously computed deflections of the "
180   PRINT "compliant layer as intial estimates of bearing clearance"
190   PRINT "A series of uniform pressures of magnitude Pn and extent"
200   PRINT "Rn are used to approx. the actual pressure profile and hence"
210   PRINT "determine deflections of compliant layer."
211   PRINT "The programme computes results for a series of poisson's"
212   PRINT "ratio values (for compliant layer) stored in data file at"
213   PRINT "end of programme"
220   WAIT 1000
230   PRINT PAGE
240   ! ****************************************************************
250   ! A description of important parameters in programme is as follows
260   ! ****************************************************************
270   ! Gc=SHEAR MODULUS of compliant layer
280   ! Hf=LOCAL FILM THICKNESS
290   ! Hm=Bearing LIFT OFF
300   ! Io(),Ii(),Ko()&Ki() are modified BESSEL functions
310   ! Ka=(1-Vc)^0.5/Tc
320   ! Cn=2*Vc*Pn*Tc^2/(Gc*Rn^2)
330   ! Po=RECESS PRESSURE across bearing inlet port.Note this is assumed
340   ! uniform over 0<=R<=Ro.
350   ! Pf=Bearing FILM PRESSURE at radius R
360   ! Pfn=Computed new bearing FILM PRESSURES at radius R
370   ! Pfr=FILM PRESSURES for a rigid bearing of film clearance Hm
380   ! Pff=FILM PRESSURE profile fitted using LEAST SQUARES method
390   ! Pn=MAGNITUDE of pressure for a parabolic profile at R=0
400   ! R=RADIAL POSITION
410   ! Rb=BEARING RADIUS
420   ! Rc=RADIUS of compliant layer
430   ! Rn=RADIUS of PARABOLIC pressure profile
440   ! Ri=RECESS RADIUS
450   ! Tc=THICKNESS of compliant layer
460   ! W=Bearing LOAD CAPACITY
470   ! Wr=LOAD CAPACITY for a rigid bearing
480   ! Wc=DEFLECTION of compliant layer
490   ! Vq=VOLUMETRIC FLOW RATE to bearing
500   ! Uv=Lubricant VISCOSITY
510   ! Dap=Linear damper to improve convergence of solution
520   ! ****************************************************************
530   ! The following are dimensionless parameters for comparison with
540   ! V.Castelli's and M.K.Benjamin's analytical results
550   ! ****************************************************************
560   ! Wd=Dimensionless LOAD CAPACITY
570   ! Qd=      "       FLOW RATE
580   ! Pd=      "       RECESS PRESSURE
590   ! Cd=      "       bearing LIFT OFF based on compliant layer thickness
600   ! Cdd=     "          "     "    "     "    " bearing radius
610   ! Wcd=     "       DEFLECTION of compliant layer
620   ! Rd=      "       RADIAL POSITION
630   ! Pfd=     "       FILM PRESSURE
640   !
650   DIM Hf(28),Pf(14),Pfr(14),R(18),Rn(13),Pn(13),Pff(14),F(14,14),Bm(13)
660   DIM Ann(13,13),Am(13,13),Wc(36),As(28),An(2),Bn(2)
670   DIM Ass(14),Pfn(14),Wcd(36),Rd(36),Pfd(14),Wcn(36),Rs(36),C(8),Cda(10)
680   ! **********************
690   ! IMPUT bearing details
700   ! **********************
710   INPUT "SHEAR MODULUS of compliant layer Gc=?",Gc
720   ! INPUT "POISSON'S RATIO of compliant layer Vc=?",Vc
730   ! IF (Vc<0) OR (Vc).5) THEN 720
731   READ Vc
740   INPUT "RADIUS of compliant layer Rc=?",Rc
750   INPUT "RADIUS of bearing Rb=?",Rb
760   INPUT "RECESS RADIUS Ri=?",Ri
770   IF (Rb<=Rc) AND (Ri<Rb) THEN 820
780   PRINT "RADIUS Rc=>Rb>Ri.TRY AGAIN"
790   PAUSE
```

```
800   PRINT PAGE
810   GOTO 740
820   Cab=0
830   INPUT "Does supply port pass through compliant layer YES or NO ?",Caa$
840   IF Caa$="YES" THEN 880
850   IF Caa$="NO" THEN 890
860   INPUT "You have mistyped YES or NO.TRY AGAIN.",Caa$
870   GOTO 840
880   Cab=1
890   INPUT "THICKNESS of compliant layer Tc=?",Tc
1050  INPUT "Lubricant VISCOSITY Uo=?",Uo
1060  Vab=0
1070  PRINT "Do you want to input a constant supply pressure or"
1080  PRINT "a constant flow rate."
1090  INPUT "INPUT YES or NO for constant supply pressure.",Vaa$
1100  IF Vaa$="YES" THEN 1140
1110  IF Vaa$="NO" THEN 1160
1120  INPUT "You have mistyped YES or NO.TRY AGAIN.",Vaa$
1130  GOTO 1100
1140  INPUT "RECESS PRESSURE Po=?",Po
1150  GOTO 1180
1160  Vab=1
1170  INPUT "VOLUMETRIC FLOW RATE to bearing Vq=?",Vq
1180  PRINT PAGE
1190  Xab=0
1200  Xad=0
1210  INPUT "Input increment of Pd for output of results",N12
1220  IF N12<=0 THEN 1210
1230  INPUT "Do you want a hardcopy of results.YES or NO ?",Xaa$
1240  IF Xaa$="YES" THEN 1280
1250  IF Xaa$="NO" THEN 1290
1260  INPUT "You have mistyped YES or NO ?.TRY AGAIN.",Xaa$
1270  GOTO 1240
1280  Xab=1
1290  INPUT "Do you want PRESSURE & DEFLECTION profiles in results,YES or NO?",X
aj$
1300  IF Xaj$="YES" THEN 1340
1310  IF Xaj$="NO" THEN 1420
1320  INPUT "You have mistyped YES or NO ?.TRY AGAIN.",Xaj$
1330  GOTO 1300
1340  Xad=1
1350  INPUT "How many profiles do you want listed in results (max 10)",N10
1360  IF (N10<=0) OR (N10>10) THEN 1350
1370  PRINT "Input values of Cd for which profiles are required"
1380  FOR I=1 TO N10
1390  INPUT "Cd=",Cda(I)
1400  PRINT "Cd(";I;")= ";Cda(I)
1410  NEXT I
1420  IF Rc>1.4*Rb THEN 1450
1430  Ir=Rc/Rb*14
1440  GOTO 1460
1450  Ir=18
1460  Xah=0
1470  PRINT "INPUT range of results for analysis"
1480  INPUT "LARGEST clearance",Hml
1490  INPUT "LARGEST value of Pd",Pds
1500  PRINT PAGE
1501  Ka=(1-Vc)^.5/Tc
1502  Zz=Ka*Ri
1503  GOSUB 5250
1504  GOSUB 5320
1505  Iii=Ii
1506  Kii=Ki
1507  Zz=Ka*Rc
1508  GOSUB 5200
1509  GOSUB 5250
1510  GOSUB 5300
1511  GOSUB 5320
1512  Ioc=Io
1513  Iic=Ii
1514  Koc=Ko
1515  Kic=Ki
1540  Hm=Hml
1550  Pdo=0
1560  Dap=1
1570  FOR I=0 TO 14
1580  IF I>8 THEN 1610
1590  R(I)=I*(Rb-Ri)*.1+Ri
1600  GOTO 1620
1610  R(I)=(I-8)*(Rb-Ri)*.2/6+.8*(Rb-Ri)+Ri
1620  NEXT I
1630  FOR K=0 TO 12
```

```
1640  Rn(K)=(R(K)+R(K+1))/2
1650  NEXT K
1660  Rn(13)=Rb
1670  IF Rc=Rb THEN Rn(13)=(R(13)+R(14))/2
1680  FOR J=0 TO Ir STEP .5
1690  IF J>14 THEN 1750
1700  IF J>8 THEN 1730
1710  Rs(2*J)=J*(Pb-Ri)*.1+Ri
1720  GOTO 1760
1730  Rs(2*J)=(J-8)*(Rb-Ri)*.2/6+.8*(Rb-Ri)+Ri
1740  GOTO 1760
1750  Rs(2*J)=(J-14)*(Rb-Ri)*.1+Rb
1760  NEXT J
1770  Count=1
1780  N11=0
1790  Xai=1
1800  Xaj=0
1810  Yax=0
1820  Yay=0
1830  Xag=0
1840  Xag=Xag+1
1850  IF Xag>1 THEN 2110
1860  PRINT PAGE
1870  PRINT "Programme executing for M.Evans research student"
1880  ! ******************************************
1890  ! Compute PRESSURE PROFILE for a rigid bearing
1900  ! ******************************************
1910  IF Vab=1 THEN 2020
1920  ! For constant recess pressure Po
1930  Vqr=Po*PI*Hm^3/(LOG(Rb/Ri)*6*Uv)
1940  IF Xaj=1 THEN 2110
1950  FOR I=0 TO 14
1960  Pfr(I)=Po*LOG(Rb/R(I))/LOG(Rb/Ri)
1970  Pf(I)=Pfr(I)
1980  NEXT I
1990  Vq=Vqr
2000  GOTO 2110
2010  ! For constant flow rate Vq
2020  Ca=6*Uv*Vq/(PI*Hm^3)
2030  FOR I=0 TO 14
2040  Pfr(I)=Ca*LOG(Rb/R(I))
2050  Pf(I)=Pfr(I)
2060  NEXT I
2070  ! ********************************************************************
2080  ! Fit a series of uniform pressures of magnitude Pn and extent Rn
2090  ! to the actual pressure profile.
2100  ! ********************************************************************
2110  FOR I=0 TO 13
2120  Pn(I)=Pf(I)-Pf(I+1)
2130  NEXT I
2140  ! ******************************************
2150  ! Compute DEFLECTION PROFILE of compliant layer
2160  ! ******************************************
2170  MAT Wc=(0)
2180  FOR I=0 TO 13
2190  ! ************************************************************
2200  ! Construct matrix for determination of constants in equation
2210  ! for deflection of compliant layer.
2220  ! ************************************************************
2230  Zz=Ka*Rn(I)
2240  GOSUB 5200
2250  GOSUB 5250
2260  GOSUB 5300
2270  GOSUB 5320
2280  Ion=Io
2290  Iin=Ii
2300  Kon=Ko
2310  Kin=Ki
2320  IF Cab=0 THEN 2440
2330  C(1)=Kii/Iii
2340  C(3)=(Ka*Koc+Kic/(2*Rc))/(Ka*Ioc-Iic/(2*Rc))
2350  C(4)=-Pn(I)*Vc/(2*Gc)
2360  C(5)=Ka*Ion*Kin/Iin+Ka*Kon
2370  C(7)=-Kin+Iin*Kii/Iii
2380  C(8)=-Kin-Iin*(Ka*Koc+Kic/(2*Rc))/(Ka*Ioc-Iic/(2*Rc))
2390  Bn(2)=C(4)/C(5)/(C(8)/C(7)-1)
2400  Bn(1)=C(4)/C(5)+Bn(2)
2410  An(1)=-Bn(1)*C(1)
2420  An(2)=Bn(2)*C(3)
2430  GOTO 2510
2440  C(3)=(Ka*Koc+Kic/(2*Rc))/(Ka*Ioc-Iic/(2*Rc))
2450  C(4)=-Pn(I)*Vc/(2*Gc)
```

```
2460  C(5)=Ka*Ion*Kin/Iin+Ka*Kon
2470  Bn(2)=-C(4)/C(5)
2480  Bn(1)=0
2490  An(2)=Bn(2)*C(3)
2500  An(1)=An(2)+Bn(2)*Kin/Iin
2510  ! ++++++++++++++++++++++++++++++++++++++++++++++++++++++++++++++++
2520  ! The constants in equations for deflection of compliant layer are
2530  ! An(1),An(2),Bn(1) and Bn(2).Know compute deflections.
2540  ! ++++++++++++++++++++++++++++++++++++++++++++++++++++++++++++++++
2550  FOR J=0 TO Ir STEP .5
2560  IF Rc>Rb THEN 2580
2570  ! IF (J>13) AND (J<=14) THEN 2980
2580  Zz=Ka*Rs(2*J)
2590  GOSUB 5200
2600  GOSUB 5300
2610  IF Rs(2*J)>Rn(I)+.05*Rb THEN 2660
2620  IF (I=13) AND (Rc=Rb) THEN 2640
2630  IF (Rs(2*J)<=Rn(I)+.05*Rb) AND (Rs(2*J)>=Rn(I)-.05*Rb) THEN 2680
2640  Wc(2*J)=-(1-2*Vc)*Pn(I)*Tc/(2*Gc*(1-Vc))-2*Tc*Vc*Ka*(An(1)*Io-Bn(1)*Ko)/(3
*(1-Vc))+Wc(2*J)
2650  GOTO 2840
2660  Wc(2*J)=-2*Tc*Vc*Ka*(An(2)*Io-Bn(2)*Ko)/(3*(1-Vc))+Wc(2*J)
2670  GOTO 2840
2680  Rca=Rn(I)-.05*Rb
2690  IF Rca<=0 THEN Rca=0
2700  IF (Cab=1) AND (Rca<=Ri) THEN Rca=Ri
2710  Zz=Ka*Rca
2720  GOSUB 5200
2730  GOSUB 5300
2740  Wca=-(1-2*Vc)*Pn(I)*Tc/(2*Gc*(1-Vc))-2*Tc*Vc*Ka*(An(1)*Io-Bn(1)*Ko)/(3*(1-
Vc))
2750  Rcb=Rn(I)+.05*Rb
2760  IF Rcb>=Rc THEN Rcb=Rc
2770  Zz=Ka*Rcb
2780  GOSUB 5200
2790  GOSUB 5300
2800  Wcb=-2*Tc*Vc*Ka*(An(2)*Io-Bn(2)*Ko)/(3*(1-Vc))
2810  Wc(2*J)=(Wcb-Wca)*Rs(2*J)/(Rcb-Rca)+Wca-(Wcb-Wca)*Rca/(Rcb-Rca)+Wc(2*J)
2820  GOTO 2840
2830  Wc(2*J)=(Wc(26)-Wc(24))*(2*J-26)/2+Wc(26)
2840  NEXT J
2850  NEXT I
2860  ! ++++++++++++++++++++++++++++++++++++++++++++++++++++++++++++++++
2870  ! Damp deflections of compliant layer using a linear damper
2880  ! ++++++++++++++++++++++++++++++++++++++++++++++++++++++++++++++++
2890  FOR I=0 TO Ir STEP .5
2900  Wcn(2*I)=Wc(2*I)*Dap+Wcn(2*I)*(1-Dap)
2910  NEXT I
2920  ! ************************************
2930  ! Determine new FILM CLEARANCE profile
2940  ! ************************************
2950  FOR I=0 TO 14 STEP .5
2960  Hf(2*I)=-Wcn(2*I)+Hm
2970  NEXT I
2980  ! ************************************
2990  ! Determine new FILM PRESSURE profile
3000  ! ************************************
3010  ! ++++++++++++++++++++++++++++++++++++++++++++++++++++++++++++++++
3020  ! Evaluate values of 1/(R(I)*Hf(I)^3) for intergration using
3030  ! SIMPSON'S RULE
3040  ! ++++++++++++++++++++++++++++++++++++++++++++++++++++++++++++++++
3050  FOR I=0 TO 14 STEP .5
3060  As(2*I)=1/(Rs(2*I)*Hf(2*I)^3)
3070  NEXT I
3080  ! ++++++++++++++++++++++++++++++++++++++++++++++++++++++++++++++++
3090  ! Evaluate strip intergrals from R=(I-2) TO R=(I) using
3100  ! SIMPSON'S RULE
3110  ! ++++++++++++++++++++++++++++++++++++++++++++++++++++++++++++++++
3120  FOR I=2 TO 28 STEP 2
3130  Ass(I/2)=(As(I)+4*As(I-1)+As(I-2))*(Rs(I)-Rs(I-2))/6
3140  NEXT I
3150  ! ++++++++++++++++++++++++++++++++++++++++++++++++++++++++++++++++
3160  ! Sum the strip intergrals from R=Rb to R(I) and hence determine
3170  ! new film pressures
3180  ! ++++++++++++++++++++++++++++++++++++++++++++++++++++++++++++++++
3190  Bs=6*Uv*Vq/PI
3200  MAT Pfn=(0)
3210  FOR I=14 TO 1 STEP -1
3220  Pfn(I-1)=Bs*Ass(I)+Pfn(I)
3230  NEXT I
3240  IF Vab=1 THEN 3320
3250  Axx=Pfn(0)/Po
```

```
3260  FLOAT 4
3270  PRINT "Axx=";Axx
3280  Vq=Vq/Axx
3290  FOR I=0 TO 14
3300  Pfn(I)=Pfn(I)/Axx
3310  NEXT I
3320  ! ************************************************************************
3330  ! Determine changes in pressure profile.If all changes are greater then
3340  ! 0.1% compute new pressures
3350  ! ************************************************************************
3360  ! Aaa=0
3370   FOR I=0 TO 14
3380  ! IF I=14 THEN 3690
3390  ! Pdiff=(Pfn(I)-Pf(I))/Pf(I)*100
3400  ! IF ABS(Pdiff)<.1 THEN 3690
3410  ! Aaa=1
3420   Pf(I)=Pfn(I)
3430   NEXT I
3440  Xaj=1
3450  Count=Count+1
3460  PRINT "Count=";Count
3470  IF Count>=20 THEN Dap=Dap/2
3480  IF Count>=20 THEN Count=1
3490  ! IF Aaa=1 THEN 1920
3500  IF (Axx<.9999) OR (Axx>1.0001) THEN 1840
3510   Count=1
3520  ! ************************************************************************
3530  ! Compute LOAD CAPACITY of bearing by numerical intergration using
3540  ! SIMPSON'S RULE
3550  ! ************************************************************************
3560  W=Pf(0)*PI*Ri^2
3570  FOR I=0 TO 12 STEP 2
3580  W=PI*(Rs(2*I+4)-Rs(2*I))*(Rs(2*I+4)*Pf(I+2)+4*Rs(2*I+2)*Pf(I+1)+Rs(2*I)*Pf
(I))/3+W
3590  NEXT I
3600  ! ********************************
3610  ! Load capacity for rigid bearing
3620  ! ********************************
3630  Wr=Pfr(0)*PI*(Rb^2-Ri^2)/(2*LOG(Rb/Ri))+Pfr(0)*PI*Ri^2
3640  BEEP
3650  ! *************
3660  ! PRINT results
3670  ! *************
3680  Qd=6*Uv*Vq/(PI*Gc*Tc^3)
3690  Pd=Pf(0)/(Gc*Qd^.25)
3700  Cd=Hm/(Tc*Qd^.25)
3710  IF Pd-Pdo>=N12 THEN 3740
3720  Xac=0
3730  GOTO 3760
3740  Xac=1
3750  Pdo=Pd
3760  IF Xab=0 THEN 3780
3770  PRINTER IS 0
3780  IF Xac=0 THEN 4220
3790  IF Yax=1 THEN 3920
3800  STANDARD
3810  PRINT "SHEAR MODULUS of compliant layer Gc=";Gc
3820  PRINT "POISSON'S RATIO for compliant layer Vc=";Vc
3830  PRINT "RADIUS of compliant layer Rc=";Rc
3840  PRINT "RADIUS of bearing Rb=";Rb
3850  PRINT "RECESS RADIUS Ri=";Ri
3860  PRINT "THICKNESS of compliant layer Tc=";Tc
3870  PRINT "Lubricant VISCOSITY Uv=";Uv
3880  IF Vab=1 THEN 3910
3890  PRINT "RECESS PRESSURE Po=";Po
3900  GOTO 3920
3910  PRINT "VOLUMETRIC FLOW RATE to bearing Vq=?";Vq
3920  FLOAT 3
3930  PRINT "Bearing LIFT OFF Hm=";Hm
3940  PRINT !
3950  FIXED 3
3960  PRINT "LOAD CAPACITY for compliant bearing W=";W
3970  IF Vab=1 THEN 4010
3980  FLOAT 3
3990  PRINT "VOLUMETRIC FLOW rate to compliant bearing Vq=";Vq
4000  GOTO 4030
4010  FLOAT 3
4020  PRINT "RECESS PRESSURE for compliant bearing Po=";Pf(0)
4030  PRINT !
4040  FLOAT 3
4050  PRINT "Dimensionless FLOW RATE Qd=";Qd
4060  FIXED 3
```

```
4070  PRINT "   ~     ~      LOAD CAPACITY Wd=";W/(PI*Rb^2*Gc*Qd^.25)
4080  PRINT "   ~     ~      RECESS PRESSURE Pd=";Pd
4090  PRINT "   ~     ~      bearing LIFTOFF Cd=";Cd
4100  FLOAT 3
4110  PRINT "   ~     ~      bearing LIFTOFF Cdd=";Hm/(Rb*Qd^.25)
4120  PRINT !
4130  FIXED 3
4140  PRINT "LOAD CAPACITY for rigid bearing Wr=";Wr
4150  IF Vab=1 THEN 4190
4160  FLOAT 3
4170  PRINT "VOLUMETRIC FLOW rate to rigid bearing Vqr=";Vqr
4180  GOTO 4210
4190  FIXED 3
4200  PRINT "RECESS PRESSURE for rigid bearing Po=";Pfr(0)
4210  PRINT !
4220  IF Xad=0 THEN 4330
4230  Cdiff=Cdo-Cd
4240  N11=0
4250  FOR I=1 TO N10
4260  IF (Cda(I)<=Cd+Cdiff/2) AND (Cda(I)>=Cd-Cdiff/2) THEN 4280
4270  GOTO 4290
4280  N11=1
4290  NEXT I
4300  ! PRINT "Cd+Cdiff/2=";Cd+Cdiff/2
4310  ! PRINT "Cd-Cdiff/2=";Cd-Cdiff/2
4320  ! PRINT "N11=";N11
4330  IF (Xad=0) OR (N11=0) THEN 4860
4340  IF Yay=1 THEN 4470
4350  PRINT "+++++++++++++++++++++++++++++++++++++++++++++++++++++++++++"
4360  PRINT "+ Pf=Film pressure for a compliant bearing                +"
4370  PRINT "+ R=Radial position                                       +"
4380  PRINT "+ Wc=Deflections of compliant layer                       +"
4390  PRINT "+                                                         +"
4400  PRINT "+ Pfd=Dimensionless film pressures for compliant bearing  +"
4410  PRINT "+ Rd=    ~     ~      radial position                     +"
4420  PRINT "+ Wcd=   ~     ~      deflections of compliant layer      +"
4430  PRINT "+++++++++++++++++++++++++++++++++++++++++++++++++++++++++++"
4440  ! ++++++++++++++++++++++++++++++++
4450  ! Compute dimensionless parameters
4460  ! ++++++++++++++++++++++++++++++++
4470  PRINT !
4480  FLOAT 3
4490  PRINT "DIMENSIONLESS bearing LIFTOFF Cd=";Hm/(Tc*Qd^.25)
4500  PRINT "   ~     ~      bearing LIFTOFF Cdd=";Hm/(Rb*Qd^.25)
4510  FOR I=0 TO 14
4520  Pfd(I)=Pf(I)/(Gc*Qd^.25)
4530  Rd(2*I)=Rs(2*I)/Rb
4540  Wcd(2*I)=Wcn(2*I)/(Tc*Qd^.25)
4550  NEXT I
4560  FOR I=15 TO Ir
4570  Wcd(2*I)=Wcn(2*I)/(Tc*Qd^.25)
4580  Rd(2*I)=Rs(2*I)/Rb
4590  NEXT I
4600  PRINT !
4610  IMAGE 3A,14X,A,10X,3A,12X,2A
4620  IMAGE M3D.3DE,4X,2D.3D,4X,M3D.3DE,4X,D.3D
4630  PRINT "*************************"
4640  PRINT "* Film pressure profile *"
4650  PRINT "*************************"
4660  PRINT !
4670  PRINT USING 4610;" Pf","R","Pfd","Rd"
4680  PRINT !
4690  FOR I=0 TO 14
4700  PRINT USING 4620;Pf(I),Rs(2*I),Pfd(I),Rd(2*I)
4710  NEXT I
4720  PRINT !
4730  IMAGE 3A,11X,A,10X,3A,10X,2A
4740  IMAGE MD.3DE,4X,2D.3D,4X,MD.3DE,4X,D.3D
4750  PRINT "***************************************"
4760  PRINT "* Compliant layer deflection profile *"
4770  PRINT "***************************************"
4780  PRINT !
4790  PRINT USING 4730;" Wc","R","Wcd","Rd"
4800  PRINT !
4810  FOR I=0 TO Ir
4820  PRINT USING 4740;Wcn(2*I),Rs(2*I),Wcd(2*I),Rd(2*I)
4830  NEXT I
4840  PRINT !
4850  PRINT "-----------------------------------------"
4860  PRINTER IS 16
4870  IF Xac=0 THEN 4890
4880  Yax=1
```

```
4890  IF Xad=0 THEN 4910
4900  Yay=1
4910  IF Xab=1 THEN 4960
4920  PRINT "Press continue key to continue"
4930  ! PAUSE
4940  PRINT PAGE
4950  PRINT "Programme executing for M.Evans research student"
4960  ! Dii=Hm*Rb*Gc*.196/(Tc*Po*.67)
4970  ! IF Dii>Bii THEN 5120
4980  ! READ Aii,Bii,Cii
4990  ! IF (Dii<=Aii) AND (Dii>Bii) THEN 5100
5000  ! GOTO 5070
5010  ! Hm=Aii*Tc*Po*.67/(Rb*Gc*.196)
5020  ! Dii=Aii
5030  ! Hm=Hm-Cii*Tc*Po*.67/(Rb*Gc*.196)
5040  Cdo=Cd
5050  Hm=Hm-.05*Hf(28)
5060  IF Pd>Pds THEN 5130
5070  ! Dap=.15
5080  PRINTER IS 0
5090  ! PRINT "Pd=";Pd;"Pdo=";Pdo;"Hm=";Hm;"Dap=";Dap
5100  PRINTER IS 16
5110  Xag=0
5120  GOTO 2950
5130  READ Vc
5131  IF Vc=0 THEN 5139
5133  GOTO 1501
5139  PRINT PAGE
5140  PRINT "Computer ready for next user"
5150  END
5160  ! ************************************************************************
5170  ! The following are sub routines for evaluating MODIFIED BESSEL functions;
5180  ! Io,Ii,Ko & Ki
5190  ! ************************************************************************
5200  IF Zz>2 THEN 5230
5210  Io=1+.25*Zz^2+.015625*Zz^4+4.34027E-4*Zz^6
5220  GOTO 5240
5230  Io=.3989*EXP(Zz)*(1+.125/Zz+.0703125/Zz^2+.0732421/Zz^3)/Zz^.5
5240  RETURN
5250  IF Zz>3 THEN 5280
5260  Ii=Zz*(.5+.0625*Zz^2+2.60416E-3*Zz^4+5.42534E-5*Zz^6)
5270  GOTO 5290
5280  Ii=.3989*EXP(Zz)*(1-.375/Zz-.1172/Zz^2-.102539/Zz^3)/Zz^.5
5290  RETURN
5300  Ko=1.2533*EXP(-Zz)/Zz^.5*(1-.125/Zz+.0703125/Zz^2-.0732421/Zz^3)
5310  RETURN
5320  Ki=1.2533*EXP(-Zz)/Zz^.5*(1+.375/Zz-.1171875/Zz^2+.102539/Zz^3)
5330  RETURN
5340  ! DATA Aii,Bii,Cii
5350  ! DATA 4.8,1.6,0.8
5360  ! DATA 1.6,0.96,0.32
5370  ! DATA 0.96,0.64,0.16
5380  ! DATA 0.64,0.48,0.08
5390  ! DATA 0.48,0.16,0.04
5400  ! DATA 0.16,0.128,0.032
5410  ! DATA 0.128,0.096,0.016
5420  ! DATA 0.096,0.08,0.008
5430  ! DATA 0.08,-0.08,0.004
5440  ! DATA for Vc
5450  DATA 0.5,0.49,0.45,0
```

APPENDIX 4

CONSTANTS b_1 and b_3 IN EQUATIONS FOR DEFLECTIONS OF THE POROUS PAD IN BENDING

From boundary conditions (ii) in section 3.5 the radial bending moment m_r at $r = r_b$, between the porous pad and its adhesive bond, must be in equilibrium. The bending moment induced in the porous pad bond by deflections of the porous pad is given by equation 3.83 of section 3.5;

$$m_r = k_b . \frac{du_b}{dr} \qquad \text{at} \quad r = r_b \qquad \text{A4.1}$$

Deflections of the porous pad u_b are given by equation 3.90 of section 3.5;

$$u_b = \frac{1}{D_b} . \sum_{n=0,2}^{k_3} \left(\frac{a_n . r^{n+4}}{(n+2)^2 . (n+4)^2} \right) + \frac{b_1 . r^2}{4} + b_3 \qquad \text{A4.2}$$

(Note by boundary condition (i) in section 3.5, $b_2 = 0$ and is therefore omitted from equation A4.2).

Differentiating equation A4.2 gives;

$$\frac{du_b}{dr} = \frac{1}{D_b} . \sum_{n=0,2}^{k_3} \left(\frac{a_n . r^{n+3}}{(n+2)^2 . (n+4)} \right) + \frac{b_1 . r}{2} \qquad \text{A4.3}$$

Substituting for $\frac{du_b}{dr}$ in equation A4.1 using A4.3 gives;

$$m_r (\text{at } r = r_b) = k_b . \left[\frac{1}{D_b} . \sum_{n=0,2}^{k_3} \left(\frac{a_n . r_b^{n+3}}{(n+2)^2 . (n+4)} \right) + \frac{b_1 . r_b}{2} \right] \qquad \text{A4.4}$$

Equation A4.4 gives the radial bending moment m_r in the porous pad bond at $r = r_b$. In the porous pad itself the radial bending moment m_r for a thin plate in bending is given (47) by the following equation;

$$m_r = - D_b \left(\frac{d^2 u_b}{dr^2} + \frac{\nu_b}{r} . \frac{du_b}{dr} \right) \qquad \text{A4.5}$$

Differentiating equation A4.3 gives;

$$\frac{d^2 u_b}{dr^2} = \frac{1}{D_b} . \sum_{n=0,2}^{k_3} \left(\frac{(n+3) . a_n . r^{n+2}}{(n+2)^2 . (n+4)} \right) + \frac{b_1}{2} \qquad \text{A4.6}$$

Substituting for $\frac{du_b}{dr}$ and $\frac{d^2u_b}{dr^2}$ in equation A4.5 using equations A4.3 and A4.6, gives at $r = r_b$ the following:

$$m_r(\text{at } r=r_b) = -\left[\sum_{n=0,2}^{k_3}\left(\frac{(n+3).a_n.r_b^{n+2}}{(n+2)^2.(n+4)}\right) + \nu_b.\sum_{n=0,2}^{k_3}\left(\frac{a_n.r_b^{n+2}}{(n+2)^2.(n+4)}\right) + \frac{D_b.b_1.(1+\nu_b)}{2}\right] \qquad \text{A4.7}$$

Equation A4.7 gives the bending moment m_r in the porous pad itself at $r = r_b$. The radial bending moments given by equations A4.4 and A4.7 are in equilibrium. Therefore equating these two equations to eliminate m_r at $r = r_b$ gives after re - arranging an expression for the constant b_1 in equation A4.2;

$$b_1 = -\frac{2}{(B_b+D_b)}\left[\frac{B_b}{D_b}.\sum_{n=0,2}^{k_3}\left(\frac{a_n.r_b^{n+2}}{(n+2)^2.(n+4)}\right) + \sum_{n=0,2}^{k_3}\left(\frac{(n+3).a_n.r_b^{n+2}}{(n+2)^2.(n+4)}\right)\right] \qquad \text{A4.8}$$

where $$B_b = k_b.r_b + D_b.\nu_b \qquad \text{A4.9}$$

An expression for the constant b_3 in equation A4.2 is obtained using boundary condition (iii) in section 3.5. This states that the deflections of the porous pad due to bending only, are zero at $r = r_b$. Substituting this condition into equation A4.2 gives;

$$b_3 = -\frac{1}{D_b}.\sum_{n=0,2}^{k_3}\left(\frac{a_n.r_b^{n+4}}{(n+2)^2.(n+4)^2}\right) - \frac{b_1.r_b^2}{4} \qquad \text{A4.10}$$

where b_1 is given by equation A4.8.

APPENDIX 5

EQUATIONS FOR THE DETERMINATION OF ELASTIC PROPERTIES E, K AND G FROM BULK MODULUS AND SHEAR SPECIMENS

(i) YOUNG'S MODULUS E

For a linear - elastic material Young's modulus E is defined by the equation;

$$E = \frac{\text{stress}}{\text{strain}} \qquad \text{A5.1}$$

As described in section 4.4.3, the cylindrical specimen (figure A5.1a) for the bulk modulus tester, undergoes initial axial compression for small loads on the tester prior to bulk compression at higher loads. Therefore for axial compressions of the bulk modulus specimen;

$$\text{stress} = \frac{\text{load}}{\text{area}} = \frac{4.L}{\pi.d_k^2} \qquad \text{A5.2}$$

$$\text{and strain} = \frac{\text{deflection}}{\text{specimen height}} = \frac{\delta}{h_k} \qquad \text{A5.3}$$

Equation A5.1 therefore becomes;

$$E = \frac{4.h_k}{\pi.d_k^2}.\left(\frac{L}{\delta}\right) \qquad \text{A5.4}$$

In equation A5.4 the ratio L/δ is equal to the slope of the load versus deflection line obtained from measurements of the bulk modulus specimen in axial compression.

(ii) BULK MODULUS K

The bulk modulus K is defined (64) by the equation;

$$K = \frac{\text{mean stress}}{\text{volumetric strain}} = \frac{\bar{\sigma}}{\varepsilon_{vol}} \qquad \text{A5.5}$$

For a cylindrical specimen the mean stress $\bar{\sigma}$ in equation A5.5 is given (64) as;

$$\bar{\sigma} = \frac{\sigma_r + \sigma_z + \sigma_\theta}{3} \qquad \text{A5.6}$$

and the volumetric strain ε_{vol} is;

$$\varepsilon_{vol} = \varepsilon_r + \varepsilon_z + \varepsilon_\theta \qquad \text{A5.7}$$

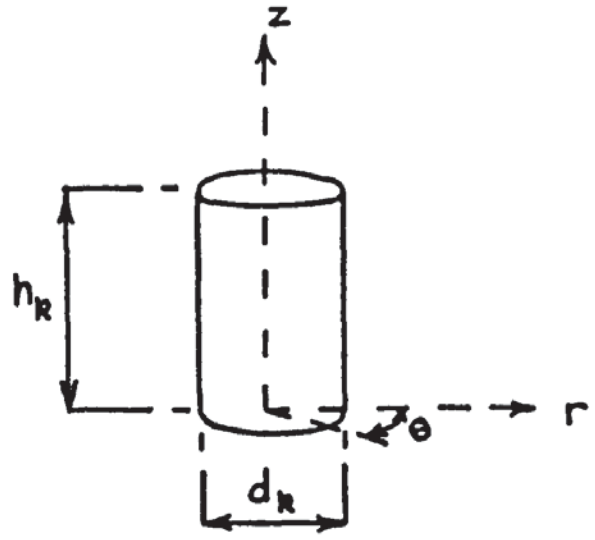

(a) Bulk modulus specimen

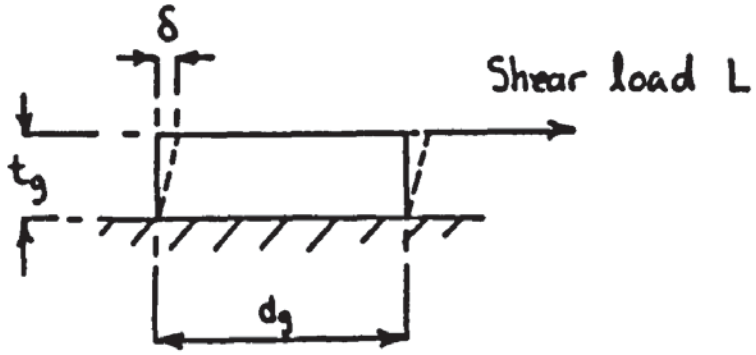

(b) Shear specimen

Figure: A5.1 Specimens for the measurement of elastic properties E, G and K

For a linear - elastic isotropic and homogeneous material the stress - strain relationships in three dimensional cylindrical co - ordinates are;

$$E.\varepsilon_r = \sigma_r - \nu.(\sigma_\theta + \sigma_z) \qquad \text{A5.8}$$

$$E.\varepsilon_z = \sigma_z - \nu.(\sigma_\theta + \sigma_r) \qquad \text{A5.9}$$

$$E.\varepsilon_\theta = \sigma_\theta - \nu.(\sigma_r + \sigma_z) \qquad \text{A5.10}$$

If straining of the compression cylinder walls of the bulk modulus tester is negligible then for the bulk modulus specimen $\varepsilon_r = \varepsilon_\theta = 0$. Therefore in equations A5.8 and A5.10;

$$\sigma_r = \nu.(\sigma_\theta + \sigma_z) \qquad \text{A5.11}$$

and $$\sigma_\theta = \nu.(\sigma_r + \sigma_z) \qquad \text{A5.12}$$

The simultaneous solution of equations A5.11 and A5.12 gives;

$$\sigma_r = \sigma_\theta = -\frac{\nu.\sigma_z}{(\nu - 1)} \qquad \text{A5.13}$$

Also in equation A5.7;

$$\varepsilon_{vol} = \varepsilon_z \qquad \text{A5.14}$$

For an elastomer layer material which is incompressible, i.e. Poisson's ratio $\nu = 0.5$, equation A5.13 becomes;

$$\sigma_r = \sigma_\theta = \sigma_z \qquad \text{A5.15}$$

In equation A5.6 therefore;

$$\bar{\sigma} = \sigma_z \qquad \text{A5.16}$$

Substituting for σ and ε_{vol} in equation A5.5, using equations A5.14 and A5.16 gives;

$$K = \frac{\sigma_z}{\varepsilon_z} \qquad \text{A5.17}$$

Equation A5.17 is for the special case where $\nu = 0.5$. In the more general case where $0 < \nu < 0.5$, substituting equation A5.13 into A5.9 gives;

$$E = \frac{\sigma_z}{\varepsilon_z}\left(1 + \frac{2.\nu^2}{(\nu - 1)}\right) \qquad \text{A5.18}$$

and since the relationship (47) between E, K and ν is;

$$E = 3.K.(1 - 2.\nu) \qquad \text{A5.19}$$

then equation A5.18 can be written;

$$K = \frac{1}{3}.\frac{\sigma_z}{\varepsilon_z}.\frac{(1 + \nu)}{(1 - \nu)} \qquad \text{A5.20}$$

Equation A5.20 reduces to A5.17 when $\nu = 0.5$. The axial stress σ_z acting on the specimen in bulk compression is;

$$\sigma_z = \frac{L}{\pi.a^2} \qquad \text{A5.21}$$

and the axial strain ε_z is;

$$\varepsilon_z = \frac{\delta}{h_k'} \qquad \text{A5.22}$$

where the compressed height h_k' of the specimen when bulk compression begins may be estimated by assuming the specimen volume remains constant during axial compression from height h_k to h_k' i.e.;

$$h_k'.\pi.a^2 = h_k.\frac{\pi.d_k^2}{4}$$

$$\text{therefore} \quad h_k' = h_k\left(\frac{d_k}{2.a}\right)^2 \qquad \text{A5.23}$$

From equations A5.21 and A5.22;

$$\frac{\sigma_z}{\varepsilon_z} = \frac{h_k'}{\pi.a^2}\left(\frac{L}{\delta}\right) \qquad \text{A5.24}$$

and substituting for h_k' in equation A5.24 using A5.23 gives;

$$\frac{\sigma_z}{\varepsilon_z} = \frac{h_k . d_k^2}{4.\pi.a^4} . \left(\frac{L}{\delta}\right) \qquad \text{A5.25}$$

Therefore equation A5.20 for bulk modulus K becomes;

$$K = \frac{h_k . d_k^2}{12.\pi.a^4} . \frac{(1 + \nu)}{(1 - \nu)} . \left(\frac{L}{\delta}\right) \qquad \text{A5.26}$$

which reduces to the following when $\nu = 0.5$;

$$K = \frac{h_k . d_k^2}{4.\pi.a^4} . \left(\frac{L}{\delta}\right) \qquad \text{A5.27}$$

In equations A5.26 and A5.27 the ratio L/δ is equal to the slope of the load versus deflection line for the bulk modulus specimen in bulk compression. However the measurements of δ are taken from the top of the piston plunger (see figure 4.32 of section 4.4.3) and bulk compressions of the specimen are comparatively small. It is therefore necessary to take into account compression of the piston plunger along its length. The true deflection of the specimen due to a load L may be expressed as:

$$\delta_{true} = \delta_{measured} - \delta_{plunger} \qquad \text{A5.28}$$

where $\delta_{measured}$ is the deflection at the top of the piston plunger and $\delta_{plunger}$ is the compression taking place along the length of the piston plunger due to the load L. Since the same load acts on both the piston plunger and the specimen then equation A5.28 may be written;

$$\left(\frac{\delta}{L}\right)_{true} = \left(\frac{\delta}{L}\right)_{measured} - \left(\frac{\delta}{L}\right)_{plunger} \qquad \text{A5.29}$$

Re - arranging equation A5.29 gives;

$$\left(\frac{L}{\delta}\right)_{true} = \frac{\left(\frac{L}{\delta}\right)_{measured}}{1 - \left(\left(\frac{\delta}{L}\right)_{plunger} \times \left(\frac{L}{\delta}\right)_{measured}\right)} \qquad \text{A5.30}$$

The axial stress in the plunger due to load L is;

$$\sigma_z = \frac{L}{\pi.a^2} \qquad \text{A5.31}$$

and the axial strain along a plunger length l_t is;

$$\varepsilon_z = \frac{\delta_{plunger}}{l_t} \qquad \text{A5.32}$$

Knowing Young's modulus E_t for the plunger material then using equations A5.31 and A5.32;

$$E_t = \frac{\sigma_z}{\varepsilon_z} = \frac{l_t}{\pi.a^2}.\left(\frac{L}{\delta}\right)_{plunger} \qquad \text{A5.33}$$

Re - arranging equation A5.33;

$$\left(\frac{\delta}{L}\right)_{plunger} = \frac{l_t}{\pi.a^2.E_t} \qquad \text{A5.34}$$

Substituting equation A5.34 into A5.30 gives;

$$\left(\frac{L}{\delta}\right)_{true} = \frac{\left(\frac{L}{\delta}\right)_{measured}}{1 - \left(\frac{l_t}{\pi.a^2.E_t}.\left(\frac{L}{\delta}\right)_{measured}\right)} \qquad \text{A5.35}$$

In equation A5.35 the ratio $(L/\delta)_{measured}$ is equal to the slope of the load versus deflection line obtained from the bulk modulus tester when the specimen is in bulk compression. However the true ratio $(L/\delta)_{true}$ for the specimen must be obtained using equation A5.35. This value is then substituted for (L/δ) in either equation A5.26 or A5.27 for bulk modulus K.

(iii) SHEAR MODULUS G

For a linear - elastic material the apparent shear modulus G_g is defined by the equation;

$$G_g = \frac{\text{shear stress}}{\text{shear strain}} \qquad \text{A5.36}$$

Figure A5.1b shows the shear specimen subject to a shear load L producing a deflection δ. The shear stress is given by;

$$\text{shear strain} = \frac{\text{shear force}}{\text{area}} = \frac{4.L}{\pi.d_g^2} \qquad \text{A5.37}$$

$$\text{and shear strain} = \frac{\text{deflection}}{\text{specimen thickness}} = \frac{\delta}{t_g} \qquad \text{A5.38}$$

Therefore substituting for shear stress and shear strain in equation A5.36 gives;

$$G_g = \frac{4.t_g}{\pi.d_g^2}.\left(\frac{L}{\delta}\right) \qquad \text{A5.39}$$

Equation A5.39 gives a value of the apparent shear modulus G_g assuming the specimen is in pure shear. The ratio L/δ is equal to the slope of the load versus deflection line obtained from measurements of the shear specimen in shear. However in equation A5.39 if the ratio t_g/d_g exceeds 0.25 an additional deflection of the shear specimen due to bending must be taken into account (93). The actual deflection due to shear only is therefore less than the measured deflection δ in equation A5.39. A true value of shear modulus for a cylindrical specimen is given (93) as;

$$G = G_g.(1 + 16.t_g^2/(36.d_g^2)) \qquad \text{A5.40}$$

APPENDIX 6

EQUATION FOR THE DERIVATION OF BEARING CLEARANCE h_d AT $r = r_b$

In section 3.2 the modified Reynolds equation for flow in the bearing clearance was introduced. This equation (equation 3.19) in non - dimensional form is;

$$\frac{1}{R}.\frac{\partial}{\partial R}\left(\frac{R}{A_r}.\frac{\partial(P^2)}{\partial R}\right) = \left(\frac{\partial(P^2)}{\partial Z}\right)_{Z=1} \qquad \text{A6.1}$$

Equation A6.1 is applicable to a non - uniform bearing clearance where $h_r = f(r)$. From Darcy's law (equation 3.1 of section 3.2.1) the axial flow velocity crossing the porous pad - bearing clearance boundary is given by;

$$v_z = -\frac{\Phi_z}{\eta}.\frac{\partial p}{\partial z}\bigg|_{z=h_b} \qquad \text{A6.2}$$

The total mass flow rate m passing through the bearing and entering its clearance, can be obtained from the summation of flow velocities passing normal to the porous pad - bearing clearance interface, i.e.;

$$m = 2.\pi \int_0^{r_b} (r.v_z.\rho)_{z=h_b}\,\partial r \qquad \text{A6.3}$$

Applying assumption (iii) of section 3.2.1, the density of this flow is given by;

$$\rho = \frac{p}{R_{gas}.T} \qquad \text{A6.4}$$

Substituting for v_z and ρ in equation A6.3 using equations A6.2 and A6.4 gives;

$$m = -\frac{2.\pi.\Phi_z}{R_{gas}.T.\eta}\int_0^{r_b}\left(r.p\,\frac{\partial p}{\partial z}\right)_{z=h_b}\partial r$$

and since $\dfrac{\partial(p^2)}{\partial z} = 2.p.\dfrac{\partial p}{\partial z}$ then;

$$m = - \frac{\pi . \Phi_z}{R_{gas} . T . \eta} \int_0^{r_b} \left(r \frac{\partial (p^2)}{\partial z} \right)_{z=h_b} \partial r \qquad \text{A6.5}$$

Equation A6.5 may be expressed in non - dimensional form as follows:

$$M = - \frac{2}{P_s^2 - 1} \int_0^1 \left(R \frac{\partial (P^2)}{\partial Z} \right)_{Z=1} \partial R \qquad \text{A6.6}$$

Equation A6.1 may be integrated to give;

$$\frac{R}{\Lambda_r} \frac{\partial (P^2)}{\partial R} = \int_0^R \left(R \frac{\partial (P^2)}{\partial Z} \right)_{Z=1} \partial R \qquad \text{A6.7}$$

Applying equation A6.7 at the bearing clearance exit R = 1;

$$\frac{1}{\Lambda_d} \left(\frac{\partial (P^2)}{\partial R} \right)_{R=1} = \int_0^1 \left(R \frac{\partial (P^2)}{\partial Z} \right)_{Z=1} \partial R \qquad \text{A6.8}$$

and using equation A6.6, equation A6.8 can be written;

$$\frac{1}{\Lambda_d} \left(\frac{\partial (P^2)}{\partial R} \right)_{R=1} = - \frac{M . (P_s^2 - 1)}{2}$$

$$\text{hence} \qquad \Lambda_d = - \frac{2}{M . (P_s^2 - 1)} \left(\frac{\partial (P^2)}{\partial R} \right)_{R=1} \qquad \text{A6.9}$$

Equation A6.9 is independant of the bearing clearance geometry h_r. It can therefore be used to derive the bearing clearance h_d at $r = r_b$ for the porous and compliant aerostatic thrust bearing as described in section 4.5.2.

APPENDIX 7
COMPUTER PROGRAMME FOR THE COUPLED SOLUTION TO THE LUBRICATION AND ELASTICITY EQUATIONS FOR THE POROUS AND COMPLIANT AEROSTATIC THRUST BEARING

```
20    ON KEY #1 GOTO 1030        !RETURN TO MENUE
30    ! ON KEY # 0 RETURN TO MENUE DURING ANALYSIS
40    ! Ab40
50    ! ************************************************************************
60    !
70    ! THIS PROGRAMME PROCESSES EXPERIMENTAL DATA AND OBTAINS ANALYTICAL
80    ! SOLUTIONS FOR A CIRCULAR POROUS (AND COMPLIANT) AEROSTATIC THRUST
90    ! BEARING.THE RESULTS ARE PRESENTED IN GRAPHICAL FORM.
100   !

110   ! ************************************************************************
120   !
130   ! DIMENSIONLESS BEARING PARAMETERS
140   !
150   ! Pds=DIMENSIONLESS SUPPLY PRESSURE
160   ! Sb=ASPECT RATIO OF POROUS PAD
170   ! Kp=RATIO OF PERMEABILITIES IN RADIAL AND AXIAL DIRECTIONS
180   ! Mf=MAGNITUDE FUNCTION FOR DEFLECTION OF POROUS PAD IN BENDING
190   ! Sf=SHAPE FUNCTION   ~      ~     ~    ~     ~     ~     ~
200   ! Sc=ASPECT RATIO OF COMPLIANT LAYER
210   ! Ke=RATIO OF RADIUS OF COMPLIANT LAYER TO RADIUS OF POROUS PAD
220   ! Gdc=DIMENSIONLESS SHEAR MODULUS FOR COMPLIANT LAYER
230   ! Vc=POISSON'S RATIO FOR COMPLIANT LAYER
240   !
250   ! DIMENSIONLESS BEARING PERFORMANCE VARIABLES
260   !
270   ! Bnc=BEARING No (BASED ON BEARING APPROACH)
280   ! Bnd=BEARING No (BASED ON BEARING CLEARANCE AT FILM EXIT)
290   ! Bno=BEARING No (BASED ON MIN. FILM CLEARANCE)
300   ! Wdl=DIMENSIONLESS LOAD CAPACITY
310   ! Gdm=      ~       FLOW RATE
320   ! Xdc=     ~       STATIC STIFFNESS (BASED ON BEARING APPROACH)
330   ! Xdd=     ~       STATIC STIFFNESS (BASED ON BEARING CLEARANCE AT FILM
340   ! EXIT
350   !
360   ! OTHER PARAMETERS AND VARIABLES USED IN PROGRAMME
370   !
380   ! Ca=BEARING APPROACH
390   ! Dh=SLOPE OF BEARING CLEARANCE AT RADIUS R
400   ! Gm=MASS FLOW RATE
410   ! Gc=SHEAR MODULUS OF COMPLIANT LAYER
420   ! Gv=GAS VISCOSITY AT Tm
430   ! Hb=THICKNESS OF POROUS PAD
440   ! Hf=BEARING FILM CLEARANCE AT RADIUS R
450   ! Hfd=DERIVED BEARING CLEARANCE AT R=Rb
460   ! P=PRESSURES IN POROUS MEDIA (ABSOLUTE)
470   ! Pa=AMBIENT PRESSURE
480   ! Pd=DIMENSIONLESS PRESSURES IN POROUS MEDIA
490   ! Pf=FILM PRESSURES IN BEARING CLEARANCE (ABSOLUTE)
500   ! Pdf=DIMENSIONLESS FILM PRESSURES
510   ! Ps=SUPPLY PRESSURE (ABSOLUTE)
520   ! R=RADIAL CO-ORDINATE
530   ! Rd=DIMENSIONLESS RADIAL CO-ORDINATE
540   ! Rb=RADIUS OF POROUS PAD
550   ! Rc=RADIUS OF COMPLIANT LAYER
560   ! Rg=GAS CONSTANT
570   ! Ta=AMBIENT TEMP
580   ! Tc=THICKNESS OF COMPLIANT LAYER
590   ! Tm=MEAN TEMP OF FLOW IN POROUS PAD
600   ! Ts=SUPPLY TEMP
610   ! Wc=DEFLECTIONS OF COMPLIANT LAYER
620   ! Wb=    ~       ~  POROUS PAD IN BENDING
630   ! Wl=LOAD CAPACITY
640   ! Vr,Vz=PERMEABILITY COEFFICIENTS IN R AND Z DIRECTIONS
650   ! Z=AXIAL CO-ORDINATE
660   ! Zd=DIMENSIONLESS AXIAL CO-ORDINATE
670   !
680   ! ************************************************************************
690   !
700   ! DIMENSION STATEMENTS
710   !
720   SHORT Bnd(100),Bnc(100),Bno(100),Wdl(100),Gdm(100),Xdc(100),Kdc(100)
730   DIM Xc(100),Ca(100),Yp(100),Xp(100),Xpo(100),Ypo(100)
740   DIM Gm(100),Hf(100,11),Hfd(100),P(11,11),Pd(11,11),Pf(100,11),Pdf(100,15)
750   DIM R(15),Rd(15),Rn(14),Wc(100,15),Wb(100,11),Wl(100),Z(11),Zd(11)
760   DIM F(10,100),B2(51),Y1(100),B1(50),Bmn(4),Mm(50),B(1,100),Am(4,4),Bm(4)
770   DIM Bn(4,4),Tac(2),Tad(2,2),Tae(2,2),Taf(2),Ap(4),Dh(11),Ab6(11),Af(4)
780   DIM Pdfo(11),Dwb(11),Wbo(11),Dwbo(11),Dwc(11),Dwco(11),Wco(15)
790   !
800   ! ************************************************************************
810   !
820   ! ZERO FLAGS
```

```
830   !
840   Aa9=0
850   Aa10$="N"
860   Aa11$="N"
870   Aa13$="N"
880   Aa17$="N"
890   Aa31$="0"
900   Aa63=0
910   Ab7$="N"
920   !
930   ! ***************************************************************************
940   !
950   ! OTHER STATEMENTS
960   !
970   MASS STORAGE IS ":F8"
980   !
990   ! ***************************************************************************
1000  !
1010  ! MAIN PROGRAMME MENUE (FOR TYPE OF PROCESSING REQUIRED)
1020  !
1030  PRINTER IS 16
1040  PRINT PAGE
1050  PRINT "TYPE OF PROCESSING REQUIRED"
1060  PRINT !
1070  PRINT "SELECT FROM THE FOLLOWING MENUE !"
1080  PRINT !
1090  PRINT "(1): INPUT BEARING PARAMETERS"
1100  PRINT "(2): INPUT EXPERIMENTAL READINGS AND PROCESS"
1110  PRINT "(3): READ A FILE OF PROCESSED EXP. OR THEO. RESULTS FROM DISC"
1120  PRINT !
1130  PRINT "OBTAIN THEO. RESULTS USING:"
1140  PRINT !
1150  PRINT "(4): THE SOLUTION BY JONES ET AL"
1160  PRINT "(5)-(7): THE ROSCOE TECHNIQUE,TO INCLUDE DEFLECTIONS OF THE:"
1170  PRINT "(5): COMPLIANT LAYER"
1180  PRINT "(6): POROUS PAD"
1190  PRINT "(7): COMPLIANT LAYER AND POROUS PAD"
1200  PRINT !
1210  PRINT "(8): STORE A FILE OF PROCESSED EXP. OR THEO. RESULTS ON DISC"
1220  PRINT "(9): PLOT RESULTS IN GRAPHICAL FORM"
1230  PRINT "(10): END"
1240  INPUT "input 1 or 2,3,etc ?",Aa1
1250  IF (Aa1<1) OR (Aa1>11) OR (Aa1<>INT(Aa1)) THEN 1240
1260  PRINT PAGE
1270  ON Aa1 GOTO 1350,2100,7010,7100,7100,7100,7100,6750,4010,1290
1280  !
1290  END
1300  !
1310  ! ***************************************************************************
1320  !
1330  ! INPUT BEARING PARAMETERS
1340  !
1350  PRINT "INPUT THE FOLLOWING:"
1360  PRINT "(Note,when a parameter is not required input 0 !)"
1370  PRINT !
1380  INPUT "input BEARING SPECIFICATION No ?",Aa31$
1390  PRINT "BEARING SPEC. No.= ";Aa31$
1400  IF Aa13$="N" THEN INPUT "Pa=?                                    (AMBIENT PRE
SSURE in bars)",Pa
1410  PRINT "Pa=";Pa;" bars"
1420  IF Aa13$="N" THEN INPUT "Ts=?                                     (SUPPLY T
EMP in kelvin)",Ts
1430  PRINT "Ts=";Ts;" kelvin"
1440  IF Aa13$="N" THEN INPUT "Ta=?                                     (AMBIENT T
EMP in kelvin)",Ta
1450  PRINT "Ta=";Ta;" kelvin"
1460  IF Aa13$="N" THEN DISP "Gv=?          (AIR VISCOSITY in Ns/m^2 at";(Ta+Ts
)/2;"kelvin)";
1470  IF Aa13$="N" THEN INPUT Gv
1480  IMAGE 3A,D.3DE,1X,6A
1490  PRINT USING 1480;"Gv=";Gv;"Ns/m^2"
1500  IF Aa13$="N" THEN INPUT "Hb=?                                   (POROUS PAD TH
ICKNESS in mm)",Hb
1510  PRINT "Hb=";Hb;" mm"
1520  IF Aa13$="N" THEN INPUT "Rb=?                                    (POROUS PAD
 RADIUS in mm)",Rb
1530  PRINT "Rb=";Rb;" mm"
1540  IF Aa13$="N" THEN INPUT "Vr=?                                (POROUS PAD RADIAL
PERM. in mm^2)",Vr
1550  IMAGE 3A,D.3DE,1X,4A
1560  PRINT USING 1550;"Vr=";Vr;"mm^2"
```

```
1570  IF Aa13$="N" THEN INPUT "Vz=?                                    (POROUS PAD AXIAL
PERM. in mm^2)",Vz
1580  IMAGE 3A,D.3DE,1X,4A
1590  PRINT USING 1580;"Vz=";Vz;"mm^2"
1600  IF Aa13$="N" THEN INPUT "Mf=?                  (MAGNITUDE FACTOR FOR POROUS P
AD IN BENDING)",Mf
1610  IMAGE 3A,D.3DE
1620  PRINT USING 1610;"Mf=";Mf
1630  IF Aa13$="N" THEN INPUT "Sf=?                      (SHAPE FACTOR FOR POROUS P
AD IN BENDING)",Sf
1640  IMAGE 3A,D.3DE
1650  PRINT USING 1640;"Sf=";Sf
1660  IF Aa13$="N" THEN INPUT "Tc=?                          (THICKNESS OF COMPLIAN
T LAYER in mm)",Tc
1670  PRINT "Tc=";Tc;" mm"
1680  IF Aa13$="N" THEN INPUT "Rc=?                             (RADIUS OF COMPLIAN
T LAYER in mm)",Rc
1690  PRINT "Rc=";Rc;" mm"
1700  IF Aa13$="N" THEN INPUT "Gc=?                  (SHEAR MODULUS OF COMPLIANT LA
YER in N/mm^2)",Gc
1710  IMAGE 3A,D.3DE,1X,6A
1720  PRINT USING 1710;"Gc=";Gc;"N/mm^2"
1730  IF Aa13$="N" THEN INPUT "Vc=?                          (POISSON'S RATIO FOR CO
MPLIANT LAYER)",Vc
1740  PRINT "Vc=";Vc
1750  PRINT !
1760  PRINT "DIMENSIONLESS BEARING PARAMETERS:"
1770  PRINT !
1780  Sb=Hb/Rb
1790  IMAGE 30A,D.3D
1800  PRINT USING 1790;"ASPECT RATIO OF POROUS PAD Sb=",Sb
1810  Kp=Yr/Vz
1820  IMAGE 34A,D.2DE
1830  PRINT USING 1820;"RATIO OF PERM'S FOR POROUS PAD Kp=",Kp
1840  IF Rc=0 THEN 1940
1850  Sc=Tc/Rc
1860  IMAGE 31A,.3D
1870  PRINT USING 1860;"ASPECT RATIO OF COMP. LAYER Sc=",Sc
1880  Ke=Rc/Rb
1890  IMAGE 33A,D.2D
1900  PRINT USING 1890;"DIM EXTENT OF COMPLIANT LAYER Ke=",Ke
1910  Gdc=Gc/(Pa*.1)
1920  IMAGE 20A,D.2DE
1930  PRINT USING 1920;"DIMEN SHEAR MOD Gdc=",Gdc
1940  IF Aa13$="Y" THEN 2020
1950  INPUT "DO YOU WANT A HARDCOPY Y/N ?",Aa13$
1960  IF (Aa13$<>"N") AND (Aa13$<>"Y") THEN 1950
1970  IF Aa13$="N" THEN 2040
1980  PRINTER IS 0
1990  PRINT "INPUTS"
2000  PRINT !
2010  GOTO 1390
2020  PRINTER IS 16
2030  Aa13$="N"
2040  GOTO 1050
2050  !
2060  ! ***************************************************************************
2070  !
2080  ! INPUT EXP. READINGS AND PROCESS
2090  !
2100  INPUT "HAVE YOU INPUTED BEARING PARAMETERS Y/N?",Aa8$
2110  IF (Aa8$<>"Y") AND (Aa8$<>"N") THEN 2100
2120  IF Aa8$="N" THEN 1350
2130  IF Aa9=1 THEN INPUT " DO YOU WISH TO CHANGE PREVIOUSLY INPUTED EXP.READING
S Y/N?",Aa10$
2140  IF (Aa9=1) AND (Aa10$<>"N") AND (Aa10$<>"Y") THEN 2130
2150  IF Aa10$="Y" THEN PRINT LIN(10)
2160  IF Aa10$="Y" THEN PRINT "Ps=";Ps-Pa;" bars gauge"
2170  INPUT "Ps=?              (SUPPLY PRESSURE in bars gauge)",Ps
2180  Ps=Pa+Ps
2190  PRINT PAGE
2200  IF Aa10$="Y" THEN 2330
2210  INPUT "HOW MANY BEARING CLEARANCES HAVE YOU TAKEN READINGS ? (100 max)",Aa
2
2220  IF (Aa2<=0) OR (Aa2>=100) THEN 2210
2230  INPUT "HOW MANY RADII HAVE YOU MEASURED FILM PRESSURES ? (7 max)",Aa3
2240  IF (Aa3<=0) OR (Aa3>=7) THEN 2230
2250  FOR I=1 TO Aa3
2260  IF I=1 THEN Aa4$="st"
2270  IF I=2 THEN Aa4$="nd"
2280  IF I=3 THEN Aa4$="rd"
2290  IF I>3 THEN Aa4$="th"
```

```
2300  DISP "INPUT";I;Aa4$;" RADIUS        (AT WHICH A FILM PRESSURE IS MEASURED)
";
2310  INPUT R(I)
2320  NEXT I
2330  IMAGE 5A,3X,8A,5X,4A,5X,4A,8X,14A
2340  PRINT USING 2330;"POINT","APPROACH","LOAD","MASS","FILM PRESSURES"
2350  IMAGE 19X,8A,3X,4A,9X,12A
2360  PRINT USING 2350;"CAPACITY","FLOW","(bars gauge)"
2370  IMAGE 30X,4A,8X,14A
2380  PRINT USING 2370;"RATE","AT RADIUS (mm)"
2390  IMAGE 10X,4A,6X,5A,3X,9A
2400  PRINT USING 2390;"(um)","(Kgs)","(Kgs/sec)"
2410  IMAGE #,30X,5A,3X
2420  PRINT USING 2410;"1*E-5"
2430  FOR I=1 TO Aa3
2440  IMAGE #,3D.D,1X
2450  PRINT USING 2440;R(I)
2460  NEXT I
2470  PRINT LIN(1)
2480  IF (Aa10$="N") AND (Aa11$<>"Y") THEN DISP "ENTER VALUES INTO ABOVE TABULAR
 FORM PRESSING CONT AFTER EACH VALUE";
2490  FOR I=1 TO Aa2
2500  GOSUB Tabularinput
2510  NEXT I
2520  IF Aa11$="Y" THEN 2800
2530  INPUT "DO YOU WISH TO MAKE ANY CORRECTIONS Y/N?",Aa6$
2540  IF (Aa6$<>"N") AND (Aa6$<>"Y") THEN 2530
2550  IF Aa6$="N" THEN 2710
2560  INPUT "WHICH POINT DO YOU WISH TO CHANGE ?",I
2570  DISP "ENTER NEW VALUES !";
2580  Aa7=I-1
2590  FOR K=1 TO Aa2-Aa7
2600  PRINT USING "#,K";CHR$(27)&"&a-1R"
2610  NEXT K
2620  IMAGE 79X
2630  PRINT USING 2620
2640  PRINT USING "#,K";CHR$(27)&"&a-1R"
2650  GOSUB Tabularinput
2660  FOR K=1 TO Aa2-Aa7
2670  PRINT USING "#,K";CHR$(27)&"&a+1R"
2680  NEXT K
2690  PRINT USING "#,K";CHR$(27)&"&a-1R"
2700  GOTO 2530
2710  Aa9=1
2720  INPUT "DO YOU WANT A HARDCOPY Y/N ?",Aa11$
2730  IF (Aa11$<>"N") AND (Aa11$<>"Y") THEN 2720
2740  IF Aa11$="N" THEN 2820
2750  PRINTER IS 0
2760  PRINT LIN(1)
2770  PRINT "Ps=";Ps-Pa;" bars gauge"
2780  PRINT !
2790  GOTO 2330
2800  PRINTER IS 16
2810  Aa11$="N"
2820  PRINT PAGE
2830  !
2840  ! DETERMINE VALUES OF Hfd
2850  !
2860  ! (1) fit the following equation to film pressure profile
2870  !     Pft=B(0)(1-(Rr)^B(1))
2880  FOR I=1 TO Aa2
2890  B2(1)=2
2900  FOR K=1 TO 50
2910  FOR J=1 TO Aa3
2920  F(0,J)=1-(R(J)/Rb)^B2(K)
2930  Y1(J)=Pf(I,J)
2940  NEXT J
2950  Aae=0
2960  Aaf=Aa3
2970  GOSUB Leastsquares
2980  B1(K)=Bmn(0)
2990  Mm(K)=0
3000  FOR J=1 TO Aa3
3010  Mm(K)=(Y1(J)-B1(K)*F(0,J))^2+Mm(K)
3020  NEXT J
3030  B2(K+1)=.8*B2(K)^(1/3)+B2(K)
3040  NEXT K
3050  ! Fit quadratic equation to values of Mm(K) and B2(K)
3060  ! in region of minimum Mm(K)
3070  ! i.e. Mm(K)=A0+A1*B2(K)+A2*B2(K)^2
3080  Taa=1E99
3090  FOR K=1 TO 50
```

```
3100  IF Mm(K)>=Taa THEN 3130
3110  Taa=Mm(K)
3120  Tab=K
3130  NEXT K
3140  FOR L=0 TO 2
3150  IF (Tab<>2) AND (Tab<>50) THEN Tac(L)=Mm(Tab-1+L)
3160  IF Tab=2 THEN Tac(L)=Mm(Tab+L)
3170  IF Tab=50 THEN Tac(L)=Mm(Tab-2+L)
3180  FOR J=0 TO 2
3190  IF (Tab<>2) AND (Tab<>50) THEN Tad(L,J)=B2(Tab-1+L)^(2-J)
3200  IF Tab=2 THEN Tad(L,J)=B2(Tab+L)^(2-J)
3210  IF Tab=50 THEN Tad(L,J)=B2(Tab-2+L)^(2-J)
3220  NEXT J
3230  NEXT L
3240  MAT Tae=INV(Tad)
3250  MAT Taf=Tae*Tac
3260  B(1,I)=-Taf(1)/(2*Taf(0))
3270  FOR J=1 TO Aa3
3280  F(0,J)=1-(R(J)/Rb)^B(1,I)
3290  Y1(J)=Pf(I,J)
3300  NEXT J
3310  Aae=0
3320  Aaf=Aa3
3330  GOSUB Leastsquares
3340  B(0,I)=Bmn(0)
3350  NEXT I
3360  ! (2) determine theoretical bearing clearance by iteration using
3370  ! Newtons Method
3380  FOR I=1 TO Aa2
3390  ! correction to merasured pressure profile for zero error
3400  FOR J=1 TO 5
3410  W11=PI*B(0,I)*(Rb*1E-3)^2*B(1,I)*1E5/(B(1,I)+2)
3420  Perror=(W1(I)*9.81-W11)/(PI*(Rb*1E-3)^2)
3430  Bn0=Perror*1E-5+B(0,I)
3440  Ct=(Bn0-Perror*1E-5-B(0,I)*(1-.9^B(1,I)))/Bn0
3450  Bn1=-21.85*LGT(Ct)
3460  B(0,I)=Bn0
3470  B(1,I)=Bn1
3480  NEXT J
3490  Dp=-B(0,I)*B(1,I)*1E5/(Rb*1E-3)
3500  Hfd(I)=(-12*Gm(I)*1E-5*287*(Ta+Ts)*Gv/(4*PI*Rb*100*Pa*Dp))^(1/3)      ! int
ial est.
3510  Fh=Rb*1E-3*(Hfd(I)^2+6*Vz*1E-6)*Hfd(I)*2*Pa*1E5*Dp+12*Gm(I)*1E-5*287*(Ta+T
s)*Gv/(PI*2)
3520  Fhh=Rb*1E-3*(3*Hfd(I)^2+6*Vz*1E-6)*Dp*2*Pa*1E5
3530  Hfdn=Hfd(I)-Fh/Fhh                                    ! new est.
3540  IF (Hfdn-Hfd(I))/Hfd(I)<1E-4 THEN 3570
3550  Hfd(I)=Hfdn
3560  GOTO 3510
3570  NEXT I
3580  Aa14=PI*(Rb*1E-3)^2*(Ps-Pa)*1E5
3590  Aa15=Gv*287*(Ta+Ts)*Hb*1E-3/(PI*(Rb*1E-3)^2*(Ps^2-Pa^2)*1E10*Vz*1E-6)
3600  Aa16=12*Vz*1E-6*(Rb*1E-3)^2/(Hb*1E-3)
3610  FOR I=1 TO Aa2
3620  Wd1(I)=W1(I)*9.81/Aa14
3630  Gdm(I)=Gm(I)*Aa15*1E-5
3640  Bnd(I)=Aa16/(Hfd(I)*(Hfd(I)^2+6*Vr*1E-6))
3650  Bnc(I)=Ca(I)*1E-6*((Ca(I)*1E-6)^2+6*Vr*1E-6)/Aa16
3660  Bno(I)=0
3670  Xc(I)=0
3680  Xdc(I)=0
3690  Kdc(I)=0
3700  NEXT I
3710  PRINT LIN(1)
3720  PRINT TAB(7);"EXP RESULTS IN DIMENSIONLESS FORM"
3730  PRINT !
3740  Pds=Ps/Pa
3750  PRINT TAB(7);"FOR DIM. SUPPLY PRESS. Pds=";Pds
3760  PRINT !
3770  IMAGE 8A,10X,10A,12X,4A,5X,4A
3780  PRINT USING 3770;"APPROACH";"BEARING No";"LOAD";"FLOW"
3790  IMAGE 39X,8A,3X,4A
3800  PRINT USING 3790;"CAPACITY";"RATE"
3810  PRINT !
3820  IMAGE 1X,6A,8X,3A,8X,5A,9X,3A,6X,3A
3830  PRINT USING 3820;"Ca(um)";"Bnd";"1/Bnc";"Wd1";"Gmd"
3840  IMAGE M3D.2D,4X,5D.D,5X,M3D.4D,8X,.3D,5X,.3D
3850  FOR I=1 TO Aa2
3860  PRINT USING 3840;Ca(I),Bnd(I),Bnc(I),Wd1(I),Gdm(I)
3870  NEXT I
3880  IF Aa17$="Y" THEN 3940
3890  INPUT "DO YOU WANT A HARD COPY OF RESULTS Y/N?",Aa17$
```

```
3900  IF (Aa17$<>"N") AND (Aa17$<>"Y") THEN 3890
3910  IF Aa17$="N" THEN 3940
3920  PRINTER IS 0
3930  GOTO 3710
3940  PRINTER IS 16
3950  Aa17$="N"
3960  DISP "NOW STORE RESULTS IN A FILE ?"
3970  PAUSE
3980  GOTO 1050
3990  !
4000  ! ************************************************************************
4010  !
4020  ! PLOT RESULTS IN GRAPHICAL FORM
4030  !
4040  Aa70=0
4050  PRINT "TYPE OF GRAPH REQUIRED"
4060  PRINT !
4070  PRINT "SELECT FROM THE FOLLOWING"
4080  PRINT !
4090  PRINT "(1):BEARING LOAD CAPACITY  ~  BEARING No"
4100  PRINT !
4110  PRINT "(2):FLOW RATE  ~  BEARING No"
4120  PRINT !
4130  PRINT "(3):STATIC STIFFNESS (Xdc) ~  BEARING No"
4140  PRINT !
4150  PRINT "(4):STATIC STIFFNESS (Kdc) ~  BEARING No"
4160  INPUT "input 1 or 2,3 ?",Aa21
4170  IF (Aa21<1) OR (Aa21>4) OR (Aa21<>INT(Aa21)) THEN 4160
4180  PRINT PAGE
4190  PRINT "SELECT FROM THE FOLLOWING MENUE"
4200  PRINT LIN(2)
4210  PRINT "(1): PLOT TO SCREEN"
4220  PRINT !
4230  PRINT "(2): PLOT GRAPH using HP 9872A"
4240  PRINT !
4250  PRINT "(3): PLOT GRAPH using BENSON PLOTTER"
4260  INPUT "input 1,2 or 3,etc ?",Aa32
4270  IF (Aa32<1) OR (Aa32>5) OR (Aa32<>INT(Aa32)) THEN 4260
4280  PRINT PAGE
4290  GOSUB Limits
4300  DISP "ARE THE RESULTS EXP. OR THEO.";
4310  INPUT "input E or T ?",Aa40$
4320  IF (Aa40$<>"T") AND (Aa40$<>"E") THEN 4310
4330  IF Aa40$="T" THEN 4490
4340  PRINT "EXP POINT TYPE"
4350  PRINT !
4360  PRINT "SELECT FROM THE FOLLOWING"
4370  PRINT !
4380  PRINT "(1): +"
4390  PRINT !
4400  PRINT "(2): *"
4410  PRINT !
4420  PRINT "(3): ><"
4430  PRINT !
4440  PRINT "(4): SQUARE"
4450  INPUT "input 1,2,3 or 4 ?",Az1
4460  IF (Az1<>1) AND (Az1<>2) AND (Az1<>3) AND (Az1<>4) THEN 4450
4470  PRINT PAGE
4480  GOTO 4510
4490  INPUT "line type for theo. curve (1 TO 10) ?",Az2
4500  IF (Az2<1) OR (Az2>10) OR (Az2<>INT(Az2)) THEN 4490
4510  ON Aa32 GOTO 4520,4570,4610
4520  PLOTTER IS 13,"GRAPHICS"
4530  PRINTER IS 16
4540  LIMIT 0,180,0,140
4550  LOCATE 25,100,20,70
4560  GOTO 4660
4570  PLOTTER IS 7,5,"9872A"
4580  PRINTER IS 7,5
4590  PRINT "VS2"
4600  GOTO 4630
4610  PLOTTER IS 5,"INCREMENTAL",.05
4620  PRINTER IS 16
4630  LIMIT 0,275,0,200
4640  ! LOCATE 31.25,106.25,20,70
4650  LOCATE 26,130,27.5,77.5
4660  GRAPHICS
4670  DEG
4680  SCALE Xamin,Xamax,Yamin,Yamax
4690  IF Ab23=1 THEN AXES 1,.05,Xamin,Yamin,1,2
4700  IF Ab23=2 THEN AXES Tick,.05,Xamin,Yamin,Co,2
4710  LORG 5
```

```
4720  LDIR 0
4730  CSIZE 2
4740  IF Ab23=2 THEN 4800
4750  FOR X=Xamin TO Xamax
4760  MOVE X,Yamin-.05*(Yamax-Yamin)
4770  LABEL 10^X
4780  NEXT X
4790  GOTO 4840
4800  FOR X=Xamin TO Xamax STEP Tick*Co
4810  MOVE X,Yamin-.05*(Yamax-Yamin)
4820  LABEL X
4830  NEXT X
4840  LORG 5
4850  FOR Y=Yamin TO Yamax STEP .1
4860  MOVE Xamin-.05*(Xamax-Xamin),Y
4870  LABEL Y
4880  NEXT Y
4890  IF Ab23=2 THEN 5020
4900  FOR I=1 TO 9
4910  Sca(I)=LGT(I)
4920  NEXT I
4930  FOR J=Xamin TO Xamax
4940  FOR I=1 TO 9
4950  X=J+Sca(I)
4960  MOVE X,Yamin
4970  DRAW X,(Yamax-Yamin)*.02+Yamin
4980  PENUP
4990  NEXT I
5000  NEXT J
5010  MOVE (Xamin+Xamax)*.5,Yamin-.1*(Yamax-Yamin)
5020  IF Aa32<>1 THEN 5400
5030  ! LORG 5
5040  ! IF Aa30=1 THEN LABEL "BEARING No (based on approach)"
5050  ! IF Aa30=2 THEN LABEL "BEARING No (based on film clearance)"
5060  ! LDIR 90
5070  ! MOVE Xamin-.1*(Xamax-Xamin),.5*(Yamin+Yamax)
5080  ! IF Aa21=1 THEN LABEL "BEARING LOAD CAPACITY"
5090  ! IF Aa21=2 THEN LABEL "DIMENSIONLESS MASS FLOW RATE"
5100  ! IF Aa21=3 THEN LABEL "DIMENSIONLESS STATIC STIFFNESS"
5110  ! LDIR 0
5120  LORG 8
5130  MOVE .8*Xamax+.2*Xamin,1.25*Yamax-.25*Yamin
5140  LABEL "THEORY LINE"
5150  UNCLIP
5160  MOVE .83*Xamax+.17*Xamin,1.25*Yamax-.25*Yamin
5170  DRAW .93*Xamax-.07*Xamin,1.25*Yamax-.25*Yamin
5180  CLIP Xamin,Xamax,Yamin,Yamax
5190  MOVE .8*Xamax+.2*Xamin,1.18*Yamax-.18*Yamin
5200  LABEL " EXP RESULT"
5210  LORG 2
5220  MOVE .83*Xamax+.17*Xamin,1.18*Yamax-.18*Yamin
5230  LABEL "+"
5240  LORG 8
5250  MOVE .785*Xamax+.215*Xamin,1.1*Yamax-.1*Yamin
5260  LABEL "-"
5270  MOVE .8*Xamax+.2*Xamin,1.08*Yamax-.08*Yamin
5280  IMAGE 2A
5290  IMAGE 1X,1A,,1X,2D,3D
5300  LABEL USING 5280;"Ps"
5310  LORG 2
5320  MOVE .8*Xamax+.2*Xamin,1.08*Yamax-.08*Yamin
5330  LABEL USING 5290;"=",Pds
5340  LORG 5
5350  MOVE .5*(Xamax+Xamin),Yamin-.2*(Yamax-Yamin)
5360  CSIZE 2.5
5370  IF Aa21=1 THEN LABEL "FIG.     LOAD CAPACITY VERSUS BEARING No FOR BEARING
 ";Aa31$
5380  IF Aa21=2 THEN LABEL "FIG.     FLOW RATE VERSUS BEARING No FOR BEARING ";A
a31$
5390  IF (Aa21=3) OR (Aa21=4) THEN LABEL "FIG.     STATIC STIFFNESS VERSUS BEARI
NG No FOR BEARING ";Aa31$
5400  CSIZE 2
5410  LORG 5
5420  IF Ab23=2 THEN 5460
5430  Xpmin=LGT(Aa22)
5440  Xpmax=LGT(Aa23)
5450  GOTO 5480
5460  Xpmin=Aa22
5470  Xpmax=Aa23
5480  FOR I=1 TO Aa2
5490  IF Aa21=1 THEN Yp(I)=Wdl(I)
5500  IF Aa21=2 THEN Yp(I)=Gdm(I)
```

```
5510  IF Aa21=3 THEN Yp(I)=Xdc(I)
5520  IF Aa21=4 THEN Yp(I)=kdc(I)
5530  GOSUB Xplot
5540  NEXT I
5550  IF Xp(Aa2)>Xp(1) THEN 5640
5560  FOR I=1 TO Aa2
5570  Xpo(I)=Xp(Aa2-I+1)
5580  Ypo(I)=Yp(Aa2-I+1)
5590  NEXT I
5600  FOR I=1 TO Aa2
5610  Xp(I)=Xpo(I)
5620  Yp(I)=Ypo(I)
5630  NEXT I
5640  I1=1
5650  Iu=Aa2
5660  FOR I=1 TO Aa2-1
5670  IF (Xp(I)<=Xpmin) AND (Xp(I+1)>=Xpmin) THEN I1=I+1
5680  IF (Xp(I)<=Xpmax) AND (Xp(I+1)>=Xpmax) THEN Iu=I
5690  NEXT I
5700  FOR I=I1 TO Iu
5710  Yp(I+1-I1)=Yp(I)
5720  Xp(I+1-I1)=Xp(I)
5730  NEXT I
5740  Ab40=Iu+1-I1
5750  FOR I=1 TO Ab40
5760  IF Aa40$="T" THEN 5950
5770  MOVE Xp(I),Yp(I)
5780  IF Az1=1 THEN LABEL "+"
5790  IF Az1=2 THEN LABEL "*"
5800  IF Az1<>3 THEN 5840
5810  LABEL "/"
5820  MOVE Xp(I),Yp(I)
5830  LABEL "\"
5840  IF Az1<>4 THEN 5920
5850  Axsq=(Xamax-Xamin)*.75/208
5860  Aysq=(Yamax-Yamin)*.75/100
5870  MOVE Xp(I)-Axsq,Yp(I)-Aysq
5880  DRAW Xp(I)+Axsq,Yp(I)-Aysq
5890  DRAW Xp(I)+Axsq,Yp(I)+Aysq
5900  DRAW Xp(I)-Axsq,Yp(I)+Aysq
5910  DRAW Xp(I)-Axsq,Yp(I)-Aysq
5920  GOTO 6010
5930  ! FIT CURVE TO RESULTS FOR PLOTTING
5940  ! Yp=Ap(0)+Ap(1)*Xp+Ap(2)*Xp^2+Ap(3)*Xp^3
5950  F(0,I)=1
5960  F(1,I)=Xp(I)
5970  F(2,I)=Xp(I)^2
5980  F(3,I)=Xp(I)^3
5990  F(4,I)=Xp(I)^4
6000  Y1(I)=Yp(I)
6010  NEXT I
6020  IF Aa40$="E" THEN 6200
6030  Aae=3
6040  Aaf=Ab40
6050  GOSUB Leastsquares
6060  MAT Ap=Bmn
6070  IF Ab23=1 THEN Xpp=LGT(Aa22)
6080  IF Ab23=2 THEN Xpp=Aa22
6090  LINE TYPE Az2
6100  Ypp=Ap(0)+Ap(1)*Xpp+Ap(2)*Xpp^2+Ap(3)*Xpp^3+Ap(4)*Xpp^4
6110  MOVE Xpp,Ypp
6120  FOR I=1 TO 100
6130  IF Ab23=1 THEN Xpp=(LGT(Aa23)-LGT(Aa22))*I/100+LGT(Aa22)
6140  IF Ab23=2 THEN Xpp=(Aa23-Aa22)*I/100+Aa22
6150  Ypp=Ap(0)+Ap(1)*Xpp+Ap(2)*Xpp^2+Ap(3)*Xpp^3+Ap(4)*Xpp^4
6160  DRAW Xpp,Ypp
6170  NEXT I
6180  PENUP
6190  LINE TYPE 1
6200  IF Aa32=1 THEN PAUSE
6210  EXIT GRAPHICS
6220  IF Aa70=1 THEN 6340
6230  INPUT "DO YOU WISH TO CHANGE GRAPH LIMITS Y/N?",Aa71$
6240  IF (Aa71$<>"Y") AND (Aa71$<>"N") THEN 6230
6250  IF Aa71$="N" THEN 6340
6260  IF Aa32<>2 THEN 6300
6270  PRINTER IS 16
6280  DISP "PUT NEW PAPER ON PLOTTER !"
6290  PAUSE
6300  GOSUB Limits
6310  GCLEAR
6320  GRAPHICS
```

```
6330  GOTO 4670
6340  Aa70=1
6350  INPUT "DO YOU WISH TO ADD ANOTHER GRAPH Y/N",Aa72$
6360  IF (Aa72$<>"N") AND (Aa72$<>"Y") THEN 6350
6370  IF Aa72$="N" THEN 6670
6380  PRINTER IS 16
6390  CAT ":F8"
6400  INPUT "WHICH FILE DO YOU WISH TO INPUT FOR PLOTTING ?",Aa54$
6410  PRINT PAGE
6420  GOSUB Readfile
6430  DISP "ARE THE RESULTS EXP. OR THEO.";
6440  INPUT "input E or T ?",Aa40$
6450  IF (Aa40$<>"T") AND (Aa40$<>"E") THEN 6440
6460  IF Aa40$="T" THEN 6620
6470  PRINT "EXP POINT TYPE"
6480  PRINT !
6490  PRINT "SELECT FROM THE FOLLOWING"
6500  PRINT !
6510  PRINT "(1): +"
6520  PRINT !
6530  PRINT "(2): *"
6540  PRINT !
6550  PRINT "(3): ><"
6560  PRINT !
6570  PRINT "(4): SQUARE"
6580  INPUT "input 1,2,3 or 4?",Az1
6590  IF (Az1<>1) AND (Az1<>2) AND (Az1<>3) AND (Az1<>4) THEN 6580
6600  PRINT PAGE
6610  GOTO 6640
6620  INPUT "line type for theo. curve (1 TO 10)?",Az2
6630  IF (Az2<1) OR (Az2>10) OR (Az2<>INT(Az2)) THEN 6620
6640  GRAPHICS
6650  IF Aa32=2 THEN PRINTER IS 7,5
6660  GOTO 5480
6670  IF Aa32<>1 THEN 6710
6680  INPUT "DO YOU WISH TO DUMP GRAPHICS Y/N ?",Aa74$
6690  IF (Aa74$<>"Y") AND (Aa74$<>"N") THEN 6680
6700  IF Aa74$="Y" THEN DUMP GRAPHICS
6710  GCLEAR
6720  GOTO 1030
6730  !
6740  ! ************************************************************************
6750  !
6760  ! GREAT A DATA FILE FOR BEARING RESULTS
6770  !
6780  PRINT "DO YOU WISH TO:"
6790  PRINT LIN(1)
6800  PRINT "(1):GREATE A NEW FILE"
6810  PRINT !
6820  PRINT "(2):RESTORE INTO AN EXSISTING FILE"
6830  INPUT "input 1 or 2,?",Aa50
6840  IF (Aa50<1) OR (Aa50>2) OR (Aa50<>INT(Aa50)) THEN 6830
6850  PRINT PAGE
6860  CAT ":F8"
6870  INPUT "INPUT FILE NAME (MAX OF 5 CHARACTERS) ?",Aa51$
6880  IF LEN(Aa51$)>6 THEN 6870
6890  IF Aa50=2 THEN PURGE Aa51$
6900  Size=INT((17+28*Aa2)*1.2/256)+1
6910  CREATE Aa51$,Size
6920  ASSIGN #2 TO Aa51$
6930  PRINT #2;Aa31$,Pds,Aa2
6940  FOR I=1 TO Aa2
6950  PRINT #2;Bnd(I),Bnc(I),Bno(I),Wdl(I),Gdm(I),Xdc(I),Kdc(I)
6960  NEXT I
6970  ASSIGN #2 TO *
6980  GOTO 1030
6990  !
7000  ! ************************************************************************
7010  !
7020  ! READ A FILE OF RESULTS
7030  !
7040  CAT ":F8"
7050  INPUT "WHICH FILE DO YOU WISH TO INPUT ?",Aa54$
7060  GOSUB Readfile
7070  GOTO 1030
7080  !
7090  ! ************************************************************************
7100  !
7110  ! ANALYTICAL SOLUTIONS
7120  !
7130  ON KEY #0 GOTO 9160
7140  Ab11=0
```

```
7150  I=0
7160  DISP "INPUT MAX BEARING No FOR ANALYSIS BASED ON";
7170  INPUT " BEARING CLEARANCE ?",Bnb
7180  Bna=.09
7190  IF (Bna>Bnb) OR (Bna<0) THEN 7170
7200  ! INPUT "INPUT BEARING No INCREMENT FOR ANALYSIS ?",Inc
7210  ! IF (Inc<0) OR (Inc>Bnb-Bna) THEN 6140
7220  INPUT "INPUT DIMENSIONLESS SUPPLY PRESSURE ?",Pds
7230  IF Pds<1 THEN 7220
7240  INPUT "DO YOU WANT HARD COPY OF RESULTS Y/N?",Ab1$
7250  IF (Ab1$<>"N") AND (Ab1$<>"Y") THEN 7240
7260  IF Ab1$="Y" THEN PRINTER IS 0
7270  INPUT "DO YOU WANT FILM PRESSURE PROFILES etc,Y/N?",Ab2$
7280  IF (Ab2$<>"Y") AND (Ab2$<>"N") THEN 7270
7290  IF Ab2$="N" THEN 7320
7300  DISP "INPUT 4 BEARING No (BASED ON FILM CLEARANCE) AT WHICH";
7310  INPUT " YOU WISH TO HAVE PROFILES",Bn1,Bn2,Bn3,Bn4
7320  PRINT LIN(1)
7330  PRINT TAB(7);"THEO. RESULTS IN DIMENSIONLESS FORM"
7340  PRINT !
7350  PRINT TAB(7);"FOR DIM. SUPPLY PRESS. Pds=";Pds
7360  PRINT !
7370  IMAGE 8A,11X,10A,12X,4A,5X,4A,12X,6A
7380  PRINT USING 7370;"APPROACH";"BEARING No";"LOAD";"FLOW";"STATIC"
7390  IMAGE 39X,8A,3X,4A,11X,9A
7400  PRINT USING 7390;"CAPACITY";"RATE";"STIFFNESS"
7410  PRINT !
7420  IMAGE 1X,6A,6X,3A,5X,5A,5X,3A,7X,3A,6X,3A,4X,8A,2X,3A,5X,3A
7430  PRINT USING 7420;"Ca(um)";"Bnd";"1/Bnc";"Bno";"Wd1";"Gdm";"Xc(N/mm)";"Xdc"
;"Kdc"
7440  FOR J=1 TO 15
7450  Rd(J)=(J-1)/10
7460  IF J<=11 THEN Zd(J)=(J-1)/10
7470  R(J)=Rd(J)*Rb
7480  NEXT J
7490  Rn(1)=2.5*Rb/50
7500  FOR J=2 TO 8
7510  Rn(J)=Rn(J-1)+5*Rb/50
7520  NEXT J
7530  Rn(9)=40.833*Rb/50
7540  FOR J=10 TO 14
7550  Rn(J)=Rn(J-1)+1*Rb/30
7560  NEXT J
7570  IF Rc<>Rb THEN Rn(14)=Rb
7580  IF (Aa1=5) OR (Aa1=7) THEN Ka=(1-Vc)^.5/Tc
7590  IF (Aa1<>6) AND (Aa1<>7) THEN 7650
7600  Db=Pa*.1*Hb^3/(128*Mf*(1-2*Sf))
7610  IF Sf<>.25 THEN 7640
7620  Bb=1E99
7630  GOTO 7650
7640  Bb=Pa*.1*Hb^3/(16*Mf*(4*Sf-1))-Db
7650  Inc=.01
7660  Bnd(I)=Bna
7670  MAT Wbo=(0)
7680  MAT Dwbo=(0)
7690  MAT Wb=(0)
7700  MAT Dwb=(0)
7710  MAT Wco=(0)
7720  MAT Dwco=(0)
7730  MAT Wc=(0)
7740  MAT Dwc=(0)
7750  Dap=1
7760  Count=0
7770  IF (Ab7$="Y") AND (Aa1<>4) THEN 7830
7780  CALL Jones(Bnd(I),Pds^2,Sb,Kp,Pdf(*),Rd(*),I,C2)
7790  IF Aa1=4 THEN 7830
7800  FOR J=1 TO 11
7810  Pdfo(J)=Pdf(I,J)
7820  NEXT J
7830  ! DETERMINE FILM CLEARANCE FROM BEARING No.
7840  Ab4=12*Vz*Rb^2/(Hb*Bnd(I))
7850  Hfd(I)=Ab4^(1/3)              ! INT. EST.
7860  Fh=Hfd(I)*(Hfd(I)^2+6*Vr)-Ab4
7870  Fhh=3*Hfd(I)^2+6*Vr
7880  Hfdn=Hfd(I)-Fh/Fhh
7890  IF (Hfdn-Hfd(I))/Hfd(I)<1E-4 THEN 7920
7900  Hfd(I)=Hfdn
7910  GOTO 7860
7920  Hfd(I)=Hfdn
7930  IF Aa1=4 THEN 8720
7940  IF (Aa1<>6) AND (Aa1<>7) THEN 8290
7950  ! DEFLECTIONS OF POROUS PAD
```

```
7960  ! fit polynomial to film pressure profile
7970  FOR J=1 TO 11
7980  F(0,J)=1
7990  F(1,J)=R(J)^2
8000  F(2,J)=R(J)^4
8010  F(3,J)=R(J)^6
8020  Y1(J)=(Pds-Pdf(I,J))*Pa*.1
8030  NEXT J
8040  Aae=3
8050  Aaf=11
8060  GOSUB Leastsquares
8070  MAT Af=Bmn
8080  ! COMPUTE DEFLECTIONS AND SLOPES
8090  Bb1=0
8100  Bb3=0
8110  FOR J=0 TO 3
8120  Bb1=-2/(Bb+Db)*(Bb/Db*Af(J)*Rb^(2*J+2)/((2*J+2)^2*(2*J+4))+(2*J+3)*Af(J)*R
b^(2*J+2)/((2*J+2)^2*(2*J+4)))+Bb1
8130  Bb3=-1/Db*Af(J)*Rb^(2*J+4)/((2*J+2)^2*(2*J+4)^2)+Bb3
8140  NEXT J
8150  Bb3=Bb3-Bb1*Rb^2/4
8160  FOR J=1 TO 11
8170  Wbb=0
8180  Dwbb=0
8190  FOR K=0 TO 3
8200  Wbb=Af(K)*R(J)^(2*K+4)/((2*K+2)^2*(2*K+4)^2)+Wbb
8210  Dwbb=Af(K)*R(J)^(2*K+3)/((2*K+2)^2*(2*K+4))+Dwbb
8220  NEXT K
8230  Wb(I,J)=Wbb/Db+Bb1*R(J)^2/4+Bb3
8240  Dwb(J)=Dwbb/Db+Bb1*R(J)/2
8250  ! DAMP DEFLECTIONS AND CORRESPONDING SLOPES
8260  Wb(I,J)=Wb(I,J)*Dap+Wbo(J)*(1-Dap)
8270  Dwb(J)=Dwb(J)*Dap+Dwbo(J)*(1-Dap)
8280  NEXT J
8290  IF (Aa1<>5) AND (Aa1<>7) THEN 8410
8300  ! DEFLECTIONS OF COMPLIANT LAYER
8310  CALL Compliant(Pdf(*),I,Pa,Vc,Tc,Gc,Wc(*),Rc,Rb,Ka,Rn(*),R(*),Ir)
8320  FOR J=1 TO 10
8330  Dwc(J+1)=(-Wc(I,J)+Wc(I,J+2))/(.2*Rb)
8340  NEXT J
8350  Dwc(1)=0
8360  ! DAMP DEFLECTIONS AND CORRESPONDING SLOPES
8370  FOR J=1 TO 15
8380  Wc(I,J)=Wc(I,J)*Dap+Wco(J)*(1-Dap)
8390  IF J<=11 THEN Dwc(J)=Dwc(J)*Dap+Dwco(J)*(1-Dap)
8400  NEXT J
8410  ! NEW FILM CLAERANCE PROFILE
8420  FOR J=1 TO 11
8430  Hf(I,J)=Hfd(I)-Wb(I,J)-Wc(I,J)+Wc(I,11)
8440  Dh(J)=-Dwb(J)-Dwc(J)
8450  NEXT J
8460  Ab5=12*Vz*Rb^2/Hb
8470  CALL Roscoe(Pds,Sb,Kp,Pdf(*),Pd(*),Hf(*),Dh(*),I,Ab5,Vr,Rb)
8480  Ab10=0
8490  FOR J=1 TO 11
8500  IF ABS(Pdf(I,J)-Pdfo(J))/Pdfo(J)*100>.1 THEN Ab10=1
8510  NEXT J
8520  FOR J=1 TO 11
8530  Wbo(J)=Wb(I,J)
8540  Dwbo(J)=Dwb(J)
8550  Pdfo(J)=Pdf(I,J)
8560  Wco(J)=Wc(I,J)
8570  Dwco(J)=Dwc(J)
8580  NEXT J
8590  FOR J=12 TO 15
8600  Wco(J)=Wc(I,J)
8610  NEXT J
8620  IF Ab10=0 THEN 8710
8630  Count=Count+1
8640  PRINTER IS 16
8650  PRINT Count
8660  IF Ab1$="Y" THEN PRINTER IS 0
8670  IF Count<20 THEN 8700
8680  Count=1
8690  Dap=Dap/2
8700  GOTO 7940
8710  Count=0
8720  ! BEARING LOAD CAPACITY (USING SIMPSON'S RULE)
8730  Wd1(I)=0
8740  FOR J=1 TO 9 STEP 2
8750  Wd1(I)=Wd1(I)+(Rd(J)*(Pdf(I,J)-1)+4*Rd(J+1)*(Pdf(I,J+1)-1)+Rd(J+2)*(Pdf(I,
J+2)-1))
```

```
8760  NEXT J
8770  Wd1(I)=Wd1(I)*2*.1/((Pds-1)*3)
8780  ! FLOW RATE
8790  IF Aa1<>4 THEN 8820
8800  Gdm(I)=-C2/(Pds^2-1)
8810  GOTO 8910
8820  FOR J=1 TO 11
8830  Ab6(J)=Pd(J)*(Pd(J,2)^2-Pds^2)/.1
8840  NEXT J
8850  ! INTERGRATE USING SIMPSONS RULE
8860  Gdm(I)=0
8870  FOR J=1 TO 9 STEP 2
8880  Gdm(I)=Gdm(I)+.1*(Ab6(J)+4*Ab6(J+1)+Ab6(J+2))/3
8890  NEXT J
8900  Gdm(I)=-Gdm(I)*2/(Pds^2-1)
8910  IF Aa1=4 THEN Hf(I,1)=Hfd(I)
8920  Bno(I)=12*Vz*Rb^2/(Hb*Hf(I,1)*(Hf(I,1)^2+6*Vr))
8930  Ca(I)=Hfd(I)+Wc(I,11)
8940  Bnc(I)=Hb*Ca(I)*(Ca(I)^2+6*Vr)/(12*Vz*Rb^2)
8950  ! STATIC STIFFNESS
8960  IF I<=1 THEN 9080
8970  IF Ab11=1 THEN 9010
8980  Xc(I-1)=-(Wd1(I)-Wd1(I-2))*PI*Rb^2*(Pds-1)*Pa*.1/(Ca(I)-Ca(I-2))
8990  Xdc(I-1)=(1/Bnc(I)+1/Bnc(I-2))*(Wd1(I)-Wd1(I-2))/(2*(1/Bnc(I)-1/Bnc(I-2)))
9000  Kdc(I-1)=-(Wd1(I)-Wd1(I-2))/(Bnc(I)^(1/3)-Bnc(I-2)^(1/3))
9010  ! PRINT RESULT
9020  IF Ab11=0 THEN GOSUB Printresult
9030  Ab11=0
9040  IF (Bnd(I)<>.11) AND (Bnd(I)<>1.1) AND (Bnd(I)<>11) AND (Bnd(I)<>110) AND
(Bnd(I)<>1100) THEN 9080
9050  Inc=Bnd(I-1)
9060  Ab11=1
9070  I=I-1
9080  I=I+1
9090  Bnd(I)=Bnd(I-1)+Inc
9100  FOR J=1 TO 11
9110  Pdf(I,J)=Pdf(I-1,J)
9120  NEXT J
9130  IF Bnd(I)>Bnb+Inc THEN 9160
9140  IF Aa1=4 THEN GOTO 7780
9150  IF Aa1<>4 THEN GOTO 7830
9160  PRINTER IS 16
9170  Aa2=I-2
9180  DISP "NOW STORE RESULTS IN A FILE !"
9190  PAUSE
9200  PRINT PAGE
9210  GOTO 1050
9220  ! ************************************************************************
9230  ! SUBROUTINES
9240  !
9250 Printresult:   !
9260  I=I-1
9270  IMAGE M3D.2D,4X,5D.D,1X,M2D.4D,2X,5D.D,5X,.3D,5X,.3D,3X,M3DE,1X,M.3D,1X,M3
DE
9280  PRINT USING 9270;Ca(I)*1E3,Bnd(I),Bnc(I),Bno(I),Wd1(I),Gdm(I),Xc(I),Xdc(I)
,Kdc(I)
9290  IF Ab2$="N" THEN 9820
9300  IF (Bnd(I)<>Bn1) AND (Bnd(I)<>Bn2) AND (Bnd(I)<>Bn3) AND (Bnd(I)<>Bn4) THE
N 9820
9310  PRINT "-------------------------------------------------------------"
9320  PRINT "DIMENSIONLESS FILM PRESSURE PROFILE FOR BEARING No Bnd=";Bnd(I)
9330  IMAGE #,1X,3A,2X
9340  PRINT USING 9330;"Rd="
9350  IMAGE #,D.D,3X
9360  FOR K=1 TO 11
9370  PRINT USING 9350;Rd(K)
9380  NEXT K
9390  PRINT !
9400  IMAGE #,4A,1X
9410  PRINT USING 9400;"Pdf="
9420  IMAGE #,D.3D,1X
9430  FOR K=1 TO 11
9440  PRINT USING 9420;Pdf(I,K)
9450  NEXT K
9460  PRINT !
9470  IF (Aa1<>6) AND (Aa1<>7) THEN 9550
9480  IMAGE #,1X,3A,1X
9490  PRINT USING 9480;"Wb="
9500  IMAGE #,2D.2D,1X
9510  FOR K=1 TO 11
9520  PRINT USING 9500;Wb(I,K)*1E3
9530  NEXT K
```

```
9540  PRINT !
9550  IF (Aa1<>5) AND (Aa1<>7) THEN 9620
9560  PRINT USING 9480;"Wc="
9570  IMAGE #,3D.D,1X
9580  FOR K=1 TO 11
9590  PRINT USING 9570;Wc(I,K)*1E3
9600  NEXT K
9610  PRINT !
9620  IF (Aa1<>5) AND (Aa1<>6) AND (Aa1<>7) THEN 9810
9630  IMAGE #,1X,3A,1X
9640  PRINT USING 9630;"Hf="
9650  IMAGE #,3D.D,1X
9660  FOR K=1 TO 11
9670  PRINT USING 9650;Hf(I,K)*1E3
9680  NEXT K
9690  IF (Aa1<>5) AND (Aa1<>7) THEN 9800
9700  PRINT LIN(1)
9710  PRINT USING 9330;"Rd="
9720  FOR K=12 TO 15
9730  PRINT USING 9350;Rd(K)
9740  NEXT K
9750  PRINT !
9760  PRINT USING 9480;"Wc="
9770  FOR K=12 TO 15
9780  PRINT USING 9570;Wc(I,K)*1E3
9790  NEXT K
9800  PRINT !
9810  PRINT "-----------------------------------------------------------------"
9820  I=I+1
9830  RETURN
9840  !
9850 Readfile: !
9860  ASSIGN #1 TO Aa54$
9870  READ #1;Aa31$,Pds,Aa2
9880  FOR I=1 TO Aa2
9890  READ #1;Bnd(I),Bnc(I),Bno(I),Wd1(I),Gdm(I),Xdc(I),Kdc(I)
9900  NEXT I
9910  ASSIGN #1 TO *
9920  RETURN
9930  !
9940 Tabularinput: IMAGE #,3D
9950  PRINT USING 9940;I
9960  Aa12=0
9970  IF (Aa6$="Y") OR (Aa10$="N") THEN Aa12=1
9980  IF Aa11$="Y" THEN Aa12=0
9990  IF Aa12=1 THEN INPUT Ca(I)
10000 IMAGE #,5X,M3D.D
10010 PRINT USING 10000;Ca(I)
10020 IF Aa12=1 THEN INPUT W1(I)
10030 IMAGE #,5X,4D.D
10040 PRINT USING 10030;W1(I)
10050 IF Aa12=1 THEN INPUT Gm(I)
10060 IMAGE #,5X,2D.2D,3X
10070 PRINT USING 10060;Gm(I)
10080 FOR J=1 TO Aa3
10090 IF Aa12=1 THEN INPUT Pf(I,J)
10100 IMAGE #,D.3D,1X
10110 PRINT USING 10100;Pf(I,J)
10120 NEXT J
10130 PRINT LIN(0)
10140 RETURN
10150 !
10160 Leastsquares: MAT Am=(0)
10170 MAT Bm=(0)
10180 FOR P1=0 TO Aae
10190 FOR Q1=0 TO Aae
10200 FOR Is=1 TO Aaf
10210 Am(P1,Q1)=Am(P1,Q1)+F(P1,Is)*F(Q1,Is)
10220 NEXT Is
10230 NEXT Q1
10240 NEXT P1
10250 FOR P1=0 TO Aae
10260 FOR Is=1 TO Aaf
10270 Bm(P1)=Bm(P1)+F(P1,Is)*Y1(Is)
10280 NEXT Is
10290 NEXT P1
10300 MAT Bn=INV(Am)
10310 MAT Bmn=Bm*Bn
10320 RETURN
10330 !
10340 Limits:!
10350 PRINT PAGE
```

```
10360 PRINT "WHICH SCALE FOR BEARING No DO YOU WISH TO USE"
10370 PRINT !
10380 PRINT "(1): LOG(Bn)"
10390 PRINT !
10400 PRINT "(2): 1/(Bn)^1/3"
10410 INPUT "Input 1 or 2 ?",Ab23
10420 IF (Ab23<1) OR (Ab23>2) OR (Ab23<>INT(Ab23)) THEN 10410
10430 PRINT PAGE
10440 IF Ab23=2 THEN 10490
10450 INPUT "Input BEARING No RANGE (log scale) ?",Aa22,Aa23
10460 IF Aa22>=Aa23 THEN 10450
10470 IF Aa22<=0 THEN 10450
10480 GOTO 10520
10490 INPUT "Input 1/Bn^(1/3) RANGE FOR RESULTS ?",Aa22,Aa23
10500 IF Aa22>=Aa23 THEN 10490
10510 GOTO 10570
10520 Xamin=INT(LGT(Aa22))
10530 Xamax=INT(LGT(Aa23))
10540 IF Xamin>LGT(Aa22) THEN Xamin=Xamin-1
10550 IF Xamax<LGT(Aa23) THEN Xamax=Xamax+1
10560 GOTO 10630
10570 INPUT "Input scale range for X-axis ?",Ab24,Ab25
10580 IF Ab25<Ab24 THEN 10570
10590 Xamin=Ab24
10600 Xamax=Ab25
10610 INPUT "Input Tick spacing & count for X-axis ?",Tick,Co
10620 IF Tick>Xamax THEN 10610
10630 PRINT "IS THE BEARING No BASED ON:"
10640 PRINT !
10650 PRINT "(1):APPROACH"
10660 PRINT !
10670 PRINT "(2):FILM CLEARANCE"
10680 INPUT "Input 1 or 2 ?",Aa30
10690 IF (Aa30<1) OR (Aa30>2) OR (Aa30<>INT(Aa30)) THEN 10680
10700 PRINT PAGE
10710 ON Aa21 GOTO 10720,10780,10840,10840
10720 INPUT "Input BEARING LOAD CAPACITY RANGE (0,min & 1,max !) ?",Aa24,Aa25
10730 IF (Aa24<0) OR (Aa25>1) THEN 10720
10740 IF Aa24>=Aa25 THEN 10720
10750 Yamin=INT(Aa24*10)/10
10760 Yamax=INT(Aa25*10)/10
10770 GOTO 10890
10780 INPUT "Input FLOW RATE RANGE (0,min & 1,max !)?",Aa26,Aa27
10790 IF (Aa26<0) OR (Aa27>1) THEN 10780
10800 IF Aa26>=Aa27 THEN 10780
10810 Yamin=INT(Aa26*10)/10
10820 Yamax=INT(Aa27*10)/10
10830 GOTO 10890
10840 INPUT "Input STATIC STIFFNESS RANGE (0,min & 1,max !)?",Aa28,Aa29
10850 IF (Aa28<0) OR (Aa29>1) THEN 10840
10860 IF Aa28>=Aa29 THEN 10840
10870 Yamin=INT(Aa28*10)/10
10880 Yamax=INT(Aa29*10)/10
10890 RETURN
10900 !
10910 Xplot:!
10920 IF (Ab23=1) AND (Aa30=1) THEN Xp(I)=LGT(1/Bnc(I))
10930 IF (Ab23=1) AND (Aa30=2) THEN Xp(I)=LGT(Bnd(I))
10940 IF (Ab23=2) AND (Aa30=1) THEN Xp(I)=ABS(Bnc(I))^(1/3)
10950 IF (Ab23=2) AND (Aa30=2) THEN Xp(I)=1/Bnd(I)^(1/3)
10960 IF Bnc(I)<0 THEN Xp(I)=-Xp(I)
10970 RETURN
10980 !
10990 ! ************************************************************************
11000 !
11010 ! SUBPROGRAMES
11020 !
11030 SUB Jones(SHORT Bn,REAL A,S,K,P(*),R(*),J,C2)
11040 DIM Kn(200),En(200),F(20),Jo(200,2),D(200),U(20,200),C(2)
11050 REM "VALUE OF Q SELECTED FOR DESIRED ACCURACY"
11060 REM "Bn=BEARING NUMBER"
11070 REM "A=DIMENSIONLESS SUPPLY PRESSURE SQUARED"
11080 REM "S=BEARING ASPECT RATIO"
11090 REM "K=RATIO OF RADIAL PERM TO AXIAL PERM"
11100 Q=80
11110 B=S*K^.5
11120 REM "DETERMINE ROOTS OF J1=0"
11130 N=1
11140 E(0)=0
11150 GOSUB 11670
11160 D(N)=B*Kn(N)
11170 IF D(N)>110 THEN T=1E99
```

```
11180 IF D(N)<=110 THEN T=EXP(2*D(N))
11190 T=(T-1)/(T+1)
11200 REM "T=Tanh(D(N))"
11210 En(N)=D(N)/((Bn*D(N)+Kn(N)^2*T)*Kn(N)^2)
11220 En(N)=En(N)+En(N-1)
11230 IF N>Q THEN 11260
11240 N=N+1
11250 GOTO 11150
11260 C(2)=(A-1)/(Bn^2*En(N)-Bn/8-1)
11270 C2=C(2)
11280 FOR I=1 TO 10
11290 U(I,0)=0
11300 F(I)=Bn*C(2)*(R(I)^2-1)/4
11310 N=1
11320 L=1
11330 IF Kn(N)=0 THEN 11350
11340 GOTO 11390
11350 GOSUB 11670
11360 D(N)=B*Kn(N)
11370 REM "DETERMINE Jo's"
11380 REM "Jo(N,1)=Jo(Kn) and Jo(N,2)=Jo(Kn*R)"
11390 IF Jo(N,1)=0 THEN 11410
11400 GOTO 11460
11410 M=Kn(N)
11420 IF M<=8 THEN 11450
11430 GOSUB 11720
11440 GOTO 11460
11450 GOSUB 11760
11460 L=L+1
11470 M=Kn(N)*R(I)
11480 IF L>2 THEN 11500
11490 GOTO 11420
11500 IF D(N)<=220 THEN Sh=EXP(D(N))
11510 IF D(N)>220 THEN Sh=1E99
11520 Ch=(Sh+1/Sh)/2
11530 Sh=(Sh-1/Sh)/2
11540 REM "Sh=Sinh(D(N)) &Ch=Cosh(D(N))"
11550 Cn(2)=Bn*C(2)/(Jo(N,1)*(Kn(N)^2*Sh+Bn*D(N)*Ch))
11560 U(I,N)=Bn*Cn(2)*D(N)*(Jo(N,1)-Jo(N,2))*Ch/Kn(N)^2
11570 U(I,N)=U(I,N-1)+U(I,N)
11580 IF N>Q THEN 11620
11590 N=N+1
11600 GOTO 11320
11610 REM "HENCE THE DIMENSIONLESS FILM PRESSURE IS!"
11620 P(J,I)=(1+F(I)+U(I,N))^(1/2)
11630 NEXT I
11640 P(J,11)=1
11650 SUBEND
11660 REM "SUBROUTINE FOR ROOTS OF J1=0"
11670 Y=(N+.25)*PI
11680 Kn(N)=Y-.375/Y+.0234/Y^3-.2303/Y^5+6.6784/Y^7
11690 RETURN
11700 REM "SUBROUTINE TO DETERMINE VALUE OF Jo's"
11710 REM "WHEN M>8"
11720 Jo(N,L)=(2/(PI*M))^(1/2)*(SIN(M+.25*PI)+1/(8*M)*SIN(M-.25*PI))
11730 RETURN
11740 REM "SUBROUTINE TO DETERMINE VALUE OF Jo's"
11750 REM "WHEN M<=8"
11760 Ab=1-M^2/4+M^4/64-M^6/2304+M^8/147456-M^10/14745600+M^12/2.12336E9
11770 Bc=-M^14/4.16179E11+M^16/1.06542E14-M^18/3.45196E16+M^20/1.38078E19
11780 Cd=-M^22/6.68267E21+M^24/3.84939E24-M^26/2.60219E27+M^28/2.04011E30
11790 De=-M^30/1.8361E33
11800 Jo(N,L)=Ab+Bc+Cd+De
11810 RETURN
11820 ! ************************************************************************
11830 SUB Roscoe(Pds,S,K,Pdf(*),P(*),Hf(*),Dh(*),Ia,Ab5,Vr,Ro)
11840 REM "THIS PRO HAS SUCESSIVE OVER RELAXATION"
11850 DIM B(10),Q(11,11,3),Qo(11,11,1),Ho(11),Bnn(11)
11860 REM "PROGRAM FOR DETERMINING FILM PRESSURES IN POROUS AIROSTATIC"
11870 REM "BEARING UNDER STEADY STATE CONDITIONS USING ROSCOE TECH."
11880 REM "READ BEARING DETAILS FIRST IN DIMENSIONLESS FORM SECOND IN"
11890 REM "MM'S"
11900 REM "S=BEARING RATIO ,K=RATIO OF RADIAL PERM TO AXIAL PERM"
11910 REM "Bn=BEARING No,Dr&Dy ARE DIMENSIONLESS RADIAL & AXIAL GRID WIDTHS"
11920 REM "Qs=DIMENSIONLESS SUPPLY PRESSURE SQUARED"
11930 REM "Vr=RADIAL PERM. MM^2,RADIUS OF PAD MM'S"
11940 REM "Dh(I)=SLOPE OF BEARING FILM AT NODE I"
11950 REM "Ho(I)=BEARING FILM CLEARANCE AT NODE I"
11960 Dr=.1
11970 Dy=.1
11980 Qs=Pds^2
11990 A=S^2*K/Dr^2
```

```
12000 B(5)=1/Dy^2
12010 B(10)=1 D;
12020 N=1
12030 ' DET INT EST OF PAD PRESSURES FROM FILM PRESSURES
12040 FOR J=1 TO 11
12050 FOR I=1 TO 11
12060 Pb=Pdf(Ia,I)+(Pds-Pdf(Ia,I))*(11-J)/10
12070 Q(I,J,N)=Pb^2
12080 NEXT I
12090 Ho(J)=Hf(Ia,J)
12100 Bnn(J)=Ab5/(Ho(J)^3+6*Vr*Ho(J))
12110 NEXT J
12120 N=N+1
12130 REM "DET NEW EST OF PRESSURES SQUARED IN POROUS PAD BY ROSCOE TECH."
12140 REM "FOR REGION A"
12150 FOR I=2 TO 10
12160 FOR J=2 TO 10
12170 B(3)=EXP(-1/(I-1))
12180 B(4)=A/((I-1)*(1-B(3)))
12190 Q(I,J,N)=(B(4)*(Q(I+1,J,N-1)+Q(I-1,J,N-1)*B(3))+B(5)*(Q(I,J+1,N-1)+Q(I,J-1
,N-1)))/(B(4)*(1+B(3))+2*B(5))
12200 Qo(I,J,N-1)=Q(I,J,N-1)
12210 Q(I,J,N-1)=Q(I,J,N)
12220 NEXT J
12230 NEXT I
12240 REM "FOR REGION B"
12250 J=1
12260 FOR I=1 TO 11
12270 Q(I,J,N)=Qs
12280 Qo(I,J,N-1)=Q(I,J,N-1)
12290 NEXT I
12300 REM "FOR REGION C"
12310 I=1
12320 B(3)=EXP(-1)
12330 B(4)=A/(1-B(3))
12340 FOR J=2 TO 10
12350 Q(I,J,N)=((1+B(3))*B(4)*Q(I+1,J,N-1)+B(5)*(Q(I,J+1,N-1)+Q(I,J-1,N-1)))/((1
+B(3))*B(4)+2*B(5))
12360 Qo(I,J,N-1)=Q(I,J,N-1)
12370 Q(I,J,N-1)=Q(I,J,N)
12380 NEXT J
12390 REM "FOR REGION D"
12400 I=11
12410 B(3)=EXP(-.1)
12420 B(4)=A/(1-B(3))
12430 FOR J=2 TO 10
12440 Q(I,J,N)=((1+B(3))*B(4)*Q(I-1,J,N-1)+(Q(I,J+1,N-1)+Q(I,J-1,N-1))*B(5))/((1
+B(3))*B(4)+2*B(5))
12450 Qo(I,J,N-1)=Q(I,J,N-1)
12460 Q(I,J,N-1)=Q(I,J,N)
12470 NEXT J
12480 REM "FOR REGION E"
12490 J=11
12500 FOR I=2 TO 10
12510 B(7)=1/Bnn(I)*(1/((I-1)*Dr)+3*(Ho(I)^2+2*Vr)*Ro/(Ho(I)^3+6*Vr*Ho(I))*Dh(I)
)
12520 B(8)=B(7)/(Dr*(1-EXP(-B(7)*Dr*Bnn(I))))
12530 B(9)=EXP(-B(7)*Dr*Bnn(I))
12540 Q(I,J,N)=(B(8)*(Q(I+1,J,N-1)+Q(I-1,J,N-1)*B(9))+B(10)*Q(I,J-1,N-1))/(B(8)*
(1+B(9))+B(10))
12550 Qo(I,J,N-1)=Q(I,J,N-1)
12560 Q(I,J,N-1)=Q(I,J,N)
12570 NEXT I
12580 REM "FOR CORNER c"
12590 I=1
12600 J=11
12610 B(7)=1/Bnn(I)*(1/Dr+3*(Ho(I)^2+2*Vr)*Ro*Dh(I)/(Ho(I)^3+6*Vr*Ho(I)))
12620 B(8)=B(7)/(Dr*(1-EXP(-B(7)*Dr*Bnn(I))))
12630 B(9)=EXP(-B(7)*Dr*Bnn(I))
12640 Q(I,J,N)=(B(8)*(1+B(9))*Q(I+1,J,N-1)+B(10)*Q(I,J-1,N-1))/(B(8)*(1+B(9))+B(
10))
12650 Qo(I,J,N-1)=Q(I,J,N-1)
12660 Q(I,J,N-1)=Q(I,J,N)
12670 REM "FOR CORNER d"
12680 Q(11,11,N)=1
12690 Qo(11,11,N-1)=1
12700 N=N+1
12710 REM "W=SOR FACTOR"
12720 W=1.6
12730 FOR I=1 TO 11
12740 FOR J=1 TO 11
12750 Q(I,J,N)=Q(I,J,N-1)*W+(1-W)*Qo(I,J,N-2)
```

```
12760 NEXT J
12770 NEXT I
12780 FOR I=1 TO 11
12790 FOR J=1 TO 11
12800 IF ABS((Q(I,J,N)-Qo(I,J,N-2))/Qo(I,J,N-2)*100)>.01 THEN 12820
12810 GOTO 12890
12820 N=1
12830 FOR M=1 TO 11
12840 FOR O=1 TO 11
12850 Q(M,O,N)=Q(M,O,N+2)
12860 NEXT O
12870 NEXT M
12880 GOTO 12120
12890 NEXT J
12900 NEXT I
12910 FOR I=1 TO 11
12920 FOR J=1 TO 11
12930 P(I,J)=Q(I,J,N)^.5
12940 NEXT J
12950 Pdf(Ia,I)=P(I,11)
12960 NEXT I
12970 SUBEND
12980 ! ************************************************************************
12990 SUB Compliant(Pdf(*),Ia,Pa,Vc,Tc,Gc,Wc(*),Rc,Rb,Ka,Rn(*),R(*),Ir)
13000 DIM Pn(14),C(5),Bn(2),An(2)
13010 ! Fit a series of uniform pressures of magnitude Pn and extent Rn
13020 ! to the actual pressure profile.
13030 FOR I=1 TO 8
13040 Pn(I)=(Pdf(Ia,I)-Pdf(Ia,I+1))*Pa*.1
13050 NEXT I
13060 FOR I=9 TO 11
13070 Pn(I)=(Pdf(Ia,9)-Pdf(Ia,10))*Pa*.1/3
13080 NEXT I
13090 FOR I=12 TO 14
13100 Pn(I)=(Pdf(Ia,10)-Pdf(Ia,11))*Pa*.1/3
13110 NEXT I
13120 IF Rc>1.4*Rb THEN 13150
13130 Ir=INT(Rc/Rb*11)
13140 GOTO 13160
13150 Ir=15
13160 Zz=Ka*Rc
13170 GOSUB 13810
13180 GOSUB 13860
13190 GOSUB 13920
13200 GOSUB 13950
13210 Ioc=Io
13220 Iic=Ii
13230 Koc=Ko
13240 Kic=Ki
13250 ! Compute DEFLECTION PROFILE of compliant layer
13260 FOR J=1 TO Ir
13270 Wc(Ia,J)=0
13280 NEXT J
13290 FOR I=1 TO 14
13300 ! Construct matrix for determination of constants in equation
13310 ! for deflection of compliant layer.
13320 Zz=Ka*Rn(I)
13330 GOSUB 13810
13340 GOSUB 13860
13350 GOSUB 13920
13360 GOSUB 13950
13370 Ion=Io
13380 Iin=Ii
13390 Kon=Ko
13400 Kin=Ki
13410 C(3)=(Ka*Koc+Kic/(2*Rc))/(Ka*Ioc-Iic/(2*Rc))
13420 C(4)=-Pn(I)*Vc/(2*Gc)
13430 C(5)=Ka*Ion*Kin/Iin+Ka*Kon
13440 Bn(2)=-C(4)/C(5)
13450 Bn(1)=0
13460 An(2)=Bn(2)*C(3)
13470 An(1)=An(2)+Bn(2)*Kin/Iin
13480 ! The constants in equations for deflection of compliant layer are
13490 ! An(1),An(2),Bn(1) and Bn(2).Know compute deflections.
13500 FOR J=1 TO Ir
13510 Zz=Ka*R(J)
13520 GOSUB 13810
13530 GOSUB 13920
13540 IF R(J)>Rn(I)+.05*Rb THEN 13590
13550 IF (I=14) AND (Rc=Rb) THEN 13570
13560 IF (R(J)<=Rn(I)+.05*Rb) AND (R(J)>=Rn(I)-.05*Rb) THEN 13610
```

```
13570 Wc(Ia,J)=-(1-2*Vc)*Pn(I)*Tc/(2*Gc*(1-Vc))-2*Tc*Vc*Ka*(An(1)*Io-Bn(1)*Ko)/(
3*(1-Vc))+Wc(Ia,J)
13580 GOTO 13740
13590 Wc(Ia,J)=-2*Tc*Vc*Ka*(An(2)*Io-Bn(2)*Ko)/(3*(1-Vc))+Wc(Ia,J)
13600 GOTO 13740
13610 Rca=Rn(I)-.05*Rb
13620 IF Rca<=0 THEN Rca=0
13630 Zz=Ka*Rca
13640 GOSUB 13810
13650 GOSUB 13920
13660 Wca=-(1-2*Vc)*Pn(I)*Tc/(2*Gc*(1-Vc))-2*Tc*Vc*Ka*(An(1)*Io-Bn(1)*Ko)/(3*(1-
Vc))
13670 Rcb=Rn(I)+.05*Rb
13680 IF Rcb>=Rc THEN Rcb=Rc
13690 Zz=Ka*Rcb
13700 GOSUB 13810
13710 GOSUB 13920
13720 Wcb=-2*Tc*Vc*Ka*(An(2)*Io-Bn(2)*Ko)/(3*(1-Vc))
13730 Wc(Ia,J)=(Wcb-Wca)*R(J)/(Rcb-Rca)+Wca-(Wcb-Wca)*Rca/(Rcb-Rca)+Wc(Ia,J)
13740 NEXT J
13750 NEXT I
13760 SUBEND
13770 ! ************************************************************************
13780 ! The following are sub routines for evaluating MODIFIED BESSEL functions;
13790 ! Io,Ii,Ko & Ki
13800 ! ************************************************************************
13810 IF Zz>2 THEN 13840
13820 Io=1+.25*Zz^2+.015625*Zz^4+4.34027E-4*Zz^6
13830 GOTO 13850
13840 Io=.3989*EXP(Zz)*(1+.125/Zz+.0703125/Zz^2+.0732421/Zz^3)/Zz^.5
13850 RETURN
13860 IF Zz>3 THEN 13890
13870 Ii=Zz*(.5+.0625*Zz^2+2.60416E-3*Zz^4+5.42534E-5*Zz^6)
13880 GOTO 13900
13890 Ii=.3989*EXP(Zz)*(1-.375/Zz-.1172/Zz^2-.102539/Zz^3)/Zz^.5
13900 RETURN
13910 IF Zz=0 THEN Ko=1E99
13920 IF Zz<>0 THEN Ko=1.2533*EXP(-Zz)/Zz^.5*(1-.125/Zz+.0703125/Zz^2-.0732421/Z
z^3)
13930 RETURN
13940 IF Zz=0 THEN Ki=1E99
13950 IF Zz<>0 THEN Ki=1.2533*EXP(-Zz)/Zz^.5*(1+.375/Zz-.1171875/Zz^2+.102539/Zz
^3)
13960 RETURN
```

LIST OF REFERENCES

(1) Barwell,F.T.: "Bearing Systems Principles and Practice", Oxford Unv. Press, 1979.

(2) Sheinberg,S.A. and Shuster,V.G.: "Resistance to Vibrations of a Hydrostatic Thrust Bearing", Machine Tool (U.S.S.R.), Vol.31, No.11, 1960, pp 24 - 29.

(3) Robinson,C.H. and Sterry,F.: "The Static Strength of Pressure Fed Gas Journal Bearings, Porous Bearings", Atomic Energy Research Est., Harwell, Berkshire, U.K., ED/R 1672, 1958.

(4) Mori,H., Yabe,H. and Ono,T.: "Theory of Externally Pressurized Circular Thrust Bearings", Trans. A.S.M.E., Jou. of Basic Eng., Sept. 1965, pp 613 - 621.

(5) German,R.M.: "Gas Flow Physics in Porous Metals", The Int. Jou. of Powder Tech., Vol 15, No.1, 1979, pp 23 - 30.

(6) Forchheimer,P.: "Wasserbewegung Darch Boden",Zeitschrift des Verines deutscher Ingenieure", Vol. 45, 1901, pp 1781.

(7) Greenberg,D.B. and Weger,E.: "An Investigation of the Viscous and Inertial Coefficients for the Flow of Gases Through Porous Sintered Metals with High Pressure Gradients", Chem. Eng. Sci., 1960, Vol.12, pp 8 - 19.

(8) Morgan,V.T.: "Permeability of Porous Metals", Symp.Metallurge des Powders, 1964. (Edition Metaux, Paris).

(9) Taylor,R. and Lewis,G.K.: "Experience Relating to the Steady Performance of Aerostatic Porous Thrust Bearings", Proc. Instn. Mech. Engrs., Vol. 189, 22/1975, pp 383 - 390.

(10) McCrea,R.J. and Donaldson,I.S.: "The Significance of Fluid Inertia and Slip Velocity in the Steady - State Analysis of Externally Pressurized Gas - Lubricated Partially Porous Thrust Bearing", 7 th Int. Gas Bearing Symp., July 13 - 15, 1976, paper A1, pp 1 - 20.

(11) Mori,H. and Yabe,H.: "Theoretical Investigation of Externally Pressurized Gas - Lubricated Porous Journal Bearing with Surface - Loading Effect." Trans A.S.M.E., Jou. of Lub. Tech., April 1973, pp 195 - 199.

(12) Polome,J. and Gorez,R.: "The use of Ground Porous Material in Gas Lubrication", Wear, 60 (1980) pp 349 - 356.

(13) Mongomery,A.G. and Sterry,F.: "A Simple Air Bearing Rotor for Very High Rotational Speeds", A.E.R.E. ED/R 1671 Harwell, Berkshire, England, 1955.

(14) Sneck,H.J. and Yen,K.T.: "The Externally Pressurized, Porous Wall, Gas Lubricated Journal Bearing 1.", Trans. A.S.L.E., 1964, Vol.7, pp 288 - 298.

(15) Sneck,H.J. and Ewell,R.C.: "The Externally Pressurized, Porous Wall, Gas Lubricated Journal Bearing 2.", Trans. A.S.L.E., 1965, Vol.8, pp 339 - 345.

(16) Sneck,H.J. and Yen,K.T.: "The Externally Pressurized, Porous Wall, Gas Lubricated Journal Bearing 3.", Trans. A.S.L.E., 1967, Vol.10, pp 339 - 347.

(17) Mori,H., Yabe,H. and Shibayama,T.: "Theoretical Solution as a Boundary Value Problem for Externally Pressurized Porous Gas Bearings", Trans. A.S.M.E., Jou. of Basic Eng., Sept. 1965, pp 622 - 630.

(18) Barlow,E.J. and Wildman,M.: "The Axisymmetric, Perfectly Flexible Foil Bearing With Porous Inlet Restrictor", Trans. A.S.M.E., Jou. of Lub. Tech., Jan. 1968, pp 145 - 152.

(19) Garguilo,E.P. and Gilmour,P.W.: "A Numerical Solution for the Design of Externally Pressurized Porous Gas Bearings: Thrust Bearings." Trans. A.S.M.E., Jou. Lub. Tech., Oct. 1968, pp 810 - 817.

(20) Ishizawa,S. and Hori,E.: "The Flow of a Viscous Fluid through a Porous Wall into a Narrow Gap." Bul. J.S.M.E., Vol.9, No.36, 1966, pp 719 - 730.

(21) Beavers,G.S. and Joseph,D.D.: "Boundary Conditions at a Naturally Permeable Wall." J. Fluid Mech., Vol.30, 1967, pp 197 - 207.

(22) Beavers,G.S., Sparrow,E.M. and Magnuson,R.A.: "Experiments on Coupled Flow in a Channel and a Boundary Porous Medium." Trans. A.S.M.E., J. Basic Eng., Vol.92, 1970, pp 843.

(23) Jones,O.K., Mickalski,J. and Lewis,G.K.: "The Steady State Performance of an Externally Pressurized Gas Lubricated Porous Thrust Bearing with a Uniform Film." Externally Pressurized Bearings, Instn. of

Mech. Engrs., Paper C12, 1971, pp 23 - 42.

(24) Taylor,R.: "The Steady - State and Dynamic Performance of Gas Lubricated Uniform Film Porous Thrust Bearings." Phd Thesis, The University of Aston in Birmingham (U.K.), 1975.

(25) Taylor,R. and Lewis,G.K.: "Steady State Solutions for an Aerostatic Thrust Bearing with an Elastic Porous Pad." 6th Int. Gas Bearing Symp. at Uni. of Southampton (U.K.), March 1974, Paper C5, pp 57 - 74.

(26) Roscoe,D.: "The Numerical Solution of the Three - Dimensional Viscous Navier - Stokes Equations." Ph.D. Thesis, Department of Mathematics, University of Aston in Birmingham, 1975.

(27) Murti,P.R.K.: "Analysis of Externally Pressurized Gas Porous Bearings." Trans. A.S.M.E., Jou. Lub. Tech., July 1974, pp 354 - 360.

(28) Murti,P.R.K.: "Effect of Velocity Slip in an Externally Pressurized Porous Thrust Bearing Working with an Incompressible Fluid." Trans. A.S.M.E., Jou. Lub. Tech., Sept. 1976, pp 404 - 408.

(29) Verma,L.: "Effect of Velocity Slip in an Externally Pressurized Porous Circular Thrust Bearing." Wear, Vol.63, 1980, pp 239 - 244.

(30) Kilmister,G.T.F.: "The use of Porous Materials in Externally Pressurized Gas Bearings." Powder Metallurgy, 1969, Vol.12, No.24, pp 400 - 409.

(31) Donaldson,I.S. and Patterson,E.B.: "Some Experiments on Plain Externally Pressurized Air Bearings with Porous Inserts at Supply Pressures up to 3.1 MN/m ." Gas Bearing Symp. at Uni. of Southampton (U.K.), March 1971, Paper 26, pp 1 - 8.

(32) Donaldson,I.S. and Patterson,E.B.: "The use of Porous Inserts in Plain Externally Pressurized Air Thrust Bearings at High Supply Pressures." 6th Int. Gas Bearing Symp. at Uni. of Southampton, March 1974, Paper C6, pp 75 - 88.

(33) Majumdar,B.C. and Schmidt,J.: "Design of Externally Pressurized Rectangular Porous Thrust Bearings." Wear, Vol.32, 1975, pp 1 - 8.

(34) Rao,N.S.: "Effect of Slip Flow in Aerostatic Porous Rectangular Thrust Bearings." Wear, Vol.61, 1980, pp 77 - 86.

(35) Rao,N.S.: "Analysis of Aerostatic Porous Rectangular Thrust Bearings with Offset Loads." Wear, Vol.59, 1980, pp 333 - 344.

(36) Naaum,A.G. and Lewis,G.K.: "The Steady Performance of Externally Pressurized Porous Rectangular Pad Gas Bearings Incorporating Viscous and Inertia Dominated Flow." I.Mech.E., Jou Mech. Eng. Sci., Vol.22, No.4, 1980, pp 203 - 205.

(37) Howarth,R.B.: "Externally Pressurized Porous Thrust Bearings." Trans. A.S.L.E., Vol.19, No.4, 1976, pp 293 - 300.

(38) Capone,A., Capone,E., Agostino,V.D. and Kirvonosov,V.: "Permeability Distribution in Sintered Bearings." Tribology Int., 1978, pp 333 - 336.

(39) Gorez,R.: "A Study of the Stability of Externally Pressurized Gas Bearings with Porous Wall by Liapunov's Direct Method." Trans. A.S.M.E., Jou. Lub. Tech., April 1973, pp 204 - 207.

(40) Dah - Chen Sun.: "Stability Analysis of an Externally Pressurized Gas - Lubricated Porous Thrust Bearing." Trans. A.S.M.E., Jou. Lub. Tech., Oct. 1973, pp 457 - 468.

(41) Dah - Chen Sun.: "On the Stability of Gas - Lubricated Porous Thrust Bearings." Trans. A.S.M.E., Jou. Lub. Tech., April 1975, pp 332 - 334.

(42) Gorez,R. and Szwarcman,M.: "Externally Pressurized Gas Bearings with Partially Porous Wall." 6th Int. Gas Bearing Symp. at Uni. of Southampton (U.K.), March 1974, Paper C7, pp 89 - 102.

(43) Taylor,R. and Lewis,G.K.: "The Dynamic Performance of Aerostatic Porous Thrust Bearings with Uniform Films." 7th Int. Gas Bearing Symp. held at Churchill College, Cambridge, England, July 1976, Paper A4, pp 49 - 66.

(44) Taylor,R.: "A Numerical Solution of the Dynamic Characteristics of an Aerostatic, Porous Thrust Bearing having a Uniform Film Subject to Linear Axial Load Variations." I. Mech. E, Jou. Mech. Eng. Sci., Vol.19, No.3, 1977, pp 122 - 127.

(45) Peaceman,D.W. and Rachford,H.H.Jnr.: "The Numerical Solution of Parabolic and Elliptic Differential Equations." Jou. Soc. Ind. Appl. Math., Vol.3, No.1, 1955.

(46) McAdam,G.D.: "Some Relations of Powder Characteristics to the Elastic Modulus and Shrinkage of Sintered Ferrous Compacts.", Jou. Iron and Steel Int., Vol. 168, 1951, pp 346 - 358.

(47) Benham,P.P. and Warnock,F.V.: "Mechanics of Solids and Structures.", Pitman Int. Text, 3rd edition, 1978.

(48) Squire,A.: "Density Relationships of Iron - Powder Compacts.", Trans. A.I.M.E., Vol. 171, 1947, pp 405 - 409.

(49) Spriggs,R.M.: "Expression for the Effect of Porosity on Elastic Modulus of Polycrystalline Refractory Materials, Particularly Aluminum Oxide.", Jou. Am. Ceram. Soc., Vol. 44, 1961, pp 628 - 629.

(50) Dewey,J.M.: "The Elastic Constants of Materials Loaded with Non - Rigid Fillers.", Jou. Appl. Phys., Vol. 18, 1947, pp 578 - 583.

(51) Mackenzie,J.K.: "The Elastic Constants of a Solid Containing Spherical Holes.", Proc. Phys. Soc. B., Vol. 63, 1950, pp 2 - 9.

(52) Eshelby,J.D.: "The Determination of the Elastic Field of an Ellipsoidal Inclusion and Related Problems.", Proc. R. Soc., Vol. 241, 1957, pp 376 - 380.

(53) Skorokhod,V.V.: "Electrical Conductivity, Modulus of Elasticity and Viscosity Coefficients of Porous Media.", Powder Metall., Vol. 12, 1963, pp 183 - 192.

(54) Leheup,E.R. and Moon,J.R.: "Elastic Behaviour of High - Density Powder - Forged Samples of Iron and Iron - Graphite.", Powder Metall., No. 1, 1980, pp 15 - 22.

(55) Wang,J.C.: "Young's Modulus of Porous Materials, Part 1: Theoretical Derivation of Modulus - Porosity Correlation.", Jou. of Mat. Sci., Vol 19, 1984, pp 801 - 808.

(56) Dowson,D. and Taylor,C.M.: "Elastohydrostatic Lubrication of Circular Plate Thrust Bearings.", Trans. A.S.M.E., Jou. of Lub. Tech., July 1967, pp 237 - 244.

(57) Elrod,H.G.: Exact and Approximate Theory for Linearly - Compliant Layer with Inflexible Adhesive Backing.", Lub. Research Lab., Dept. of Mech. Eng., Columbia University, New York, July 1965, Tech. Report No. 2.

(58) Pirvics,J. and Castelli,V.: "Characteristics of the

Elastohydrostatic Gas Lubricated Axisymmetric Thrust Bearing.", Lub. Research Lab., Dept. of Mech. Eng., Columbia University, New York, Nov. 1966, Tech Report No. 8.

(59) Castelli,V., Rightmire,G.K. and Fuller,D.D.: "On the Analytical and Experimental Investigation of a Hydrostatic Axisymmetric Compliant - Surface Thrust Bearing.", Trans A.S.M.E., Jou. of Lub. Tech., Oct. 1967, pp 510 - 520.

(60) Castelli,V. and Rightmire,G.K.: "Design Guide for Hydraustatic Axisymmetric Compliant - Surface Thrust Bearings.", Lub. Research Lab, Dept. of Mech. Eng., Columbia University, New York, Nov. 1969, Tech. Report No. 16

(61) Benjamin,M.K.: "Compliant Surface Bearings, An Analytical Investigation.", Lub. Research Lab, Dept. of Mech. Eng., Columbia University, New York, 1969, Tech. Report No. 15.

(62) Benjamin,M.K., Rightmire,G.K. and Castelli,V.: "Compliant - Surface, Fluid Film Bearings: Theory and Experiment for the Circular - Face Thrust Bearing and Theory for the Journal Bearing.", Rev. Roum. Sci. Techn. - Mec. Appl., Bucarest, 1971, Tome 16, No.2, pp 427 - 458.

(63) Rightmire,G.K.: "An Experimental Method for Determining Poisson's Ratio of Elastomers.", Trans. A.S.M.E., Jou. of Lub. Tech., July 1970, pp 381 - 388.

(64) Holownia,B.P.: "Effect of Carbon Black on the Elastic Constants of Elastomers.", Jou. Inst. Rubber Ind., 1974, Vol.8, No.4, pp 157 - 160.

(65) Holownia,B.P.: "Effects of Different Types of Carbon Black on Elastic Constants of Elastomers.", Plastics and Rubber: Mat. and Appl., August 1980, pp 129 - 132.

(66) Stanojevic,M. and Lewis,G.K.: "A Comparison of Two Test Methods for Determining Elastomer Physical Properties.", Polymer Testing, 1983, Vol.3, pp 183 - 195.

(67) Levy,S.B. and Coogan,J.R.: "Flexible Membrane Hydrostatic Air Bearing.", Trans. A.S.M.E., Jou. of Lub. Tech., Jan. 1968, pp 184 - 191.

(68) Pirvics,J. and Castelli,V.: "Elastomer Inertia Effects in Compliant Surface Bearings.", Trans.

A.S.M.E., Jou. of Lub. Tech., 1973, Vol.95, pp 372 - 380.

(69) Pirvics,J. and Castelli,V.: "Elastomer Viscoelasticity Effects in Compliant Surface Bearings.", Trans. A.S.M.E., Jou. of Lub. Tech., 1973, Vol.95, pp 363 - 371.

(70) Buckholz,R.H.: "On the Role of a Compliant Surface in Long Squeeze Film Bearings.", Trans A.S.M.E., Jou. of Applied Mech., Dec. 1984, Vol.51, pp 885 - 891.

(71) Lowe,I.R.G.: "Some Experimental Results from Compliant Air Lubricated Thrust Bearings.", Trans A.S.M.E., Jou. of Lub. Tech., Oct. 1974, pp 547 - 553.

(72) Lowe,I.R.G.: "Characteristics of Externally Pressurized Thrust Bearings with One Compliant Surface.", 6th International Gas Bearing Symp. at the Univ. of Southampton (U.K.), March 1974, Paper A4, pp 43 - 60.

(73) Gupta,P.K.: "Incipient Lift - off in Preloaded Plane Externally - Pressurized Compliant Surface Bearings.", Proc. of I.Mech.E., 1974, Vol.188, No.42, pp 447 - 455.

(74) Rybricki,E.F., Strenkowski,J.S., Tamm,M.A. and Glaeser,W.A.: "A Finite Element Model for Compliant Bearing Lubrication Using a Minimization Algorithm.", Wear, 1978, Vol.47, pp 279 - 292.

(75) Lau.H. and Harman,C.M.: "Externally Pressurized Compliant Air Bearing Operating on a Rough Moving Surface.", Trans. A.S.M.E., Jou of Lub. Tech., Jan. 1975, pp 63 - 68.

(76) Christensen,H. and Tonder,K: "The Hydrodynamic Lubrication of Rough Bearing Surfaces of Finite Width.", Trans A.S.M.E., Jou. of Lub. Tech., July 1971, pp 324 - 330.

(77) Stanojevic,M.: "The Steady Performance of Compliant - Surface Aerostatic Thrust Bearings.", Phd Thesis, Uni. of Aston in Birmingham (U.K.), 1976.

(78) Smith,R.L.: "Developement of Compliant Bearing Designs for Directional Central Gyroscope.", Prepared for Army Missle Command, 25 April 1973, Dist. by National Tech. Infor. Service, U.S. Dept. of Commerce, Report No. AD - 762 0 36.

(79) Field,G.J. and Nau,B.S.: "An Optical Interference

Method of Studying the Lubrication of a Compliant Bearing.", Trans. A.S.M.E., Jou. of Lub. Tech., Oct 1976, pp 486 - 490.

(80) Hori,Y., Kato,T., and Narumiya,H.: "Rubber Surface Squeeze Film." Trans. A.S.M.E., Jou. of Lub. Tech., July 1981, Vol.103, pp398 - 404.

(81) Ikeuchi,K., Mori,H., Okubo,T., and Ichi,S.: "Study on Circular EHD Squeeze Films under Periodic Motion.", Bull. of the J.S.M.E., April 1982, Vol.25, No.202, pp 646 - 653.

(82) Hayashi,K.: "Investigation on Externally Pressurized, Gas - Lubricated, Circular Thrust bearing with Flexible Surface.", 8th Inter. Gas Bearing Symp. at Leicester Poly. (U.K.), April 1981, Paper 1, pp 1 - 18.

(83) Lindley,P.B.: "Engineering Design with Natural Rubber.", The Natural Rubber Producers Research Association, 3rd edition, 1970.

(84) Moghe,S.R. and Neff,H.F.: "Elastic Deformations of Constrained Cylinders.", Trans A.S.M.E., Jou. of App. Mech., June 1971, pp 393 - 399.

(85) Timoshenko,S. and Goodier,J.N.: "Theory of Elasticity.", Eng. Soc. Monographs, 2nd edition, McGraw - Hill Book Company, 1951.

(86) Otter,J.R.H., Cassel,A.C. and Hobbs,R.E.: "Dynamic Relaxation.", Proc. Instn. Civil Eng., Paper No. 6986, 1967, pp 633 - 656.

(87) Holownia,B.P.: "Effect of Poisson's Ratio on Bonded Rubber Blocks.", Inst. of Mech. Eng., Jou. Strain Analysis, Vol.7, No.3, 1972, pp 236 - 242.

(88) Collins,F., Derby,T. and Moses,C.: "Performance Evaluation using Finite Element Analysis and Simple Material Properties.", Rubber World, Part 1: July 1982, pp 19 - 24, Part 2: August 1982, pp 29 - 35.

(89) Gent,A.N. and Lindley,P.B.: "The Compression of Bonded Rubber Blocks.", Proc. Inst. Mech. Eng., Vol.173, No.3, 1959, pp 111 - 121.

(90) Mclachan,N.W.: "Bessel Functions for Engineers.", Oxford Eng. Science Series, 2nd edition, 1955.

(91) Mayhew,Y.R. and Rogers,G.F.C.: "Thermodynamic and Transport Properties of Fluids.", Oxford Basil Blackwell, 2nd edition, 1977.

(92) Gerald,C.F.:"Applied Numerical Analysis.", Addison - Wesley Series in Mathematics, 1970.

(93) Rivilin,R.S. and Saunders,D.W.:"Cylinderical Shear Mountings.", Trans. of the I.R.I., Vol.24, No.6, 1949, pp296 - 306.